

Archived NIST Technical Series Publication

The attached publication has been archived (withdrawn), and is provided solely for historical purposes. It may have been superseded by another publication (indicated below).

Archived Publication

Series/Number:	Special Publication (NIST SP) - 960-16
Title:	NIST Recommended Practice Guide: Fractography of Ceramics and Glasses
Publication Date(s):	September 26, 2006
Withdrawal Date:	May 11, 2016
Withdrawal Note:	Superseded by SP 960-16e2

Superseding Publication(s)

The attached publication has been **superseded by** the following publication(s):

Series/Number:	Special Publication (NIST SP) - 960-16e2
Title:	NIST Recommended Practice Guide Fractography of Ceramics and Glasses
Author(s):	Quinn, George D. D.
Publication Date(s):	May 11, 2016
URL/DOI:	http://dx.doi.org/10.6028/NIST.SP.960-16e2

Additional Information (if applicable)

Contact:	george.quinn@nist.gov
Latest revision of the attached publication:	
Related information:	
Withdrawal announcement (link):	

Date updated: June 9, 2015

NATL INST. OF STAND & TECH



A11107 049437

NIST
PUBLICATIONS

REFERENCE

Fractography of Ceramics and Glasses



George D. Quinn

reco m m e n d e d
NIST

QC
100
.457
#960-16
2007

NIST
National Institute of
Standards and Technology
Technology Administration
U.S. Department of Commerce

Special
Publication
960-16





Fractography of Ceramics and Glasses

NIST Special Publication SP 960-16

May 2007

Pages 1-9 and 1-10 should be renumbered to 2-1 and 2-2.

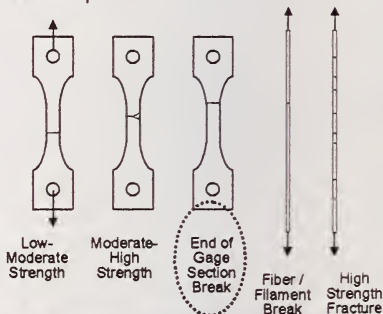
Page 3-10, 3-11 A note should be added here to say that JPEG images sometimes may be saved with adjustable amounts of compression. They should be saved with little or no compression.

Page 3-43 Figure 3.38 The marker bar was cropped off the bottom figure. Both a and b were at the same magnification. The depth of the semi elliptical precrack (from the image bottom to the white arrow) was 250 μm .

Page 4-13 Figure 4-8

The middle tensile specimen is labeled wrong.

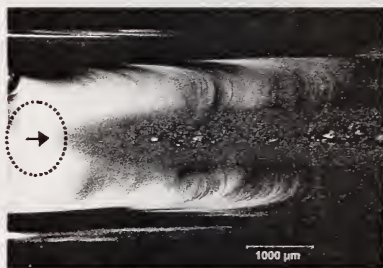
It should be:
"End of Gage Section Break"



Page 4-30 Line 13, delete the words: "a later chapter"

Page 5-28 Figure 5.19a

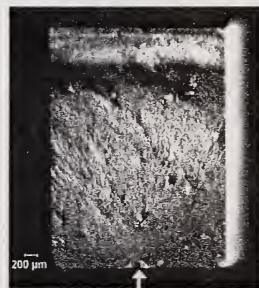
The black arrow should be moved down so that it marks the onset of the mist in the middle of the piece.



Page 5-33 Figure 5.21d

The Figure is missing the white arrow on the bottom that marks the semi elliptical surface crack.

It should appear as shown here.



Page 5-39 Figure 5.25 There is a checkerboard pattern superimposed on the image. This is an artifact of a process when the photo was scanned.

Page 5-41 Line 3 in the definition of Wallner line. Change the word "they" to "it"

Page 5-43 The definition of primary Wallner line is missing the word "such":

Primary Wallner line. A Wallner line formed by an elastic pulse generated by some portion of the crack front with a singularity in the specimen such as a discontinuity at the free surface or within the specimen, or with any localized stress field or elastic discontinuity.

Page 6-16
 Page 6-24
 Page 7-18

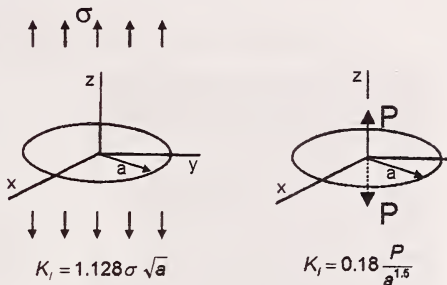
Figure 6.13 last line. Delete the word "incidental."
 4th paragraph. Change Figure 4.17 to Figure 4.18
 second paragraph, change Figure 7.10 to Figure 7.12 in lines 1 and 8

Page 7-19

first line, change "where γ_f is the fracture stress" to
 "where σ_f is the fracture stress"

Page 7-24

Figure 7.15a,b
 The radius arrow and the letter "a" are displaced from the center of the circle in Figs. a and b.
 The z axis is also displaced from the center of the circle in Fig. b.
 They should appear as shown here.



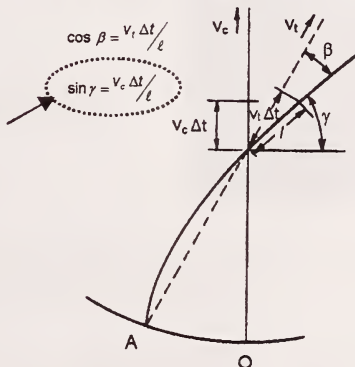
Page 7-25

third paragraph, line 7+8, change "... the flaw size for equation 7.2 is .." to
 "... the flaw size for equation 7.6 is .."

Page 7-28

Figure 7.27a
 top left, change

sin β to sin γ as shown here



Page 7-43

top line, change the word
 "maximum" to "minimum"

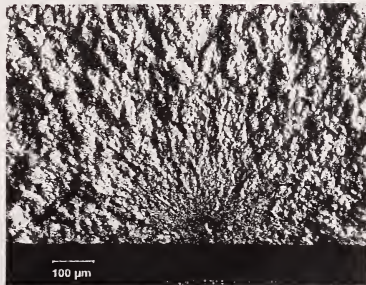
Page 7-48

last line, change from
 "... they will become shallower semi ellipses the deeper they go ..." to:
 "... they will become more elongated the deeper they go...."

Page D-9

Figure D6.b
 The wrong photo is shown.
 It is a duplicate of Figure D6a.

The correct Figure D6.b is shown here.
 It is an optical photo with a close-up of the origin and mirror. It is about the same magnification as the SEM image shown in Fig. D-2c. The intent was to show matching optical and SEM images in b and c at the same magnifications for comparison.



NOTE: If additional mistakes are found, please inform G. Quinn at: george.quinn@nist.gov

This errata sheet will be updated if necessary and posted on the NIST Ceramics Division web site that includes this and other Guides in .pdf form.

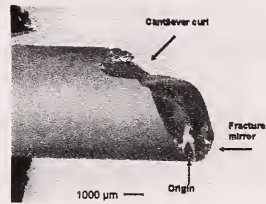
See: <http://www.ceramics.nist.gov/pubs/practice.htm>



Page 5-2

Figure 5.1

The words "Fracture mirror" and the black arrow with it point to the wrong location. Move them down 15 mm.



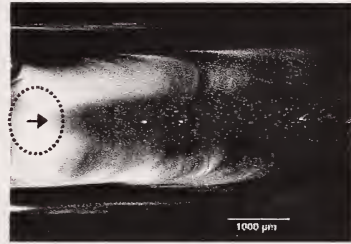
Page 5-13

There is a minor omission. At the end of the second paragraph, add: "Strong Wallner lines may also trigger mist formation in fracture mirrors."

Page 5-28

Figure 5.19a

The black arrow should be moved down so that it marks the onset of the mist in the middle of the piece.

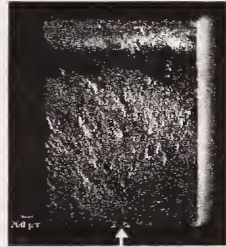


Page 5-33

Figure 5.21d

The Figure is missing the white arrow on the bottom that marks the semi elliptical surface crack.

It should appear as shown here.



Page 5-39

Figure 5.25 There is a checkerboard pattern superimposed on the image. This is an artifact of a process when the photo was scanned. I could not obtain an original photo.

Page 5-41

Line 3 in the definition of Wallner line. Change the word "they" to "It"

Page 5-43

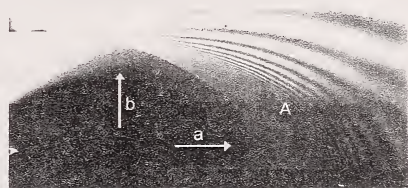
The definition of primary Wallner line is missing the word "such":

Primary Wallner line. A Wallner line formed by an elastic pulse generated by some portion of the crack front with a singularity in the specimen such as a discontinuity at the free surface or within the specimen, or with any localized stress field or elastic discontinuity.

Page 5-54

Fig. 5.36c.

The bottom half of Fig. c was printed poorly in many books. It should look as shown here:



See opposite side.

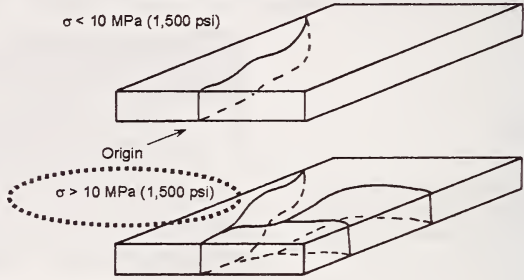
Page 5-58 Lines 6 + 7. Tsirk only studied "use chips."
Therefore delete the clause: "either when the implements were made or"

Page 5-58 Fig. 5-58 caption. Delete the word "Sierra".
The figures do show scarps, but not the specific Sierra scarp type.

Page 6-16 Figure 6.13 last line. Delete the word "incidental."

Page 6-24 4th paragraph. Change Figure 4.17 to Figure 4.18

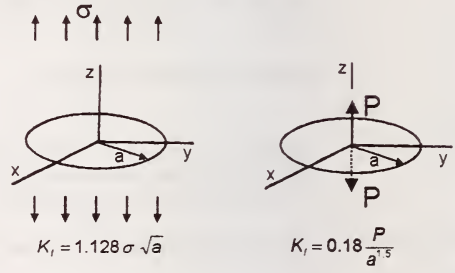
Page 7-2 Fig. 7.1 The stress range for the bottom figure should show greater than: ">"



Page 7-18 second paragraph, change Figure 7.10 to Figure 7.12 in lines 1 and 8

Page 7-19 first line, change "where γ_f is the fracture stress" to
"where σ_f is the fracture stress"

Page 7-24 Figure 7.15a,b
The radius arrow and the letter "a" are displaced from the center of the circle in the figure on the left.
The z axis is also displaced from the center of the circle in the figure on the right.



They should appear as shown here.

Page 7-25 third paragraph, line 7+8, change "... the flaw size for equation 7.2 is .." to
"... the flaw size for equation 7.6 is .."

Page 7-26 Figure 7.16 caption, last line, change: "... given in table 7.1" to
"... given in **page 7-29.**"

Page 7-28 Equation 7-12 is missing a term. It should be:

$$M = \left[1.13 - 0.09 \left(\frac{a}{c} \right) \right] + \left[-0.54 + \frac{0.89}{0.2 + \left(\frac{a}{c} \right)} \right] * \left(\frac{a}{h} \right)^2 + \left[0.5 - \frac{1}{0.65 + \left(\frac{a}{c} \right)} + 14 * \left(1 - \left(\frac{a}{c} \right) \right)^{24} \right] * \left(\frac{a}{h} \right)^4$$

(The missing term in the printed Guide is circled above.)
(Incidentally, this "M" term is a combination of the M₁, M₂, and M₃ terms from the original 1981 Newman and Raju paper.)

Equation 7.16 should be corrected from:

$$S = [1.1]^* \sqrt{\left(\frac{a}{c}\right)} \quad \text{to:} \quad S = \left(1.1 + 0.35 \left(\frac{a}{h}\right)^2 \right) \sqrt{\left(\frac{a}{c}\right)}$$

(The shorter version is valid if the crack is very small and $a/h \approx 0$. Note that errata sheets prior to this errata sheet #5 were also wrong and had a "*" symbol instead of the appropriate plus sign "+" on the right side.)

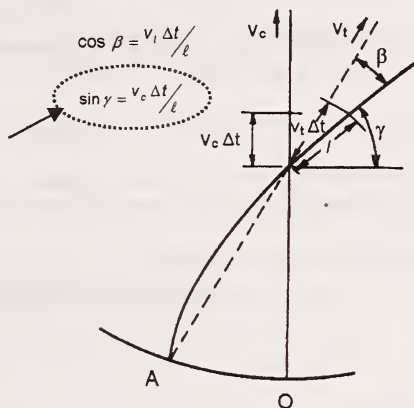
Change the section heading number from 7.7 to 7.8

4 lines up from the bottom, change the word: "overcomes" to "overtakes"

top line, change the word: "maximum" to "minimum"

Figure 7.27a
top left, change

$\sin \beta$ to $\sin \gamma$ as shown
here



last line, change from
"... they will become shallower semi ellipses the deeper they go .." to:
"... they will become **more elongated** the deeper they go...."

Figure D6.b
The wrong photo is shown.
It is a duplicate of Figure D6a.

The correct Figure D6.b is shown here.
It is an optical photo with a close-up of the origin and mirror. It is about the same magnification as the SEM image shown in Fig. D-2c.
The intent was to show matching optical and SEM images in b and c at the same magnifications for comparison.



Errata sheet 6 March 12, 2008

Unfortunately, there are a number of errors in the printed version of the Guide. Many of the stray arrows, equation mistakes, and mislabeled figures stem from software compatibility problems. Other errors were oversights on my part. Also, there was no editor for the book, so there certainly are sections that could be worded better.

A *corrected* .pdf version of the Guide is available on line at:

<http://www.ceramics.nist.gov/>

Click on the right side for the **NIST Recommended Practice Guides**.

Caution: it has a large file size (31.7 MB).

Printed books may be requested, *at no charge*, on this web site or by contacting me.

This errata sheet will be updated and posted on the same web site as necessary. I have also been making some hand corrections to the books as I mail them out.

If you find something you believe is wrong, please let me know at:
george.quinn@nist.gov

George Quinn
March 12, 2008

CORRECTIONS:

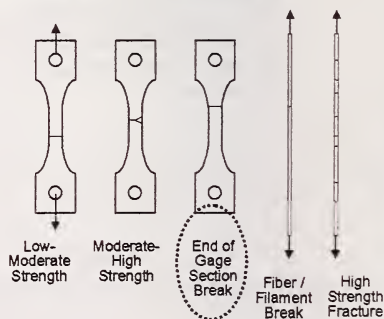
Pages 1-9 and 1-10 should be renumbered to 2-1 and 2-2.

Page 3-10, 3-11 A note should be added here to say that JPEG images may be saved with adjustable amounts of compression. They should be saved with little or no compression.

Page 3-43 Figure 3.38 The marker bar was cropped off the bottom figure. Both a and b were at the same magnification. The depth of the semi elliptical precrack (from the image bottom to the white arrow) was 250 μm .

Page 3-54 Figure 3.46 caption, change the word "comparator" to "profilometer"

Page 4-13 Figure 4-8
The middle tensile specimen is labeled wrong.
It should be:
"End of Gage Section Break"



Page 4-30 Line 13, delete the words: "a later chapter"

Special Publication 960-16

Fractography of Ceramics and Glasses

George D. Quinn

Materials Science and Engineering Laboratory,
National Institute of Standards and Technology

Special Publications

2007



U.S. Department of Commerce

Carlos M. Gutierrez, Secretary

Technology Administration

Robert C. Cresanti, Under Secretary of
Commerce for Technology

National Institute of Standards and Technology

Dr. William Jeffrey, Director

Certain commercial entities, equipment, or materials may be identified in this document in order to describe an experimental procedure or concept adequately. Such identification is not intended to imply recommendation or endorsement by the National Institute of Standards and Technology, nor is it intended to imply that the entities, materials, or equipment are necessarily the best available for the purpose.

National Institute of Standards and Technology

Special Publication 960-17

Natl. Inst. Stand. Technol.

Spec. Publ. 960-17

546 pages (April 2007)

CODEN: NSPUE2

U.S. GOVERNMENT PRINTING OFFICE

WASHINGTON: 2006

For sale by the Superintendent of Documents

U.S. Government Printing Office

Internet: bookstore.gpo.gov Phone: (202) 512-1800 Fax: (202) 512-2250

Mail: Stop SSOP, Washington, DC 20402-0001

Preface

Fractography is a powerful but underutilized tool for the analysis of fractured glasses and ceramics. It is applicable to fractures created under controlled conditions in the laboratory and to component failures in service. Fractography can identify the cause of failure and can even provide quantitative information about the loading conditions.

The goal of this Guide is to make fractographic analysis of brittle materials less an art and more an engineering practice for scientists and engineers. This guide emphasizes practical approaches for problem solving and failure analyses.

Fractographic analysis is to large degree pattern recognition. This Guide includes a wealth of illustrations to aid fractographers in pattern recognition. The Guide also includes an extensive bibliography and a tabulation of published case studies so that the reader can pursue topics of specific interest.

Acknowledgements

The author derived much inspiration from the late Professor Van Derck Fréchette of Alfred University. Van made many important contributions to the science of fractography of brittle materials, not the least of which was his 1990 seminal book: *Failure Analysis of Brittle Materials*. Van solved many practical, vexing, and spectacular cases and trained hundreds of fractographers including this author over his long and distinguished career.

The author has had a continuing and fruitful collaboration with Professor James Varner at Alfred University. Dr. Varner and the author continue the Van Fréchette legacy by training a new generation of fractographers.

The author thanks Dr. Jeffrey Swab, of the U.S. Army Research Laboratory; Aberdeen, Maryland and Mr. Michael J. Slavin (formerly of ARL) for their help in crafting a framework for fractographic analysis that was used to create the U.S. Army Military Handbook (MIL HDBK) 790 in 1990. This MIL HDBK was the precursor to American Society for Testing and Materials standard (ASTM) practice C 1332 adopted in 1996. This was the first formal standard for fractographic analysis of ceramics and brittle materials in the world. Many of the concepts in this Guide stem from our collaboration on those standards.

The author has learned much from discussions with and readings of the prolific writings of Mr. Roy Rice, Prof. Jack Mecholsky, and Dr. Stephen Freiman. They have significantly advanced the state of the art of materials science through their fractographic work.

Dr. Roger Morrell of the National Physical Laboratory has been an inspiration, particularly with his astute practical applications of fractography to failure analysis and his own Guide to Fractography.

The author would be remiss in not acknowledging the insightful contributions of Dr. Janet B. Quinn of the American Dental Association, who is making her own contributions to the science of brittle materials fractography and never fails to present challenging fractographic problems to her spouse.

TABLE OF CONTENTS

Preface

1.	Introduction	1-1
2.	Resources	2-1
3.	Tools and Equipment	3-1
3.1	Low Power Optical Examination and Component Fracture Documentation	3-2
3.2	Photographing the Overall Component.	3-7
3.3	Stereo Binocular Microscope	3-11
3.4	Stereoptical Microscope Camera Port.	3-14
3.5	Discussion Stereomicroscope	3-15
3.6	Illumination Sources	3-15
3.7	Coatings.	3-20
3.8	Size Measurements	3-23
3.9	Compound Optical Microscope	3-26
3.10	Compound Microscope with Digital Camera and Image Z-axis Scanning	3-29
3.11	Digital Image Processing and Reconstruction	3-29
3.12	Replication Equipment	3-30
3.13	Scanning Electron Microscope	3-35
3.14	Stereo SEM Imaging	3-49
3.15	Field Emission SEM	3-50
3.16	Environmental SEM	3-51
3.17	Transmission Electron Microscope.	3-51
3.18	Atomic Force Microscope (AFM)	3-52
3.19	Optical Profilometer	3-52
3.20	Confocal Scanning Light Microscope.	3-53
3.21	Stress Wave and Ultrasonic Fractography	3-53
3.22	High Speed Photography.	3-56
3.23	X-ray Topography	3-56
3.24	Dye Penetration and Staining	3-56
3.25	Other Equipment.	3-59
3.26	Other Resources	3-60
3.27	The Future	3-61
4.	General examination and fracture patterns	4-1
4.1	Specimen Reconstruction	4-2
4.2	Crack Branching Patterns	4-3
4.3	Crack Branching Angles	4-6

4.4	Crack Branching Distances	4-10
4.5	Fragmentation Patterns	4-10
4.6	Laboratory Strength Test Fracture Patterns.	4-12
4.6.1	Tension strength.	4-13
4.6.2	Flexural strength	4-14
4.6.3	Biaxial flexural strength	4-18
4.6.4	Laboratory test specimen analysis: additional tips	4-20
4.7	Component Fracture Patterns - General	4-22
4.8	T Intersections and Crossing Cracks	4-26
4.9	Invisible cracks	4-27
4.10	Plates and Windows	4-28
4.11	Tempered Windows.	4-30
4.12	Thermally Induced Plate and Window Fractures	4-31
4.13	Bottles and Pressure Vessels	4-33
4.14	Torsional Fractures	4-36
4.15	Chipping	4-37
4.16	Laboratory Test Fractures and Component Fractures.	4-40
4.17	Controlled Component Fractures	4-40
4.18	Finite Element Analysis	4-40
4.19	Characteristics of Some Common Fracture Modes	4-41
4.19.1	Mechanical overload fracture	4-41
4.19.2	Thermal fracture	4-41
4.19.3	Impact or contact fractures	4-42
4.19.4	Corrosion or oxidation.	4-43
4.19.5	Residual stress.	4-43
4.19.6	Time dependent fracture	4-44
5.	Fracture Surface Examination.	5-1
5.1	Introduction	5-1
5.2	Fracture Mirrors, A Fractographer's Best Friend	5-3
5.2.1	Fracture mirrors in glass	5-3
5.2.2	Fracture mirrors in ceramics.	5-14
5.2.3	Fracture mirrors, special cases	5-18
5.3	Hackle	5-29
5.3.1	Coarse hackle	5-29
5.3.2	Wake hackle.	5-31
5.3.3	Twist hackle.	5-34
5.3.4	Other hackle	5-39
5.4	Wallner Lines	5-41
5.4.1	Introduction	5-41
5.4.2	Primary Wallner lines	5-43
5.4.3	Secondary Wallner lines	5-47

5.4.4	Tertiary Wallner lines	5-50
5.4.5	Wallner Lambda lines	5-55
5.5	Arrest Lines	5-55
5.6	Scarps	5-57
5.7	Glue Chips	5-59
5.8	Transgranular and Intergranular Fracture	5-60
5.9	Stable Crack Growth	5-63
5.9.1	Slow crack growth (SCG) at ambient temperature	5-63
5.9.2	Stable extension from local residual stress or R-curve effects	5-66
5.9.3	High temperature slow crack growth in ceramics	5-67
5.9.4	High temperature creep fracture	5-70
6.	Origins of Fracture	6-1
6.1	Origins, Flaws, and Defects	6-1
6.2	The Spatial Distribution of Flaws	6-1
6.3	Are Flaws Intrinsic or Extrinsic?	6-3
6.4	Matching Fracture Halves	6-5
6.5	External Surfaces	6-6
6.6	Volume-Distributed Flaws	6-6
6.6.1	Pores	6-6
6.6.2	Porous regions	6-6
6.6.3	Porous seams	6-6
6.6.4	Agglomerates	6-6
6.6.5	Inclusions	6-12
6.6.6	Compositional inhomogeneities	6-12
6.6.7	Large grains	6-12
6.6.8	Grain boundaries	6-12
6.7	Surface-Distributed Flaws	6-17
6.7.1	Surface voids	6-17
6.7.2	Pits	6-17
6.7.3	Handling scratches and polishing scratches	6-17
6.7.4	Sharp object impact or contact	6-21
6.7.5	Blunt object impact or contact	6-23
6.7.6	Grinding and machining cracks	6-28
6.7.7	Chips	6-37
6.8	Other Flaws	6-38
6.8.1	Processing cracks in ceramics	6-38
6.8.2	Artificial or controlled flaws, glasses and ceramics	6-38
6.8.3	Other glass origins	6-41
6.9	Fracture Oddities	6-48
6.10	Contaminants	6-49

6.11	Combined or Hybrid Flaws	6-49
6.12	Baseline Microstructure Origins	6-53
6.13	Flaw Size	6-54
6.14	Partially-Exposed Flaws	6-54
6.15	Microfault Pockets	6-55
6.16	Polished Microstructural Sections	6-58
6.17	What to Report	6-58
7.	Quantitative Analysis	7-1
7.1	Introduction	7-1
7.2	Stresses from the Extent of Fragmentation	7-2
7.2.1	Annealed parts	7-2
7.2.2	Fragmentation of tempered parts	7-5
7.3	Stresses from the Branching Distances	7-7
7.3.1	Annealed plates and bars	7-7
7.3.2	Tempered plates	7-8
7.4	Stresses from the Mirror Size	7-10
7.4.1	Mirror analysis and constants	7-10
7.4.2	How to measure mirror sizes	7-13
7.5	Fracture Mechanics Analysis of the Flaw Size	7-18
7.5.1	Introduction to fracture mechanics	7-18
7.5.2	The Newman-Raju Y Factors	7-28
7.5.3	Irregularly-shaped surface cracks	7-34
7.5.4	Three-dimensional, blunt, and inclined flaws	7-35
7.6	Relationship of K _{Ic} and A	7-36
7.7	Mirror to Flaw Size Ratios	7-36
7.8	Comparing Measured to Calculated Flaw Sizes	7-38
7.9	Crack Velocities from Wallner Line Analysis	7-40
7.10	Slow Crack Growth	7-46
7.11	R- curve Behavior	7-50
7.12	Indentation Mechanics	7-58
7.13	Fractal Analysis	7-60
7.14	Estimation of Residual Stresses	7-62
7.15	Weibull Analysis	7-65
8.	Single Crystals	8-1
8.1	General	8-1
8.2	Preferred Cleavage Planes	8-2
8.3	Fractographic Techniques	8-5
8.4	Fracture Surface Markings	8-8
8.5	Origins	8-20
8.6	Other Sources	8-27

9.	Ceramic and Glass Composites	9-1
9.1	Particulate, Whisker, or Self-Reinforced Ceramic Composites . . .	9-1
9.2	Fiber-Reinforced Composites	9-2
10.	Case Studies	10-1
Case 1	Ruptured Rotor (Ceramic gas turbine rotor)	10-1
Case 2	Busted Barrel (Silicon carbide gun liner)	10-9
Case 3	Conflicting Carbide Data (Silicon carbide flaws and slow crack growth)	10-12
Case 4	Vulnerable Vials (Broken medicinal bottles)	10-16
Case 5	Troublesome Tubes (Sapphire in a plasma asher)	10-17
Case 6	Suffering Setter Plate (Silicon carbide furnace plate)	10-20
Case 7	Ruptured Radomes (Fused silica missile nosecones)	10-22
Case 8	Maligned Machinists (Bend bars made by different machine shops)	10-25
Case 9	Modeler's Match (Fracture origins in MEMS scale SiC micro tensile specimens)	10-27
Case 10	Fractious Fractographers (A fractography round robin)	10-29
Case 11	Perilous Prostheses (Four ceramic dental crowns)	10-33
11.	Conclusions	11-1
Appendix A Bibliography		
Appendix B Fractographic Case Studies		
Appendix C Fracture Mirror and Branch Constants		
Appendix D Guidelines for Measuring Fracture Mirrors		

Index

1. Introduction

Why did it break? Where is the origin? Did it break as expected or from an unexpected cause? Was there a problem with the material or was the part simply overloaded or misused? Why did this part break and others not? What was the stress at fracture? Was the laboratory strength test successful or was there a misalignment? These are common practical questions and the fractographer can often give straightforward definitive answers.

The curse of brittle materials is that they are prone to catastrophic fracture. Brittle fracture is fracture that takes place with little or no plastic deformation. Nature has partially compensated for this shortcoming by furnishing clear fracture patterns and fracture surface markings that provide a wealth of interpretable information. Indeed, in many respects, fractographic analysis of ceramics and glasses is easier and can produce more quantitative information than the fractographic analysis of metals or polymers.

Figure 1.1 shows broken glass and ceramic rods. Using the techniques described in this Guide, fractographers are able to determine that the rods were broken in bending, from surface flaws, and even determine the fracture stress.

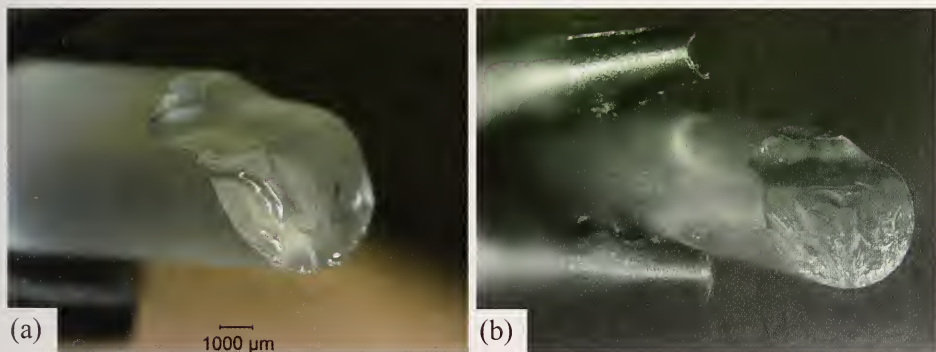


Figure 1.1 Fractured glass (a) and ceramic (b) rods.

This Guide takes a broader view of fractography than merely the examination of the fracture surfaces. Fréchette¹ described the science of fractography as the study of fragments and their interpretation in terms of material properties and conditions leading to failure. ASTM standard 1322² defines fractography as:

fractography, n - means and methods for characterizing fractured specimens or components

Examination of the fracture surfaces of broken pieces is an important element of fractographic analysis, but much can be gleaned by first looking at the sizes, shapes, and breakage patterns of the fragments. In some cases, the breakage pattern is all that is necessary and examination of fracture surfaces is unnecessary. For example, even novices can recognize an impact site on an automobile windshield without examining the fracture surfaces. A simple visual examination can tell the observer whether a component fracture was thermally or mechanically driven, whether the stress was large or small, and whether the stresses were uniaxial or multiaxial.

It is surprising how many instances there are in the literature where undue attention was spent on small fracture surface regions that were probably not even in the area of fracture initiation. It behooves one to look at the overall breakage pattern first before one jumps to a microscopic examination of the fracture surfaces.

Most people recognize that fractography is a valuable tool for failure analysis, but fewer appreciate its value in routine mechanical testing or support of materials processing. Although thousands of ceramic or glass items and test specimens are broken daily, only a tiny fraction are examined fractographically. A wealth of information is lost about the causes of fracture and the nature of the material. The flaw type may be just as important as the fracture stress in a strength test. Rice rued this state of affairs in 1977:³

"The most significant experimental procedure that can aid the understanding of mechanical properties is a study of fracture surfaces, especially to identify fracture origins.... It is indeed amazing the number of mechanical properties studies conducted that were extensively concerned directly or indirectly with the size and character of flaws and microstructure from which failure originated in which no attempt was made to experimentally observe and verify the predicted or implied flaw character."

Some of the reluctance to apply fractographic analysis is that it is unfamiliar to most engineers and scientists. Although there are a few notable exceptions, fractography is not commonly taught in schools and is often learned gradually and autodidactically by experience over many years. Some regard fractographic analysis as a subjective practice that can only be applied by masters. Others deem it as too interpretive. The reality is that what may seem mysterious to some is in fact objective and quantitative to an experienced fractographer.^a Interpretation is an essential step, but brittle materials often leave unequivocal markings on fracture surfaces that even a novice can inter-

pret with confidence. The markings are the direct consequence of crack perturbations during propagation. An important element of fractographic analysis is **pattern recognition**. Certain types of fracture leave telltale fracture patterns on the fracture surfaces, or in the breakage patterns or shapes of the fragments. For example, hackle lines radiating from a fracture mirror are telltale features that even novices can identify. They intuitively lead an observer back to the origin. Other markings may be more subtle and can be overlooked by the casual or inexperienced observer. With a little practice and experience, any material scientist or engineer should be able to analyze brittle fractures and make an interpretation, or at least recognize what pieces should be brought to the attention of a more experienced fractographer. The novice may be tentative at first, but fractography is a cumulative learning experience. The more fractography one does, the easier it becomes.

A colleague who was trained in archeology once described an analogous situation to the author.^b While walking through the countryside in the American southwest, she noticed small mounds and depressions on the ground, exposed potsherds, and fragments of flint arrowheads and hammers. Companions with her who were unfamiliar with archeology did not notice them and were oblivious to the evidence of human activity around their feet.^c

A good starting place to gain fractographic experience is by examining test coupons broken in laboratory conditions. Flexural strength specimens are a common starting point. Pattern recognition skills can be reinforced by seeing multiple examples in a set of specimens. Component failure analysis is often much more difficult, especially if only a single example is available or the fracture occurred under unknown loading conditions.

Fractographers ideally should have knowledge of materials science, microscopy, mechanics (stresses and strains), and an aptitude for problem solving and troubleshooting. They should be comfortable with microscopy, since many of the features to be studied are smaller than the unaided eye can

^a This is reminiscent of Arthur C. Clarke's Third law, which is: "Any sufficiently advanced technology is indistinguishable from magic." Profiles of the Future: An Inquiry into the Limits of the Possible, A. C. Clarke, Bantam, 1973.

^b Dr. Jane Adams, U. S. Army Research Laboratory.

^c The author has had similar experiences when searching for buried ancient Roman ruins in Germany along the great 95 km long Wasserleitung (waterway) from the Eifel forest to Cologne and also along the 500 km long Limes from Bonn to Regensburg. The Limes were a frontier fortification similar to Hadrian's Wall, but constructed of less durable materials.

discern. Some experience in materials science is necessary since strength-limiting flaws and crack propagation behavior are controlled by processing and the microstructure. Cracks propagate in response to stresses and strains, so fractography often comes quite naturally to mechanical engineers. That is not to say that physicists and geologists don't make good fractographers, but they will have to learn the fundamentals of stress analysis. At a minimum, a fractographer should be comfortable with concepts of uniaxial tensile stresses (stresses primarily in one direction, such as in a direct tensile strength test specimen), uniaxial bending stresses (such as in a beam loaded in bending), and biaxial stresses (whereby there are tensile stresses in two different directions such as in a pressurized plate, a pressurized bottle, or a disk loaded

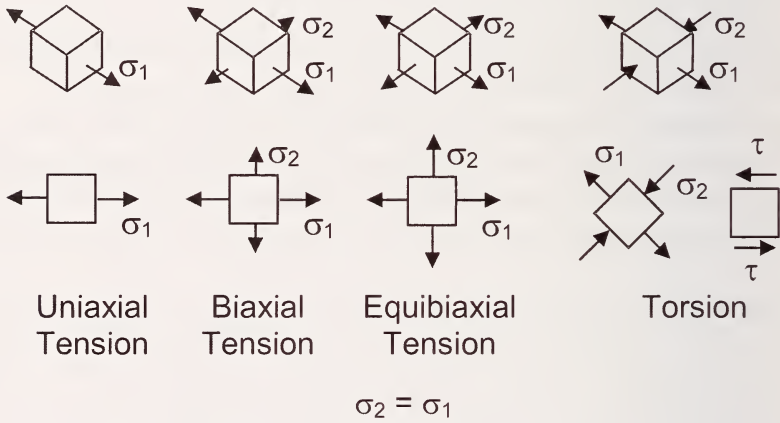


Figure 1.2. Stress states may be represented by forces (arrows) acting on the surfaces of tiny differential volume elements. They are shown here as 3-dimensional (top row) or 2-dimensional (bottom row) views. The lengths of the arrows are in proportion to the stress magnitude. σ_1 and σ_2 are normal stresses and τ are shear stresses.

in ring-on-ring flexure). These stress configurations are illustrated in Figure 1.2. It should also be borne in mind that most parts and laboratory specimens have stress gradients. It is rare that a component has a uniform stress throughout. Simple loading configurations are typically covered in the first chapters of an elementary strength of materials engineering textbook, which may be consulted to gain a basic familiarity with stresses and strains.

Part of the skill of a fractographer is knowing where to look and how to look. A specimen that breaks into only two pieces may not be too difficult to interpret. Medium to high strength specimens with multiple fractures can initially

be confusing, but with a little experience and a few simple precautions, one can find the primary fracture. Component or service failures may be difficult since the loading conditions may be unknown. Key pieces may be missing or the evidence incomplete or contradictory. Multiple crack systems from different causes and events may intersect and confound an interpretation.

The author suspects one reason that fractography is sometimes held with suspicion or is deemed subjective is that some incautious fractographers have jumped to conclusions and reached questionable interpretations. It is unwise to make conclusions based on limited or incomplete evidence. Novices often force fit a fracture scenario to their limited experience base. Some fracture patterns may be difficult to detect or very subtle and may not be recognized. Good fractographers recognize their strengths and the limitations of their experience base and do not overreach or extrapolate. They should be alert to unusual or new fractographic markings or failure modes with which they are not familiar and should be ready to search the literature, consult colleagues, or try to create comparable markings in the laboratory. No fractographer is born with a built-in data base of fractographic patterns in the brain, so step-by-step accumulation of experience is necessary. One may consult textbooks, reference articles, and even this Guide to help acquire knowledge, but there is no substitute for hands-on direct eyeball and microscopy experience.

There is a wealth of information in the technical literature about fractography of glasses and ceramics, but it is scattered in textbook chapters, in journals, and conference proceedings. Fréchette's seminal book, *Failure Analysis of Brittle Materials*,¹ is a good starting point for the practical fractography of glasses, but there is no analogous book for ceramics. This Guide helps fill that gap and presents practical information for both glasses and ceramics. It also includes an extensive bibliography. There are formal standard practices in the American Society for Testing and Materials² and European Committee for Standardization⁴ for fractographic analyses of glasses and ceramics.

Fractography is a tool for the broader topic of failure analysis. Figure 1.3 suggests a simple but apt analogy. The fractographer is called upon to solve a fracture mystery. The detective uses his or her powers of observation to study the scene of the fracture and meticulously collects and preserves the available evidence. The clues are contemplated and weighed against the available background information furnished by witnesses. Comparable cases are considered to determine whether there are similarities and whether there is a pattern. Scientific analysis of the material may be done to verify its quality, composition, and authenticity. Pondering all the information, and keeping an open mind for all possible scenarios, the fractographer detective formulates a

hypothesis and checks it against the known facts. The fractographer communicates the findings to the client, management, engineer or processor in a manner that is convincing and fathomable. Sometimes the findings must be presented in formal legal settings. In summary, fractographic analysis is not merely looking at fracture surfaces, but is the integration of knowledge from a variety of sources to solve the puzzle of how fracture occurred (Figure 1.4).



Figure 1.3. The fractographer as detective.

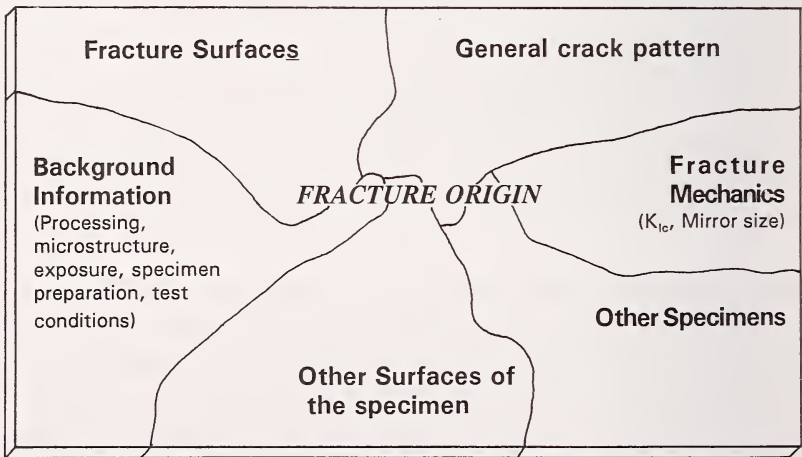


Figure 1.4. Fractographic analysis is more than examining fracture surfaces.⁵

One definition of failure analysis is: “A process that is performed in order to determine the causes or factors that have led to an undesired loss of function.”⁶ Failure may be due to fracture, corrosion, excessive deformation, or wear. Hence, fracture is a subset of a larger class of failure causes. The readers interested in the broader topic of failure analysis in general, including concepts and philosophies about how to conduct an analysis, should refer to the ASM handbook on Failure Analysis and Prevention.⁶ That volume has multiple chapters and extensive discussions about failure analysis in general, and has such pragmatic recommendations as: “don't jump to conclusions,” “keep an open mind,” and “avoid 5-minute best guess analyses.”

At this point it is appropriate to point out a critical aspect of fracture analysis problems. Final fracture often occurs after a chain of events. One event may create a flaw, but then a second or even third event may be necessary to cause fracture. For example, drinking glasses commonly sustain internal impact damage from eating utensils that are carelessly dropped into the glass. Subsequent thermal stresses generated in the dishwasher may cause cracks to extend gradually around the base. If the large crack is not noticed, an unwary user who picks up a liquid filled glass may have an unpleasant surprise. What was the cause of failure in this case: the user pouring a liquid into the glass and lifting it to quench a thirst, the initial impact damage, or the thermal stresses that cause the crack to grow? The answer is all of the above.

Certain commercial equipment, instruments, or materials are identified or shown in this Guide to specify adequately the experimental procedure or to show examples of fractographic equipment. Such identification does not imply recommendation or endorsement by the National Institute of Standards and Technology, nor does it imply that the materials or equipment identified are necessarily the best available for the purpose.

Chapter 1 References

1. V. D. Fréchette, "Failure Analysis of Brittle Materials," *Advances in Ceramics*, Vol. 28, American Ceramic Society, Westerville, OH, 1990.
2. ASTM C 1322-02a, "Standard Practice for Fractography and Characterization of Fracture Origins in Advanced Ceramics," Annual Book of Standards, Vol. 15.01, ASTM Int., West Conshohocken, PA, 2003. (The original version was adopted in 1996.)
3. R. W. Rice, "Microstructure Dependence of Mechanical Behavior of Ceramics," pp. 199 - 381 in *Treatise on Materials Science and Technology*, Vol. 11, Academic Press, New York, 1977.
4. CEN prEN 843-6, "Advanced Technical Ceramics - Monolithic Ceramics – Mechanical Properties at Room Temperature – Part 6: Guidelines for Fractographic Examination," European Committee for Standardization, Brussels, 2004.
5. J. J. Swab and G. D. Quinn, "The VAMAS Fractography Round Robin: A Piece of the Fractography Puzzle," pp. 55 – 70 in *Fractography of Glasses and Ceramics III*, Ceramic Transactions, Vol. 64, eds., J. R. Varner, V. D. Fréchette, and G. D. Quinn, ACS, Westerville, OH, 1996.
6. *Failure Analysis and Prevention*, ASM Handbook, Vol. 11, American Society for Materials, Materials Park, OH, 2002.

2. Resources

This Guide is designed to be a stand-alone resource. There is a wealth of additional information scattered in books and technical articles that delve into specific topics in more detail.

Appendix A is a bibliography featuring many good publications of special interest to the glass and ceramic communities. The topics include books on fractography, compilations of conference proceedings, overview papers on fractography, reports on fractography round robins, compilations of fracture mechanics stress intensity factors, and papers on microscopy, fracture origin types, fracture mirrors, and fracture mechanics analyses of flaw sizes.

There are two ongoing conference series devoted exclusively to the fractography of glasses and ceramics. One is in the United States and one is in Europe. The conferences have been held at four or five year intervals. The longest running and most famous was begun by Professors Van Derck Fréchet and James Varner in 1986 at Alfred University in New York State. Five conference proceedings have excellent information on a range of theoretical and applied problems by leaders in the field. Dr. Jan Dusza of the Institute of Materials Research of the Slovak Academy of Sciences, Košice, Slovakia began a new conference series in 2001 and had one sequel in 2004.

Appendix B is a unique Case Study bibliography that lists a series of publications dealing with specific case studies. These include fracture of windows, bottles, pressure vessels, and various ceramic parts. Some of the cases deal with the mundane and some with the exotic. It is included for the benefit of readers who wish to investigate specific problems.

Appendix C is the most complete tabulation of fracture mirror constants ever compiled for ceramics and glasses. It is an expansion of a similar listing in ASTM C 1322-02a.

Each chapter of this Guide also contains a specific list of references for topics covered in the chapter.

It is beyond the scope of this Guide to chronicle the history of fractographic analysis of brittle materials. Readers who wish to pursue this topic may enjoy the writings of Smekal,^{1,2,3,4} Wallner,⁵ Preston,⁶ Shand,⁷ Poncelet,⁸ Murgatroyd,⁹ and Fréchet.¹⁰

Chapter 2 References

- 1 A. Smekal, "The Nature of the Mechanical Strength of Glass," *J. Soc. Glass Tec.*, 20 (1936) 430 - 448.
- 2 A. Smekal, "Über die Natur der Mechanischen Festigkeitseigenschaften der Gläser," *Glastech. Ber.*, 7 (1937) 259 - 270.
- 3 A. Smekal, "Die Festigkeitseigenschaftenb Spröder Körper," *Ergebnisse der Exacten Natur Wissen.*, 15 (1936) 106 - 188.
- 4 A. Smekal, "Verfahren zur Messung von Bruchfortpflanzungs-Geschwindigkeiten am Bruchflächen," *Glastechn. Ber.*, 23 [3] (1950) 57 - 67.
- 5 H. Wallner, "Linienstrukturen an Bruchflächen," *Zeitschrift für Physik*, 114 (1939) 368 - 378.
- 6 F. W. Preston, "Bottle Breakage-Causes and Types of Fractures," *Bull. Amer. Ceram. Soc.*, 18 [2] (1939) 35 - 60.
- 7 E. B. Shand, "Experimental Study of Fracture of Glass: II, Experimental Data," *J. Amer. Ceram. Soc.*, 37 [12] (1954) 559 - 572.
- 8 E. F. Poncelet, "The Markings on Fracture Surfaces," *J. Soc. Glass Technol.*, 42 (1958) 279T - 288T.
- 9 J. B. Murgatroyd, "The Significance of Surface Marks on Fractured Glass," *J. Soc. Glass Technol.*, 26 (1942) 155 - 171.
- 10 V. D. Frechette, "Characteristics of Fracture-exposed Surfaces," *Proc. Brit. Ceram. Soc.*, 5 (1965) 97 - 106.

3. Tools and Equipment

The most important tools of the fractographers craft are the binocular stereoptical microscope and the scanning electron microscope. The stereoptical microscope affords to the eyes a magnified, naturally-appearing, three-dimensional view of the fracture surface that retains all color and reflectivity information. Fracture origins and flaws in ceramics and glasses can often be detected with the stereoptical microscope, but higher magnifications are often needed to see the flaw more clearly. The scanning electron microscope serves this need and has good depth of field, high magnification capability, and chemical analysis features. Other tools such as hand magnifiers, compound optical microscopes, or even atomic force microscopes play supportive roles.

In the early 21st century, dramatic advances in digital camera technology, computer software, computer memory, and processing speeds are revolutionizing imaging technology. The new technologies are quite affordable and are rendering film photography obsolete and are opening up marvelous new capabilities not heretofore available. The shortcomings of conventional compound microscopes (*e.g.*, limited depth of field) or of scanning electron microscopes (*e.g.*, flat-appearing images) can be overcome or mitigated. The blending of optical microscopy with the new digital imaging technologies are leading to clever new microscope designs based upon interferometry or processing of multiple images. For example, virtual three-dimensional images can be constructed with automatically rastering optical microscopes or by analysis of multiple scanning electron microscope images taken with slightly different specimen tilts. The pseudo three-dimensional images can be displayed, tilted, and rotated to afford different perspectives. Various quantitative numerical analyses of surface topography (*e.g.*, surface roughness or even fractal dimension analysis) can be performed at almost no extra effort since the surface topography has been recorded digitally.

Simple low-cost software programs are now available that can simply and conveniently overcome the depth of field limitations of virtually any microscope. A series of photos at the same magnification are taken while slightly readjusting the focus in sequential steps. The software interprets the regions that are in focus and stitches these together to create a single image with an infinite depth of field.

In this chapter, traditional and new tools of the trade and are reviewed with an emphasis on their applicability to fractography.

3.1 Low Power Optical Examination and Component Fracture Documentation

The examination of fractured pieces begins with a visual examination using the unaided eye. Some fractographer prefer to use lint free gloves when handling fragments, but gloves usually are not necessary. Ceramics and glasses are hard, durable materials and may be cleaned fairly easily.

It may be tempting to rush to a microscopic examination of the fracture surfaces, but study of the general fracture and the overall condition of the component is time well spent. This examination and reconstruction of the specimen may be aided by a simple (1.2 X to 1.4 X) magnifying glass, whether hand-held or mounted on a stand as shown in Figure 3.1. A stand-mounted lens frees the fractographer's hands for manipulation of the specimen. Larger versions with built in ring lamps are ideal. A clean, tidy table or bench top is desirable, lest the fractographer inadvertently knock critical fragments onto the floor or against each other, or contaminate or damage the fracture surfaces.



Figure 3.1. Simple magnifiers.

Small jeweler's loupes as shown in Figures 3.2 and 3.3 also are handy, particularly in the field. Their working distances range from 50 mm for the low power (5 X) loupe, to about 25 mm for a 10 X loupe. Some practitioners may be adept at holding a watchmaker's loupe in one eye without using a hand, thereby freeing up both hands. Most fractographers will use one hand to hold



Figure 3.2. Hand loupes and optical comparators. From the left, 5 X and 7 X watchmaker loupes; a 20 X loupe, a 7 X comparator with an internal 20 mm scale marked in 0.1 mm increments, and a 8 X to 16 X zoom comparator with an 16 mm scale marked in 0.1 mm increments.

the loupe and the other to hold the examined fragment. Machinist loupes and pocket optical comparators with magnifications up to 20 X (two are shown on the right of Figure 3.2) have built-in measuring scales with graduations as fine as 0.1 mm (0.005 in). Rapid measurements of mirror sizes or even fracture origin sizes may be made with these inexpensive tools. Remember, the more



Figure 3.3. Loupes (5 X to 20 X) may either be held by the eye or by hand. The part is a single crystal silicon rod.



Figure 3.4. A jeweler's or hobbyist's head mounted magnifier (2 X to 3.5 X) can be helpful



Figure 3.5. Specimen holders. Clockwise from the lower left are: a bend bar holder made with an alligator clip on a bendable (10 gage electrical) wire with electrical tape wrapped around the teeth to cushion the specimen, two aluminum jigs with slots and grooves for bend bars or tension strength specimens, an aluminum block with hole, and three aluminum holders comparable in size to a glass microscope slide with groves to hold bend bars both on their flats and on edge for chamfer examination.

powerful the magnification, the smaller the field of view and the shallower the depth of field, so a good general duty loupe or comparator with a 7 X or 10 X magnification may be perfectly suitable and more versatile than one with a 20 X magnification. At these low magnifications, illumination is usually not a problem and ambient light is adequate.

Simple holders or clamps may be useful as shown in Figures 3.5 and 3.6, particularly if the fractographer is examining repetitive examples of a particular type specimen or component. It can be exasperating to hold a part in one hand at just the right angle, while holding a magnifier with the second, but then need an extra hand to apply some alcohol with a cotton swab to clean the part. Similarly, the fractographer may wish to jot down some important information as part of a written record.

Conventional clays should not be used for mounting specimens unless there is no alternative. Clay is a pernicious material that can easily contaminate the fracture surfaces and blend into the fracture features. Clays have colors and compositions similar to ceramic products and are next to impossible to clean off. Their surface charge and extremely fine plate-like structure cause them to cling to the fracture surface. Clays often have an oil to keep them plastic that makes things even worse, since the oils can smear over the fracture surfaces even on glasses. Clay often gets on one's hands and then tends to get on everything. More information on clay contamination is in section 6.10.

A completely satisfactory alternative is polymer clay that is available from arts and crafts stores.^a Some polymer clays can be easily dissolved and cleaned with paint thinner, acetone, and even ethanol. The color in these polymer clays can easily be distinguished on the fracture surfaces. The best colors are deep blues or greens. White or gray should not be used since they cannot be distinguished from many ceramics. Garish colors should not be used, since they are a distraction in photographs.

Simple cleaning tools and markers such as shown in Figure 3.7 should be conveniently located at the examination work station. Acetone, ethanol, or methanol with tissues and cotton swab applicators are handy for cleaning. Compressed air from air lines should be used with caution since there may be traces of oil mixed with the air. Water soluble ink pens are handy for marking the specimen. Ceramic fracture surfaces should never be cleaned with metallic tools or probes. It may be tempting to try to scrape or poke off a

^a Sculpey III Polymer. "Oven bake clay" made by Polyform products, Elk Grove Illinois is easily dissolved by paint thinner and acetone.



Figure 3.6. Component or specimen holders. Clockwise from the lower left: a homemade plastic platform mounted on a swivel base; a pivoting wooden holder; a cork ring; a clamp on a stand, an alligator clip on a stand, an inverted miniature wood flower pot with a hole, and two wooden candleholders with dolls heads and polymer mounting clay. The balls can be rotated to obtain optimum illumination angles onto the specimen's surface.



Figure 3.7. Convenient tools and cleaning agents

contaminant, but metallic tools are abraded by the harder ceramic causing metallic traces to be smeared on the fracture surface. Some fractographers prefer to handle fragments while wearing white cotton gloves.

3.2 Photographing the Overall Component

It is often prudent to photograph the entire specimen or component. An overall photo provides an essential context for subsequent close up photos. A variety of scales or rulers should be available, which may be set alongside the component in order to show the size or scale. In this day and age, when photos and images are manipulated and expanded or shrunk digitally, it is prudent to get size markers on the recorded image as soon as possible, otherwise much time can be wasted afterwards deducing or guessing what magnification was used. It is very easy to make mistakes with the size markers added after the fact. Fractographers would do well to follow the example of the archeological community, wherein rulers and meter sticks are ubiquitous features of any formal record of a dig site. In lieu of scales, simple props such as coins or other common objects may be set alongside the component, but perhaps on the side or bottom where they subsequently can be cropped or replaced with marker bars in subsequent reports or publications.

A variety of camera types may be used to photograph an entire component. Digital cameras are rapidly becoming the tool of choice for virtually all such work, but film based cameras are still effective.

A conventional single lens reflex (SLR) film camera with 35 mm film (Figure 3.8) can be used at very close distances from the object when using the macro option or supplemental close up lenses that are screwed onto the front of the main lens. The single lens reflex mode (whereby the photographer sees the object to be photographed through the main camera lens) is essential to ensure that the object is properly framed by the camera lens. ASA/ISO film speeds of 100 to 400 may be used. Faster films are usually too grainy. The great drawback of conventional film photography is that the fractographer must deliver the film to a processor with an attendant time delay of hours or days. Digital renditions of the images may be prepared by the film processor or by scanning the color prints, preferably at 120 dots per cm (300 dots per inch) or finer resolutions. Another drawback is the difficulty in using a flash at close distances if the light levels are low. A tripod and camera shutter release chord are needed for exposures longer than $1/30^{\text{th}}$ of a second. Illumination is important and a simple flash on the camera usually is unsatisfactory due to the proximity of the specimen to the camera. A platform with multiple illumination sources may suffice, but rudimentary light bulbs or spotlights may produce unsatisfac-



Figure 3.8. 35 mm single lens reflex camera with conventional film, tripod, and close-up lenses.

tory results due to unwanted shadows. In some cases the best results can be obtained by photographing the component outdoors with ambient lighting on a neutral-colored background, such as a white or gray poster board. The author



Figure 3.9. Camera stand with built-in lamps. A fiber optic light source is also on the platform to furnish vicinal (described below) and highlight illumination.

often photographs specimens on the window sill of his office on a white poster board base. An additional white cardboard is placed vertically as a reflector on the inside of the room to reflect some external light to back-fill the lighting on the specimen.

A dedicated macrophotography camera stand such as shown in Figure 3.9 has traditionally been useful for fractographic record keeping. The particular model shown in the figure is equipped with an old Polaroid type instant film camera with a variety of interchangeable objective lenses and an adjustable bellows. Overall photos of an entire component or close-ups of fracture surfaces may be shot. Magnifications up to 35 X are possible with a 17 mm lens and full bellows extension. Exposures have to be made on a trial-and-error basis with wastage of film until the optimum exposure time and lens f-stop settings are found. Most such photography has been done in black and white. Color photos were possible, but film speeds were slow causing long exposure times and often the colors were not rendered faithfully. Most users have replaced instant film cameras with digital cameras.

Digital cameras, either professional high-resolution models or simple consumer versions such as shown in Figure 3.10, have revolutionized fractographic photography. They have both manual and auto focus and exposure controls and can capture good images in ambient lighting without a flash. Small liquid crystal display monitors on the rear of the cameras allow fractographer to see what the primary lens will capture when the image is snapped.



Figure 3.10. Digital camera with macro capability, auto exposure, and auto focus.

The digital camera has the added virtue that it can immediately display the captured image. Remedial action can be taken immediately and a new image captured. This is very efficient. Another advantage is that images taken with digital cameras seem to be less sensitive to the color of the illumination. Color film often produces odd colored images if outdoor balanced film is used indoors with tungsten filament bulbs or fluorescent lamps. Another great advantage of the digital cameras is that they need less light to make a good quality image. Ambient illumination usually suffices. Flash lamps used with film cameras often over- or underexpose an object and create harsh shadows.

Digital cameras should have no less than 2 megapixel to 3 megapixel resolution. Many publications now require no less than 3 megapixel resolution and images must be presented at 120 dots per cm (300 dots per inch). The LCD monitor should be bright and large (at least 37 mm). The camera should have auto focus and auto exposure options and, most importantly, have a macrophotography option for close ups at distances as short as 100 mm. File storage format should include a Joint Photographic Experts Group (JPEG) or Tagged Image File Format (TIFF) option. Some professionals prefer RAW format, which is image data with very little processing or compression. TIFF is either an uncompressed format or a LZW (Lempel-Ziv-Welch) compressed format. LZW compression translates common patterns in an image into short codes and is best at preserving all the image data and achieving good compression. It doesn't achieve the high compression ratios that JPEG does. LZW is available for monochrome, grayscale, palette, and true color images.

JPEG files are compressed and are as much as 1/5th to 1/10th the size of an uncompressed TIFF file, with very little or no loss of detail. JPEG is available only for true color or grayscale images. JPEG reduces the number of bits in the image by eliminating repetitive image data or image data that is hard to see. The software may allow various compression levels and the higher the level of compression, the lower the quality of the image. In most cases, a low compression level produces a result that is indistinguishable from an original image. JPEG may compress more than other methods and the results may not be fully reversible. A JPEG file is automatically uncompressed when it is opened. At higher compression ratios (> 20:1) JPEG can degrade the quality of the image.

The RAW format is used by manufacturers to contain the (actual) raw data from the image sensor in a digital camera. They are minimally processed data. RAW file formats are proprietary. RAW files can differ greatly from one manufacturer to another and sometimes between cameras made by one manufacturer. RAW files are normally only used when additional computer processing is intended. Skilled users can adjust images with more control than

the other processed image file types. Although the term “raw” describes files in the classical sense of “raw data,” they typically are slightly processed in the camera. Usually the processing is limited to algorithms connected to the camera hardware. Some noise reduction processing is common. The proprietary nature of RAW files poses severe problems that fractographers should keep in mind. Photographers will find their older images inaccessible, as future software versions lose support for older cameras. In the worst cases, entire camera brands and RAW format subtypes may disappear.

The author typically saves and presents his images in JPEG format. Virtually all the photographic images in this Guide were saved in the JPEG format. Text and line art, and graphs were saved in LZW compressed TIF files.

The digital camera should be capable of easily transferring images to a computer, either through a cable to a USB or FireWire port on the computer or via a docking port. Common consumer digital cameras that have these features now cost less than a few hundred dollars. More elaborate single lens reflex (SLR) digital cameras have more options, more versatile lenses, and higher resolutions. Some may have extremely high resolutions, but it should be borne in mind that the stored image file sizes may be very large. SLR cameras should be ordered with close up lenses as an option.

3.3 Stereo Binocular Microscope

More powerful magnification will be needed in most cases to observe small fracture origins or fractographic markings on the fracture surfaces. The fractographer's single most valuable tool is the stereoptical binocular microscope or stereomicroscope (Figure 3.11). The stereomicroscope is designed such that each eyepiece views the object from a slightly different angle thereby creating two different images. The brain interprets these as a three-dimensional view. The stereomicroscope is in reality two separate microscopes. Older rudimentary Greenough design stereoscopes had two completely different optical paths, one for each eye. They had very limited capabilities. Most contemporary stereomicroscopes use a common objective lens and then two internal optical light paths in the body up to the eyepieces. Parfocality, whereby the object remains in focus while the magnification is changed, is a very advantageous feature of the microscope.

Stereomicroscopes present an image that is right side up and is laterally correct. The images are therefore easy to correlate to a specimen held in the hands or on the stage. The long working distance from the objective lens and the good depth of field make it possible to clearly see surface features despite

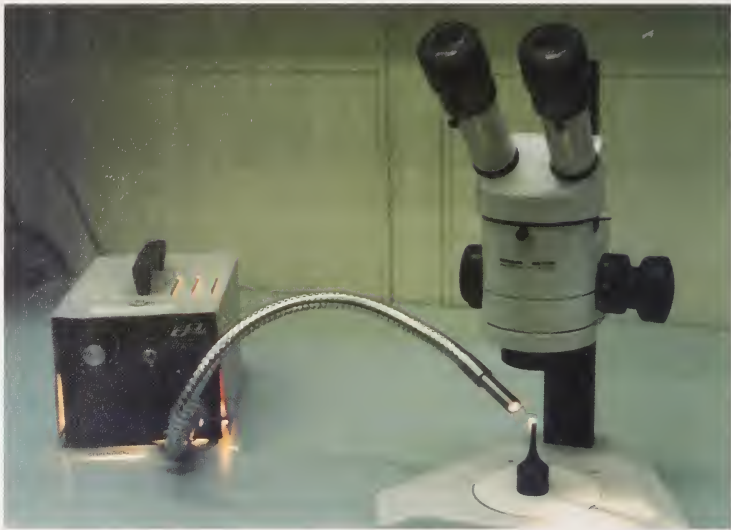


Figure 3.11. Stereo binocular microscope with a fiber optical light source for directional illumination. This is an indispensable tool for the ceramic and glass fractographer. Low incident angle or "vicinal illumination" is illustrated in the picture. In other cases, a ring light mounted on the objective lens of the microscope may be suitable. This particular microscope has interchangeable 0.63 X, 1.0 X and 2.0 X objective lenses, a body zoom magnification range of .65 X to 4 X, and 25 X eyepieces for an overall magnification range of 10 X to 200 X. The moderately tall (300 mm) mounting post enables large specimens up to 150 mm tall to be placed under the microscope.

the inherent roughness or curvatures of fracture surfaces. Some stereomicroscopes also have diaphragm apertures that can be stopped down to enhance the depth of field. Many stereomicroscopes are modular and easily modified or expanded.

The total magnification of a stereomicroscope is the product of the magnifications of the objective lens, the body, and the eyepieces. There often are different objective lenses (0.5 X to 2.0 X) that screw into the bottom of the microscope. Low power 0.5 X or 0.63 X lenses are useful for examining or photographing an entire test specimen or viewing large areas of the fracture surface. Higher power lenses (1.6 X or 2.0 X) may be screwed in for close-up examination. It may come as a surprise that the objective lenses have such low magnifying power, but a large diameter lens is needed to create the two optical views at slightly different viewing angles. The low power also means that the working distance from the objective lens to the object is very large, on the order of 20 mm to 200 mm. This is a very important and desirable feature for the examination of irregular components. One advantage of the long

working distance is that illumination sources such as fiber optic gooseneck light guides can be brought into close proximity to the work piece and the angle can be adjusted with plenty of room. A good fractographic examination set up should have both a low power objective lens (0.5 X or 0.63 X) and a high power lens (1.6 X or 2.0 X). An intermediate power lens (1.0 X) may also be handy. Objective lenses can cost anywhere from \$ 400 to \$ 4,000 each.

Much of the magnification occurs in the body of the stereomicroscope. Most bodies have multiple magnifications either through the use of discrete lenses that can be rotated into the optical path, or better, through stepless zoom magnification. Modern stereomicroscopes have been vastly improved over earlier generation models that may have only had a 2 X or 4 X zoom range. Modern bodies can steplessly zoom over a 10 X or even 16 X range while keeping the object in focus. A very desirable feature is discrete click stops on the zoom knob corresponding to specific magnifications. This feature is critical for size measurement purposes, either by the use of a graduated reticule in the eyepiece, or by a camera mounted on the microscope.

Final magnification is provided by the wide field eyepieces that are usually 10 X, 16 X, or 25 X. Stereomicroscopes may be used either with or without eyeglasses. The eyepiece tubes usually can be adjusted for the interpupillary distance. Eyepieces can be ordered either for persons with normal vision or for spectacle wearers. Rubber boots that attach to or slide up and down over the eyepieces are helpful for screening out stray light coming into the eyes. These can be removed or slid out of the way for eyeglass wearers. Typical overall magnifications can range from as low as 5 X to as high as 200 X. Some modern stereomicroscopes can achieve as much as 300 X to 400 X magnification with 16 X body magnifications and 1.6 X objectives.

The stereoptical microscope should be mounted on a tall mounting post so that large objects can be placed on the stage. Often it is necessary to mount long specimens end on so that the fracture surface is viewed directly. Figure 3.11 shows a model with about a 300 mm post that allows specimens as large as 100 mm to 150 mm tall to be placed on the stage. A serious shortcoming of some inexpensive so called “student microscope” models is their rudimentary mount that has a very limited clearance between the objective lens and the base. Such budget microscopes should be avoided. The fractographer quickly learns that he or she cannot even get the broken pieces in focus due to the long working distance of the lens and the limited body clearance.

It is also advisable to have one or both eyepieces adjustable, so that the operator can focus each eyepiece independently. One reticule should have a cross hair, which is valuable if one wishes to show a colleague a particular feature or the microscope will be used for size measurement if it is used in conjunction with a traversing stage as will be described below. If no independent measurement system is incorporated, then a built in graduated reticule should be mounted in one of the eyepieces. The reticule readings will have to be calibrated at various magnifications.

A very valuable but expensive optional feature is a tilting eyepiece head that may be adjusted up or down so that the viewer does not have to extend or bend his or her neck to see through the eyepieces, or to have to move a chair or stool up or down. A tilt head can cost between \$ 3,000 and \$ 4,000.

3.4 Stereoptical Microscope Camera Port

Stereomicroscopes may be equipped with a camera port for a video or digital camera. The port will be in line with either the left or right optical paths. The camera cannot record or display both images that the eyes see and the mind interprets as a three-dimensional image. Some microscope bodies have a lever switch that directs the light to either the eyepiece or to the camera. This scheme is extremely inconvenient. A much better scheme is a beam splitter that can simultaneously direct half of the light to the eyepiece and half to the camera so that the image can be viewed at the same time it is projected onto a monitor.

Instant film cameras were common in the past but are now obsolete. They have been supplanted by video cameras or digital cameras connected to a computer. Even video cameras are being rendered obsolete as digital cameras have become more capable, less expensive, and easy to use.

Video cameras with red, green, blue (RGB) signal output were inexpensive and commonly used in the 1980s and 1990s to feed a video signal to a television monitor. These were attached to the microscope port via an adapter. C-mount adapters were and still are the most common. Often a video printer was added to the system to produce hard copies. These provided a convenient color print, but at less resolution and clarity than a photo. The video cameras typically captured images with a 640 x 480 or 768 x 500 picture element resolution. This was adequate for conventional television images, which could change rapidly and were convenient for keeping fresh images on the screen while refocusing or changing magnifications, but the resolution was poor. Sometimes the video camera could be connected to a frame grabber board

installed in a computer. The frame grabber would “snap” an image and feed it to software that would display the image on a separate computer monitor.

Digital cameras, which have vastly superior resolutions and which are quite fast, are rapidly replacing video cameras. They can show “live” images at nominally reduced resolutions on the computer monitor. Once the object is framed and focused, a higher quality image can be acquired or “snapped.” The price of these cameras is becoming cost effective and resolutions of 3 megapixels or more are common at prices less than \$ 4,000 as this Guide was written. The camera input can be fed to free software provided with the digital camera as part of a complete package, or to a separate image processing software package. In the past there inevitably were compatibility problems with software and cameras and all the usual annoying nuances of computer programs. Contemporary digital cameras and software packages are much more user friendly and the fractographer need not be a computer expert. Nevertheless, it probably is best to have digital cameras and their software installed by a camera or microscope company representative who has experience trouble shooting installation and compatibility problems.

3.5 Discussion Stereomicroscope

Figure 3.12 shows a “discussion stereoptical microscope” that enables two observers to simultaneously see the identical image. A beam splitter diverts half of the light to the auxiliary viewing station. The configuration shown is a side-by-side model which is preferred for most fractographic analysis. Discussion microscopes often have a built in moveable pointer that can be seen by both observers. Discussion microscopes are extremely valuable for training new fractographers or for showing features to clients or colleagues. The auxiliary viewing station should also have adjustable eyepieces so that the secondary observer can adjust the focus to match the focus of the primary observer. A camera port can be included with another beam splitter so that the image can be projected onto a monitor at the same time it is viewed through the eyepieces.

3.6 Illumination Sources

Figure 3.13 shows some options for specimen illumination. Bright light sources are advisable to facilitate the examination of dark ceramics and the use of high magnifications. The most common illumination source for fractographic analysis is a ring light that clamps to the objective lens. This provides uniform lighting but may not be effective in highlighting ridges or valleys. Directional illumination can be achieved with one or more fiber optic goose-



Figure 3.12. A discussion stereoptical microscope that allows two observers to simultaneously view an object. Note the very tall post (800 mm) on which the microscope body is mounted. The entire assembly can be moved up or down as required to facilitate examination of very large or very small specimens. Beam splitters in the optical path enable simultaneous viewing through the eyepieces at the same time the digital camera views the object. The digital camera is connected to a computer and monitor.



Figure 3.13. Illumination sources for use with a stereomicroscope. Clockwise from the middle left: a ring light intended to be clamped to the objective lens, a ring dark light illuminator on an adjustable stand, a line light source on a stand, and a transmitted light platform.

neck light guides that direct an intense light beam onto the fracture surface at an angle. Dual gooseneck guides from a single light source as shown in Figure 3.14 are convenient so that one guide may be used for illuminating the key features while the second can be used as filler. Vicinal illumination, or low angle grazing illumination, is very effective for accentuating peaks and valleys on fracture surfaces as shown in Figure 3.15. The ability to adjust the angle of the illumination source is important. Easily adjustable holders are a great time saver.



Figure 3.14. Dual "gooseneck" fiber optic light guides allow flexibility in directional illumination.

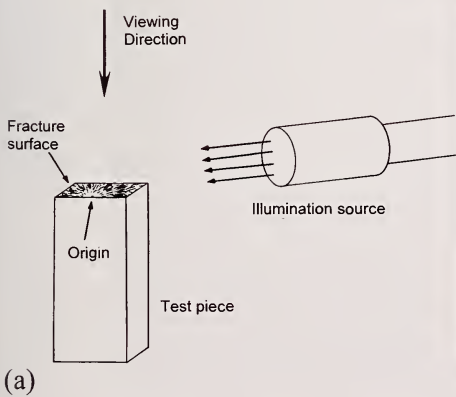


Figure 3.15. Low angle or "vicinal" illumination (a) is effective in highlighting fracture surface topography as shown in (b), which is the fracture surface of a ceramic rod broken in flexure.

Dark field illuminators such as shown in Figure 3.16 may also be handy. The dark field illuminator is similar to a normal ring light, but the light is directed sideways from the ring periphery towards an object in the middle. This sideways illumination accentuates subtle surface features and scratches.



Figure 3.16. Dark field illumination of the fracture surface of a fractured steel railroad coupler pin. The arrow points to a fatigue crack.

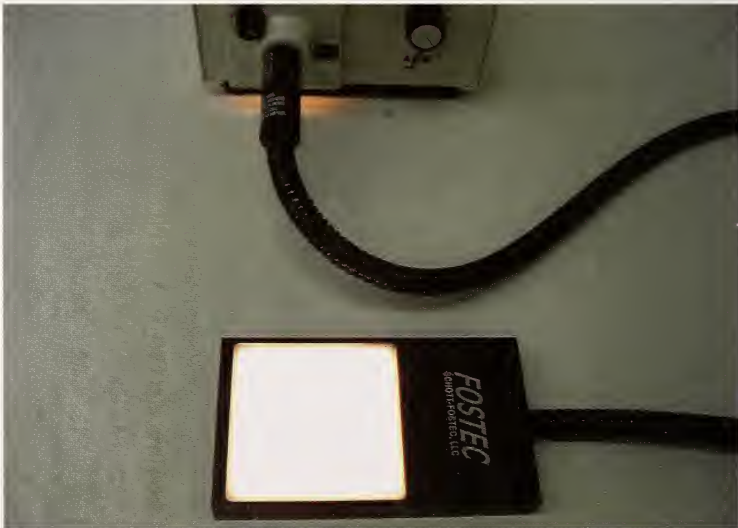


Figure 3.17. Illuminator plate for transmitted illumination.

Some stereomicroscopes have illumination sources in the base for transmitted illumination that is useful for glasses and transparent ceramics. Illuminated bases as shown in Figure 3.17 may also be used. A transmitted light stage can be improvised as shown in Figure 3.18.



Figure 3.18. *An improvised stage made of Plexiglas, white paper, and a mirror for transmitted illumination. A fiber optic light source can be directed onto the tiltable inclined plane so that light is reflected up through a specimen mounted on the top.*

Some translucent or transparent specimens may be illuminated by transillumination. The fiber optic light source is directed through the material from one side. Usually the side surface nearest the light guide will be washed out, but internal features and subtle fracture surface features may stand out elsewhere on the fracture surface. Figure 4.1 in the next chapter shows an example.

Polarizers may be valuable for examining transparent materials. They may reveal residual strains in glasses or twins in single crystals (Figure 3.19). One polarizing filter may be placed between the transmission light source and the specimen and an analyzer (another polarizing filter) attached to the objective lens. The analyzer can be rotated as required to achieve the desired color or brightness differences.

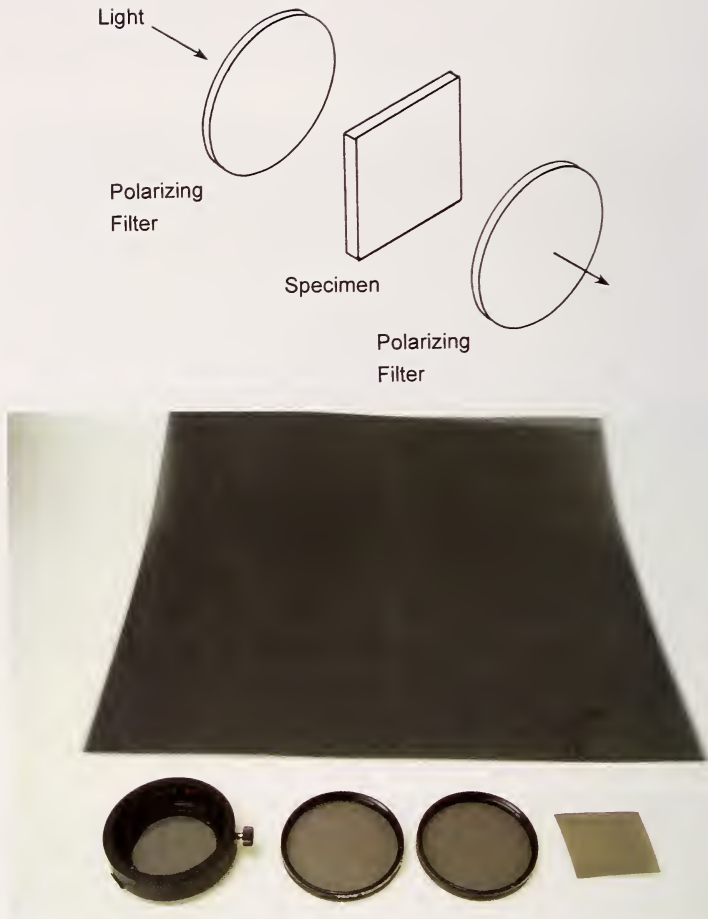


Figure 3.19. Crossed polarizing filters or plastic sheets. Polarizers can either be dedicated accessories for the stereoscope, or can be improvised from ordinary single lens camera lens attachments or sheets of plastic polarizing film.

3.7 Coatings

Coatings may be applied to specimens that have poor reflectivity or which are translucent and scatter light from beneath the surface thereby washing out the surface detail. A thin layer of gold or platinum may be sputtered onto the specimen surface in a small vacuum chamber. Such equipment is commonly used to prepare a specimen for scanning electron microscope examination, but the coating may enhance optical examinations as well as shown in Figure 3.20. A simpler expedient that works very well for many white or gray ceramics is a

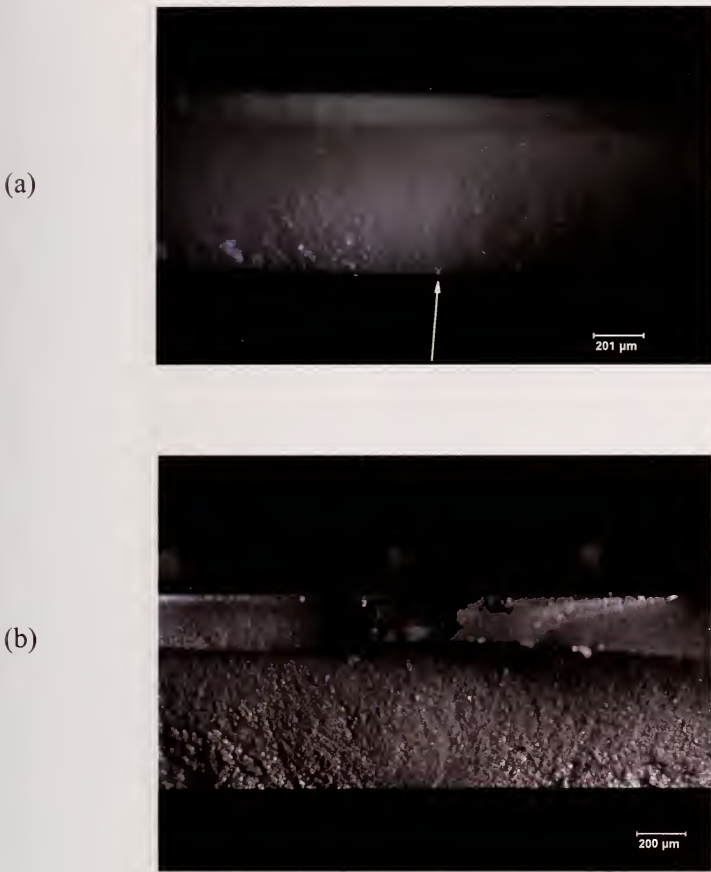


Figure 3.20. Two views of a fractured yttria-stabilized tetragonal zirconia disk with reflected light illumination. (a) shows the uncoated fracture surface and (b), the same region after a thin gold coating was applied.

common felt tip pen as shown in Figures 3.21 and 3.22. Green felt tip pens work the best, partly because the eye is most sensitive to green wavelengths, but probably also due to the character of the green dye.^b The dyes can easily be removed with ethanol and the process repeated in a matter of seconds. Most of the dye will come off, but some may penetrate into crack branches or undercuts in the fracture surface and may be more persistent. Additional dye and staining techniques are discussed in section 3.24 later in this chapter.

^b Paper mate Flair, 1.1 mm, Sanford Corporation, Division of Newell, Rubbermaid

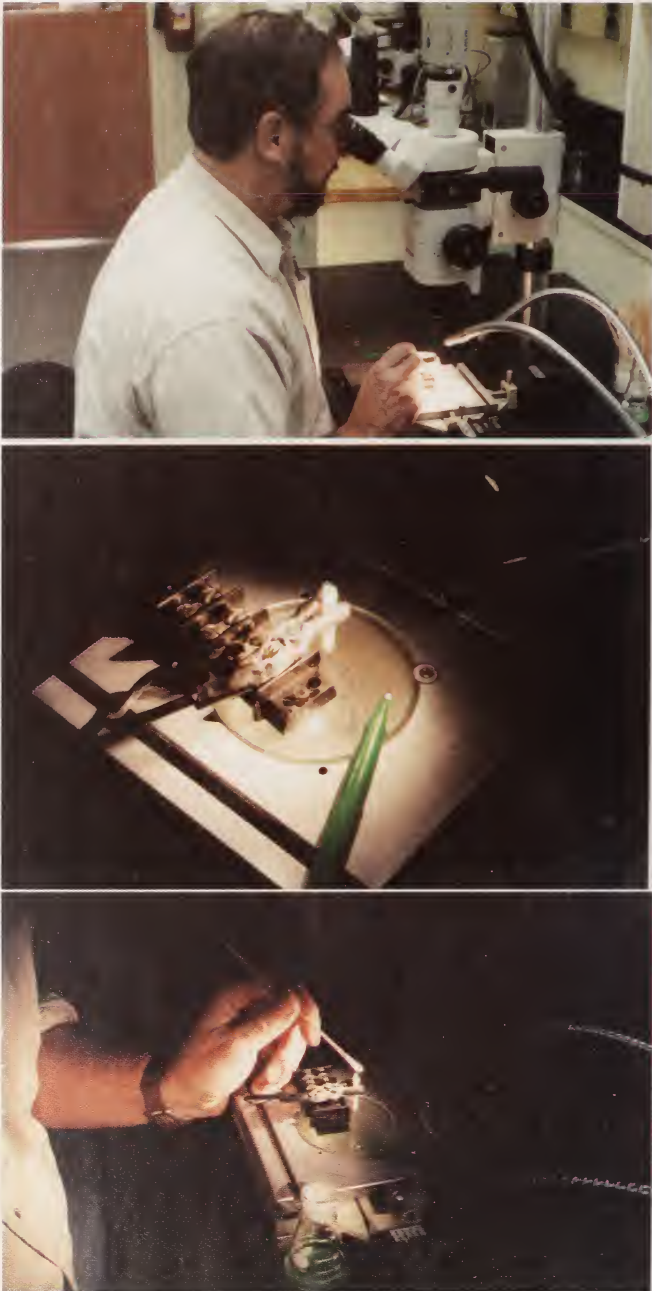


Figure 3.21. A simple but effective coating technique for white ceramics is to stain the surface with a green felt tip pen. The staining can be watched in real time through the microscope. The green stain can be easily removed with ethyl alcohol on a cotton swab applicator and the process repeated.

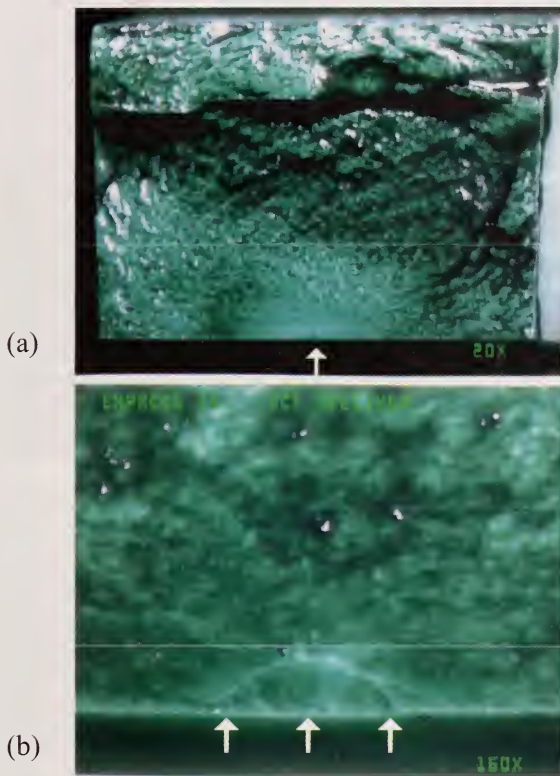


Figure 3.22. An example of green dye staining on a dental glass ceramic bend bar. (a) shows the entire fracture surface illustrating how the stain drains into valleys and accentuates hackle lines and ridges and how easily the fracture mirror region stands out (arrow). The bottom view shows the fracture origin: an artificially created surface crack (arrows) made by Knoop indentation for a fracture toughness measurement. The pictures were medium resolution video prints and the thin horizontal line is an artifact from a defect in the print head.

3.8 Size Measurements

Sizes may be measured by means of a graduated reticule in a microscope eyepiece. The graduations must be calibrated by means of a stage micrometer such as shown in Figure 3.23. Users should be cautious about the accuracy of stage micrometers. Some are rudimentary and only meant to furnish an approximate magnification for photography and can be as much as several percent in error. Others may be very accurate. If a stereomicroscope has a zoom capability, it is best that the body have discrete click steps or detents so that precise magnifications can be calibrated and recorded at the discrete steps.

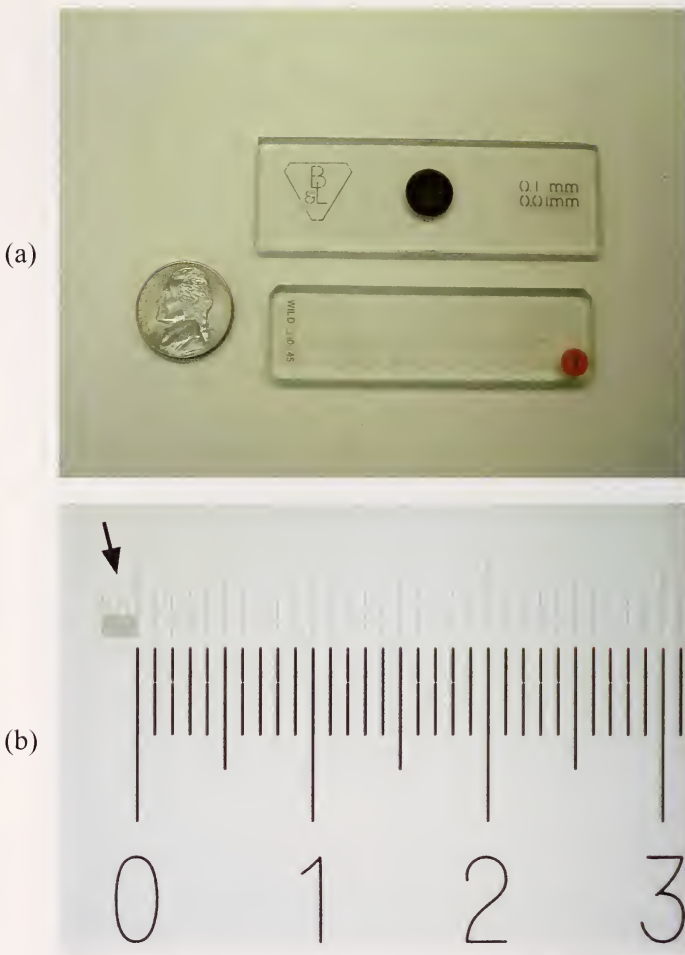


Figure 3.23. Two stage micrometers (a). A close-up of the bottom one is in (b). The numbers show 1 mm spacings. The thin lines on the top right are 100 μm apart and on the top left (arrow) are 10 μm apart. This model was accurate to an amazing 0.01 %.

A powerful accessory to a microscope is a traversing X-Y stage with micrometer positioning heads such as shown in Figure 3.24. This accessory is especially valuable for precisely aligning a specimen in the field of view, particularly when photographing an image. The micrometer heads, in conjunction with a crosshair in one eyepiece, also facilitate accurate size measurements of features. One advantage of such a system is that if the fracture surface is viewed directly from above through both eyepieces, and the fracture plane is horizontal, then the micrometer-measured sizes need not be

corrected for foreshortening, as long as the surface being examined is parallel to the X-Y stage.

If size measurements are made on recorded images, care must be taken to ensure that the optical axis of the camera is perpendicular to the fracture surface plane. A little more care is needed with a camera mounted on a stereoscope. Since the stereomicroscope camera views the fracture surface at an angle to the fracture surface, its view may be foreshortened. The specimen may have to be tilted a few degrees to obtain a true view of the size of the fracture surface.

An additional advantage for the X-Y stage measurement is that the size readings are independent of the magnification used to view the specimen. In contrast, images captured by the camera must be calibrated for the exact magnification.

One drawback to the traversing stage is that it takes up vertical space and hence the microscope body must be moved up higher and possibly may limit the working range under the objective if the microscope is mounted on a short post. As noted above, stereomicroscope for fractographic examination should be mounted on tall posts for maximum versatility.



Figure 3.24. A X-Y traversing stage with digital micrometer heads is very convenient for positioning a specimen and also for making accurate size readings.

3.9 Compound Optical Microscope

Compound optical microscopes such as shown in Figures 3.25 and 3.26 may be used for fractographic analysis, but are less versatile than stereomicroscopes. Compound microscopes are best suited for small specimens with relatively flat surfaces. They magnify much more (up to 1600 X) than a stereomicroscope, but three-dimensional topographical effects are lost. Virtually all work is now done with air lenses. Oil immersion lenses are no longer needed.

Objective lenses from 5 X to 100 X may be used in the lens turret, but in practice the limited depth of field makes it difficult to see a fracture surface in focus at larger magnifications. Only portions of a fracture surface may be in focus even at lower magnifications. Working distances are also very small, and care must be taken not to contact the objective lens with a specimen. Long focal length objectives are ideal. These have greater working distances, but at the cost of some loss of light collecting power and resolution. The author uses a compound microscope with long focal length lenses. For example, the 100 X objective has a 1.3 mm clearance and 0.8 numerical aperture. Some 100 X lenses are available with working distances as long as 13 mm, but these have lower numerical apertures (0.5 to 0.6) and thus less resolving capability. The clearance between a stage and the objective lenses may also preclude examination of large fractured pieces. Vicinal illumination is difficult to achieve with compound microscopes, especially at greater magnifications.

Dark field illumination may be effective for examining cleavage planes in single crystals. Direct reflected light illumination may be too bright or wash out details due to the mirror-like reflection from a cleaved crystal surface. Dark field illumination blocks the central portion of the illumination light coming through an objective, allowing only oblique rays in a ring to strike the specimen. Only the light that is scattered by features on the fracture surface is reflected back up into the objective for the viewer to see. Fracture surfaces appear as small bright spots and lines against a dark background. Dark field can highlight subtle cleavage steps and make the symmetry of a fracture mirror more evident.

Compound microscopes are useful for measuring very small features, such as tiny fracture mirrors in optical fibers or other strong test specimens. Compound microscopes can also be used in transmitted illumination mode.

Compound microscopes may be very useful for examining fine detail in replicas. Thin polymer replicas of curved surfaces may be flattened by taping the ends of a replica on a glass microscope slide, or the replica may be placed between two glass slides so that the curved surface can be flattened and examined at high magnification in either transmitted or reflected light.

Compound microscopes are essential for examining polished specimens for microstructural analysis, a useful adjunct to the fractographic analysis.



Figure 3.25. Compound reflected light microscope. Although the microscope has twin eyepieces, they both view the same image collected by the objective lens. Overall magnifications can be as much as 1000 X, but the working distances and the depths of field are very small. Only relatively flat specimens may be examined.

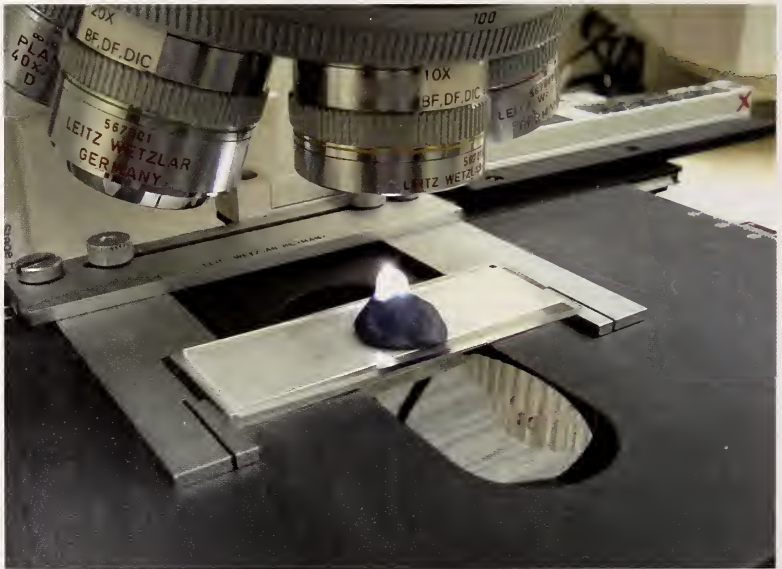


Figure 3.26. A research compound microscope with a digital camera and computer installation. Linear encoders with a 1 micrometer resolution are attached to the traversing X-Y stage and facilitate rapid size measurements. The instant film camera on the top was a common accessory in the 1970s to 1990s, but has been rendered obsolete by digital cameras such as the one marked by the arrow. A fractured glass rod mounted on blue polymeric clay is on the stage. The fracture mirror can be viewed through the eyepieces at the same time it is projected on the monitor.

3.10 Compound Microscope with Digital Camera and Image Z-axis Scanning

A new adaptation of a compound microscope is to direct the image from the objective lens directly to a digital camera. An eyepiece is not fitted. The camera software interprets which portions of the field of view are in focus. The microscope (or the sample mount) Z-position is changed slightly, and the process repeated. Gradually a three-dimensional virtual image of the surface is constructed by the computer software and a pseudo three-dimensional rendition is displayed on a computer monitor. This process effectively increases the depth of field of the microscope system, thereby overcoming one of the great shortcomings of a common compound microscope. In principal, a high power, high numerical aperture objective (*e.g.*, 100 X, 0.9 NA) could be used to examine surfaces at much higher magnifications than possible with a stereoptical microscope. Multiple images of different regions can be digitally stitched together to create image mosaics thereby increasing the effective field of view. An additional advantage is that once the surface topography is digitally stored, it can be tilted and rotated. Various quantitative analyses of the surface topography can be conducted. Drawbacks may be that an image may take longer to acquire, oblique or vicinal illumination may be difficult or impossible to do, and the human eye is no longer in the loop. Color and reflectivity effects may be lost.

3.11 Digital Image Processing and Reconstruction

Digital image technology is revolutionizing techniques for processing images. As an example, inexpensive commercial software now overcomes the depth of field limitations of common microscopes. A series of ten or so JPEG or TIFF digital images of an object are taken by an ordinary digital camera with the focus adjusted slightly between each photo. Only a portion of the object is in focus in each image. The software evaluates each image, assesses which portions are in focus, and then constructs a composite final image with all elements in focus. It does not matter whether the images are from a camera mounted on a tripod, an optical microscope, or a scanning electron microscope. Figures 3.27 and 3.28 show examples. The practical ramifications of this technology is that infinite depths of field are achievable with all microscopes, dramatically enhancing the versatility of all microscopes.

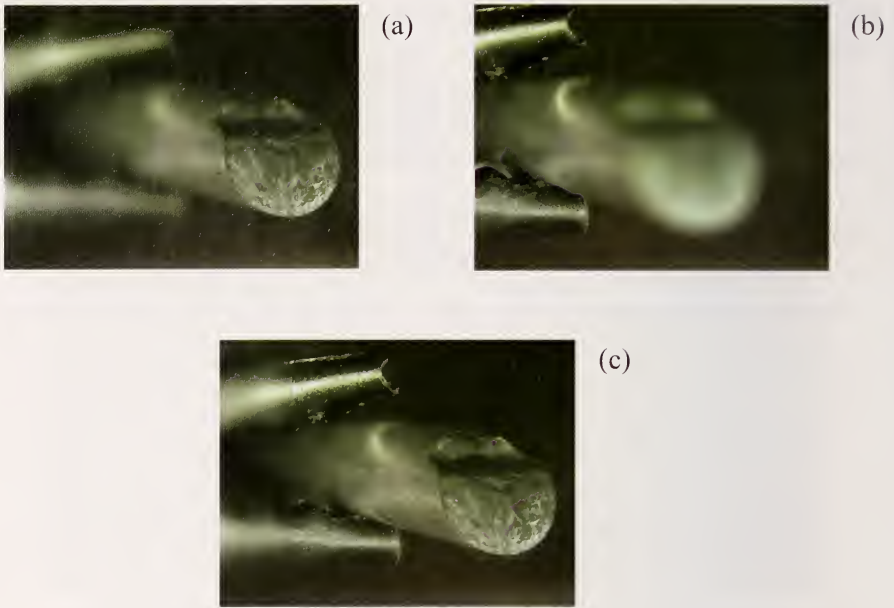


Figure 3.27. A silicon nitride 6 mm diameter rod broken in flexure (801 MPa). (a) and (b) show stereoptical microscope digital images. Even though the microscope has great depth of field, the cantilever curl and holder are out of focus in (a). (b) shows the holder in focus. (c) shows the digital reconstructed composite image from 15 separate images.

3.12 Replication Equipment

Replicas of fracture surfaces may be valuable in some instances. Some fractured parts may be so large or unwieldy that it may be difficult to position them under an optical microscope. In other instances, the fractured part may be a critical piece of evidence that cannot be removed to the fractography laboratory. Replicas can also be an important backup source of critical fracture surface information if the component is lost or damaged.

In other cases, fracture surface features may actually be easier to observe on the replica than on the original surface. In many transparent or translucent ceramics such as porcelains or coarse grain ceramics, light scattering from below the surface can obscure the fracture surface details. For example, subtle wake hackle lines behind pores may be easier to see on replicas. Curved surfaces can be made more amenable to high magnification examination, since a replica can be flattened. Since the replica usually is a negative of the fracture surface, depressed features such as pores or cracks are converted to raised

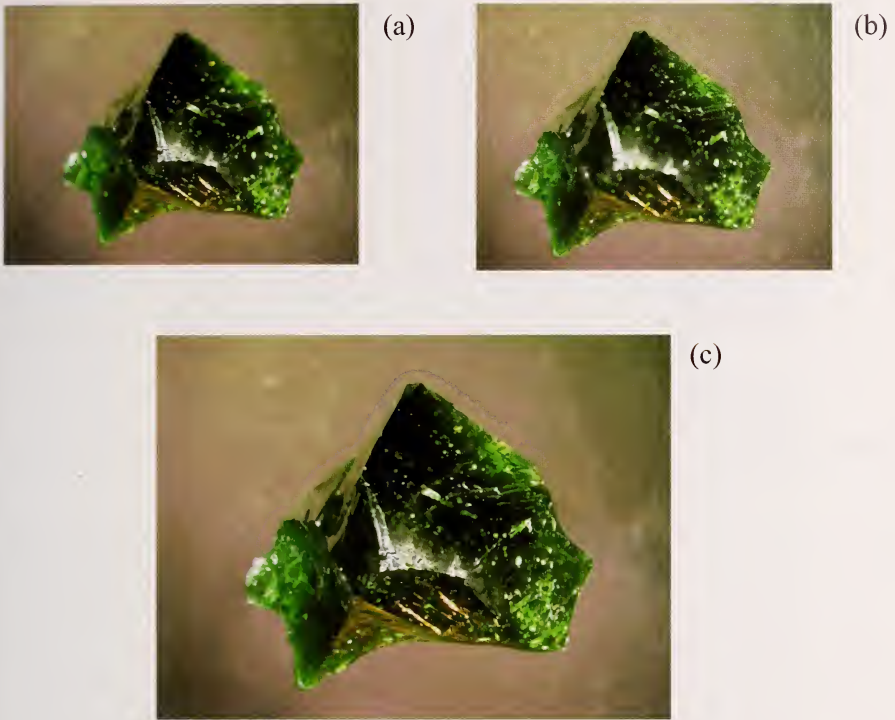


Figure 3.28. A 25 mm glass fragment. (a) and (b) show typical images made by a stereoptical microscope at low magnification. Although the microscope has excellent depth of field, portions of the fragment are out of focus in each view. (c) shows the digitally reconstructed image made from 16 separate images focused from the top to bottom of the fragment. The digital reconstruction took less than 1 minute.

features on the replica that sometimes are more easily imaged in the scanning electron microscope.

Cellulose acetate tapes or films (such as used in transmission electron microscopy) are convenient replica materials that may be made at room temperature as shown in Figure 3.29. The specimen surface should be clean. A short strip of tape is cut from the sheet or roll and then wetted with acetone. Thick tapes or films may be immersed in acetone for 10 s to 15 s, whereas thin tape may be wetted by a few drops from an applicator. The specimen surface may also be wetted by acetone, although that step is not always necessary. The tacky film or tape is applied to one side of the fracture surface and then is gradually brought into contact with the remainder. The replica material



Figure 3.29. Thin cellulose acetate replica tape, acetone, applicator, and bend bar specimens.

should be applied so as not to entrap any air. Pressure is firmly applied to the replica for 15 s up to two or three minutes as required, taking care to not slide or shift the replica material. A small pad (or if the specimen is small enough, a finger or thumb) may be used to apply the pressure. The pressure is carefully removed without disturbing the replica which remains in contact with the fracture surface for 10 min to 15 min more drying time. The replica is peeled from the fracture surface (or it may pop off) and may be trimmed with scissors or mounted on a glass microscope slide such as shown in Figure 3.30. Replicas made with polyvinyl chloride or silicon elastomers may also be used, but these require heating of the specimen as described by Fr chet te.¹ If PVC is used, the specimen is heated and the PVC applied with a Teflon rod.

Replicas may be viewed with reflected or transmitted illumination in an optical microscope. Gold or carbon coatings can be sputtered onto a replica. A detailed section on replication techniques is in the transmission electron microscopy (TEM) chapter in the ASM Handbook on Fractography.²

Since many replicas are negatives of the fracture surface, it is prudent to label them clearly as to their location on the component, lest the fractographer confuse top-bottom, or left-right orientations. Special care should be taken to avoid artifacts in the replicas such as trapped air pockets, tears, or handling artifacts. Replicas should be kept clean and carefully stored in containers.

An exception to the rule about replica orientation applies to dental replicas that are actually *positive* duplicates as shown in Figure 3.31. Extraction of a damaged dental crown typically requires its destruction. Therefore it is prudent to make a replica before the crown is extracted.

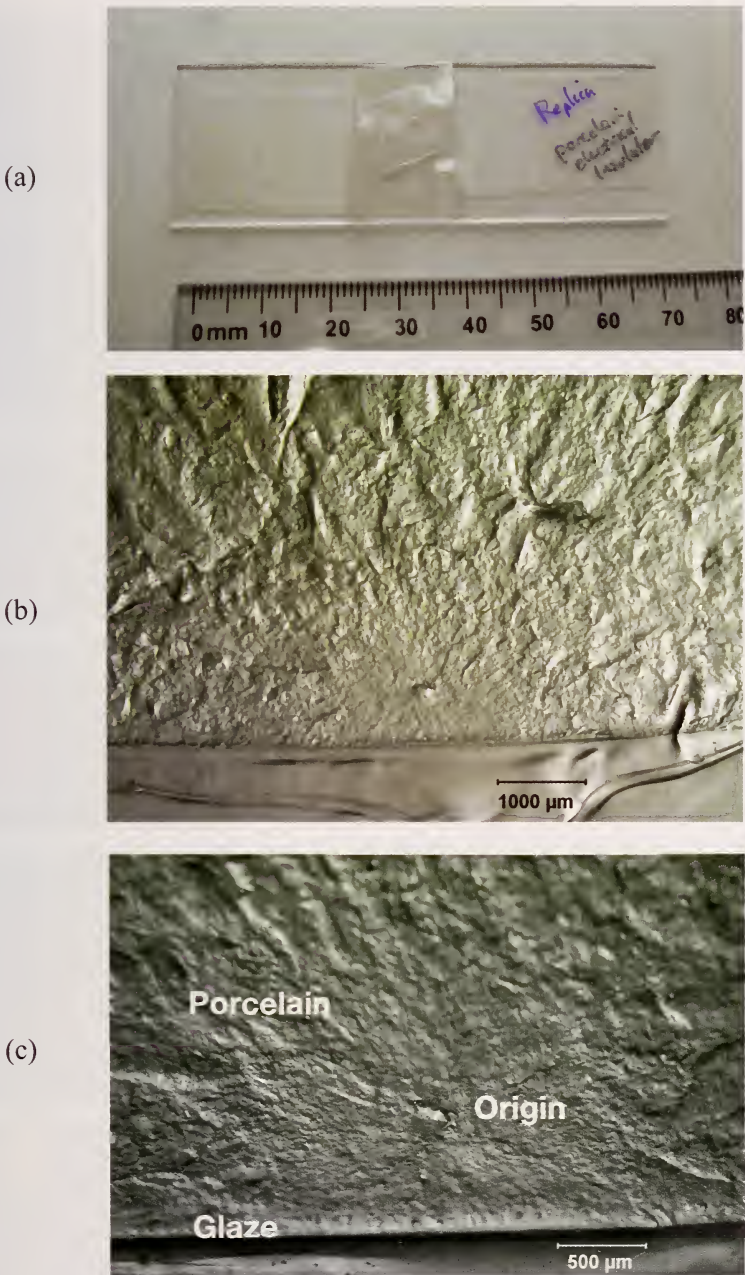


Figure 3.30. Cellulose acetate replica of a fracture surface of a porcelain electrical insulator. (a) shows the replica taped to a glass microscope slide. (b) and (c) show close-ups of the replica which reveals the mirror and an inclusion flaw.

(a) Top view of the fractured all-ceramic crown (first upper left molar) in the patient's mouth. The broken crown is cleaned with alcohol on a cotton swab.



(b) The crown is water spray rinsed and air dried.



(c) A light body precision impression material is injected around the fracture surface.



(d) The whole crown is covered with more impression material.



(e) The mold is removed.



(f) A positive replica is cast with epoxy resin and gold coated for SEM examination.



Figure 3.31. Steps in the preparation of a dental replica that is a positive duplicate of a fractured crown. Figure 6.50 has additional views of this fractured crown.

(Photos and technique courtesy of S. Scherrer, Univ. Geneva)



Figure 3.32. A conventional scanning electron microscope.

3.13 Scanning Electron Microscope

Despite the versatility of optical microscopy, there inevitably will be cases where the fracture initiating flaw is too small to be clearly discerned and the scanning electron microscope (SEM) is required (Figure 3.32). The SEM is a complementary tool to the optical microscope. They “see things” differently. It is best to examine specimens with the optical microscope first, since much valuable information such as color, reflectivity, and internal flaws in translucent or transparent materials cannot be detected by the SEM. Nevertheless, the SEM is a versatile tool that can view large portions of a specimen at low magnifications and yet instantly zoom in for high-resolution close-ups of regions of interest without adjusting the specimen. It can also provide compositional information. The practical limits of magnification for fractographic analysis are of the order of 10 X to 20,000 X.

Modern SEMs are not difficult to use and materials scientists and engineers can perform their own routine examinations without the need of an expert operator. The advent of commercial SEMs and transmission electron microscopes in the 1960s led to a quantum jump in the quality of fractography of ceramics and glasses. Researchers and engineers could finally see and characterize the strength-limiting flaws that previously were too small to be clearly discerned with optical microscopy. It is fair to say that the SEM opened up a whole new world of possibilities for fractographers, processors, and

◆ Fractography of Ceramics and Glasses

mechanical testers and led to many major advances in materials science and engineering.^c

The SEM uses electrons as a signal source and, since the probe size can be made smaller than the wavelength of light, smaller features can be resolved and much greater magnifications achieved. A vacuum is necessary to remove gas that would interfere with the electron beam. The SEM has superb depth of field over a broad magnification range. For a working distance of 20 mm, the depth of field may be 0.4 mm at 100 X or 40 μm at 1000 X and 4 μm at 10,000 X.³ Sometimes the SEM is preferred for this reason at even low magnifications (100 X to 500 X) that are well within the range of optical microscopes. On the other hand, SEM images often look flat and tend to de-emphasize large surface topography changes. The SEM image can also be deceptive and it may be confusing to interpret whether a feature projects above the surface or is a depression below the surface. Stereo SEM viewing, described below, can help solve this dilemma. A great advantage of the SEM is that compositional analysis can also be done using accessories that detect X-rays emitted from the fracture surface.

Specimens must fit into the vacuum chamber and are usually cut and mounted on a small aluminum stub that will be placed into the SEM as shown in Figure 3.33. The SEM should have a large opening to accommodate broken fragments and test specimens without having to cut or trim them to small sizes. The stage has external controls that permit the specimen to be positioned in X, Y, and Z directions, rotated, and tilted. The size of the chamber and the mount station, plus the clearance to the electron optics all put limits on the size of specimens than can be examined. A good SEM for fractography has a large chamber, a large entry way, and can pump down with a minimum of difficulty.

Specimens on an aluminum stub are shown in Figure 3.33(b) and 3.34. It is convenient to cut the specimens so that they will sit square and facing upward. Irregular specimens can be propped up by small metallic pieces. It is best to cut multiple specimens to have similar lengths to minimize refocusing time when viewing in the SEM. A small laboratory cut off wheel with a thin diamond wafering saw is also handy for cutting long specimens into manageable lengths for the SEM. The specimens should be cut so that the fracture surface is approximately perpendicular to the incident beam in order to avoid

^c The coincidental advent of modern fracture mechanics in the late 1950s, described in a later chapter, also led to major breakthroughs in the study of ceramics and glasses.

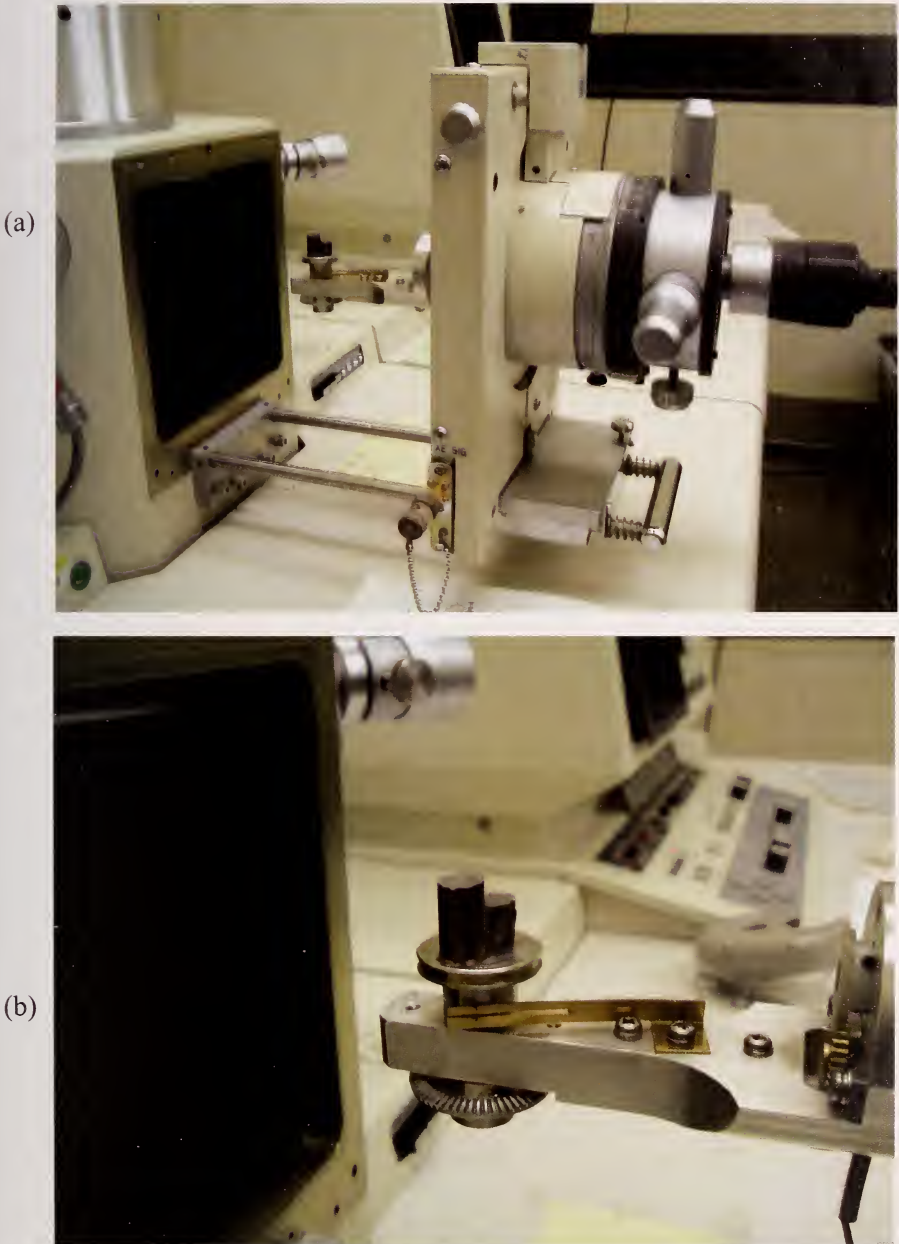


Figure 3.33. (a) shows an open SEM vacuum chamber showing the specimen station on the left and the positioning controls on the right, outside of the chamber. (b) shows a close up of the two fracture specimens on their stub on the examination mount. Both fragments had to be cut from longer pieces to fit in the chamber. This model has a large opening and the stage can accommodate specimens as tall as 25 mm.



Figure 3.34. Two matching fracture halves of a broken round tension specimen on a stub in a protective plastic box. Silver paint was used to attach the specimens to the stub. Ideally, the halves should have been cut to similar lengths to save time refocusing in the SEM.



Figure 3.35. SEM specimen preparation tools. Clockwise from the top left are two SEM length calibration standards, two silver paint bottles, a double-sided conductive adhesive tape roll, two sheets of double-sided conductive adhesive disks, and an assortment of aluminum stubs.

distortions from foreshortening. Once in the SEM, the specimen can be tilted to enhance the emissions and signal responses if necessary.

Figure 3.35 shows some common accessories and tools for SEM examination. The specimens must be cleaned carefully of greases, dust, or debris. It can be exasperating to find a tiny piece of dust right on top of the origin site when the specimen is in the chamber. Soaking the specimen in a small beaker of acetone in an ultrasonic bath for a minute or so is often effective. After removal, a gentle blast of compressed air can eliminate any acetone residue. Sometimes it may be sufficient to swipe the fracture surface with a cotton swab soaked in acetone. Small trays or plastic boxes are convenient for holding the specimens and protecting them from contamination prior to examination. Special containers are available for mounting stubs. The best procedure is to keep the specimens as clean as possible from the moment the fragments are recovered.

There must be a good electrical contact between the specimen and the stub. The specimen can be affixed to the stub by silver paint or by conductive carbon double-sided sticky tape. If multiple specimens are placed on a stub, *it is a good idea to make a hand drawn sketch or map to show which specimen is where on the stub*, lest the viewer become confused when viewing the array in the SEM. Furthermore *all the specimens should be oriented in a similar way*. For example, if a series of bend bar fracture surfaces are being examined, they all should have their tensile surfaces facing the same way. Otherwise, much time can be lost getting oriented or searching the wrong areas during the SEM session. A set of optical photos of the fracture surface can be handy when the specimens are examined in the SEM.

The next step for most SEM examinations is to apply a thin 5 nm to 40 nm conductive gold, gold-palladium, or carbon coating by means of a sputter coater (such as shown in Figure 3.36) or a thermal evaporator. The former is preferred for rough surfaces. The coatings are needed for ceramics and glasses in order to eliminate surface charge build up from the electron bombardment. For most applications, the coating does not interfere with the image. A coating is not needed for conductive ceramics in the SEM or for examinations with low accelerating voltages (1 keV to 5 keV). Low accelerating voltage examinations may have a diminished resolution, however. Carbon coatings are used if X-ray information of lighter atomic weight elements is desired. Coating with gold or carbon is a simple procedure that only takes a few minutes. Sometimes a gold coating may be applied to facilitate some optical microscopy examinations, since the coating eliminates reflected light that is scattered back up through a fracture surface in translucent or transparent speci-



Figure 3.36. A gold sputter coater used to apply conductive coating.

mens. The sputter coater will preferentially coat from one direction, and sometimes it is advantageous to position the specimen and the stub at an angle so that shadow coating will occur on the surface. Slight charging on some edges of the fracture surface may enhance the image by promoting contrast. Coating along the specimen sides may be incomplete, so sometimes it is wise to add a thin silver paint line along the specimen sides from the fracture surface to the stub. Of course, the silver paint should be kept well away from the fracture origin or any features of interest on the fracture surface. The conductive coating step may be omitted for some modern SEMs that operate at low accelerating voltages and low vacuums as described in a later section on environmental SEMs. Additional details and tips on coatings for SEM examination may be found in the paper by Healy and Mecholsky.⁴

The SEM can be operated in several modes. A focused beam of high-energy electrons (typically 1 keV to 30 keV) is rastered over a rectangular portion of the specimen. Some electrons interact with the specimen surface and some penetrate into the volume. Figure 3.37 shows that the interaction volume is larger than the size of the incident beam, which may be as small as 10 nm diameter.⁵ The three most important signals are secondary electrons, backscattered electrons, and X-rays. Secondary electrons reveal the surface topography. Backscattered electrons give a combination of the topography and atomic number and crystallographic information. X-rays reveal compositional information.

The initial working distance can be adjusted to enhance the field of view and the depth of field. Long working distances allow a lower minimum magnification which is sometimes helpful in initial orientation or in photographing the whole part or as much as possible. A longer working distance also allows the specimen to be tilted more. On the other hand, longer working distances reduce resolution and may reduce X-ray signal acquisition. Image clarity is also affected by specimen tilt. As noted above, having the surface perpendicular to the incident beam minimizes foreshortening, but secondary electron and X-ray collection can be maximized by tilting the specimen towards the detectors.

Initial inspections on a cathode ray tube (CRT) display often are typically with 500 line scans, but when a image is recorded on film, a higher resolution CRT with 2000 or more line scans is used. The raster of the beam on the specimen is synchronized with that of the electron beam that rasters across the display CRT.

The secondary electron mode of operation provides the best spatial resolution and produces a surface topographical image. Secondary electrons are low energy electrons (10 eV to 50 eV) primarily produced from the material close to the surface. Since they are low energy, a positively charged detector off to one side can capture the emitted electrons for the image. These electrons may

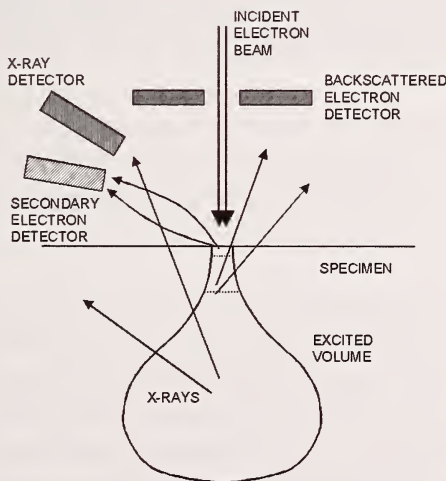


Figure 3.37. The electron beam interacts with the specimen surface and volume creating emissions that may be analyzed. Signals are generated in all directions, but they come from different depths of the material. The beam is rastered over the surface and an image is sequentially formed.

even follow a curved trajectory from the surface to the detector. Edge charging can be a problem with very rough surfaces or those with sharp corners and cracks, in which case gamma adjustments to the image may help.

Gamma adjustments can suppress bright areas and enhance dark areas. For some edge charging cases, backscattered imaging may be preferred. In the early days of SEM, the sample was tilted at 45° to enhance the secondary electron signal responses, but this caused foreshortening of the image. Contemporary SEMs typically examine specimens with the fracture surface perpendicular to the electron beam and the detector well off to the side.

Backscattered electrons are higher energy electrons (5 keV to 40 keV), up to the energy of the incident beam and are emitted from a larger volume than the secondary electrons. The backscattered electrons travel in straight lines and are registered by a different detector that may have to be slid into proximity with the fracture surface. They often have a central hole for the incident electron beam. Backscattered electrons include both topographical and compositional responses. Detectors can be split ring or four quadrant (or more) versions and, by turning different elements on or off in the detector, it is possible to emphasize topographical or compositional information. Backscattered electron imaging is effective in detecting phase distributions in heterogeneous or composite microstructures and also aberrant features such as inclusions or second phase concentrations. Such information is often completely missed by secondary electron imaging.

Figures 3.38 through 3.40 show matching secondary electron and backscattered electron images of fracture origins. Figure 3.38 shows how the backscatter mode can even help highlight a controlled semi-elliptical flaw made by a Knoop indenter.

X-ray emissions provide valuable information about the elemental composition. This energy-dispersive spectroscopy by X-ray analysis (EDS or EDX) is especially useful for detecting and characterizing inclusions, second phase variations, or compositional inhomogeneities, which all may act as strength-limiting flaws. The analysis is over a region of the order of size of a few micrometers, but penetrates into the interior $1\ \mu\text{m}$ to $2\ \mu\text{m}$. With most SEMs and with coated surfaces, elements from sodium ($Z = 11$) or heavier can be detected simultaneously. Lighter elements such as boron or carbon cannot be readily detected. A better resolution of the lighter elements is obtained with very thin gold or carbon coatings, or even uncoated specimens with low accelerating voltage.

(a)



(b)

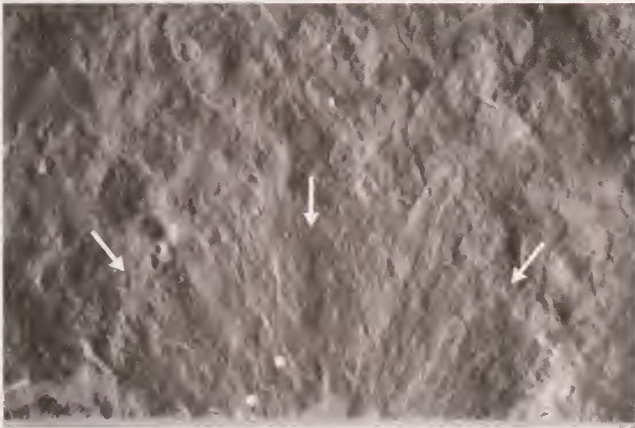


Figure 3.38. Comparative secondary electron (a) and backscattered electron (b) images of the fracture surface of a Knoop semi-elliptical precrack in a silicon nitride fracture toughness test specimen. The edge charging in (a) emphasizes certain features, but (b) shows that the flattening effect of the backscattering mode tends to better reveal the overall crack (arrows).

An X-ray scan may require several minutes as the electron beam illuminates the surface and the detector accumulates a sufficient signal of a range of emitted X-rays. A typical scan appears as shown in Figure 3.41b where signal intensity is plotted versus X-ray energy or wavelength. The specimen response is compared to known characteristic wavelengths of the various elements to identify which elements are present. A common procedure is to scan the critical feature, then rescan a different area away from the feature and compare the patterns. The accelerating voltages should be high enough to activate emissions from the elements. This should be 1.5 times the threshold energy of the element. So for example, for copper $K\alpha$ X-rays of 8.0 keV, it is best to use an accelerating voltage of 12 keV or greater. Otherwise if the volt-

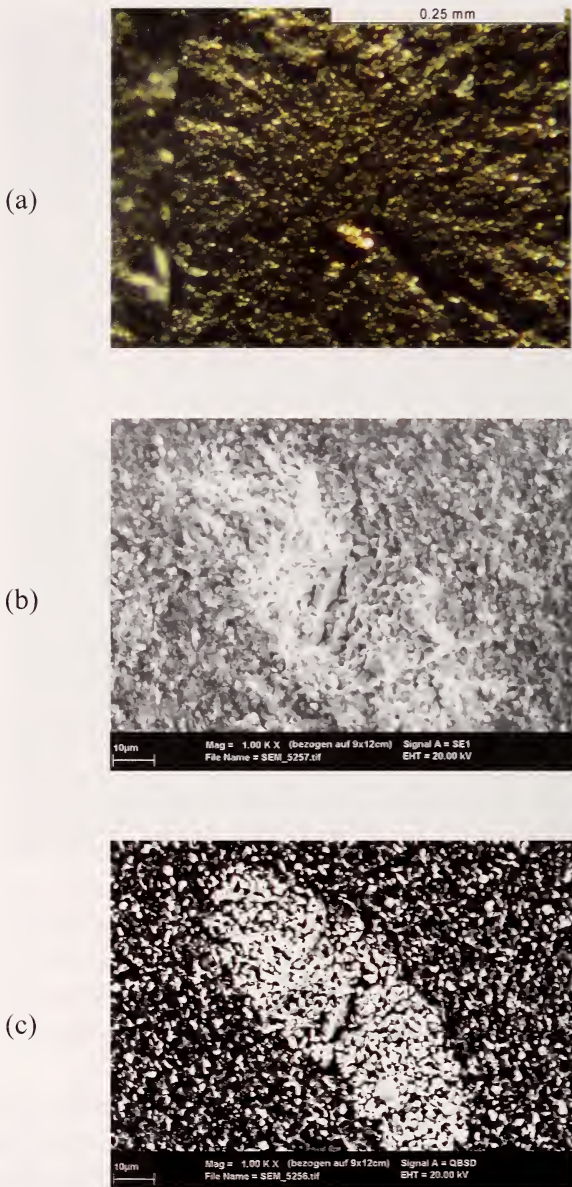


Figure 3.39. Backscattered mode electron scanning electron microscopy is effective in showing compositional difference of fracture origins flaws relative to the background. (a) is an optical image of a silicon nitride with 30 mass % TiN bend bar illustrating the origin has a gold color (722 MPa). (b) is an SEM secondary electron image of the origin. (c) is a backscattered electron image of the flaw. This origin may be termed either a TiN agglomerate or a compositional inhomogeneity. (Courtesy J. Kübler, EMPA).

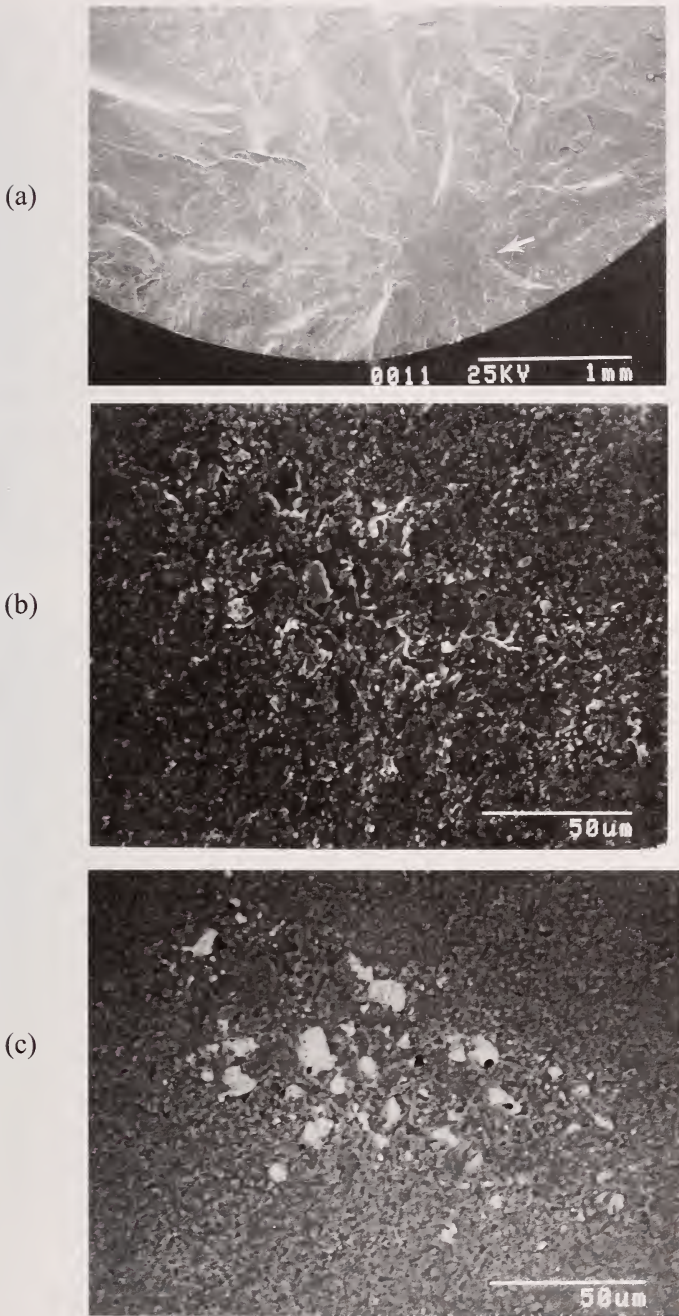


Figure 3.40. A cluster of iron particles acting as an origin in a silicon nitride rod broken in flexure. The origin is below the surface. The stress at the origin was 682 MPa. (a) and (b) show secondary electron images and (c) is the backscattered image at the same magnification as (b).

age is too low, then the X-rays will not be emitted or detected, even if copper is present.⁶

X-ray compositional maps, tailored to a particular element, may be made of the region being examined. The areas that contain the element in question emit X-rays and create bright spots on the map, whereas regions without the element appear dark. Digital image maps may be constructed with false colors representing areas of similar composition.

Figure 3.41 shows matching secondary electron and backscattered electron images of an inclusion in a silicon nitride tension specimen. Figure 3.42 shows the EDX analysis from a closeup view of the inclusion. In this case the iron peak stands out prominently. At other times, the inclusion peaks may appear only as a small fraction of the intensity of the primary constituent (Si in this case) due to the averaging effect of the area being imaged. Several peaks at different energies and intensities characterize each element and sometimes these will overlap with peaks from other elements, which can confuse the interpretation. Gold or palladium peaks from the coating may also be present. EDX analysis is usually semi quantitative, and even under the most ideal conditions, the mass fraction concentration is only precise and accurate to $\pm 1\%$.⁷ The minimum concentrations that can be detected are 0.5 to 1.0 mass fraction % under ideal conditions, but more typically is several mass fraction % or more.

Magnifications displayed on the SEM monitor (*e.g.*, 1000 X) may not be accurate. Brooks and McGill state that accuracies of 5 % are typical.⁷ The superimposed micrometer bars on the photos or images are usually better than a nominal magnification, but are not necessarily exact either. If quantitative measurements are made with the SEM, then care should be taken to ensure the fracture surface is not foreshortened. An SEM length calibration standard such as shown in Figure 3.43 should be used to check the magnifications. Some older SEMs have magnifications that vary across the field of view and which are not the same vertically and horizontally.

A paper by Healey and Mecholsky on SEM techniques and their application to brittle materials is very instructive.⁴ An excellent, detailed article on the use of the SEM for fractography is by Brooks and McGill.⁷

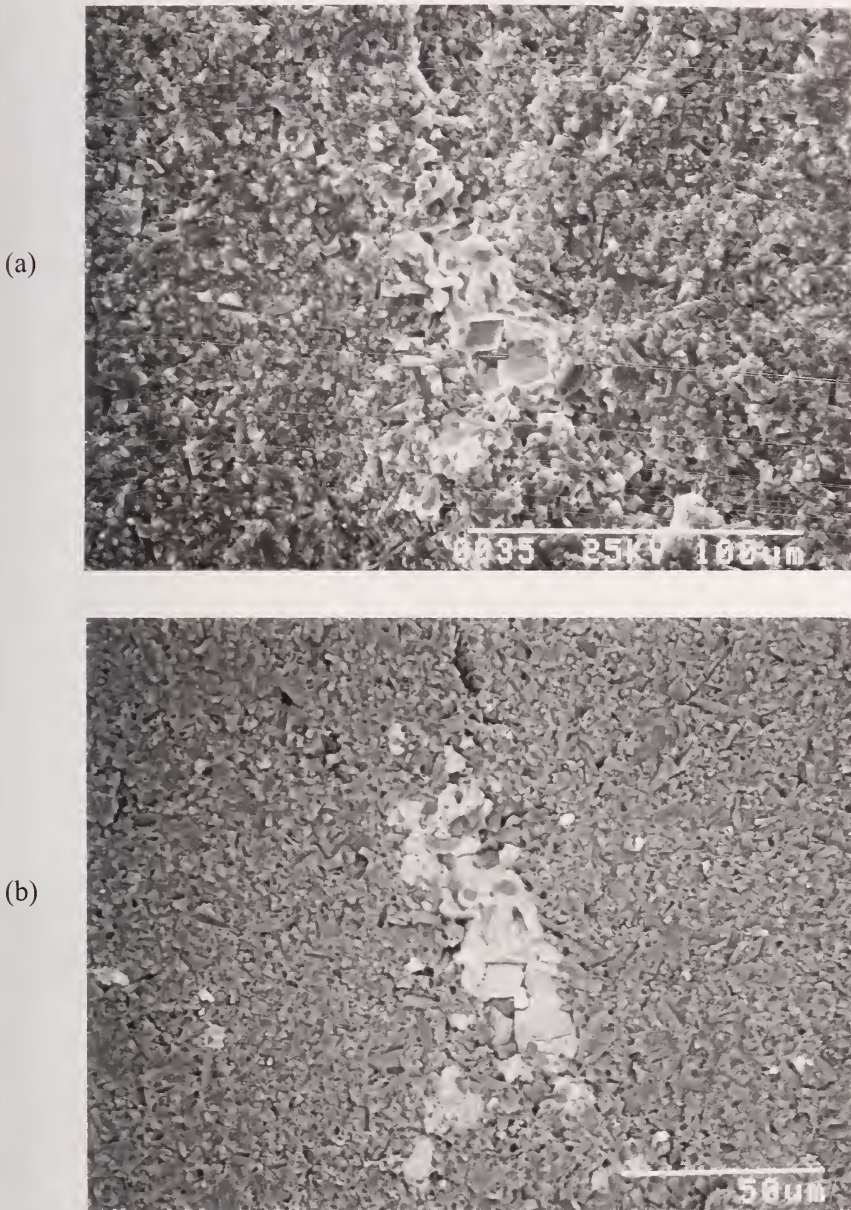


Figure 3.41 Matching secondary electron (a) and backscattered electron (b) images of a strength limiting inclusion in a silicon nitride rod (684 MPa).

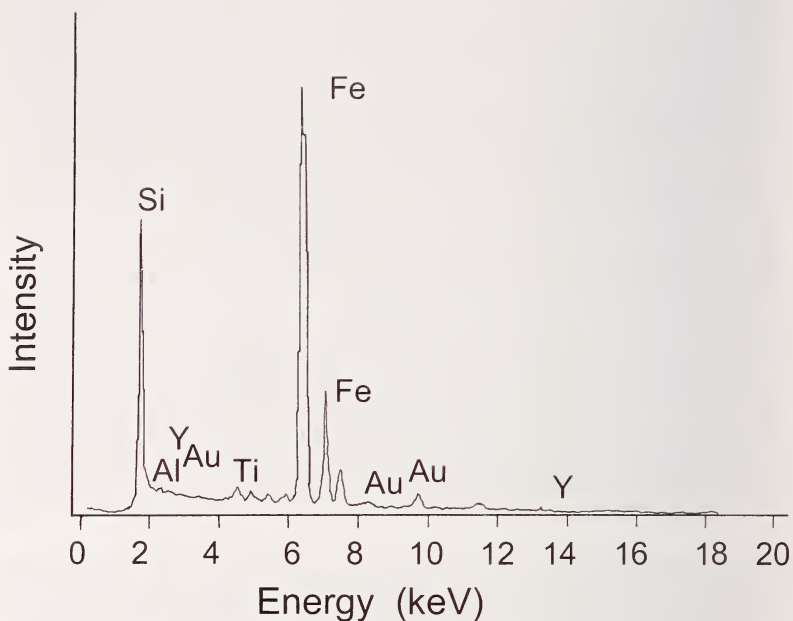


Figure 3.42. The EDX pattern of the flaw in the previous figure clearly identified the origin as an iron inclusion.

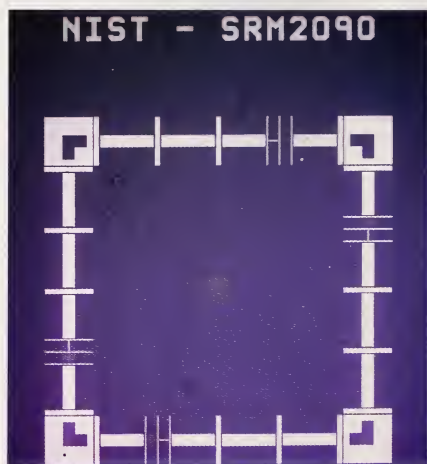


Figure 3.43. A NIST Standard Reference Material SEM length calibration standard. Finely spaced reference lines are located at intervals along the sides of the box on the right close up view.

3.14 Stereo SEM Imaging

The SEM takes pictures that make the surface look flat and do not show the topography clearly. A much better sense of the full topography can be revealed by the simple process of taking matching stereo photographs. Two photos of the same area are taken, but with the specimen tilted 5° to 15° in the SEM chamber between shots. A minor adjustment to the brightness and contrast may be necessary for the second photo, but is not essential. Some people are able to hold the two images in front of their eyes and focus the left eye on the left photo and the right eye on the right photo. The distance between the photos is adjusted and the eyes are “relaxed.” The brain merges the images and interprets them as a single three-dimensional view. Most people find it easier to put the images under a stereo viewing optical device as shown in Figure 3.44. The fractographer looks into two eyepieces and the photos are spaced apart and adjusted slightly back and forth until the three dimensional effect is achieved. It may take a little practice to get the two images to register, but the usual trick is to focus each eye on an identical feature or spot in the two photos. Initially the two eyes will discern the spot as two separate images, but by carefully sliding one or the other photos around, the spots can be made to merge. At that instant the three-dimensional effect should be detected since each eye will be viewing the same surface, but from different perspectives. This may take a little practice, but the viewer helps make it easy for most people. One curious effect is that the perception of what features are up or down may change depending upon which photo is on the left and which

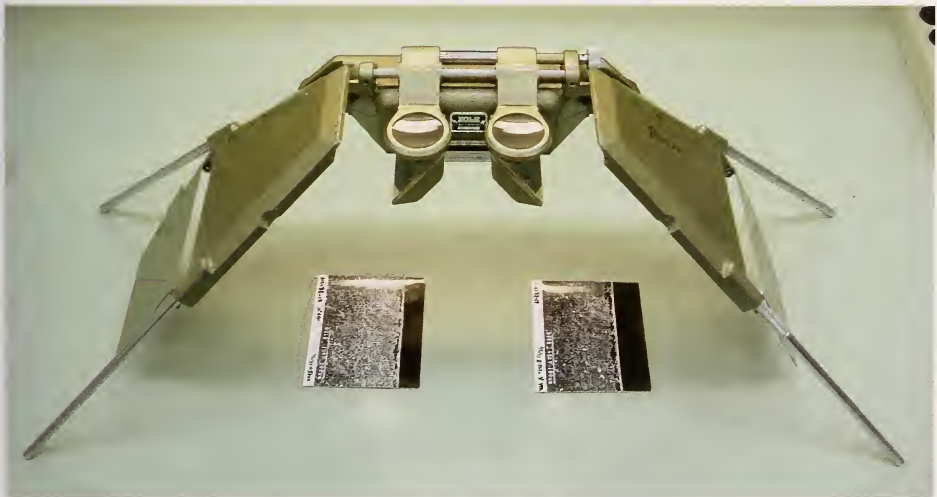


Figure 3.44. Stereoscope viewer. The two photos are placed under the viewer and the viewer looks into the two eyepieces. The photos are moved around slightly until they appear as one image in three dimensions.

is on the right. It may be necessary to swap the photos to get the correct rendition. The orientation of the photos may have to be turned 90° as well in order to match the tilt angle used in the SEM.

Some modern SEMs can digitally capture the pair or of tilted images, or even three images at different tilts. Image analysis software can then interpret the multiple images and constructs a pseudo three-dimensional rendition that is displayed on a monitor. The computer image can be rotated or displayed from different vantage points and height profiles through various sections can be displayed. Quantitative analysis may be done by a procedure known as stereophotogrammetry. A few applications to ceramics so far were hampered by contrast limitations or lack of computing power,⁹ but the latter problem will be of less concern in the future.

3.15 Field Emission SEM

Field emission scanning electron microscopes (FESEM) offer dramatic increases in magnifications (600,000 X) compared to the SEM and improved resolutions down to 1 nm (Figure 3.45). They rival the resolution and contrast of many transmission electron microscopes. The field emission cathode replaces more conventional tungsten cathodes on the common SEM. A small-



Figure 3.45. A field emission scanning electron microscope

er probe beam is used. Accelerating voltages are lower and conductive coatings are not needed in many cases. Energy dispersive X-ray spectroscopy (EDX) can be applied to smaller regions than in a conventional SEM. The FESEM is used much the same way that a conventional SEM is used for fractographic analyses.

3.16 Environmental SEM

The environmental scanning electron microscope (ESEM) is designed to operate either in a high or low vacuum unlike conventional scanning electron microscopes, which require a high vacuum. The environmental SEM can operate with environments having water vapor or other gases. A specimen coating is not needed, as static charges do not develop on the specimen since the gasses ionize and can neutralize excess electron charge build up on the specimen. Magnifications up to 100,000 are possible, but resolutions are less than that from a conventional SEM. One advantage of the ESEM is that dynamic processes such as corrosion or chemical reactions can be studied by time-lapse imaging. The ESEM is primarily used for biological materials or with materials when it is undesirable to apply a coating.

3.17 Transmission Electron Microscope

The transmission electron microscope (TEM) is capable of extraordinarily high magnifications and high resolutions (< 0.1 nm). It is limited to specimens about $0.5 \mu\text{m}$ or less in thickness, however. The TEM can reveal critical microstructural details. Prior to the advent of modern scanning electron microscopy, TEM was applied to replicas of fracture surfaces in order to study the fracture morphology. Today, the TEM is not used for routine fractographic analysis, but is a critical tool for research projects studying the effect of microstructure on properties. It can reveal crucial information about defect densities in grains, grain boundary sliding and cavitation, twin formation, damage accumulation, phase changes, fracture mode (intergranular or transgranular), and grain boundary phases and their thickness. TEM specimens are cut from the bulk and then electrochemically or ion milled to very thin foils that are transparent to electrons. Alternatively, carbon replicas may be made for examination. Since the TEM examines only tiny portions of the material, it is almost never used to find and characterize fracture origins or classical fracture surface markings.

3.18 Atomic Force Microscope (AFM)

The AFM is a powerful microscope that uses a tiny tip (radius about 2 nm to 20 nm) at the end of a cantilever to probe the surface. The tip is brought into close proximity to the sample surface and either gently contacts the surface or taps it while the tip is oscillated close to the cantilever's resonant frequency. The probe is held at a fixed location in the X-Y plane and the surface to be examined is rastered in the X-Y plane. The Z-deflection of the cantilever is magnified by a laser beam that reflects off the cantilever into a position sensitive photo detector or interferometer. A computer records the X-Y and Z displacements and a three-dimensional image of the surface can be constructed. The AFM is capable of extremely fine resolution (10 pm) and does not require any special specimen preparation or testing environment, but the specimen must be very nearly flat and has to be mounted flat on a holder. The AFM is most frequently used in microelectronic and biological studies. It has been applied to the study of fatigue crack markings in metals and fracture mirror roughness measurements in glasses. There are limitations to the AFM. The scanned area is usually quite small, depending upon the resolution it can be as small as 1 μm square to as large as 150 μm square. The vertical surface features can only be a few micrometers in size. Acquisition times may be long. Color and reflectivity information are lost. Therefore the AFM is almost never used to search for fracture origins or other telltale fracture markings, but instead is used for very close up, high-resolution examination of surface roughness detail or coating evaluations. Hull used it to study the nature of mist and hackle lines in brittle epoxies.³

3.19 Optical Profilometer

Optical profilometers are designed to make non-contact three-dimensional surface roughness measurements from 0.1 nm to several millimeters. The sub nanometer resolution for an optical system with white light illumination source (halogen bulb) may seem surprising, but interferometry allows the small height variations to be resolved. Optical profilometers either translate the specimen vertically or, if the specimen is tilted slightly, laterally in front of an interferometer. Reflected light from the specimen and a reference surface are combined to form fringes that are projected onto a digital camera. Height variations are denoted by color and contrast differences in a computer generated image as shown in Figure 3.46. One advantage of the optical interferometer is that precise height and roughness variations are quantitatively recorded and can be interpreted by the program software.

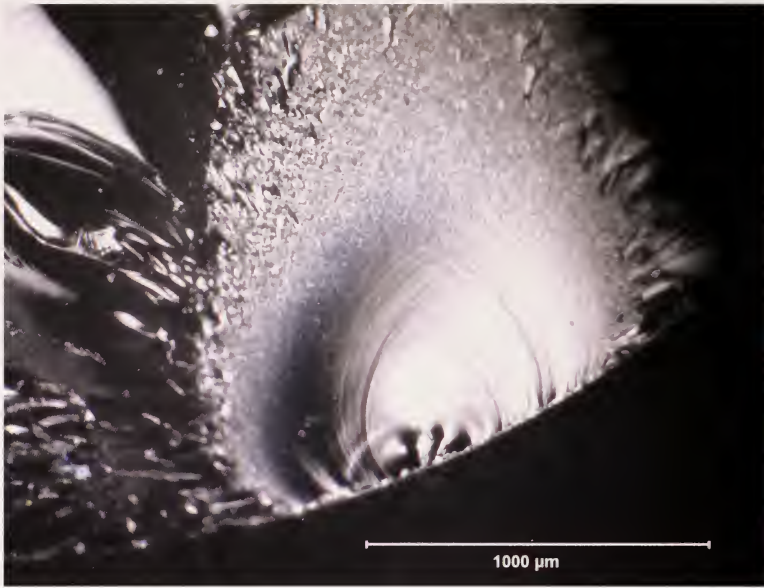
3.20 Confocal Scanning Light Microscope

This is a variant of an optical microscope. Rather than broadly illuminate a fracture surface, a point source of light (often from a laser) is scanned over the surface and reflected into the microscope through a pinhole aperture. A lens with a large numerical aperture is used and on uneven surfaces only a small portion of the surface will be in focus. A photo-multiplier tube records the strong return signal from the in-focus regions. Optical slices of in-focus surface are registered and recorded by a computer as the focus is finely adjusted. The final product is a computer generated three-dimensional topographic map of the specimen surface, often in false color corresponding to the surface heights. Figure 3.47 shows an example for a glass fracture mirror. Resolutions are of the order of $0.25\ \mu\text{m}$ or greater. The primary virtue of the confocal microscope is that in-focus images can be collected that would not otherwise be possible due to the limited depth of field of the light microscope. Quantitative information about height differentials can also be recorded. Confocal microscopes usually have longer image acquisition times than common optical microscopes with cameras, although some contemporary models can acquire and display images in as fast as $1/30^{\text{th}}$ s which is suitable for video rate imaging. A full topographical characterization can require 10 s or more.

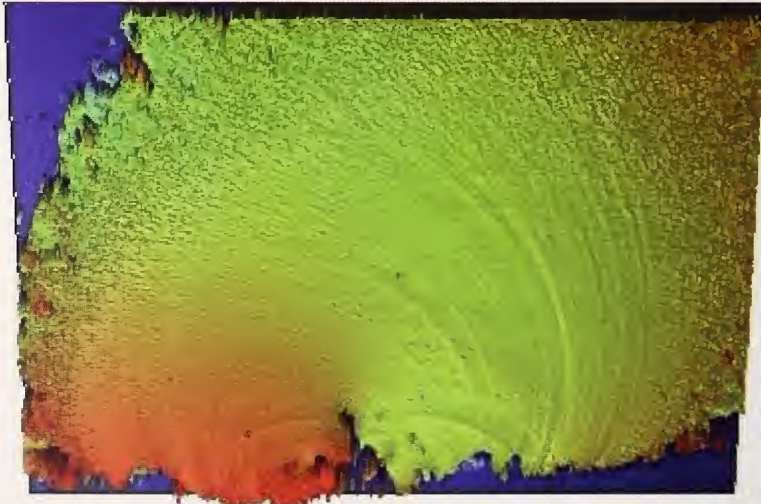
Some fracture surfaces are difficult to view with a confocal microscope. Carbon and graphite surfaces reflect very little light back up to the lens. Single crystals can act as specular mirrors and reflect light away from the lens. Diffuse reflection may be enhanced by application of a coating in such cases.

3.21 Stress Wave and Ultrasonic Fractography

Ultrasonic or stress wave fractography is an effective fractographic tool in the laboratory that was pioneered by Kerkhof.^{10,11} A transducer attached to the specimen creates continuous elastic waves at a specific frequency. The elastic waves create ripples on the fracture surface as shown in Figure 3.48. Local crack velocity can be simply calculated on the basis of the spacing between the lines and the frequency of the pulses. Richter and Kerhof¹¹ used 5 MHz lead zirconate titanate transducers to measure cracks running at terminal velocities in glass. Their review article has a wealth of additional details about this method and many fascinating examples of its use. Additional examples of their work are in section 5.4.4 on tertiary Wallner lines.

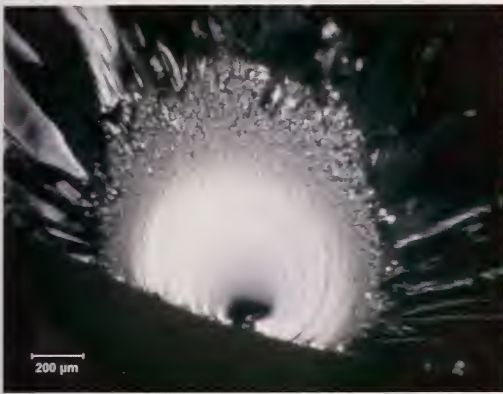


(a)

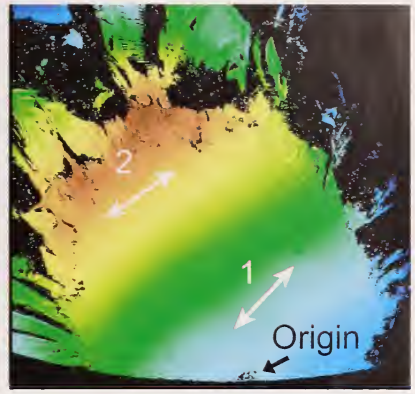


(b)

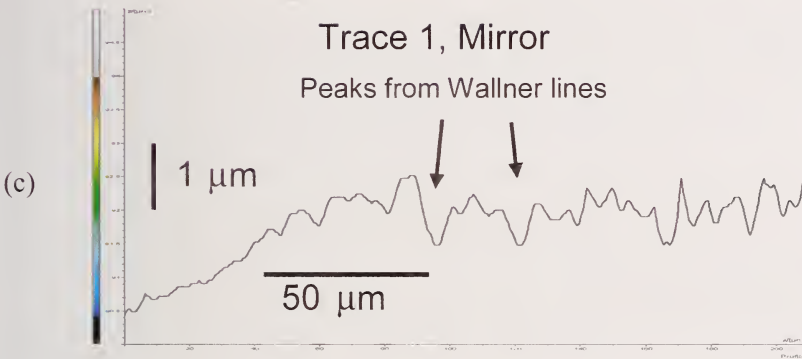
Figure 3.46. Matching (a) optical microscope and (b) lateral scanning optical comparator images of a fracture mirror in a ground glass rod. (b) shows an area 1.0 mm tall x 1.3 mm wide. The colors correspond to the scale range shown on the right (+7.9 μm to -16.3 μm). Wallner lines and mirror mist are readily detected and displayed. The origin is a surface crack from a scratch. (b is courtesy of R. Gates)



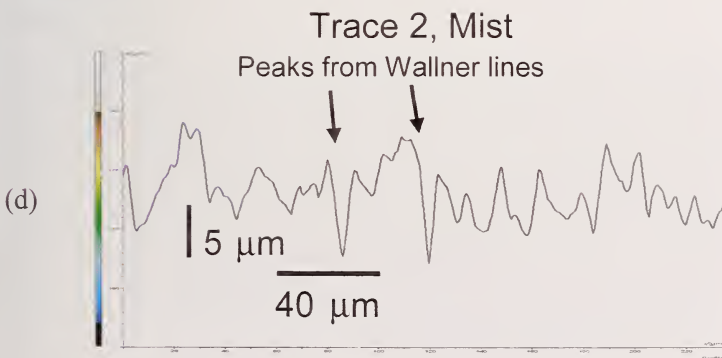
(a)



(b)



(c)



(d)

Figure 3.47. Matching stereoptical (a) and confocal microscope image (b) of a glass rod fracture mirror. Height profiles for tracks 1 and 2 are shown in (c) and (d). The major peaks are from Wallner lines. The minor peaks show the inherent roughness in the mirror and mist regions. (b) and traces are courtesy of J. López-Cepero Borrego and A. Ramirez de Arellano Lopez, Univ. Seville.)

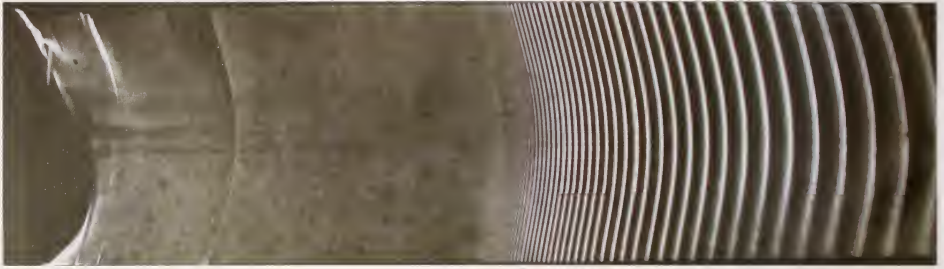


Figure 3.48. Fracture in a glass plate. Fracture originated at the left and accelerated to the right as attested to by the increased spacing between the timing ripples. (Courtesy H. Richter)

3.22 High Speed Photography

Studies of impact fractures have benefited from high speed photographic techniques. Field's review is good starting point.¹² The first extensive use of high-speed photography to study fracture in glasses was by Schardin and colleagues.¹³ In 1937, he and Struth used a multiple spark camera to observe that the terminal velocity of cracks in soda lime glass was about 1500 m/s.

3.23 X-Ray Topography

X-ray topography is a specialized technique for single crystals.^{14,15} An X-ray beam illuminates the test specimen and images formed using the diffracted beams are recorded. The image from an ideal crystal is completely homogeneous, but imperfections that distort or "strain" the crystal lattice produce image contrast. Often the defects themselves are not visible. It is the disturbances to the lattices that are revealed, and these are often magnified in size relative to the defect size. X-ray topographs will reveal dislocations, stacking faults, inclusions, and surface damage. Since diffracted X-rays form the image, interpretation is not always straightforward. Figure 3.49 shows examples of X-ray topographs. They reveal handling damage on and below the polished surfaces of a sapphire hemispherical domes and which were not visible with the optical or scanning electron microscopes

3.24 Dye Penetration and Staining

Dye penetration is a staple of nondestructive testing, but it also has value for fractographic analysis. It is commonly used to search for hidden cracks in a

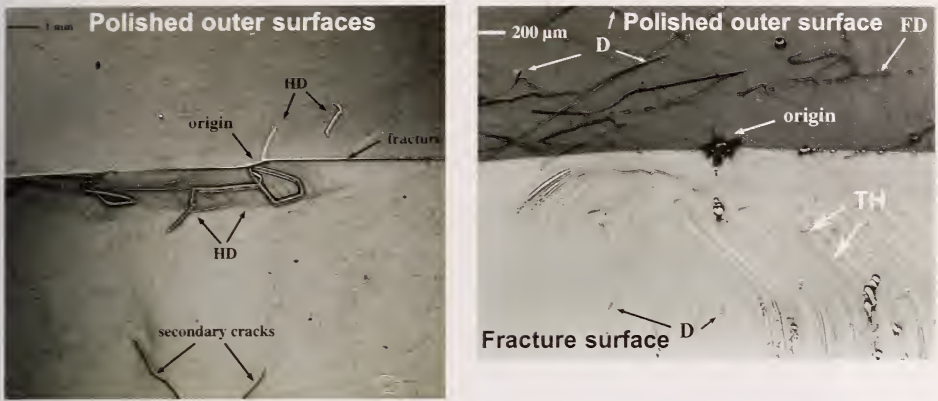


Figure 3.49. X-ray topographs of a fractured sapphire hemispherical dome. (a) shows the outer polished surfaces of the matching fracture halves and reveals handling damage (HD) cracks not readily visible to the optical or scanning electron microscopes. (b) shows a close up of one half tilted to show the fracture surface and outer polished surface with twist hackle - cleavage step lines (TH), dislocations (D), and fabrication damage (FD). (Courtesy D. Black).

ceramic part prior to usage or after exposure to some loading or environmental conditions. Simple staining with common dyes such as the felt tip pens shown in section 3.7 can aid post-fracture interpretation in porous or coarse-grained materials that are otherwise very difficult to interpret. The dye can be applied to the fractured parts. For example, Figure 3.50 shows a portion of a fractured porcelain toilet tank. Simple staining revealed tiny incomplete crack branches that gave a clear indication of the direction of crack propagation.

Dye penetration is sometimes used with ceramics to try to penetrate grinding induced cracks, but these are often very small and tight, making penetration problematic. There often are compression residual stresses a few micrometers deep on the outer surface of a ground part. These tend to clamp the crack faces shut. Sometimes a dye solution with a heavy metal element such as palladium nitrate is used so that the dye may be detectable in the SEM.¹⁶ Detection of tiny grinding induced cracks on the outer ground surface is very difficult. Examinations of the fracture surfaces are done after fracture to ascertain whether the dye has penetrated beneath the ground surface. Dye "bleeding" can be a problem if the dye migrates into the fracture surface either during the fracture event or afterwards.

Simple colored staining dyes or felt tip pens may be used with white ceramics. Fluorescent dyes are used with dark ceramics. Level 4 ultrahigh sensitivity

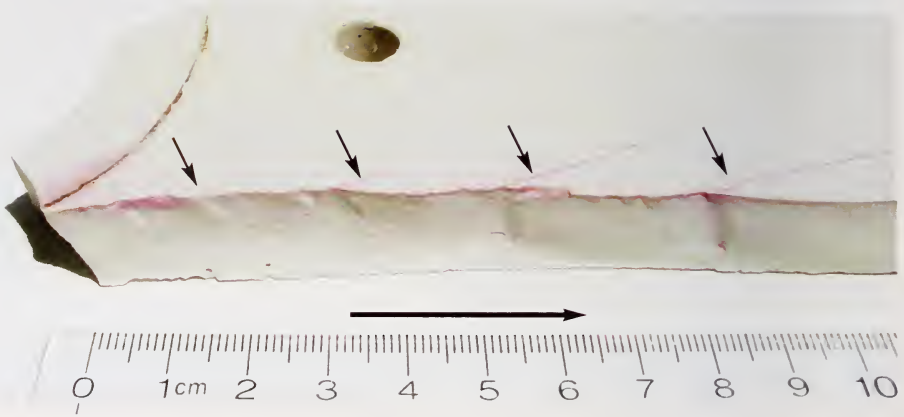


Figure 3.50. Fractured porcelain part with dye penetration by a common felt-tip pen. The dye reveals crack branching patterns (small arrows) and thus the direction of crack propagation (large arrow).

fluorescent dyes are needed to get into the tiny cracks. Special precleaning and soaking steps sometimes are necessary to facilitate dye penetration. Sometimes it may even be necessary to heat or vacuum treat a part to eliminate adsorbed gasses on the crack faces prior to dye penetration. After pene-



Figure 3.51. Fluorescent dye penetration equipment.

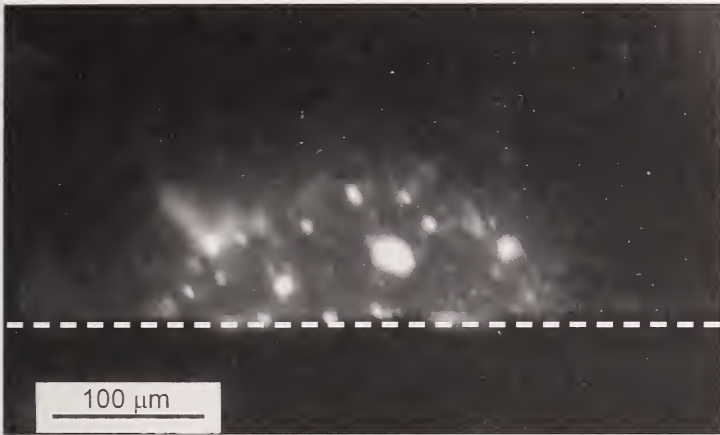


Figure 3.52. Fracture surface of a silicon nitride specimen with a Knoop surface crack that was penetrated by a fluorescent dye prior to fracture. The dye highlights the semielliptical surface precrack. The dashed line is the specimen bottom surface. This photo was made with a compound microscope with xenon bulb illumination and a fluorescence filter at a nominal 200 X magnification. The dim blurred image is typical for the weakly-emitting dye penetrant. This photo was made with instant-developing film that was exposed for several minutes.

tration, ultraviolet or “black lamp” illumination (Figure 3.51) is used to excite the dye such that it fluoresces and can be seen by the eye. Parts may be examined under a stereoscope, but the images are dim since the amount of light emitted is very slight. It is difficult or impossible to photograph features under these conditions. Compound optical microscopes, on the other hand, may be used with intense xenon light sources and fluorescent filters so that images may be captured as shown in Figure 3.52. The photo shows an image made on instant developing film. Digital cameras might give better recorded images.

3.25 Other Equipment

A common scanner such as shown in Figure 3.53a is handy for converting print images to digital JPEG or TIFF files. Figure 3.53b shows a simple ultrasonic cleaner that is helpful for cleaning small specimens prior to SEM examination. The specimens may be placed into small beakers with a solvent such as acetone and then placed into the sonic cleaner bath which is partially filled with water. Methyl alcohol is effective in removing finger prints. A few minutes vibration is usually sufficient to remove common contaminants and cutting debris. Simple cutoff or wafering machines (Figure 3.54) are handy for



Figure 3.53. Other useful equipment for a fractography laboratory. Digital scanner (a) and ultrasonic cleaning bath (b).



Figure 3.54. Wafering and cut off wheel machines.

cutting large specimens to sizes that can be mounted in optical or scanning electron microscopes. Cutting should be done wet to flush debris away and to minimize heating of the specimen.

3.26 Other Resources

The ASM Handbooks Volume 11 on Failure Analysis and Prevention and Volume 12 on Fractography have articles on fractographic equipment.^{17,18} Appendix A of this Guide lists additional sources of information.

3.27 The Future

New technologies will revolutionize many of the tools of the trade. Digital camera imaging is replacing processed film photography. Digital enhancement of contrast, color, or image clarity is an enormous advantage. Infinite depths of field will be achieved in camera by means of automated capture of multiple slightly refocused images. Programs will stitch together the in-focus to create a single composite focused image.

Productivity will be vastly enhanced. Virtual imaging with computer generated topographical images will become commonplace. One must be careful, however, not to over-do digital adjustments as anyone who ever has over adjusted gamma settings on a digital image appreciates. Despite all the advantages of the new tools and advanced technologies, they will never replace direct optical imaging. The stereoptical microscope will always be a primary tool since it is easy to use and retains color and reflectivity information and can capture internal reflections. Most of the new digital technologies emphasize topographic detail to the exclusion of all else.

New computer software and digital camera technologies will enhance the capabilities of the conventional compound optical microscope so that it partially replaces the scanning electron microscope. The latter is most commonly used at 200 X to 1000 X for fractographic work, since this is all the magnification that is ordinarily needed to find and record 5 μm to 100 μm size flaws. These magnifications are well within the reach of enhanced compound optical microscopes with Z-axis rastering and software that constructs three-dimensional images to overcome the inherent depth of field limitation of optical microscopy with glass objective lenses. On the other hand, the chemical (energy dispersive x-ray analysis) and structural analysis (electron diffraction) capabilities of the SEM will ensure it is a staple of the fractographers tool box for many years to come.

Perhaps one of the greatest current limitations of the art of image storage and display is that it is all two-dimensional. Fracture surfaces are by their very nature three-dimensional, so something is lost when an image of a fracture surface is captured and stored in a computer's memory. This is partially solved by new image analysis computer programs used in conjunction with multiple SEM images (taken with different tilts) or optical microscopes with Z-axis rastering such that a computer generated model or depiction of the surface can be displayed. Such virtual images can be color enhanced and can be tilted, rotated, or viewed from different angles. Nonetheless, they are all displayed on two-dimensional computer monitors.

One can imagine the future fractographer donning special eyepieces or a visor that enable him or her to traverse over or “fly over” a virtual fracture surface. These will certainly have considerable novelty value, but one wonders whether they will lead to better diagnoses than those made by an experienced observer looking through a simple stereoptical microscope. It is very common for the fractographer, while wiggling and tilting a fracture surface under a stereoptical microscope, to detect a fleeting reflection or stray subtle fracture line, which upon further examination unlocks the secret of a particular problem. Will future computer software and image analysis programs ever match this skill?

Perhaps the great breakthrough will occur when technology is invented that can capture genuine three-dimensional images that retain full color, reflectivity, and internal reflection information *and display* them with full fidelity in three dimensions. The author can personally attest to the hours of desperate struggle to acquire the best two-dimensional image to capture a critical detail, only to feel despair when showing the image later and realizing that it just doesn't show what the eyes saw.

Chapter 3 References

1. V. D. Fréchet, *Failure Analysis of Brittle Materials*, Advances in Ceramics, Vol. 28, American Ceramic Society, Westerville, OH, 1990.
2. Anonymous, “Transmission Electron Microscopy,” pp. 179 - 192 in *Fractography*, Vol. 12, ASM Handbook, ASM Int., Materials Park, OH, 1987.
3. D. Hull, *Fractography, Observing, Measuring and Interpreting Fracture Surface Topography*, Cambridge University Press, Cambridge, 1999.
4. J. T. Healy, and J. J. Mecholsky, Jr., “Scanning Electron Microscopy Techniques and Their Application to Failure Analysis of Brittle Materials,” pp. 157-181 in *Fractography of Ceramic and Metal Failures*, ASTM STP 827, ASTM, 1984.
5. B. L. Gabriel, “Scanning Electron Microscopy,” pp. 166 - 178 in *Fractography*, Vol. 12, ASM Handbook, ASM Int., Materials Park, OH, 1987.
6. L. S. Chumbley and L. D. Hanke, “Scanning Electron Microscopy,” pp. 516 - 526 in *Failure Analysis and Prevention*, Vol. 11, ASM Handbook ASM Int., Materials Park, OH, 2002.

7. C. R. Brooks and B. L. McGill, "The Application of Scanning Electron Microscopy to Fractography," *Mater. Charact.*, 33 (1994) 195-243.
8. H. U. Marschall, R. Danzer, and R. Pippin, "Three-Dimensional Analysis of Decorated Ceramic Fracture Surfaces by Automatic Stereophotogrammetry," *J. Am. Ceram. Soc.*, 83 [1] 223 - 225.
9. T. D. Fletcher, J. J. Petrovic, and J. E. Hack, "Quantitative Fractography of SiC Whisker-Si₃N₄ Matrix Composites," *J. Mat. Sci.*, 26 (1991) 4491 - 4498.
10. F. Kerkhof, "Bestimmung der Maximalen Bruchgeschwindigkeit Verschiedener Gläser Nach Der Ultraschalmethode," *Glasstechnische Bericht*, 35 (1955) 267 - 272.
11. H. G. Richter and F. Kerkhof, "Stress Wave Fractography," pp. 75 - 109 in *Fractography of Glass*, eds., R. C. Bradt and R. E. Tressler, Plenum, NY, 1994.
12. J. E. Field, "High-Speed Photography," *Contemp. Phys.*, 24 [5] (1983) 439 - 459.
13. H. Schardin and W. Struth, "Neuere Ergebnisse der Funken-kinemographie," *Zeitschrift Tech. Phys.*, 18 (1937) 474 - 477.
14. D. R. Black and G. G. Long, *X-Ray Topography*, NIST Recommended Practice Guide, NIST Special Publication 960-10, April 2004.
15. D. Black and G. D., Quinn, "X-ray Topography for Fractography of Ceramic Single Crystals," *Journal of Failure Analysis and Prevention*, 6 [3] (2006) 69 - 76.
16. W. Kanematsu, M. Sando, L. K. Ives, R. Marinenko, and G. D. Quinn, "Determination of Machining Crack Geometry by Dye Penetration Technique," *J. Amer. Ceram. Soc.*, 84 [4] (2001) 795-800.
17. *Fractography*, Vol. 12, ASM Handbook, ASM Int., Materials Park, OH, 1987.
18. *Failure Analysis and Prevention*, Vol. 11, ASM Handbook, ASM Int., Materials Park, OH, 2002.



4. General Examination and Fracture Patterns

Analysis begins with a simple visual examination of the broken pieces. The general patterns of crack extension and branching not only point the way back to a fracture origin, but also provide information about the cause of fracture, the energy of fracture, and the stress state. The majority of brittle fractures start at one origin and radiate outward. Severe thermal stresses or impact loadings can create multiple origin sites. Fréchette¹ defined the fracture origin as: “that flaw (discontinuity) from which cracking begins.” A slightly broader definition considers that the fracture origin is both a location and a flaw:

fracture origin: the source from which brittle fracture begins.

Even if the primary objective is to find the fracture origin, the overall breakage pattern should be examined first. Most of this chapter is concerned with breakage patterns in general and examination of the fracture surfaces is deferred until Chapter 5. An experienced fractographer may simultaneously examine the general breakage pattern and the fracture surfaces.

The overall fracture pattern reveals information about the fracture event and component stress state. This is true for both laboratory test coupons and component fractures. Breakage may be sudden, unstable, and catastrophic as in a laboratory strength test or a dropped glass. Alternatively it may be in stages as in a fractured dental crown restoration or a crack growing in an automobile windshield.

Most but not all origins in glass are from surface- or edge-located flaws. Ceramics fracture from volume, surface, or edge sources. The fracture origin is the site that had the worst combination of tensile stress and flaw severity. The latter is determined by the flaw size, shape, and thermoelastic or chemical interactions with the matrix. A large flaw may not necessarily trigger fracture, especially if it is located in a portion of a part that has low stress or it is very blunt such as a spherical pore. The severity of a flaw and whether local stresses are sufficient to trigger fracture are covered by principles of fracture mechanics presented in Chapter 7.

This chapter begins with some generic breakage patterns and shows some common examples, both for laboratory tested specimens and component fractures. The end of the chapter has some general observations about fractures caused by mechanical overload, impact or contact, thermal, corrosion or oxidation, and some observations on how residual stresses may affect fracture patterns.

4.1 Specimen Reconstruction

The general examination often begins with specimen reassembly. Ideally all fragments are available. Even if the pieces with the origin are lost, valuable information can be gleaned from the fragments. With some experience and with a familiar breakage pattern, irrelevant shards or ordinary secondary fracture fragments may be ignored. At this point the fractographer should take care not to introduce contamination to the fragments and especially the fracture surfaces.

Sometimes an experienced fractographer is able to look at fragments of a familiar component or test specimen type and be able to immediately find the piece with the fracture origin. For example, experienced fractographers are able to sift through a bucket of tempered glass fragments and find the origin pieces on the basis of their telltale morphology.

A common concern is whether it is safe to put the pieces together. This step is discouraged when conducting analysis of polymer or metal fractures. In contrast, ceramic and glasses are hard and durable materials. The pieces usually fit perfectly together. It is acceptable to fit pieces together gently, taking care to avoid abrasion or chipping. Single crystals and glasses are more sensitive to chipping than polycrystalline ceramics and must be handled more carefully.

Simple adhesive tapes may be used to temporarily hold pieces together. Apply the tape sparingly and only on an external surfaces and not between fracture surfaces. Small strips of masking tape may be used judiciously, but it should be borne in mind there is a risk of contamination. Whatever tape is used, it should be a type that is easily removable. Keep in mind that a reassembled body held together by tape strips may be unwieldy.

In complex cases with multiple fragments, it may even be necessary to glue fragments together. Glues should be used sparingly and preferably in a tack-bonding mode away from candidate fracture origin regions. Avoid getting glue on the fracture surfaces. The overall assembly will fit better if there is no build up or misfits from glue joints between fracture planes. Simple cheap nitrocellulose air-drying cements^a are suitable and set fast. They can easily be removed by peeling off with a fingernail or razor knife or by dissolving with common solvents. In special cases it may be necessary to use a strong cement to glue the pieces together on their fracture surfaces. Cyanoacrylate ester

^a Duco cement or Scotch "All purpose adhesive, Super strength".

("super") glues may be used since they can set with very thin bonds such that cumulative misfits are held to a minimum. Such glues can be removed by soaking in acetone or nail polish remover. *In any case, glues should be used sparingly and every precaution taken to prevent them from coming into contact with fracture origin areas.*

During reconstruction it may be helpful to mark the pieces with a number or letter scheme in order to expedite the examination and to minimize specimen-to-specimen refitting exercises. Judicious marking with a pencil or fine tip felt tip marker pens are effective, but care should be taken to avoid contaminating the fracture surfaces or the fracture origin. Felt tip pen markings can usually be removed with alcohol or acetone.

During the initial examination it may be advantageous to try *transillumination* on white and translucent ceramics. Transillumination, whereby the part is illuminated from behind or from the side, may reveal internal cracks, flaws, and microstructural irregularities not detected by examination of the outer surface. Figure 4.1 shows two examples.

4.2 Crack Branching Patterns

Crack branching and radiating patterns may be interpreted before the fracture surfaces are examined. Much of the fractographer's craft is in the observation and interpretation of these patterns. Crack branch patterns can lead back to an origin and also tell much about the stress state and magnitudes. A simple example is a glass biaxial strength test specimen shown in Figure 4.2. The radiating pattern is intuitive and leads the observer back the origin which is in the disk middle. Sometimes multiple fractures can be simultaneously triggered. Examples are severe thermal shock fractures, or mid body fractures on each side of an impacted bottle. Secondary origins are often present in components that initially break from one origin, but then the fragments themselves fracture.

The first general rule is that a *crack propagates normal to the direction of the local principal tension stress*. As the crack propagates, minor perturbations in the direction of local principal tension can modify the plane of cracking. These minor perturbations can create telltale markings such as Wallner lines or hackle on the fracture surface as described in Chapter 5. Internal stresses or inhomogeneities can also cause crack local deviations.

◆ Fractography of Ceramics and Glasses

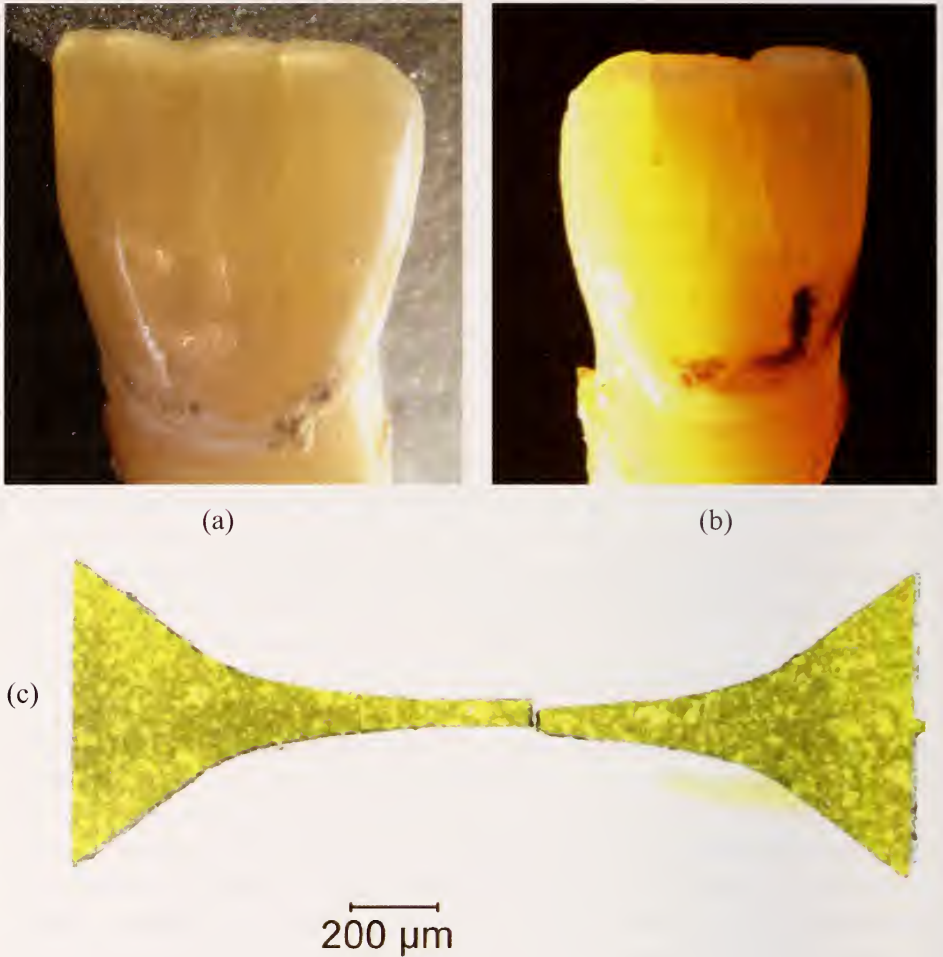
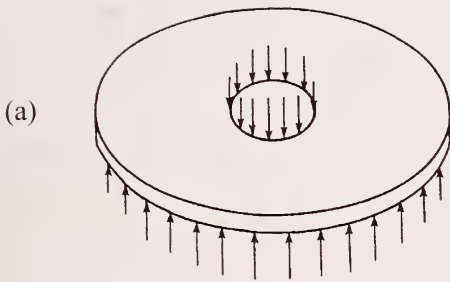
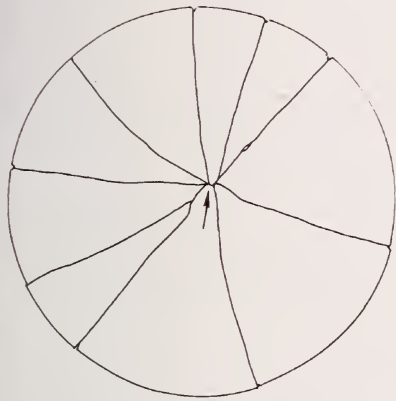


Figure 4.1 Transillumination (sideways) through a part (a) and (b) show internal cracks in an extracted intact human enamel tooth from an approximately 80 year old patient. (courtesy S. Scherrer) (c) shows transmitted (through) illumination with a chemical vapor deposited SiC micro tensile specimen. Very coarse grains acted as light pipes through the body. Relatively pure SiCs are green.



(a)



(b)



(c)

Figure 4.2 Fracture patterns in a moderately strong glass disk tested in ring-on-ring biaxial strength test. (a) shows the test arrangement, (b) shows a schematic of a fracture pattern. The arrow marks the origin. (c) shows an example in a borosilicate crown glass disk.

Once fracture has commenced, the propagating crack can fork or branch into multiple propagating cracks. These may be at non-normal angles to the far field stress direction. Nevertheless, the initial fracture starts out as a single radiating crack that separates the part into two pieces. Often the search for the fracture origin entails studying the branching patterns and tracing them back to the region of first fracture where the two pieces with the origin join across a flat surface as shown in the center of Figure 4.2b.

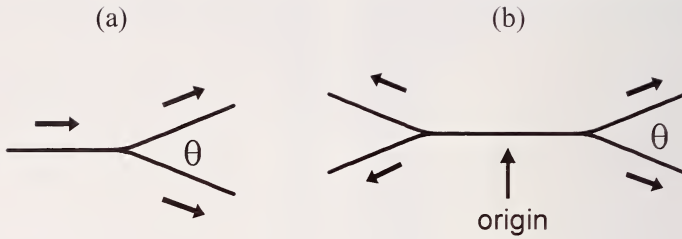


Figure 4.3 Crack branching indicates the direction of crack propagation.

4.3 Crack Branching Angles

Cracks which have reached their terminal velocity (normally about 50 % to 60 % of the shear wave velocity) may split into two cracks with an acute angle between them as shown in Figure 4.3a. Fréchet¹ terms this *velocity branching*, *velocity forking*, or *velocity bifurcation*. Branching patterns are a valuable aid in diagnosing the direction of crack propagation. For example, a pair of branches in opposite directions typically brackets the origin as shown in Figure 4.3b.

Another very useful pattern is that the angle of forking varies with the stress state as shown in Figure 4.4. The trend shown by the solid line was reported by Preston in 1935 for the fracture of glass articles². Uniaxially stressed parts, such as a tension strength specimen or a bend bar, fork at about 45°. Equibiaxially stressed parts, such as a uniformly loaded thick window that has an origin near the center, fork at as much as 180°. Pressurized bottles, which have circumferential hoop stresses that are double the axial stresses, fork at about 90°. Torsion fractures, wherein the ratio of the principal stresses is negative (one stress is tensile, the other is compressive), have very small forking angles. Preston said that the angles were very consistent and varied by only a few degrees, but other investigators have observed much greater variability.

It now appears that systematic variations can occur due to component shape, the exact loading configuration, the stress level, and possibly the material properties. For example, the 180° branching angle for equibiaxial tension (“drumskin tension”) reported by Preston occurs for pressure loaded, thick windows that fracture at high loads. Shinkai³ shows such a fracture (his Figure 22a) in a 1.7 m x 0.9 m x 6 mm building window. On the other hand, most laboratory scale disk specimens tested with ring-on-ring equibiaxial

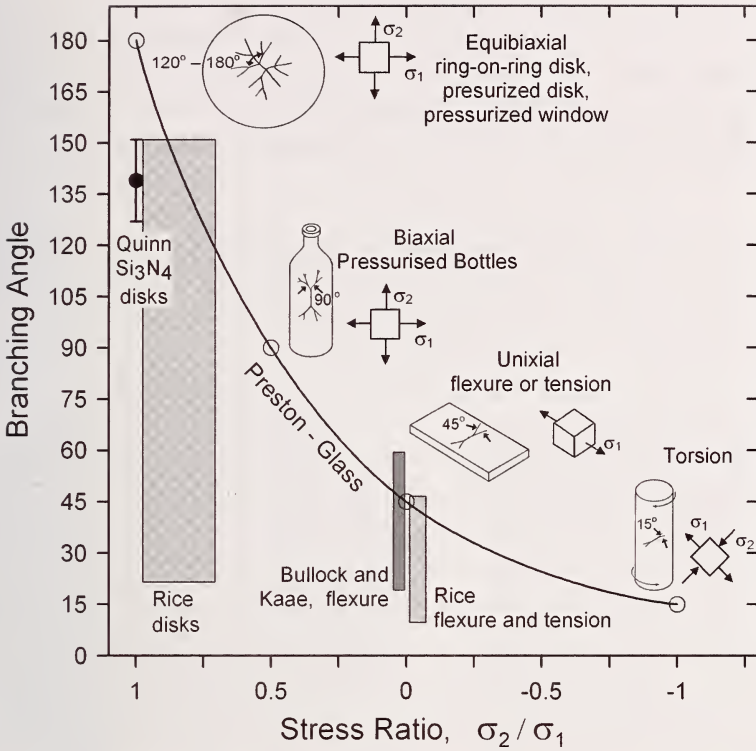


Figure 4.4 Branching angle versus stress state. The solid line is the trend for glass shown by Preston.² The shaded bands show Rice's data⁴ ranges for several ceramics and Bullock and Raae's range for a glassy carbon.⁵ The author's data for silicon nitride ring-on-ring disks are also shown.⁶

loading (Figure 4.2) have smaller angles from 120° to 155° and only approach 180° if the specimen is very strong and has much stored elastic energy at fracture. Laboratory scale specimen data by Rice⁴ on a range of ceramic materials, Bullock and Raae⁵ on glassy carbon, and the author on silicon nitride⁶ tend to confirm Preston's general trend, but with smaller angles. Most of Bullock and Raae's uniaxial angles were 30°. The exact biaxial stress ratio for Rice's data for his thermally-shocked and ring-on-ring loaded disks is unclear and therefore is shown as a band in Figure 4.4. Some of the fractures were outside the inner loading ring where the hoop and radial stresses are not the same. Some of his data was for ball-on-ring loaded specimens which were also not equibiaxial unless fracture began at the exact center. Nevertheless, Rice made a number of useful observations about the details of branching angle. A number of measurements were made and the standard deviations indicated there was some variability in branch angles even in uniaxially loaded

specimens. In some instances, the branching angle depended somewhat on whether the crack split into two branches or into three, including an extension of the original crack. He also noted that even along a given branch the angle did not necessarily stay constant. If a branch started out at an unusually low angle, it tended to curve to increase the angle. The converse was also observed.

Rice suggested that branching patterns tend to split the broken component into regions of approximately similar area.⁴ This implies that the cracks partition the component into pieces with comparable areas and strain energies, a reasonable supposition. Bullock and Raae also noted that the branching angles diminished with progressive branching.⁵

Unfortunately there is no consensus on how to measure branching angles. Both Preston and Fréchette recommended that the angle be measured close to the point of forking, but it may be more appropriate to measure the angle once it has stabilized. Close inspection shows that a branch starts at a shallow angle and then increases to its stable configuration as shown in Figures 4.5 and 4.6. Preston's original sketch (his Figure 2) for the equibiaxial disk pattern in fact shows such a gradual curvature at the origin and the angle reached 180° only after a small extension. J. Quinn used magnification to study branch angles in biaxially stressed glass disks and also observed angles that started small, but then stabilized at a larger angle.⁷ She observed that there was a stress magnitude dependence of the final angle: highly stressed disks had angles that approached the 180-degree limit, whereas lower stressed disks had smaller final angles. Rice evidently measured the angles after they had been fully developed. Branching angles often vary within a broken part, usually due to spatial variations of the stresses. So for example, in a ring-on-ring loaded disk the stresses are equal in the middle circle, but the radial and hoop stresses drop off at different rates outside the inner circle out to the rim. Furthermore, as cracks progressively branch they may begin to interact with other branching cracks. Hence, it is common for an initial branch angle to be large in the middle near an origin in a biaxially stressed disk, but the subsequent branch angles diminish out towards the rim.

So in summary, although there are discrepancies in the reported data, and the optimum manner of measuring the angles is unresolved, branching angles provide at least a qualitative indication of the stress state. There may be material property or component shape effects. Nonetheless, the general trends of branching angles may prove helpful to a fractographer.

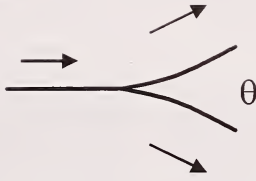


Figure 4.5 Close up of the branching point.



(a)



(b)

Figure 4.6 Fracture pattern in a 44.5 mm silicon nitride ring-on-ring (10 mm x 40 mm) equibiaxial strength test disk. The stress at fracture in the inner ring was 447 MPa. The branching is curved near the origin. Successive secondary branching occurs over short distances. (b) is a close up of the origin area showing that the initial branch angles are 140° and 145°. Additional branching is minimized as the crack propagated into lower stress areas away from the disk center.

4.4 Crack Branching Distances

The distance a propagating crack travels before branching is directly related to the stresses and stored energy in the component. The greater the stored energy, the shorter the distance to branching. If the crack travels through a region of constant stress, the empirical relationship is:

$$\sigma \sqrt{R_b} = A_b$$

where σ is the stress, R_b is the branching distance (radius), and A_b is a material constant called the fracture branching constant. A table of branching constants is in Appendix C. Additional details about this relationship are discussed in chapter 7 on Quantitative Analysis. There is some evidence that A_b may not be a material constant^{8,9}, and may depend upon geometry and stress state.

4.5 Fragmentation Patterns

A general quantitative assessment about the stresses in a part can be made from the number of fragments. Low stress, low energy fractures create minimal branching and hence few fragments. High energy fractures cause extensive fragmentation. The extent of fragmentation depends upon the stress state throughout the body and the total energy available for fracture. A small pebble or BB gun shot creates only localized damage in a window, but a hurled brick will cause window bending in addition to localized impact damage. Sometimes a general observation about fragmentation patterns is sufficient for a diagnosis. For example, if a fracture occurs at an unexpectedly low stress the fractographer might suspect and search for a gross material, handling, or impact flaw that has weakened a part. Many thermal breaks are low energy fractures. High local or transient stresses may precipitate initial crack propagation, but the stress levels may be low in most other portions of a part. Low energy fractures often have few or no telltale markings on the fracture surfaces, as discussed in the next chapter.

Processing cracks that occur on firing also generate minimal fragmentation. Differential shrinkage or out-gassing often create local stresses that can initiate a crack in the green state or during final firing, but the stresses may relax as the crack opens. Figure 4.7 shows an example. Such cracks are often rough, twisted, and winding. Their internal fracture surfaces may have telltale thermal rounding or discoloration from being exposed during processing.

Moderate-stress failures create more fragments that can be reassembled so that branching patterns can be interpreted. There may be more fracture surface markings.

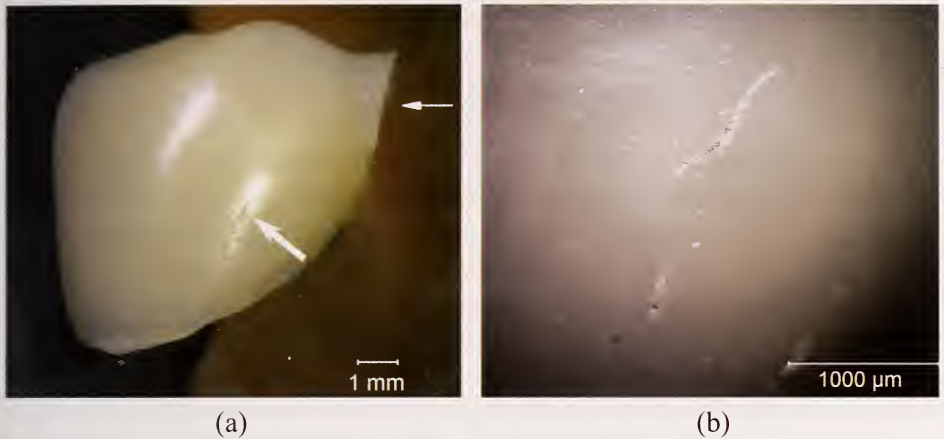


Figure 4.7 Processing cracks in an alumina three unit dental bridge. (a) shows a frontal (facial) view of the end unit which has fractured at the narrow connection to the next unit (small white arrow). A sintering crack is evident on the front face of the crown (large white arrow). It did not cause fracture in this instance. (b) shows a close-up of the processing cracks.

On the other end of the spectrum, high-energy fracture may be so virulent and create so many fragments that reconstruction may be impractical. Critical pieces may be lost. That is not to say fractographic analysis is hopeless. Sometimes telltale pieces that contain the origin can be culled out of a mass of fragments and the critical information gleaned while the majority of pieces are ignored. Analysis of the fracture surfaces can reveal whether fracture was caused by tension or bending, as will be discussed in the next chapter.

Uneven stress states may be manifested in many ways. For example, Fréchette¹ showed an example of a tempered high-powered lamp that cracked spontaneously as a result of heating in-service. In the fracture origin area, the fragments were large, attesting to a low to moderate stress level. Elsewhere in the lamp, extensive fragmentation and dicing typical of tempered glass was observed. Fréchette concluded that the intense heating in service caused the middle of the lamp to lose its temper and weaken such that it was more susceptible to fracture from thermal stresses.

Although similar techniques are applied to analyze laboratory-generated fractures and component service fractures, it is convenient to treat them separately in the following paragraphs. Even if one is primarily interested in component analysis, the experience gained with laboratory fractures can help with the former.

4.6 Laboratory Test Fracture Patterns

In the laboratory the cause of fracture is known. Fractographic analysis may be done to identify strength limiting flaws or to study crack microstructure interactions. It may be done to verify that the test was done correctly and that the fixtures and specimen were aligned properly. It may be done to gain valuable experience in examining fracture patterns in a particular material that can help with component failure analysis.

A simple precaution should be taken before the testing commences: *Shielding or buffering material should be placed around the specimens to catch all the fragments and to minimize secondary fractures and impact damage.* Cotton or tissue buffering and paper shields can be placed around the test specimens. In some instances the specimens may be partially taped before the test so that the pieces remain attached to the tape after fracture. This must be done judiciously and in no instance should tape interfere with the load application. Tape should never be on the tensile stressed surfaces. This step is very helpful with biaxial ring-on-ring loaded disks wherein the compression side of the specimen may have a tape circle inside the loading ring and a tape annulus outside the inner loading ring. The surface in contact with the loading ring should not be taped.

Specimens should be premarked with orientation or location marks. This preliminary step can dramatically aid post fracture analysis. For example, the orientation of round specimens tested in tension should be marked to ascertain whether fracture occurs preferentially from one side or another. Similarly, flexural strength specimens should always have the loading points marked on the side once the specimen has been inserted and preloaded in the bend fixtures. The marks will help ascertain whether breakages occur at the load pins. Sometimes a grid may be marked on a specimen to help with reconstruction. This may help with biaxial disks loaded in flexure, but again, any such markings should be on the compression side of the specimen.

4.6.1 Tension strength

This category includes machined specimens with grip holes or shoulders, glass optical fibers pulled in tension, or long tubes or rods that are pulled apart. Direct tension is conceptually one of the simplest loading configurations, but in practice it can be tricky to achieve. Slight loading misalignments or test specimen irregularities can create superimposed bending stresses. Breakage patterns in properly aligned specimens are usually quite simple as shown in Figure 4.8. Fractures initiate and run perpendicularly to the loading axis until and if they branch. Moderate-to-high strength specimens may branch with the telltale 30° to 45° angle as discussed in section 4.3. Fractures at a nonperpendicular angle to the loading direction (or with cantilever curls as discussed in the next section) should be cause for concern and suggest misalignments in the load train. It is especially important to ascertain whether fracture origins are located on the specimen surface, in the interior, or at an edge as will be discussed in the next chapter. Breakages in a group of test specimens should be randomly distributed within the gage section. An occasional break near the end of the gage section is probably not too serious, but if all specimens break from the end, then the tester should review the test specimen design. The stress concentration at the end of the gage section, the fixture and grip alignments, and the machining of the blend junction at the end of the gage section should be checked.

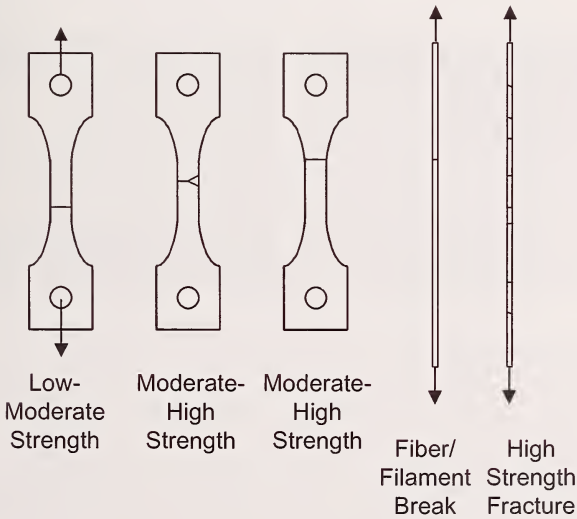


Figure 4-8 Tension specimen and fiber fractures.

High strength fibers have the added complication that secondary fractures are common. After initial fracture, the intense stored elastic energy in the fiber releases, sending stress waves through each broken portion. Reverberations and fiber whipping cause additional breakages. Fragmentation may be so thorough that it may be impractical to find a primary fracture. Testing in oil or coating the fibers with grease may minimize the whipping and secondary breakage, at the risk of contaminating the primary fracture and altering the environmental sensitivity of fiber strengths.

4.6.2 Flexural strength

Flexural strength testing with rod or bar specimens is often done in lieu of direct tension testing. Flexure is much easier to do. Specimens and testing equipment cost considerably less. A drawback is that much less volume and area are exposed to the full tensile stresses. Hence, flexural strengths are typically greater than direct tension tests strengths. Reference 10 is a review of flexural strength testing of ceramics. For our purpose here, it is convenient to briefly review the stress state as shown in Figure 4.9. The bending loading creates a stress distribution such that the maximum tensile stress is on the bottom as shown in (b) and (c). The stresses diminish into the interior until

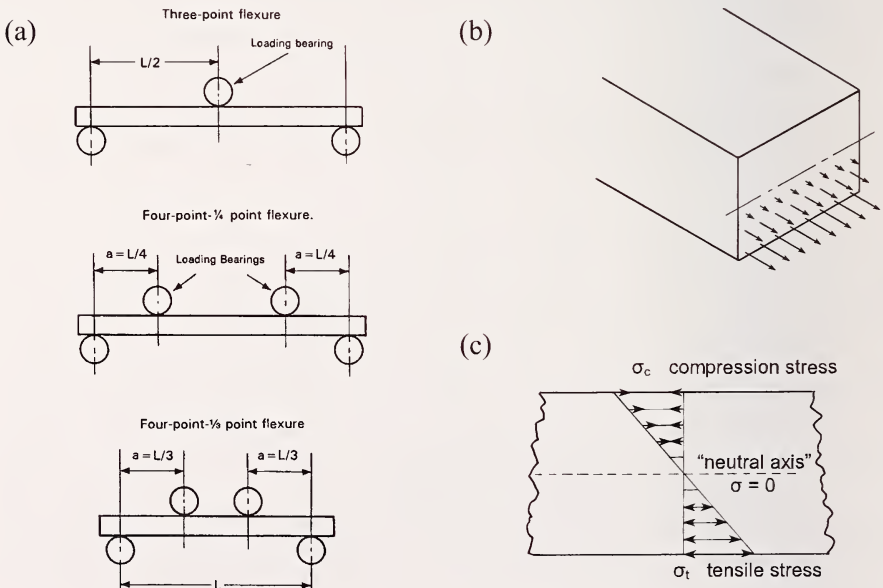


Figure 4.9 Three- and four-point flexure test configurations are shown in (a). The stress distribution on a cross section is illustrated in (b) and (c).

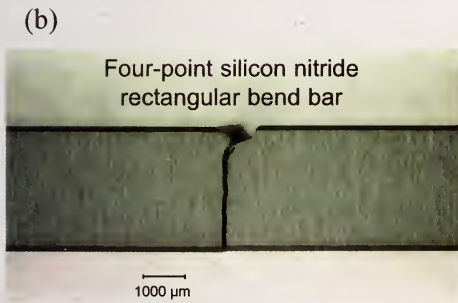
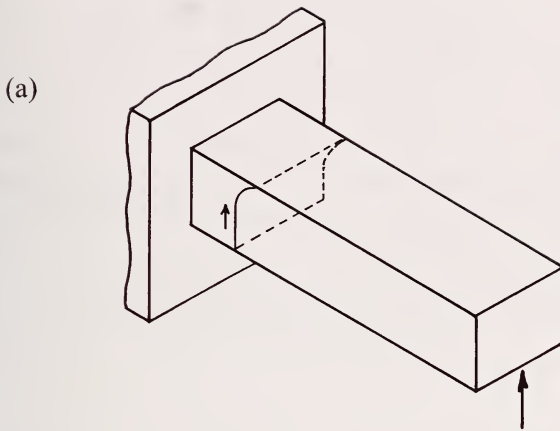


Figure 4.10 Compression or cantilever curls are a telltale feature of flexural fractures. In each case the tension surface is on the bottom and the compression surface is on top. (b) - (e) show side views of four-point flexure specimens.

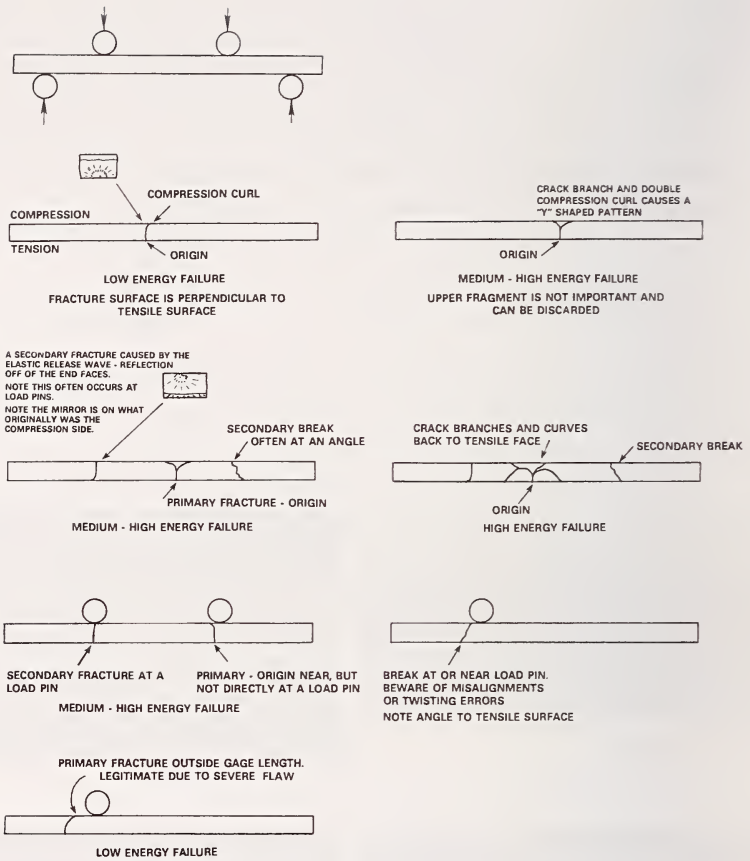


Figure 4.11 Fracture patterns in four-point flexure specimens. Cushioning material under the specimens minimizes damage to the fracture surface edge.

they are zero in the middle, at the “neutral axis.” The tensile stresses are balanced by compression stresses on the opposite side. The maximum stress exists only directly opposite the middle loading point in three-point loading and diminishes with distance from the middle loading point to the outer support points. The maximum stress occurs over a larger region between the two inner loading points in four-point flexure.

A very telltale feature of bend fractures is the *compression curl*, also known as the *cantilever curl*, shown in Figure 4.10. Once the crack has propagated from the tensile half of the specimen into the compression side, it slows down and changes direction. In stronger specimens the crack can branch, creating a double curl. The existence of a compression curl is an important sign that the

specimen either was loaded primarily in bending or had a strong bending component. Compression curls are not normally present in direct tension specimens, unless they were badly misaligned. The origin of fracture on a fracture surface is opposite the compression curl. The presence or absence of compression curls may be important for interpreting not only test specimens but component fractures as well. Thermal fractures usually do not have compression curls.

Figure 4.11 shows a variety of fracture patterns in bend bars. Low strength fractures are often the easiest to interpret since the specimen breaks into only two or three pieces. Often a small “T” shaped piece will be opposite the origin, but this fragment can be ignored since it never has the origin on it. The origin is below the “T” fragment on the two matching pieces nearer to the tensile stressed surface. Sometimes it is handy to keep the “T” fragments to confirm the other fragments do fit together.

Higher strength bars have two or more fractures and it must be deduced which was primary. Secondary fractures are caused by reverberations and stress reflections after the first fracture has occurred.^{11,12} Secondary breaks frequently occur at the loading points. If there are two fractures and one is located at an inner loading point and the other is in the inner gage section, the latter is probably the primary fracture with the first origin. If the two breaks are close to the two inner loading points, then the exact locations on the tensile surface should be examined closely. Often one fracture will be right under a loading point, whereas the other may be as close but not right at the loading point. The latter is usually the primary fracture. If both are exactly under the two inner points, it may be difficult to deduce which was first. There is also the possibility the specimen might have been loaded unevenly causing stress concentrations at both sites. If this occurs for more than a couple of specimens in a test set, then the fixture should be checked. Properly aligned specimens and fixtures almost always cause a perpendicular primary fracture in the middle gage section. Secondary fractures are often but not always at a slight non-perpendicular angle to the specimen axis. An unusually large flaw outside the gage section can trigger a fracture with crack plane tilted towards an inner loading pin. Specimens with such low strength fractures usually do not have secondary breaks. *Fractures outside the inner gage section in properly aligned specimens and fixtures are usually completely valid and a warning that unusually large flaws are present in some specimens.* They should not be cavalierly dismissed as invalid tests. Misaligned specimens or fixtures can cause twisted crack planes as shown in Figure 4.12.

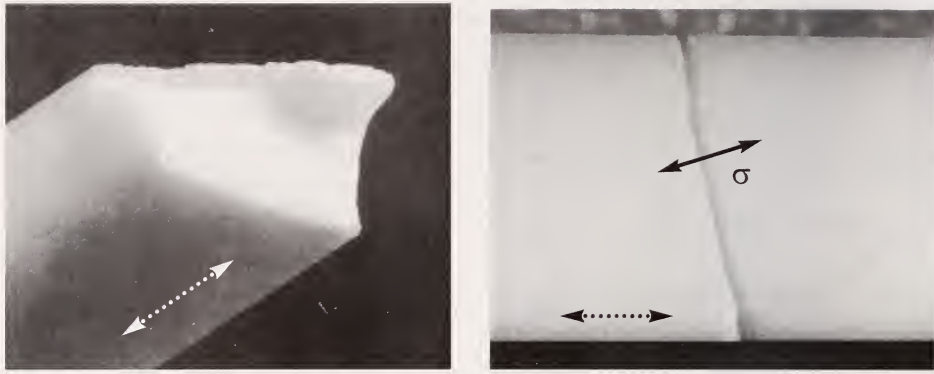


Figure 4.12 A twisted fracture surface in a misaligned alumina bend bar in a fixture that did not articulate properly. (a) shows the fracture surface and (b) the tensile surface of both halves. The principal stress direction (solid black arrow) was 14 degrees off the expected direction (dotted arrows). Twisted or angled fracture planes should prompt the tester to check the fixture articulation and specimen alignment procedures.

4.6.3 Biaxial flexural strength

Plates or disks may be tested in biaxial tension by a variety of methods including: pressure-on-ring, ring-on-ring, piston-on-ring, ball-on-ring, and ball-on-three balls.

Pressure-on-ring loading (whereby a specimen is supported on a ring and is loaded by a uniform pressure on the opposite surface) has the virtue that a large area is stressed biaxially. There are no loading point or stress concentration problems with the inner loaded area. Ring-on-ring loading, which is more commonly done since it is simpler to do, creates an equibiaxial stressed region in the inner circle. Pressure-on-ring and ring-on-ring are best used with specimens that have flat and parallel surfaces for even contact with the loading and support rings. Figure 4.13 shows fracture patterns in ring-on-ring specimens.

The single ball loading schemes have the drawback that only a tiny spot directly under the loading point experiences the maximum stress, and the concentrated forces of the ball may even distort the stress field in the vicinity. Fracture almost always starts directly below the loading ball.

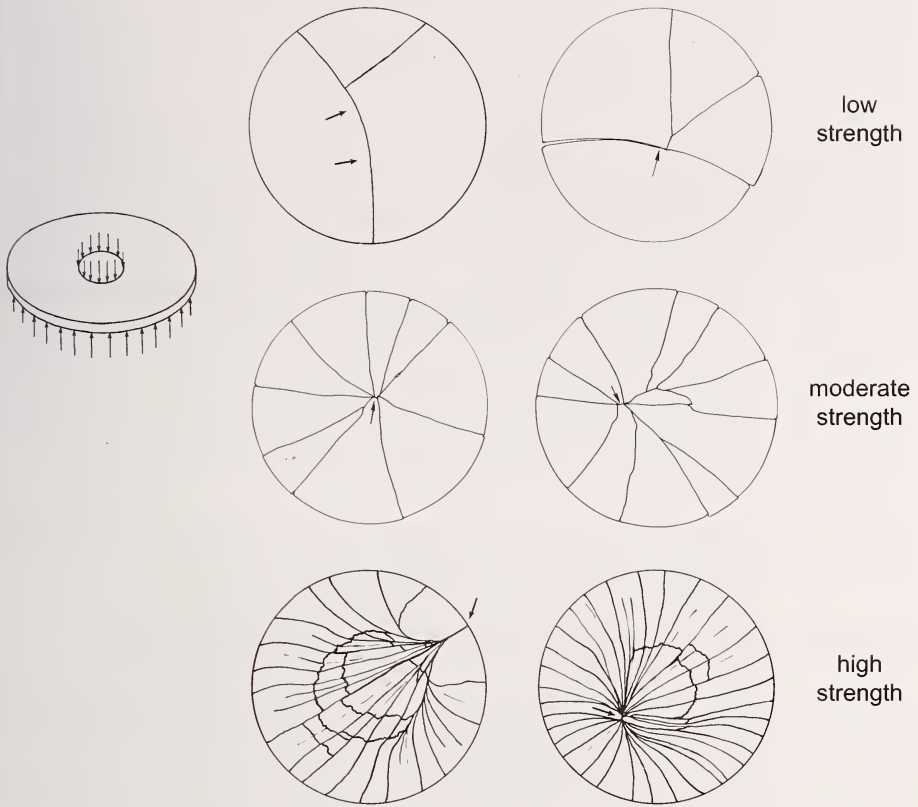


Figure 4.13 Fragmentation patterns in ring-on-ring loaded specimens. The small arrows mark likely origin areas. In low strength parts, after the first break has occurred, the larger remnant may still bear load from the inner loading ring, and it in turn will break in bending. In moderate to high strength disks, secondary circumferential cracking occurs near the inner loading ring.

The ball-on-three ball or piston-on three-ball schemes are better suited for uneven specimens, but the stress state is not very symmetric. Cracks often align themselves to run between the supporting balls. Excessively thick test specimens should not be used, since breaking forces are so high that contact cone cracks can be initiated at the loading sites. These disturb the stress state and, in the worst case, will propagate through the specimen thickness and reach the tensile side and cause unintended fracture.

A common misperception about ring-on-ring testing is that the edge condition is unimportant, since the maximum stresses are within the inner loading circle.

This notion is only partly correct. Figure 4.14 shows one of several fractured glass specimens that were part of a large set of specimens intended to generate a comprehensive design and reliability database. The overall fracture pattern showed the origin was on the rim. Fracture surface examination confirmed that outer rim grinding cracks caused fracture. Stress analyses for ring-on-ring specimens (e.g., Fessler and Fricker¹³) show that the maximum hoop and radial stresses are in the inner circle. The radial stresses gradually diminish to zero out at the rim. Hoop stresses also diminish, but are finite at the rim and depend upon the specimen dimensions, the fixture sizes, and Poisson's ratio. In the case of the disk shown in the Figure, the hoop stresses were as large as 50 % of the maximum stresses in the middle. It was not surprising that with a highly-polished tensile surface, the disk instead fractured from grinding flaws on the rim. In this testing episode, the problem was detected early after only six disks had been tested. The remaining disks were reground and acid etched to diminish the severity of the grinding cracks. Subsequent fracture testing was successful and almost always initiated fracture from the central disk region. If this precaution had not been taken and the remaining disks tested to fracture, the database would have been nearly worthless.

4.6.4 Laboratory test specimen analysis: additional tips

It is often helpful to look at contact marks or scuff marks where the specimen was loaded, whether it was in tension, uniaxial or biaxial bending. Such surface marks are one type of *witness marks*. These are marks on a specimen surface that attest to contact with a foreign body. In this manner it may be possible to ascertain whether loading was in fact uniform or not. Contact marks in a bend specimen may also help with the interpretation of whether a break occurred directly opposite a loading pin.

Test specimens are often broken in batches of ten, thirty, or more. Which specimens should be examined first? The pragmatic answer is that the weakest ones should be examined first, since they are the easiest to interpret. The experience gained from these easy specimens facilitates examination of the more complex fractured specimens, since the fractographer will be better prepared to recognize primary fractures and distinguish them from secondary breaks.

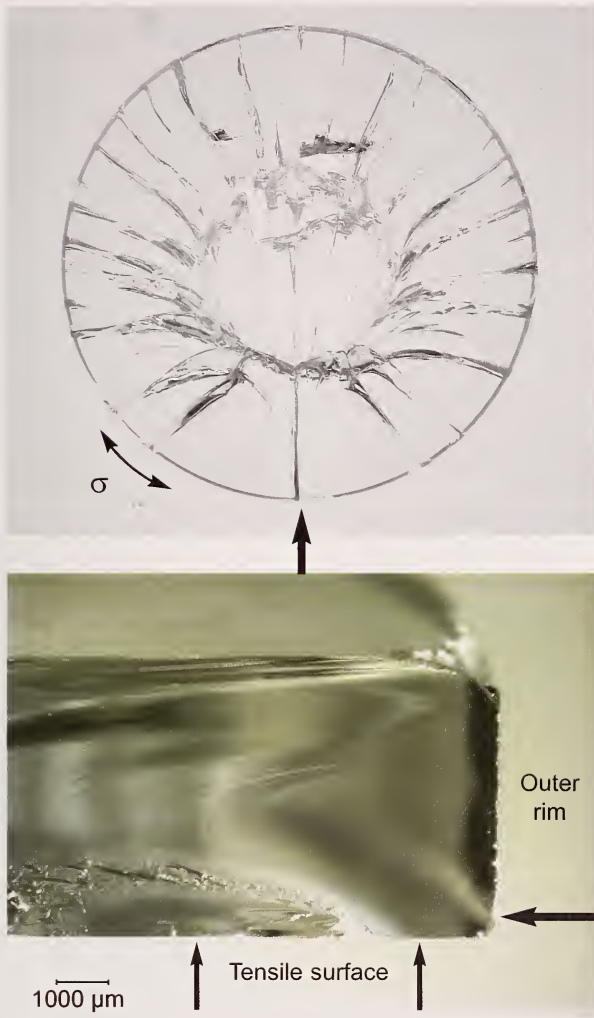


Figure 4.14 A fractured glass ring-on-ring tested disk. (a) shows the overall breakage pattern. Fracture started on the rim (large arrow) in response to the uniaxial hoop stress σ (small arrows), propagated towards the middle, and branched in response due to the greater biaxial stresses in the middle. (b) shows the fracture surface. The origin is a grinding crack on the outer rim (large arrow).

4.7 Component Fracture Patterns - General

Component fractures have the complication that the state of stress or the cause of failure may be unknown. The general fragmentation pattern can provide powerful clues. The fractographer first should obtain whatever ancillary information is possible about the component. What exactly was the material? What were the circumstances of the fracture? Was it an isolated case or part of a series? Had some change been made to the material or the loading conditions? Was there a noise (e.g., shattering sounds or water hammer)? Were there other parts or evidence found with the fractured material (impact debris)? Was there a witness? Is the witness honest? Does the witness have a good memory? Background information such as this may be crucial for the broader failure analysis.

A wise precaution is to retrieve as many pieces as possible. In some instances where there is an obvious pattern, the fractographer can cull out important fragments. On the other hand, if other people have the fragments, then one cannot expect them to know which are the important pieces. They should retrieve all pieces. If remnants are in a mount or assembly, then they should not be retrieved or extracted until after the fractographer has had an opportunity to examine them in situ. Of course, this may not always be practical, but the fractographer should make an effort to see the fracture scene and fragments in as close to in situ state as possible. At the minimum, photographs of the overall fracture pattern and close-ups as necessary should be taken. Figures 4.15 illustrate some of these recommendations for a practical failure problem. This window fracture also illustrates how witness marks or traces of the impactor material aided the interpretation.

The impulse is to jump directly to an examination of the fracture surfaces to find an origin. While there may be no harm in this (and it is human nature for most fractographers to take this step), there is one extra step that is prudent to take, especially if a moderate or great amount of time has been spent in specimen reconstruction or the part is involved in serious failure analysis or litigation problem:

The entire component or part should be photographed or sketched.

There are several reasons why it is wise to capture an image of a whole structure or sketch it at an early stage. There are obvious instances, for technical or legal purposes, why a permanent record is required. It is best to make the record as soon as possible, lest pieces be lost, misplaced, or mangled in handling. An early record is essential if pieces need be cut up for



Figure 4.15 Window fracture problem. Evidence collected at the scene included foreign material attached to the impact site as shown in (d). The crack patterns indicated impact from the exterior. That plus the height of the impact above the ground, the tuft of fur, the time of the year (November, the rutting season) and similar occurrences elsewhere suggested the cause of failure shown in (e).

microscopic examination. If the pattern of fracture is complex and an origin location not obvious, the fractographer may have to examine many pieces in order to track the cracking pattern back to the origin. A sketch or photo that can be marked up aids this process. Figure 4.16 shows an example of a broken component and an accompanying sketch with work notes. (Fréchette suggested a labeling scheme that some fractographers might find useful (Figure 8.1 of Ref. 1.)

An overall sketch or photo will help the analyst show other fractographers, engineers, managers, or clients the overall context of the fracture origin or fracture pattern. Is the fracture from the same location as other parts, is the pattern of breakage the same, or has a new failure mode been triggered? Much time and accuracy may be lost in orally explaining or drawing sketches from memory the fracture patterns days or weeks later. A handy overall photo of the part can save time and reassure others that the correct fracture origin photos indeed have been taken. Many closeup images of fracture features in the technical literature are unconvincing or may in fact have nothing to do with a bona fide fracture origin.

If many examples of a particular part are to be studied, then a sketch or photo of an *unbroken* part may be useful as a blank onto which fracture patterns may be sketched or drawn.

A ruler, magnification marker, or a common object such as a coin should be placed next to the component when a photo is taken.

Some common fracture patterns are shown in the following examples. The reader is referred to the bibliography for more information. Fractographers who are dealing with specific component failures are strongly advised to search the literature for prior examples and documentation of similar fracture patterns. Appendix B of this guide is a compilation of specific fractographic case studies.

(a)



(b)

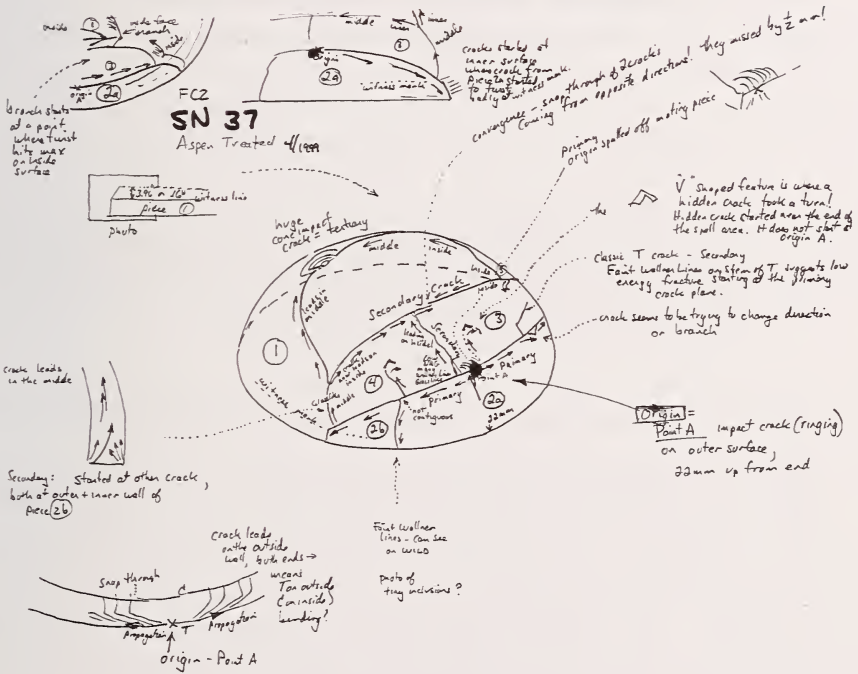


Figure 4.16 Fractured single crystal sapphire hemispherical dome and working sketch with notes. The crack progression along individual pieces was used to back track to the origin (arrow). The sketch helped integrate and keep track of the information from examination of the individual pieces. The origin is marked by the arrow in (a) and is labeled "origin" in (b).

4.8 T Intersections and Crossing Cracks

Intersecting cracks may pose interpretation problems in component fracture analysis. A fractographer may initially be confused by the multitude of intersecting cracks. Which came first? Which way was the crack going? With a little experience and applying the process of deduction, it usually is not too difficult to answer these questions. Figure 4.17 offers some guidance.

Crack branching creates markings shown in (a). The branch angle depends upon the stress state as shown previously in section 4.3. Even with biaxial loading and branch angles near 180° , a close examination of the branching point will show which way the crack was moving as it split. Hence the determination of the crack propagation direction is easy. Intersecting cracks as shown in (b) are also easy to interpret. The first crack passes through the plate undisturbed. The second crack approaches and is stopped at the intersection since it is unable to traverse the previously cleaved material. Intersections are commonly at 90° since the second crack moves at right angles to tensile stresses and tensile stresses cannot be carried across the previously cleaved crack. Figure 4.16 shows an example. Examination of the fracture surfaces (to be discussed in the next chapter) will also corroborate the interpretation, since the fracture surface of the first crack is planar and undisturbed though the intersection. Wallner lines and hackle lines for the first crack plane are continuous and connected on each side of the intersection.

The scenario shown in Figure 4.17c is less common, but occurs in cases where an initial crack does not completely cleave the plate. This can easily occur with bending fractures wherein the crack leads on one side that is in tension, but does not necessarily go all the way through on the compression side. The window in Figure 4.15c was such an example. In such cases, the remnant ligament of unbroken material provides a path for a crossing crack to traverse the first crack. The key feature to look for is a disturbance in the fracture surface features. The fracture surface markings (Wallner lines and hackle) on the first plane are continuous on either side of the intersection, but there is a pronounced change in the markings on the second crack plane, often a jog, or a hook around and up to complete the fracture just on the other side of the first crack. Sometimes two cracks seem to cross exactly over each other at exactly 90° , but a very close inspection of the exact intersection will show that one (the second crack) has a slight offset or step where it intersects the other.

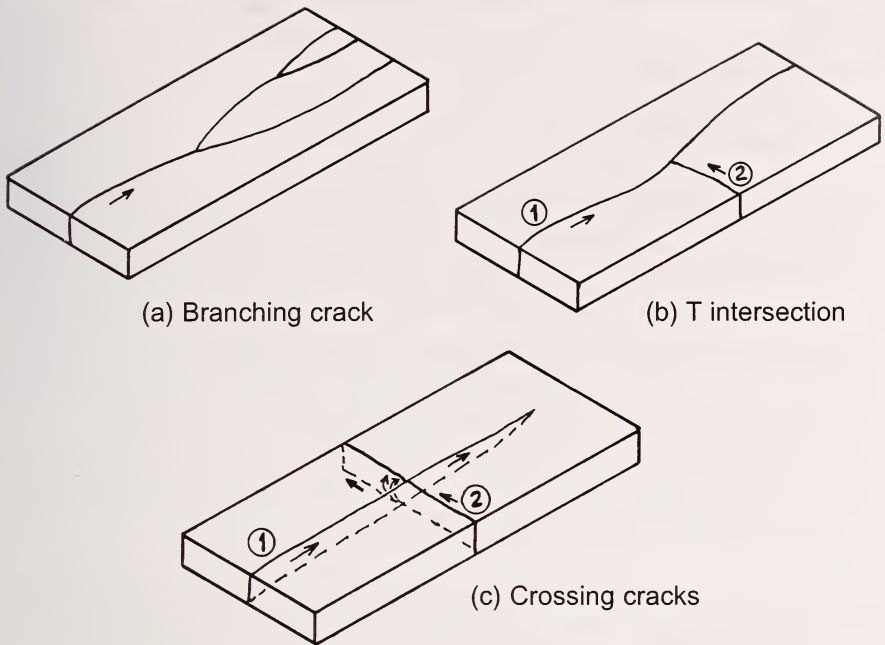


Figure 4.17 *Intersecting cracks. (a) shows common crack branching, which can be distinguished by the gradual forking. (b) shows a T intersection. The numerals indicate the first and second cracks. (c) shows a crossing crack, which may occur if the first crack does not completely cleave the part.*

4.9 Invisible Cracks

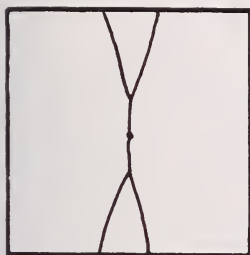
Incomplete fractures sometimes create cracks that are difficult or impossible to see. The interfacial separations may be less than the wavelengths of light and the cracks are not visible even under a microscope. The cracks may even be partially healed. Interfacial adhesion may be due to hydrogen bonding from water molecules adsorbed onto the fresh surfaces following the initial crack opening.¹⁴ When a crack is created but closes quickly, as in the case of a window impact, pockets of air may be trapped between the crack faces. These pockets may be visible if light is reflected off the glass-air interface. Sometimes the light is refracted creating elusive but colorful reflections that are visible only at certain angles. (This is one reason why it is wise to rotate and shift a piece while inspecting it, or to move around it if the piece is stationary.) “Chill check” cracks, described in section 6.8.3 and shown in Figure 6.33, are tiny cracks formed by transient, very-localized thermal shock. They can be very difficult to see. Sometimes crack segments will *appear* to be isolated and not connected to other cracks or to an origin, but they are in

fact connected by invisible segments. Fréchette described a case wherein a tight long crack in an intravenous feeding bottle went unnoticed in a hospital, leading to a fatality (case 10.8 in Ref. 1).

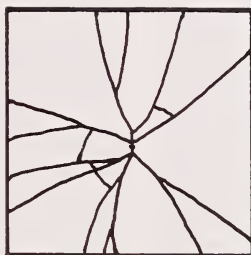
4.10 Plates and Windows

Plates and windows can exhibit a wide variety of fracture patterns. Some common modes are shown in Figure 4.18. An excellent article on the fracture of flat glass is by Shinkai, reference 3. His article shows subtle variations in the fracture patterns depending upon whether the plate edges are freely supported or are built in. Variations also occur with plate thickness. The extent of residual stress in tempered glass plates may also be estimated from the size of the diced fragments as will be discussed in 7.2.2. Heat strengthened glasses also have compressive residual stresses such that the glass is twice as strong as an annealed plate, but the pieces do not dice into small fragments and break into triangular shards.

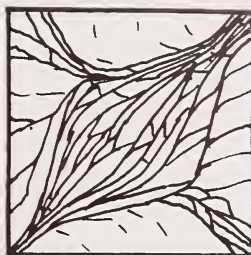
Blunt objects may create a cone crack that penetrates partially or completely through the plate. Such a flaw may or may not necessarily constitute a failure, since the plate is essentially intact except for the impacted site. At higher velocities, radial cracks may be generated that emanate from the impact site. Radial cracks also may be triggered by impact of sharp objects. In other cases, the bending forces from the impact may cause the crack (once it is away from the immediate impact site) to run on the opposite side of the plate from the direction of impact. At even higher velocities, the continued loading of the plate causes the radially-fractured segments to bend inward, leading to circumferential secondary cracking. In this case, the maximum tension is on the impacted side of the plate. These form rings around the impact site, but the rings are often offset at the radial cracks, confirming that the latter occurred first. Figures 4.15c and 4.18 show examples. Sometimes a secondary ring crack may step across a radial crack if the latter has not completely severed the plate. Very blunt objects may not necessarily create cracking at the impact side. Bending forces can create tension opposite the impact side and can trigger crack growth from flaws on the opposite side. In some instances, the very blunt object can generate bending forces in the plate that triggers a crack from a flaw at the plate edge. A crack runs to the impact site, and then radiates and branches repeatedly outward. In analyzing such fracture sequences, it is often very useful to combine the overall crack pattern analysis with an examination of the fracture surfaces, as described in the next chapter. The fracture surface examination reveals whether the crack was running uniformly through the thickness or was leading on the inside or outside plate surfaces. The latter information can establish whether the plate was in bending, and if so, which side was in tension.



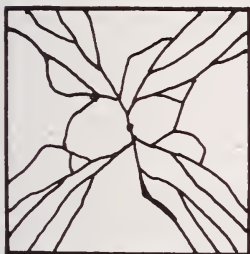
Uniaxial bending
Supported on the sides



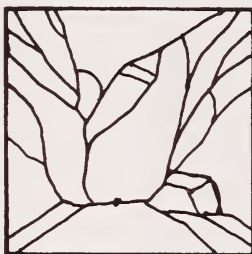
Pressure loaded
Supported all around



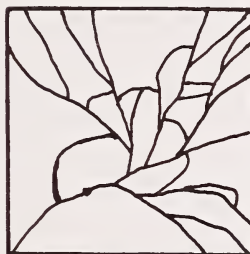
Diagonal compression
(after Ref. 3)



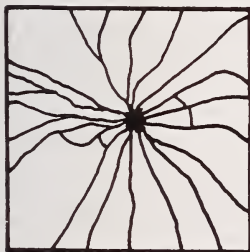
Pressure loaded
Freely supported
(After Ref. 3)



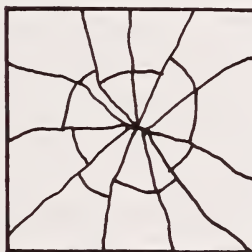
Pressure loaded
Freely supported
(After Ref. 3)



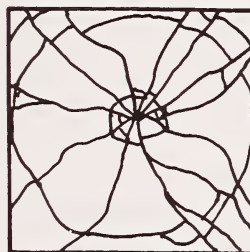
Pressure loaded
Freely supported
(After Ref. 3)



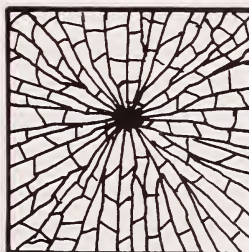
Ball impact
Freely supported



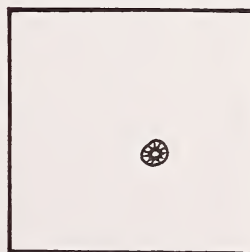
Center impact
Secondary ring cracks



Center impact
Secondary ring cracks



Sharp impact
Tempered glass



Blunt impact
(BB hit)

Figure 4.18 Plate and window fracture patterns. Figure 4.14c shows an example of a center impact plate with secondary ring cracks.

4.11 Tempered Windows

Tempered glasses fracture into many small fragments. Occasionally such fractures are triggered by internal flaws such as nickel sulfide inclusions. More commonly, the fracture is triggered by impact or sharp contact loading on the surface. If the loading is sufficient, it drives a surface crack through the surface compression temper zone and into the interior tensile stresses. Once this occurs, the plate will spontaneously fracture into many small fragments, since the internal stresses are more than sufficient to cause propagation and branching. Often the diced glass remains in place and does not fall apart. The origins can often be deduced from the branch crack patterns as shown in Figure 4.19. Close examination of the origin area often reveals that in moderate impact or loading cases, the crack branching creates matching symmetrical hexagonal shaped pieces at the origin as shown in Figure 4.19c. Indeed, as will be discussed in section 7.3.2 and figure 7.6, a later chapter, the first branch distances may be used to estimate the temper stress. An excellent article on the fracture of tempered flat glass is by Shinkai, reference 3. Shinkai states that some higher energy impacts may not have the two telltale fragments at the origins, and may instead have cone cracks that penetrate from the surface.

Finding the origin fragments may seem hopeless for extensively fractured tempered plates if the fragments have fallen out of a frame, but the hexagonal (or pentagonal or heptagonal) fragments are distinctive and can be found by simply sifting through the rubble. With persistence and a little luck, the patient fractographer may be rewarded.^b In some instances, tempered plates do not break up into uniform fragments. The existence of atypical fragments is often a sign that the temper was non-uniform either by design (e.g., Shinkai Ref. 3, p.288) or not (e.g., Fréchette, Ref. 1, case 10.18), or relieved by high temperature exposure (e.g., Fréchette, Ref 1, case 10.22).

^b Professor J. Varner has singled out origin pieces from a bucket full of swept up fragments.

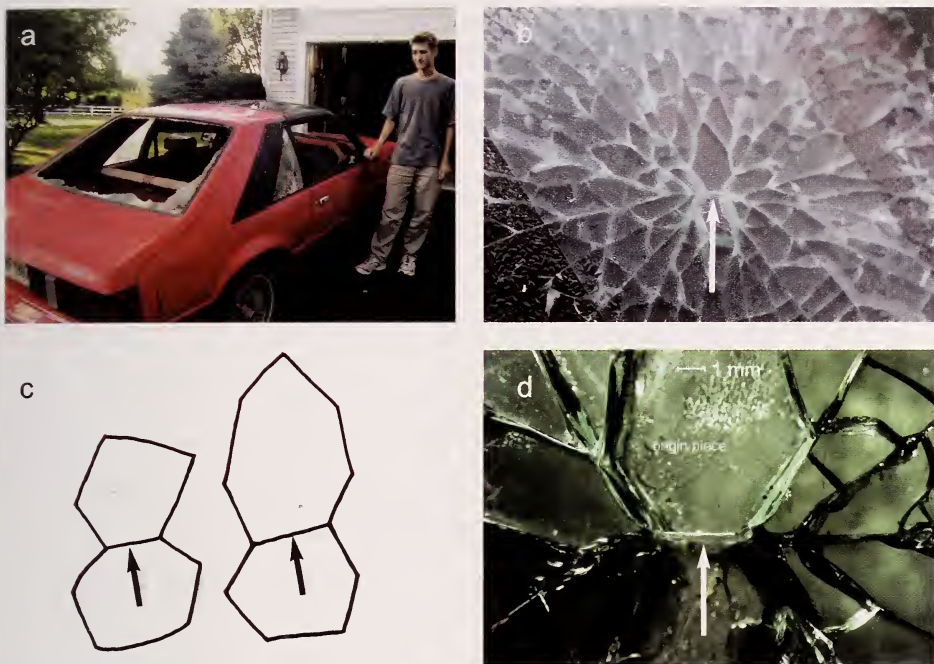


Figure 4.19 Tempered glass fractures in the author's son's car. Flying debris from a tornado in College Park, Maryland in September, 2001 caused the impact fractures (a,b,d). The arrows show the actual origin in one window and (c) shows some variations of shape of typical matching origin pieces. The fracture surface of the origin piece is shown in Figure 5.19b.

4.12 Thermally Induced Plate and Window Fractures

A center-heated plate is one which is heated in the middle while the rim is cooler. Differential strains put the middle of the plate into compression and the rim into tension. The plates fracture as shown in Figure 4.20. The crack starts from an edge origin in tension and initially propagates at 90° to the edge, but then changes to a meandering wavy pattern as it approaches the initially compressively stressed portions of the plate. The waves are often periodic as shown in (b). Figure 4.21 shows a thermal failure in an alumina plate. Case 6 in Chapter 10 shows another example in a SiC furnace plate. Fréchette¹ noted that a meandering cracks are not proof of thermal stresses and they can also form in impact cases in the final stages of breakup.

Thermal stress fractures often have localized tensile stresses that start fracture, but diminish away from the origin site. Branching may be minimal and the fracture surfaces may be relatively featureless and flat in regions away from

the origin. Wallner lines or hackle lines (discussed in the next chapter) are rare. On the other hand, there may be multiple arrest lines attesting to stepwise propagation of the crack. Scarps may be present on the fracture surface if the part was thermally shocked by a cooler fluid.

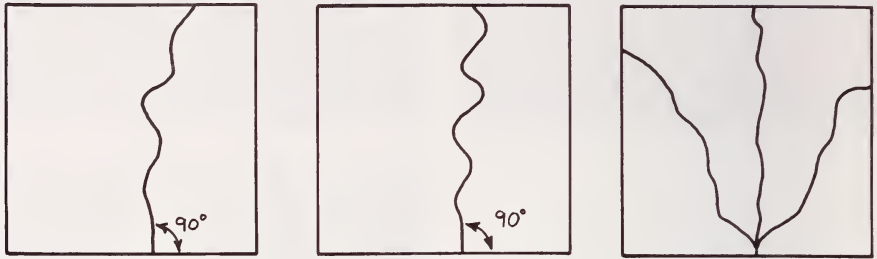


Figure 4.20 Fractures in center-heated plates. (a) and (b) are low stress fractures (less than 10 MPa {1,500 psi} in glass), and (c) is a higher stress fracture such that branching occurred.

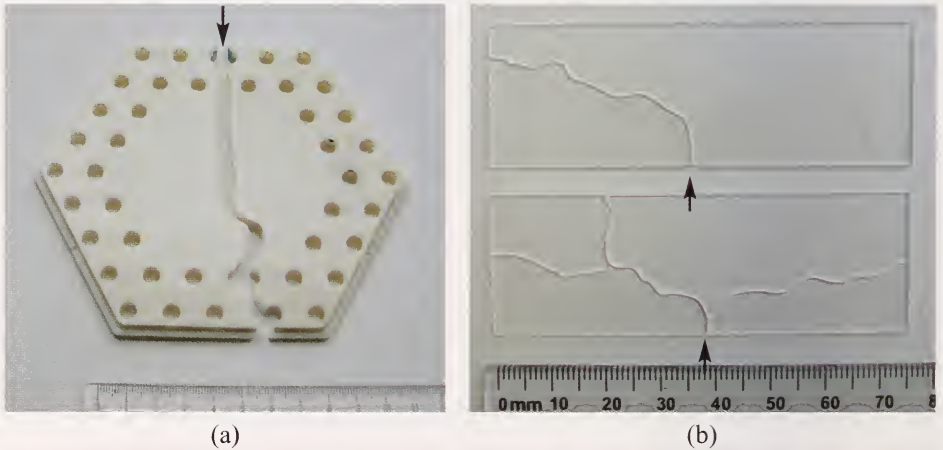


Figure 4.21 Thermal fractures with origin marked by arrows. (a) shows an alumina furnace baffle plate. Fracture started from grinding cracks associated with a hole. (b) shows glass slides broken by simply heating them on a hot plate.

4.13 Bottles and Pressure Vessels

Bottles and pressure vessels are susceptible to a variety of failure scenarios. Figure 4.22 shows some common modes, but this illustration is by no means complete. The reader is referred to the excellent review article by Kepple and Wasylyk¹⁵ for a more detailed presentation with more illustrations. Preston's article¹⁶ in 1939 was an outstanding early contribution. Fréchet¹ also illustrated a number of interesting glass bottle fractures.

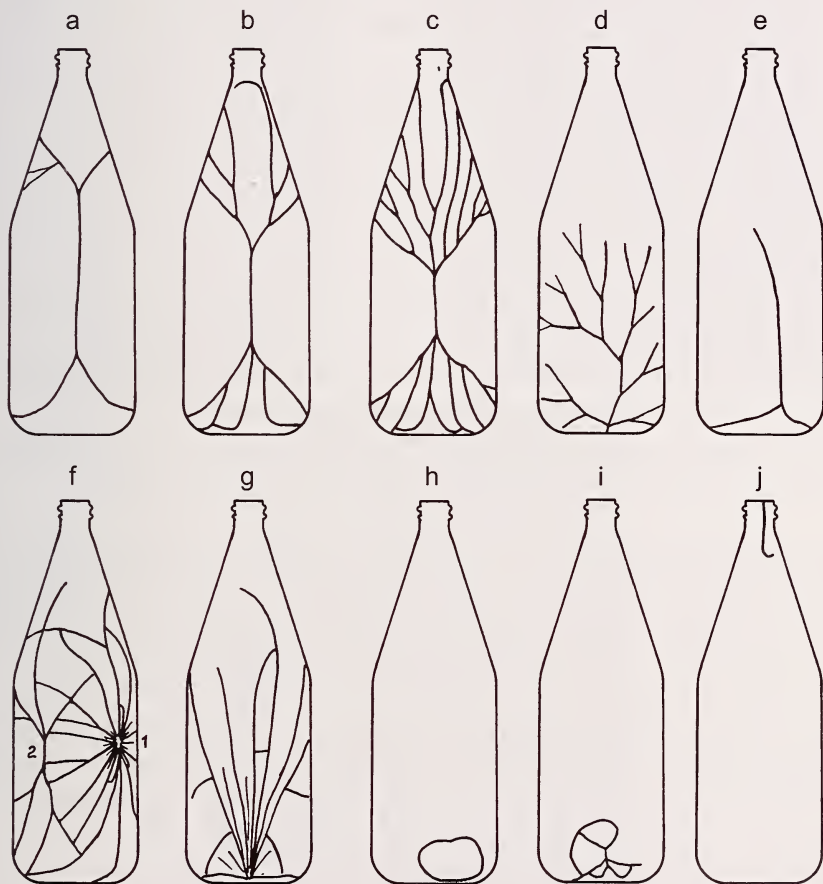


Figure 4.22 Bottle fracture patterns. (a-c) sidewall fractures due to internal pressure at progressively greater pressures; (d) internal pressure fracture starting from the base; (e) is a thermal fracture from sudden cooling of the base; (f) is an impact fracture on the right side (labeled 1) with a hinge fracture on the side (labeled 2); (g-i) show water hammer fractures and (j) shows a fracture from diametral rim clamping.

Fractures from internally pressurized bottles (e.g., carbonated beverages, Fig. 4.22 a-c) have vertical initial cracks, since hoop tensile stresses are double the axial stresses. Fractures initiate on the outside wall and branch in a symmetrical pattern about the vertical axis. The number of branches is proportional to the stress in the glass. Fractures start on the outside wall since larger flaws are more apt to be present there, but as the crack propagates it will extend to the interior and then lead slightly on the internal surface, since the stress is slightly higher there. Secondary breaks from bending have crack fronts that strongly lead on the inside surface. Pressure fractures from the base will also have extensive forking as shown in Figure 4.22d.

Thermal fractures have very little or no branching as shown in Figure 4.22e. Sudden temperature differentials can occur in a variety of different ways. Tensile stresses are generated when a portion of the body is suddenly cooled and attempts to shrink. The warm portions resist the contraction and put the cooler portions into tension. The temperature gradients can be either through the thickness or from one part of the body to another. Exposure of a hot vessel to a cold liquid often leads to thermal shock fracture. Fracture often starts and runs around the base and may extend up into the sidewall. Sometimes impact damage sites may be found around the base, either on the inside or the outside. Impact damage sites on the inside are often due to careless dropping of eating utensils into the glasses. Fréchette¹ and Kepple and Wasylyk¹² cover more thermal stress fractures of glass containers.

External impact fractures often have a starburst pattern at the impact site as shown in Figure 4.22f and 4.23. The principal crack system is not necessarily started at the impact site, however. The force of impact can cause the sidewall of the vessel to flex outwards creating a bending stress in the side of the vessel. This can trigger so-called “hinge fractures” 45° to the side of the impact site. Wallner lines indicate that fracture starts on the outside surface of the hinge fracture sites. A network of cracks from the impact site can start on either the inside or outside of the impact site, depending upon the sharpness of the impactor. The impact site may create the initial fractures, but in many cases the hinge origins fracture first. They then send a *leader crack* over to the impact site that triggers or exacerbates the fragmentation at the original impact site. Figure 4.23 shows an example of this in a glass tube. Filled glass containers dropped on their side trigger fracture from origins on the inside surface.

Water hammer is a phenomenon that can cause vessel fractures as shown in Figures 4.22g-i. The sudden arrest of a liquid in motion or a surge of liquid

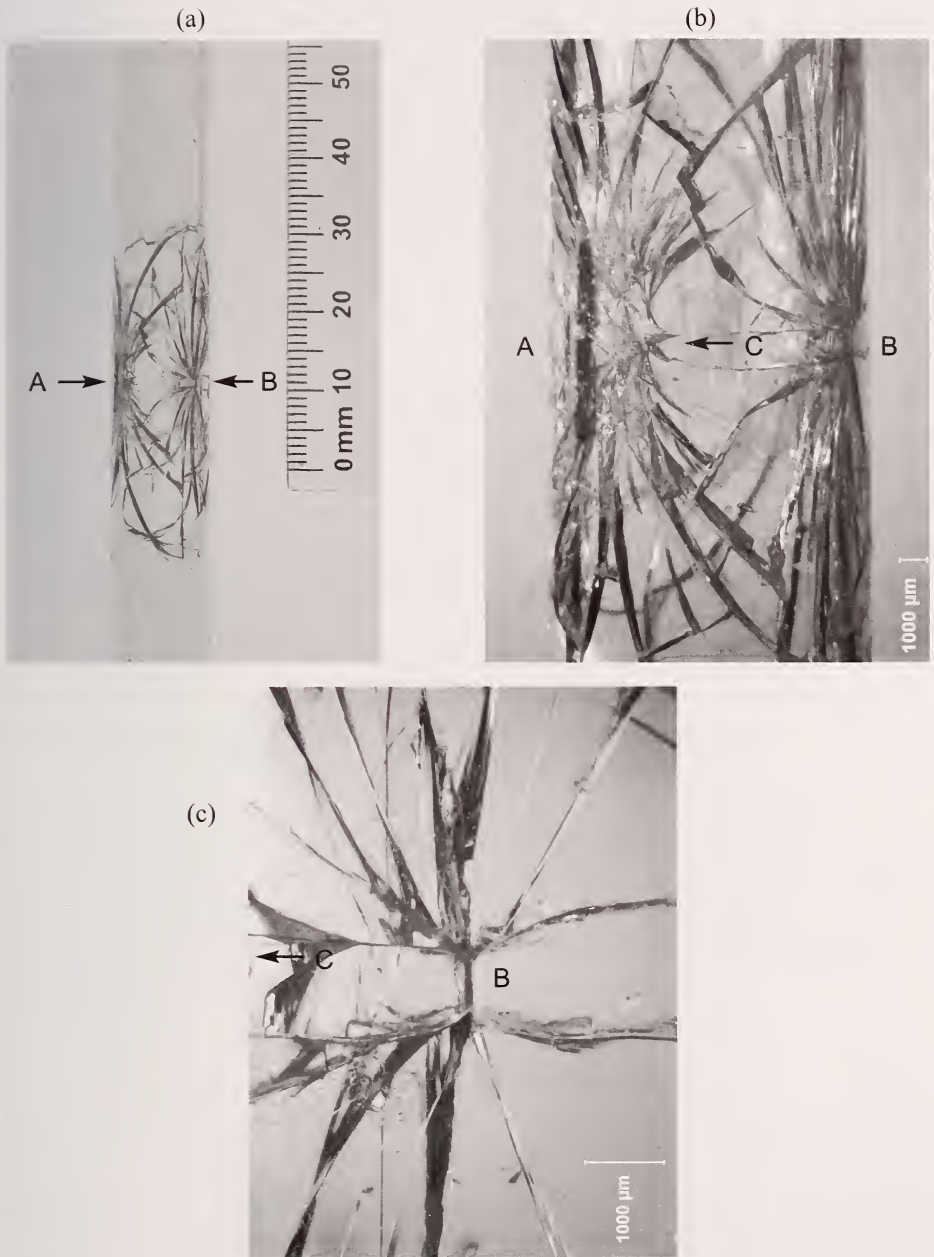


Figure 4.23 Small glass tube loaded diametrically at opposing points Point A (only the front is shown). Fracture started at the side hinge point B which generated an array of radiating cracks. One of these is the "leader crack" C (arrows in b and c) which went to the loading site A where it branched repeatedly and fanned out yet again. (Tube courtesy of W. Haller.)

that collapses a void in a partially-filled vessel can create transient intense internal localized pressures. Figure 4.22g shows a base fracture initiated by water hammer when a filled bottle was dropped. There may be a high concentration of cracks at the origin, but little branching afterwards since the stresses were focused at the base. Collapse of a void can occur in vacuum-sealed or incompletely-filled vessels. Base fractures shown in Figures 4.22h,i can result. Vessel necks are vulnerable to many forms of damage from chipping to capping-clamping stresses. Figure 4.22j shows a crack triggered by diametral clamping around the rim.

4.14 Torsional Fractures

Torsional loadings such as shown in Figure 4.24 produce twisted fracture surfaces at an angle to the part length. Torsional stresses usually do not induce a special failure mode in ceramics or glasses. Fracture starts at a flaw and the crack propagates normal to the plane of maximum normal tensile stress, which is aligned at 45° to the shear stress direction. In other words, the shear stress (τ) state is equivalent to one in which a material element is pulled in tension

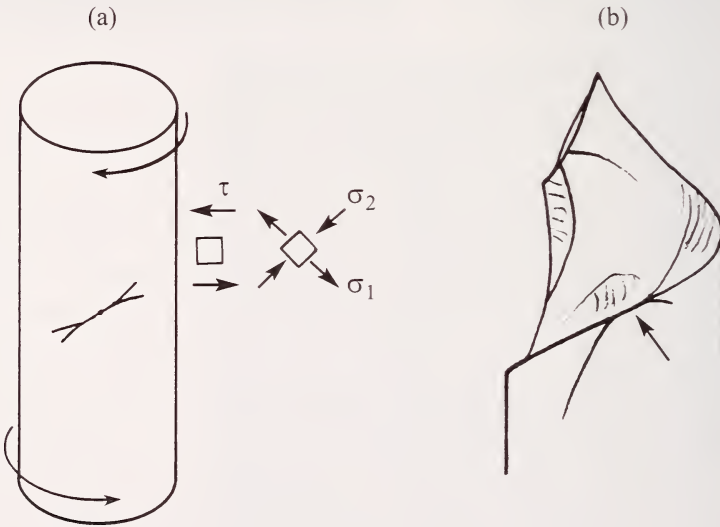


Figure 4.24 Torsional loading causes fractures at an angle to the longitudinal axis of a part. The shear stresses are τ . These generate equivalent principal stresses σ_1 in tension and σ_2 in compression as shown in (a). Fracture occurs perpendicular to σ_1 . (b) shows a schematic of a glass rod fractured in torsion (after Michalske, ref. 17). The origin is at the arrow. Note how branching occurs to either side of the origin, but that only one branch in each case continues giving rise to the curved fracture surface.

(σ_1) in one direction and compressed laterally (σ_2) as shown in the middle of Figure 4.24. Fracture primarily occurs due to σ_1 tensile stress and fracture propagates perpendicular to σ_1 . Many parts that fail in torsional loading also have some bending as well. Fracture surfaces often have ample twist hackle markings as discussed later in section 5.3.3. Figure 4.12 shows an example of a fracture in a bend bar that had superimposed bending and torsional stresses. Figure 5.25c shows the fracture surface of a glass rod with mixed tension and torsional loading.

4.15 Chipping

Concentrated loads near an edge can chip off a portion of the body. Figure 4.25 shows some examples. The load to cause fracture depends upon the shape of the object that applies the contacting force, the distance from the edge, the angle of the applied force P , the angle of the edge, and the material's fracture toughness. Several papers on edge chipping were given in a session at the 2000 Alfred Conference on Fractography of Ceramics and Glasses listed in the bibliography. Edge chipping also has been a topic in the lithic fracture literature and flint knappers have a good practical knowledge on the topic. The shape of chips varies with the angle of the applied load as shown in Figure 4.26.¹⁸ This has practical significance, since the shape of the chip can tell a fractographer the direction of the force that caused the chip.

Edge chips are very common as *secondary fractures* on broken ceramic or glass fragments. They easily occur if fragments bump into each other or impact other objects during breakage or subsequent handling. If there is any doubt as to whether an edge chip is a secondary or a primary fracture, compare the matching fracture halves. If the chip is only on one half, then it is a secondary fracture.

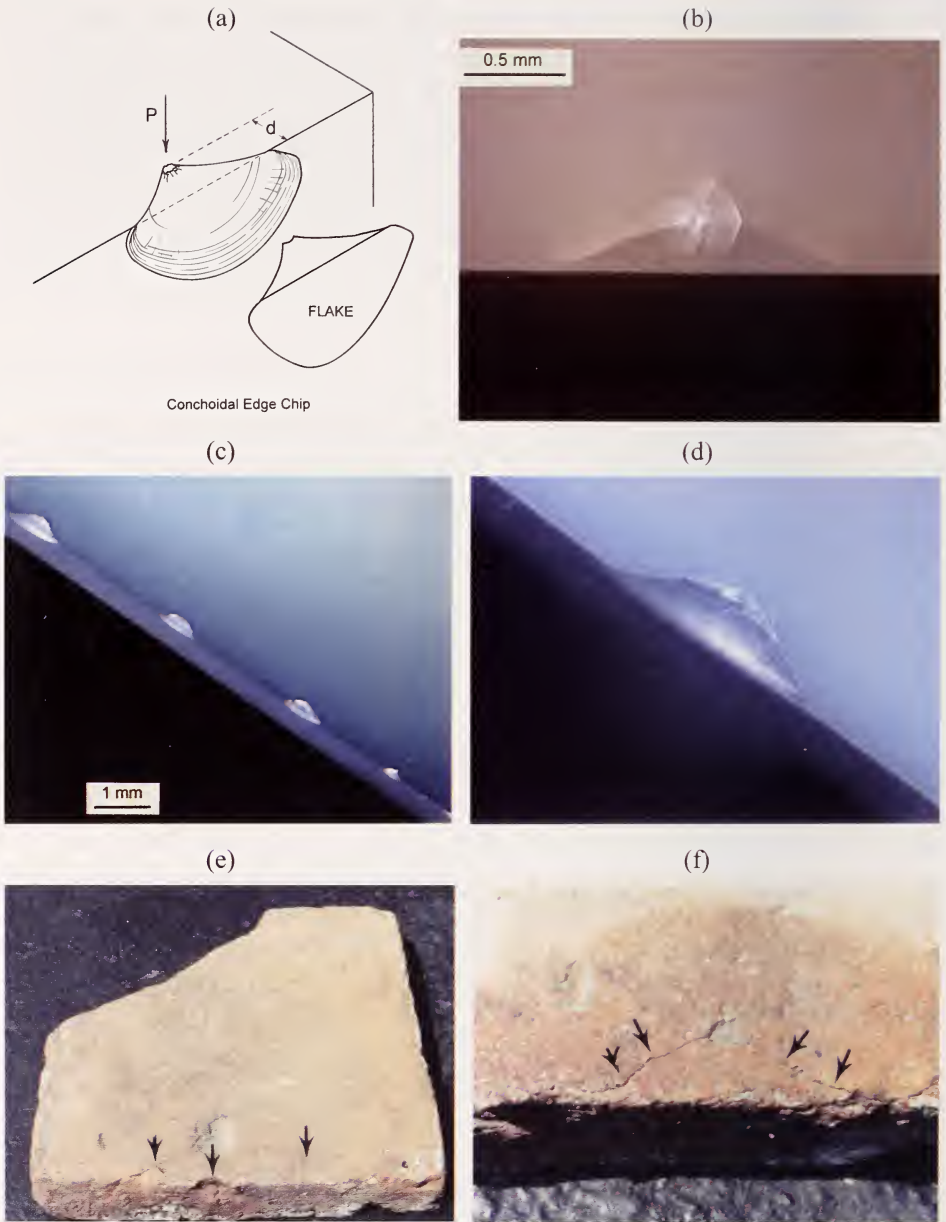


Figure 4.25 Examples of chip fractures. (a) is a schematic that shows how a chip is formed and the telltale shape. (b) shows a top view of a chip that is just about to pop off a lithium silicate foundation dental glass-ceramic. The loading point is obvious. (c) shows a row of edge chips created in porcelain under controlled conditions in the laboratory. (d) is a close-up. (e) and (f) show edge chips in an ancient Roman (circa 300 AD) 22 cm square x 3.4 cm thick hypocaust stone from Trier, Germany. (b,c,d, courtesy J. Quinn)

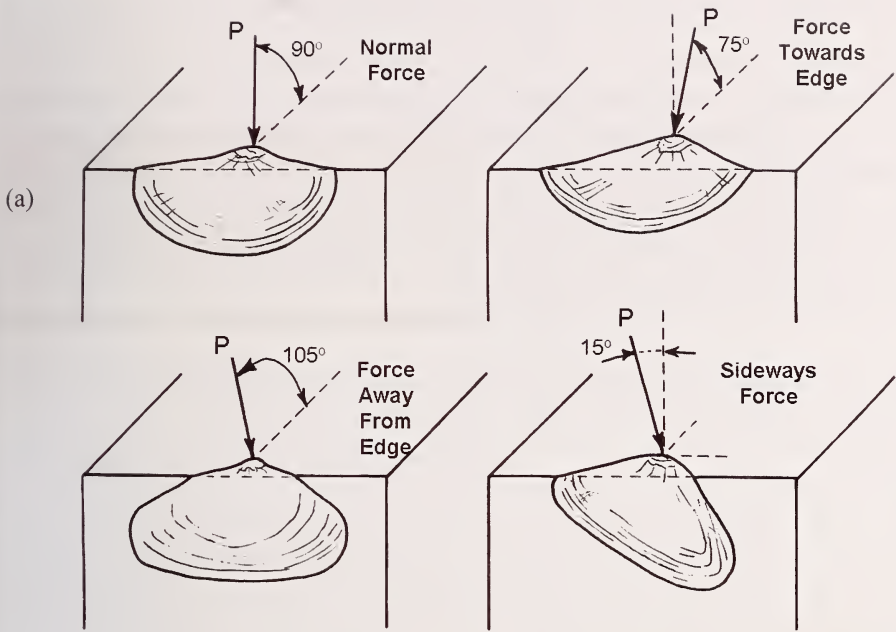


Figure 4.26 The angle of the applied load affects the shape of edge chips. (a) is a schematic that shows the patterns and (b) shows front views of two chips in glass (at different loads and distances from the edge) made by a conical indenter tool angled away from the edge at 105° . (after J. Quinn and R. Mohan, Ref. 18).

4.16 Laboratory Test Fractures and Component Fractures

Examination of laboratory test coupon fracture surfaces can often aid interpretation of component failures. It is not unusual to be confronted with only one or two component fractures. The fracture surface markings may be unfamiliar and common fracture markings such as hackle lines or cantilever curls may be hard to recognize. A few broken bend bars, tension specimens, or fracture toughness specimens of the same material may be invaluable in such cases. The fractographer can study the crack propagation behavior and markings for these familiar configurations.

The author used this approach to aid the interpreting of broken large (≈ 1 m) sintered porous fused silica missile radomes in the mid 1980s. This is case 7 discussed in Chapter 10. Only a few broken components were available and an initial examination of the weak material with its rough fracture surfaces was unsuccessful. Examination of bend bar and double torsion fracture toughness specimens gave the author more experience in interpreting crack propagation directions. Optimum examination conditions for detecting hackle and Wallner lines were discovered. This know-how was then applied to the full size components, with the result that fracture surfaces which initially confounded the author became tractable on the reexamination. The origins were found.

4.17 Controlled Component Fractures

Sometimes one must resort to controlled laboratory fractures of components themselves in order to simulate expected or actual fracture modes. Morrell et al.¹⁹ and Richter²⁰ have documented two superb examples of this approach for ceramic hip joint balls. Morrell et al.¹⁸ supplemented their component testing with biaxial disk and bend bar fracture testing.

4.18 Finite Element Analysis

Stress solutions may be straightforward for simple shapes and loadings, but many components have complex shapes and asymmetrical loadings. Closed-form solutions for the stress state may not be available. Finite element analysis (FEA) is a valuable tool for such problems. FEA models partition a body into small elements and uses computer analysis to obtain the stresses and strains in each using the theory of elasticity. In principle, the entire stress distribution in a body can be analyzed, provided that the loading conditions are accurately simulated. Software for FEA is becoming increasingly easy to use, but some skill is needed in setting up the problem, applying a good mesh,

and identifying the correct boundary conditions. Richter utilized FEA results to help interpret the ceramic hip ball fractures.²⁰

FEA analysis can be a case of “garbage in and garbage out.” Modelers may be so enamored of the models with their assumed loading conditions and anticipated fracture modes that they are unreceptive to obvious evidence that a component is not fracturing “the way it is supposed to break.” A good modeler should be flexible and not afraid to modify or adapt the simulation based on the fractographic findings. Reference²¹ reviews several case studies and compared model predictions to actual fracture modes.

4.19 Characteristics of Some Common Fracture Modes

4.19.1 Mechanical overload fracture

This chapter has illustrated only a sampling of mechanical fractures. The general breakage patterns can sometimes lead one directly back to an origin site, but often it is necessary to examine the fracture surfaces to interpret the directions of crack propagation as shown in chapter 5. Once a fracture pattern is recognized and an origin site identified, the next step is to assess whether the flaw is intrinsic to the manufacture of the part (as in a pore or inclusion), or from surface finishing, or from handling, contact or impact damage, or environmental attack (e.g., corrosion, oxidation, or erosion). Origins are covered in chapter 6.

4.19.2 Thermal fracture

Thermal stresses are created by differential strains created when portions of the body try to stretch or contract, but are constrained by other portions of the body at different temperatures. Thermal stresses may either be steady state (invariant with time) or time dependent. Gradual or linear spatial temperature gradients usually do not generate thermal stresses. Two types of thermal stress cases occur: (a) components with stresses arising from overall temperature gradients between portions of the body and (b), surface and interior stresses caused by through-thickness temperature gradients.

The center-heated plate problem discussed in section 4.12 is a classic case of (a). The differential expansion of the middle regions of the structure relative to the rim creates uniaxial hoop type tensile stresses at the rim that trigger fracture from an edge origin. The crack initially propagates perpendicularly to the edge but then slows down and meanders in the interior biaxial compression stress field. The interior stresses are of insufficient magnitude to cause crack

branching. The fracture surface markings (discussed in the next chapter) may be sharp and clear near the origin but then fade away to a very smooth featureless appearance as the crack slows down in the interior. Case 6 in chapter 10 is an example of a center heated plate fracture in a silicon carbide furnace part. Center-cooled plates have the opposite stress state: tension in the interior and compression at the rim. Fracture is less likely to occur in this case since the edge, which is likely to have the more serious flaws, is in compression.

Thermal stresses and strains occur during transient cool down or heat up events. Sudden temperature changes are called “thermal shock.” Thermal shock can cause strains between portions of a body or through-thickness stresses. Ceramics and glasses are most susceptible to sudden cool down thermal stresses, since tensile stresses are created at the surface. The surface layer of the part cools quickly and tries to contract, but the hotter interior portion prevents the contraction thereby creating tensile strains and stresses in the outer layer. Compressive stresses are generated in the interior. Suddenly cooling the surface with a fluid such as water can generate substantial tensile stresses and fracture since the fluid promotes rapid heat transfer from the surface. Some procedures, such as laboratory quenching of hot bend bars into water, create sharp stress gradients with a biaxial stress state at the surface. This leads to the formation of a two-dimensional network of surface cracks that may not necessarily penetrate completely into the interior.

Very-localized thermal fractures from contact of an article surface with a cooler contacting object can create “chill checks” that are very localized tiny cracks (Figure 6.33). These do not penetrate far or very deep since thermal strains are very localized. The cracks are susceptible to extension leading to fracture by subsequent events or loadings.

4.19.3 Impact or contact fractures

Impacts may create localized damage sites that can become the origin of fracture if the impactor is small or sharp, but can also cause fracture by imposing bending stresses on a structure such that fracture initiates on the side opposite the impact site or elsewhere in the body. Section 4.13 shows both scenarios. Sharp and blunt impacting objects create different types of localized damage origins as shown in sections 6.7.4 and 6.7.5. When an impact or contact fracture is suspected, the surface should be carefully examined for “witness marks.”

4.19.4 Corrosion or oxidation

Oxidation and corrosion can weaken a part and leave it susceptible to fracture. Telltale surface reactions are often readily apparent on the surface in the form of numerous pits, discoloration, and surface scale. Sometimes the damage is confined to small localized pits, bubbles, or blisters as shown in Figure 6.15. In some difficult to interpret cases, the reactions are localized along grain boundaries and can only be discerned with the SEM. Chemical analysis can show cation migration to or from a reaction site. It can also indicate contamination or reaction with the environment or furnace linings or insulation. Richerson²² shows several examples of corrosion-oxidation damaged silicon nitrides.

4.19.5 Residual stresses

Residual stresses can arise from many sources. They can be intentional as in tempered glass or unintentional as in ceramics sintered in furnaces with thermal gradients. They may be very localized as in the case of stresses around an inclusion that has different thermal contraction than a matrix or from a damage zone underneath a hardness indentation impression. Residual stresses can be through the thickness of a part or between portions of a body. The fractographer may be tipped off to the existence of residual stresses by the overall fracture patterns as shown in this chapter. A sudden change in crack propagation direction may be another sign. They can also be indicated by abrupt, seemingly spontaneous fractures when a component is being cut or machined. They may also be signaled by Wallner line markings on the fracture surfaces as shown in the next chapter. Distortions in the size and shape of a fracture mirror can be evidence of residual stresses. Quantitative analysis of flaw sizes can also be used to estimate residual stresses as shown in section 7.14.

Fréchette²³ described a case of boron carbide blanks fracturing during machining. Fractographic analysis showed that the fracture started at the root of the machine cut and then spread rapidly along the centerline of the slabs and then outward to the free surfaces. This indicated the interior was in tension and the outer portions were in compression. The firing schedule was reviewed and it was learned that the part was allowed to free cool between 1950 °C to 1800 °C followed by very gradual cooling thereafter. The free cooling occurred in a range where creep was possible which could have set up a final stress state not unlike tempered glass. No matter how carefully the slicing was done, once it reached the tensile interior stresses, the part fractured. The problem was simply remedied by changing the cool down rate

through the creep regime to minimize differential strains during the cool down, thereby eliminating the source of the residual stresses.

4.19.6 Time-dependent fracture

Delayed fracture can occur due to slow crack growth from preexistent flaws. The loading conditions and stresses may initially be insufficient to cause breakage, but a flaw may slowly grow when it is under load until it reaches a critical condition and then triggers breakage. The rate of crack growth is very sensitive to the stresses and stress intensities acting on a flaw, and growth can be very slow or rather fast. For constant stress, cracks accelerate with time in accordance with fracture mechanics analyses shown in section 7.10. There may be little or no warning of the imminent failure since the extent the crack grows to become critical may be very small. Sometimes the slow crack growth leaves telltale markings on a fracture surface as shown in section 5.9.

Chapter 4 References

- 1 V. D. Fréchet, *Failure Analysis of Brittle Materials*, Advances in Ceramics, Vol. 28, American Ceramic Society, Westerville, OH 1990.
- 2 F. W. Preston, "The Angle of Forking of Glass Cracks as an Indicator of the Stress System," *J. Am. Ceram. Soc.*, 18 [6] (1935) 175 - 176.
- 3 N. Shinkai, "The Fracture and Fractography of Flat Glass," pp. 253 - 297 in *Fractography of Glass*, eds. R. C. Bradt and R. E. Tressler, Plenum Press, NY, 1994.
- 4 R. W. Rice, "Ceramic Fracture Features, Observations, Mechanism and Uses," pp. 5 - 103 in *Fractography of Ceramic and Metal Failures*, Special Technical Publication 827, American Society for Testing and Materials, West Conshohocken, PA, 1984.
- 5 R. E. Bullock and J. L. Kaae, "Size Effect on the Strength of Glassy Carbon," *J. Mat. Sci.*, 14 (1979) 920 - 930.
- 6 G. D. Quinn and G. Wirth, "Multiaxial Strength and Stress Rupture of Hot Pressed Silicon Nitride," *J. Eur. Ceram. Soc.*, 6 (1990) 169-177.
- 7 J. B. Quinn, "Extrapolation of Fracture Mirror and Crack-Branch Sizes to Large Dimensions in Biaxial Strength Tests of Glass," *J. Am. Ceram. Soc.*, 82 [8] (1999) 2126 - 2132.

- 8 D. Shetty, A Rosenfield, and W. Duckworth, "Crack Branching in Ceramic Disks Subjected to Biaxial Flexure," *Comm. Amer. Ceram. Soc.*, Jan. 1983, C10-C12.
- 9 D. Hull, "Influence of Stress Intensity and Crack Speed on the Fracture Surface Topography: Mirror to Mist to Macroscopic Bifurcation," *J. Mat. Sci.*, 31 (1996) 4483 – 4492.
- 10 G. D. Quinn and R. Morrell, "Design Data for Engineering Ceramics: A Review of the Flexure Test," *J. Am. Ceram. Soc.*, 74 [9] (1991) 2037-2066.
- 11 J. Miklowitz, "Elastic Waves Created During Tensile Fracture, The Phenomenon of a Second Fracture," *J. Appl. Mech.*, Mar. 1953, 122 – 130.
- 12 H. Kolsky, "The Waves Generated by Brittle Fracture in Glass," *Trans. Soc. Rheology*, 20 [3] (1976) 441 – 454.
- 13 H. Fessler and D. C. Fricker, "A Theoretical Analysis of the Ring-on-Ring Loading Disk Test," *J. Am. Ceram. Soc.*, 67 [9] (1984) 582 – 588.
- 14 D. G. Holloway, "The Fracture Behavior of Glass," *Glass Technol.*, 27 [4] (1986) 120 -133.
- 15 J. B. Kepple and J. S. Wasylak, "Fracture of Glass Containers," pp. 207 – 252 in *Fractography of Glass*, ed. R. C. Bradt and R. E. Tressler, Plenum, NY, 1994.
- 16 F. W. Preston, "Bottle Breakage—Causes and Types of Fractures," *Bull. Am. Ceram. Soc.*, 18 [2] (1939) 35-60.
- 17 T. A. Michalske, "Quantitative Fracture Surface Analysis," pp. 652 – 662 in *Engineered Materials Handbook Ceramics and Glasses, Volume 4*, ed. S. Schneider, ASM Int., Metals Park, OH 1991
- 18 J. B. Quinn and R. Mohan, "Geometry of Edge Chips Formed at Different Angles," *Ceram. Eng. Sci. Proc.*, 26 [2] (2005) 85 – 92.

- 19 R. Morrell, L. Byrne, and M. Murray, "Fractography of Ceramic Femoral Heads," pp. 253 – 266 in *Fractography of Glasses and Ceramics IV*, eds. J. Varner and G. D. Quinn, Ceramic Transactions Vol. 122, American Ceramic Society, Westerville, OH 2001.
- 20 H. Richter, "Fractography of Bioceramics," pp. 157 - 180 in *Fractography of Advanced Ceramics*, ed J. Dusza, Key Engineering Materials, Vol. 223 (2003), Trans Tech Publ., Switzerland.
- 21 G. D. Quinn, "Design and Reliability of Ceramics, Do Modelers, Designers and Fractographers See the Same World?" *Ceram. Eng. and Sci. Proc.*, 26 [2] (2005) 239 – 252.
- 22 D. W. Richerson, Chapter 16 in *Modern Ceramic Engineering, 2nd edition*, Marcel Decker, NY, 1992.
- 23 V. D. Fréchet, "Fractography and Quality Assurance of Glass and Ceramics," pp. 227 - 236 in *Quality Assurance in Ceramic Industries*, eds. V. D. Fréchet, L. D. Pye, and D. E. Rase, Plenum, NY, 1978.

5. Fracture Surface Examination

5.1 Introduction

The origin may range from a type and location anticipated by the fractographer (as in a broken bend bar) to an unexpected type from an unexpected location or cause (as in a broken component). With familiar laboratory strength test specimens, the fractographer may proceed directly to the primary fracture surface and quickly locate the origin area. Usually the fractographer seeks a fracture mirror, a key feature centered on the origin. Figure 5.1 shows an example. The origins are often very small and magnification by a microscope is necessary. Stereoptical microscopes are ideal for initial fracture surface examinations. Sometimes this examination may be all that is needed for a full characterization of the origin. In other instances, the flaw at the origin is so small that scanning electron microscopy is needed.

Unexpected failure modes or component fractures require more time to study. The crack propagation markings on fracture surfaces allow one to evaluate the state of stress, the crack velocities, and interpret crack propagation paths back to an origin. In instances where an origin is not obvious, it may be necessary to study many fragments and carefully determine the local direction of crack propagation. Stereoptical microscopes are ideal for this initial fracture surface examination. Wallner lines and hackle markings are helpful indicators of the direction of crack propagation. It may be helpful to mark which way the crack was running in a fragment. This can be repeated for other fragments and then the pieces reassembled so that the lines of crack propagation can be tracked back to an origin site. Even very complex fractures may be interpreted if the fractographer is patient and systematic.

The greater the stress in the part at fracture, the more the stored energy, and the richer the fracture markings. Weak parts with low stored energy are often difficult to interpret. The part breaks into two pieces with relatively featureless fracture surfaces. Very porous or coarse-grained materials also can mask fracture surface fractographic markings. On the other hand, very strong components such as some glass optical fibers may have so much stored elastic energy at fracture that excessive fragmentation occurs and the origin cannot be found.

The nomenclature of fracture markings is varied. For example, “twist hackle” is also referred to as “river delta” lines. The Guide adopts the nomenclature system devised by Fréchette.¹ His system is practical, logical, and designed to

be easily remembered. Some of the definitions in the next sections are from Fréchet and some are new.

“Conchoidal fracture” and “cleavage fracture” are terms commonly used in the geological community. Cleavage fractures are smooth and planar fractures such as those on preferred breakage planes in single crystals. Conchoidal fractures do not follow natural planes of separation and often are curved, sometimes in a manner reminiscent of curved seashells. Conchoidal is derived from the Greek word for a mussel shell. Glass and many ceramic fractures are conchoidal. “Joint” is a common term in the geological community and means a fracture surface. Joints are defined as a fracture or crack in a rock mass along which no appreciable movement has occurred. “Parting” is another geological term describing flat fractures in a mineral, but is not necessarily along preferred cleavage planes. Parting is sometimes associated with twinning.

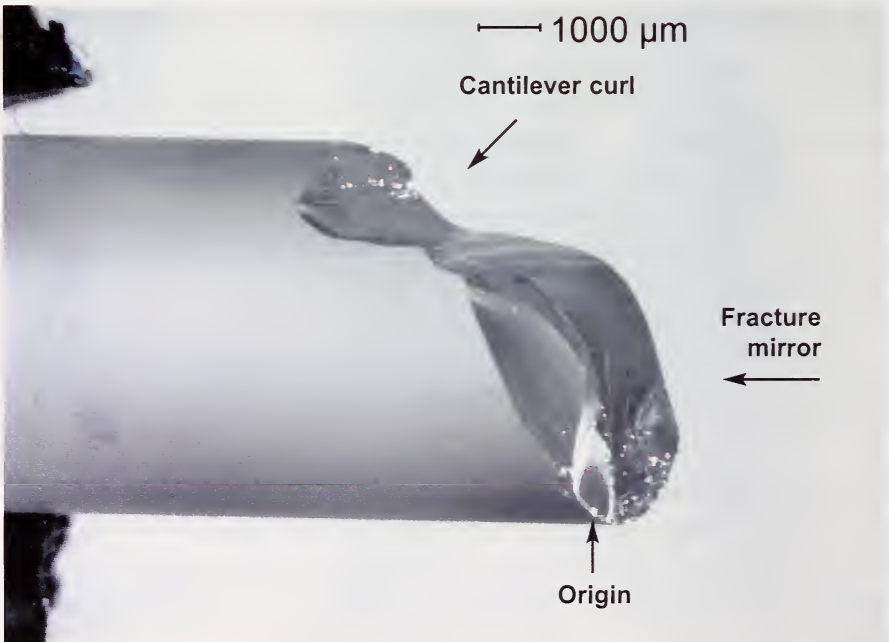


Figure 5.1 A fused silica rod fractured in bending at 88.5 MPa (12.8 ksi).

5.2 Fracture Mirrors, A Fractographer's Best Friend

5.2.1 Fracture mirrors in glass

Fracture mirrors: Relatively smooth regions surrounding and centered on the fracture origin. (ASTM C 1322 and C 1145)

Once a fractographer finds a mirror, he is reasonably sure that the fracture origin has been found. Figures 5.1 to 5.3 show mirrors in glass. They are telltale features that can be recognized by even novice fractographers. In strong specimens they are approximately circular or semicircular in shape, but significant deviations may occur as discussed later. Usually there is only one mirror corresponding to a single fracture origin, but there are exceptions that are discussed later in this chapter. There won't always be a fracture mirror and, if the fractographer cannot find one, he or she should not worry. More about this will be covered later in this chapter, but for now let us take a closer look at the fractographer's best friend.

The fracture mirror is the region where a crack radiates outwards from a flaw at the fracture origin. The crack accelerates from near zero velocity to terminal velocity within the mirror region. Using ultrasonic stress wave fractography on soda lime silica specimens, Richter and Kerkhof² and Field³ showed that a crack accelerates to between one-half to the full terminal velocity (≈ 1500 m/s) by the time the mirror-mist markings formed. Smekal⁴ arrived at the same conclusion from his analysis of the Wallner lines (described later) inside fracture mirrors. This remarkable acceleration over a very short distance occurs in microseconds.

The terminal velocity in glasses ranges from 700 m/s to 2500 m/s depending upon composition and elastic properties. It is even faster in ceramics. Table 5.1 lists some values. The terminal velocity is about 0.5 to 0.6 times the Raleigh surface wave velocity in an elastic body, or about 0.38 times the longitudinal (dilatational) stress wave velocity. The Raleigh wave velocity is less than the longitudinal wave velocity, $v_1 = \sqrt{E/\rho}$, where E is the elastic modulus and ρ is the density. The terminal velocity of the crack is limited by the speed that elastic energy is transferred to the crack tip. In principle, the crack can travel as fast as the Raleigh wave speed, but in practice the local deviations of the crack front that create mist and hackle limit the crack speed. Some atypical shock loading cases can drive a crack faster than the normal terminal velocity provided that the crack does not develop mist, hackle, or branching. Maximum crack velocities in single crystals whereby mist and hackle formation are suppressed can reach a greater fraction of the Raleigh

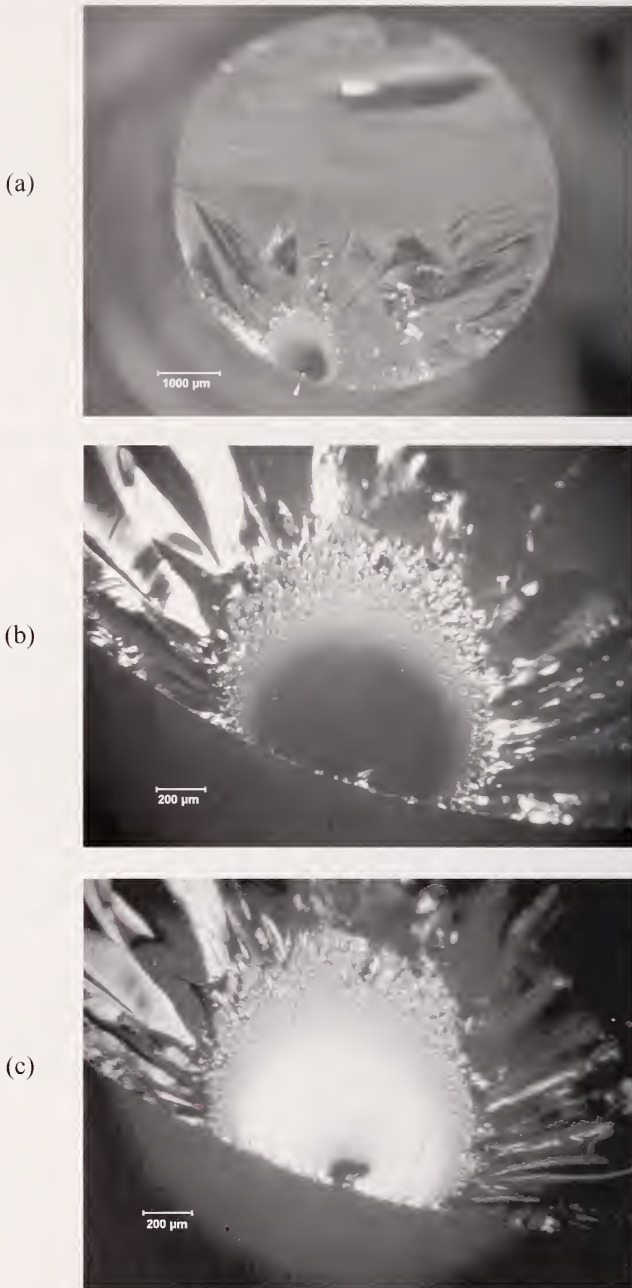


Figure 5.2 Three views of a fracture mirror in fused silica glass rod broken in bending at a high stress level (96.2 MPa, 13.9 ksi). (a) shows the entire fracture surface. (b) is a close-up of the mirror; and (c) is the same region but with the illumination adjusted. Maximum tension was at bottom center in view (a). The mirror is asymmetric due to the bending stress field.

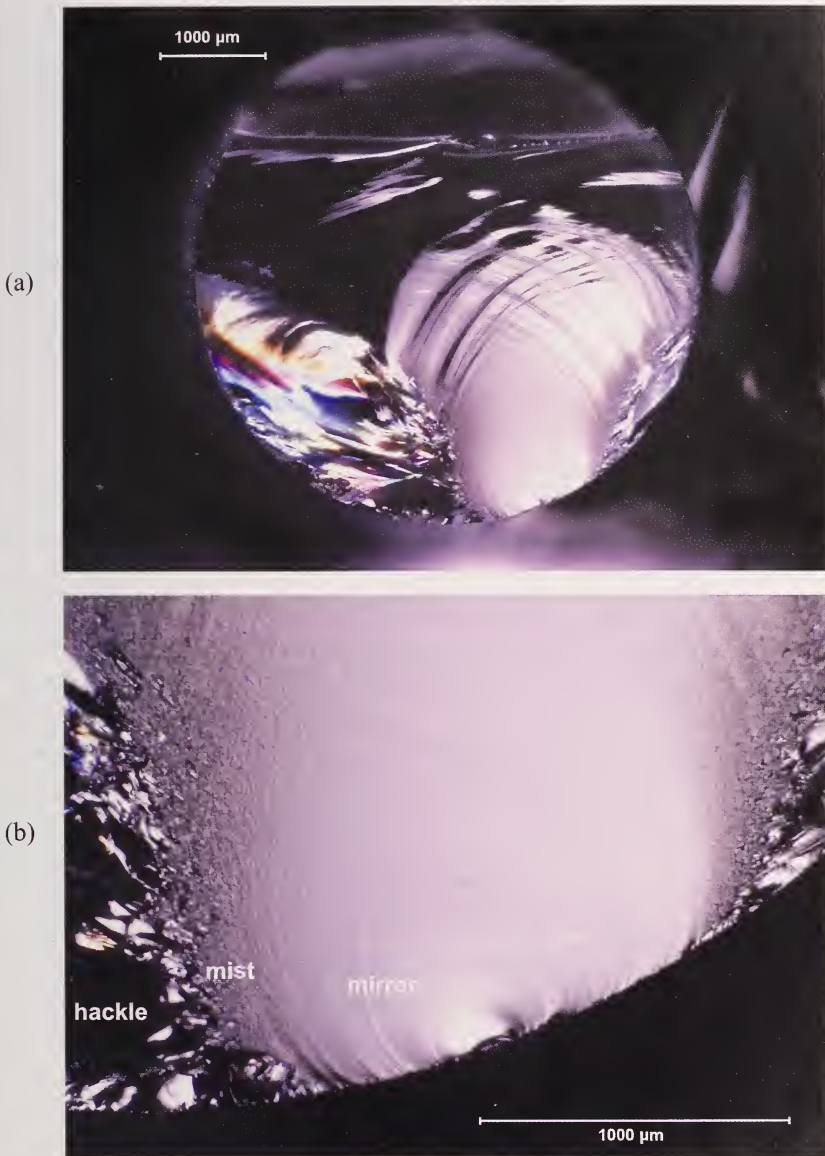


Figure 5.3 Two views of a fracture mirror in a moderate strength (76.2 MPa, 11.0 ksi) fused silica glass rod broken in bending. The mirror is incomplete since it was large relative to the cross section size. The advancing crack propagated into a decreasing stress field in the interior and did not have sufficient energy to form the mist and hackle in a complete circle. If this rod had been loaded in direct tension instead of bending, the mirror would have been fully formed and semicircular. The incomplete mirror in the direction of the interior is a telltale sign of bending.

wave speed than glass and polycrystalline ceramics. In some ballistic impact conditions, a *damage wave* of cracking in glass can proceed at velocities 80 % to 90 % of the *longitudinal* wave speed.^{5,6} High speed photography revealed that individual crack segments traveled no more than the conventional terminal velocity of 1480 m/s, but that secondary cracks nucleated right behind the shock wave.

If the stresses acting on the advancing crack decrease, the crack can decelerate and even stop. This is not unusual in thermal shock cases where stress gradients can be large.

Material	Maximum Crack Velocity (m/s)	Ref.
Soda lime glass	1510	7
Soda lime glass	1580	3
Soda lime glass	1540	11
Soda lime glass	1600	8
Soda lime glass	1500	10
Soda lime glass	1460	6
Various flint glasses	750 - 1400	7
Heavy flint glasses	700 - 1095	8
Mirror glass	1520	8
Borosilicate crown glass (BK-7)	1677	8
Borosilicate crown glass (BK-7)	1800	4
Fused silica	2100	4
Fused silica	2500	10
Fused silica	2155	7
Reaction bonded Si ₃ N ₄ (AME)	2950	9
Hot pressed Si ₃ N ₄ (HS 130)	3500	9
KCl, single crystal	700	3
LiF, single crystal	1700	3
MgO, polycrystalline (85% dense, 15 μm)	1800	9
MgO, single crystal, cleavage {100}	5100	3
Diamond, cleavage {111}	7200	3
Al ₂ O ₃ , single crystal sapphire, cleavage on {10 $\bar{1}$ 0}	4500	3
Al ₂ O ₃ , polycrystalline (Lucalox 15 μm)	2000	9
Tungsten	2200	3
Tool Steel	1700	9
Resin Plastic	420	8
PMMA	770	9

Table 5.1 Terminal crack velocities from Field (3), Smekal (4), Schardin et al. (7), Kerkhof (8), Congleton and Denton (9), Chaudhri (10), and Winkler et al. (5), and Barstow and Edgerton (11).

The term mirror came in to being as a result of early optical microscope examinations of glasses wherein the mirror region was so smooth that it reflected light like a mirror. Figure 5.2c shows a bright mirror region. (The illumination in this figure also accentuates the faint curved Wallner lines within the mirror, about which more shall be said later in this chapter.) In polycrystalline ceramics or composites, the qualifier “relatively,” as in “relatively smooth,” must be used, since there is an inherent roughness from the microstructure even in the area immediately surrounding the critical flaw.

The underlying principal that accounts for the micro and macro branching has been attributed to the crack reaching a critical velocity,¹² a critical energy level,¹³ a critical stress intensity,¹⁴⁻¹⁷ or a critical strain intensity.¹⁸ A velocity criterion for crack branching was discounted by data shown by Congleton and Petch.¹⁵ Richter and Kerkhof,² Field,³ and Döll¹⁹ used ultrasonic fractography to show that cracks approached terminal velocity before the formation of the mist boundary and there was no pronounced change in velocity when the mirror formed. Kirchner et al.^{16, 17} showed convincing evidence that a stress intensity criterion accounts for the mirror sizes and shapes. Congleton and Petch¹⁵ demonstrated that a stress intensity criterion controlled branching. They also showed that the Johnson and Holloway energy criterion¹³ was related to the stress intensity criterion. Tsai and Mecholsky²⁰ have pointed out that for isotropic materials it is difficult to distinguish between the energy, stress intensity, or strain intensity criteria since they are all related. This topic will be discussed again in Chapter 7 on Quantitative Analysis and in Appendix D on Guidelines for How to Measure Fracture Mirrors.

Careful electron microscopy and atomic force microscopy now have shown that the formation of the mirror is a gradual progression of very localized crack path deviations from the main plane. Figures 5.4 a-e show super-resolution electron microscope images of various regions in a mirror collected by Beauchamp.^{21, 22} Poncelet²³ showed comparable images in 1958, but Gölz may have been the earliest with extraordinary electron microscope photos published in 1943.²⁴ Rounded ridges that are elongated in the direction of crack propagation gradually coarsen in amplitude. At some point, they develop slight hackle steps where over running and under running fingerlike crack segments link. This point, where nano-micro scale hackle lines begin to form, could be an important transition point. Close examination of Beauchamp's Figure 5.4 b shows they are not present inside the mirror, but they are just visible in his Figure 5.4c near the mirror-mist boundary. Surface roughness could change significantly at this point. Attempts to correlate the

mirror boundaries with a simple surface roughness parameter have had only limited success, however, as discussed in more detail in Appendix D. Hull²⁵ pointed out that different surface roughness characterization devices such as atomic force microscopes (AFMs), mechanical profilometers, and laser optical profilometers all have different advantages, disadvantages, sensitivities and scanning zone sizes. AFMs can measure tiny regions with very high sensitivities, but may miss large hackle steps in a mist or hackle zone. These latter features can dramatically alter the average or root mean square roughness. Mist and hackle regions may have different roughness at different scales. Hull discusses these various scales of roughness in some detail in his book.²⁵

The mirror markings can be explained with reference to Figures 5.2, 5.3b, and 5.4. The explanation below closely follows Fréchet's¹ general discussion as well as Beauchamp's²¹ convincing analysis. As the crack accelerates away from the origin, micro portions of the crack front begin to twist slightly or tilt up and down out of the main fracture plane. These local deviations occur as consequence of the stress field in front of a fast crack having maxima that are out of plane, unlike the case for a static or slowly moving crack.¹² The momentary tilting or twisting does not persist for very long since crack plane deviations are restricted by the energetic cost of creating additional crack surface. The slight tilt or twist variations in crack plane quickly rejoin the main propagating crack plane. These tiny local crack perturbations exist well within the mirror region, but are too small to be optically discernable. As the crack advances, they eventually become large enough to be just discernable with the optical microscope as the "mist" zone surrounding the origin (Figure 5.4d). The mist has a slight frosty appearance such as when water condenses on a reflecting mirror. As the crack continues to advance, the local perturbations increase and begin to oscillate and form larger tongue-like segments that may deviate from the average fracture plane to the degree that micro steps are generated running parallel to the direction of crack propagation. (Some have described the out-of-plane perturbations as "fingers.") The perturbations gradually coarsen such that the tongue-like elements can overcut other portions of the crack front thereby generating large "velocity hackle" lines that run parallel to the direction of crack propagation. Beauchamp^{21, 22} pointed out that many of these features are similar in character from within the mirror out to the hackle zone. They differ only in scale. The transitions between the regions are gradual and are usually described as not abrupt. One intriguing observation by Beauchamp²¹ was that tilted or twisted hackle segments that rejoin with the main crack plane may generate elastic

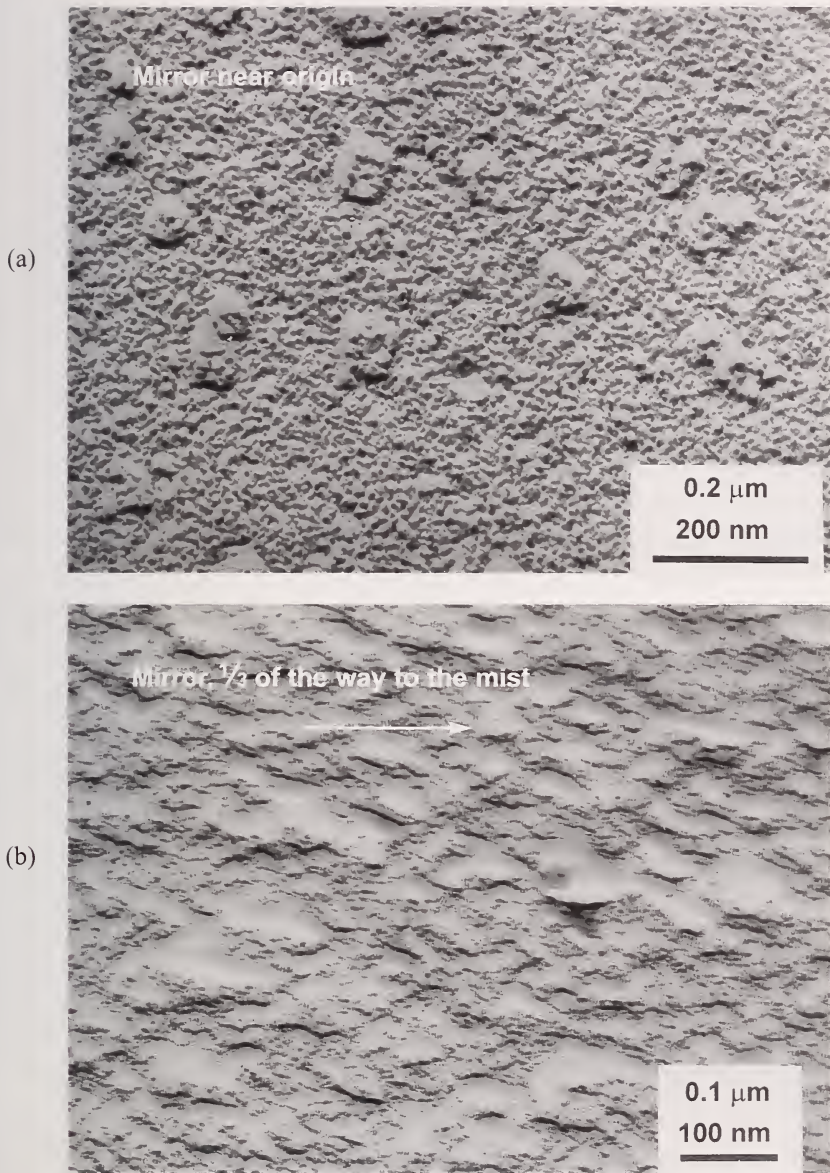
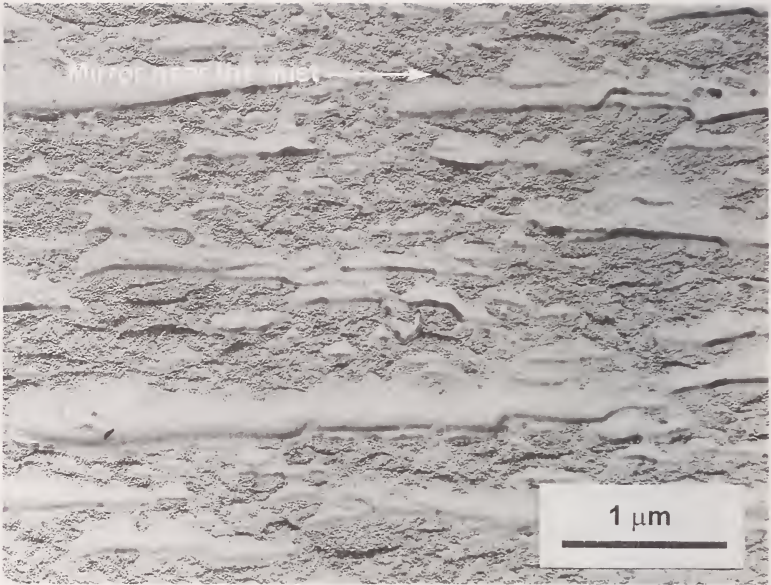


Figure 5.4 Transmission electron microscope pictures from parts of the fracture mirror in a lightly tempered soda lime glass sheet. (courtesy E. Beauchamp, refs. 21, 22) (a) is in the smooth mirror area near the critical flaw. The tiny black dots are an artifact of the specimen preparation, but the larger (50 nm) round bumps are genuine. (b) is in the mirror region about $\frac{1}{3}$ rd of the way to the mirror/mist boundary. The arrow shows the direction of crack propagation. The ridges and valleys are elongated in the direction of crack propagation, but they are too small to be detected optically.

(c)



(d)

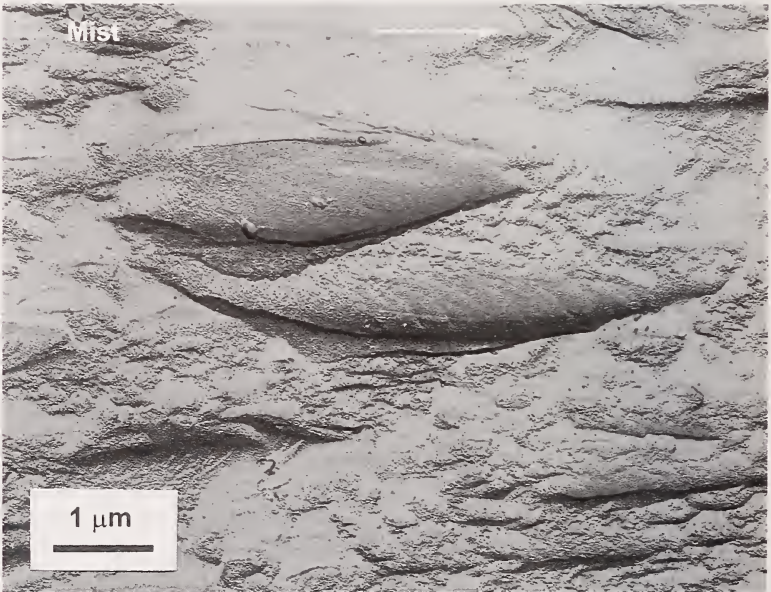


Figure 5.4 continued (c) is a region still inside mirror but close to the mist boundary. The ridges are longer and wider. (d) is in the mist, just beyond the mirror/mist boundary. The features are similar to the prior figure, except that they are now large enough to be detected optically. Close examination of (c) and (d) reveals faint but distinct twist hackle lines in some of the large features, attesting to some localized lateral crack growth.

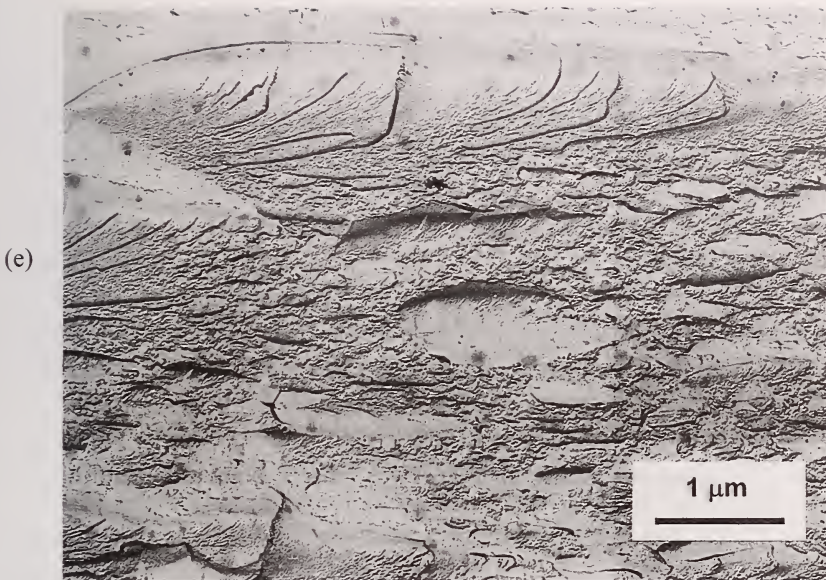


Figure 5.4 continued (e) shows features in the hackle zone. The features are now larger than $10\ \mu\text{m}$, but are similar in character to those in the mist and mirror zones.

pulses and Wallner lines, (described later in this chapter) that could trigger additional hackle along the crack front. This could be the impetus to form a band of hackle along the crack front and hence the mist-hackle boundary.

In summary, although the process of roughening through the boundaries has often been described as gradual, there are two potential transition points. The mirror-mist boundary may be a transition where nano-micro steps form between ridges that are tens of nanometers tall. The mist-hackle transition boundary may be where a band of microhackle forms that is triggered by self-generated or external elastic pulses (Wallner lines).

Fréchette¹ defined hackle and mist hackle. This Guide adopts his definition for the former, but makes a slight modification to the latter:

Hackle: *A line on the surface running in the local direction of cracking, separating parallel, but noncoplanar portions of the crack surface.*
(Ref.1, Fréchette)

Mist hackle: *Markings on the surface of an accelerating crack close to its effective terminal velocity, observable first as a misty appearance and with increasing velocity revealing a fibrous texture, elongated in the direction of cracking.*

Mist is fairly obvious in glasses, but is difficult or impossible to discern in ceramics due to the microstructure. Fréchette's definition of mist hackle originally also included the words "and coarsening up to the stage at which the crack bifurcates" which suggests it encompassed all mirror markings including hackle right up to the point of crack branching. It seems reasonable to distinguish the mist region from hackle region for practical reasons that will become evident when ceramic mirrors are discussed below. Therefore this Guide adds the following term:

Velocity hackle: *Hackle markings formed on the surface of the crack close to its terminal velocity, observable as discrete elongated steps aligned in the direction of cracking.*

Mirrors are very important since they not only draw attention to the fracture origin, but their size may be used to estimate the stress in the part at the moment of fracture. For a long time it was common practice to interpret the mirror as having distinct boundaries between the mirror and mist and between the mist and hackle. Extensive empirical work showed that the relationship between the mirror size and the stress at the instant of fracture is:

$$\sigma \sqrt{R} = A \quad (5-1)$$

where σ is the tensile stress at the origin at the instant of fracture, R is the mirror radius, and A is a constant, known as the "mirror constant" and is considered by many to be a material property constant. It has unit of stress $\sqrt{\text{length}}$, which are the same units as stress intensity which is discussed in detail in section 7.5.5. The mirror radius may either be the mirror-mist boundary or the mist-hackle boundary for glasses. There are different A 's for each boundary. For polycrystalline ceramics there usually is simply a single mirror-hackle boundary. Equation 5-1 is discussed in more detail in Chapter 7, Quantitative Analysis and in Appendix D (where guidance is given on how to actually make the measurement), but for the moment we need only consider some general ramifications.

This simple relationship has tremendous practical value. It is not necessary to have a-priori information about the how the part was loaded. The smaller the mirror, the larger is the stress at the origin site. A small mirror is proof that the part was strong and had a small strength-limiting flaw. Conversely, large mirrors mean the failure stress was lower and implies a large defect. In some instances, a part may be so weak that the mirror size is larger than the part cross-section and hence the mirror markings are not visible. That, in and of

itself, is valuable information. The existence of a mirror boundary implies that the part was stressed to a moderate or high level. Alternately, very strong parts (e.g., pristine optical fibers) may have such high strengths that mirrors are so small as to be not practically measurable with optical microscopes or the mirror may not even be found due to excessive fragmentation.

Mist and hackle are sometimes triggered earlier than they would otherwise form by material flaws or microstructural features. Figure 5.5 shows an example. Surface irregularities often cause a fracture mirror centered on a surface origin to depart from a semicircular shape and turn slightly inward towards an origin as shown in Figures 5.2 and 5.3.

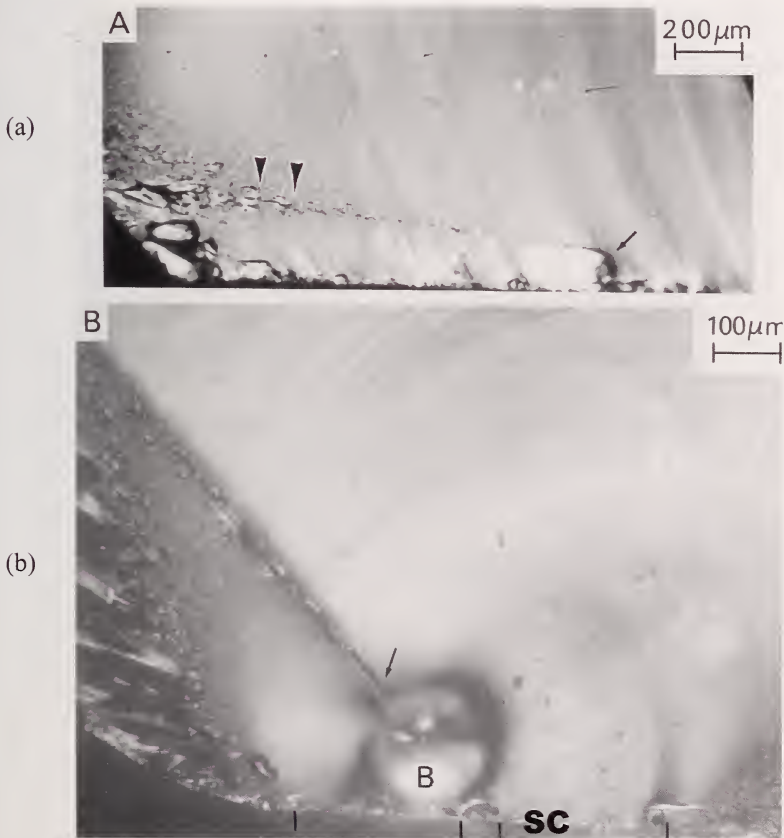


Figure 5.5 Early mist and hackle associated with defects. (a) shows mist and hackle triggered by a surface crack in a soda lime glass specimen at 65 MPa. The origin was well to the right, beyond the photo edge. (b) shows early mist and hackle triggered by a large bubble "B" in a 70 MPa strength specimen. The origin is a surface crack "SC." (Courtesy R. Rice.)

5.2.2 Fracture mirrors in ceramics

The microstructure and polycrystalline nature of most ceramics obscures most of the fine details of fracture mirrors. Figures 5.6 - 5.8 show some variants of mirrors in ceramics. Mist is usually not recognizable. Sometimes coarse microstructural elements or flaws in a mirror may trigger early hackle lines within the mirror, prior to the onset of the generalized velocity hackle that forms the mirror boundary. The mode of crack propagation, whether it is trans- or intergranular, also affects the mirror markings. Transgranular fracture is a mode whereby the crack propagates directly through grains on cleavage planes, whereas intergranular fracture is a mode whereby the crack takes paths along grain boundaries between grains. These modes will be discussed later in section 5.8.

Mirrors may be easier to see in materials that start out with transgranular fracture but then develop increasing fractions of intergranular fracture. On the other hand, it may be more difficult to define mirrors when the fracture mode is intergranular from the origin right through the entire mirror. For these reasons it is appropriate to add the qualifier "relatively" as in relatively smooth when describing the mirror region since there is an inherent roughness from the microstructure even in the area immediately surrounding the origin.

Rice observed that mirrors are more detectable in strong specimens and are less clear in weak specimens.²⁶ Mirrors may not be detectable in coarse grained materials or those with more than 10 % porosity. Mist can only be detected in fine-grained ceramics or those that fracture transgranularly.²⁷

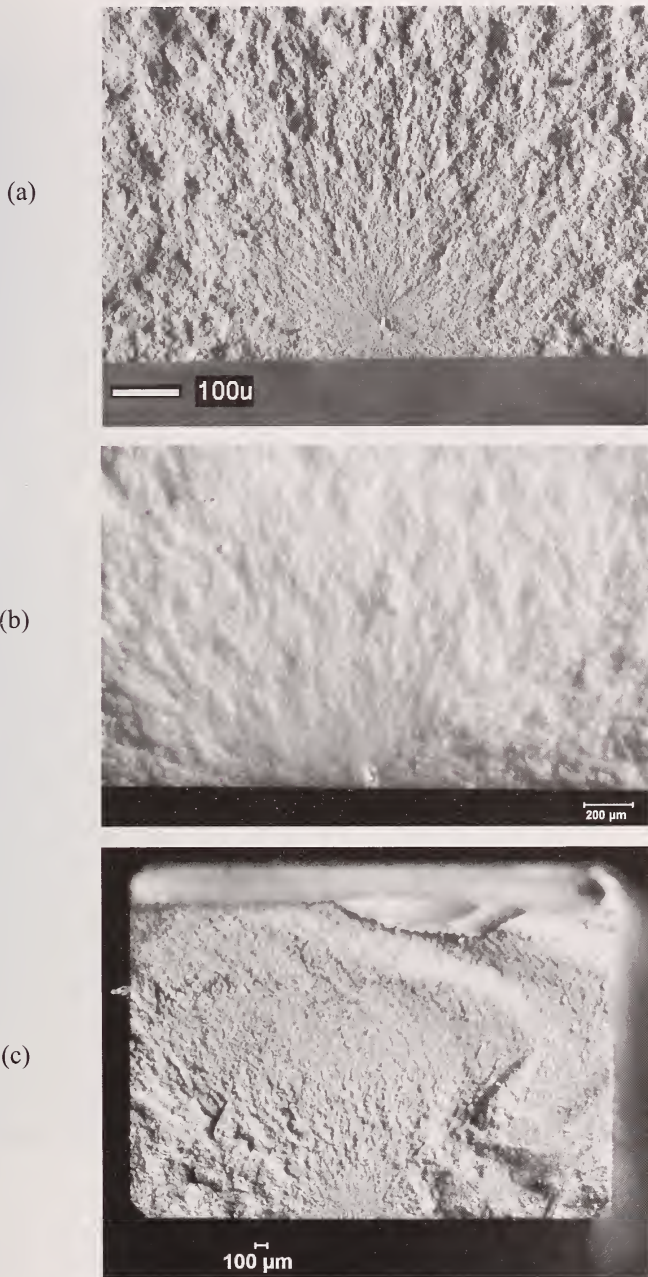


Figure 5.6 Mirrors in ceramics. (a) is a strong bend bar (1024 MPa) of Y-tetragonal zirconia polycrystal (Y-TZP) material for dental crowns as seen on the SEM. (Courtesy J. Quinn) (b) is another Y-TZP bend bar (486 MPa) for an engine application as photographed by a stereoptical microscope. (c) is a silicon nitride bend bar (487 MPa).

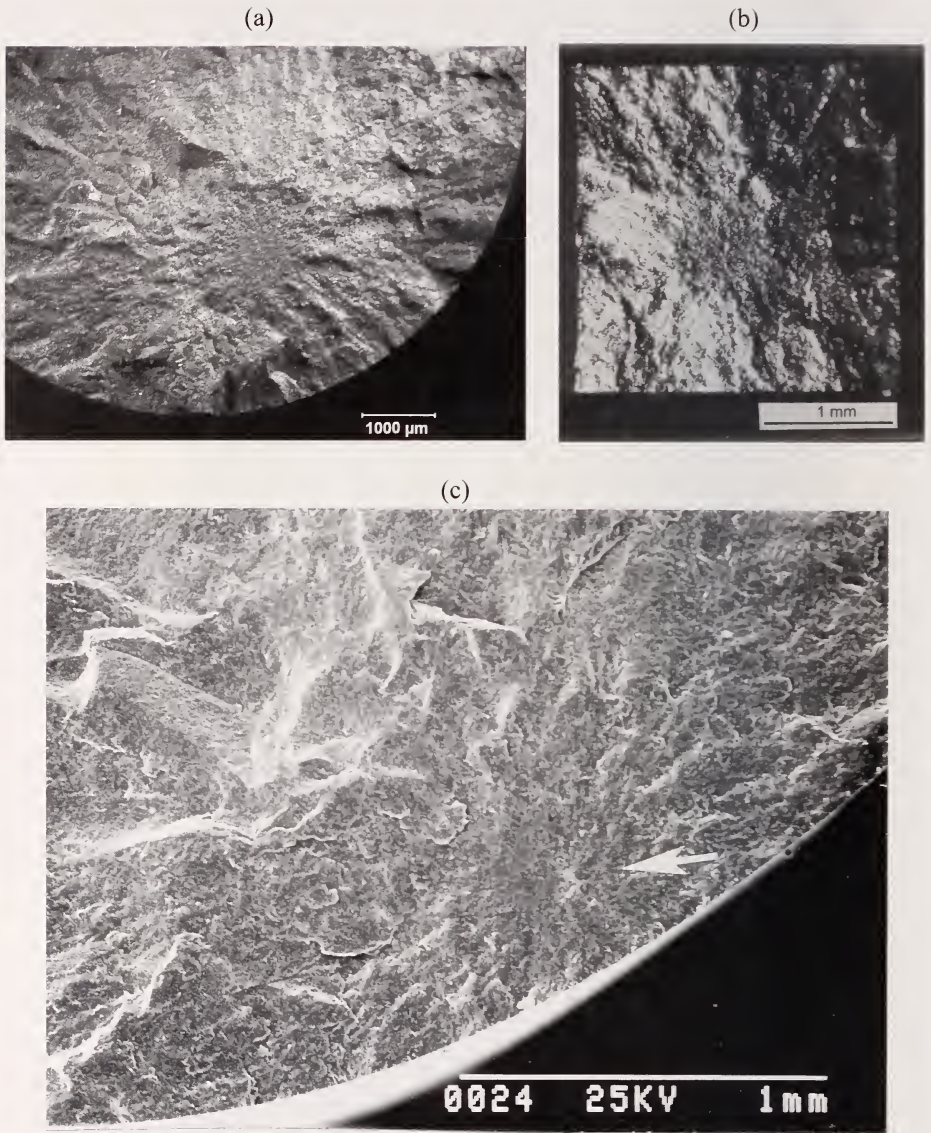


Figure 5.7 Mirrors in ceramics. (a) is a hot pressed silicon carbide tensile specimen (371 MPa). (b) is a silicon carbide tension specimen and (c) is a silicon nitride rod broken in flexure. Many beams and rods broken in flexure have internal flaw origins if the specimens are ground carefully.

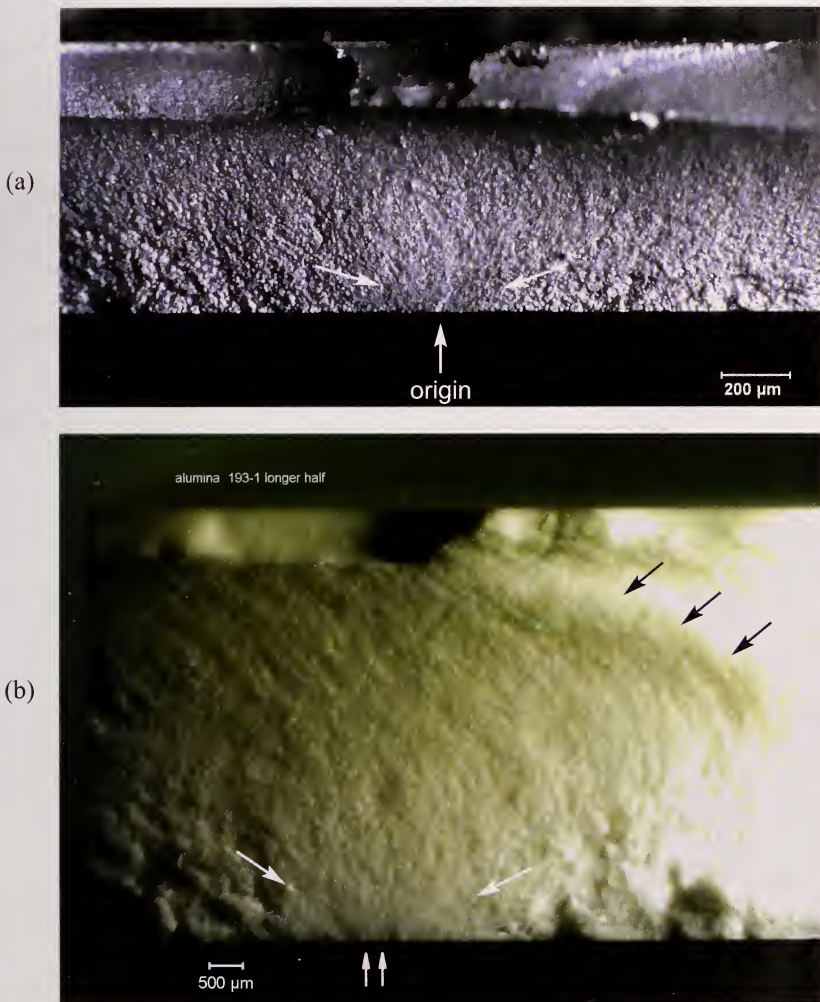


Figure 5.8 Examples of incomplete ceramic mirrors due to bending stress fields. (a) shows a gold coated biaxial Y-TZP zirconia disk photographed by a stereoscope camera. The arrows mark the origin and the mirror. (b) is an alumina bend bar with vicinal illumination to reveal the mirror in this stereoptical microscope image of this translucent material. The small white arrows mark the origin (a grinding crack) and the large white arrows mark the mirror. The black arrows mark a Wallner line arc.

5.2.3 Fracture mirrors, special cases

Multiple fracture mirrors

In many cases, only one origin is activated and there is only one fracture mirror. The crack propagates and reaches terminal velocity after only a short extension and in a period of microseconds. In rare instances, two virtually identical flaws may be triggered simultaneously in a laboratory strength test such as shown in Figure 5.9.

Sometimes there will be multiple simultaneously-activated origins in a component or test specimen due to severe loadings such as laser heating or thermal shock by water quenching.²⁸ Another example is a side impacted bottle as shown in Figure 4.12f whereby the impact causes the sidewalls of the vessels to flex outwards. The bending stresses activate “hinge fractures” to either side of the impact site. When there are multiple origins, each generates a crack system and the fractographer must deduce the sequence of events that causes them. Sometimes, once one origin starts a crack system, the component stresses are redistributed and a second origin is then activated. The burst turbine rotor case 1 in chapter 10 is an example.

Secondary fractures can occur due to a variety of causes. Elastic wave reverberations after an initial fracture can cause secondary fractures. These complicate the interpretation of high strength four-point bend specimens and it can be difficult to determine which one was the primary fracture. An observation that a fracture mirror is on what once was the *compressively* loaded surface in a bend bar is proof the break was secondary, as shown in Figure 4.11. If there are two fracture planes with mirrors on the tensile side in the inner gage section, the larger mirror may be the primary break and the smaller mirror may be secondary due to stress reverberations that momentarily created a greater local stress.

Concentric mirrors have been reported by Ramulu et al.²⁹ and correspond to a crack front that is alternately decelerating and accelerating. Such markings also occur in high strength tensile specimens when a crack branches repeatedly. At each branch, the crack slows down somewhat, then accelerates back to near terminal velocity and branches again.

Steps or jogs in a mirror

In some cases there may be a pronounced step or jog starting at the origin. This usually occurs when the critical flaw is irregular, three dimensional, or inclined at an angle to the principal stress. Crack extension from the irregular flaw may occur on slightly offset, parallel planes and thereby create a step

(a)



(b)

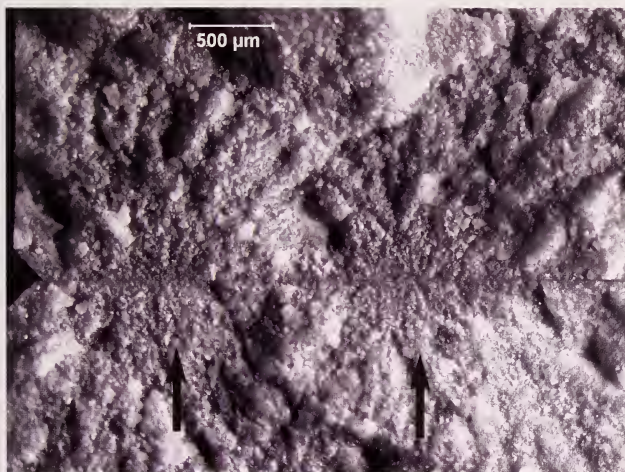


Figure 5.9 Multiple mirrors from grinding damage in a silicon nitride bend bar. (b) is a close-up of (a). Grinding damage caused fracture in these examples and the origins in each mirror were nearly identical. (Ref. 30)

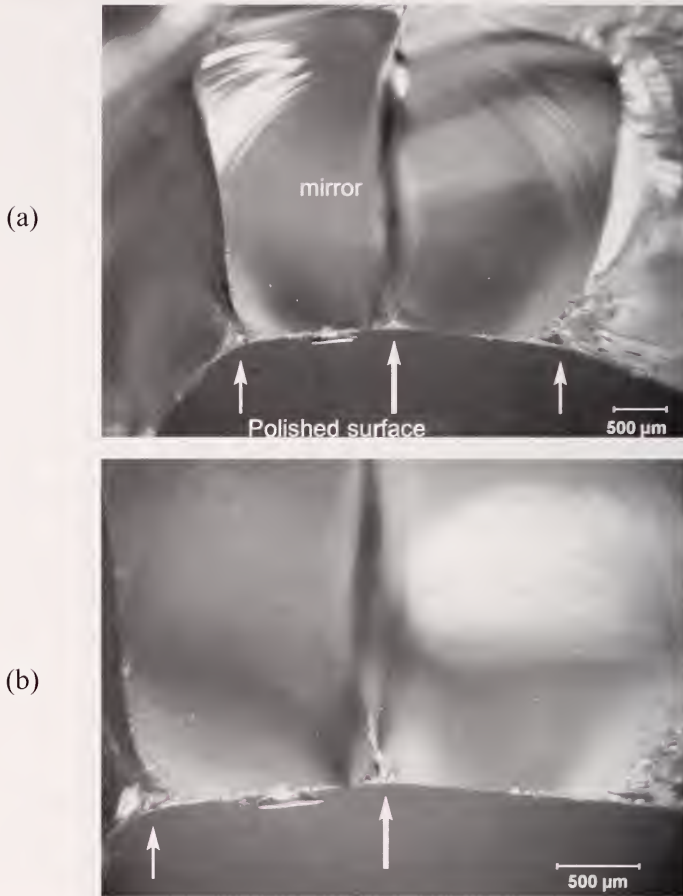


Figure 5.10 Bent mirror in a borosilicate crown glass ring-on-ring disk strength specimen. The origin was a Vickers indentation flaw (large white arrows) with multiple radial and median cracks. (a) and the close-up (b) show the fracture surface with the specimen tilted back to show the outer polished surface where the indentation (white arrows) started fracture. Fracture started from Vickers indentation radial cracks oriented in different directions. A hackle line extends from the origin straight up through the mirror. Notice how main crack branching occurs (small white arrows) soon after the mirror boundaries formed in this equibiaxial-loaded specimen. Notice also that the branching angle initially is small then flares out to its final configuration.

or jog which may persist up into the mirror or even further. These steps are one type of “hackle” as described later in section 5.3. They usually point back to the origin and are an additional aid to locating the origin flaw.

Curved or bent mirrors

Cracks propagate perpendicular to the maximum principal tension stress, but some parts may have maximum stresses that are invariant with orientation. Equibiaxial stressed ring-on-ring test coupons (Figure 4.2) are an example. Curved or wavy fracture mirrors may occur in equibiaxial-loading cases. Figure 5.10 shows an example of a bent mirror.

Non circular mirrors

Mirror shape distortions may reveal important information about flaws or the stress distributions in a part. Mirrors that are not circular or semicircular indicate stress gradients, residual stresses, or elongated flaws at the origin.

Most fracture mirrors that form around a volume-distributed flaw in the interior of a part are circular. Oblong or elliptical mirrors in the interior of a strong part are less common. Figure 5.7 shows three internal fracture origins and mirrors in ceramic test specimens. In one case, the part was tested in flexure, but the mirror was relatively small and showed no obvious distortion or elongation.

On the other hand, parts with surface origins often have flared or elongated mirrors, especially if the part was stressed in flexure. The bending loading mode usually creates a stress gradient with a maximum tension at the surface, zero stress at the middle (“the neutral axis”), and compression on the opposite surface as shown in Figure 4.9. As the crack accelerates from the surface origin, it traverses through a diminishing stress field towards the interior. This slows down the crack and elongates the mirror shape towards the interior as shown in Figures 5.11 and 5.12. It can even eliminate the mirror markings altogether if the mirror is large relative to the specimen cross-section size. The stress gradient does not affect the markings along the tensile surface. There often is a small cusp on either side of the mirror pointing back to the origin in glasses. The cusp is accounted for by fracture mechanics considerations. (A crack that connects to a free surface experiences a slightly greater stress intensity factor right at the surface, than a comparable crack in the interior of a body.) The small cusp is inconsequential for most analysis, except when fracture mirror sizes are measured as discussed in chapter 7 and Appendix D.

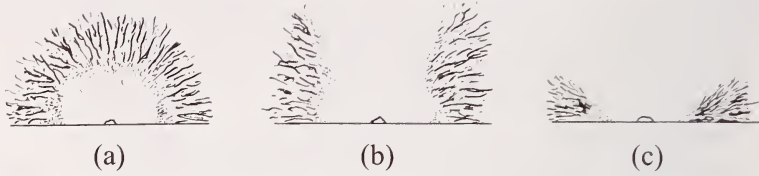


Figure 5.11 Mirror shapes around surface origins. (a) is common for tension specimens, or flexure specimens or plates in bending if the mirror is small relative to the thickness. (b) and (c) show mirrors that flare or are incomplete into the interior. This occurs when the mirror is large in a part loaded in bending.



Figure 5.12 Fracture mirrors in four glass rods broken in flexure. The maximum tensile stress was on the bottom in each case. Origins on the rod sides had pronounced flair or were incomplete due to the stress gradient.

The elongations in Figures 5.11 and 5.12 are common. Flexural stress gradients always cause elongations towards the interior. On the other hand, there are several important cases whereby elongations along the outer surface of the part occur as shown in Figure 5.13. Elongated flaws may generate elongated mirrors and sometimes even mirrors with side protuberances. Figure 5.14 shows two possible scenarios for the formation of such elongated mirrors. Machining/grinding cracks and polishing scratches cause such markings.^{30, 31} Figures 5.15 and 5.16 show examples.

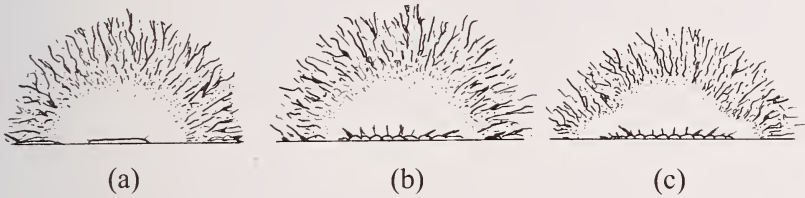


Figure 5.13 Mirror elongations along the surface can occur if the origin is a scratch or a long parallel grinding crack. (a) shows a single elongated crack at the origin, (b) shows a grinding zipper crack (see section 6.7.6), and (c) shows a zipper crack that generated lobes on the sides of the mirror.

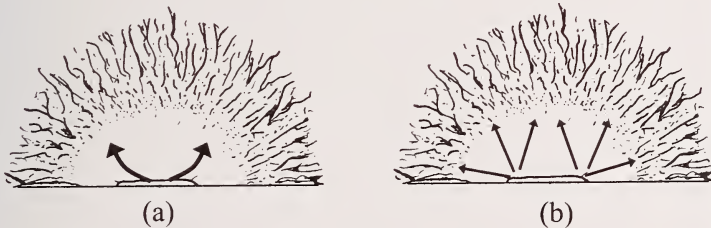


Figure 5.14 Two scenarios that could account for mirror elongations along the surface from long flaws. (a) shows how a crack could unzip or propagate quickly along the surface. (b) shows that criticality could be reached at several points on the flaw periphery and fracture commences accordingly.

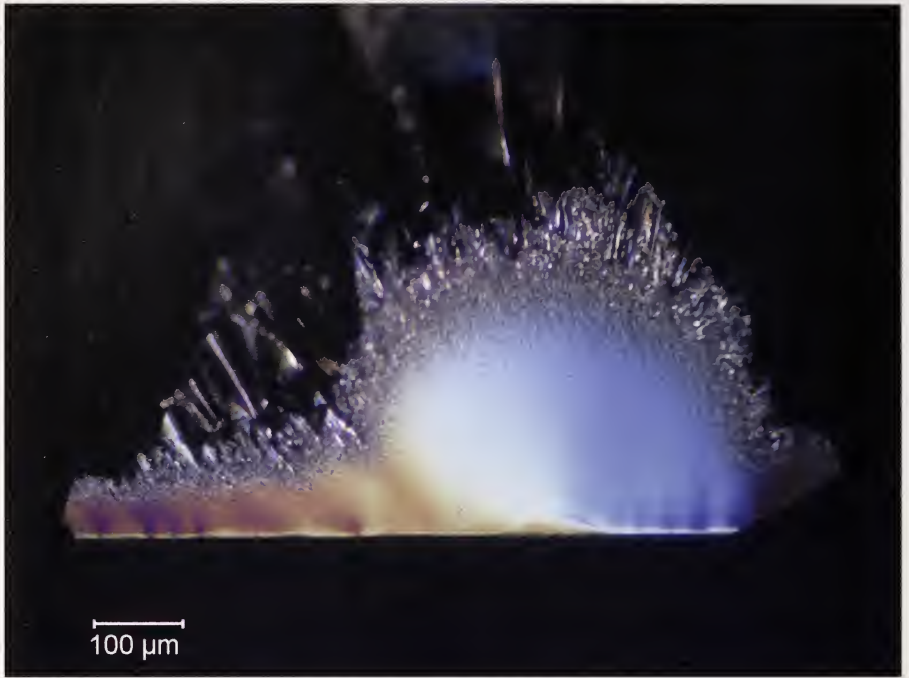


Figure 5.15 Elongated mirror in a fully-annealed borosilicate crown glass ring-on-ring disk strength specimen tested in inert conditions (dry nitrogen). (146 MPa, 21.2 ksi). The origin was a 7.3 μm deep long crack presumably from a scratch in the polished surface although all surface traces of the offending scratch had been eliminated by the final polishing. An SEM image of the origin flaw is shown in figures 6.17 b, c and 7.20 b, c. In this optical photo the initial flaw appears as a thin white band on the bottom. Notice the slightly deeper penetration of the flaw in the middle of the mirror suggesting that it grew to criticality here first. The crack then fanned out to form the elongated non-circular mirror; but also unzipped along the surface to the left and right. The shadow bands extending up from the flaw are Wallner lines generated by minor flaw perturbations extending up into the mirror. Differential interference contrast image from a reflected light compound microscope.

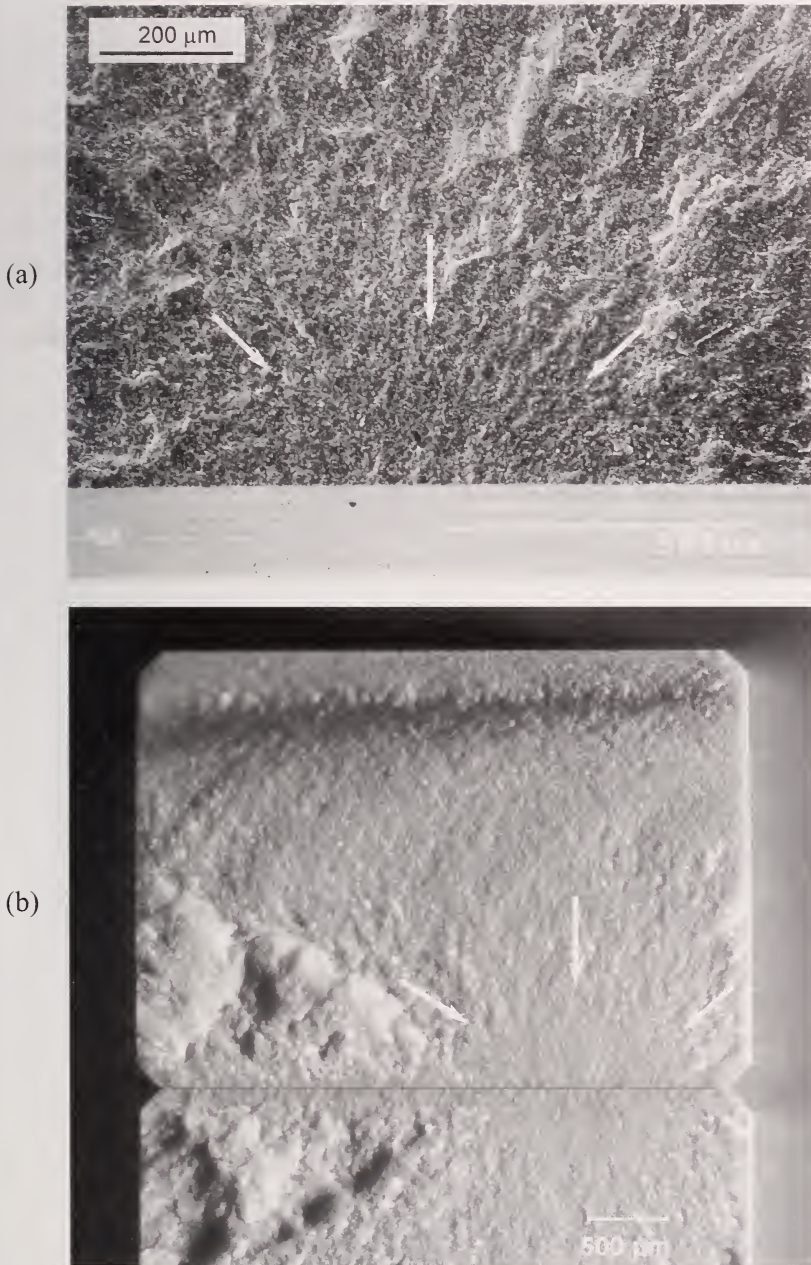


Figure 5.16 Sideways-elongated mirrors from grinding flaws in ceramic bend bars. (a) zipper crack (section 6.7.6) in sintered reaction bonded silicon nitride. (542 MPa) (b) zipper crack in sintered silicon nitride. (432 MPa)

Residual surface stresses may also alter mirror shapes. The shape distortion depends upon the magnitude, sign and depth of the residual stresses. Figure 5.17 shows a typical parabolic residual stress distribution in glass from thermal tempering.³² Stresses are strongly compressive at the surface, decrease to zero about 21% of the thickness in from each surface (assuming the two surfaces are cooled at the same rates), and change to tensile in the interior. The compressive stress at the surface is twice the magnitude of the interior tensile stress. Figure 5.18 shows a mirror in a heat strengthened glass plate. For a surface origin, the compressive surface residual stresses suppress mirror formation along the outer surface. Compensating residual internal tensile stresses shorten the mirror dimensions into the interior. A more detailed discussion of discussion of mirror shapes in tempered plates is in Appendix D and Figure D.8 in particular. Diced pieces from fully-tempered glass show mist and velocity hackle in the interior in Figure 5.19.

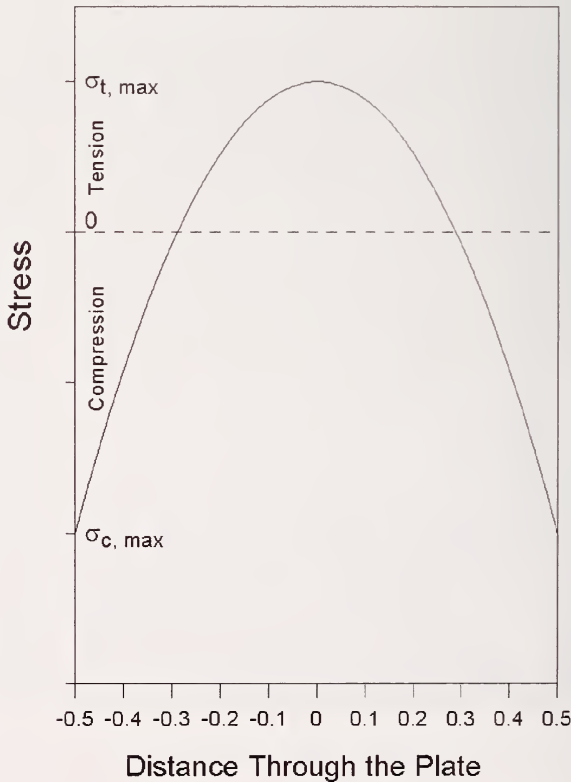


Figure 5.17 Residual stresses in thermally tempered glass plates.

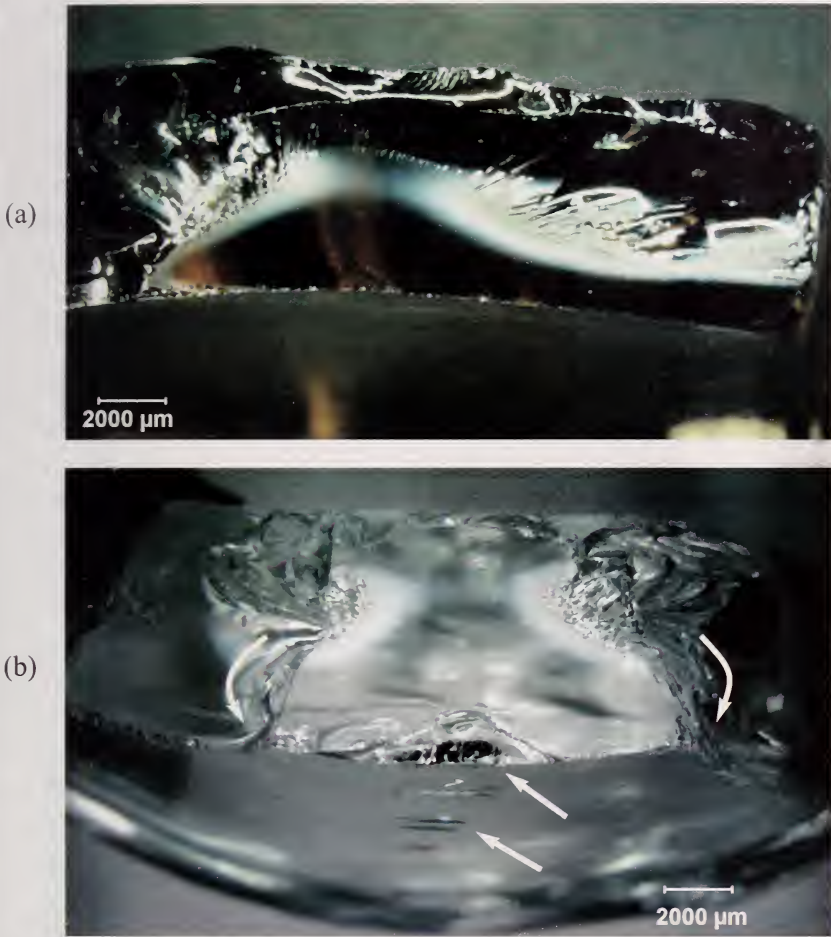


Figure 5.18 Residual stresses alter the mirror shape. These images show thermally strengthened glass consumer wares. The piece in (a) shows a complete suppression of mirror boundary markings along the lower right surface, but they are present to the left of the origin. This indicates the piece was thermally strengthened with emphasis to protect the rim. The mirror is well developed into the depth since residual tensile stresses there help form the mist and hackle. (b) shows a piece with mirror markings into the interior, but not along the bottom surface. The crack branched from the mirror sides in the interior of the piece then hooked back around to sever the fragment as shown by the arrows. The origin is one or a series of chatter cracks (white arrows).

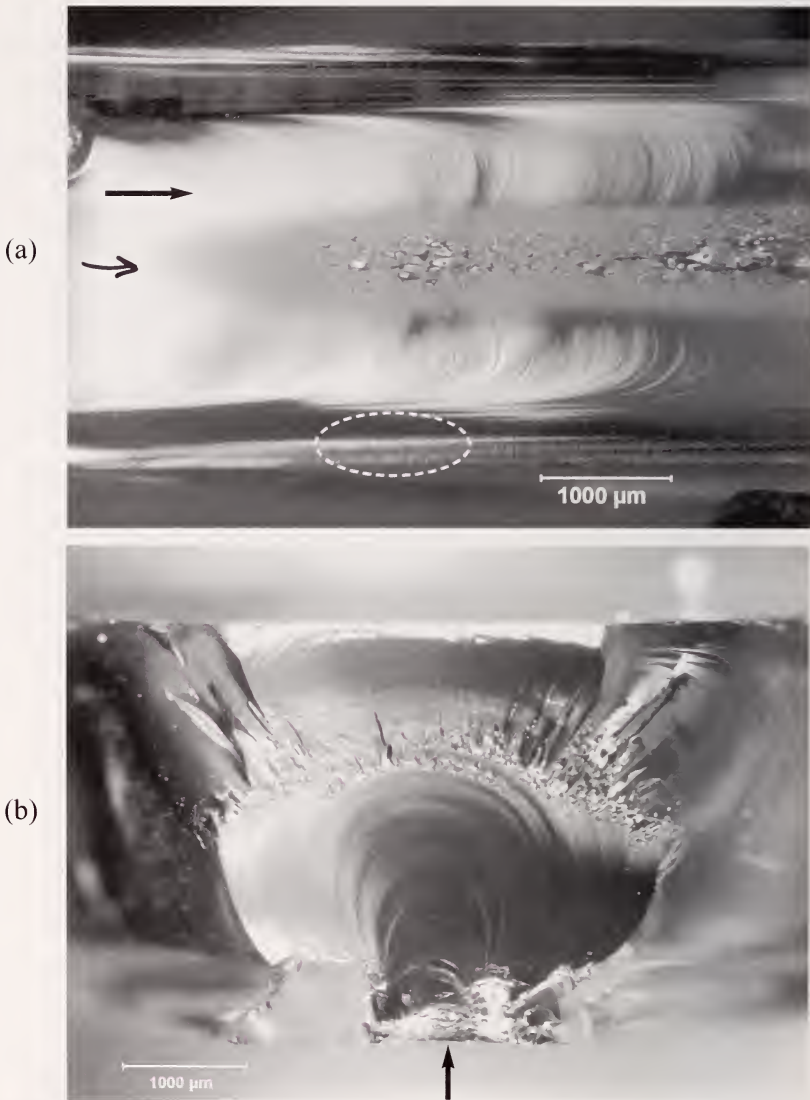


Figure 5.19 Mist and velocity hackle in tempered glass. (a) shows the crack reached terminal velocity in the interior where the tensile stresses were greatest. The black arrow shows the direction of crack propagation and the onset of mist. Each diced piece usually has this pattern since cracks slow at a branch then accelerate to terminal velocity again. Crack propagation was retarded at the outer surfaces due to the compression. Final breakage through to the surface has vertical twist hackle (white dashed ring). (b) shows the impact origin (arrow) and mirror. These photos are of the same auto window pieces in Figures 4.19b and d.

5.3 Hackle

In addition to the mist hackle and velocity hackle described above in the mirror section, which are self initiated by the crack at terminal velocity, there are other types of hackle that are very useful for ascertaining the direction of crack propagation. These markings enable the fractographer to trace crack propagation back to an origin. Hackle lines are sometimes called “lances” and less commonly “striations,” but this latter term is not recommended.

5.3.1 Coarse hackle

Microstructural hackle: Large broad hackle lines that form in ceramics from non-specific sources, but most likely variations in the microstructure.

Ceramics often develop general coarse hackle lines even in the absence of mirrors or other well-defined fracture surface markings. This occurs in low strength or porous ceramics and often is the only marking on a fracture surface that can indicate a direction of crack propagation. The microstructure or some geometric irregularity causes portions of the crack to advance on non coplanar regions separated by rounded ridges as opposed to sharp steps. Figures 5.20 (a - c) show examples.



Figure 5.20 Coarse hackle in ceramics. (a) shows matching fracture surface halves of a split cylinder flexural strength specimen of a coarse-grained ($50\ \mu\text{m}$ to $80\ \mu\text{m}$) magnesia partially-stabilized zirconia. It has a very rough clumpy fracture surface, but vicinal illumination shows the coarse hackle lines (black arrows) radiating from the origin region (white arrow).

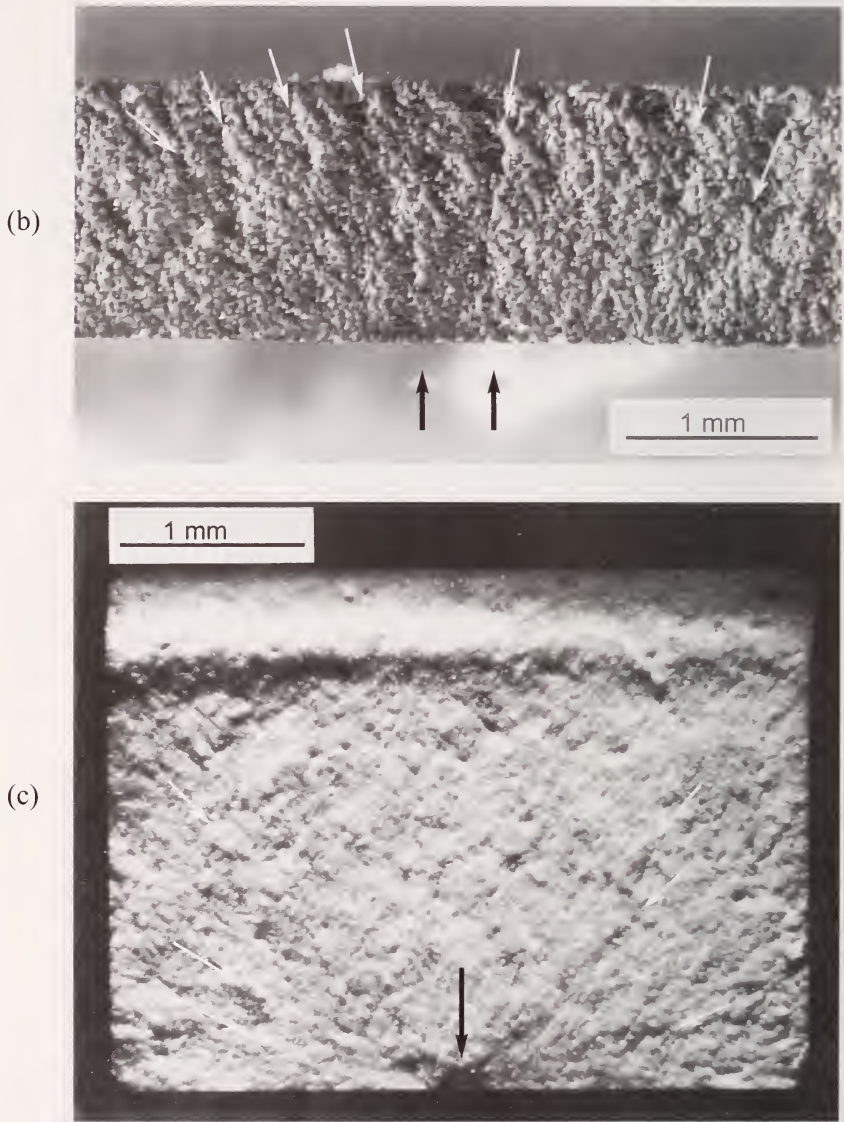


Figure 5.20 Continued (b) is a broken O-ring specimen of a ceramic membrane material. (c) is a silicon nitride bend bar with a controlled Knoop artificial flaw on the bottom middle. Coarse microstructural hackle lines guide the observer back to the origins (arrows). The only other fractographic feature observable is the cantilever curl in (c). Both specimens are so weak that fracture mirrors are larger than the cross sections.

5.3.2 Wake hackle

Wake hackle: A hackle mark extending from a singularity at the crack front in the direction of crackling.

When an advancing crack encounters an elastic singularity such as an inclusion or a pore, the crack front may split at the object and sweep past it on both sides. As the two fronts pass the obstacle they often end on slightly different planes and create a step or "tail" between them. The tail may fade away quickly or persist for long distances. These markings are very recognizable and may either be large or very small. They serve as miniature "weather vanes" which tell the direction of local crack propagation. Figure 5.21 shows examples.

Wake hackle in *glazes or veneers* often is the only recognizable fracture surface feature in kitchenware, electrical insulators, and some dental ceramics. The core ceramic materials in these instances are often coarse grained, porous, or weak and few fracture surface markings are evident. Sometimes in even the most difficult materials, tiny porosity will aid the fractographer by serving as a source of wake hackle.³³



Figure 5.21 Wake hackle, the fractographers "weather vane" for crack propagation. (a) shows wake hackle from bubbles in glass. The crack was running in the direction of the arrow. Many bubbles are beneath the surface in this view.

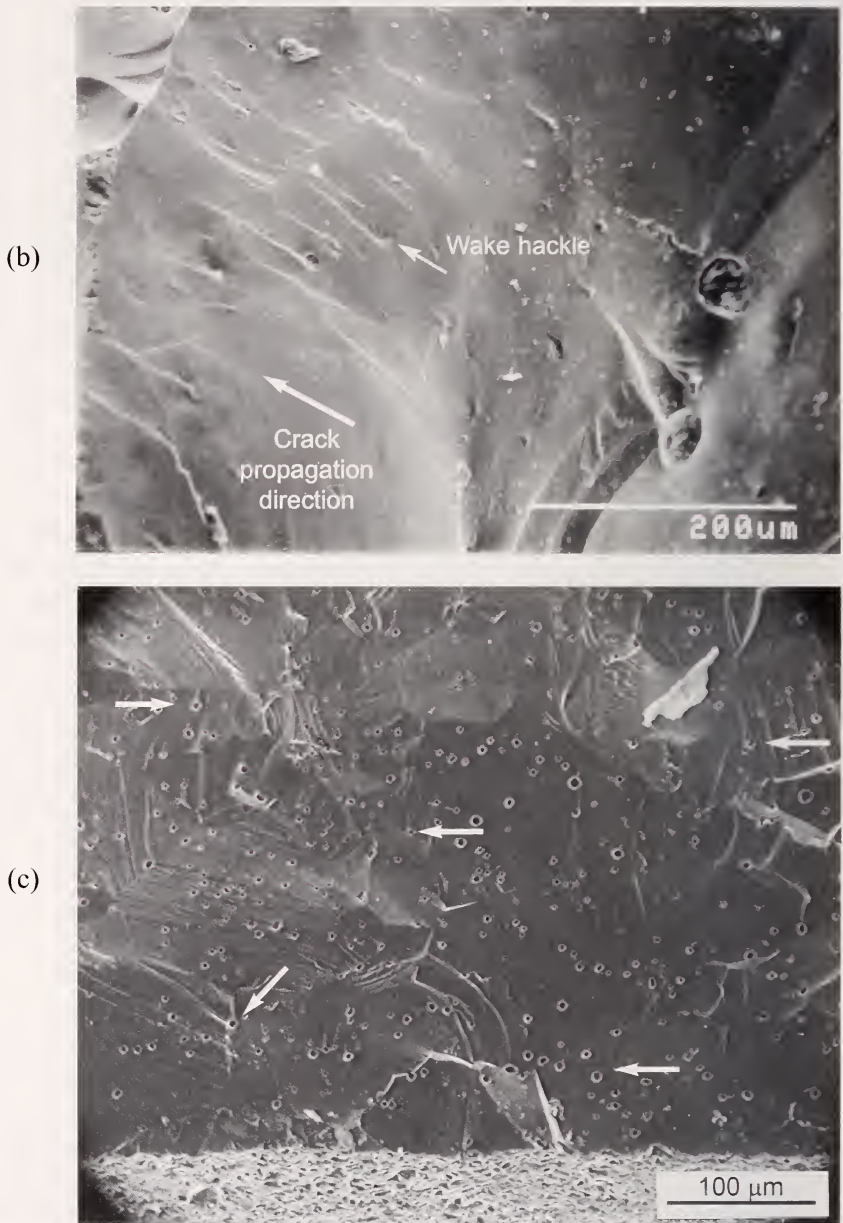


Figure 5.21 continued (b) shows an array of wake hackle from pores in an Empress II dental veneer. The crack was running in the direction of the arrow. Notice that some hackle is triggered even though the crack did not cleave the pore (small white arrow). (c) shows an example of transgranular fracture from a large grain origin in polycrystalline AlON. Wake hackle was triggered by grain boundaries and some tiny pores (small arrows).

(d)

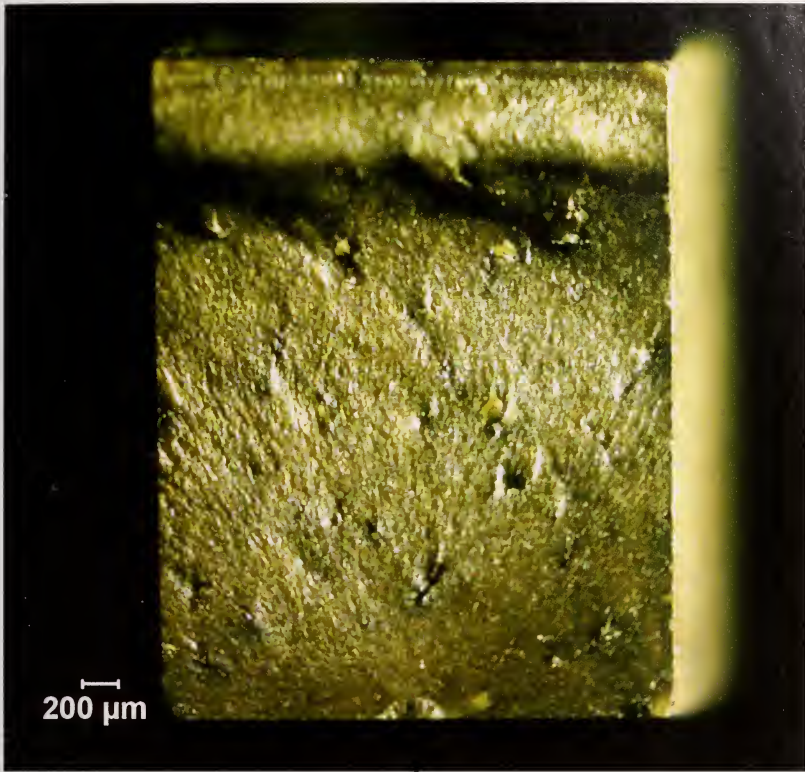


Figure 5.21 continued (d) shows wake hackle from inclusions in a lead zirconium titanate bend bar. They point back to the origin on the bottom. The tensile surface is on the bottom and a cantilever curl is on the top. The origin is a semi elliptical surface crack (arrow) generated by a Knoop indentation.

Irregularities such as pores or inclusions are not the only sources of wake hackle in ceramics. Grain boundaries and local crack path redirection as a crack propagates from one grain to another with a different crystallographic orientation, or local density or other microstructural variations all can trigger “microstructural wake hackle.” Sometimes meticulous observations of within-grain cleavage, micro wake hackle, and micro twist hackle lines can allow the fractographer to backtrack to an origin.

Kerkhof and Summer used ultrasonic fractography to show that a crack accelerates in the immediate vicinity of a hole in glass, but then is retarded as the crack runs past the hole.³⁴ Figure 5.36d later in this chapter shows an example.

5.3.3 Twist hackle

Twist hackle: *Hackle that separates portions of the crack surface, each of which has rotated from the original crack plane in response to a lateral rotation or twist in the axis of principal tension. (Fréchette, Ref 1.)*

Twist hackle are very telltale markings as illustrated in Figures 5.22 and 5.23. They are also known as delta patterns, river deltas, river patterns, lances, and sometimes even in the geological community as striations. (Striations in this instance are not to be confused with fatigue striations, a well known metallurgical fracture surface marking). The roughly parallel segments point in the direction of *local* crack propagation. Twist hackle can be generated by the primary crack as it travels directly through the body, especially as it goes around corners or geometric irregularities, or as the stress conditions changed.

Twist hackle can also occur as a result of final breakage between local crack segments or through to the side of a specimen that had initially had strong thermal or stress gradients. Twist hackle shows the *local* direction of crack propagation. For example, plates in bending often have curved cracks that run quickly on the tension stressed side, but do not quite break through to the surface. The crack later snaps through to the opposite surface leaving twist hackle markings as shown in Figure 5.24a. Double torsion fracture mechanics type test specimens sometimes have such markings. Figure 5.19a shows a similar circumstance whereby final breakthrough of tempered glass has twist hackle on both outer surfaces. This final localized break through can occur on a micro-size scale as well, as for example between two nearby wake hackle crack segments.

In polycrystalline ceramics, twist hackle marking within coarse grains can serve as very helpful markers. They are local indications of crack propagation and it is often possible to track a propagating crack back to an origin by reading the local “weather vanes.” Figure 5.25b shows examples. The fractographer may be surprised to see that twist hackle line within separate grains may not all line up the same way. It is quite common for cracks to take local detours through the microstructure in response to local conditions.

Sommer³⁵ analyzed the formation conditions of twist hackle and concluded that in glasses a stress redirection of 3.3° is needed to initiate the twist hackle. Torsional stresses superimposed on tension stresses can create twist hackle markings as shown in Figure 5.25c.

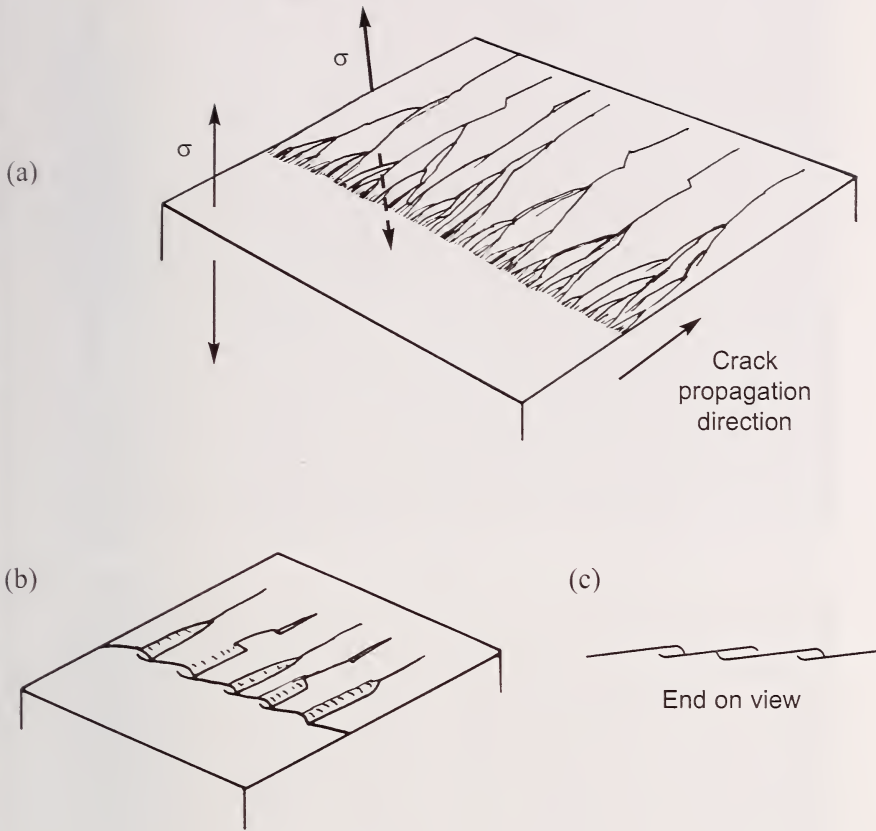
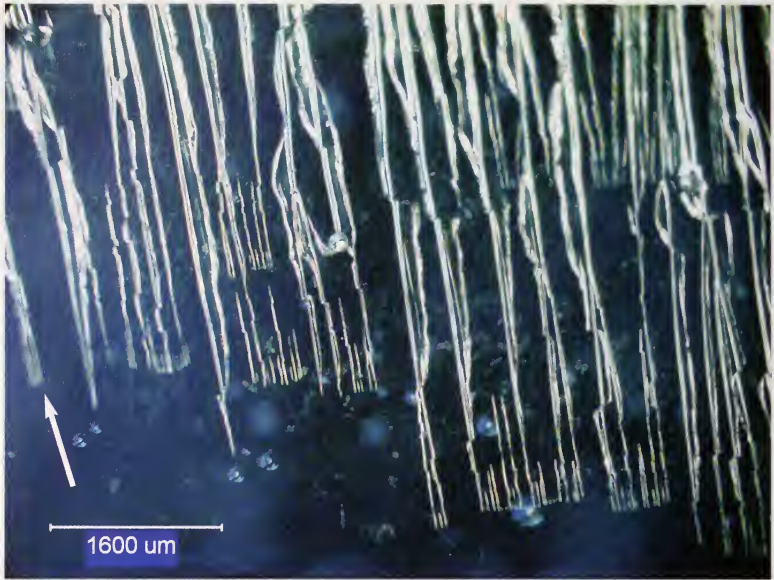


Figure 5.22 Twist hackle schematics. (a) shows how twist hackle is formed. A crack propagating from left to right runs perpendicular to the initial stress field as shown on the left. The axis of principal stress then tilts as shown on the top middle. The crack is unable to rotate all at once in response to the new stress direction, so it breaks into small, unconnected segments. The steps are "hackle lines" or "lances." Lateral breakthroughs occur between the micro segments as shown in (b) and (c). Note in (c) how the micro segments can link either by a top segment breaking through to a bottom segment or vice versa. On any given lance, the link up can alternate between either segment creating a barbed appearance. Sometimes an incomplete segment can breakthrough long after the main fracture has occurred, generating faint tinkling sounds and creating very sharp needle like fragments that fall free from the fracture surface. The small hackle lines gradually merge into coarser hackle lines and so on until the new crack plane is aligned perpendicular to the new tensile stress axis. Usually crack propagation is in the direction of fine to coarse hackle.

(a)



(b)



Figure 5.23 Twist hackle. (a) and (b) show close-ups of twist hackle in glass. The crack was running in the direction of the arrow in (a). (b courtesy J. Varner)

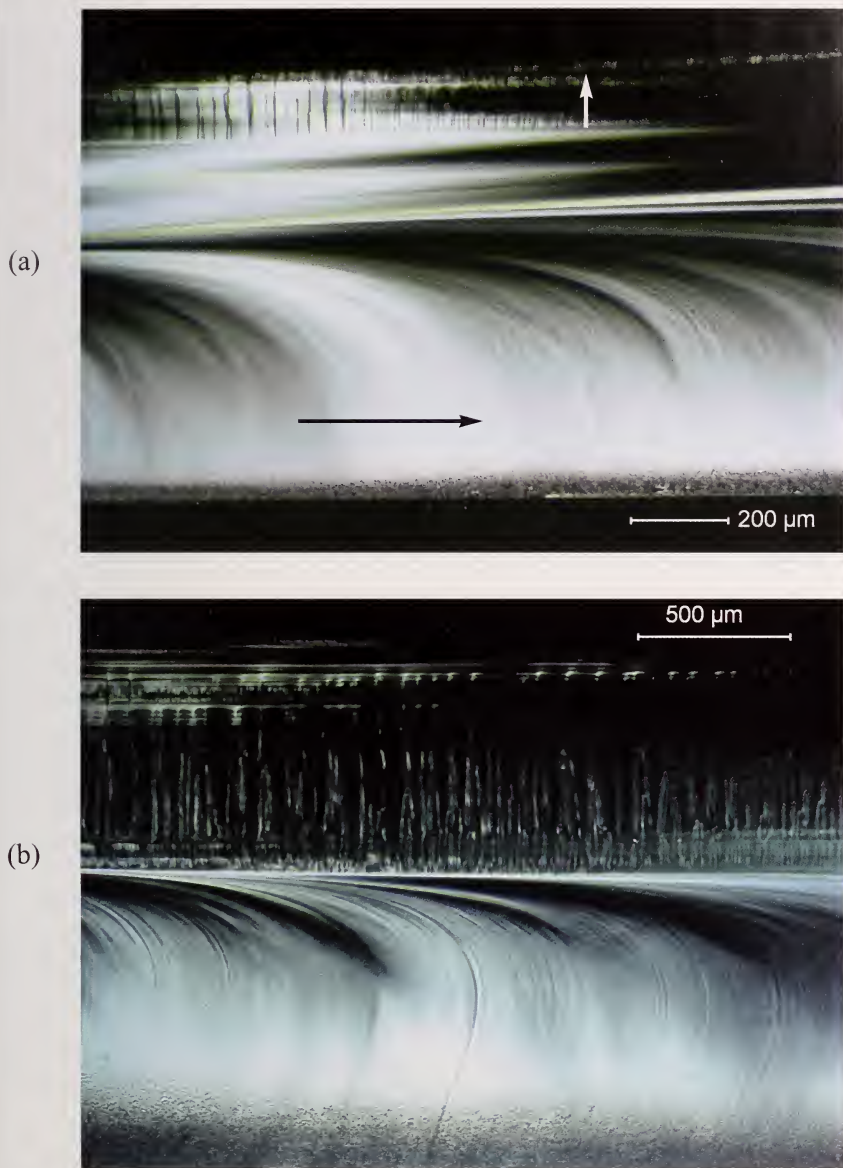


Figure 5.24 Twist hackle. (a) shows a glass microscope slide that was broken in bending with a little superimposed torsion. The main crack fracture from left to right, leading on the bottom surface as attested to by the profusion of mist and secondary Wallner lines and an occasional primary Wallner line (described in the next section). Final break through to the top surface (white arrow) created the twist hackle along the top. Tempered glass fragments often have this appearance as shown in (b), but with matching top and bottom halves as shown in Figure 5.19a.

(a)



(b)

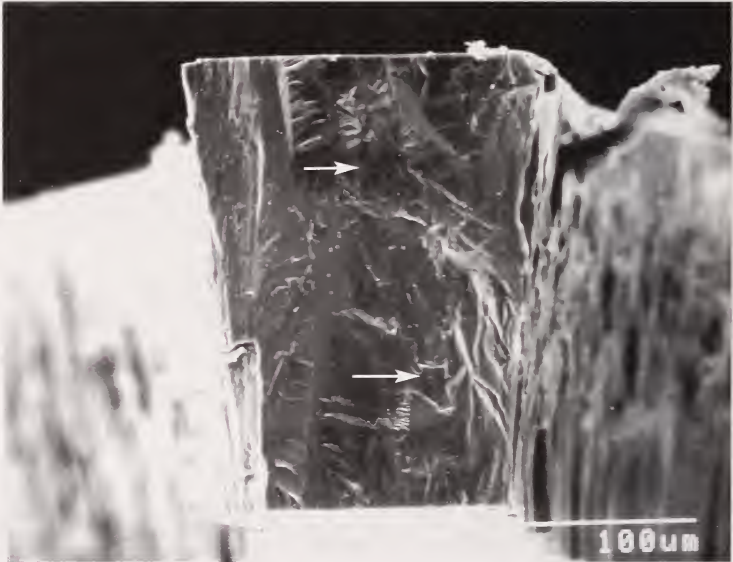


Figure 5.25 Twist hackle in grains. (a) and (b) show fracture surfaces of chemical vapor deposition (CVD) silicon carbide micro tensile specimens. CVD materials often have coarse columnar grains. Such grains run from top to bottom in this view. Twist hackle in these grains in both images show that fracture propagated from left to right as shown by the arrows. Fracture occurred from cracks located at the bottom of the grooves on the left side in each case.

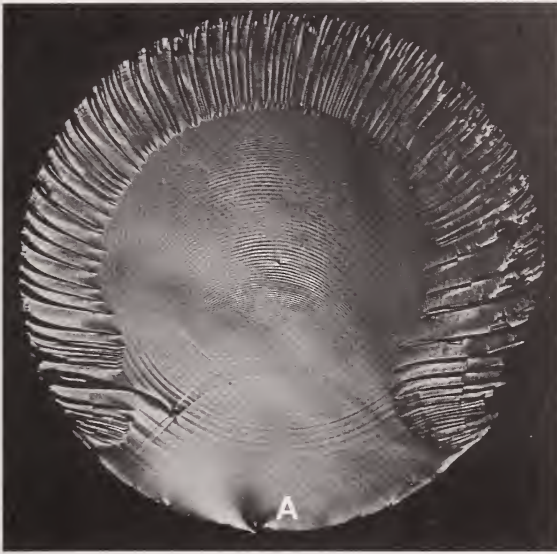


Figure 5.25 continued c. Twist hackle around the circumference of a 15 mm diameter glass rod broken in tension (induced by lateral fluid pressure compression around the periphery while the rod ends were free) with some superimposed torsion. The wavy lines are tertiary Wallner lines (described in the next section) created by ultrasonic fractography. Fracture started at the bottom at point A and progressed into the rod interior. Final breakthrough to the outer surface generated the twist hackle. (Kerkhof and Sommer, ref. 34, and Richter and Kerkhof, ref. 2.)

5.3.4 Other hackle

Shear hackle: A particular form of twist hackle that occurs in the lazy loops generated in the latter stages of fracture of a hollow specimen. (Fréchette, Ref 1.)

Initially this definition may seem peculiar, but once the fractographer has seen an example such as Figure 5.26a, it becomes clear what Fréchette had in mind.¹ He said: “Far from the fracture origin, it is common to see the crack turn through 90° and develop a cupped surface, inclined at 45° to the free surface, from whose centerline a spray of twist hackle emerges. It has little significance in reconstructing a failure event in industry, but it is useful in problems of rock fractures.”

Corner hackle: A fan like array of hackle lines created when a crack goes around a corner of a component or curves in a plate.

Figures 5.26 b and c show two examples. The fan like array spreads outwards in the direction of crack propagation.

Hackle can be generated from steps or irregularities in the origin flaw. A good example is “grinding crack hackle” shown in section 6.7.6 in the chapter on origins. “Cleavage step hackle” is covered in chapter 8 on single crystals.



Figure 5.26a Shear hackle in a glass plate. The crack was perpendicular to the glass surface and was slowing as it moved in the direction of the arrow. It then turned 90° parallel to the surface and finally broke through to the surface at about 45° , producing the spectacular fan shaped shear hackle. Shear hackle is a variant of twist hackle.

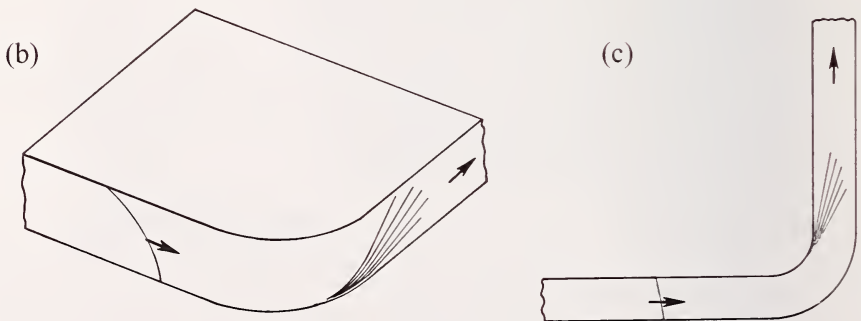


Figure 5.26(b) and (c) show two types of corner hackle. (b) shows a fan like pattern that occurs when a crack that is leading on the bottom surface curves in another direction. (c) shows a fan like pattern that occurs when a crack goes around a corner of a container or vessel.

5.4 Wallner Lines

5.4.1 Introduction

Wallner line: *A rib shaped mark with a wavelike contour caused by a temporary excursion of the crack front out of plane in response to a tilt in the axis of principal tension. They may also form from passage of the crack front through a region with a locally shifted stress field, as at an inclusion, pore, or surface discontinuity. (adapted from Fréchette, Ref. 1)*

Also known as “ripples” or “rib marks,” Wallner lines were named for Helmut Wallner who first explained how they formed in 1939.³⁶ He showed beautiful images (similar to Figures 5.2 and 5.3 of this Guide) of fracture mirrors in flexurally tested glass rods with the lines within the mirrors. He presented a splendid sketch showing how an expanding crack front was overtaken by an expanding elastic wave. The Wallner line is the locus of the elastic wave and the crack front intersections. The elastic wave momentarily causes the crack to ripple out of plane like a wave on a pond surface. The shape of the line depends upon the respective shapes and speeds of the elastic wave and the crack front as well as the direction the wave approaches and intersects the crack front. Wallner lines are invaluable in determining the direction of crack propagation. As will be shown, they usually do not have the exact same shape as the crack front, but they are usually curved (bowed) in the direction of crack propagation. They are best understood by the examples that follow.

Wallner lines are very shallow hillocks on a fracture surface. They look like a thin shadow band and they tend to shift slightly as illumination is adjusted. This is in marked contrast to crack arrest lines that are sharp and do not appear to move as light is adjusted. Wallner lines are very easy to see on fracture surfaces once the lighting is adjusted, but they are very difficult to see on the scanning electron microscope, since they produce almost no contrast and are very shallow.

There are several types of Wallner lines depending upon the source of the elastic wave. Fréchette¹ has thoughtfully categorized these as primary, secondary, and tertiary. This Guide follows his scheme and adopts his definitions. His figures showing the evolution of the loci are instructive but have been revised and expanded into separate illustrations in this Guide to make them easier for the beginner to understand. Keep in mind that a crack front through a plate may be straight or have different shapes according the stress state as shown in figure 5.27.

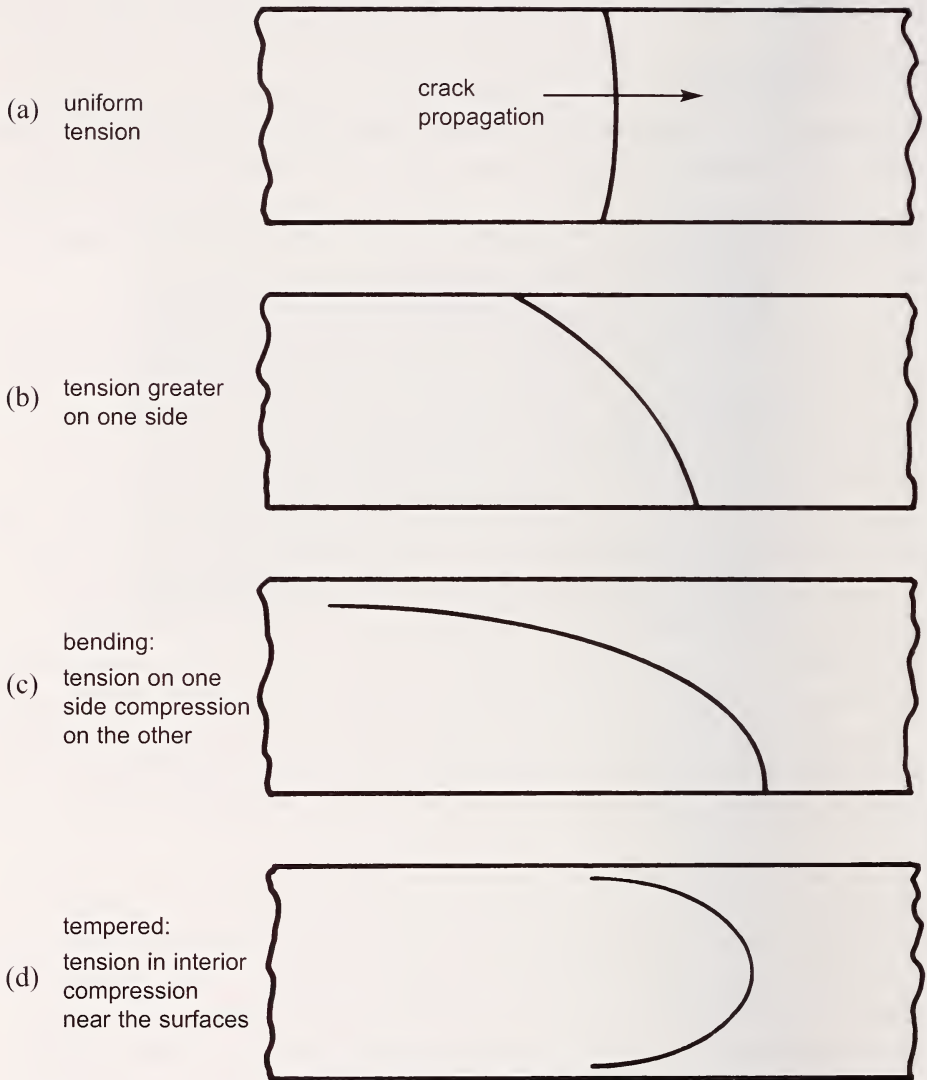


Figure 5.27 Crack front variations due to stress distributions through the thickness. (a) shows a crack front in a uniform tensile loaded plate. (b) has a greater tensile stress on the bottom. (c) has a plate in bending such that the bottom is in tension and the top in compression. (d) is a tempered plate with tensile stresses in the interior and compressive stresses at the surface.

5.4.2 Primary Wallner lines

Primary Wallner line. *A Wallner line formed by an elastic pulse generated by some portion of the crack front with a singularity in the specimen as a discontinuity at the free surface or within the specimen, or with any localized stress field or elastic discontinuity. (Adapted from Fréchette, ref. 1)*

Primary Wallner lines commonly are generated by surface blemishes and irregularities such as scratches, pits, or edge chips. Figure 5.28 shows examples and Figure 5.29 illustrates how they are formed. If a Wallner line is seen to emerge from such a surface blemish, it is evidence that the surface fault was present at the instant the crack ran by. Alternatively, if a large blemish or chip is on a glass fracture surface, but there is no Wallner line from it, the blemish occurred afterwards and was not initially on the piece.

Unless the crack is moving very slowly (and the elastic wave overtakes the entire crack front very quickly), primary Wallner lines do not show the exact crack front profile. Nevertheless, they are curved in the same direction and can help the fractographer deduce which way a curved crack was running. It is fairly easy to show that straight crack fronts generate straight but tilted primary Wallner lines.

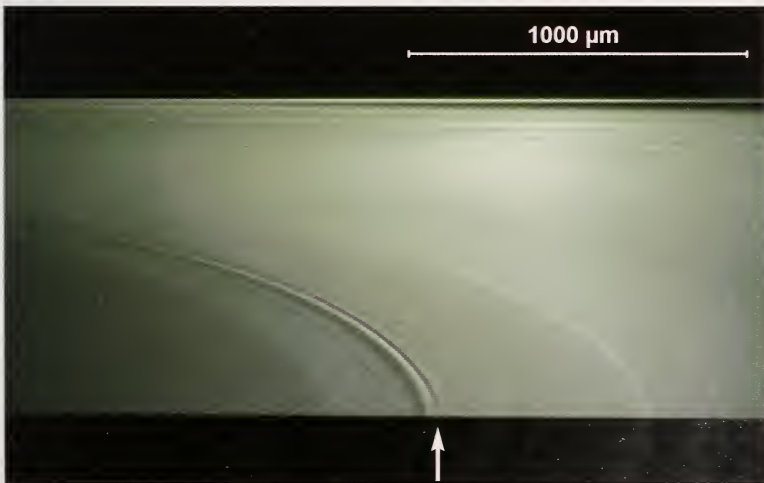


Figure 5.28 *Primary Wallner line in a glass slide broken in bending. A simple scratch on the surface (arrow) triggered the strong Wallner line as the crack ran from left to right. Other tiny faults triggered fainter primary Wallner lines.*

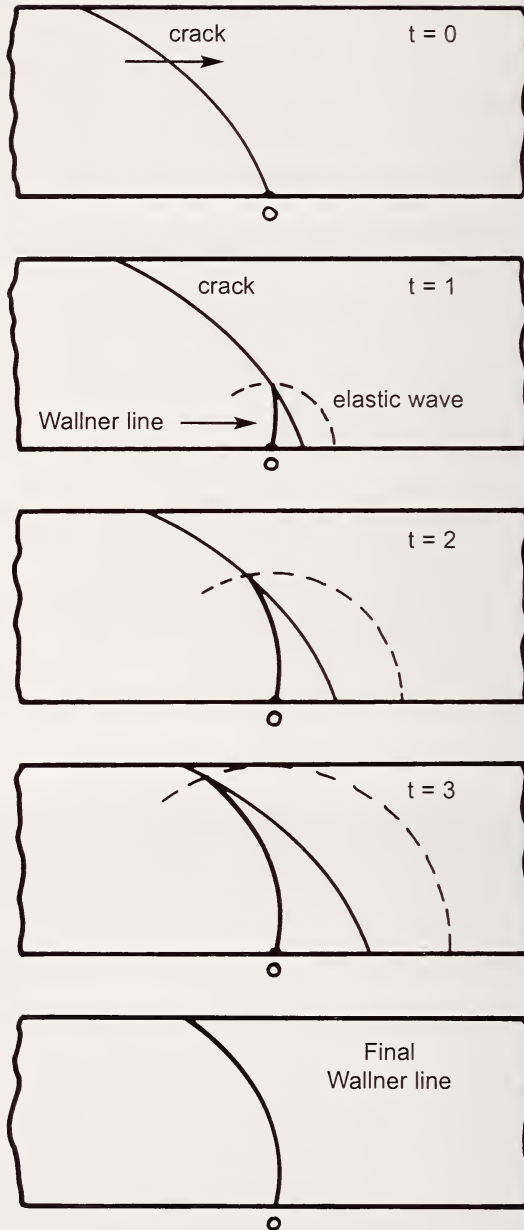


Figure 5.29 Primary Wallner lines. This schematic series shows the progressive advance of the crack at successive time intervals. The elastic wave that forms the Wallner line (thick line) starts at "O," a surface irregularity. The crack leads on the bottom surface, but is moving at constant velocity in this example.

Wallner lines are less easy to see in ceramics. Figures 5.8b and 5.30 show examples. In porous, granular, or coarse-grained ceramics, large broad ridges that are Wallner lines may be the only recognizable marking on the fracture surface. If so, the ridge may have been caused by microstructural irregularities or surface flaws on one side of the origin or to a geometric irregularity (e.g., an inside corner in a formed ware or a ridge on a plate).

Figure 5.31 shows “gull wings,” a variant of primary Wallner lines.

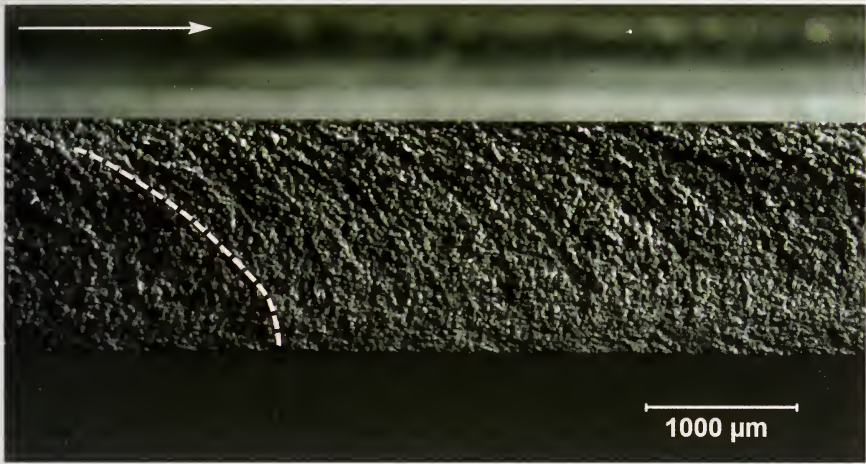


Figure 5.30 Wallner lines are more difficult to see in polycrystalline ceramics. This is an optical image of a silicon nitride double torsion fracture toughness specimen. The crack was running in the direction of the white arrow. The double torsion configuration bends a specimen so that the bottom is in tension and the top in compression. The cracks lead on the bottom surface. Primary Wallner lines formed with arcs shown by the white dashed curve.

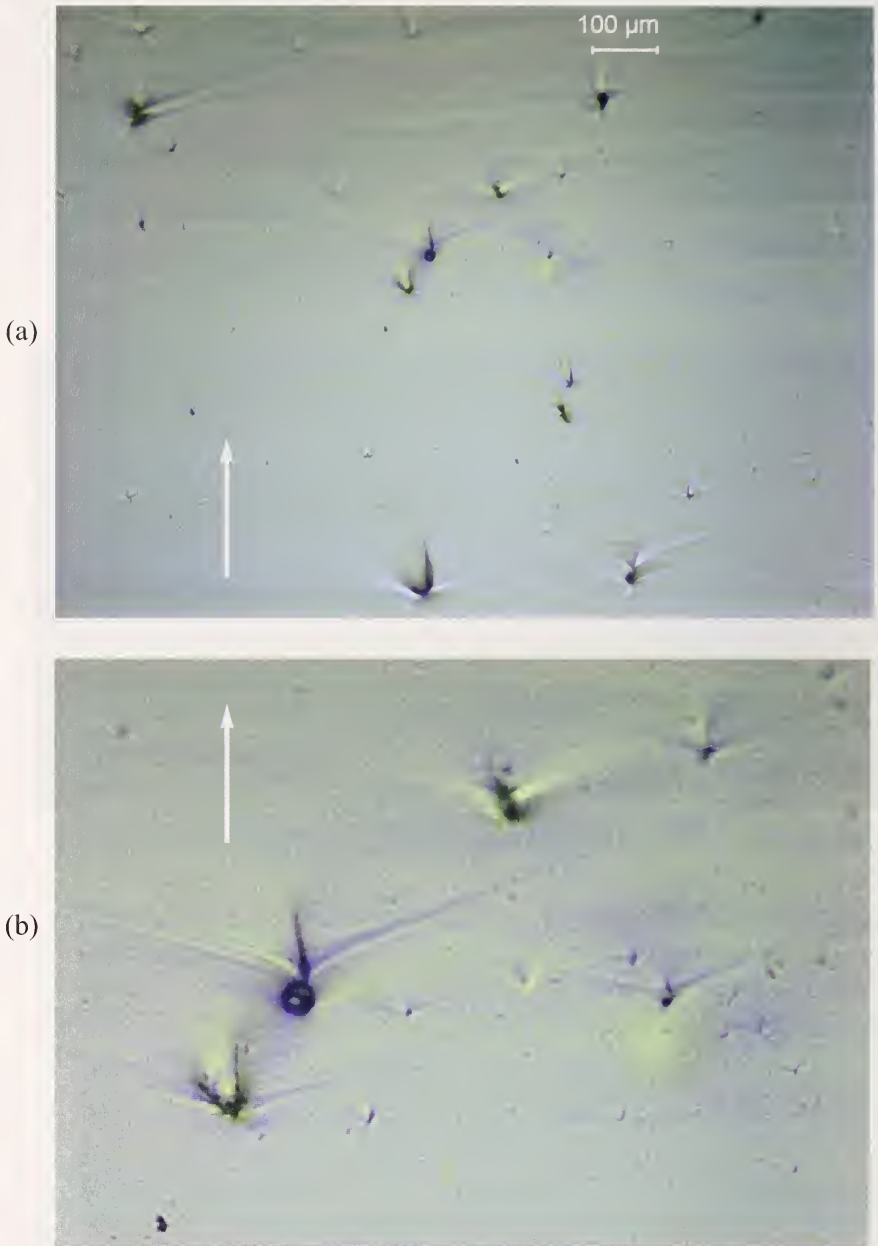


Figure 5.31 Gull wings are a variant of primary Wallner lines. (b) is a close-up of (a). Most of these pores also have wake hackle as well. These images are from obsidian with crack propagation from bottom to top as shown by the arrows. The wing angles can be used to measure crack velocity (section 7.9). (specimen courtesy A. Tsirk)

5.4.3 Secondary Wallner lines

Secondary Wallner line: *A Wallner line generated by an elastic pulse released by a discontinuity in the progress of the crack front, typically one of the rough details which arise as the crack approaches its effective terminal velocity. (After Fréchette, Ref 1.)*

Unlike the primary Wallner lines that form as a result of a crack encountering an external feature, secondary Wallner lines occur from features the crack generates itself. Mist and hackle are disturbances created by crack running at or near terminal velocity. The mist and hackle generate copious secondary Wallner lines. Figure 5.32 shows their formation sequence and Figure 5.33 shows examples. It is very common for both primary and secondary Wallner lines to be present. They can be distinguished by their different curvatures. Secondary Wallner lines are more hooked (like a fish hook) than primary Wallner lines. As was the case with primary Wallner lines, secondary Wallner lines do not show the exact crack front profile. Nevertheless, they are curved in the same direction and can help the fractographer deduce which way a curved crack was running.

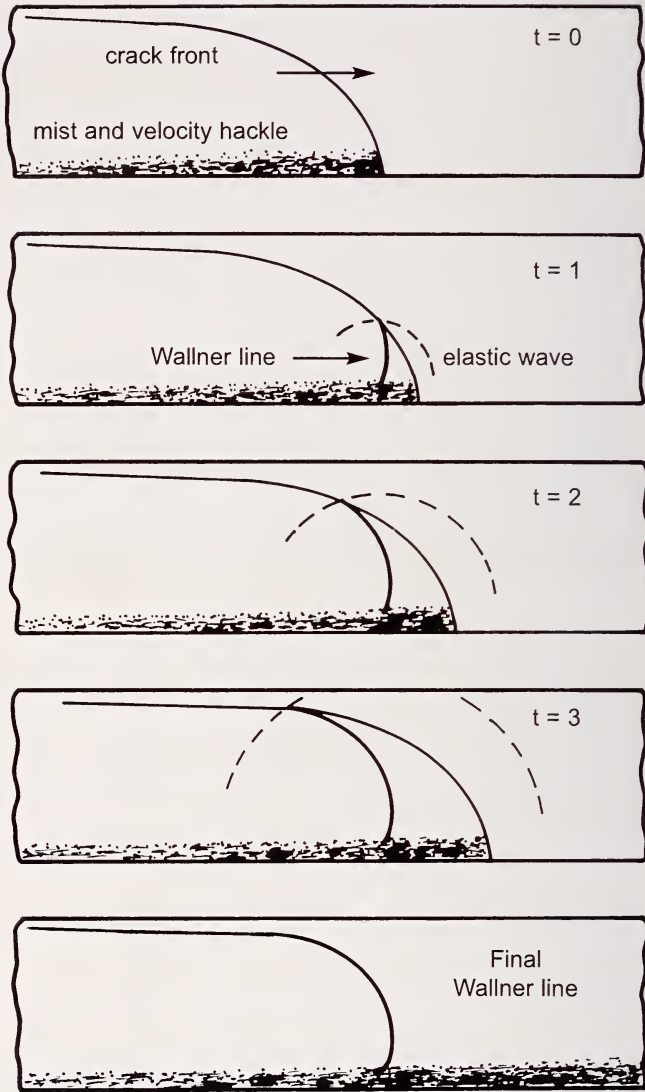


Figure 5.32 Secondary Wallner lines are formed by the crack itself. This schematic series shows the progressive advance of the crack and the elastic pulse that forms the secondary Wallner line (dark line) in a plate with a stress gradient. Notice the hook final shape, a consequence of the stress gradient caused by the variation in the crack velocity from a maximum on the bottom to close to zero at the top.

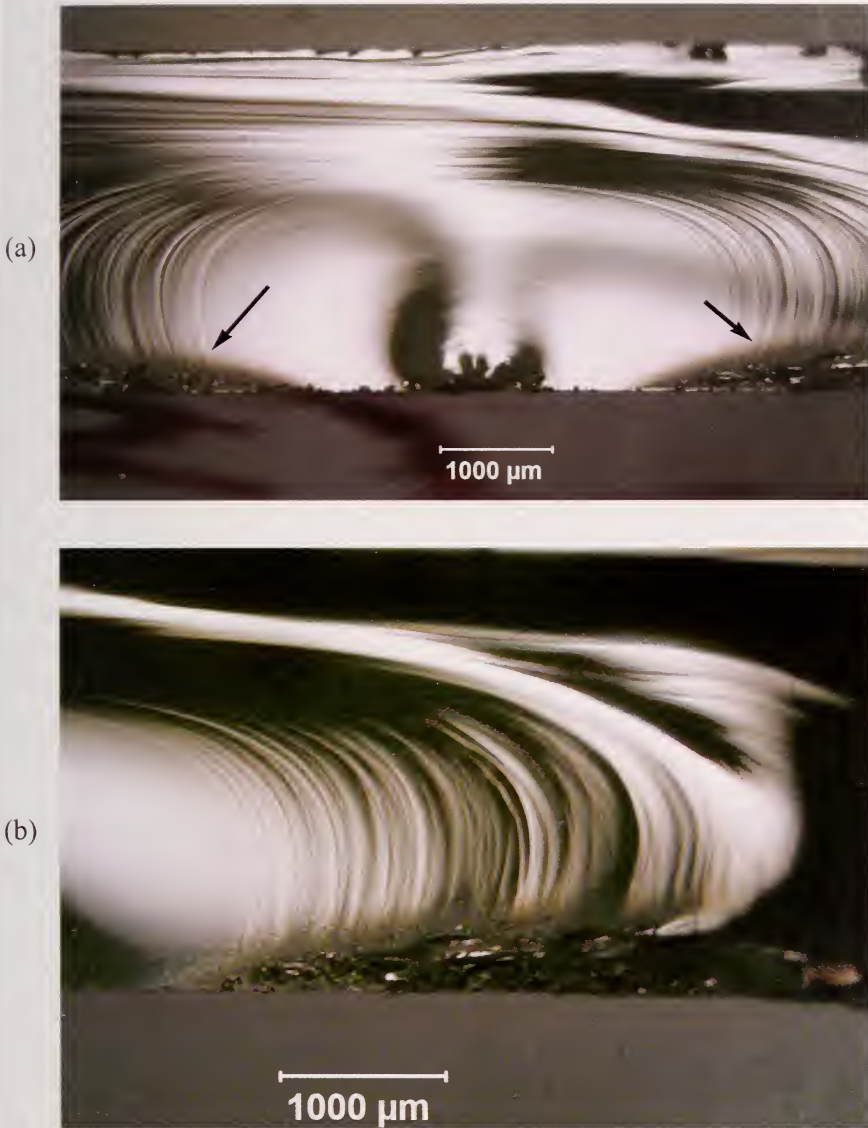


Figure 5.33 Examples of secondary Wallner lines in glass microscope slides. (a) and (b) show Wallner lines from the sides of a mirror. (b) is a close-up of the right side of (a). Mist and hackle triggered the secondary Wallner lines (arrows). There also are fainter primary Wallner lines inside the mirror. Notice their different arcs. (c) is a slide broken in bending. The arrow shows the direction of crack propagation.

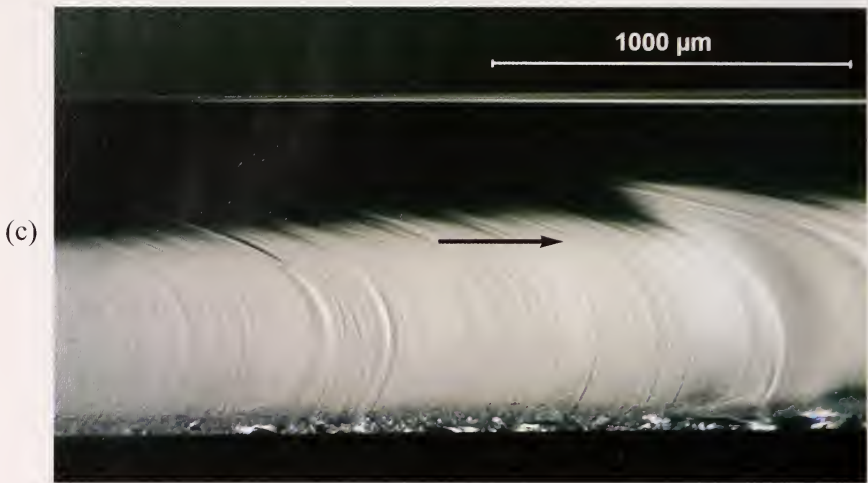


Figure 5.33 Continued

5.4.4 Tertiary Wallner lines

Tertiary Wallner lines are lines caused by elastic pulses generated from outside the crack front. (Fréchette, Ref. 1)

Vibration or shock from a source other than the crack itself can create waves that intersect with and cause momentary deviations in the crack front. Depending upon the source of the elastic pulse relative to the crack plane, the interaction may generate Wallner lines that may be very close to the shape of the crack front, or it may produce an arc formed by a progression of intersections as in the examples shown above. For example, if the crack is moving relatively slowly the fast elastic wave will overtake all portions of the crack front nearly simultaneously, producing a Wallner line “snapshot” of the crack front.

If the pulse source is located at a site normal to the fracture plane, the pulse may reach all portions of the crack front simultaneously also producing a “snapshot” of the crack front. The impacted glass shown in Figure 5.34 is a good example. Notice how the tertiary Wallner lines are concentric about the impact sites. The impact site not only generated the cracks. But the elastic pulses as well. (In contrast note how the primary and secondary Wallner lines in Figures 5.3 and 5.33a cross over each other on top of the origin.) Impact typically results in a ringing within the specimen that may be short



Figure 5.34 Tertiary Wallner lines in a large chunk of glass that was hammered into pieces. There are multiple impact sites marked by arrows, the most prominent of which is marked by the larger white arrow. Notice how the tertiary Wallner lines are concentric about the impact sites. This was one of Professor Fréchet's demonstration pieces.

lived, but will be long enough to endure for the period a crack traverses through a body.

On the other hand, a sudden stress relief may create a brief vibration when a crack pops in or propagates. This may be accompanied by an audible snap, but only generates faint elastic pulses so that only a few tertiary Wallner lines form near the origin. Fréchet¹ noted that window panes that are cracked by thermal stresses may have only a few tertiary Wallner lines near the origin and are featureless elsewhere.

A schematic case of a pulse overtaking a crack from the rear is shown in Figure 5.35. The reader is reminded that Wallner lines do not always create a "snapshot" of the crack front shape. Tertiary Wallner lines are not always formed by pulses arriving from a source so conveniently located as in test pieces studied with ultrasonic fractography. They may come from any direction including from sources that are out of the crack plane.

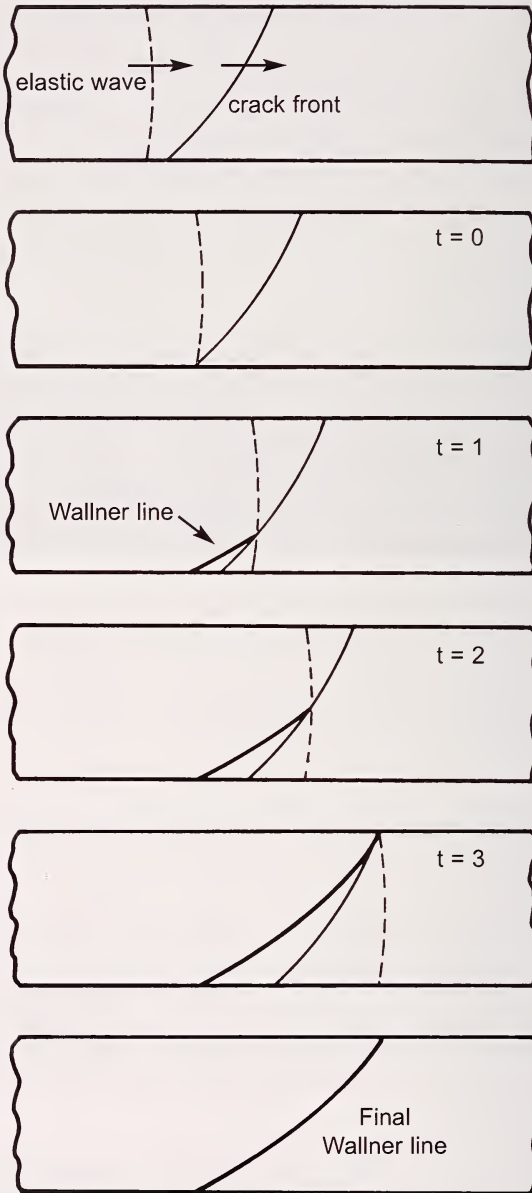


Figure 5.35 Schematic showing the stages of formation of a tertiary Wallner line for a curved crack front overtaken by an elastic wave from behind the crack. The Wallner line has a similar concavity as the crack front, but the loci are different.

Ultrasonic or stress wave fractography,^{2,37} previously mentioned in section 3.21, deliberately uses externally generated elastic waves to create tertiary Wallner lines on the running crack. Figures 5.36 a-d show some examples from Richter and Kerkhof's work.² Local crack velocity can be simply calculated on the basis of the spacing between the lines and the frequency of the pulses. They were able to measure cracks running at terminal velocities in glass with 5 MHz lead zirconium titanate transducers. Their review article² has many fascinating examples of the application of this method to study crack front profiles and velocities.

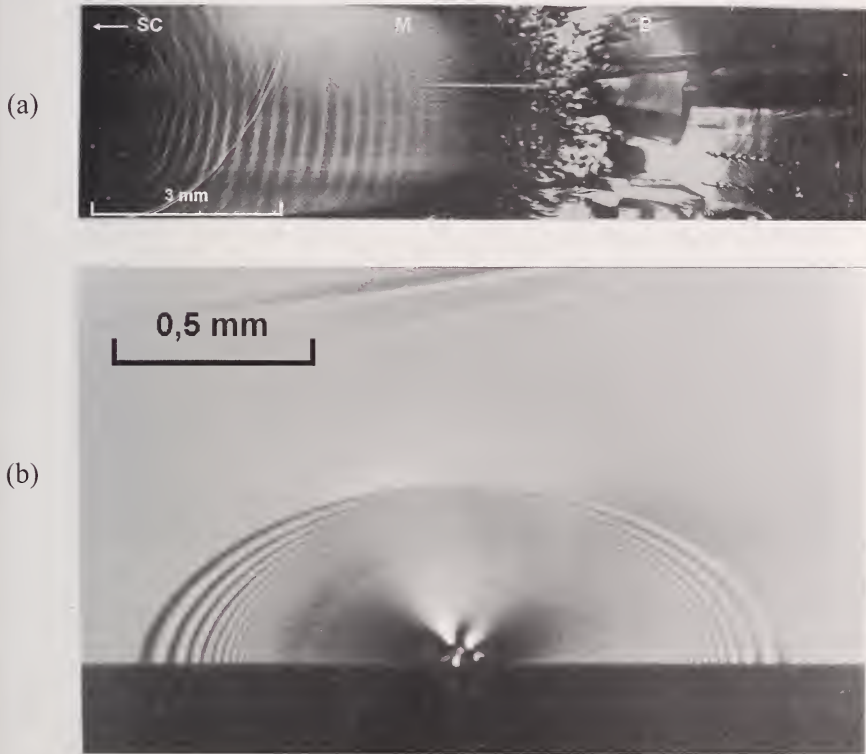


Figure 5.36 Examples of tertiary Wallner lines from ultrasonic fractography. A transducer created elastic pulses that created “snapshots” of the crack fronts they propagated through glass test specimens. (a) is a notched tension specimen loaded to fracture. The crack started at “SC” and ran to the right forming mist at M and branching at B. The crack reached a terminal velocity of 1540 m/s two waves to the right of the letters SC, before the mist formed. (b) shows an accelerating crack that grew from an indentation flaw in a bend bar. The ellipse shapes are in perfect accordance with fracture mechanics predictions from the Newman-Raju stress intensity shape factors discussed in section 7.5.2. (Courtesy, H. Richter)

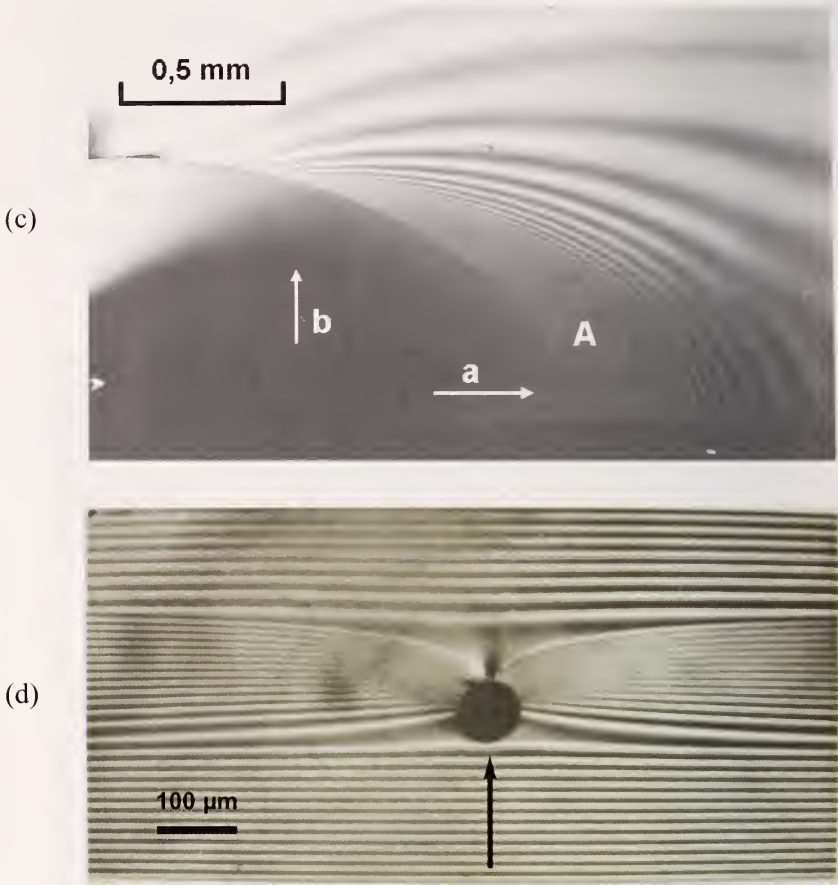


Figure 5.36 continued (c) shows a surface crack in a bend bar that went unstable from one side when growing by slow crack growth in water. The bending stress field caused the crack to grow faster along the surface (arrow *a*) than into the depth (arrow *b*). The crack went unstable on the side “A” and then rapidly fanned out and around the still slowly advancing main crack. See also Figure 5.44. (d) shows a crack front approaching a capillary tube void at 60 m/s. The arrow shows the crack propagation direction. The crack locally accelerated to 60 m/s as it approached the void, but then slowed down to 20 m/s as it passed around it, and then jumped at a faster velocity after passing around the void. (Ref. 2, photos courtesy of H. Richter)

5.4.5 Wallner Lambda lines

Elastic waves can reflect off free surfaces creating a lambda shaped line on the fracture surface as shown in Figure 5.37. These are typically formed by primary or secondary Wallner lines. Crack velocity can be calculated from the spacing of the Wallner lines as discussed in section 7.8.

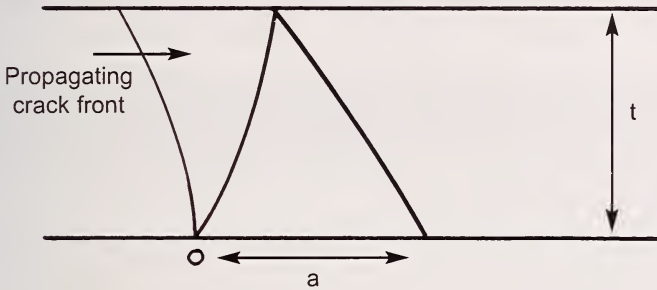


Figure 5.37 Wallner lambda line mark. The schematic shows the advancing crack (thinner line) encounters a discontinuity at point O. An elastic pulse creates a primary Wallner line that runs upward to the top surface. When the elastic wave reflects from the opposite surface, the Wallner line continues back downward.

5.5 Arrest Lines

Arrest Line A sharp line on the fracture surface defining the crack front shape of an arrested or momentarily hesitated crack prior to resumption of crack propagation under a more or less altered stress configuration.

This is a slightly modified version of Fréchette's definition.¹ His definition included the words "rib mark" as in "rib shaped," but this author has seen straight arrest lines in thermally-stressed plates, so a more general definition seems in order. The words "momentarily hesitated" are also added to Fréchette's definition. Arrest lines are different than Wallner lines in two key respects: arrest lines are sharp and, unlike most Wallner profiles, arrest lines show the crack front profile at an instant in time. The sharp line usually corresponds to where a crack hesitates or stops. Subsequent propagation may be at a slightly different angle if the loading axis changes slightly. On the other hand, Fréchette suggested that the arrest lines can also occur even if cracks do not actually stop but can occur due to a sudden redirection of the axis of principal tension. If the change involves a twist, then twist hackle lines will also form leading away from the arrest line.

Michalske showed that cracks that arrested after slow crack growth sometimes require extra loading to repropagate after aging.³⁸ The crack tip blunts slightly during the aging and the crack has to resharpen before repropagation. This process occurs with slight variations along the crack front so that when the crack repropagates there are slight humps and valleys along the crack front and tiny hackle lines leading away from the arrest line.

Fatigue crack markings are much less common in ceramics and glasses than in metals. Many fine-grained equiaxed-microstructure ceramics and nearly all

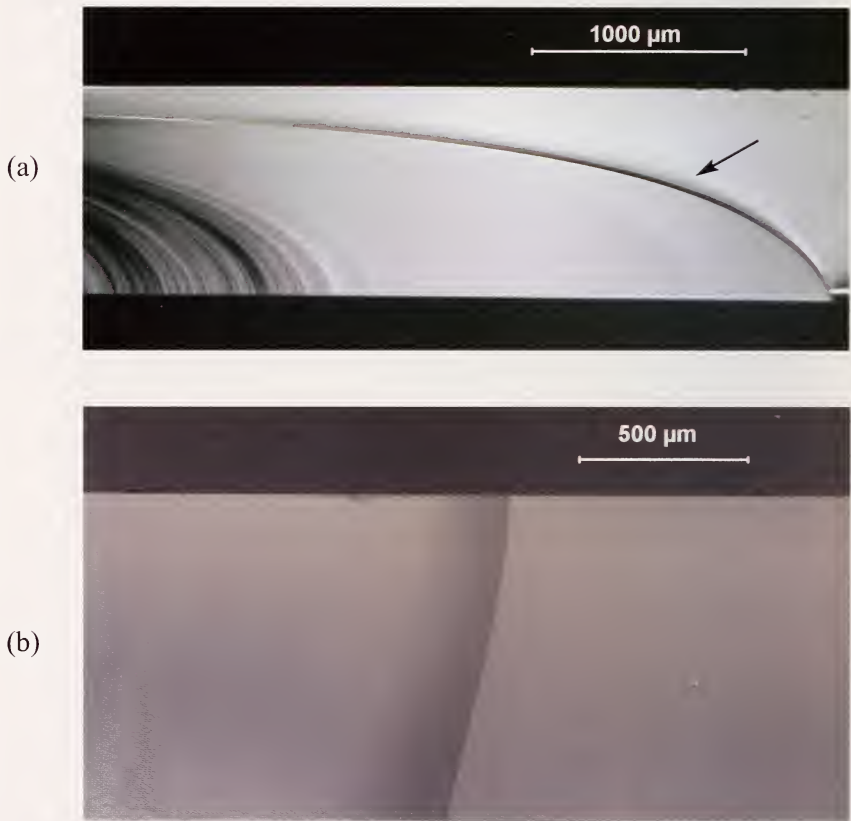


Figure 5.38 Crack arrest line examples. (a) shows a glass microscope slide broken in bending and the arrest line is on the right (arrow). The lines to the left are primary Wallner lines. Wallner lines are not as sharp as arrest lines. (b) shows an arrest line in a glass slide that broke from thermal stresses.

glasses are not susceptible to classic fatigue crack growth, by which iterative cyclic loading to a crack causes damage nucleation, accumulation, and stepwise growth with periodic spaced striations on the fracture surface. Polycrystalline ceramics having coarse-grained or elongated grain microstructures and anisotropic properties may be susceptible to classic cyclic crack growth, but these microstructures are not conducive to leaving evidence of progressive crack extension. On the other hand, many ceramics and all silicate glasses are *susceptible* to incremental crack growth during cyclic loadings simply due to the accumulated effect of the slow crack growth phenomena described in section 5.8.2. If fatigue crack markings are present at all in ceramics or glasses, they usually will be manifested as a series of concentric or parallel crack arrest lines. Evans showed a good example in glass in Reference 39.

5.6 Scarps

Scarps are subtle curved lines on a fracture surface caused by interaction of a propagating crack and a liquid or a reactive environment. The liquid can act to retard a crack front or can cause it to accelerate, sometimes in a discontinuous fashion. The scarps mark sudden transitions in crack velocities that occur due to interactions of the crack with liquid. They usually correspond to transitions in the crack tip environment, including changing from wet to dry, dry to wet, humid air to dry air, etc. They even can occur in totally wet environments if the crack accelerates so fast that the viscous liquid cannot keep pace and instead cavitates behind the crack tip. This topic is briefly covered in section 7.10. Scarps are usually only detected in glasses and single crystals. Scarps could exist in polycrystalline ceramics, but the inherent roughness from the microstructure masks their presence.

Fréchette has identified several types of scarps and accounted for their formation.¹ Scarps can vary from as simple as a single faint line across the fracture surface perpendicular to the direction of crack propagation (cavitation scarp), to a complex network of curves such as shown in Figure 5.39. Fréchette called some of these “Sierra scarps” due to their similarity to familiar mountains. “Cavitation scarps” occur when an accelerating crack causes void formation or cavitation in the water between the fracture surfaces that is trying to keep up with the crack tip. Once cavitation occurs the crack outruns the fluid water. In this guide it is not necessary to delve into the details of scarp formation. The *practical significance* of scarps is that they are evidence that fracture occurred in the presence of a fluid, most commonly water. They also can help confirm the local direction of crack propagation.

Scarps are very subtle, and are best seen in an optical microscope with the specimen tilted to create a mirror like reflection from the fracture surface. They usually exist in only a portion of the specimen and usually where the crack is moving at a slow to moderate speed. Tsirk³⁹ has studied a variety of scarps in knapped obsidian arrowheads and knives formed by pressure flaking. Some of the scarps were generated in antiquity either when the implements were made or when they chipped during usage. Tsirk has postulated that the shape of scarps may depend upon the nature of the fluid and possibly the viscosity. Scarps formed in water or saliva are different then those formed in blood.⁴⁰ The reader is referred to Fréchette's book¹ and references^{38, 40-43} for details on scarps.

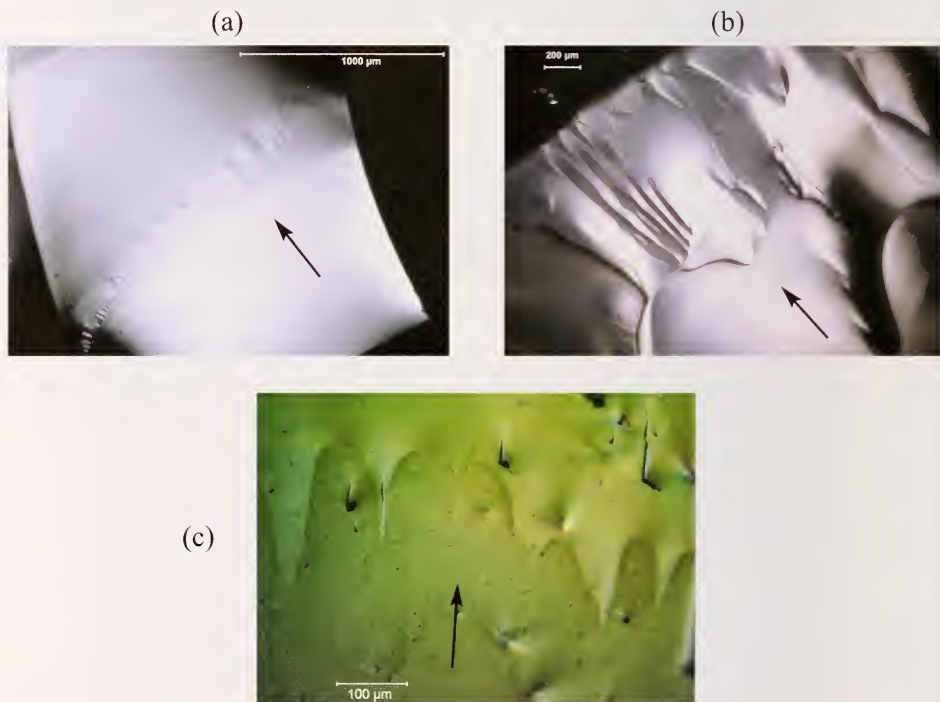


Figure 5.39 Examples of Sierra scarps, which are liquid-induced fracture markings. The arrows show the direction of crack propagation. (a) is a fractured medicinal vial. The liquid was the medicine within the vial. (b) is in a single crystal sapphire hemispherical dome broken by water quench thermal shock. This differential interference contrast optical photo shows the scarps have some variability in height. (c) is in an obsidian shard formed by knapping (courtesy A. Tsirk). The faint vertical lines within the scarps are subcavitation hackle, a precursor to complete cavitation.

5.7 Glue Chips

Glue chipping is a process used by artists to create surface decorations on glass. Figure 5.40 illustrates the geometries. Glue is coated onto a lightly abraded glass surface. The plate is warmed causing the glue to contract. Shallow cracks enter the glass at the edge of the glue at about 45 degrees then run parallel to the surface. The glue is peeled away removing scalloped chips in the glass. Fréchette noted that the chips formed by this artistic process closely resemble flaws generated in glasses in architectural and structural applications.⁴⁴

The conventional wisdom in many joining problems is to choose a metal or other material that contracts more than the ceramic or glass. During cool down from the elevated temperature joining process, the ceramic or glass is put into residual compression. This indeed is what happens, *except right at the edge of the joint* where a localized tensile stress can introduce cracks as shown in Figure 5.40. If the cracks remain shallow and come back to the surface joint, they are harmless. Alternately, if they remain where subsequent tensile loadings activate them, or they tilt down away from the joint, they can cause severe strength degradation. Glue chips, when exposed so as to reveal their fracture surfaces, have ample twist hackle, arrest lines, and tertiary Wallner lines.

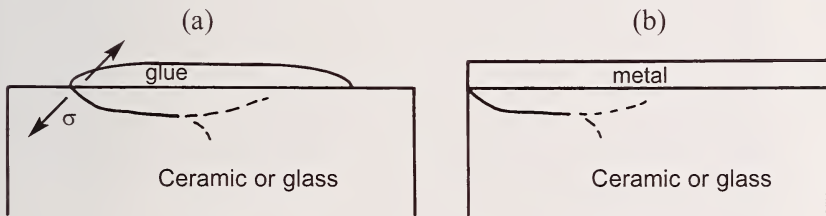


Figure 5.40 Glue chipping cracks. (a) show a sectional view with a glue applied to the surface of the glass of ceramic. Contraction causes a crack to enter at about 45° to the surface. (b) shows a comparable geometry with a metal bonded to a glass or ceramic. If the metal contracts more than the ceramic, edge cracks can be created.

Glue chips were the origins of fracture in some spectacular failures of very large window panels in a Boston skyscraper in the 1970s.⁴⁴ The glue chips were formed by a brazing compound that was sprayed onto the window edges. The compound was applied unevenly, causing some coarse droplets to form rather than the intended fine spray. Contraction of the droplets caused edge chips to form. Subsequent mechanical and thermal loadings caused the cracks to propagate and the windows eventually fractured. All the windows in the skyscraper had to be replaced.

5.8 Transgranular and Intergranular Fracture

In addition to finding the fracture origin, in polycrystalline ceramics it is often important to observe whether crack propagation is transgranular and cleaves through grains or is intergranular whereby the crack runs around the grains along grain boundaries. Figures 5.41 and 5.42 show examples. Sometimes the word *intragranular* is used interchangeably with transgranular, but the former word is not recommended, since it is so similar to *intergranular* that it often creates confusion.

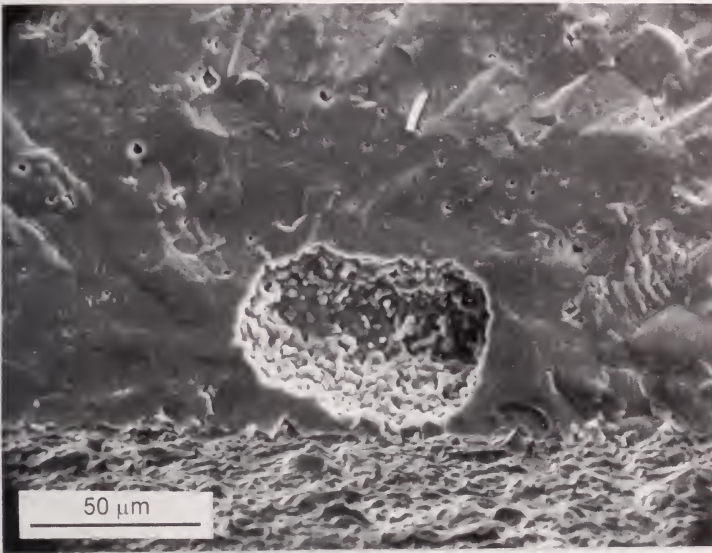
Material scientists are concerned with the mode of propagation since it provides information about how cracks interact with the microstructure. Intergranular fracture may indicate weak boundary strength. It may be a manifestation of between-grain stresses due to elastic or thermal anisotropies, especially in non-cubic ceramics. It is usually necessary to have scanning electron micrographs of the fracture surface for this characterization. Mixed inter- and transgranular fracture modes are common. It is customary to make approximations or estimates of the fraction of inter- and transgranular fracture and to show an illustration. There is clearly some interpretation involved and what may be a 50 % to 50 % mix for one observer might be reported as a 40 % to 60 % mix by another.

Fracture mirrors in polycrystalline ceramics may initially have transgranular fracture but change to mixed trans- and intergranular fracture as the crack radiates outwards.²⁶

Slow crack growth or environmentally-assisted crack growth usually occurs intergranularly. Grain boundaries are weaker than matrix grains and secondary phases or glasses often are distributed along the grain boundaries.

Transgranular fracture through grains often generates twist hackle and/or cleavage steps within the grains as the crack twists and turns to follow preferred cleavage planes within the microcrystals. These markings can be interpreted to evaluate the local direction of crack propagation.

(a)



(b)

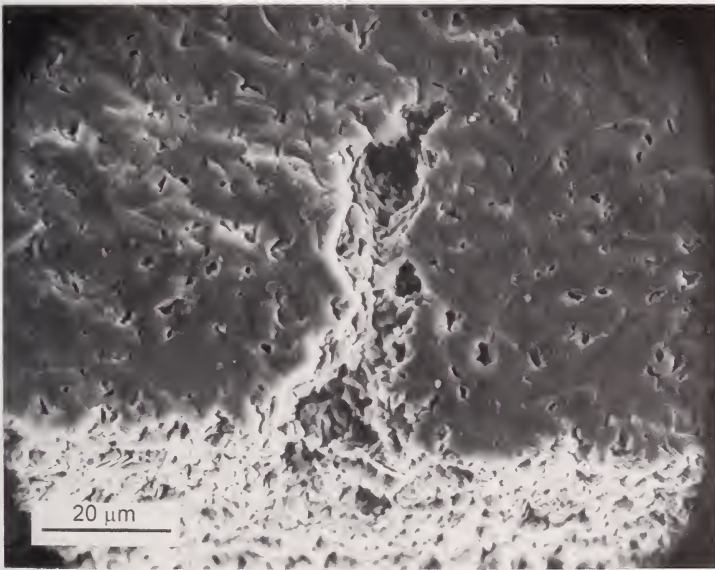


Figure 5.41 Transgranular fracture examples around fracture origins. (a) is aluminum-oxynitride. Notice also the wake hackle triggered by the grain boundaries and some small pores. (b) is a sintered alpha silicon carbide.

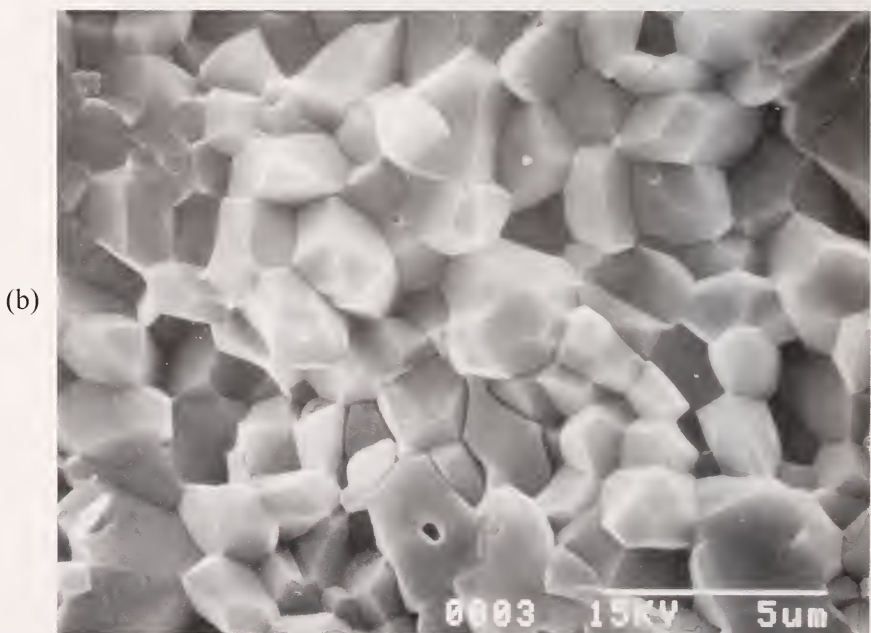
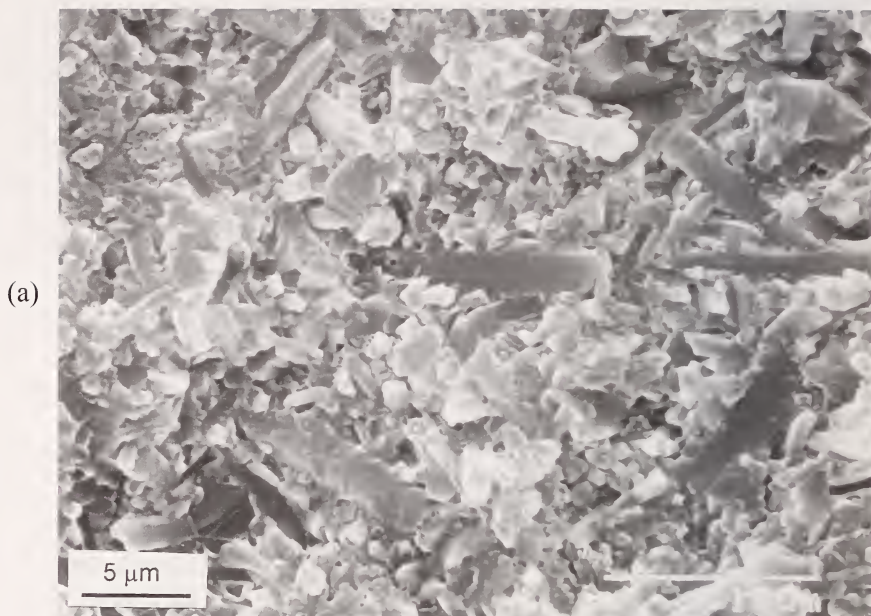


Figure 5.42 Examples of intergranular fracture surfaces. (a) is an elongated grain silicon nitride. (b) is a 99.9 % sintered alumina.

5.9 Stable Crack Growth

5.9.1 Slow crack growth (SCG) at ambient temperature

Many glasses, oxide ceramics, and nonoxide ceramics with an oxide sintering aid are susceptible to environmentally-assisted slow crack growth (SCG). The expression “slow crack growth” usually is used in the context of stable crack extension due to combined effects of stress and environment. (It is also commonly used to describe high temperature stable crack extension as described in section 5.9.3.) Water, either in liquid or as a vapor, is the most common reactive species that causes slow crack growth, although other polar molecules can attack silicates. Slow crack growth requires both a stress to open the crack faces and a reactive species to chemically react with the strained atomic bonds at the crack tip. Hence, it is sometime called “stress corrosion cracking.” Slow crack growth can lead to weakening and/or time dependent fracture.

All glasses are susceptible to slow crack growth. Many other ceramics are too, particularly if they are bonded by a glassy boundary phase, no matter how thin. Covalently-bonded ceramics are not susceptible to SCG at room temperature, unless there is an oxide boundary phase. Section 7.10 has more qualitative information about the mechanics of slow crack growth and Table 7.2 lists materials that are or are not susceptible.

Sometimes it is possible to detect evidence of the stable crack extension. Slow crack growth is usually intergranular in polycrystalline ceramics. If the fast, unstable fracture mode is transgranular or mixed, then the difference in propagation morphology may be detectable as a SCG “halo” on a fracture surface as shown in Figure 5.43.

Slow crack growth halo: *A region or band around a flaw in a ceramic caused by stable crack extension. The band is caused by changes in the mode of crack propagation.*

SCG halos can often be detected with both optical and SEM microscopy as shown in Figure 5.43. The usual remedies to eliminate the slow crack growth in laboratory strength testing are to test either at a very fast loading rate or in an inert atmosphere. Comparative tests have shown that the SCG halos disappear when testing is done in inert atmosphere.⁴⁵

There is no crack-microstructure morphology change in glasses, but a subtle partial elliptical line that sometimes appears on the fracture surface provides a

strong clue that SCG has enlarged a flaw as shown in Figures 5.36c and 5.44.^{46,47} The part elliptical line is a slight step that forms as a result of the intersection of the unstable crack portion that wraps around the portion of the crack that has not gone unstable.

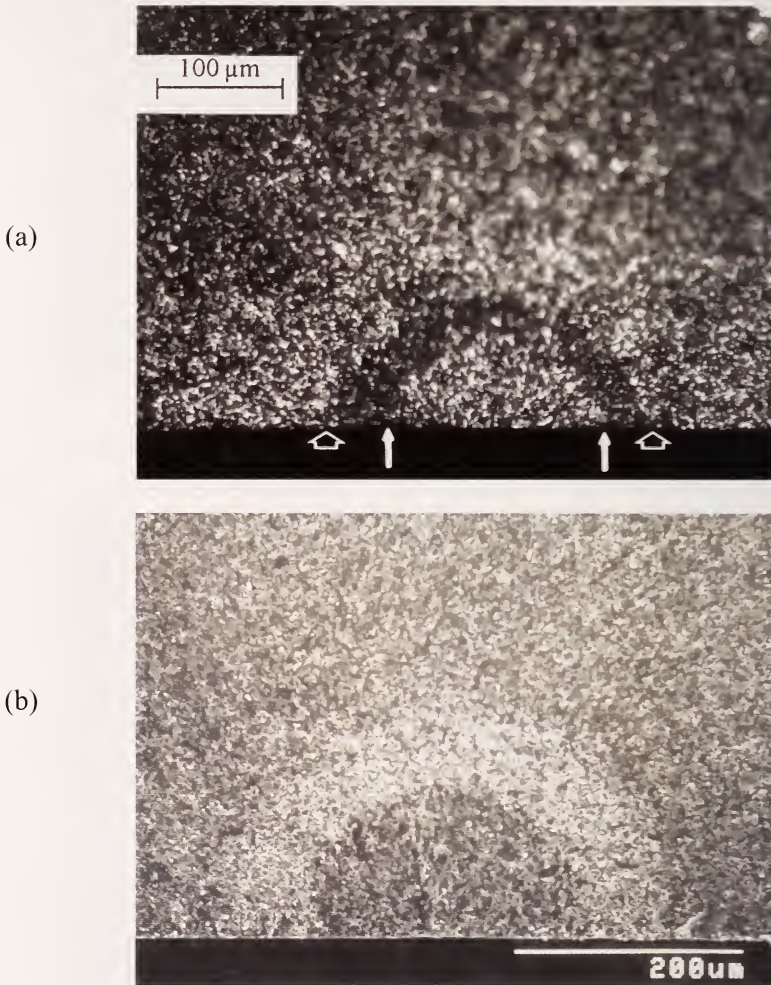


Figure 5.43 Artificial Knoop semicircular flaws made at different loads in two specimens are surrounded by slow crack growth “halos” in a sintered 99.9 % alumina. (a) is an optical image of a 29 N indentation flaw (Courtesy J. Swab), and (b) is a SEM image of a 49 N flaw. The initial precracks are mixed transgranular-intergranular, the halo is mostly intergranular, and the fast fracture is mixed transgranular-intergranular. The crack growth that enlarged the flaw occurred in only a few seconds during an ordinary strength test. Notice that the rougher intergranular surface appears dark in the optical photo since it scatters light, whereas it appears light colored in the SEM.

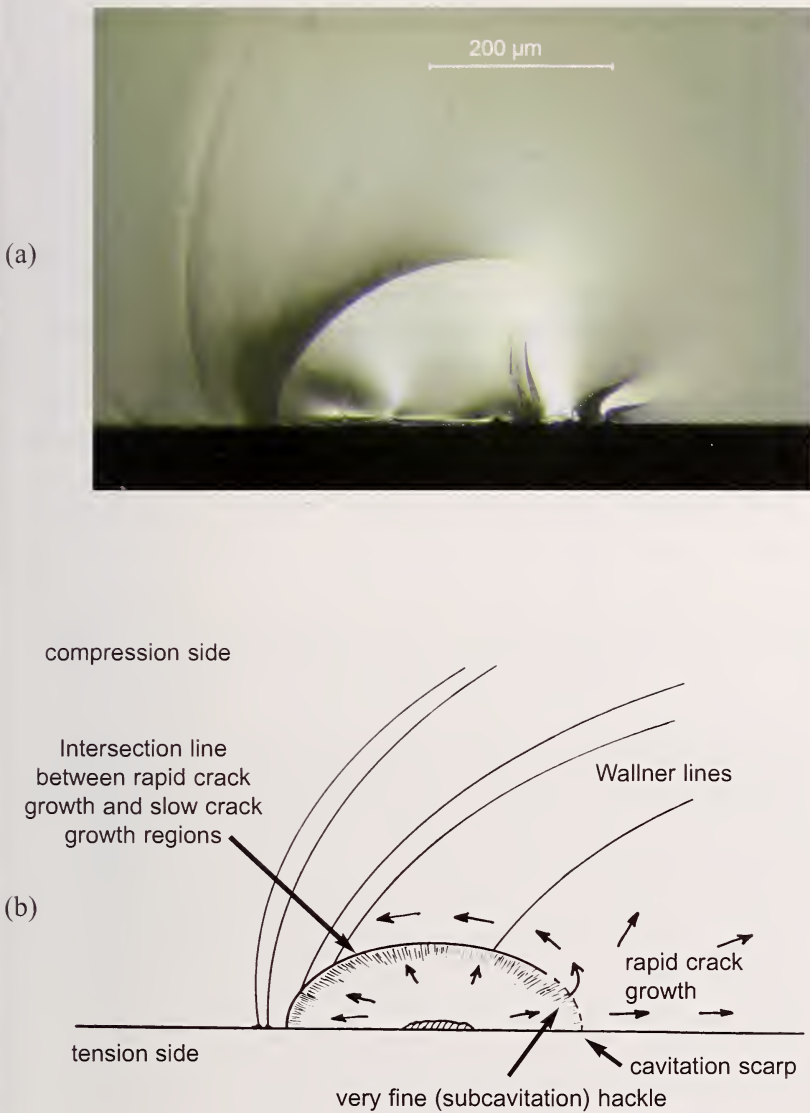


Figure 5.44 Slow crack growth in glasses sometimes leaves a partial semi-elliptical line that approximates the critical crack size. (a) shows an example for a glass disk tested in ring-on-ring biaxial flexure in water. The original flaw was an 8 μm to 10 μm deep crack from a polishing scratch. It grew approximately 20 times deeper in the bending stress field before it went unstable along the right side. Only a very faint cavitation scarp exists at that position, but a more distinct line forms around the crack front periphery as the unstable crack wraps around it. (b) shows a schematic of this sequence. See also Figure 5.36c.

5.9.2 Stable extension from local residual stress or R-curve effects

Stable crack extension can occur, even in the absence of environmental effects, if a flaw has a strong local residual tensile stresses. Indentation crack flaws made by either Vickers or Knoop indentation are good examples. Damage zones underneath the indentation can provide the tensile stresses that are the driving force for crack extension. As the crack extends away from damage zone and the crack periphery gets larger, the effect of the tensile stresses diminish and the crack slows down and arrests in the absence of externally applied stresses. Alternatively, in fast fracture tests where the specimen is loaded to fracture, there can be momentary stable crack extension of the flaw prior to rupture. Figure 5.45 shows an example of stable crack extension due to local residual stresses in a hot-pressed silicon nitride. Rising R-curves, which will be discussed in more detail in chapter 7, can also lead to stable crack extension at room temperature. There is only a small fractographic literature on this effect, in part due to the fact that the amount of stable crack extension prior to a flaw going unstable is often very small. (Stable crack extension from local residual stresses or due to R-curve effects is usually not termed “slow crack growth” in the literature.)

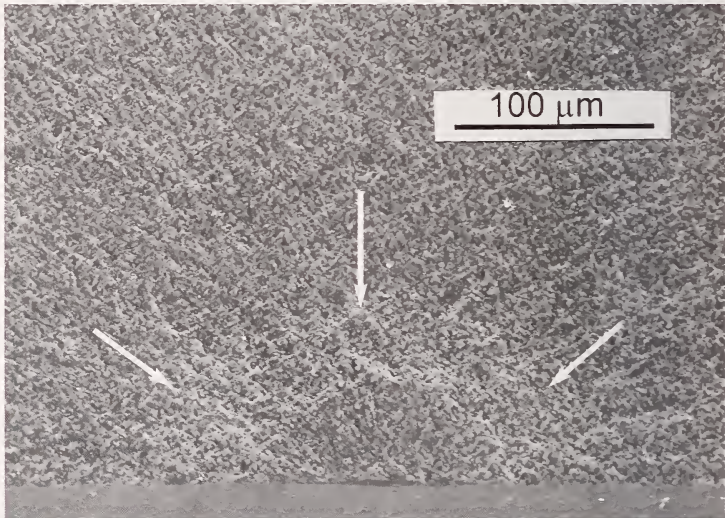


Figure 5.45 Knoop flaw (dark semi-ellipse) in silicon nitride showing stable crack extension (white arrows). The local residual stresses underneath the indentation provided the impetus for the extension. Traces of the elongated Knoop indentation can be seen on the bottom.

5.9.3 High temperature slow crack growth in ceramics

At elevated temperatures, increased atom mobility and decreases in boundary phase viscosity can lead to intergranular crack growth. This also can cause weakening or time dependent fracture. The environment may or may not play a role in slow crack growth. Figures 5.46 and 5.47 show flaws that have been altered as a result of slow crack growth. The slow crack growth zones are usually rougher than the normal fast fracture surface and are usually easy to detect due to the topography difference in the SEM or by a topography or reflectivity difference in an optical microscope. Oxidation of the material in a slow crack zone often causes a color or reflectivity difference that is also easy to detect in an optical microscope. The slow crack growth zones can be very small and may enlarge a flaw just enough to cause it to reach criticality, or at lower stresses, have extensive crack growth zones that can cover as much as one half of a fracture surface as show in Figure 5.47. In such cases, it often is impossible to locate the initial flaw from which the crack growth occurred.

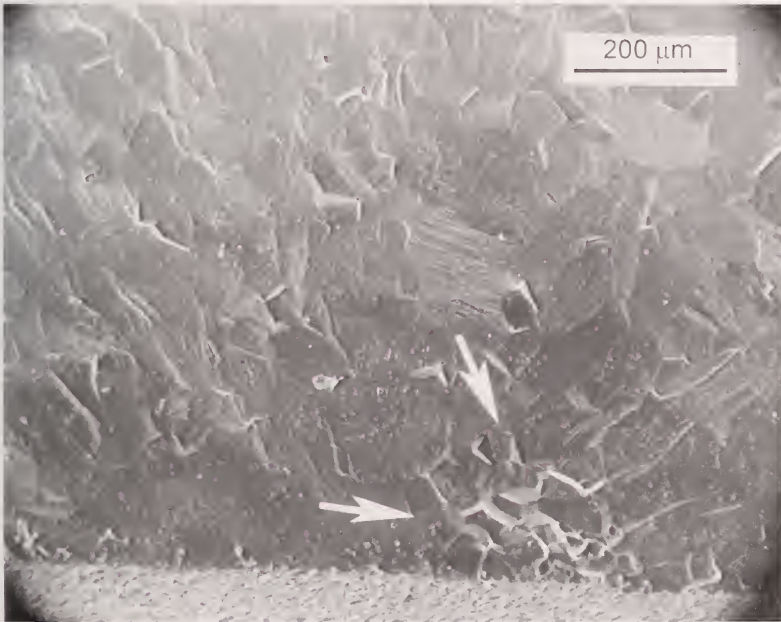


Figure 5.46 Intergranular slow crack growth in a pure AlON at elevated temperature. The slow crack growth zone (arrows) formed in the short time that was needed to break the specimen in a strength test. (1200° C, 155 MPa, 22.5 ksi)

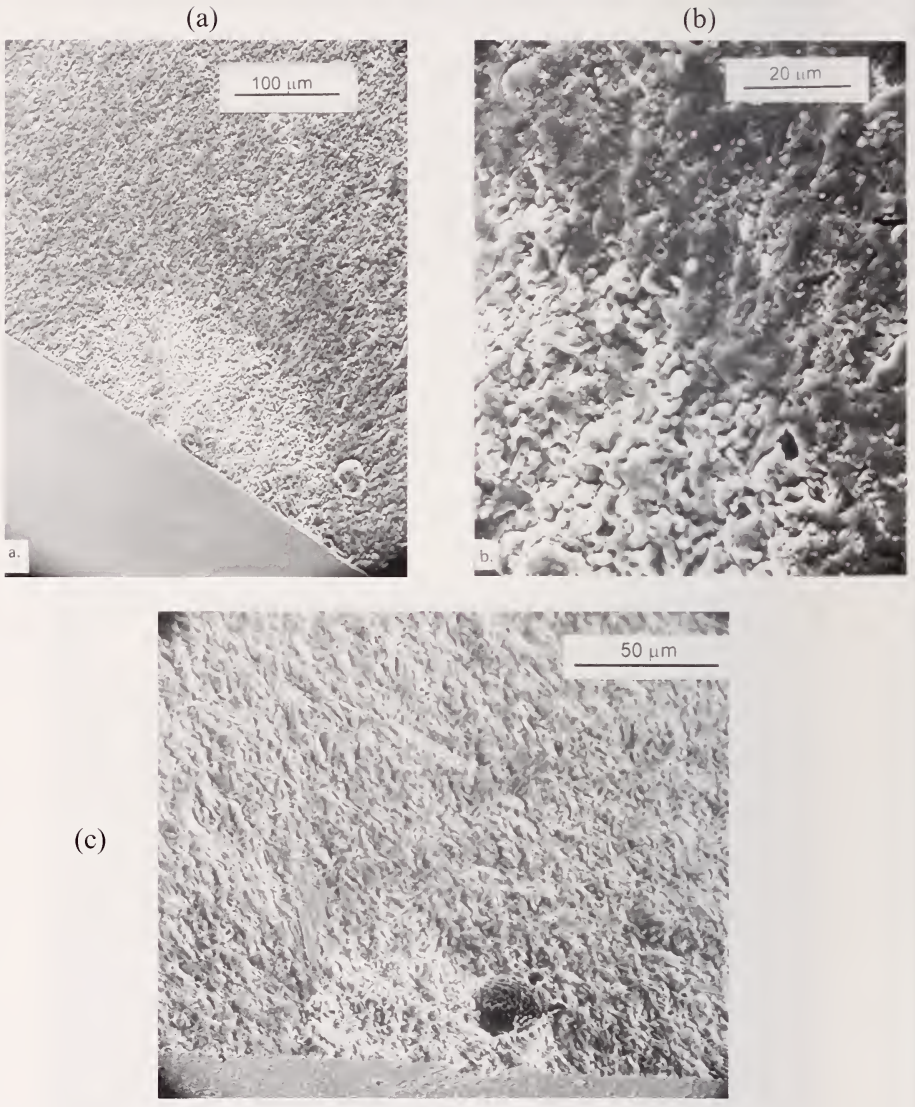


Figure 5.47 Elevated temperature slow crack growth in sintered α SiC tested in stress rupture at 1400 °C in air (a). The close-up (b) shows the boundary between the intergranular SCG and the transgranular fast fracture zones. (c) shows another α SiC specimen wherein the slow crack growth appears to have originated near a pore.

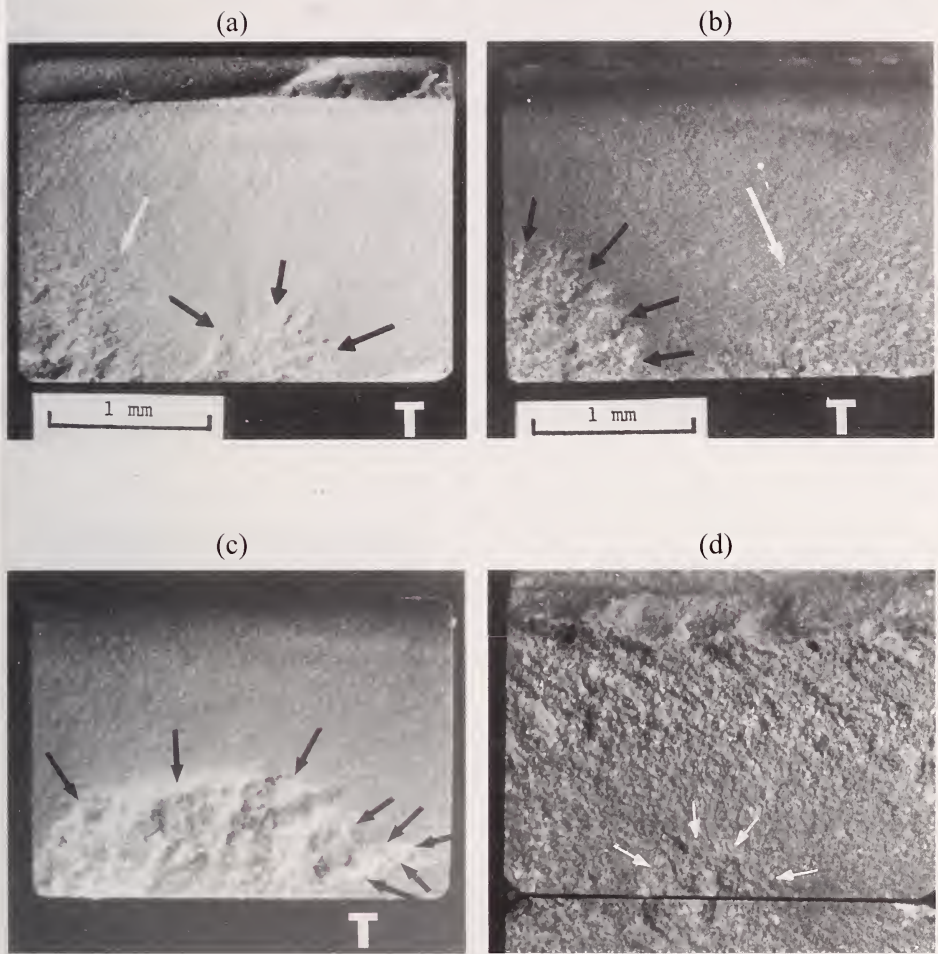


Figure 5.48 Elevated temperature slow crack growth zones in hot-pressed silicon nitride (a-d). These four bend specimens were tested at 1200 °C in air. The arrows mark the intergranular crack growth zones, which appear lighter since they have oxidized somewhat, unlike the final fracture regions. Notice the roughness of mirror-like hackle on the left side of (a) and the right of (b) as marked by the white arrows. At low magnification, this roughness could be confused with a slow crack growth zone, but closer examination shows it has directional lines typical of hackle.

5.9.4 High temperature creep fracture

Creep can cause fracture at higher temperatures and lower stresses. There is so much boundary phase ductility that sharp flaws are blunted. Fracture is due to the nucleation and growth of cavities, microcrack formation, and their coalescence. Creep fracture surfaces often look like the slow crack growth zones shown above, but with growth zones that extend across a major fraction of the fracture surface. Final rupture frequently occurs from creep crack zones connected to specimen corners. Tensile surfaces often reveal extensive tortuous microcrack patterns. A key difference between slow crack growth and creep fractures is that the former can occur with negligible bulk deformation, whereas the latter inevitably have significant permanent deformations with strains of 1% or more. Figure 5.49 shows several examples.

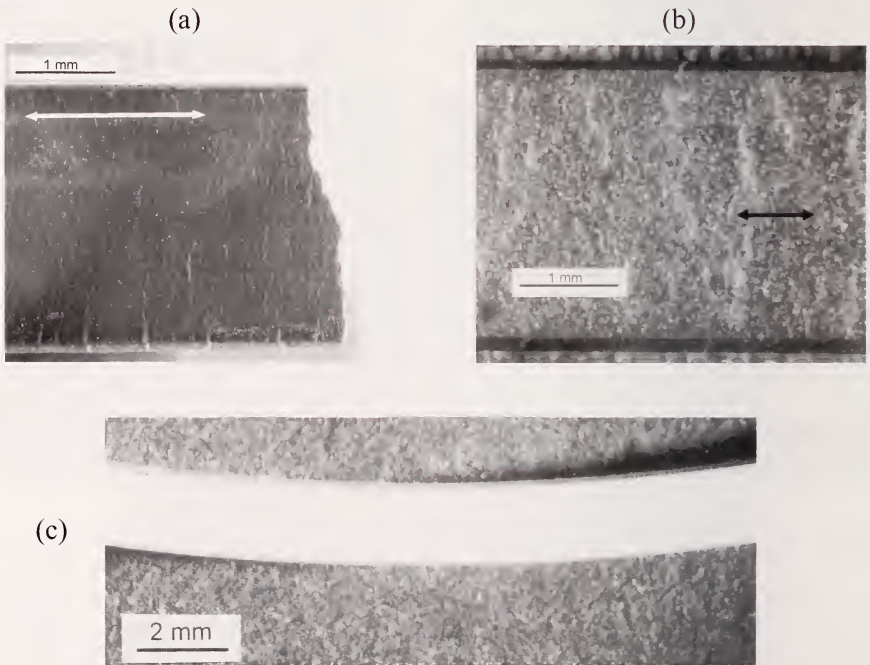


Figure 5.49 Bend specimens tested under creep fracture conditions. (a) shows the tensile surface of a hot-pressed silicon nitride specimen. Notice the extraordinarily rough fracture surface on the right side of (a). (b) shows the tensile surface of a siliconized silicon carbide specimen. Note that the microcracking is perpendicular to the axis of tensile stresses (double arrow). (c) shows a side view of a bend bar tested in creep fracture conditions.

Figure 5.50 illustrates the differences between slow crack growth and creep fracture. Glassy boundary phases such as shown in Figure 5.51 usually account for both processes. Slow crack growth occurs from preexistent flaws that grow until they reach a critical condition. Fracture toughness at elevated temperature is often greater than at room temperature due to the onset of limited plasticity. Hence, critical flaw sizes can actually be much larger at elevated temperature than at room temperature. Creep fracture on the other hand usually does not involve the initial flaws. It blunts them. Voids and microcracks are nucleated, then coalesce, and then grow leading to rupture. Specimens that fail from slow crack growth have negligible ($< 0.2\%$) permanent strain whereas creep fracture specimens have considerable permanent strain at fracture. The intergranular crack growth zone on creep fractured bend bars often extends over 33 % or more of the fracture surface.

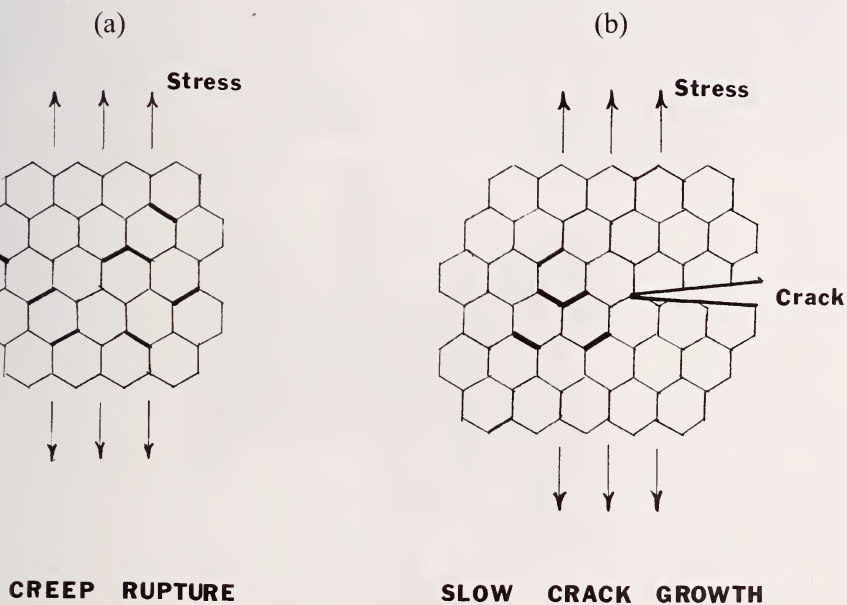


Figure 5.50 Slow crack growth and creep fracture usually are intergranular. In creep fracture, cavitation and microcrack nucleation and growth occur throughout the body in creep fracture (a), but are localized to the vicinity of a crack tip in slow crack growth (b).

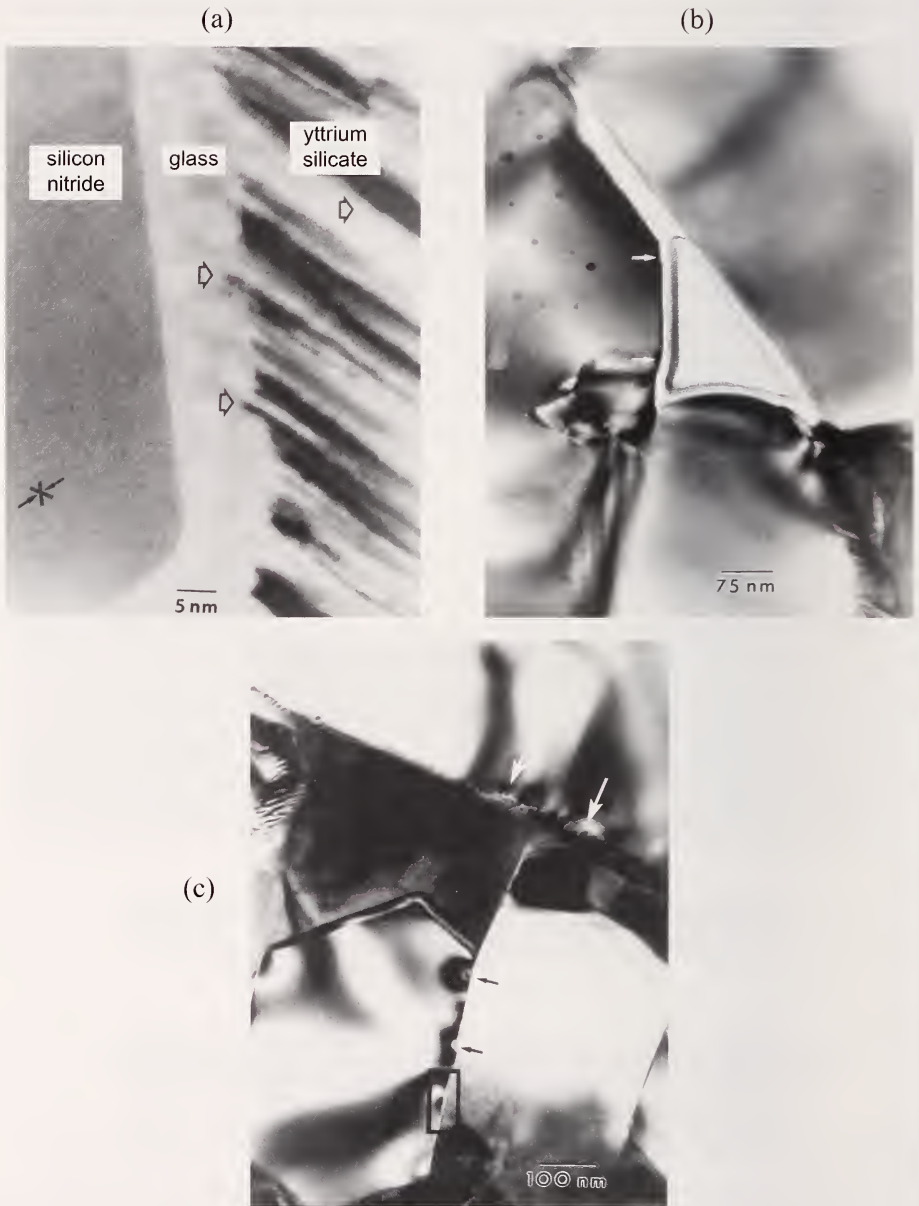


Figure 5.51 Transmission electron microscopy images show the glassy boundary phase that often is the source of intergranular slow crack growth and creep crack growth. (a) shows the boundary phase which has partially devitrified in a silicon nitride with a yttrium aluminosilicate glass sintering aid. There still is a thin glassy layer that led to SCG and creep fracture. (b) shows a creep cavity opening up at a triple grain junction. (c) shows strain sworls (black arrows) from grain boundary sliding. (Ref. 48, Photos courtesy W. Braue).

Figure 5.52 is a fracture mechanism map that puts these phenomena into context.⁴⁹ It is for a commercial silicon nitride hot pressed with about 1 mass % magnesium oxide. The sintering aid reacted with silica on the surface of the starting powders and formed a very thin silicate boundary phase glass. Depending upon the stress and temperature, flexural specimens fractured from any one of several mechanisms. At low temperature, material and grinding flaws controlled strength. At moderate temperatures in an oxidizing environment, flaws either remained unchanged and controlled strength, or they healed or blunted causing some strengthening. On the other hand, oxidation sometimes created pit flaws that weakened the body. At 1000°C and greater, intergranular slow crack growth caused flaw growth and eventual fracture in times shown in hours on the dotted lines. At low stresses and high temperature, creep fracture controlled lifetime. At low stresses and high temperature, creep fracture controlled lifetime.

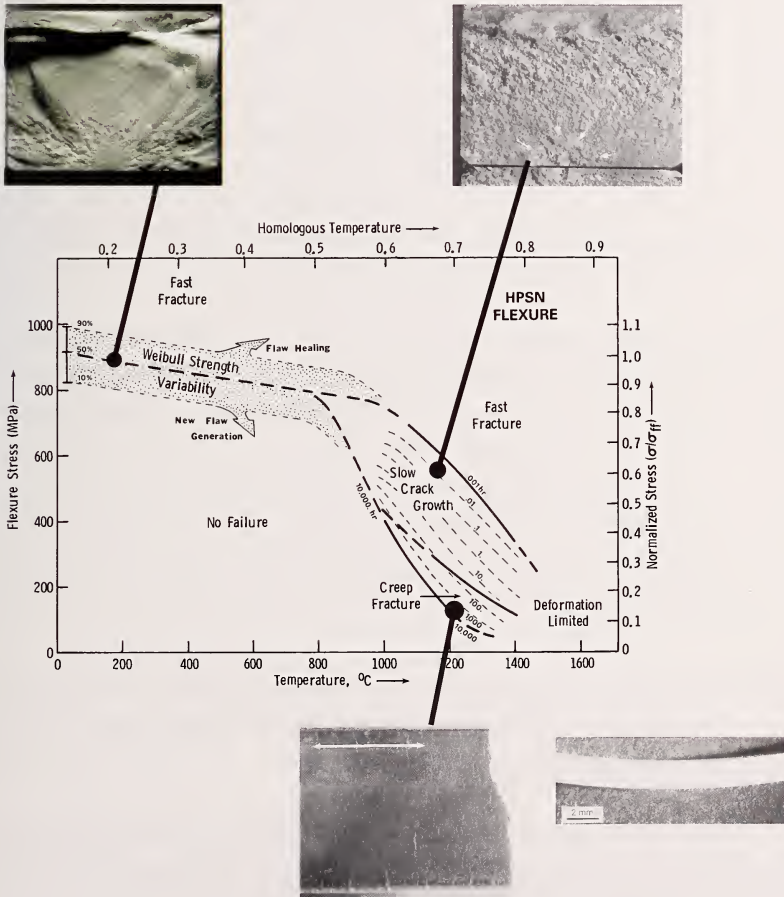


Figure 5.52 Fracture mechanism map for hot-pressed silicon nitride from Reference 49. This map is for flexurally-loaded specimens.

Chapter 5 References

- 1 V. D. Fréchette, *Failure Analysis of Brittle Materials*, Advances in Ceramics, Vol. 28, American Ceramic Society, Westerville, OH, 1990.
- 2 H. G. Richter and F. Kerkhof, "Stress Wave Fractography," pp. 75 - 109 in *Fractography of Glass*, eds., R. C. Bradt and R. E. Tressler, Plenum, NY, 1994.
- 3 J. E. Field, "Brittle Fracture: Its Study and Application," *Contemporary Physics*, 12 [1] (1971) 1 - 31.
- 4 A. Smekal, "Procedures for the Measurement of Fracture Propagation Velocities on Fracture Surfaces," *Glastechn. Ber.*, 23 [3] (1950) 57 - 67.
- 5 U. Hornemann, H. Rothenhäuser, H. Senf, J. F. Kalthoff, and S. Winkler, "Experimental Investigation of Wave and Fracture Propagation in Glass Slabs Loaded by Steel Cylinders at High Impact Velocities, pp. 291 - 298 in Int. Phys. Conf. Series No. 70, 3rd *Conference on Mechanical Properties at High Rates of Strain*, Oxford, The Institute of Physics, London, 1984.
- 6 S. Winkler, H. Senf, and H. Rothenhäusler, "High Velocity Fracture Investigation in Alumina," pp. 165 - 183 in *Fractography of Glasses and Ceramics, Advances in Ceramics*, Vol. 22, J. Varner, and V. Fréchette, eds., American Ceramic Society, Westerville, OH, 1988.
- 7 H. Schardin, L. Mücke, and W. Struth, "Bruchgeschwindigkeit von Gläsern," *Glastechn. Ber.*, 141, [5] May 1954, 19 -147. Also available translated into English in *Glass Industry*, 36 [3] (1955) 133 - 168.
- 8 F. Kerkhof, "Bestimmung der Maximalen Bruchgeschwindigkeit Verschiedener Gläser nach der Ultraschall-Methode," *Glastechn. Ber.*, 35 [6](1962) 267 - 272.
- 9 J. Congleton and B. K. Denton, "Dynamic Fracture Toughness Experiment," Final Technical Report, University of Newcastle on Tyne to U. S. Army European Research Office, July 1975.

- 10 M. M. Chaudhri, "High-Speed Photographic Investigations of the Dynamic Localized Loading of Some Oxide Glasses," pp. 87 - 113 in *Strength of Inorganic Glass*, Plenum, NY, 1985.
11. F. E. Barstow and H. E. Edgerton, "Glass Fracture Velocity," *J. Am. Ceram. Soc.*, 22 [9] (1939) 302 - 307.
12. E. H. Yoffe, "The Moving Griffith Crack," *Phil. Mag.*, 42 (1951) 739 - 750.
- 13 J. W. Johnson and D. G. Holloway, "On the Shape and Size of the Fracture Zones on Glass Fracture Surfaces," *Phil Mag.*, 14 (1966) 731 - 743.
- 14 A. B. J. Clark and G. R. Irwin, "Crack-Propagation Behaviors," *Exptl. Mech.*, 6 (1966) 321 - 330.
- 15 J. Congleton and N. J. Petch, "Crack-Branching," *Phil. Mag.*, 16 (1967) 749 - 760.
- 16 H. P. Kirchner and J. W. Kirchner, "Fracture Mechanics of Fracture Mirrors," *J. Am. Ceram. Soc.*, 62 [3-4] (1979) 198 - 202.
- 17 H. P. Kirchner and J. C. Conway, "Criteria for Crack Branching in Cylindrical Rods: I, Tension, and II, Flexure," *J. Am. Ceram. Soc.*, 70 [6] (1987) 413 - 418 and 419 -425.
- 18 H. P. Kirchner, "Brittleness Dependence of Crack Branching in Ceramics," *J. Am. Ceram. Soc.*, 69 [4] (1986) 339 - 342.
- 19 W. Doll, "Investigations of the Crack Branching Energy," *Int. J. Fract.*, 11 (1975) 184 - 186.
- 20 Y. L. Tsai and J. J. Mecholsky, Jr., "Fracture Mechanics Description of Fracture Mirrors Formation in Single Crystals," *Int. J. Fract.*, 57 (1992) 167 - 182.
- 21 E. K. Beauchamp, "Mechanisms of Hackle Formation and Crack Branching," pp. 409 - 446 in *Fractography of Glasses and Ceramics III*, eds. J. Varner V. D. Fréchette, and G. D. Quinn, Ceramic Transactions, vol. 64, American Ceramic Society, Westerville, OH, 1996.

- 22 E. K. Beauchamp, "Fracture Branching and Dicing in Stressed Glass," Sandia Laboratories Research Report, SC-RR-70-766, Jan. 1971.
- 23 E. F. Poncelet, "The Markings on Fracture Surfaces," *J. Soc. Glass Technol.*, 42 (1958) 279T - 288T.
- 24 E. Gözl, "Übermikroskopische Feinstructuren an Glassbruchflächen," (Ultramicroscopic Fine Structures on Glass Fracture Surfaces), *Zeitschrift Physik*, 120 (1943) 773 - 777.
- 25 D. Hull, Chapter 5, in *Fractography, Observing, Measuring and Interpreting Fracture Surface Topography*, Cambridge Univ. Press., Cambridge, 1999.
- 26 R. W. Rice, "Fracture Topography of Ceramics," pp. 439 - 472 in *Surface Interfaces of Glasses and Ceramics*, eds. V. Fréchette, W. LaCourse, V. L. Burlick, Plenum, NY, 1973.
- 27 R. W. Rice, "The Difference in Mirror-to-Flaw Size Ratios Between Dense Glasses and Polycrystals," *J. Am. Ceram. Soc.*, 62 [9-10] (1979) 533 - 535.
- 28 D. Lewis, III and J. R. Spann, "Fracture Features at Internal Fracture Origins in a Commercial Glass Ceramic," *Comm. Am. Ceram. Soc.*, Oct. 1982, C-173 - C-174.
- 29 M. Ramulu, R. C. Bradt, A. S. Kobayashi, and K. H. Yang, "A Dynamic Fracture Mechanics Interpretation of Multiple Mist Regions on Soda-Lime-Silicate Glass Fracture Features," pp. 215 - 227 in *Fractography of Glasses and Ceramics, Advances in Ceramics*, Vol. 22, J. Varner, and V. Fréchette, eds., American Ceramic Society, Westerville, OH, 1988.
- 30 G. D. Quinn, L. K. Ives, and S. Jahanmir, "On the Fractographic Analysis of Machining Cracks in Ground Ceramics: A Case Study on Silicon Nitride," Special Publication 996. NIST, Gaithersburg, MD, May, 2003.
- 31 G. D. Quinn, L. K. Ives, and S. Jahanmir, "On the Nature of Machining Cracks in Ground Ceramics: Part I: SRBSN Strengths and Fractographic Analysis," *Machining Science and Technology*, 9 (2005) 169 - 210.

- 32 J. Barsom, "Fracture of Tempered Glass," *J. Amer. Ceram. Soc.* 51 [2] (1968) 75 - 78.
- 33 H. Ko, "Fracture Behavior of Sintered Alumina Under Rotary Bending and Static Fatigue," pp. 15 - 29 in *Fracture Mechanics of Ceramics 12*, eds. R. C. Bradt, D. P. H. Hasselman, D. Munz, M. Sakai, V. Ya Shevchenko, Plenum, NY, 1996.
- 34 F. Kerkhoff and E. Sommer, "Das Bild der Bruchfläche (von Gläsern)," in *Handbuch der Mikroskopie der Technik, Vol. IV, Mikroskopie der Silicate*, Umschau Verlag, Frankfurt am Main, Germany, 1964.
- 35 E. Sommer, "Formation of Fracture 'Lances' In Glass," *Eng. Fract. Mech.*, 1 (1969) 539 - 546.
- 36 H. Wallner, "Line Structures on Fracture Surfaces," *Zeitschrift für Physik*, 114 (1939) 368 - 378.
- 37 F. Kerkhof, "Bestimmung der Maximalen Bruchgeschwindigkeit Verschiedener Gläser Nach Der Ultraschalmethode," *Glasstechnische Bericht*, 35 (1955) 267 - 272.
- 38 T. A. Michalske, "Fractography of Stress Corrosion Cracking in Glass," pp. 111 - 142 in *Fractography of Glass*, eds., R. C. Bradt and R. E. Tressler, Plenum, NY, 1994.
- 39 A. G. Evans, "Engineering Property Requirements for High Performance Ceramics," *Mat. Sci. and Eng.*, 71 (1985) 3 - 21.
- 40 A. Tsirk, "An Exploration of Liquid-Induced Fracture Markings," pp. 87 - 101 in *Fractography of Glasses and Ceramics, IV, Ceramic Transactions*, Vol. 122, J. Varner, and G. D. Quinn, eds., American Ceramic Society, Westerville, OH, 2001.
- 41 V. D. Fréchette, "Markings Associated with the Presence of H₂O During Cracking," pp. 71 - 76 in *Fractography of Glasses and Ceramics, Advances in Ceramics*, Vol. 22, J. Varner, and V. Fréchette, eds., American Ceramic Society, Westerville, OH, 1988.

- 42 T. A. Michalske and V. D. Fréchet, "Dynamic Effects of Liquids on Crack Growth Leading to Catastrophic Failure in Glass," *J. Am. Ceram. Soc.*, 63 [11-12] (1980) 603 - 609.
- 43 T. A. Michalske, J. R. Varner, and V. D. Fréchet, "Growth of Cracks Partly Filled With Water," pp. 639 - 649 in *Fracture Mechanics of Ceramics, Vol. 4*, eds. R. C. Bradt, D. P. H. Hasselman, and F. F. Lange, Plenum, NY, 1978.
- 44 V. D. Fréchet and M. Donovan, "Some Effects of The "Glue-Chipping" Process on Strength," pp. 407 -411 in *Fractography of Glasses and Ceramics, II, Ceramic Transactions*, Vol. 17, V. Fréchet, and J. Varner, eds., American Ceramic Society, Westerville, OH, 1988.
- 45 J. J. Swab and G. D. Quinn, "Effect of Precrack 'Halos' on K_{Ic} Determined by the Surface Crack in Flexure Method," *J. Am. Ceram. Soc.*, 81 [9] (1998) 2261 - 2268.
- 46 T. A. Michalske, "Fractography of Slow Fracture in Glass," pp. 121 - 136 in *Fractography of Ceramic and Metal Failures*, ASTM Special Technical Publication 827, eds., J. J. Mecholsky, Jr. and S. R. Powell, Jr., ASTM, West Conshohocken, PA, 1984.
- 47 T. A. Michalske, V. D. Fréchet, and R. Hudson, "Dynamic Effects of Liquids on Surface Crack Extension in Glass," pp. 1091 - 1097 in *Advances in Fracture Research*, Vol. 2, ed. D. Francis, Pergamon, NY, 1981.
- 48 G. D. Quinn and W. R. Braue, "Fracture Mechanism Maps for Advanced Structural Ceramics, Part 2, Sintered Silicon Nitride," *J. Mat. Sci.*, 25 (1990) 4377 - 4392
- 49 G. D. Quinn, "Fracture Mechanism Maps for Advanced Structural Ceramics, Part I, Methodology and Hot Pressed Silicon Nitride," *J. Mat. Sci.*, 25 (1990) 4361 - 4376.

6. Origins of Fracture

6.1 Origins, Flaws, and Defects

The origin is not only a location, but also an object. In the parlance of the engineer or scientist, the irregularities that initiate fracture are termed flaws or defects. The fractographer should use the terms “defect” and “flaw” with discretion. Scientists and engineers understand that virtually all brittle materials are imperfect and contain irregularities that can behave as flaws, but nontechnical people may misunderstand these terms. That the material contains flaws or defects does not necessarily mean that the material has been prepared improperly or is somehow faulty. Conversely, there are instances where defects or flaws do indicate defective material. The author usually avoids using the word “defect” because of its similarity to the word “defective.” “Flaw” seems a little less severe and sounds to many as a more technical term. If there is any doubt, then the fractographer may fall back upon the most innocuous term “fracture origin.” Ceramists, engineers, and researchers occasionally use the term “Griffith flaw.” A Griffith flaw is a hypothetical sharp crack, usually envisioned as a slender elliptically-shaped flaw, that concentrates stress at sharp tips. Griffith flaws and fracture mechanics are discussed in chapter 7.

6.2 The Spatial Distribution of Flaws

Flaws are either surface- or volume-distributed. For example, inclusions are almost always volume-distributed. Grinding cracks are inherently surface-distributed. Some flaws may even be edge-distributed. The distinction is important for understanding how flaws originated and whether they are from processing or from subsequent handling, finishing, or service damage. The distinction is also crucial for brittle material design engineers who often must scale the strengths of laboratory test data to predict component strengths via the Weibull theory.^{1,2,3,4,5} Strength scaling and reliability predictions may be dramatically different for area and volume scaling. Glasses usually, but not always, break from surface-distributed flaws. Ceramics can fracture from surface or internal flaws.

One aspect about the spatial distribution of flaws needs clarification as shown in Figure 6.1. A single volume-distributed flaw may be located in the volume (in the bulk), at the surface, near the surface, or at an edge. For example, an inclusion originally may have been in the interior of a ceramic plate, but when a test bar was cut out, the inclusion ended up on the surface of the test bar.

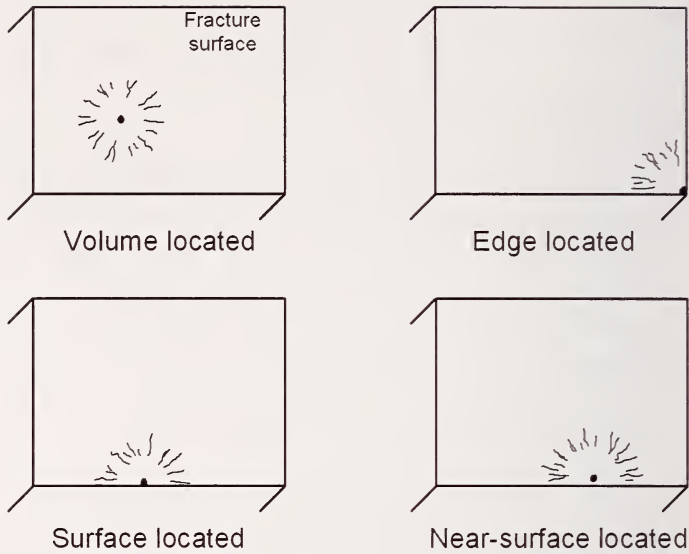


Figure 6.1. Schematics that show the four possible locations of a volume-distributed flaw type.

Surface-distributed flaws can only exist at the surface or at an edge. While the above statements may seem obvious, there are two reasons to keep the distinction clear. Firstly, if a flaw is found at a surface location, it does not necessarily mean it is a surface type flaw. It could be a volume flaw located at the surface. Some causal analysts simply look at the locations of the fracture origins. If they are located at the surface they simply interpret the origin as a surface type flaw. This is often wrong, particularly if the test data set is from bend bars or biaxially-loaded plates. It is a common misunderstanding that these two configurations always break from surface flaws. Origins indeed are often located at the surface of these bending configurations, but if reasonable precautions are taken to control the grinding damage, then they are quite likely to break from volume flaws. The following pages show many such examples. Secondly, even if the data are not intended for design, a common mistake is to assume that all surface-located flaws are machining damage.

Thus, the fractographer should be careful when answering questions like: “What were the origins?” A cavalier answer such as “surface flaws” does not convey enough information. The answer should be more specific such as: “volume-distributed inclusions located at the surface,” or “volume-type flaws located at or near the surface,” or “surface-distributed grinding cracks.”

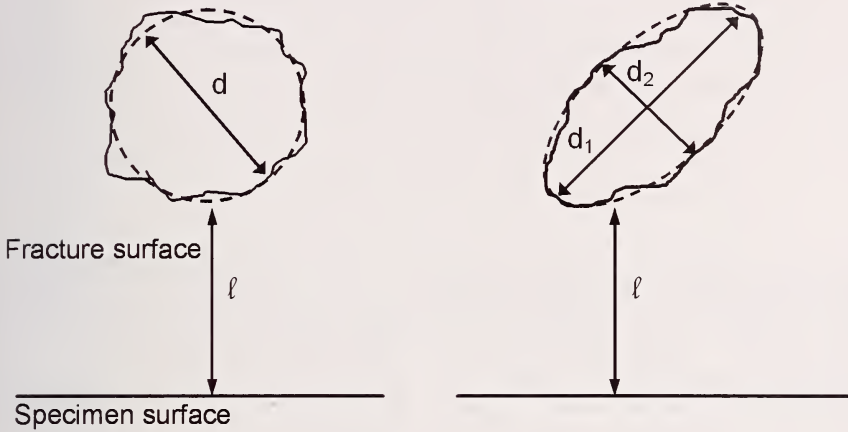
Near surface if $0 < \ell < d$ Near surface if $0 < \ell < d_1$ 

Figure 6.2. Near surface (NS) origins are no deeper (ℓ) than the flaw diameter or major axis length.

One might ask at what point is a volume type flaw “near surface.” A review of the fracture mechanics stress intensity shape factors for flaws located at various distances in proximity to a surface suggests the criterion shown in Figure 6.2. At distances closer than one diameter, the shape factor for such flaws increase by more than a few percent.

Sometimes the characterization of location is important for service-performance issues or fracture mechanics analyses of the flaws. For example, some near-surface located origins may be more susceptible to time-dependent crack growth than equivalent volume-located origins. A classic example of this for time-dependent fractures in sintered silicon carbide is case study 3 in Chapter 10 of this Guide. Pores located at or near the surface behaved differently than identical pores located in the bulk. Near surface-located origins may also be likely to link up with surface machining or impact damage or to extend subcritically to the surface prior to catastrophic fracture.

6.3 Are Flaws Intrinsic or Extrinsic?

The irregularities that act as fracture origins in advanced ceramics can develop during or after fabrication of the material. Large irregularities (relative to the average size of the base microstructure) such as pores, agglomerates, and

inclusions are typically introduced during processing. Some might deem inclusions and other irregularities as extrinsic flaws in a material, but to the extent that they occur naturally during fabrication and cannot be avoided, they alternatively could be considered intrinsic. For example, if a material customarily has a ball milling step in the process, and mill fragments flake off and become inclusions in every batch, then these may be considered intrinsic. Other origins can be introduced after processing as a result of machining, handling, impact, wear, oxidation, and corrosion. These usually can be considered extrinsic origins. However, machining damage may be considered either extrinsic or intrinsic. It is intrinsic to the manufacture to the extent that machining is a natural consequence of producing a finished specimen or component. In any case, the differentiation between intrinsic and extrinsic is often of no practical concern and it is pointless to argue the distinction.

Wherever possible, the origin should be characterized by what it is rather than a description of how it appears, since the latter may depend upon the mode of viewing. Descriptions such as the origin was a “white spot” should be avoided. It may be white in an optical microscope, but it most likely will not in a SEM (Figure 6.3). Sometimes descriptive terms may be used, but as qualifiers to the true flaw identity, e.g., “pores that appear white when viewed optically.”

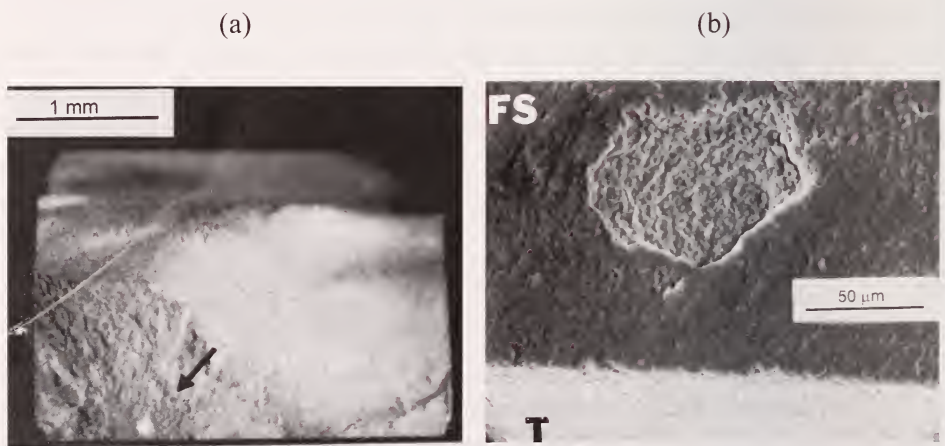
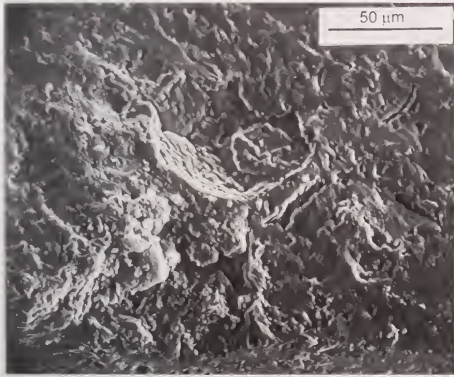


Figure 6.3. Wherever possible, describe flaws by what they are, not how they appear. (a) shows a white spot at the origin in a reaction bonded silicon nitride bend bar. The SEM image of the origin in (b) shows the origin is a pore. FS denotes fracture surface and T denotes tensile surface.

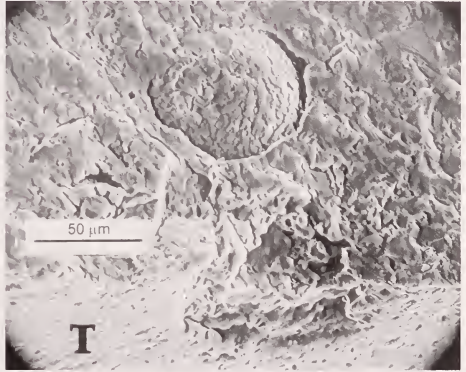
6.4 Matching Fracture Halves

Whenever possible both halves of the fracture surface should be examined since each contains information about the fracture origin. For example, Figure 6.4 illustrates a case wherein an agglomerate was strength limiting. If only the (a) half was examined, the fractographer may have interpreted the flaw as a pore.

(a)



(b)



(c)

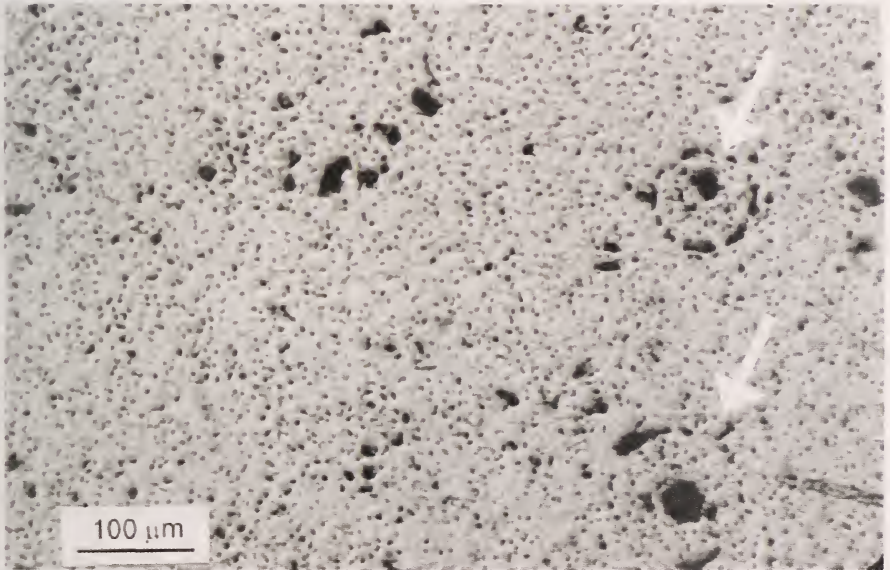


Figure 6.4. Fracture origin in a sintered alpha silicon carbide flexure specimen. (a) suggest the origin is a pore, but (b) which shows the mating half, shows an agglomerate. (c) shows a polished microstructural section for this material that reveals the agglomerates (arrows).

6.5 External Surfaces

If an origin is located at the surface, it is wise to examine the exterior surface by tilting the specimen back or by directly looking at the exterior surfaces for clues as to the flaw type as shown in Figure 6-5.

6.6 Volume-Distributed Flaws

6.6.1 Pores

Pores are one of the easiest flaws to find and identify. In ceramics they are often equiaxed but can easily assume a myriad of odd shapes as shown in Figure 6.6. Pores are volume-distributed flaws that are discrete cavities. For more information about pores as origins, see Reference 6.

6.6.2 Porous regions

Porous regions are volume-distributed flaws that are three-dimensional zones of porosity or microporosity regions. Examples are shown in Figure 6.7. These can be obvious or very subtle. SEM microscopy is usually needed to identify these flaws. Optical microscopy may not be effective since the color and contrast at the origin match the surrounding material.

6.6.3 Porous seams

Porous seams are similar to porous regions, but are more planar or two-dimensional. Examples are shown in Figure 6.8. If the material separated completely between these seams, the flaw might be more aptly described as a processing crack, as described below in section 6.8.1.

6.6.4 Agglomerates

Agglomerates are volume-distributed flaws that are a cluster of grains, particles, platelets, or whiskers or a combination thereof. They are a common flaw in ceramics made with powders that are prepared by spray drying. Spray dry agglomerates are often hollow. Agglomerates often sinter away from the matrix, creating a shell like void around the agglomerate. Since the composition is identical to the matrix, the color and reflectivity of this flaw are identical to the matrix. If agglomerates are suspected, examine more of the fracture surface for similar spherical or ring like features since if there is one, there usually are many. Examples are shown in Figures 6.4 and 6.9.

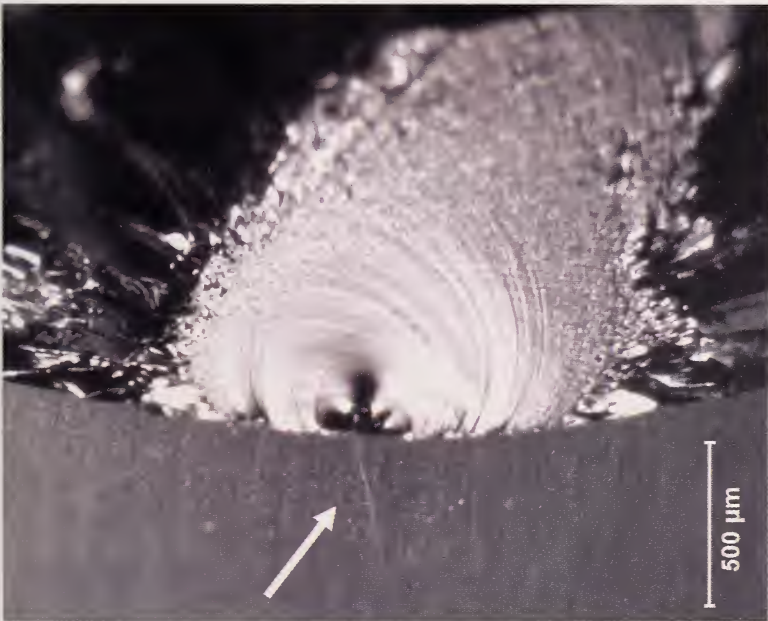
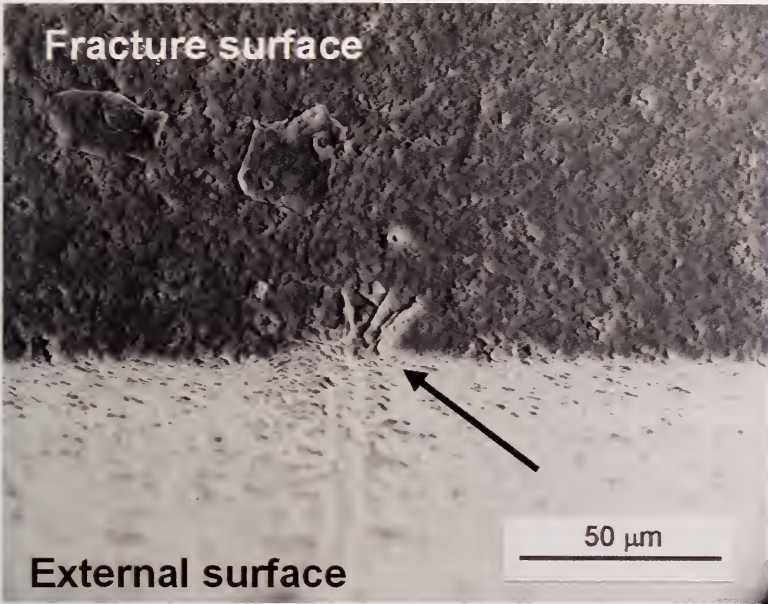


Figure 6.5. The exterior surface should be checked if the flaw is located on the surface. (a) shows an irregular flaw at the origin in a reaction bonded silicon nitride component. (b) shows the fracture origin of a fused silica rod broken in flexure. This tilted back view shows a scratch on the surface (arrow) coincident with the origin.

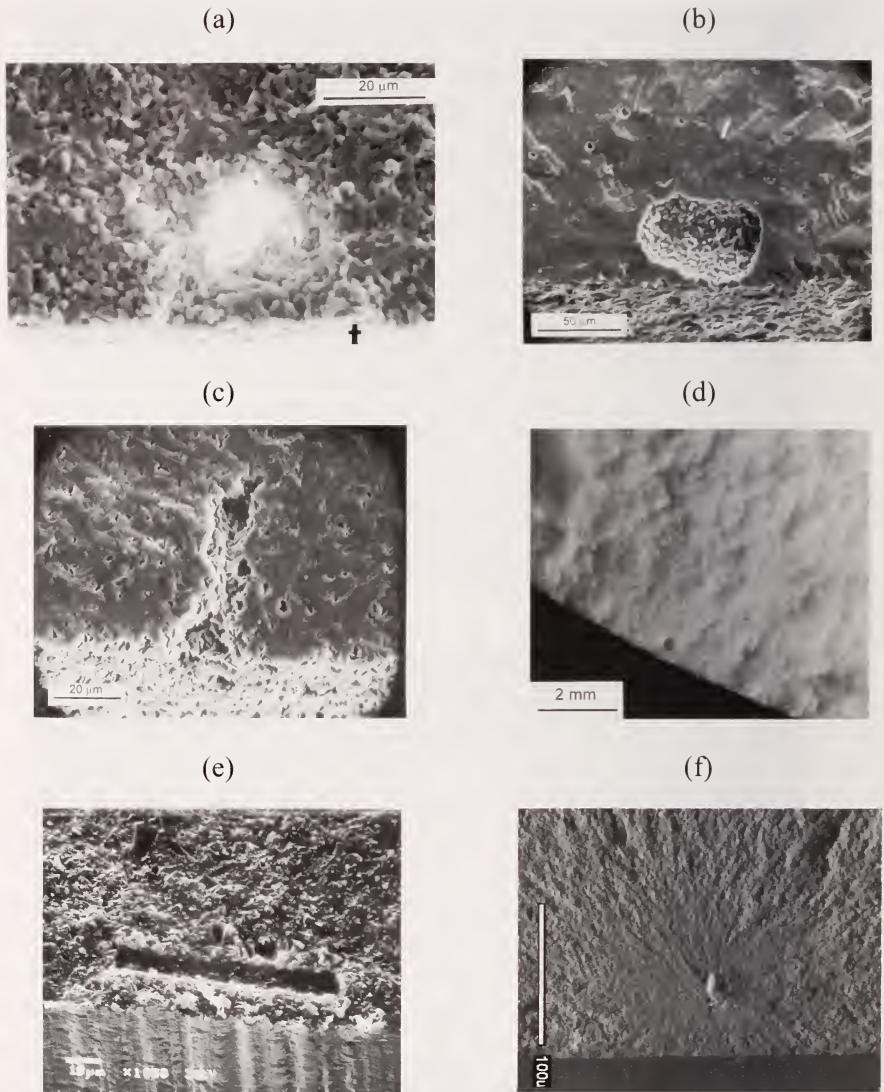


Figure 6.6. Examples of pore fracture origins in ceramics. (a) shows a SEM image of a pore in a 99.9% alumina bend bar: Electron charging created the bright spot. (b) shows a pore in an aluminum oxynitride bend bar that is within 5 μm of the surface. This is a “near surface” location example. The transgranular fracture near the pore helps the pore stand out very clearly. (c) is an irregular pore in a sintered alpha silicon carbide bend bar. (d) is a pore in a porcelain electrical insulator (courtesy J. Taylor and R. Rice). (e) is a cylindrical pore in a silicon nitride probably from a fiber or hair burn out. (f) is a pore in a Yttria-stabilized tetragonal zirconia polycrystal (3Y-TZP) (photo f is courtesy J. Quinn).

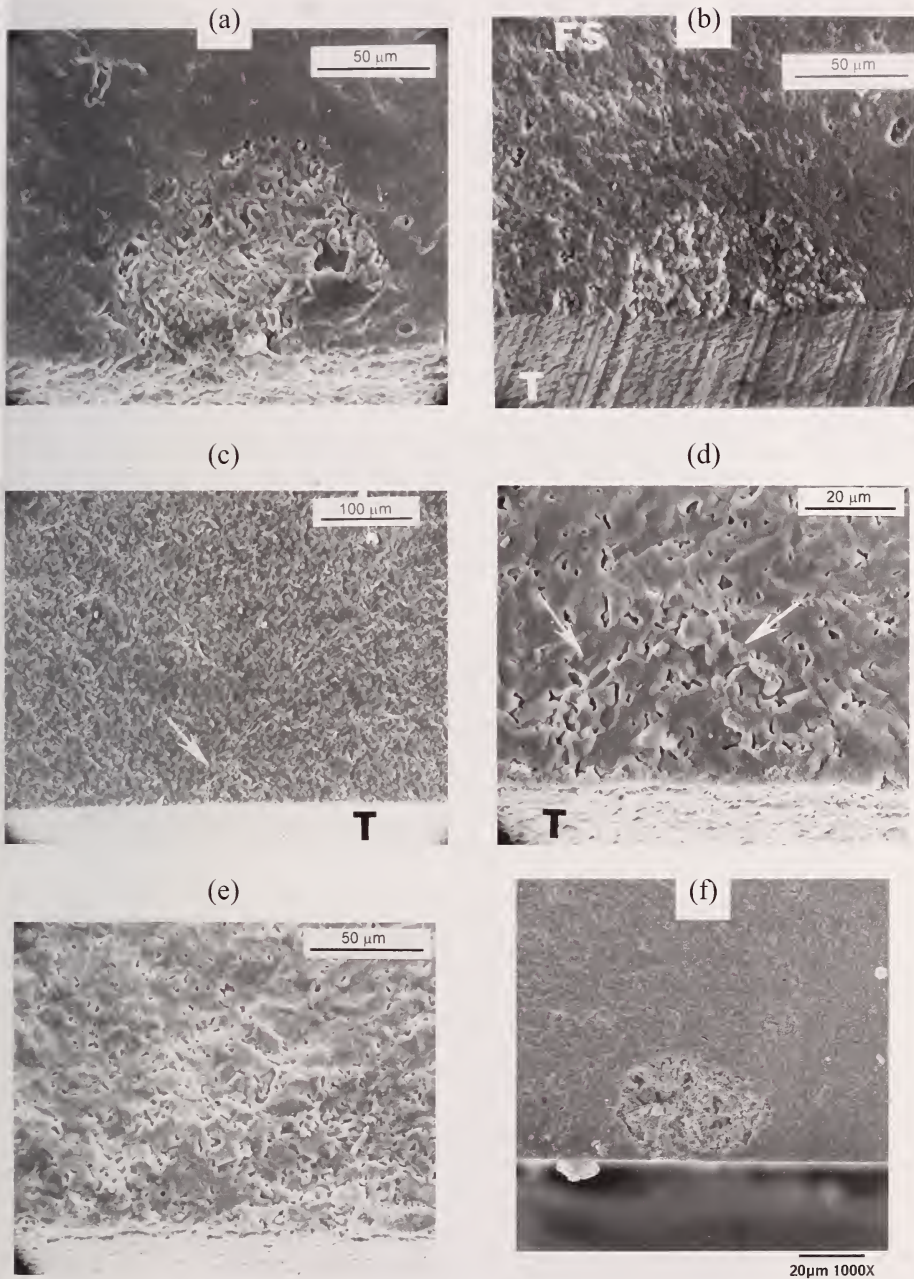
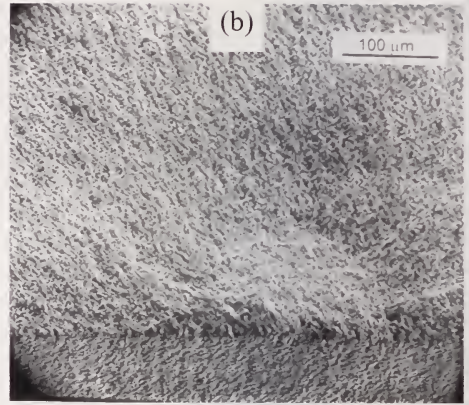
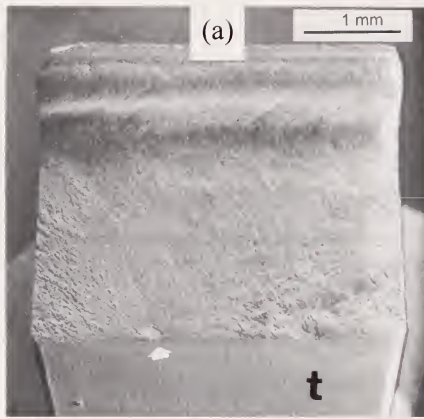


Figure 6.7. Examples of porous region fracture origins in ceramics. (a) is in sintered aluminum oxynitride. (b) is in a reaction bonded silicon nitride. (c) and (d) are both from one sintered alpha silicon carbide bend bar; (e) is also from a sintered silicon carbide. (f) is in a tetragonal zirconia polycrystal (3Y-TZP).

◆ Fractography of Ceramics and Glasses



(c)



(d)

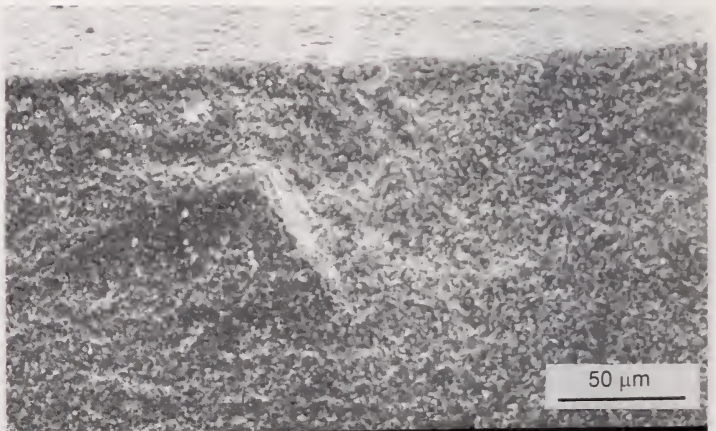
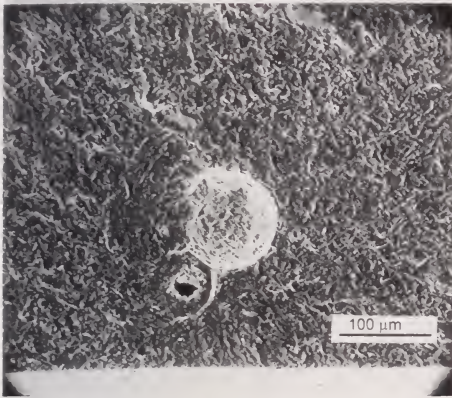
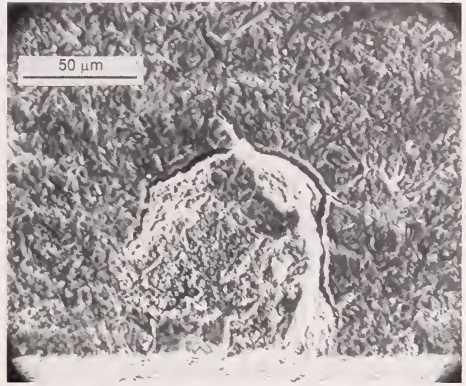


Figure 6.8. Examples of porous seam fracture origins. (a) and (b) show the origin in a fine-grained sintered 99.9% alumina. (c) and (d) show the origin in matching halves of another fine-grained sintered 99.9 % alumina bend bar.

(a)



(b)



(c)

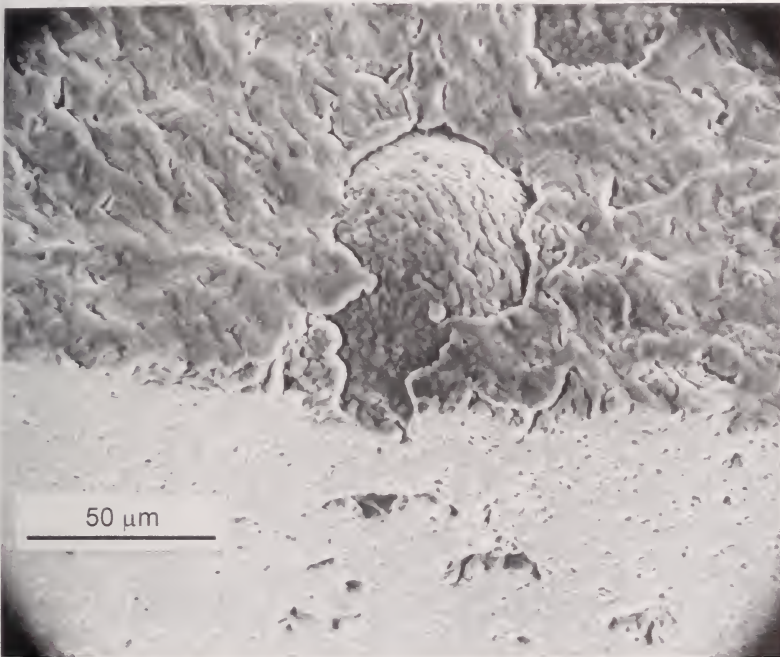


Figure 6.9. Examples of agglomerate fracture origins. (a – c) show spray dry agglomerate fracture origins in sintered alpha silicon carbide. Agglomerates often sinter away from the matrix leaving a void like crack.

6.6.5 Inclusions

Inclusions are also volume-distributed flaws that are a foreign body with a composition different than the normal composition of the glass or ceramic. They are often easy to detect due to color or reflectivity differences compared to the matrix. Sometimes they are round and equiaxed, other times they are odd shaped or fragmented. Figure 6.10 shows some examples. Not all inclusions behave the same and their effect depends upon whether their elastic and thermal properties mismatch those of the matrix.⁷ Inclusions can cause cracking in the matrix, may crack themselves, or may detach and pull away from the matrix creating a void like flaw. The nickel sulfide inclusion shown in Figure 6.10a is a particularly deleterious flaw in tempered glasses, since it can undergo a spontaneously phase transformation at room temperature with an attendant volume expansion of several percent. Nickel sulfide inclusions can trigger catastrophic breakage. The tungsten inclusion shown in Figure 6.10c and d is also unusually deleterious. The tungsten impurity, from tungsten carbide ball milling media, can form very brittle tungsten silicides that lower the fracture toughness around and in the flaw.

6.6.6 Compositional inhomogeneities

These are microstructural irregularities related to the nonuniform distribution of the primary constituents, an additive, or a second phase. They may have a color or reflectivity difference compared to the matrix. Sometimes they are pockets of glass in a ceramic. Examples are shown in Figure 6.11.

6.6.7 Large grains

Large grains can occur due to local exaggerated grain growth. They may form due to a slight compositional or density variations during sintering. The compositional variability can be from an impurity or a sintering aid. Large grains can be a single or a cluster of grains having a size significantly greater than the range of the normal grain size distribution. They can often be seen with the optical microscope due to a difference in reflectivity compared to the matrix. Examples are in Figure 6.12. Rice's book⁸ on grain size and mechanical properties of ceramics has a good discussion of large grains as fracture origins on pages 13 – 16.

6.6.8 Grain boundaries

Grain boundaries may be vulnerable areas and, if the grain size is large enough, the boundaries can act as strength limiting flaws. Such flaws are very

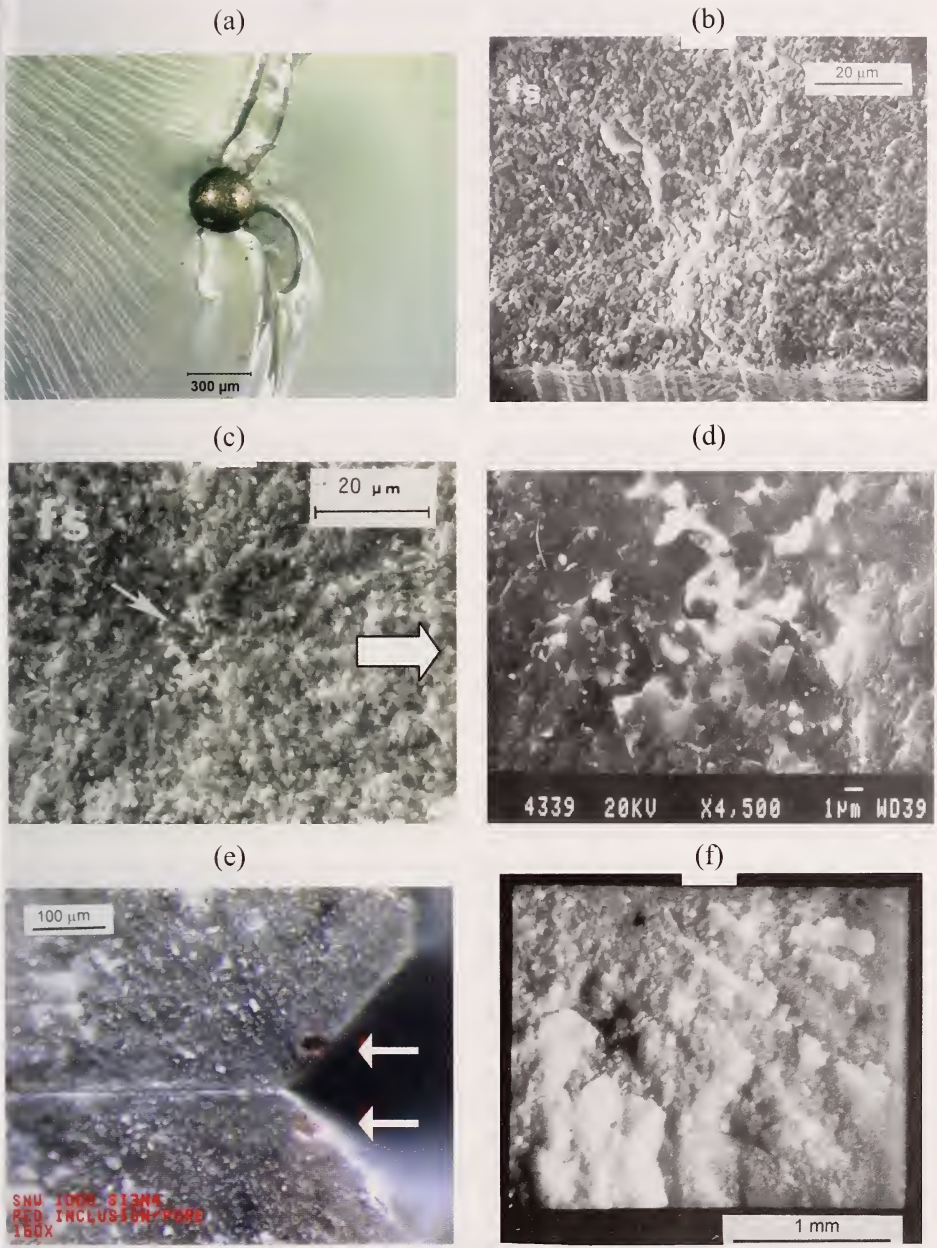


Figure 6.10. Examples of inclusion origins. (a) is a nickel sulfide in tempered glass plate that spontaneously fractured. (b) is an irregular iron and chrome inclusion in a sintered SiAlON bend bar. (c) and (d) are views of a tungsten inclusion in a hot pressed silicon nitride bend bar. (e) is a red iron inclusion in sintered silicon nitride bend bar at an edge chamfer. (f) is an inclusion in a silicon nitride tension specimen.

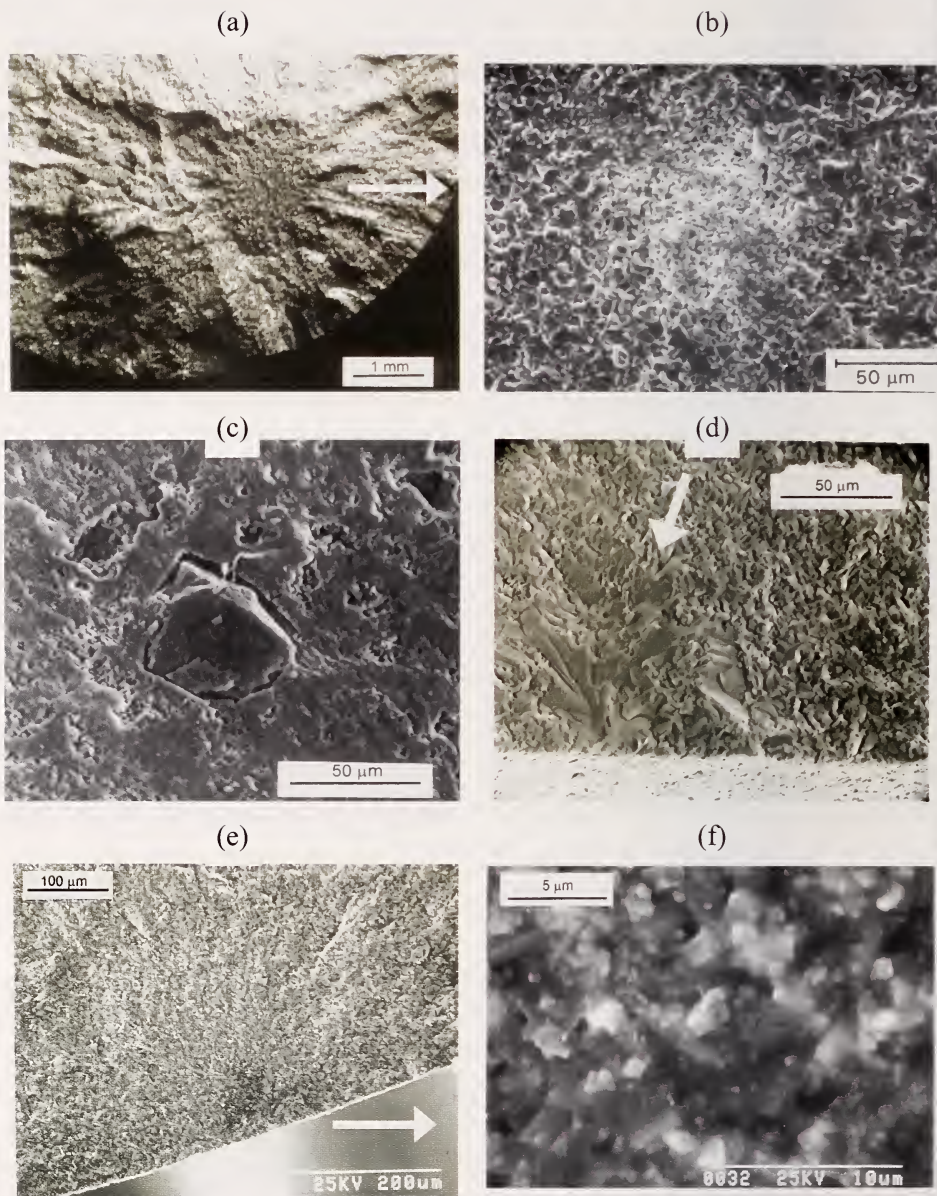


Figure 6.11. Examples of compositional inhomogeneity fracture origins. (a) and (b) show an example of an aluminum rich zone in a hot-pressed silicon carbide. Aluminum is an element in the sintering aid. (c) shows an unreacted silicon globule that pulled away from the matrix in a reaction bonded silicon nitride. (d) shows a silicon lake in a siliconized silicon carbide. (e) and (f) are an example of a local excess of sintering aid in a sintered reaction bonded silicon nitride.

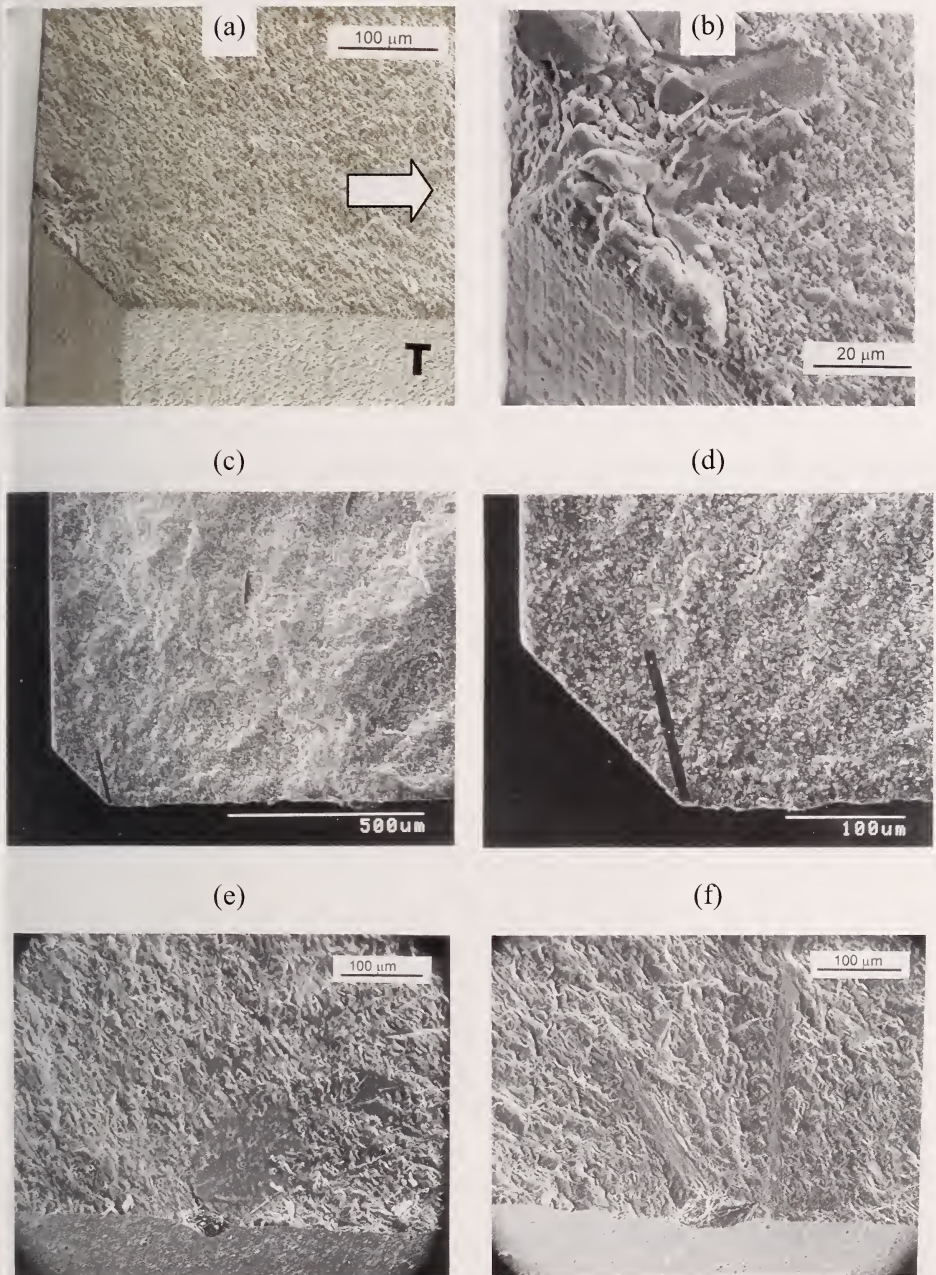


Figure 6.12. Examples of large grain fracture origins. (a,b) show a cluster of large grains at a chamfer in a 99.9% alumina bend bar. (c,d) show a single oversized grain in a silicon nitride with interlocking elongated grains intended to enhance fracture toughness. (e, f) show examples of acicular large grains in sintered alpha silicon carbide.

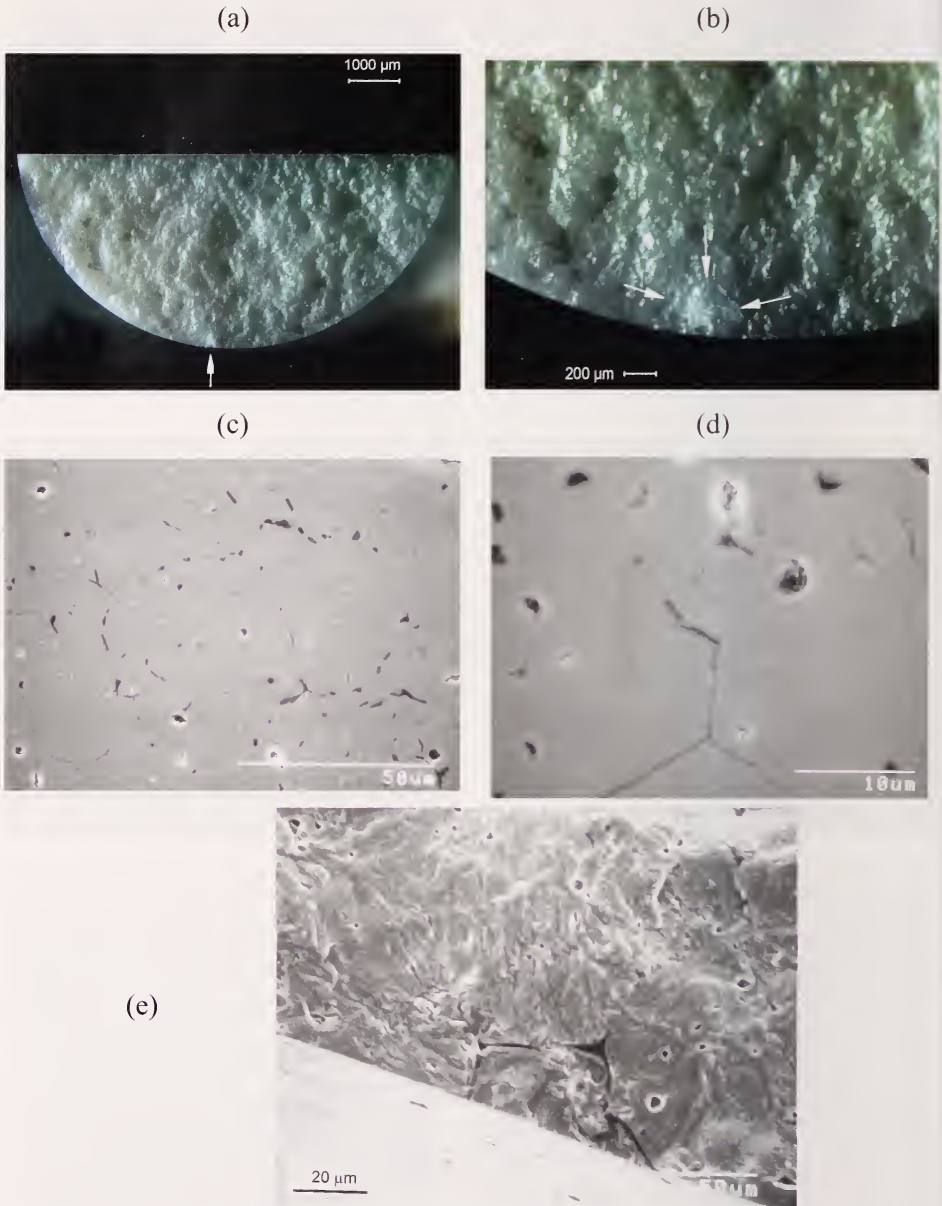


Figure 6.13. Grain boundaries may be flaws in coarse-grained materials such as Mg partially stabilized zirconia ($50\ \mu\text{m}$ to $70\ \mu\text{m}$). (a) and (b) show optical images of the rough fracture surface of a split rod flexural strength specimen. The rough surface is due in part to weak grain boundaries. (c) and (d) show SEM images of a polished surface revealing the gaps and cracks along the grain boundaries. (e) shows a grain boundary fracture origin. Tiny wake hackle from incidental several small pores radiate away from the origin.

difficult to unequivocally identify as origins since the fracture path may be intergranular and follow other grain boundaries, thereby creating a very rough fracture surface. Coarse-grained (50 μm to 70 μm) magnesia partially-stabilized zirconia typically fails from this type flaw as shown in Figure 6.13. Microstructural analysis of polished specimens is essential for the diagnosis in such cases.

6.7 Surface-Distributed Flaws

6.7.1 Surface voids

Surface voids are cavities on the surface of a component created by a reaction with the *processing* environment. They are similar to pores, except that they only arise on the surface. Surface voids can be in a reaction layer from hot-isostatic pressing with a glass encapsulation cladding or from trapped outgassing bubbles. Examples are shown in Figure 6.14.

6.7.2 Pits

Pits are surface cavities that form as a result of a reaction between a ceramic or glass and the *usage* environment. Corrosion or oxidation can create pits. Examples are shown in Figure 6.15. Richerson⁹ shows several good examples of oxidation and corrosion pits in silicon nitride. Pits have chemistry or structural differences that make them distinguishable from pores or surface voids. Sometimes the damage can be confined to grain boundaries and the flawed regions can be difficult to discern on a fracture surface.

6.7.3 Handling scratches and polishing scratches

Handling damage may be scratches, chips, cracks, or other flaws due to handling or impact. Examples are shown in Figures 6.16 and 6.17. Scratch damage varies widely depending upon the material, the sharpness or bluntness, the speed, depth of cut, and force of the scratching device or abrasive. At low load, a simple groove that is smooth with mostly plastic deformation and minimal cracking may be created. At higher loads and with more abusive tools and conditions, grooves with severe cracking may be generated. The cracking will be of several types: a crack that penetrates beneath the groove and follows the direction of the scratch, a series of shorter jagged cracks that jut out to either side of the scratch, and sometimes lateral cracks that are parallel to the surface and cause material to spall off. The depth of the cracking can be much greater (ten times or more) than the visible groove.

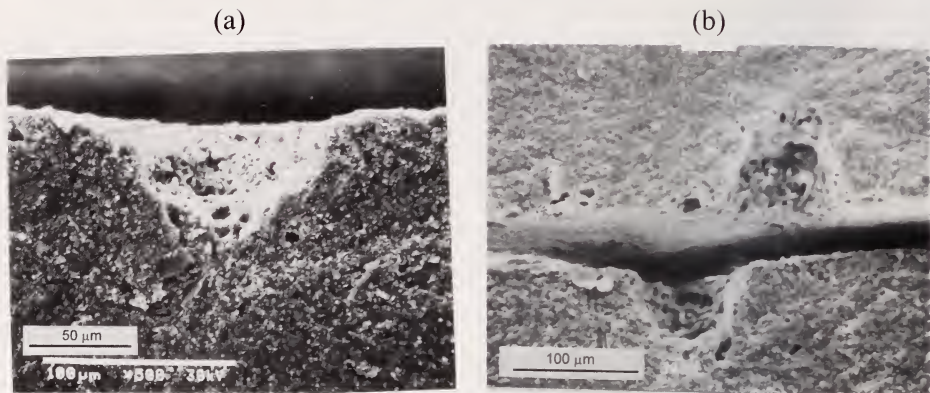


Figure 6.14. Examples of surface void fracture origins. (a) and (b) are in as-fired bend bars of injection-molded sintered silicon nitride. (Courtesy A. Pasto).

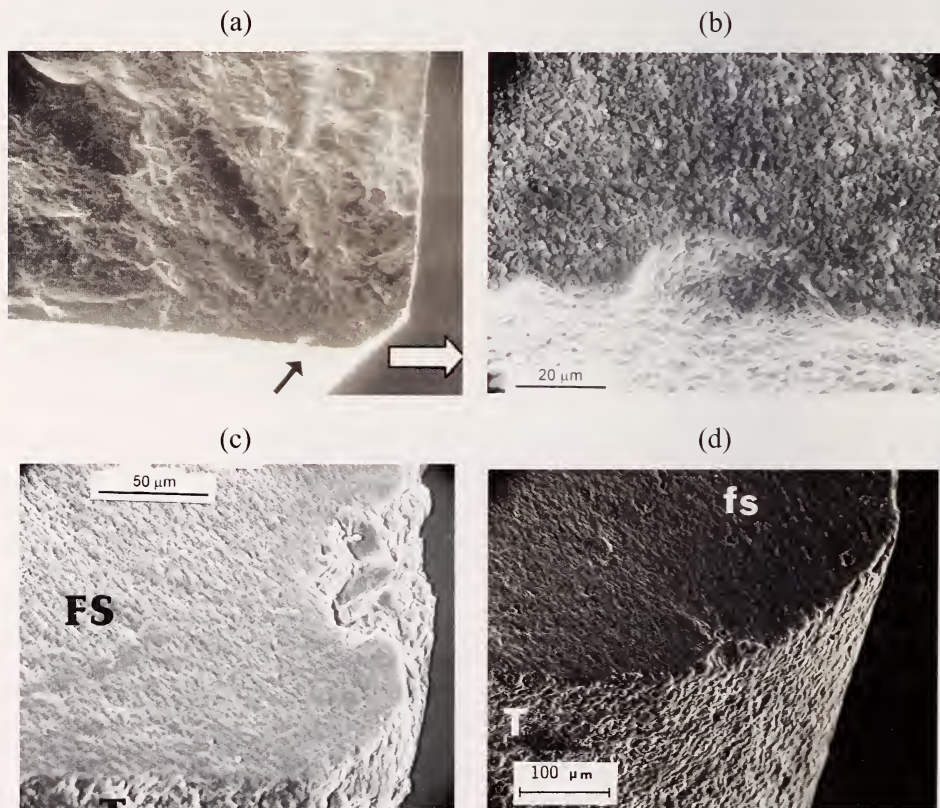


Figure 6.15. Examples of pit fracture origins. (a) – (c) are in oxidized hot-pressed silicon nitride. (b) is a close-up of (a). (d) is a reaction-bonded silicon nitride.

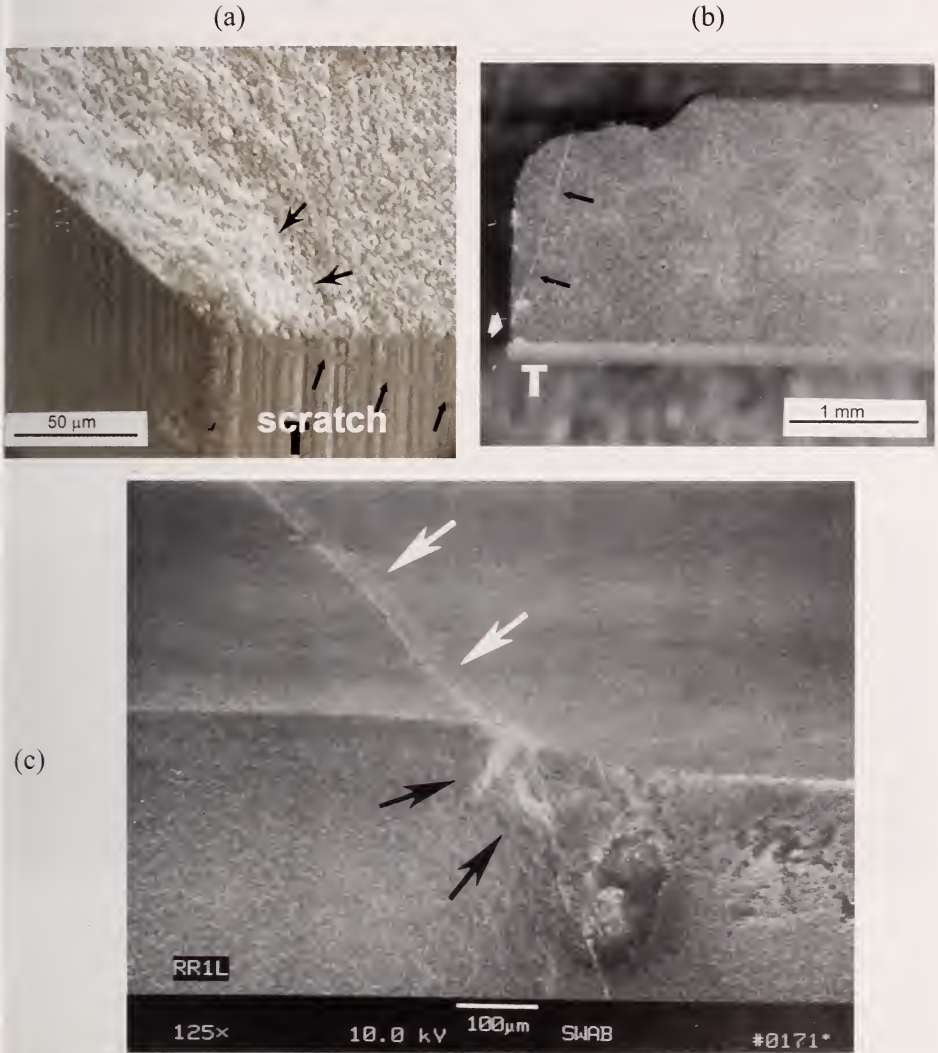


Figure 6.16. Examples of scratch origins with the scratch at an angle to the tensile stress. The cracks penetrate much deeper than the scratch groove depth. Scratches can create damage that may be mistaken for grinding cracks, so it is wise to look at the orientation of the scratch relative to the grinding striations. Scratches will be at irregular angles and are often isolated. (a) is in a SiAlON bend bar with a scratch near the chamfer. (b) is a side view of a reaction bonded silicon nitride bend bar. Scratches often require illumination at just the right angle to be seen. (c) shows a scratch on a bend bar surface (white arrows) and the continuation of it into the interior that acted as the fracture origin in a bend bar (black arrows) (c is courtesy J. Swab).

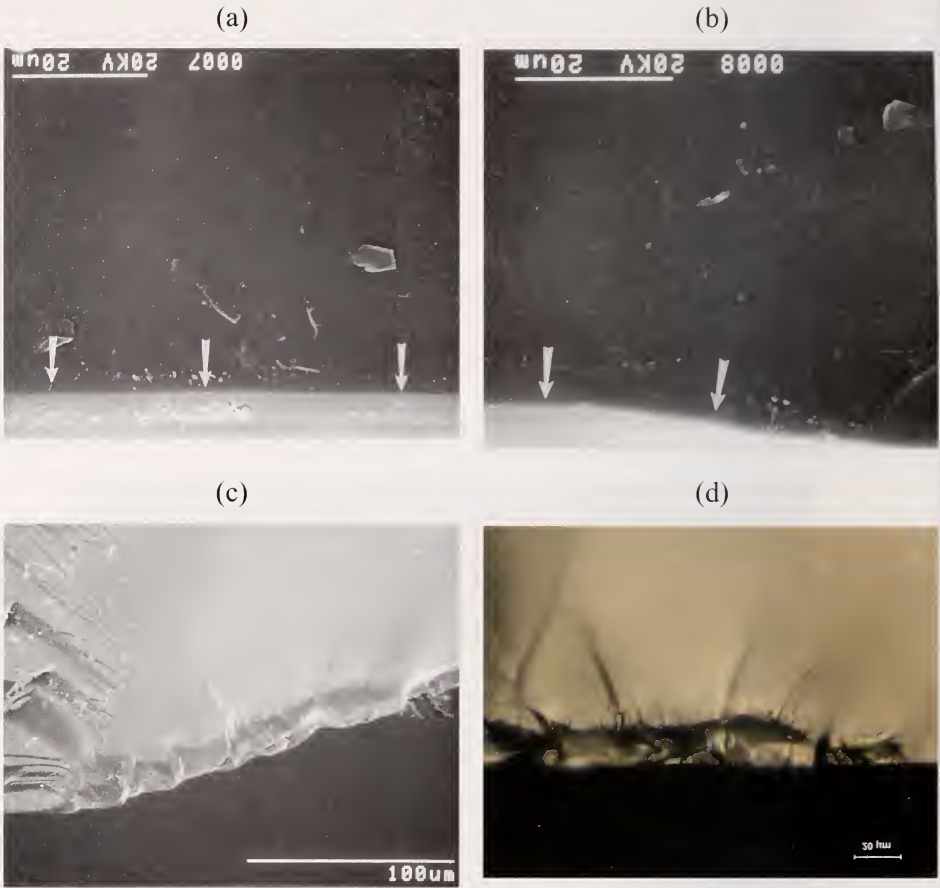


Figure 6.17. Examples of scratches with the tensile stress normal to the scratch. (a) and (b) show a very long, but smooth $7.3\ \mu\text{m}$ deep scratch crack in an annealed and polished glass disk broken in ring-on-ring flexure. Figure 5.15 shows the fracture mirror. (c) and (d) show SEM and optical images, respectively, of a polishing scratch crack in a single crystal sapphire hemispherical dome that broke in a high temperature wind tunnel test rig. In both these cases, there was no trace whatsoever of the scratch on the outer polished surface. All traces had been removed by final polishing, but the subsurface cracking damage remained.

Scratches that occur after fabrication and finishing are usually easy to identify. They are usually isolated and stand out on a surface, provided that the fractographer is careful to illuminate the part from different directions. Figure 6.5b and 6.16 show examples. It is easy to overlook a scratch on a surface if the lighting is not optimal. If scratches are suspected, then it is wise to

rotate the part under the illumination or move the illumination around while watching through a microscope. A quick momentary reflection may be the first sign a fractographer gets of a scratch. Scratches may also be overlooked on the SEM since they have very low contrast. If the tensile stresses are oriented at an angle to the axis of the scratch, then only be a small portion of the scratch may trigger a fracture as shown in Figure 6.16. The origin will be seen as an irregular crack on the fracture surface. These cracks may be so irregular as to confuse a fractographer who may mischaracterize the origin or arbitrarily assume it is machining damage. This is a good example of how, if a surface-located flaw controls strength, the fractographer should look at the exterior surface for other clues.

In other cases with biaxially loaded parts, such as pressurized vessels or plates, or laboratory ring-on-ring strength tests, there will always be a tensile stress available that is oriented perpendicular to the scratch axis. Figure 6.17 shows examples. In these cases the fracture follows the scratch for a distance. These can be tricky to diagnose if the fracture follows the entire length of the scratch, since the scratch trace on the outer surface may be overlooked or hard to see on the exact fracture edge, even if the pieces are put back together. On the other hand, fractures often veer off from the scratch axis, since the irregular jagged cracks that protrude off to the side of the scratch can redirect the main fracture.

When scratches are suspected, it is usually a good idea to look for other scratches elsewhere on the exterior surface of the part.

It is not uncommon with polished surfaces, to find a scratch-created flaw at the fracture origin, but all grooves or exterior surface traces are gone. Additional polishing after the scratch flaw was created removed all the surface traces.

6.7.4 Sharp object impact or contact

Figure 6.18 shows examples of origins created by impact or contact of a sharp object. Median and radial cracks may penetrate deeply beneath the impact site, which is often heavily damaged with small fragments missing. Vickers indentations are often used to mimic such flaws. Witness marks on the exterior surface may give clues as to the nature of the impactor. The exterior surface should be examined for other nearby impacts.

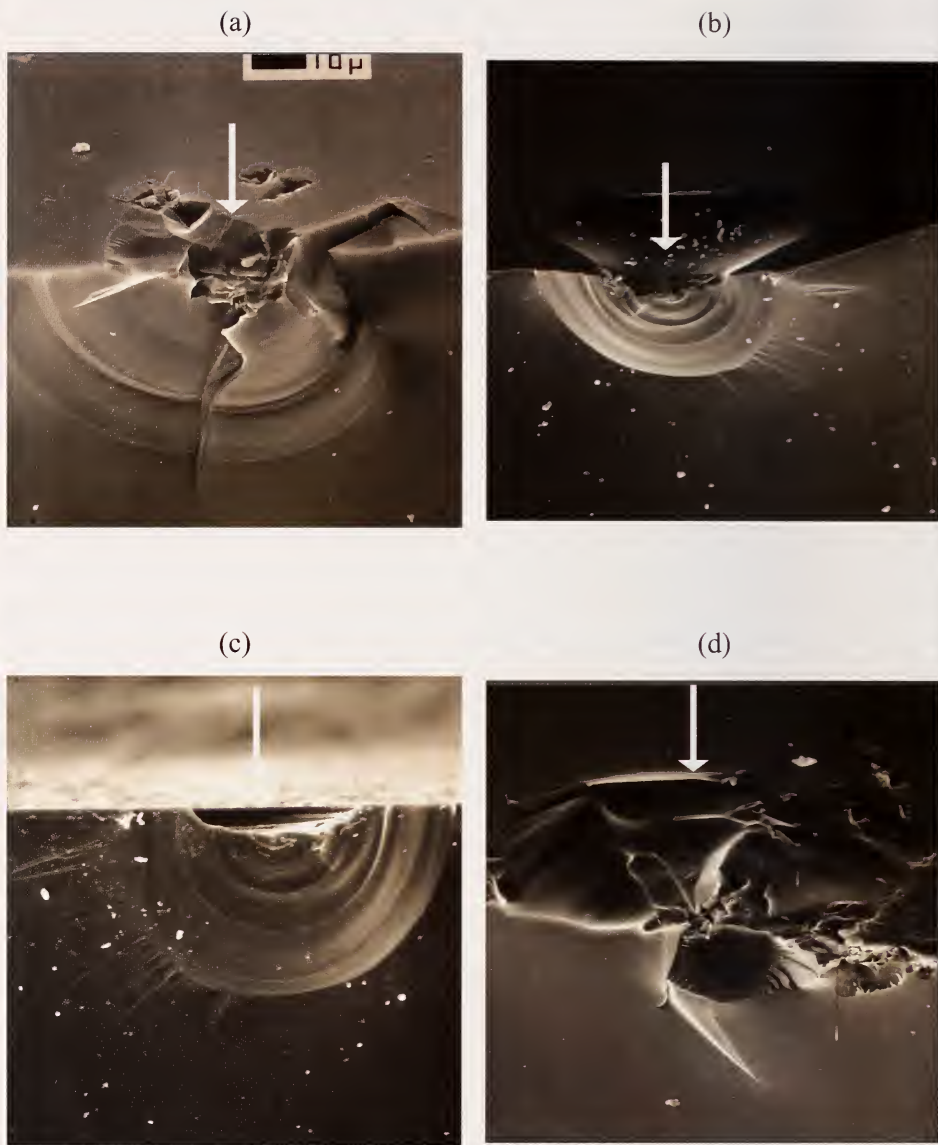


Figure 6.18. Examples of sharp particle impact origins. (a) - (d) show origins in glass. The direction of impact is shown by the arrows. All of the impacts have created penetrating median – radial cracks. (b) and (d) have pronounced lateral cracks as well. In each case the impact site has been pulverized or crushed, unlike blunt impact sites. (all Courtesy J. Varner).

6.7.5 Blunt object impact or contact

Blunt impacts or blunt contact loadings produce round Hertzian cone cracks as illustrated in Figure 6.19. These may be complete or partial rings as shown in Figures 6.20, 6.21, and 6.22. The cone crack initiates as a ring just outside the footprint of the two contacting bodies as shown in Figure 6.19a. The size of the contact area depends upon the load, geometries, and elastic properties of the two materials. A simple rule of thumb is that the contacting object is almost always several times larger than the observed ring size on the contacting surface as shown in Figure 6.19. Of course, if the blunt object penetrates through the plate and makes a large hole, then the impactor may be comparable in size to the hole. When contact damage is detected, the exterior surface should be examined for other nearby impacts.

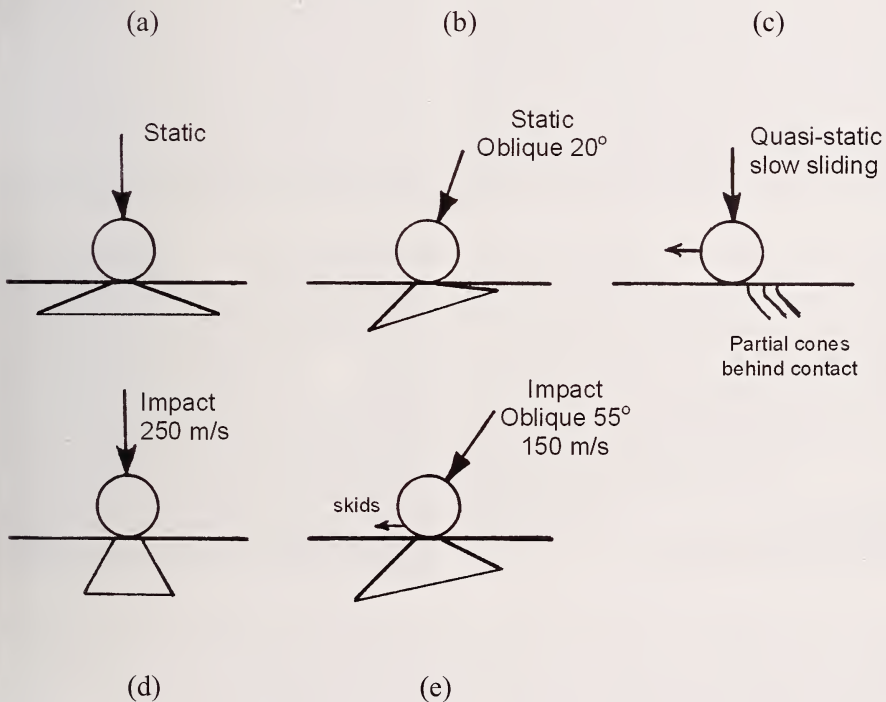


Figure 6.19. Blunt contact or blunt impact cone crack profiles. Notice the blunt impactor is larger than the size of the contact circle and first ring to form at the impact site.

Ring cracks initially pop in normal to the surface but then turn and propagate into the depth with an included angle of 125° to 135° for quasi static loading^a in glasses as shown in Figure 6.19a. The included cone angle decreases markedly with impact velocity as shown in Figure 6.19d. It may be possible to estimate the projectile velocity from the included cone angle.^{10,11,12} For example, at 250 m/s, 0.8 mm to 1 mm diameter steel balls created 60° to 80° cone cracks in glass¹⁰ and 70° to 90° cracks in silicon carbide.¹² During quasi static or impact loadings, as load increases the footprint area may expand and generate multiple concentric ring and cone cracks.

If a ball that is loaded perpendicular to the surface is slid over the surface at quasi static rates, the cone axis tilts such that the rear of the cone dips down deeper, and the front portion of the cone disappears (Figure 6.19c).¹³ Partial cone cracks are the result. This is not surprising since the forward motion of the ball creates an additional tensile stress behind the ball, but adds compressive stresses to the material ahead of the ball.

Conditions are different if the contactor is loaded (or strikes at) at non-perpendicular angles. Full cones form, but they tilt so that the backside approaches the surface while the front side penetrates deeper into the surface as shown in Figures 6.19b,e.¹⁴

Most blunt contact loadings produce a cone crack that penetrates partially or completely through a plate or body as shown in Figure 4.17. These may not cause component breakage and may merely be a cosmetic fault unless the structure is intended to seal the environment. Subsequent loading in tension or flexure may cause new crack extension from the cone crack as shown in Figures 6.20 (d) and (e). Many structures such as dental crowns may have numerous harmless cone cracks in the veneers. They are only revealed when a fracture that commenced elsewhere passes through the cone (Figure 6.20f).

Impacts at moderate or high energy create radial cracks and bending stresses that can propagate cracks far beyond the impact site and any cone cracks, thereby causing component fracture. Figure 6.22b shows an example.

^a Stationary or with slow motion.

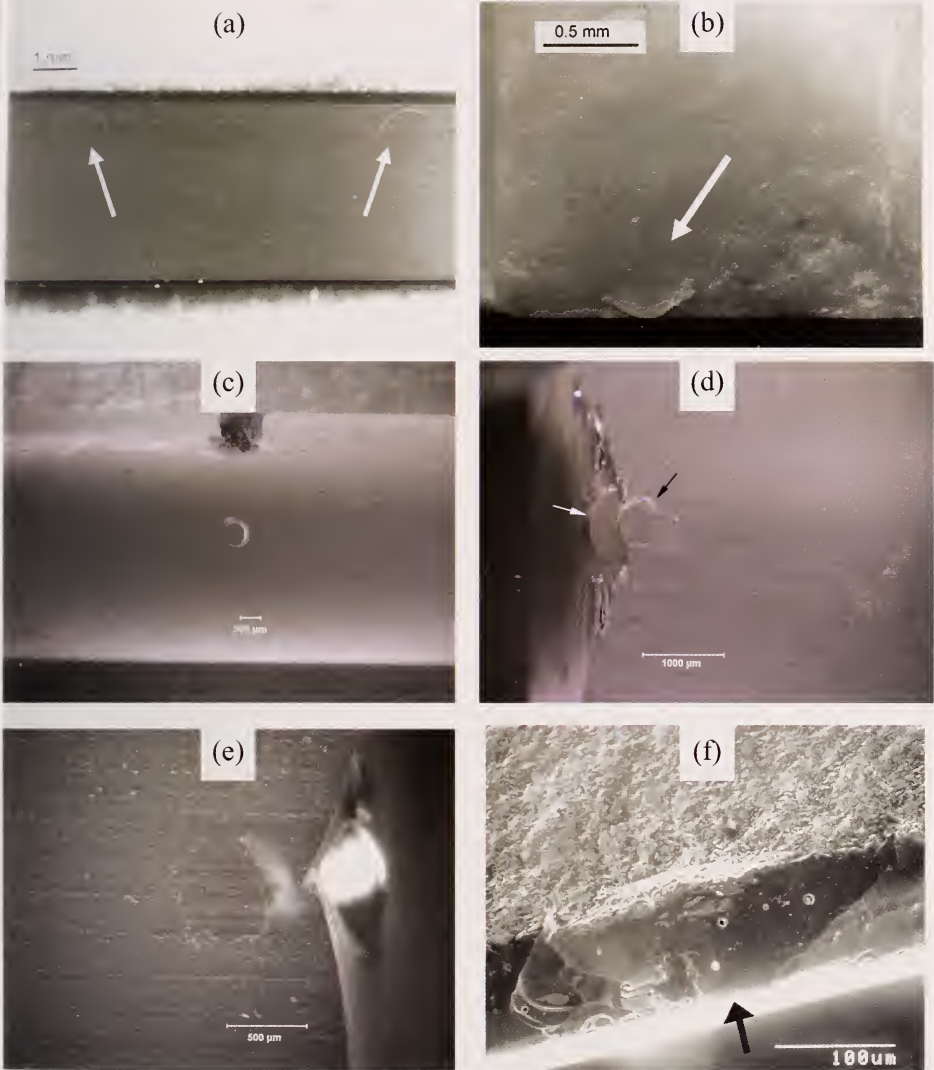


Figure 6.20. Examples of blunt impact or contact crack damage fracture origins. (a) shows the tensile surface of a silicon nitride bend bar with partial crack rings that were created by a ball tipped micrometer. Such rings were fracture origins in some other bend bars. (b) is a cone crack fracture origin from a blunt contact or impact on a rectangular bend bar. (c) shows a blunt contact crack from a loading roller on a cylindrical rod glass flexure specimen. Notice that the ring is incomplete. The cone crack can act as a strength-controlling flaw if loaded in tension as shown in (d) and (e). (f) shows a cone crack in a dental bilayer crown. The cone crack, which initiated from contact on the veneer layer, was harmless. Fracture initiated elsewhere and simply passed through the cone crack.

◆ Fractography of Ceramics and Glasses

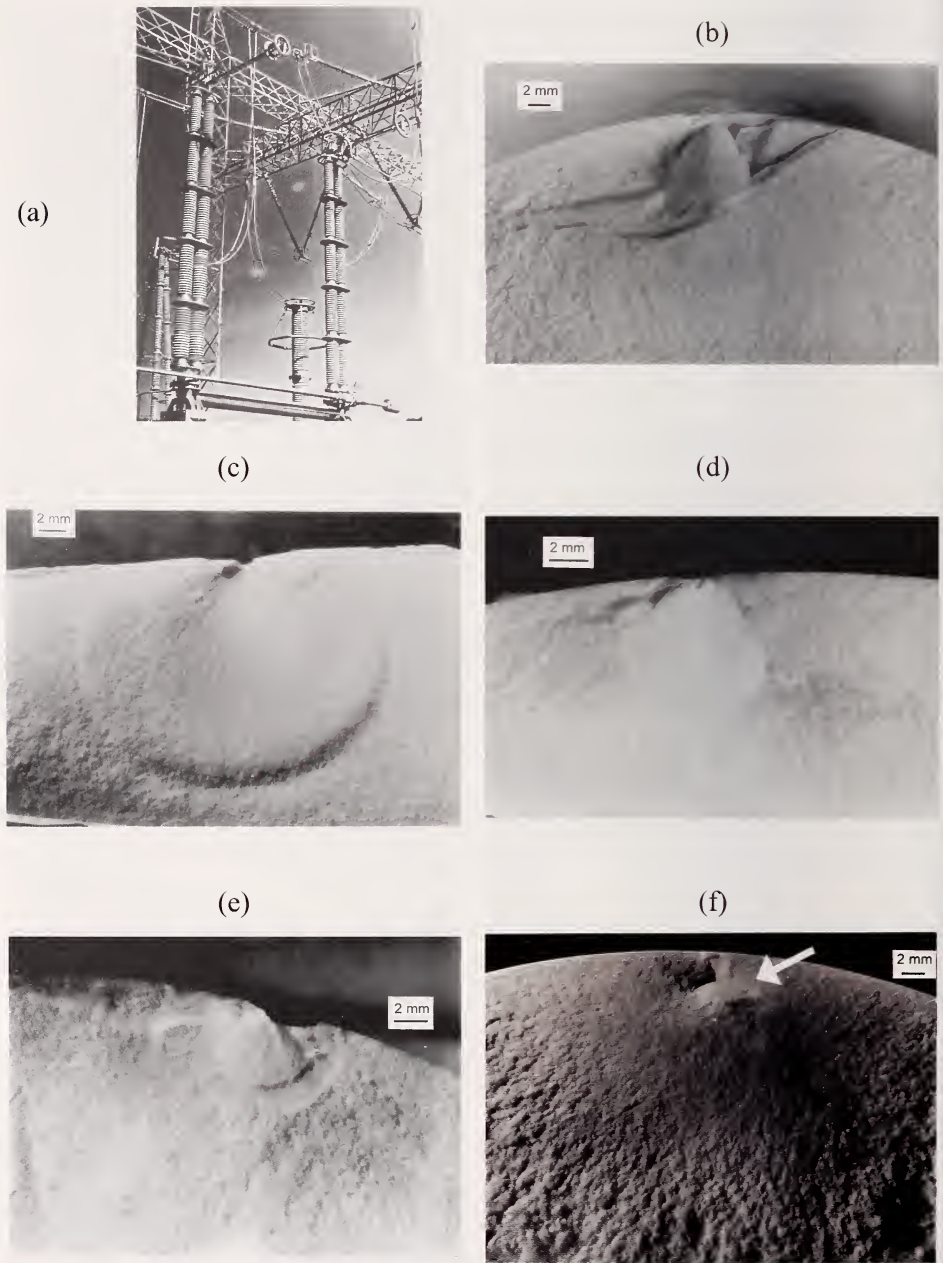


Figure 6.21. Blunt impact origins in electrical insulator porcelains. (a) shows the installed insulators. (b) and (c) are blunt impact damage from “BB” gun projectiles. (d) is damage from a sling shot projectile. (e) and (f) are impact origins from contact with support structures. Note the partially exposed cone in (f) (arrow). (Photos courtesy of J. J. Taylor and R. W. Rice)

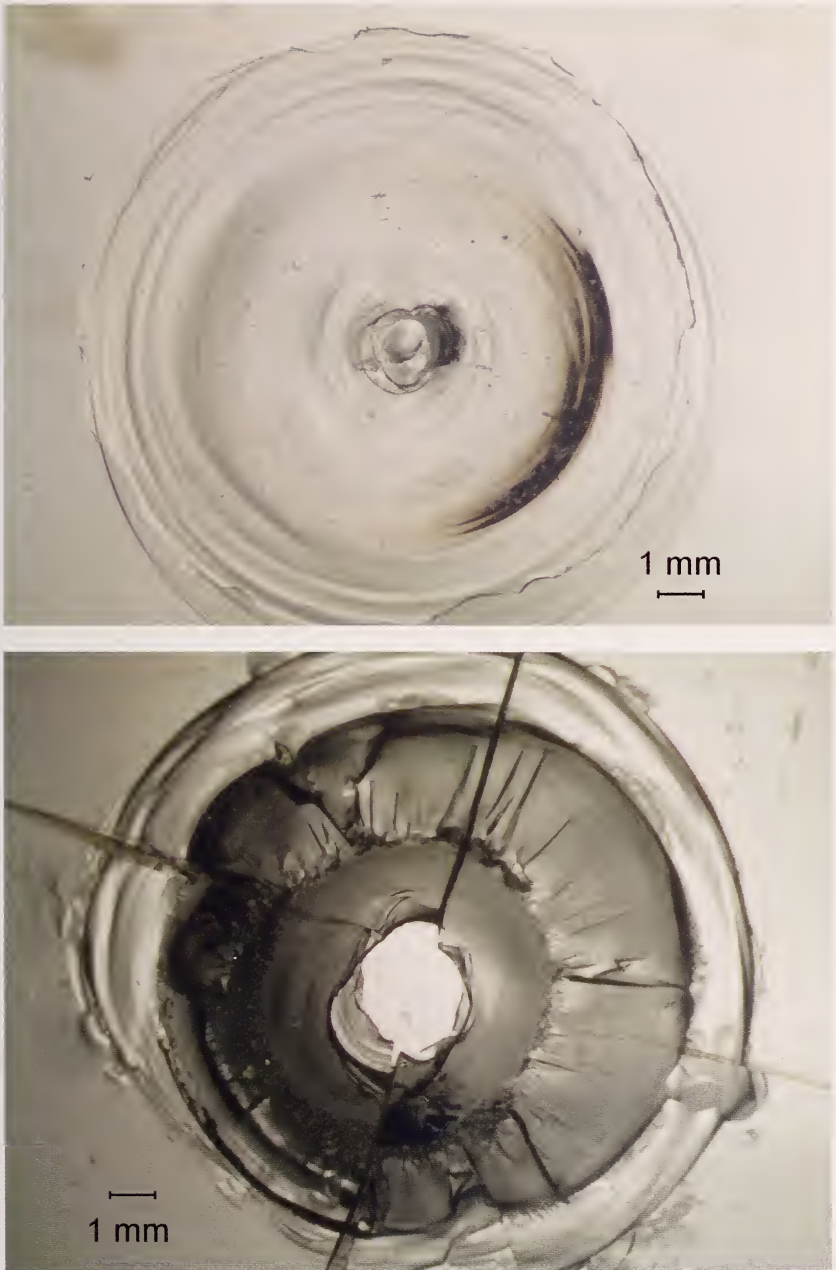


Figure 6.22. Blunt impact origins in glass plates. (a) shows a mild – moderate impact with cone cracks. The plate did not break into pieces. (b) is a severe impact that was sufficient to create cone and radial cracks. The latter caused plate fracture. (Specimens courtesy of J. Varner and V. Fréchette, Alfred University)

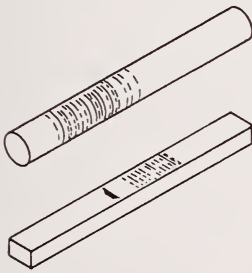
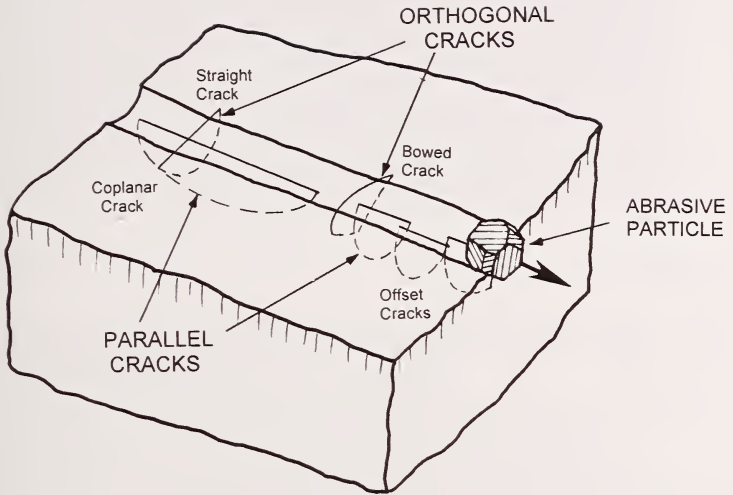
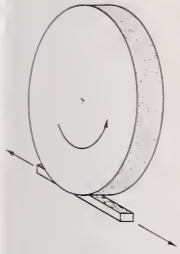
6.7.6 Grinding and machining cracks

Grinding or cutting introduces damage to the surface. The damage can be controlled, usually by using progressively finer grinding and polishing steps to remove damage introduced by prior steps. Edges are particularly susceptible to damage and can easily be cracked or chipped. Bevels and rounding are effective treatments for the latter. They are commonly applied to biaxial disks and bend bars and are carefully aligned circumferentially or lengthwise lest the beveling introduce more cracks.

Surface grinding procedures use grinding wheels as shown in Figure 6.23. The grinding process entails material removal, often by means of microcrack and microchip formation. By its very nature, cracking is introduced into the surface. Initial grinding is done with coarse wheel grits and modest depths of cut in order to facilitate material removal. Intermediate and final stage grinding is done with finer grit wheels and smaller depths of cut to reach final part dimensions and surface finish requirements, but also to remove prior damage while introducing a minimum amount of new damage.

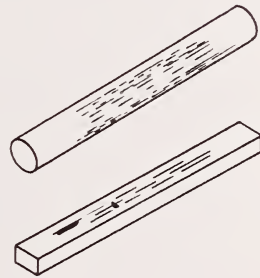
Fractographers realize that there often is no correlation between the strength of a part and the final surface finish. Sometimes there is a correlation, but just as often there is none. The reason is simple. Grinding induced cracks penetrate far deeper (10 to 20 times) below the surface than the surface undulations and striations. Sometimes the crack depths are proportional to the depth of the surface grooves, and the surface finish may correlate to strength. On the other hand, strength may be controlled by deep grinding cracks from earlier steps that are not removed in the final finishing phase. The following case illustrates the point. The author ordered a batch of conventional alumina bend bars to be cut and ground out of a billet by a new machine shop. The shop was instructed to surface grind longitudinally and not use their preferred Blanchard grinding process that creates random swirl marks and attendant cracking. The shop ignored the instructions and Blanchard ground the bend bars and then lapped them to a very fine beautiful finish. The strength of the bars was quite low however, and they fractured from severe, randomly oriented grinding cracks introduced by the Blanchard process. The final lapping did not go deep enough to remove the prior damage.

Figure 6.23, which is an adaptation of a figure by Rice and Mecholsky¹⁵, illustrates some key aspects of machining flaws. Parallel cracks oriented in the direction of grinding are longer and are the same depth or deeper than the orthogonal cracks. Thus, the parallel cracks are more deleterious to strength and give rise to a strength dependence with orientation (if grinding cracks are



Transversely-ground specimens

Flexure testing activates the parallel machining cracks



Longitudinally-ground specimens

Flexure testing activates the orthogonal machining cracks

Figure 6.23. Surface grinding (insert) creates grinding grooves (striations) and subsurface cracking. The cracking includes long deep “coplanar parallel cracks” or “offset parallel cracks” aligned with the striations in the direction of abrasive motion. Orthogonal cracks form at right angles to the striation and may be bowed in the direction of abrasive motion. Lateral cracks or spalls that are roughly parallel to the surface may also form (not shown). The axis of grinding is often chosen to align the worst cracking damage (the parallel cracks) with a specimen axis as shown on the bottom right.

the controlling flaws). Only one striation groove is shown in the schematic and it should be remembered that the ground surface actually contains a complex overlapping network of such cracks and grooves.

With some experience it is not too difficult to find grinding crack flaws in some dense materials, such as glass, single crystals, and either very coarse-grained or extremely fine-grained ceramics. Detection of grinding cracks in porous, heterogeneous, or mid grain-sized materials is very difficult, however, since the machining crack blends in to the background microstructure. This is especially true for the short orthogonal cracks. They are hard to find in nearly all materials. Figure 6.24 shows some examples of orthogonal cracks, which sometimes are described in the literature as “longitudinal grinding flaws.” Additional examples are shown in some of the papers by Rice and Mecholsky listed in the Bibliography, Appendix A.

Parallel machining cracks are much easier to detect and often can be found with routine optical microscopy, but only if low angle vicinal illumination is used. Figure 6.25 shows examples and Figure 6.26 shows a schematic of these flaws and their telltale signs. Figure 6.27 shows how “V” machining cracks form in ground round parts.

Several of these grinding crack flaws exhibit another form of hackle on the fracture surface.

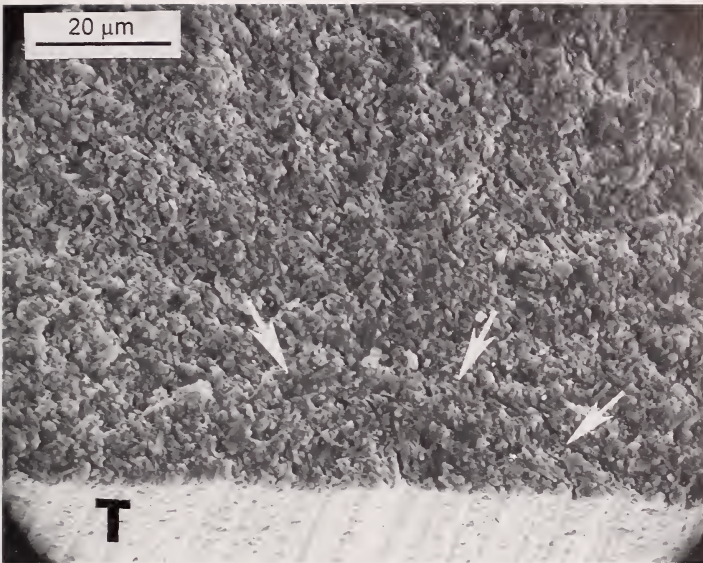
Grinding crack hackle: *Hackle formed on the fracture surface originating from irregularities and steps in grinding cracks.*

Grinding crack hackle is sometime also known as “shark’s teeth.”

The size of grinding cracks, and hence their effect on strength, depends upon the material properties such as hardness, elastic modulus and fracture resistance or fracture toughness, and the grinding wheel and machine conditions such as abrasive type, grit size and concentration, depth of cut, and wheel speed. The crack size also depends upon the grain size. Deep grinding cracks can form in very coarse-grained ceramics since the single crystal fracture toughness is less than the polycrystalline fracture toughness.

It is beyond the scope of this guide to delve into this topic other than to say that abrasive grit size is the dominant parameter for typical surface grinding procedures. Figure 6.27d shows the effect of grit size upon parallel crack depth in a commercial silicon nitride.¹⁶ The average grit size may not necessarily be the controlling parameter. Instances of “renegade” abrasive grits in a grinding wheel that caused atypical damage have been reported.¹⁶ Finally, although

(a)



(b)

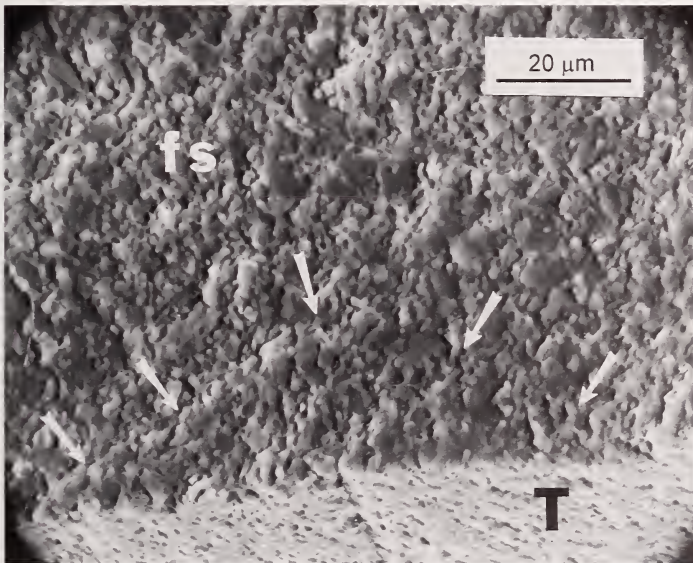


Figure 6.24. Orthogonal grinding cracks as seen in some very fine-grained ceramics. (a) shows a crack in a hot-pressed silicon nitride bend bar. (b) shows a crack in a hot-pressed silicon carbide. The bars have been tilted back in the SEM to reveal parts of the ground surface “T” which was in tension. “fs” means fracture surface. The specimens were ground longitudinally with respect to the specimen’s long axis. Slightly larger than normal striations are evident on the ground surface in each case. These orthogonal cracks are hard to find even with the SEM, since they tend to blend in with the microstructure.

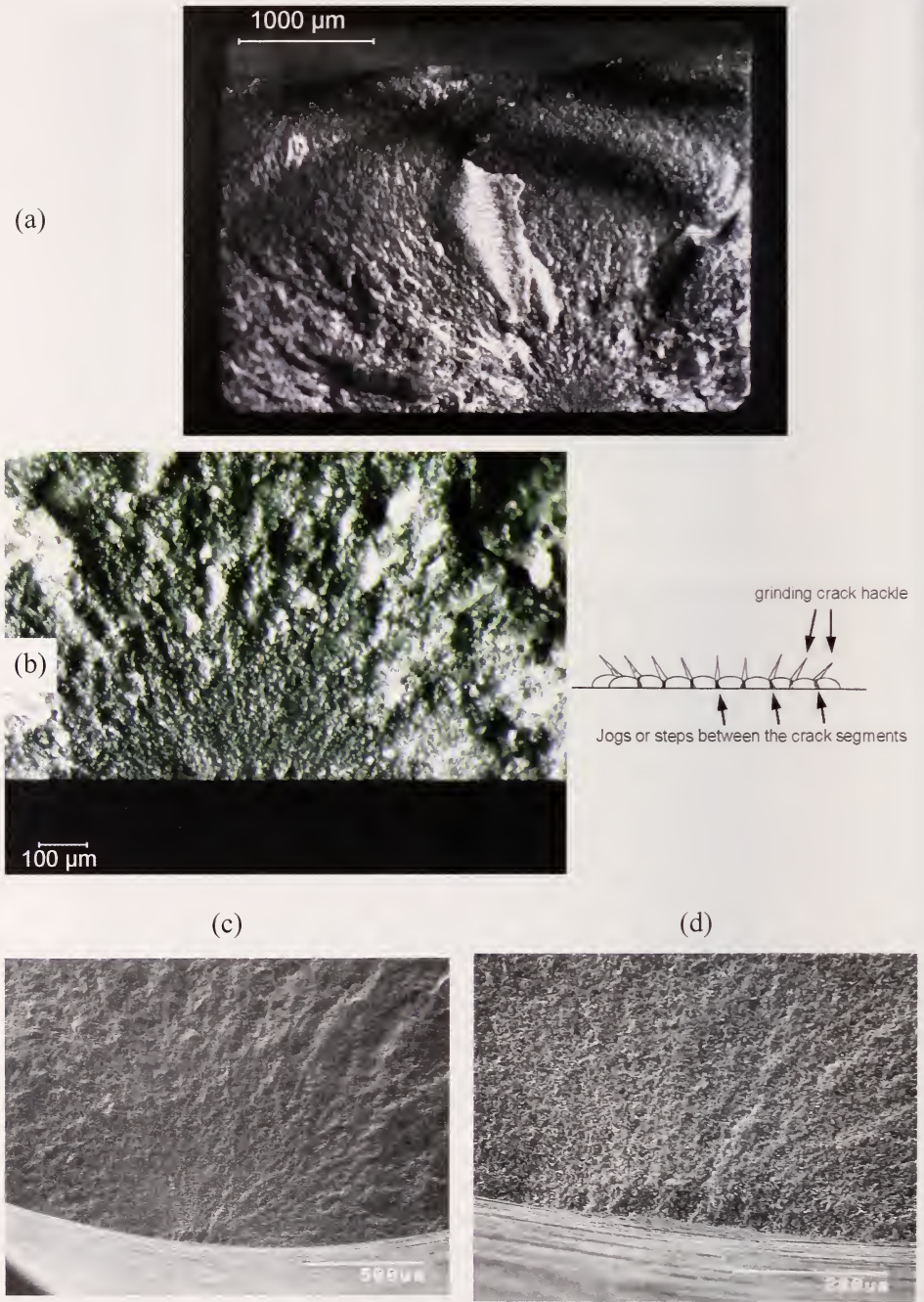
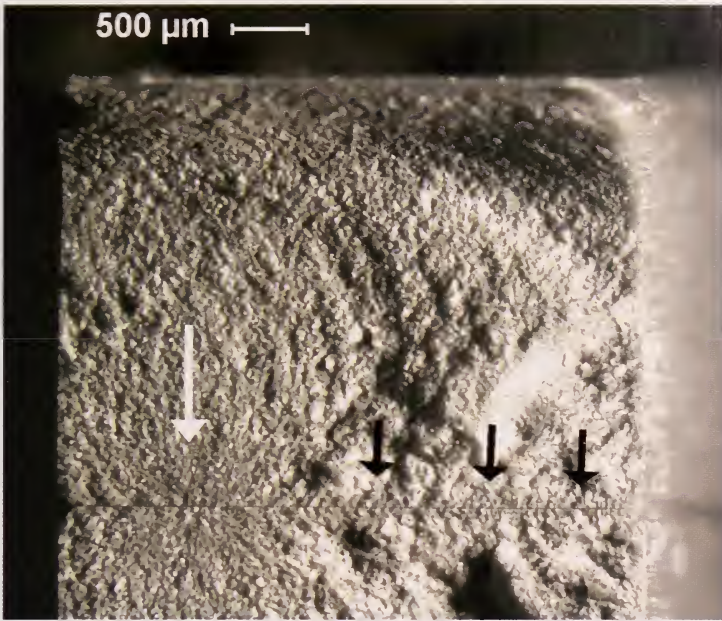


Figure 6.25. Examples of parallel grinding cracks. (a) and (b) show optical images of a “zipper crack” in a sintered silicon nitride bend bar. (c) and (d) show SEM images of a crack in a silicon nitride rod.

(e)



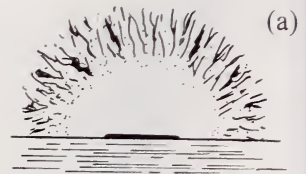
(f)



Figure 6.25. (cont'd) Examples of parallel grinding cracks. (e) shows back-to-back halves of a silicon nitride bend bar with coarse grinding (150 grit) cracks. A zipper crack is at the origin (large arrow). The small arrows show that there also is a machining crack "skin zone" along the entire surface. (f) is an alumina bend bar with vincinal illumination revealing a zipper crack.

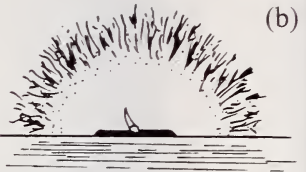
- (a) elongated “coplanar parallel crack”
(or coplanar linked semi-elliptical cracks)

A deep striation may or may not necessarily be present. The fracture mirror may be elongated along the outer specimen surface.



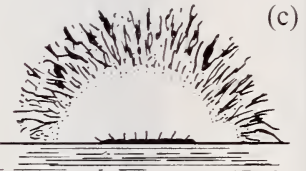
- (b) elongated “coplanar parallel crack”

linked with a natural flaw. A step in the fracture origin emanates from the material flaw.



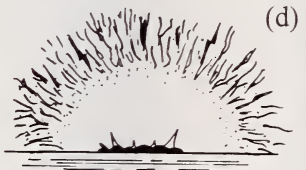
- (c) “zipper crack”

This is a series of short semi elliptical cracks which have linked. A series of short tails, or “grinding crack hackle,” emanate from the links or overlaps of the flaws and extend up into the fracture mirror. These tails may be tilted to the left or right and help confirm that fracture originated in the central region of the set. The short tails are telltale features of slightly misaligned or overlapping transverse machining cracks (or a scratch) and are often easier to see with an optical microscope with low angle lighting than with a scanning electron microscope. The fracture mirror may be elongated along the specimen outer surface or it may have one or two prominent side lobes. This origin type is common in transversely-ground rectangular flexure specimens or scratched biaxial disk specimens.



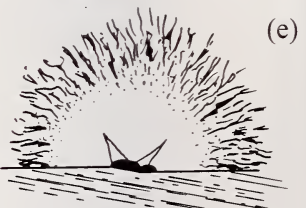
- (d) coarse “zipper crack”

This is made up of a series of irregular, less coplanar semi-elliptical cracks. Larger tails than in (c) are created. In severe cases, the tail may extend all the way to the mirror boundary. The fracture mirror may be elongated. This origin is common in transversely-ground or scratched specimens and the markings are sometimes termed “shark’s teeth.”



- (e) “V machining crack”

The crack intersects the fracture space at an angle. Only a portion of the machining crack or crack series is exposed. A pronounced step occurs in the fracture mirror. One or two (shown) tails extend well up into the fracture mirror. The machining direction is not quite perpendicular to the specimen length and uniaxial stress axis due to grinding wheel cross feed. This origin is common in cylindrical specimens prepared by centerless or cylindrical transverse grinding wherein the wheel and work pieces displace axially relative to each other.



- (f) “coarse grinding parallel crack”

The origin is a deep machining crack that extends along the entire surface. The origin is often bumpy since the origin is comprised of offset parallel cracks. Thin bands of uniform depth extend along the specimen surface on either side of the fracture mirror. The bands have the same depth as the grinding cracks. Short tails, or “machining crack hackle” which may be in the thin bands are tilted away from the origin. This origin type is common in coarse ground surfaces.



Figure 6.26. Schematics of telltale features of parallel machining cracks. These origins are common in biaxial disks, pressure-loaded plates, and transversely-ground flexural or tension strength specimens. Vicinal illumination facilitates their detection with optical microscopy. Some have elongated mirrors along the surface, an important telltale sign.

it is widely believed that materials with rising R-curves form smaller grinding cracks than materials with flat R-curves, there is evidence that just the opposite is true.¹⁷ Materials with rising R-curves are more difficult to grind, but for a given wheel speed and depth of cut, greater grinding forces are generated to overcome the removal resistance. The greater forces cause cracks to penetrate deeper than in materials with low fracture toughness or flat R-curves that cut or grind more freely.

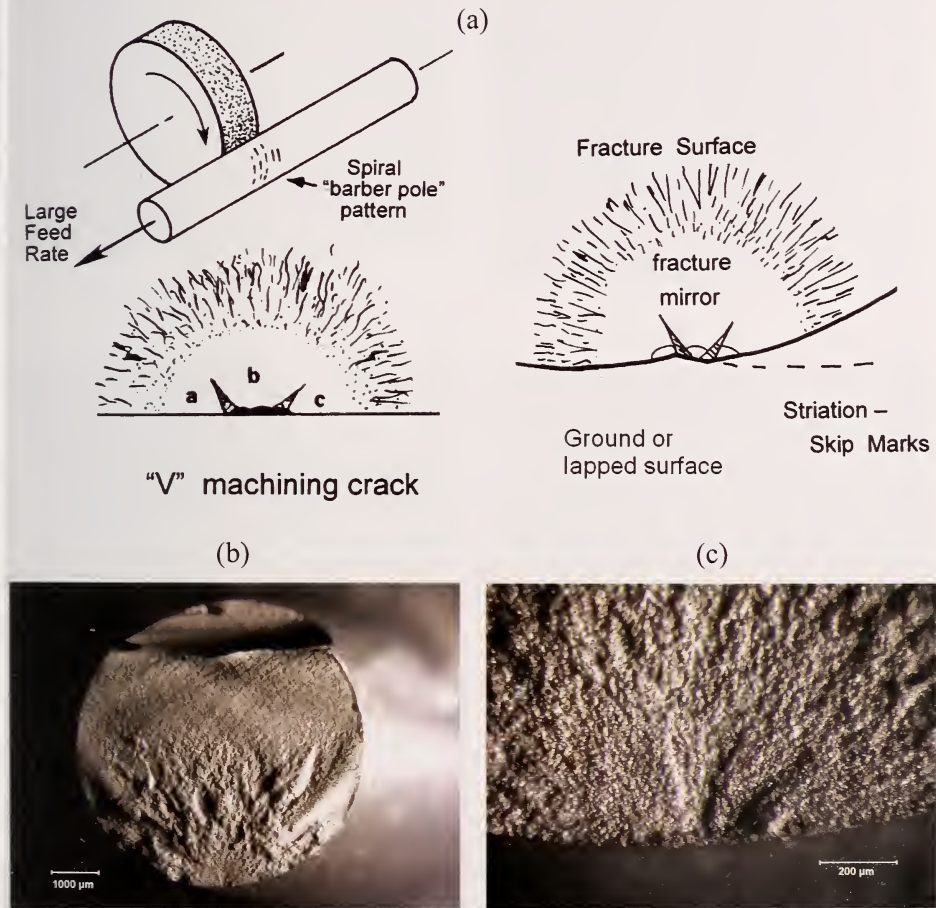


Figure 6.27. Round parts may have "V" machining cracks formed from small parallel crack segments a, b, c on different planes as shown in (a). The steps between the individual crack segments form two or more telltale hackle lines, which extend up into a mirror. Examination of the ground surface shows striations that have a small angle relative to the rod axis. (b) and (c) show optical images of an example in a silicon nitride rod. V crack flaws are easy to see even at very low magnification with vicinal illumination.

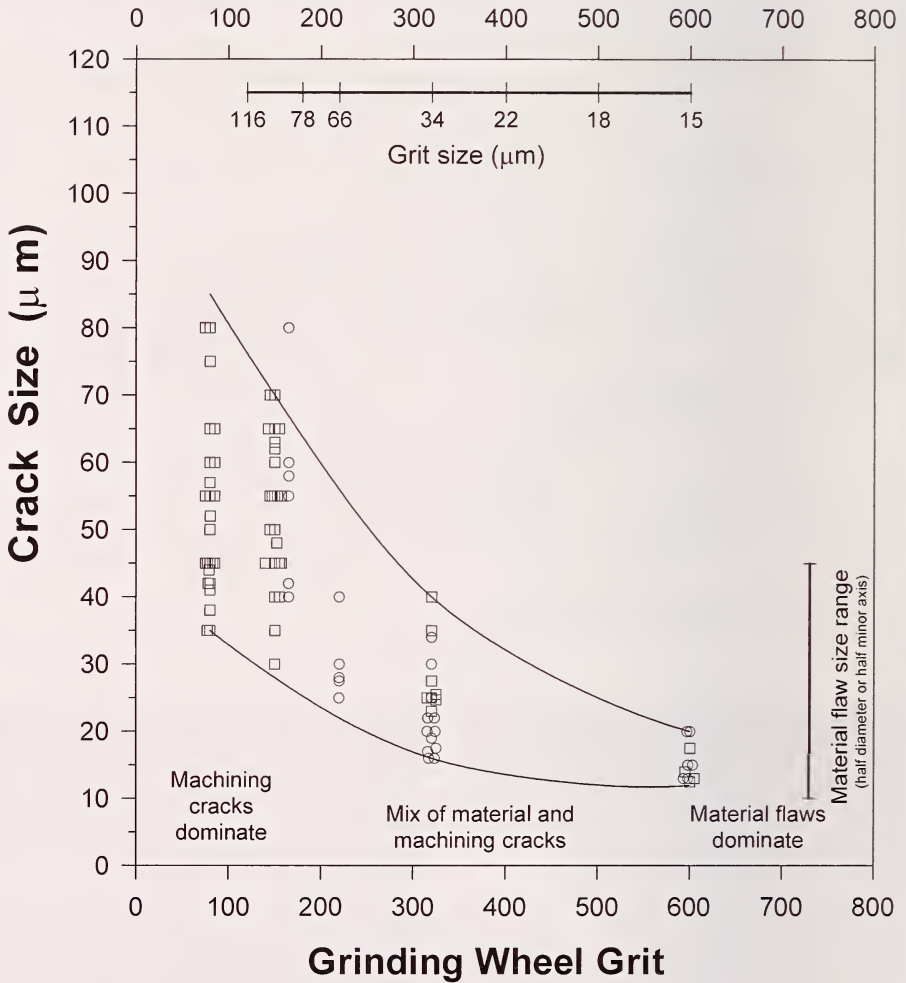


Figure 6.27d. The depth of parallel grinding cracks as a function of grinding wheel grit in a silicon nitride. The notes at the bottom show the effect upon strength. Ref. 16

6.7.7 Chips

Blunt or sharp impacts or contact loadings near an edge can chip off a piece as shown in Chapter 4. The chip can in turn become a strength limiting flaw on subsequent loadings. Figure 6.28 shows examples.

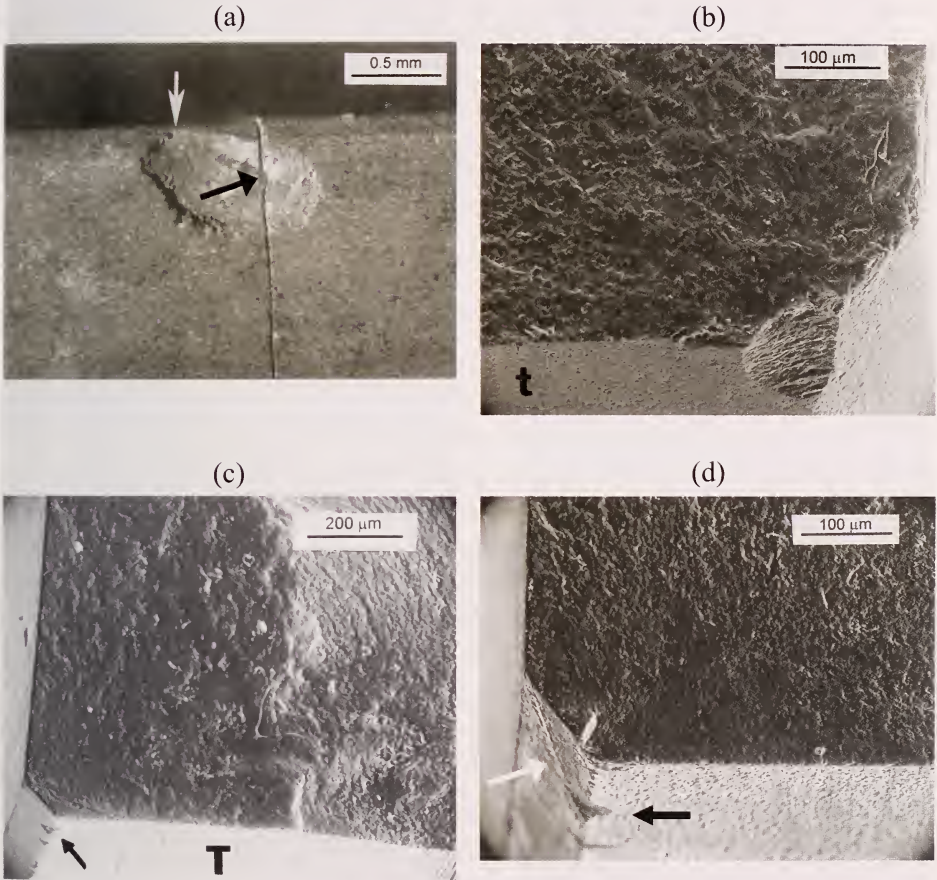


Figure 6.28. Examples of chips that acted as origins. (a) is an edge chip that acted as the flaw in a bend bar. This view shows the reassembled halves from the side. The top arrow shows the impact point that first created the chip. When broken in flexure, the fracture initiation site was found to be at the small black arrow. Notice the continuity of the chip shape on each side of the final fracture. This confirms that the chip was in the bar to begin with, and was not a secondary fracture. (b) is an edge chip in a sintered silicon carbide bend bar chamfer. (c) and (d) show chips on bend bar chamfers in hot-pressed silicon nitride. Close examination of the chamfers revealed that the grinding was not done longitudinally, but at an angle causing the chips. Notice the striation marked by the white arrow on the chamfer in (d).

6.8 Other Flaws

6.8.1 Processing cracks in ceramics

Cracks that form in the green state or during firing are quite variable and troublesome. Firing stresses can be very irregular, may be transient, and may depend upon thermal gradients in the kiln or furnace. Firing or shrinkage crack examples are shown in Figure 6.29 and Figure 4.7. Cracks that meander, are segmented, and/or are granular on the fracture surface may have formed in the green state or during firing. Since the body is not fully dense, the fracture surfaces are very granular and do not have the characteristic fracture surface markings. Close examination of interior crack surfaces may reveal thermal rounding of the particles and grains. On the other hand, cracks that are sharp and planar (and not rough and granular) may have popped in during or after cool down from the firing temperatures. Such cracks may have fracture surface markings such as hackle or arrest lines. Varner and Fréchette¹⁸ identified *dunt cracks* in whitewares. These are cracks that form during cooling when quartz particles undergo a sharp change in volume while the matrix glass is viscoelastic. The dunt crack appears as an atypical shiny transgranular fracture. *Delaminations* are a particular type of processing crack that are generally planar cracks within a material that arise from separation during green body forming, especially from mold or press release operations. They also can occur between bonded layers of dissimilar material or joints. Delaminations often occur in layered or tape cast structures, such as the two lead zirconate titanate (PZT) examples shown in Figures 6.29e and f from Reference 19. Diagnosis and remedial action for processing cracks usually requires close consultation with the processor to review the details of the fabrication and any steps that could lead to differential shrinkage, outgassing, or phase changes.

6.8.2 Artificial or controlled flaws, glasses and ceramics

Sometimes it is advantageous to deliberately create strength-controlling flaws. This is often done in fracture mechanics studies to create a controlled starting crack and then load it to fracture in order to evaluate the material's fracture resistance. Cracks made for fracture mechanics tests are typically called "precracks."

Artificial flaws are sometimes made by fractographers to help get acquainted with fracture markings on a new or difficult material. Usually a microhardness testing machine with a Knoop or Vickers indenter is used to make the controlled flaw in a bend bar or disk specimen. Unfortunately, the

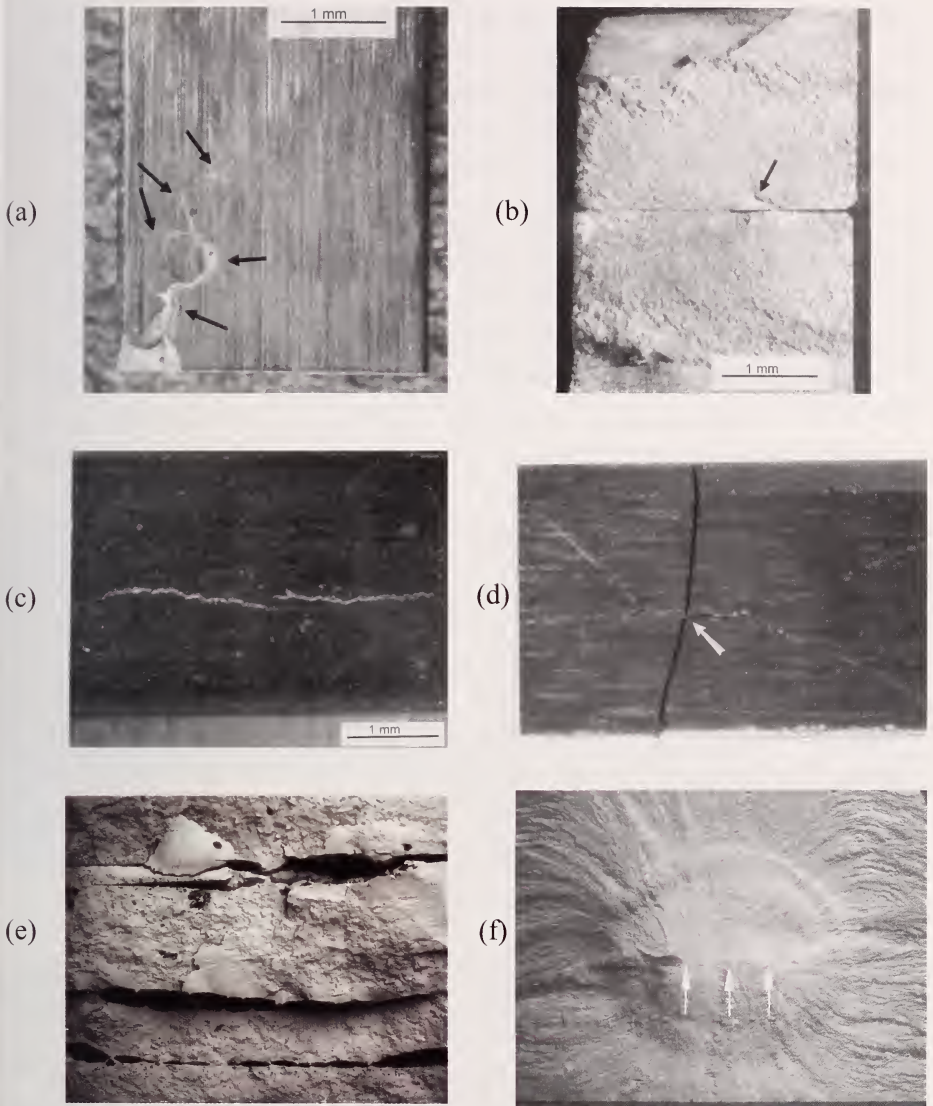


Figure 6.29. Examples of processing cracks. (a) shows the tensile surface and (b) the fracture surface of two silicon nitride bend bars which had an unstable boundary phase. (c) shows a bend bar that had a moderate strength despite a huge processing crack running perpendicular to the tensile axis. (d) shows another example of a firing crack in a bend bar. The origin was at the arrow. (e,f) show delaminations revealed on the fracture surfaces of two tape-cast PZT bend bars. (e) has severe delaminations between tape cast layers. (f) was processed much better but still had a very small horizontal delamination (arrows). The curved lines are arrest lines on the fracture surface. (e,f are courtesy Carl Wu).

indentation not only makes a crack, but significant residual stresses as well. The residual stress damage zone extends three to five times the indentation depth beneath the surface. The best remedy to deal with the residual stresses is to polish or hand-grind the residual stress damage zone off, leaving behind a stress-free semi-elliptical surface crack.

The Knoop indenter produces a much more controlled crack than the Vickers indenter. The latter creates a very complex three-dimensional crack and damage network. The Knoop indentation procedure for creating controlled flaws is described in more detail in section 7.11. Figures 3.22 and 6.30 shows examples of Knoop generated surface flaws that were fracture origins in bend bars.

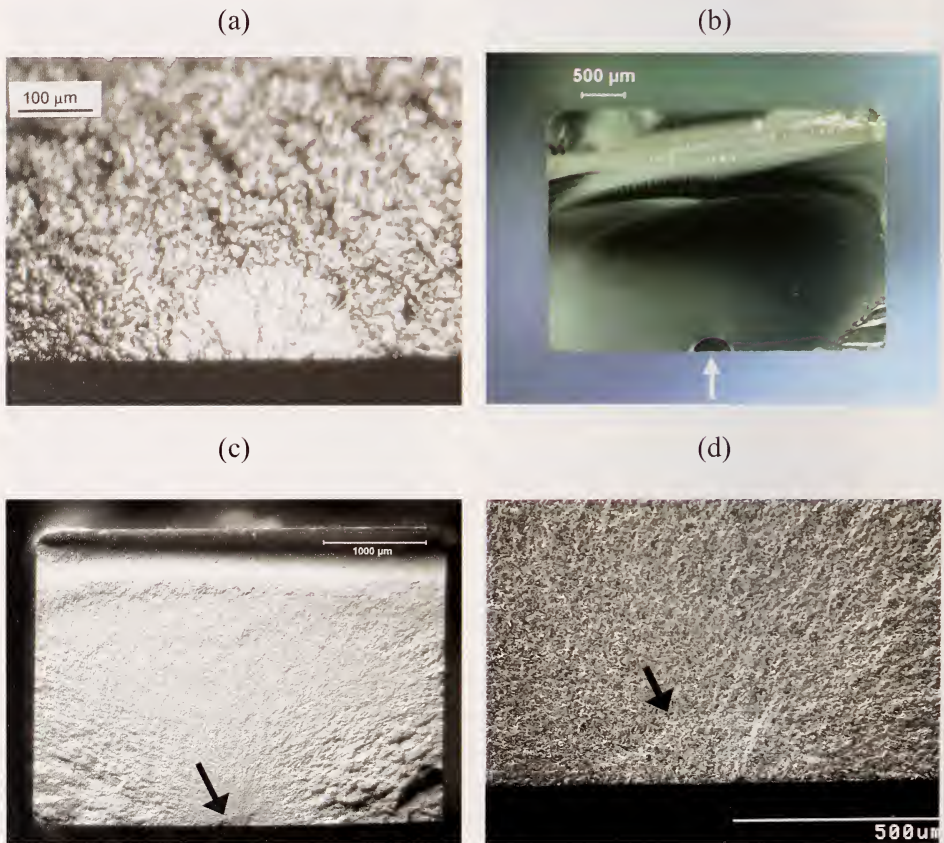


Figure 6.30. Examples of Knoop indentation flaws. (a) shows a precrack in a sintered alpha silicon carbide bend bar. (b) shows a borosilicate crown glass bend bar. (c) and (d) are optical and SEM images of cracks in a sintered reaction bonded silicon nitride.

6.8.3 Other Glass Origins

Examples of glass origins have been shown previously in this chapter: nickel sulfide inclusion in Figure 6.10a, scratches in Figures 6.5b, polishing-grinding cracks in Figure 6.17a,b, impact and contact cracks in Figure 6.18, 6.20 and 6.22, and artificial flaws in Figure 6.30b. Other flaw types that are common in glasses are shown below. Varner²⁰ and Fréchette²¹ have described the character of flaws in glass.

Flaws from the melt may come in several forms. These flaws are inclusions, pores, or compositional inhomogeneities, but have been given more specific names by the glass community.²⁰⁻²³ *Devitrification inclusions* or *devitrification stones* (Figure 6.31) can form if the glass crystallizes. *Stones* (Figure 6.32) are grains of unreacted raw material or refractory material broken off the tank or pot walls. Devitrification stones and stones have completely different chemistries and causes, so they should not be confused. Gas bubble origins are termed *blisters* if large and *seeds* if small. *Striae* are streaks of inhomogeneous, transparent glass. Their refractive index is different than the glass bulk. Very intense striae are termed *cords* and may appear as ropes or strands.



Figure 6.31. Unusually large (≈ 1 cm) glass devitrification inclusions with a blossom like structure as well as smaller seed bubbles. (Specimen courtesy of J. Varner and V. Fréchette)



Figure 6.32. Stone origins exposed on glass fracture surfaces. (a) is an example in a tempered plate (specimen courtesy of J. Varner and V. Fréchet). (b) and (c) show a stone in the middle of the wall of a glass ware.

Figure 6.33 shows *chill checks*, a pernicious flaw that is often very difficult to detect. A chill check is a small wavy and tight crack that is typically introduced into a hot glass surface by localized contact with a cooler object. Thermal stresses create the crack, but since the contact and thermal stresses are localized, the cracks are small. Glasses with high thermal expansion coefficients are most susceptible. The cracks often are difficult to detect in an unbroken component and require lighting at just at the right angle. Sometimes transmitted illumination is effective. If chill checks are suspected, then the piece or the illumination source should be manipulated a variety of ways and angles so as to try to get a momentary reflection from the crack. Chill checks form quickly and close back up very quickly. They may close so tightly (less than the wavelength of light) that they are not discernable. Nevertheless, some portions of the crack may have captured small amounts of gasses or water molecules that create slight opening pockets that are just barely detectable. These are often brightly colored, since they refract the light and may only be detectable from certain viewing angles. Once a momentary reflection is detected, the fractographer can zero in on the flaw site. Often the full extent of the crack is not visible because the crack is so tight. Fréchette¹⁶ observed that chill checks are hard to characterize since mechanical effects can also occur at the contact site. If a glass object breaks from a chill check during subsequent use and stressing, then it is likely the origin site will be irregular and may not be recognized as a chill check without examination of the outer surface. This underscores an earlier recommendation: if an origin on a fracture surface is located at the surface of the component, then it is prudent to examine the exterior surface of the part as well as the fracture surface. Varner²⁴ has compared features of chill checks and impact origins. Chill checks are curved and not flat, often have no visible outer surface damage, and, once the flaw is exposed on a fracture surface, have few markings on the flaw itself other than some twist hackle. Impact cracks are semicircular and are straighter and the outer surface has chipping and lateral cracks. Once exposed on a fracture surface, the flaw exhibits tertiary Wallner lines.

Polishing flaws from a loose abrasive rolled across a surface while under load can leave a variety of damage including indentations, scratches, Hertzian full or partial ring cracks and gouges according to Fréchette.²¹ The crack depths are typically four to five times larger than the particle diameter. They often are very elongated along the surface. Polishing, lapping or grinding glass can create sleeks which are fine, scratchlike, smooth boundaried imperfections usually caused by a foreign particle during polishing.

Chatter marks such as shown in Figures 6.34 and 6.35 often are clues to contact cracks underneath. The periodicity is a manifestation of vibration or a

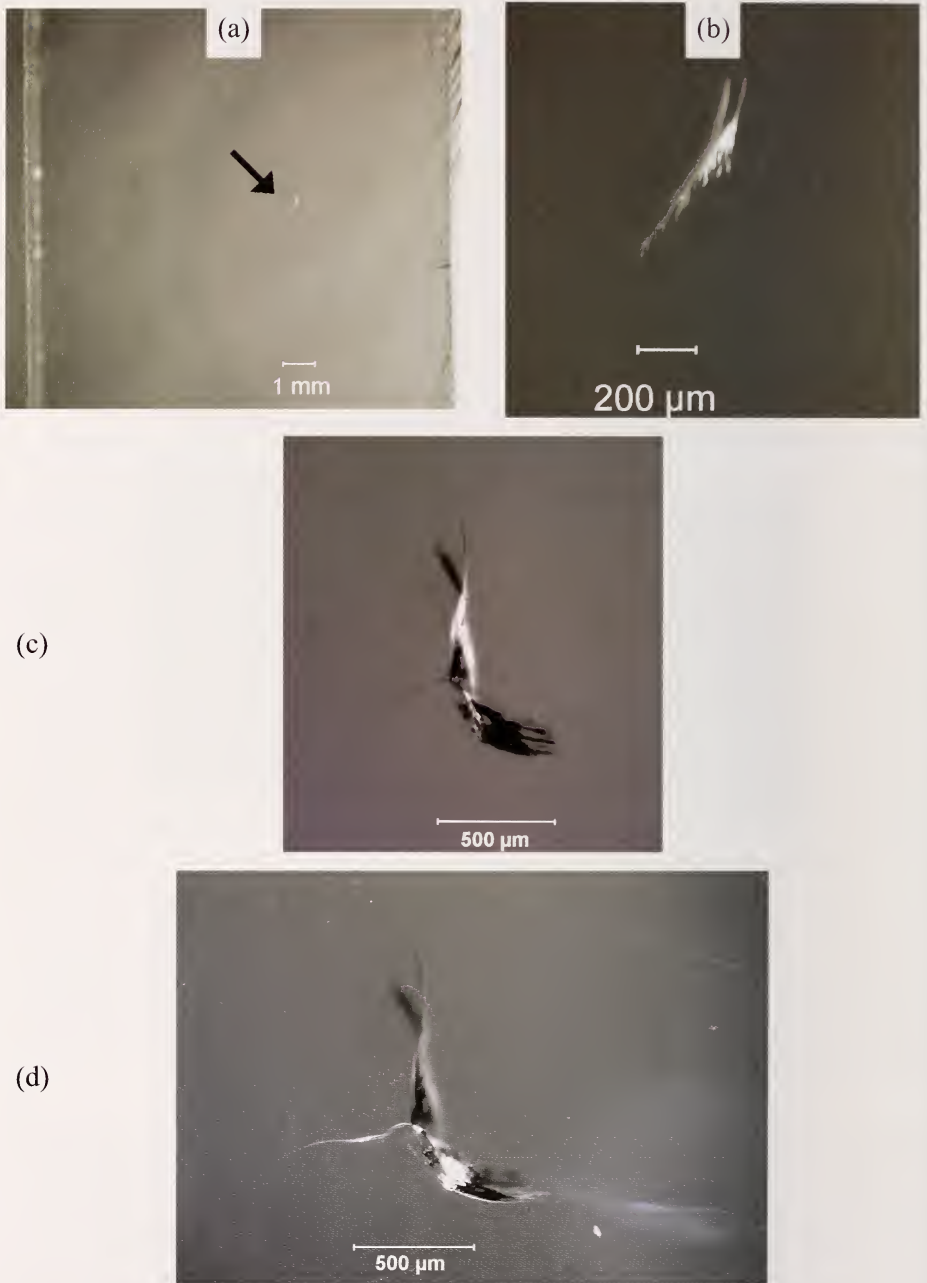


Figure 6.33. Chill check cracks on the outer surface of unbroken glass plates. (a) and (b) show the same chill check. (c) and (d) show two close-up views of another chill check and how different illumination can dramatically alter the appearance and apparent extent of the flaw. (Specimens courtesy V. Fréchet and J. Varner)

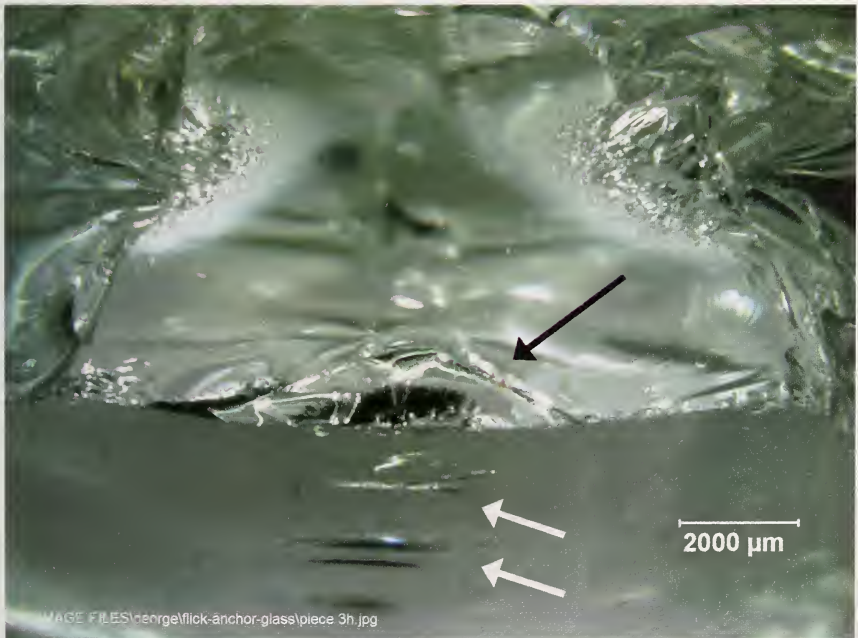
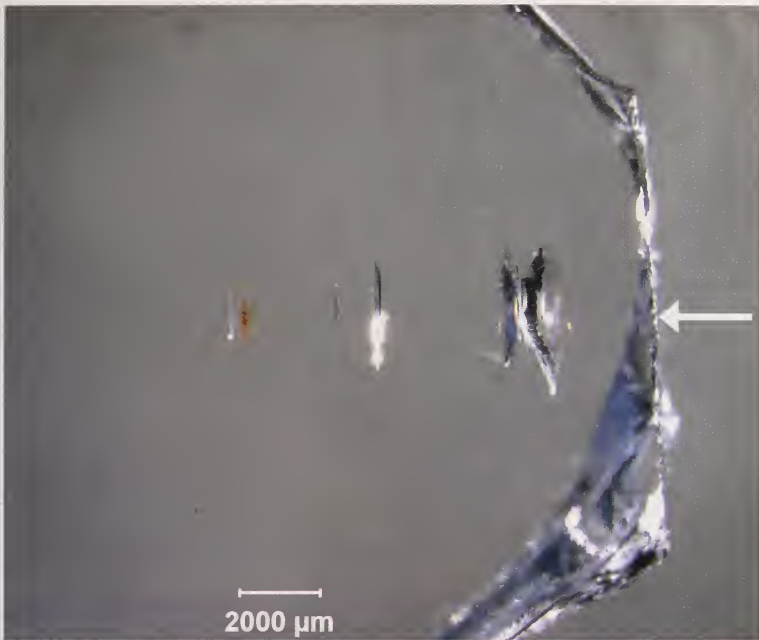


Figure 6.34. Chatter cracks from an object that contacted and slid across the surface of a heat strengthened glass vessel. (a) shows the outer surface. The arrow points to the fracture surface and the origin site. (b) shows the specimen tilted to show the origin crack on the fracture surface (large black arrow) and the other chatter cracks on the outer surface (small arrows).

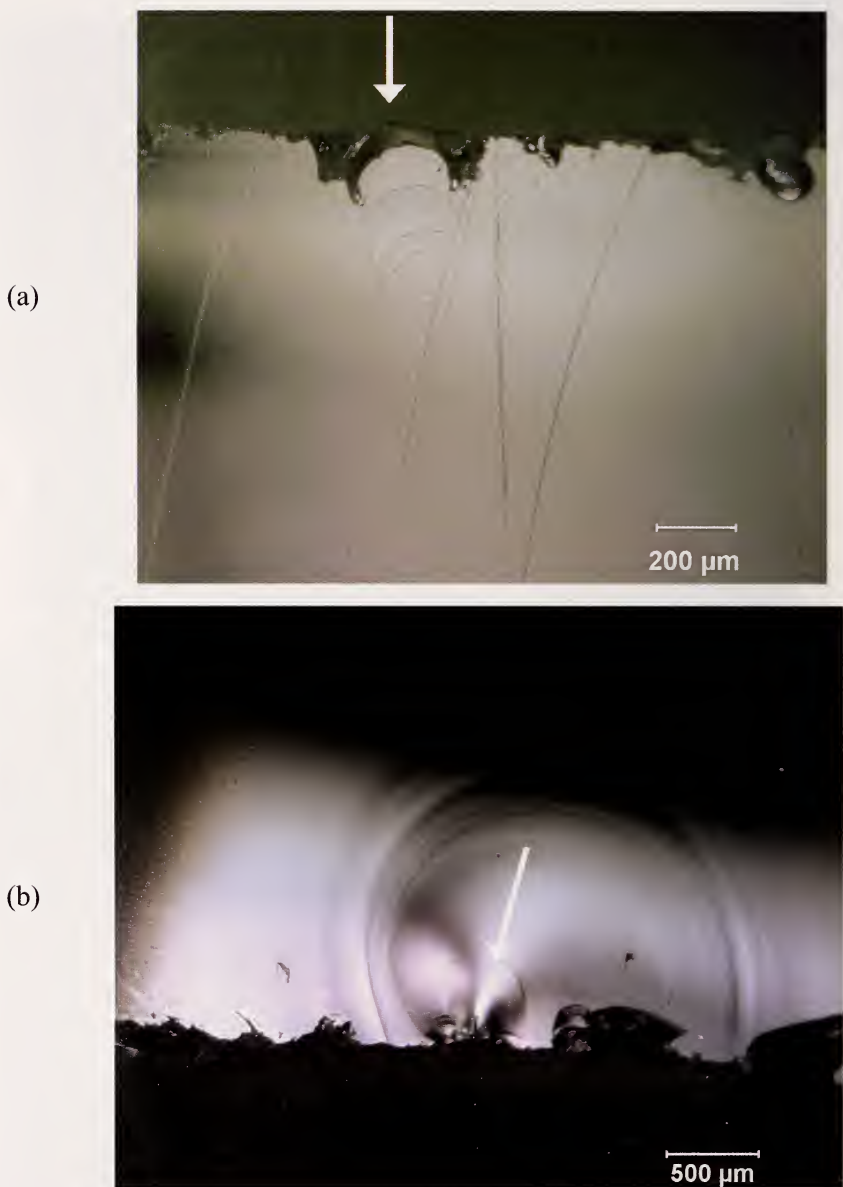
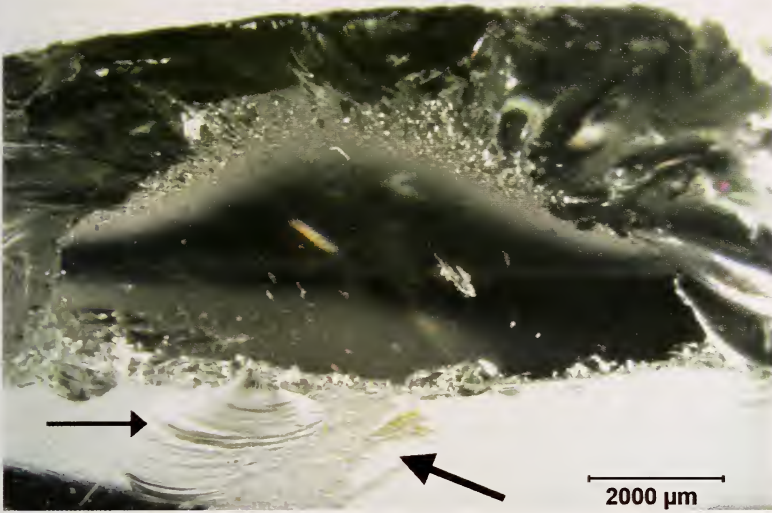


Figure 6.35. Very tiny chatter cracks from a small object that contacted and slid across the surface of a heat strengthened glass vessel. (a) shows the outer surface with an assortment of common scratches and edge chips, some of which are secondary edge chips after the main fracture. The arrow points to the exact origin site which is seen to be one of a series of curved chatter cracks. (b) shows the fracture surface. The multiple edge chips may confuse interpretation but the Wallner lines and a faint pop in arrest line are centered on the chatter crack (arrow).

(a)



(b)

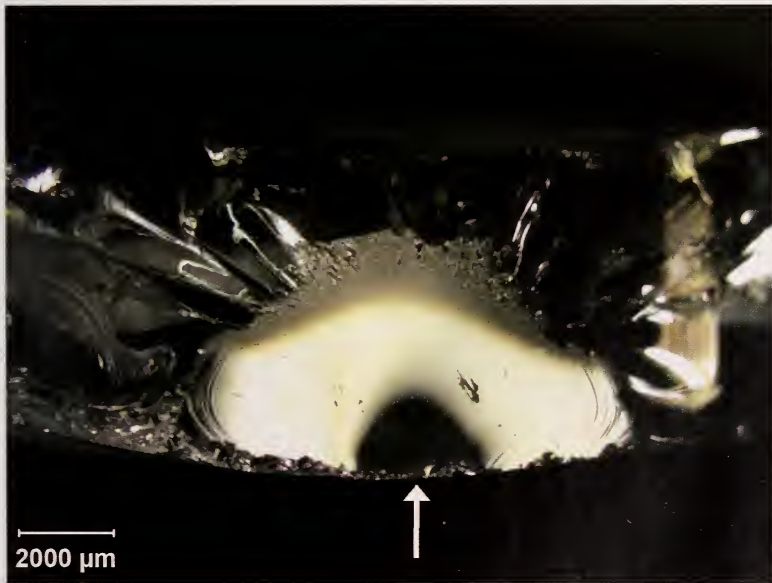


Figure 6.36. Surface abrasion can create subsurface cracks. (a) shows a piece from a broken heat-strengthened kitchenware tilted back to show the fracture surface and the elongated mirror and the outer surface with the abrasion track (large black arrow). Incidental secondary handling edge chips on the left (smaller black arrow) came from handling after fracture. (b) is the fracture surface showing an elongated mirror and the origin (white arrow). The origin region is dark due to a slight curve-wave in the fracture mirror surface.

stick slip interaction when a contacting object slides over the surface. Fracture often starts from the first or last chatter crack in a series. Abrasion tracks, which often occur around the bottom rim or sides of a glass vessel, are also vulnerable sites for localized contact damage as shown in Figure 6.36. Polishing, lapping or grinding glass can create miniature crack patterns of chatter cracks. Preston²⁵ and Ghering and Turnbull²⁶ showed numerous examples and correlated them with the forces, the surface lubrication conditions, and the abrasive or contactor types. Preston showed that a blunt contactor or ball dragged across a surface creates small partial cones cracks behind the contactor. The cracks are created by tensile stresses behind the ball or contactor as it moves and the cracks are bowed in the direction of the contactor movement such as shown in Figure 6.23. In sharp contrast, a rolling ball creates arc cracks that bow in the opposite direction. Their concave sides face the direction from which the ball came.²⁵

6.9 Fracture Oddities

Innumerable other irregularities can act as strength-limiting flaws. The fractographer should expect the unexpected. Rice²⁷ described cases of ball mills, thermocouple beads, insect carcasses and feces, dandruff, and hair as flaws. Figure 6.37 shows some oddball examples.

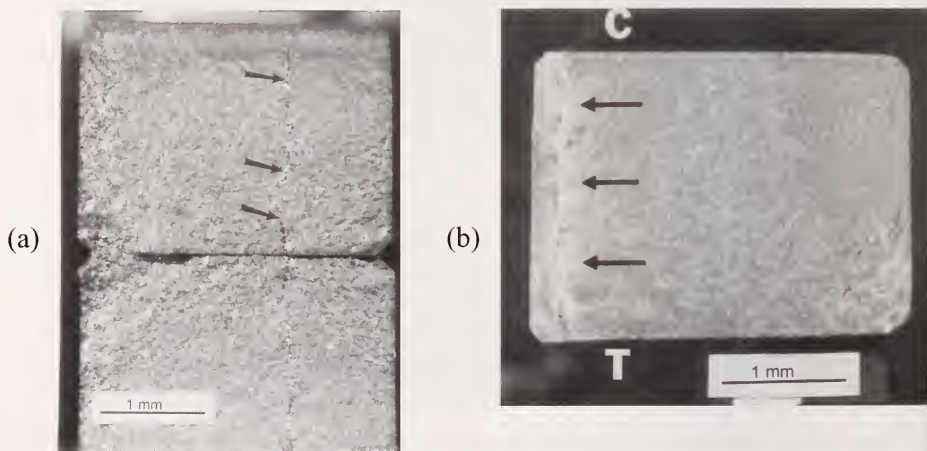


Figure 6.37. Unusual fractures. (a) shows a vein of silicon that was the strength limiting flaw in a siliconized SiC bend bar. This probably was caused by silicon infiltration of a seam or crack in the green body. (b) shows the fracture surface of a silicon nitride that had an unstable yttria silicate boundary phase. Phase changes distorted the bar shape from its original rectangular shape. Fracture occurred from the crack marked by arrows. T and C denote the tension and compression sides of the bend bar.

6.10 Contaminants

Every care should be taken to avoid contaminating the fracture surface. This is especially true during preparation of the specimens for SEM examination. During an optical examination, cleaning is not too difficult, but it is a different story if the specimen is being examined in the SEM. Once a specimen has been gold coated and is in the SEM, it can be disappointing to realize the flaw is masked by contamination or that a photo of the origin has distracting debris in the vicinity. Extraction, recleaning, and repreparation are time consuming and frustrating. Sometimes contaminants can be recognized if they appear to sit up on top of the fracture surface and are obviously not part of the material. This criterion is by no means perfect, however, as many contaminants get into the fracture surface crevices and blend in diabolically well. As noted previously, modeling clays are especially pernicious since they are fine, blend in well on the fracture surface, adhere extremely well, and are next to impossible to clean off. Figures 6.38 and 6.39 illustrates some common contaminants and how they look in the SEM. An EDX analysis of clay contamination on a fracture surface revealed aluminum, silicon, and titanium.

6.11 Combined or Hybrid Flaws

Multiple flaws may be coincident at a fracture origin. When such mixed cases arise, some judgment is required as to which origin is primary. ASTM C 1322²⁸ suggests several options for reporting such hybrid flaws. For example, if one origin type is primary then a reporting code may list it first with the secondary flaw separated by an ampersand (&). For example, Figures 6.40 (a, b) show P&LG denoting the origin is primarily a pore but with one or more associated large grains. In other cases two small flaws can link to form a strength limiting flaw. A plus sign may be used to indicate that these origin types linked together to limit the strength of the ceramic. For example, P + MD indicates a pore combined with machining damage. Origins can be difficult to characterize if they have mixed attributes. For example, porous *regions* often have large pores associated with them (Figure 6.40e).

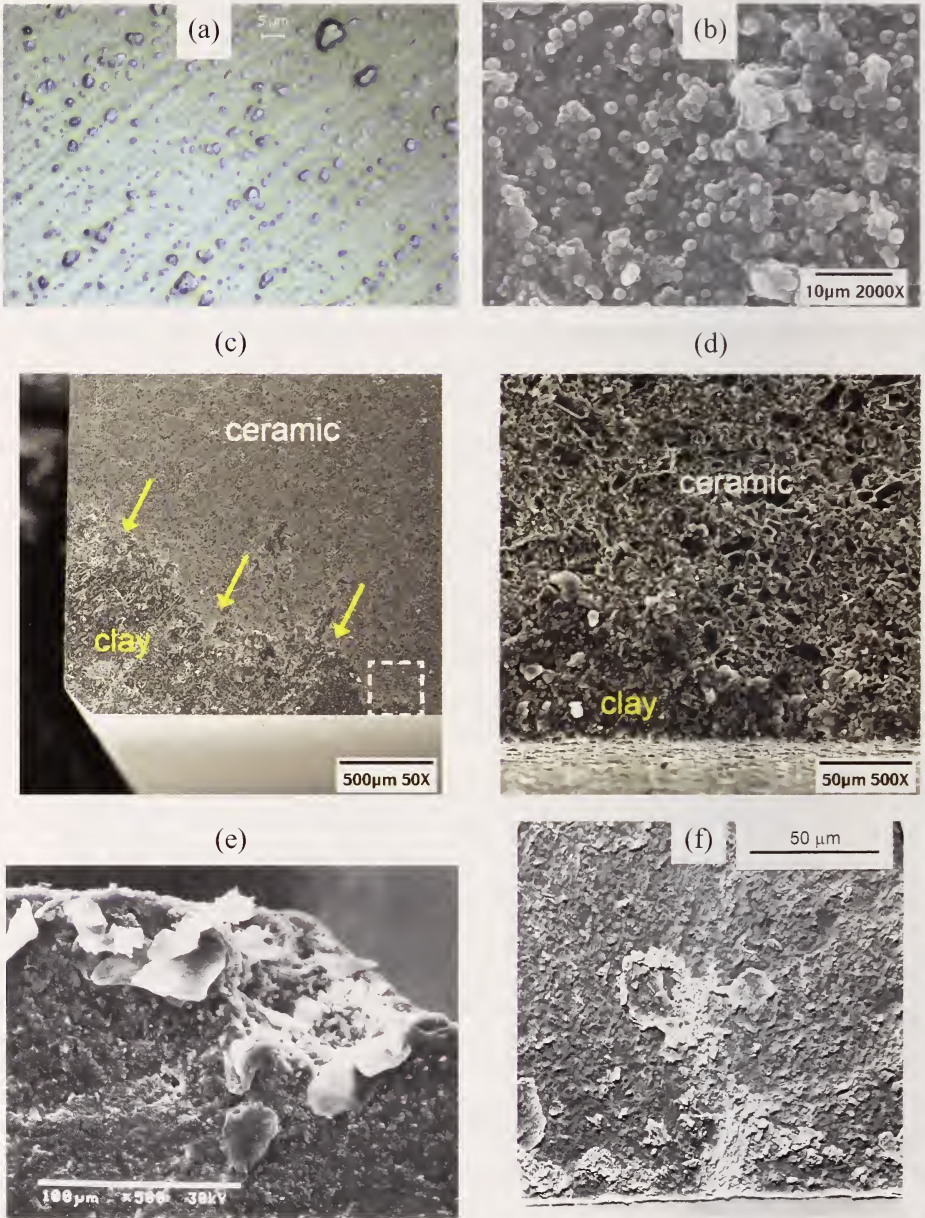


Figure 6.38. Common contaminants. (a) shows a blue clay smeared on a glass microscope slide as photographed on an optical microscope. The particles and grease smear are evident. (b) shows an SEM image of the clay. (c) shows a fracture surface of a fine grained alumina bend bar with clay swiped across the lower left corner (arrows). The boxed area is shown enlarged in (d). (e) shows human skin (courtesy A. Pasto). (f) shows an indeterminate contamination on a sintered silicon carbide.

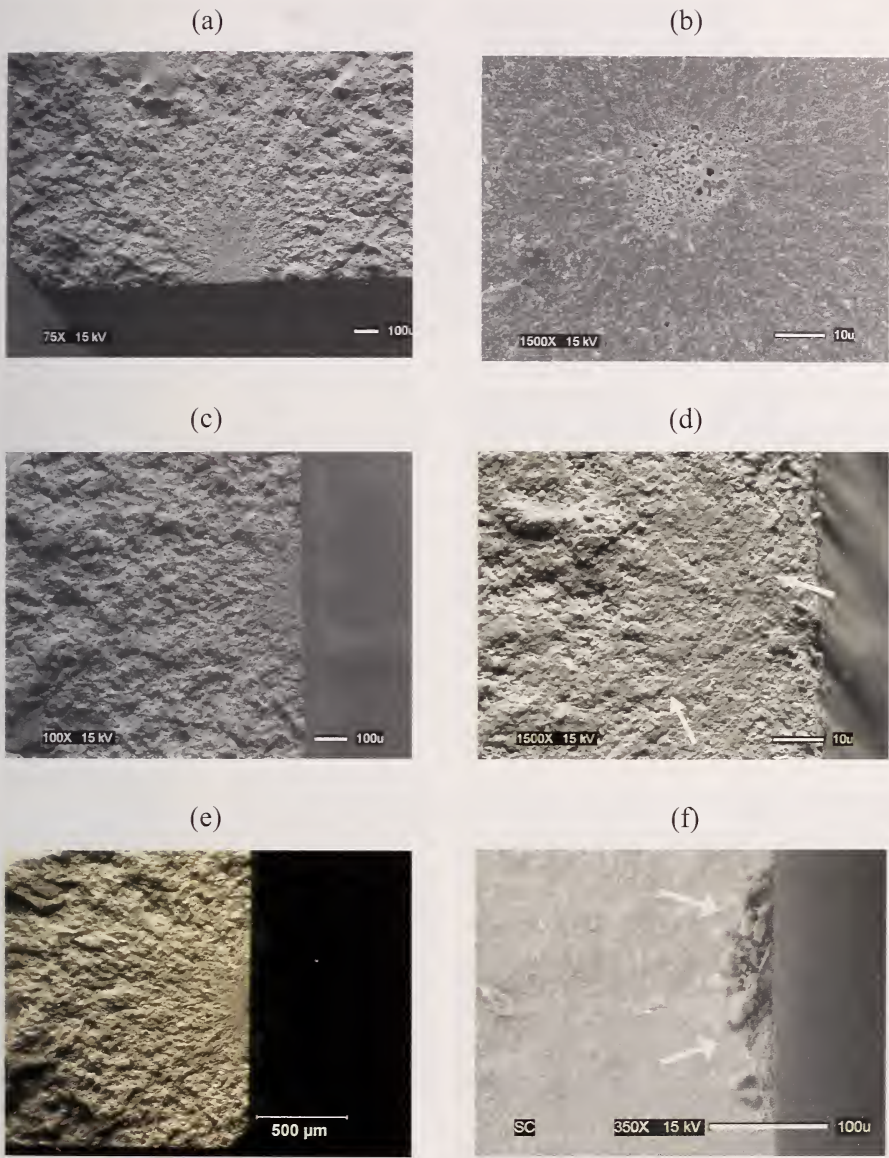


Figure 6.39. Contaminants in 3Y-TZP bend bars. (a) and (b) show a clean fracture with a well-defined fracture mirror and the common flaw in this material: a pore or porous region origin. (c) and (d) show clay smeared surface over the mirror in another specimen. Notice the parallel smear traces (arrows) from lower left to upper right in (d). The clay is not evident in the low magnification image of the mirror, but it covers the origin in (d). (e) and (f) show a mirror with an unknown contaminant covering the origin (arrows). (a-f courtesy J. Quinn)

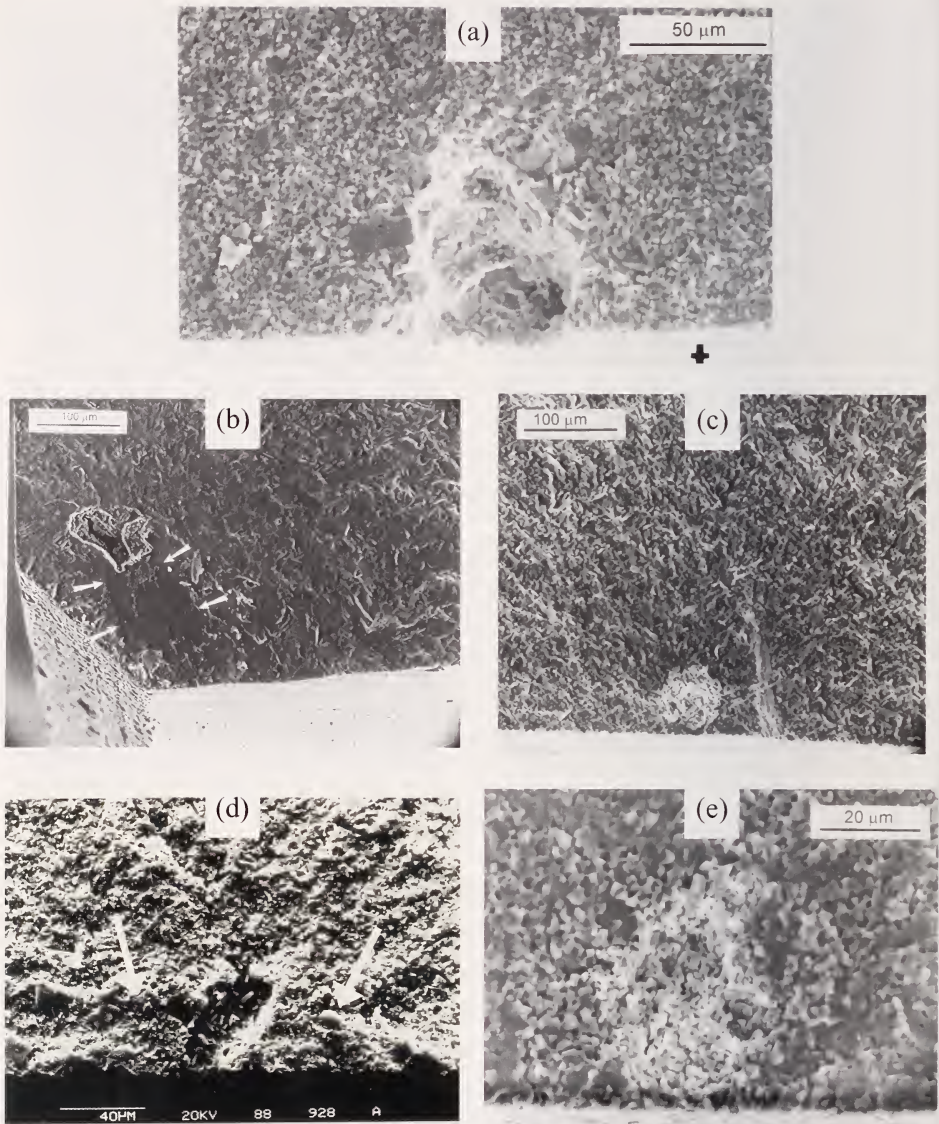


Figure 6.40. Hybrid flaw fracture origins (a) shows a flaw in a sintered 99.9 % alumina that can be described as primarily a pore, but with some large grains (P & LG). (b) is a pore/large grain (P & LG) combination in a sintered alpha silicon carbide bend bar. Note the good quality of the chamfer. Edge damage was not a factor in this case. (c) is a combination of an agglomerate and a large grain (A & LG) in sintered silicon carbide. (d) is a surface grinding crack that linked with a pore in a sintered silicon nitride (P + MD). (e) shows a flaw in a sintered alumina could be described as either a porous region or a pore.

6.12 Baseline Microstructure Origins

As fabricators improve materials by careful process control and eliminate large abnormal flaws, ceramics will break from origins that are part of the ordinary microstructure. Figure 6.41 illustrates the concept and Figure 6.42 shows an example. Once the inclusions are eliminated, grains from the large end of the grain size distribution become the strength-limiting flaws. The materials processor does not believe these are flaws, but the fracture mechanics expert does. Rice²⁷ described such origins as “mainstream microstructural features.” A shorter descriptor might be “baseline microstructure” as in: “the origin flaw was a large grain from the baseline microstructure.”

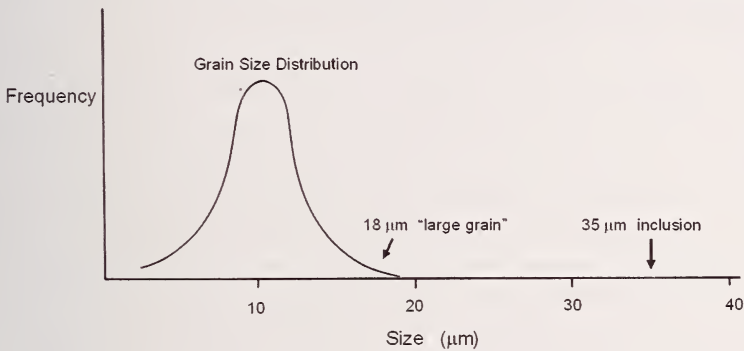


Figure 6.41. Careful processing may eliminate severe flaws such as inclusions or gross pores. In the absence of such flaws, the material may fail from “baseline microstructure” origin.

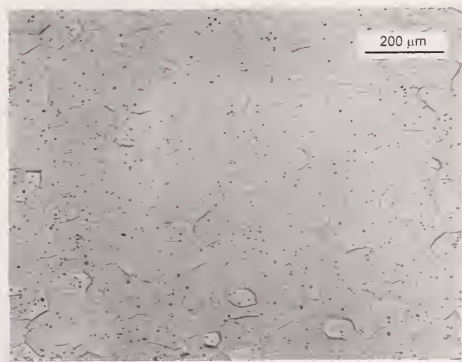
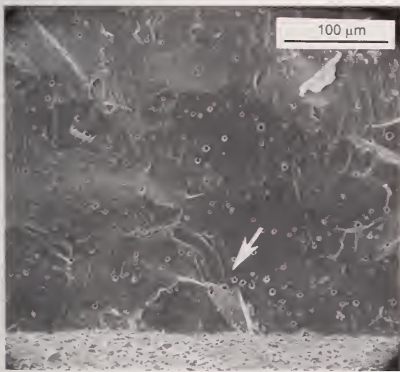


Figure 6.42. (a) shows a grain from the baseline microstructure that was the fracture origin in a sintered aluminum oxynitride four-point flexure bar. The origin in this case may actually be the grain boundary around the grain. (b) shows a polished section view of the microstructure.

6.13 Flaw Size

It may suffice to identify the nature of the flaw, but a better characterization includes at least a rough estimate of its size. A $100\ \mu\text{m}$ inclusion may not have the same source or behavior as a $20\ \mu\text{m}$ inclusion. The size need not be measured precisely if the characterization is intended to describe the general nature of the origin. On the other hand, there are some instances when a good estimate is needed, such as when it is intended to do a fracture mechanics analysis of the flaw as described in the next chapter. This may be to confirm that the fractographer has found the correct flaw. So, for example, if a fractographer has tentatively identified a $2\ \mu\text{m}$ feature as an origin, but fracture mechanics suggests the flaw should be $50\ \mu\text{m}$ in size, then the fractographer ought to reevaluate his assessment.

Measure an approximate flaw diameter, or if the flaw is elongated, approximate it with a semi-elliptical shape and measure the minor and major axis lengths as shown in Figure 6.2. The origin's true size may not be revealed on the fracture surface and exact fracture mechanics analyses of most origins are not possible due to their complex shape. An important exception to this is machining damage, wherein the origin size measurement may be very useful for the estimation of fracture toughness. When measuring the flaw size of surface located flaws, measure and record the origin depth and the width in cases when the origins are elongated. Chapter 7 and Figure 7.16 furnish more guidance.

6.14 Partially-Exposed Flaws

It should be borne in mind that flaws may not necessarily be oriented so that they are perpendicular to the principle tensile stress. Only a portion of a flaw may be exposed on a fracture surface as shown in Figure 6.43. Some of the Hertzian cone cracks shown in Figure 6.20 are good examples.

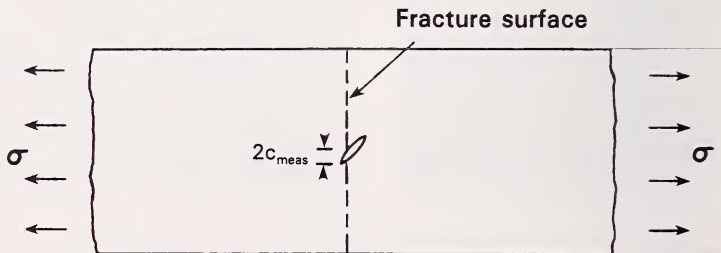


Figure 6.43. The full flaw size and shape may not necessarily be exposed on a fracture surface.

6.15 Microfault Pockets

Even if a fracture origin site can be found, there may not be an obvious flaw at the origin in some materials. Subtle porous regions or grinding damage crack at the surface can possibly be present but not detectable. This dilemma is more likely to occur with coarse-grained ceramics, porous ceramics, and heterogeneous ceramics, wherein a flaw could “hide” against the background microstructure. On the other hand, a flaw will stand out more clearly against the background in fine-grained ceramics, glasses, and single crystals.

There is another possibility why a discrete flaw may not be detectable at an origin site: There may not be one. Emphasis in this chapter up to this point has been on flaws that are discrete irregularities larger than the baseline microstructure. Alternatives are illustrated in Figure 6.44. Fracture origins

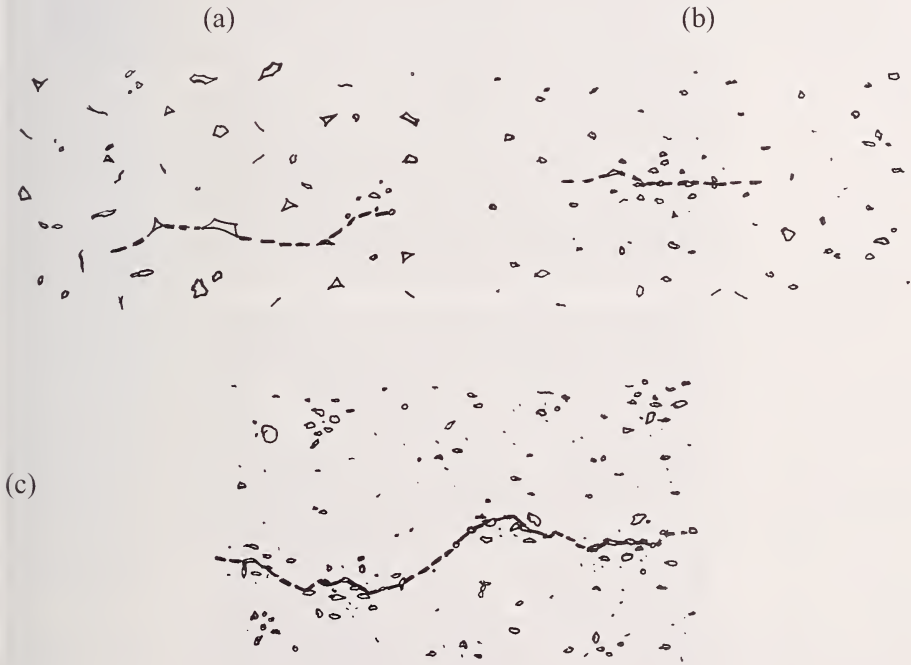
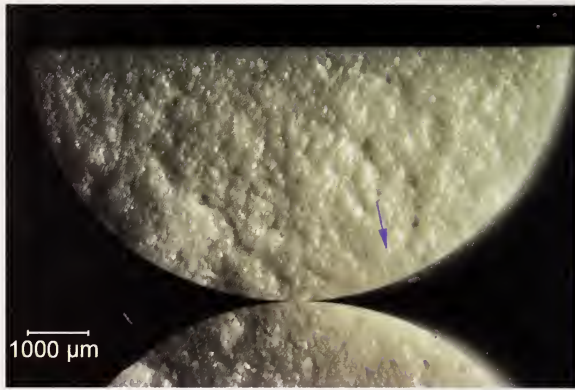
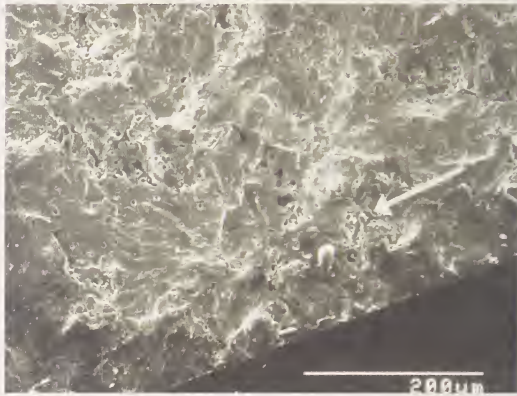


Figure 6.44. Schematics of “microfault pockets.” The fracture origin may be an array of tiny microstructural faults that are linked by microcracking. Tension stress is applied vertically. (a) is similar to a schematic by Sines and Okada.^{29,30} (b) shows an origin site that has a greater local concentration of the irregularities. (c) shows random pockets of greater than average concentration. Fracture may entail linkage of these pockets by microcracking.

(a)



(b)



(c)

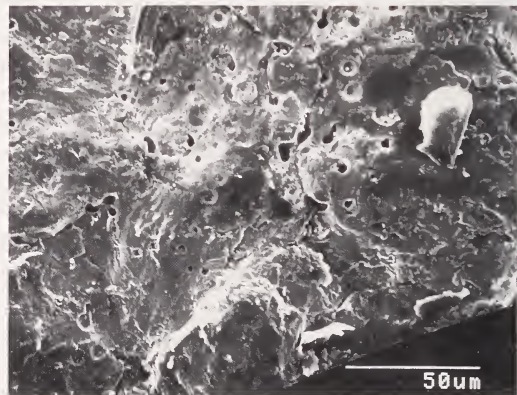


Figure 6.45. Origin in a magnesia partially-stabilized zirconia split-rod bend specimen. (a) shows the entire fracture surface which is very rough and undulating due to the coarse microstructure and irregularities in the microstructure. (b) and (c) show close-ups of the origin which is a pocket of micropores and grain boundary faults. Tiny wake and twist microhackle radiate away from the origin. Figure 6.46 shows a polished section of the same material.



Figure 6.46. Polished microstructural section of the magnesia partially-stabilized zirconia shown in the previous figure. Microflaw pockets are marked by the arrows.

may be regions of slightly or moderately greater concentration of ordinary irregularities such as micropores, grain boundary cracks or other tiny faults. The regions may be termed “microfault pockets.” By themselves, the tiny irregularities are insufficient to cause fracture, but they can link by microcracking during loading. Sines and Okada^{29,30} suggested that this could account for time-dependent fracture, but there is no reason it cannot apply to fast fracture strength as well. It should be borne in mind that a random distribution does not mean a uniform distribution. A random distribution of such tiny irregularities will have local regions of greater-than-average concentration.

Fracture origins of the types shown in Figure 6.44 would be extremely difficult to diagnose on fracture surfaces since the features at the origin look exactly like the normal microstructure. Figure 6.45 is an example. Polished specimen microstructural analysis may help with the interpretation as shown in Figure 6.46. The origin may take on the character of porous regions as shown in Figure 6.7. The literature is sparse on such flaws, no doubt because engineers and scientists are loath to show fractographs of origins that fail to show a flaw!

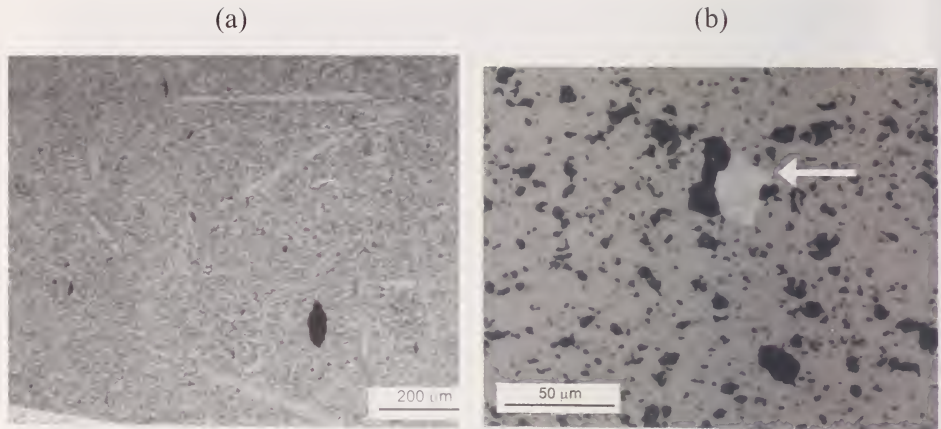


Figure 6.47. Polished microstructural sections can aid origin interpretation. (a) Sintered alpha silicon carbide often has large grain fracture origins. The acicular or platelet shape of these and their concentration are revealed by the micrograph. (b) reaction-bonded silicon nitride sometimes fails from unreacted silicon (arrow).

6.16 Polished Microstructural Sections

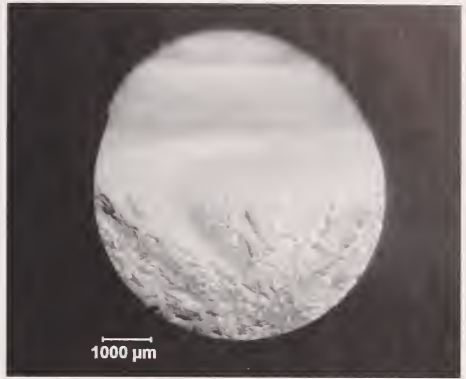
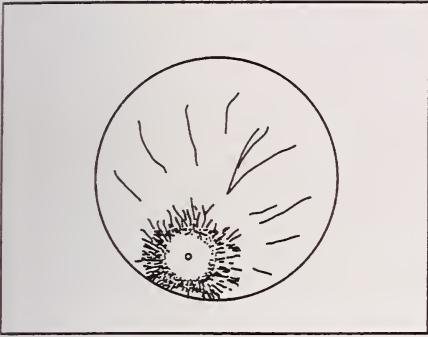
Figure 6.47 and previous Figures 6.4, 6.42 and 6.46 show examples of how polished microstructural sections can provide complimentary information about flaw types and their distributions. Polished section preparation is a staple for metals failure analysis, usually to ensure that the microstructure is as expected and the correct phases are present.

6.17 What to Report

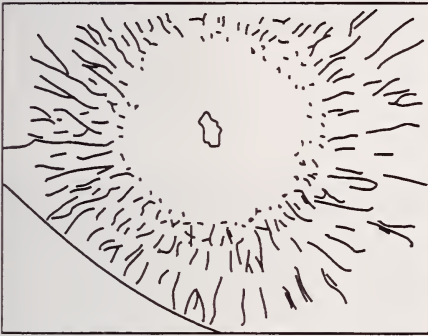
For each component, or laboratory-tested specimen, record the origin type, the location in the particular specimen, and the flaw size. If a fracture mirror is present, it may also be helpful to measure its size, especially if the fracture is in a component. Mirror size measurements in laboratory strength test specimens also may be done so that mirror constants can be estimated and published for new materials. Figure 6.48 shows the recommendations in ASTM C 1322.²⁸

Organizing a wealth of fractographic images can at times be difficult. Ideally the images should be presented in a coherent fashion with some context. A

1. Whole Fracture Surface



2. Fracture Mirror



3. Fracture Origin

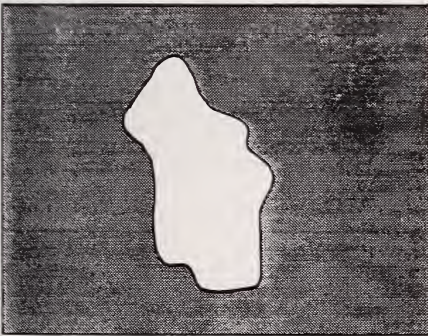


Figure 6.48. Multiple photos should be taken showing whole fracture surface, the mirror region and the origin. The right side shows an example for an inclusion in a silicon nitride rod flexural strength specimen.

◆ Fractography of Ceramics and Glasses

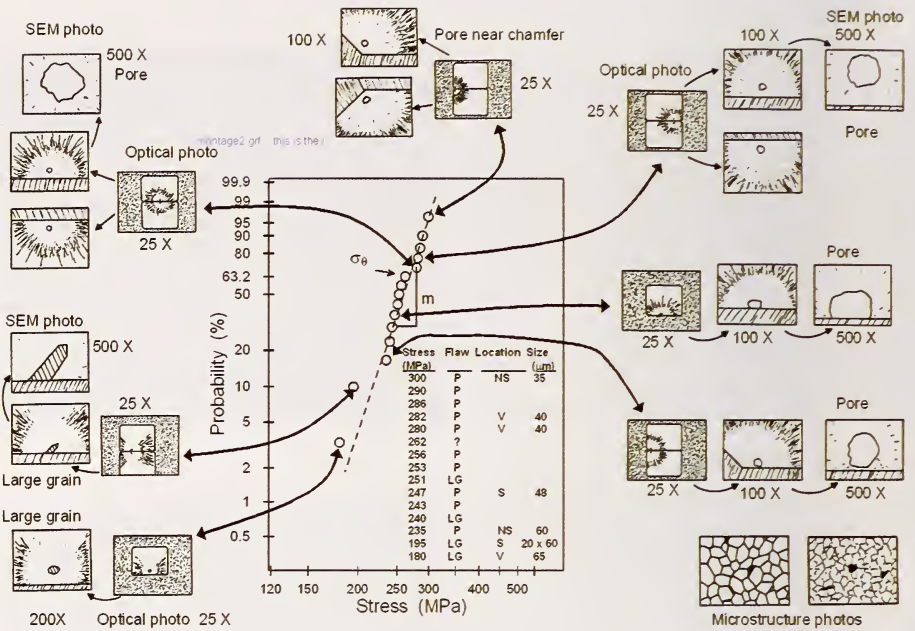


Figure 6.49. Schematic of a fractographic montage.

fractographic montage whereby images are arranged around a data plot such as a Weibull graph can be very effective as shown in Figure 6.49.

Component failure analyses often have some overall photographs of the entire structure and close-ups of various critical features. Much time and confusion can be saved if the successive images are presented in an orderly, systematic way. It is always wise to start with an overall image of the structure and then add images at progressively higher magnification at key locations. At each step the relationship of the images to each other should be clear. Figure 6.50 shows a good example for a dental crown failure.

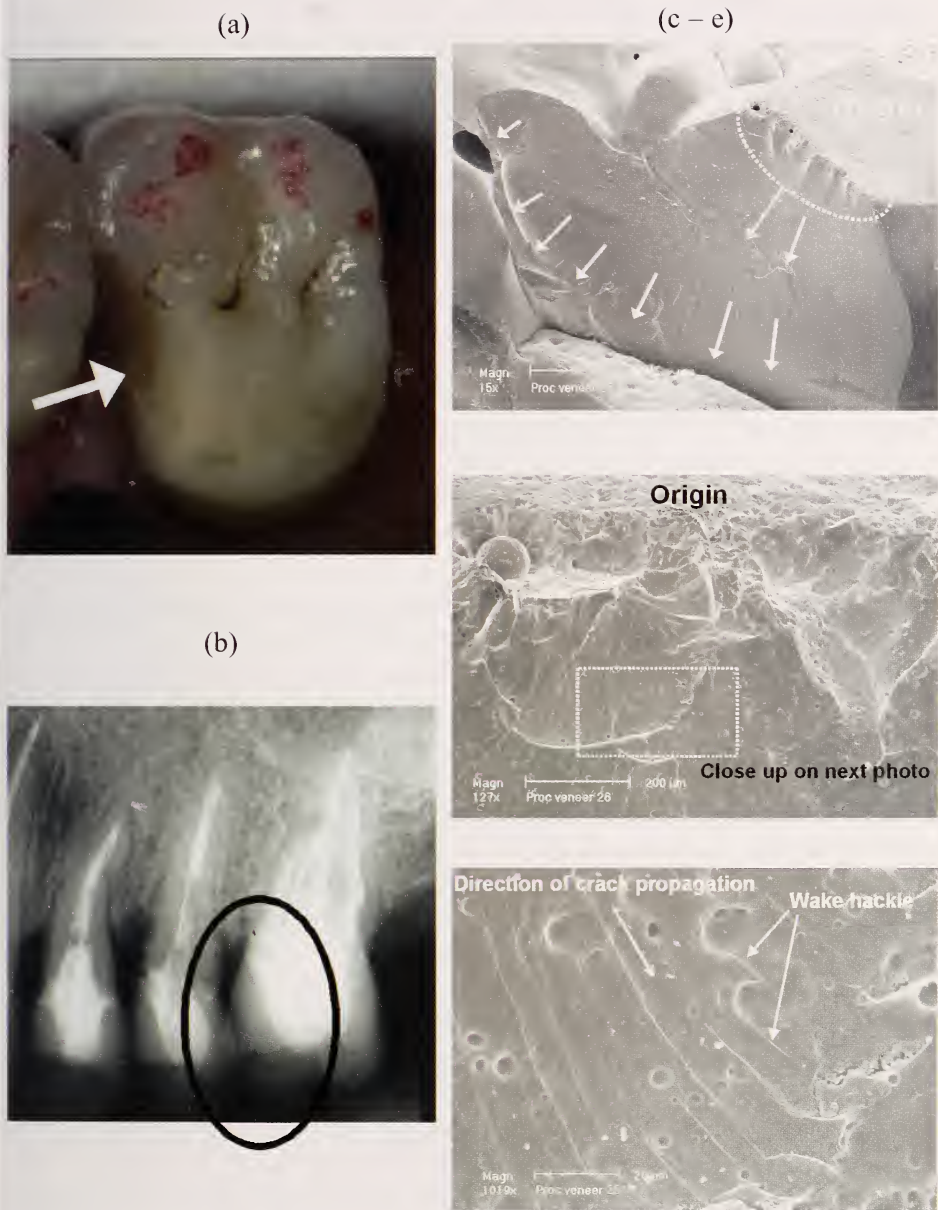


Figure 6.50. Failure of a first upper left molar crown. (a) shows a view onto the occlusal surface (the crown top) and the chipped veneer on the crown side (arrow). The porcelain veneer was inadequately supported by the alumina core as shown in the x-ray image (b). (c) – (e) show progressive close-ups of the fracture surface. This is the same crown as shown in Figure 3.31 (Courtesy S. Scherrer, Univ. Geneva)

Chapter 6 References

1. W. Weibull, "A Statistical Distribution Function of Wide Applicability," *J. Appl. Mech.*, **18** (1951) 293 – 297.
2. G. D. Quinn and R. Morrell, "Design Data for Engineering Ceramics: A Review of the Flexure Test," *J. Am. Ceram. Soc.*, **74** [9] (1991) 2037 – 2066.
3. R. W. Davidge, *Mechanical Behavior of Ceramics*, Cambridge Univ. Press, London, 1979.
4. D. Munz and T. Fett, *Ceramics, Mechanical Properties, Failure Behavior, Materials Selection*, Springer, Berlin, 1999.
5. W. E. C. Creyke, I. E. J. Sainsbury, and R. Morrell, *Design with Non-ductile Materials*, Applied Science Publ., London, 1982.
6. R. W. Rice, "Pores as Fracture Origins in Ceramics," *J. Mat. Sci.*, **19**, (1984) 895 – 914.
7. A. G. Evans, "Structural Reliability, A Processing Dependent Phenomenon," *J. Am. Ceram. Soc.*, **65** [3] (1982) 127 – 137.
8. R. W. Rice, *Mechanical Properties of Ceramics and Composites, Grain and Particle Effects*, Marcel Dekker, NY, 2000.
9. D. W. Richerson, *Modern Ceramic Engineering*, Marcel Dekker Inc., NY, 1982.
10. C. G. Knight, M. V. Swain, and M. M. Chaudhri, "Impact of Small Steel Spheres on Glass Surfaces," *J. Mat. Sci.*, **12** (1977) 1573 – 1586.
11. M. M. Chaudhri, "High-Speed Photographic Investigations of the Dynamic Localized loading of Some Oxide Glasses," pp. 87 – 113 in *Strength of Inorganic Glass*, ed. C. Kirkjian, Plenum, New York, 1985.
12. Y. Akimune, "Hertzian Cone Crack in SiC Caused by Spherical Particle Impact," *J. Mat. Sci. Lttrs.*, **9** (1990) 659 – 662.
13. B. R. Lawn, S. M. Wiederhorn, and D. E. Roberts, "Effect of Sliding Friction Forces on the Strength of Brittle Materials," *J. Mat. Sci.*, **19** (1984) 2561 – 2569.

14. M. M. Chaudhri and C. Liangyi, "The Orientation of the Hertzian Cone Crack in Soda-Lime Glass Formed by Oblique Dynamic and Quasi-static Loading with a Hard Sphere," *J. Mat. Sci.*, **24** (1989) 3441 – 3448.
15. R. W. Rice and J. J. Mecholsky, Jr., "The Nature of Strength Controlling Machining Flaws in Ceramics," pp. 351 – 378 in *The Science of Ceramic Machining and Surface Finishing II*, eds., B. J. Hockey and R. W. Rice, Special Publication 562, NBS, Gaithersburg, MD, 1979.
16. G. D. Quinn, L. K. Ives, and S. Jahanmir, "On the Nature of Machining Cracks in Ground Ceramics: Part I: SRBSN Strengths and Fractographic Analysis," *Mach. Sci. Technol.*, **9** (2005) 169 – 210.
17. G. D. Quinn, L. K. Ives, and S. Jahanmir, "On the Nature of Machining Cracks in Ground Ceramics: Part II: Comparison to Other Silicon Nitrides and Damage Maps," *Mach. Sci. Technol.*, **9** (2005) 211 – 237.
18. J. R. Varner and V. D. Fréchette, "Fractography of Whitewares," pp. 305 – 315 in *Science of Whitewares*, eds. V. Henkes, G. Y. Onoda, and W. M. Carty, American Ceramic Society, Westerville, OH, 1996.
19. B. A. Bender, C. Kim, and C. Cm. Wu, "Solid Preform Fabrication of a Piezoelectric Ceramic Torsional Actuator Motor," *Ceram. Eng. and Sci. Proc.*, **25** [3] (2004) 89 – 94.
20. J. R. Varner, "The Practical Strength of Glass," pp. 389 – 406 in *Strength of Inorganic Glass*, ed. C. Kurkjian, Plenum, NY, 1986.
21. V. D. Fréchette, *Failure Analysis of Brittle Materials*, Advances in Ceramics, Vol. 28, American Ceramic Society, Westerville, OH, 1990.
22. H. Pfaender, *Schott Guide to Glass*, Chapman and Hall, London, 1996.
23. ASTM C 162, Standard Terminology of Glass and Glass Products, *Annual Book of Standards*, Vol. 15.02, ASTM Int., West Conshohocken, PA, 1999.
24. J. Varner, private communication.
25. F. W. Preston, "The Structure of Abraded Glass Surfaces," *Trans. Opt. Soc.*, **23** [3] (1921-1922) 141 – 164.

- 26 L. G. Ghering and J. C. Turnbull, "Scratching of Glass by Metals," *Bull. Am. Ceram. Soc.*, 19 (1940) 290 – 294.
27. R. W. Rice, "Failure Initiation in Ceramics: Challenges of NDE and Processing," pp. 1057 – 1064 in *Ceramic Developments*, Sorrell, C., and Ben-Nissan, B., eds., *Materials Science Forum*, Vol. 34–36, Trans. Tech. Publ. Ltd. Switzerland, 1988.
28. ASTM C 1322-96, "Standard Practice for Fractography and Characterization of Fracture Origins in Advanced Ceramics," *Annual Book of Standards*, Vol. 15.01, ASTM int., West Conshohocken, PA (1996)
29. T. Okada, G. Sines, and D. Green, "Crack Origins and Microcracking in Delayed Fracture of Alumina," *Comm. Am. Ceram. Soc.*, May 1982, C 64 – 65.
30. G. Sines and R. Okada, "Flaws Responsible for Slow Cracking in the Delayed Fracture of Alumina," *J. Am. Ceram. Soc.*, **66** [3] (1983) 228 – 232. {with correction, *ibid*, 66 [7] (1983) 538.}

7. QUANTITATIVE ANALYSIS

7.1 Introduction

Quantitative analysis can aid the fractographic analysis and extend its value. It may be used to confirm that the right flaw has been identified as a fracture origin. It can make good estimates of the stresses in the part at failure. Four methods to estimate stress are shown in this chapter: fragmentation analysis, branching distance analysis, fracture mirror size analysis, and origin size analysis. Some analyses are empirical and others are based on the powerful tool of fracture mechanics. One goal of this chapter is to convey a working knowledge of fracture mechanics so that it can be used to solve practical problems. Table 1 includes some useful conversion factors.

Table 7.1. Conversion Factors

length

1 in	=	25.4 mm
1 micrometer (micron)	=	1×10^{-6} m
0.001 inch	=	25.4 micrometers

force

1 kgf (kilogram force)*	=	9.80 N (Newtons)
-------------------------	---	------------------

stress or pressure

1 ksi (1,000 psi)	=	6.895 MPa (Megapascal)
1 Pa	=	1 N/m ²
1 MPa	=	1 MN/m ² = 1×10^6 Pa
1 MPa	=	145.04 psi = 0.14504 ksi
1 GPa	=	1000 MPa = 1×10^9 Pa

example: 100 ksi = 690 MPa

stress intensity

1 ksi inch	=	1.10 MPa $\sqrt{\text{m}}$
example:		$5 \text{ MPa}\sqrt{\text{m}} \times \left(\frac{1 \text{ ksi}\sqrt{\text{in}}}{1.10 \text{ MPa}\sqrt{\text{m}}} \right) = 4.55 \text{ ksi}\sqrt{\text{in}}$

energy

1 erg	=	0.0000001 (1×10^{-7}) J (Joule)
1 ft-lbf (foot pound force)	=	1.355 J

energy/area

erg/cm ²	=	.001 J/m ²
---------------------	---	-----------------------

Length on Photos

1 mm	=	1 micrometer on a 1000X photo
------	---	-------------------------------

* Not an official SI unit, but included here for completeness.

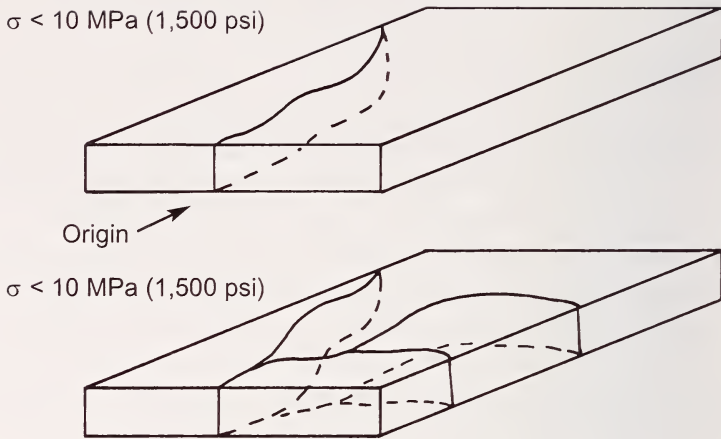


Figure 7.1 Schematic of thermal fractures of windows. Low stress fractures ($\sigma < 10$ MPa, 1,500 psi) do not cause branching. (After Fréchette¹ and Orr²)

7.2 Stresses from the Extent of Fragmentation

7.2.1 Annealed parts

A general assessment of stress levels can be made from the fracture pattern. Low stressed parts break into only two pieces. Fréchette¹ and Orr² and have suggested that 10 MPa (1,500 psi) is a threshold stress level for branching and fragmentation in glass as illustrated in Figure 7.1. Additional fragmentation occurs with increasing stress in the part, or increasing stored elastic energy. Very highly-stressed parts fragment to such a degree that laypersons are apt to describe the fracture as an “explosion.” Retrieval of the two fragments with the fracture origin may be problematic.

Fréchette and his students³ have shown fragmentation correlations with internal pressure as shown in Figure 7.2. They did similar analyses for impact velocity for impacted bottles.⁴ While their work may have been specific to certain bottle types and shapes, similar testing could be done with alternative shapes and sizes to aid in the failure analysis of new service failures.

Figure 7.3 shows how the fragmentation of ring-on-ring (32 mm and 64 mm diameters) tested glass disks (5.4 mm thick) can be correlated to fracture stress. Figure 4.13 showed examples of such test specimens and their breakage patterns. Fragmentation in Figure 7.3 was quantified by the number of radial cracks that reached the outer rim. Morrell showed a very similar graph for the

number of fragments as a function of stress in ring-on-ring tests of high purity alumina.⁵ Graphs such as these are very specific to specimen or component size, shape, and material.

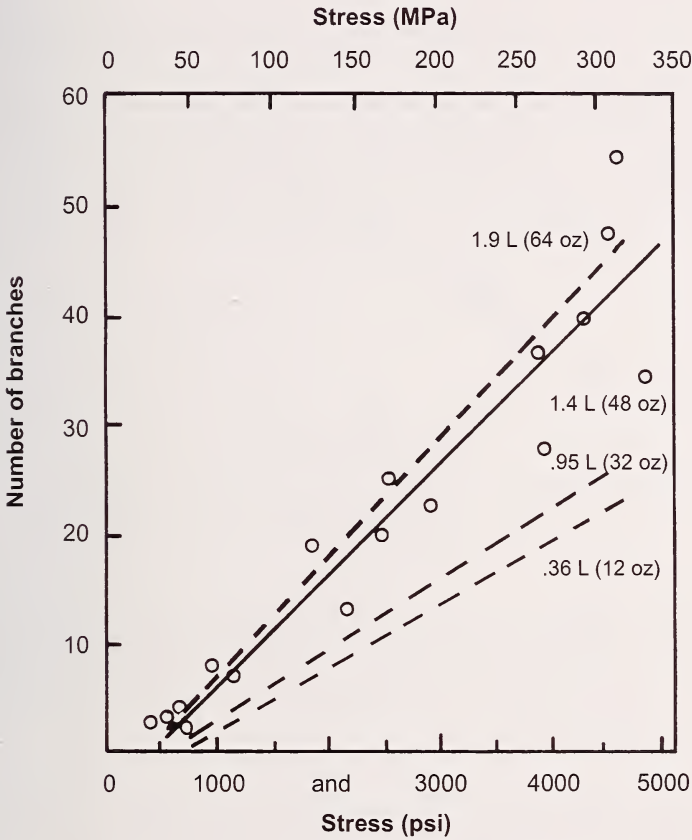


Figure 7.2 Fragmentation of internally pressurized bottles. The number of mature branches (fully developed that extend more than 13 mm beyond the first fork) are shown versus the hoop stress in the glass wall for four different sized glass containers. Data points and a solid line are shown for the 1.4 L (48 oz) bottles. Dotted lines show only the trends for the three other sizes. Some of the scatter is due to variations in the glass wall thickness. (After Fréchette and Michalske, Ref. 3)

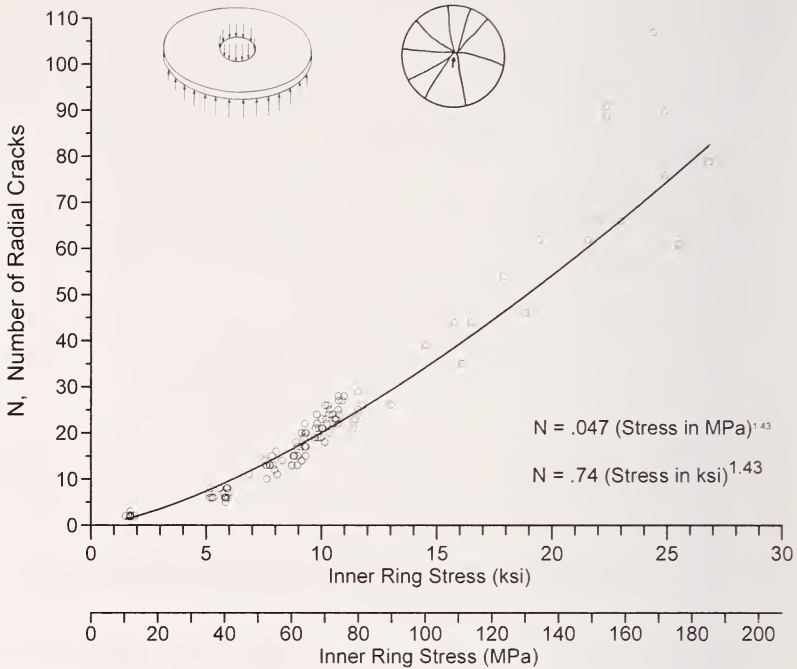


Figure 7.3 The number of radial cracks that reach the outer rim as a function of fracture stress for 76 mm diameter by 5.4 mm thick borosilicate crown glass disk broken in ring-on-ring flexure. Data were used only for fractures that initiated inside the inner loading ring.

Figure 7.3 was actually used to analyze an unexpected fracture. A similar glass disk was impacted by a hailstone that was intended to weaken the disk by creating surface damage that could be assessed in a subsequent strength test. The hailstone unexpectedly fractured the disk. The fragments were recovered and reassembled and the origin determined to be an ordinary polishing scratch on the surface opposite the impacted side. The hailstone diameter (25 mm) was similar to the inner ring diameter from the strength test set. From the number of radial cracks, the stress at failure was estimated. The estimate matched the dynamic stress estimated from an impact stress analysis, thereby confirming that the impact indeed had imparted sufficient energy to flex the disk to fracture from the ordinary surface flaw.

Often, the fractographer simply makes a qualitative stress assessment with a cursory examination. This is often sufficient for a diagnosis. For example, if a fracture occurs at an unexpectedly low stress, the fractographer might search for an unexpectedly large flaw in the component or specimen. A handling or preparation flaw may have weakened it to an unexpected level.

7.2.2 Fragmentation of tempered parts

McMaster et al.⁶ state that the most common method of inferring stress levels in tempered glass is by breaking it. They and Shinkai⁷ cite work by Akeyoshi,⁸ wherein 10 cm square tempered plates of various thickness were broken by sharp impact. The number of fragments in a 5 cm square region correlated to the internal tension temper stress as shown in Figure 7.4. For a

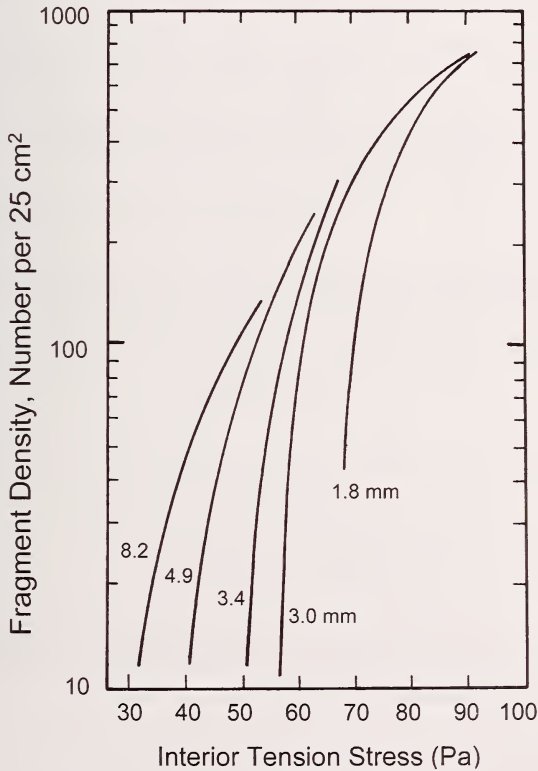


Figure 7.4 The interior tension stress in tempered soda lime glass plates may be estimated from the fragment density when the plate is broken. Each line corresponds to the plate thickness shown. (After Akeyoshi et al., Ref. 8)

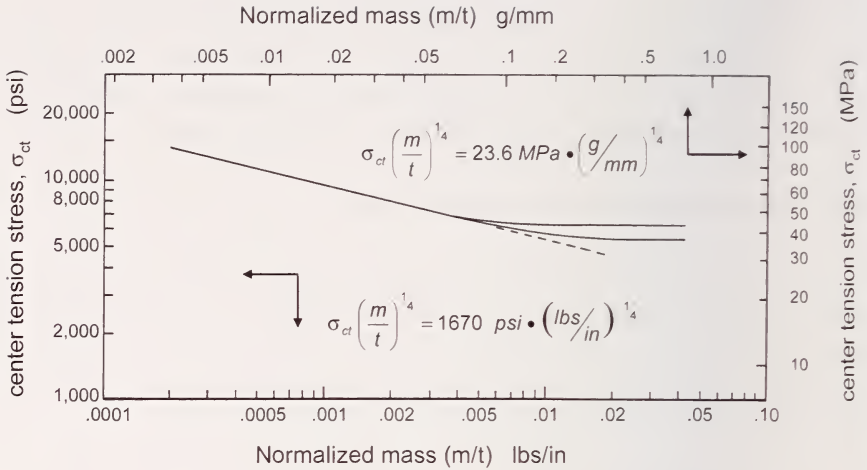


Figure 7.5 The interior tension stress in tempered soda lime sheet and plate glass may be estimated from the average fragment mass. Center tension stress is plotted versus mass normalized by the plate thickness, t . Data for five different thickness plates and sheets from 3.2 mm to 9.5 mm (1/8 in to 3/8 in) fall on the same curve. (After Barsom, ref. 9)

particular thickness plate, the data suggests there is a minimum temper stress to cause dicing. Of course, other means of assessing temper stresses are available, including polarimeter inspections and use of the stress optical coefficient, but in this Guide we are concerned with fractographic techniques.

Barsom⁹ showed that interior tension stress σ_{ct} was related to the fragment mass:

$$\sigma_{ct} \left(\frac{m}{t} \right)^{1/4} = \text{constant} \tag{7.1}$$

where m is the fragment weight (mass), t is the plate thickness. The constant has units of stress \cdot (mass/thickness)^{1/4}.

It should be borne in mind that these relationships and trends are altered if there are significant *externally* applied stresses superimposed on the temper stresses.

The fractographer should be on the lookout for irregular breakage patterns and fragment sizes that are signs of nonuniform temper stresses. Fréchette¹ showed two examples. In one case a glass cylinder was not tempered uniformly during the fabrication process (his case 10.18). A second case (his 10.22) featured a high-powered lamp that cracked spontaneously as a result of heating in service. The fragments were atypically large in the fracture origin area, but elsewhere the normal dicing fragmentation pattern was observed. Fréchette concluded that the intense heating in service caused the middle of the lamp to lose its temper. It is commonly assumed that the residual stresses are symmetric through the thickness as shown in Figure 5.17, but Menník¹⁰ illustrated the effects of asymmetric tempering of plates on the final stress distributions. Different residual compression stresses could exist on the two plate surfaces. There may even be a net tensile stress on one surface.

7.3 Stresses from the Branching Distances

7.3.1 Annealed plates and bars

The stress at fracture is related to the branching distance away from the origin by:

$$\sigma\sqrt{R_b} = A_b \quad 7.2$$

where σ is the stress, R_b is the branching radius, and A_b is a constant called the fracture branching constant. It has units of stress $\sqrt{\text{length}}$. These units are the same as for stress intensity which is described in section 7.5. The relationship between A_b and fracture toughness is discussed in 7.5.5. A similar relationship applies to mirror sizes as will be discussed in section 7.4. Rearranging shows that the branching distance is inversely dependent upon the square of the stress:

$$R_b = \left(\frac{A_b}{\sigma} \right)^2 \quad 7.3$$

This empirical relationship has been found to apply to uniaxially stressed parts such as a tensile strength specimen or a component with tensile stresses primarily in one direction. The relationship also can be applied to bend bars or components loaded in bending provided that the branching distance is measured along the surface where the tensile stresses are a maximum. The relationship

also may apply to biaxially stressed parts such as a ring-on-ring strength test disk or pressurized windows or bottles, again using matching lengths and stresses.

The term A_b may not necessarily be a material constant. It certainly does depend upon the material properties, but there is evidence that stress state and component geometry may affect it too. A_b is always greater than the fracture mirror constant that is described later in this chapter. Branching distances in biaxially-stressed parts may be less than the distances in uniaxially-stressed parts. Shetty et al.¹¹ showed that branching can occur just beyond the mirror in highly stressed, biaxially loaded disks. Hull¹² suggested that the cross section thickness of a component might influence when branching occurs. Branching A_b values are tabulated in Appendix C. Very few values are available, since most investigators have focused on fracture mirror constants instead.

The branching angle can at least be a qualitative indicator of the stress state as shown in Figure 4.4 in chapter 4. The branch angle is actually variable and curves at the exact branching location. It is recommended that the branching angle be measured close to but somewhat away from the splitting juncture, at a point where the branching angle has settled into a more or less constant value.

7.3.2 Tempered Plates

Figure 7.6 shows an interesting approach suggested by Soltesz et al.¹³ to estimate temper stresses in tempered glass plates. The lengths of the first and second branches can be correlated to internal temper stresses.

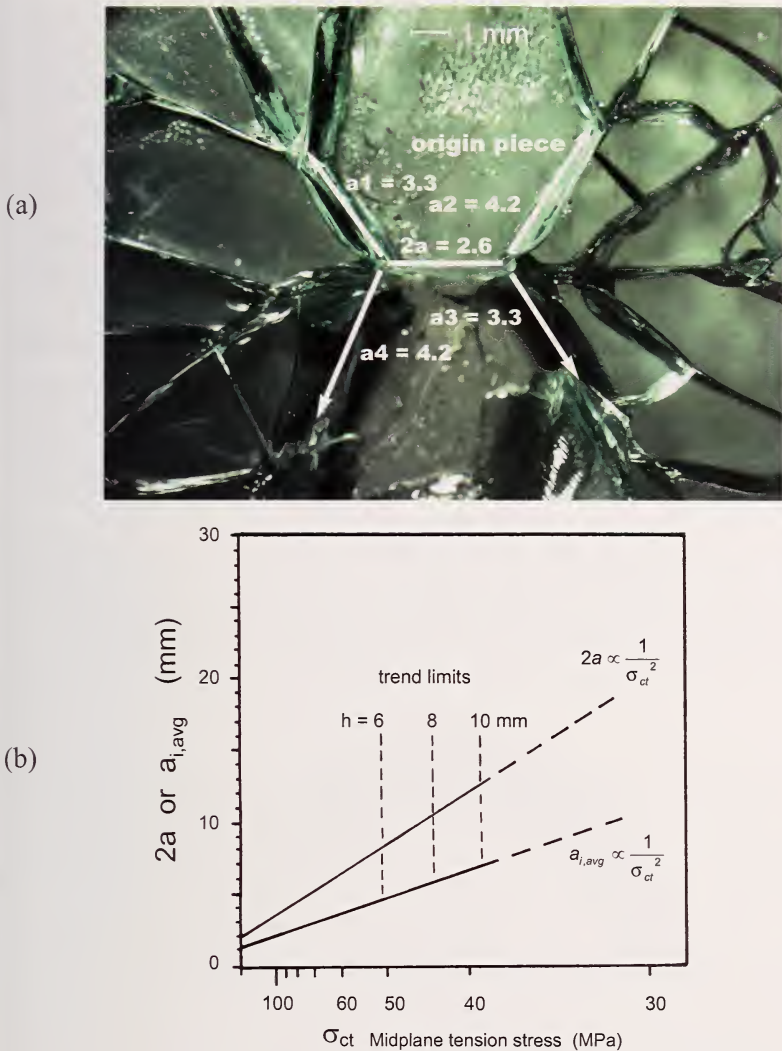


Figure 7.6 Branch distances in tempered glass may be used to estimate internal tension stresses. (a) shows an example from a 3.3 mm thick tempered automobile window. The initial branch - crack run is $2a = 2.6$ mm. The lengths of the first four branches (not including the segments that ran straight from the initial crack) are also labeled. (b) shows the initial branch distance $2a$ and the average first branch distance $a_{i,avg}$ versus the center tension stress respectively for 6 mm to 10 mm thick plates. All dimensions are in mm. Limits to the trends for different thickness plates are shown by the dashed vertical lines. Data to the right of these limits at low stresses has high scatter. (b is after Soltesz et al., Ref. 13)

7.4 Stresses from the Mirror Size

7.4.1 Mirror analysis and constants

The fracture mirror size is related to the stress at the origin. Orr's empirical mirror size relationship is:

$$\sigma \sqrt{R} = A \quad (7.4)$$

where σ is the tensile stress at the origin at the instant of fracture, R is the mirror radius, and A is the "mirror constant" with units of stress intensity ($\text{MPa}\sqrt{\text{m}}$ or $\text{ksi}\sqrt{\text{in}}$) and is considered by most as a material property. Figure 7.7 shows more details of a mirror centered on a surface flaw. This rendition also depicts the prospect that the initial flaw might grow somewhat before going critical.

Leighton Orr of the Pittsburg Plate Glass (PPG) Company was the first to systematically use equation 7.4 with the square root dependence of mirror size to solve glass fracture problems as far back as the 1940s.^{2,14,15} Johnson and

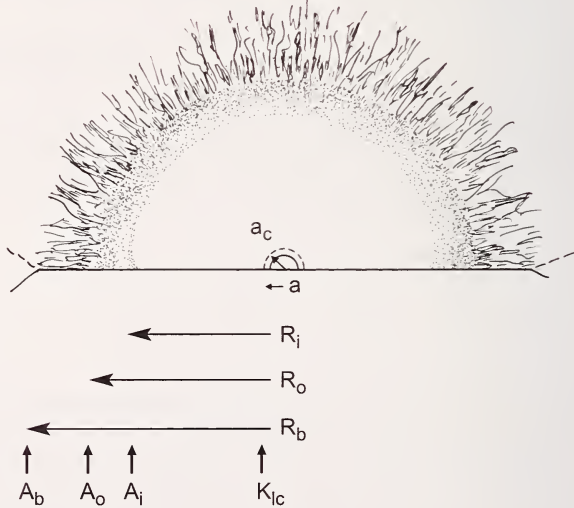


Figure 7.7 Fracture mirror schematic. An initial flaw of size "a" may go critical without any prior extension or it may grow to size a_c . R_i is the inner or mirror-mist boundary, R_o is the mist-hackle boundary, and R_b is the branching distance. The fracture toughness K_{Ic} (discussed in section 7.5.1), the mirror constants A_i and A_o and the branching constant A_b correspond to each of these boundaries. All have units of stress $\sqrt{\text{length}}$.

Holloway in 1966¹⁶ offered a physical interpretation of the relationship based on the energetics of crack propagation. Levengood,¹⁵ Shand,²⁰ Kerper and Scuderi,^{18,19} and later Kirchner et al.²⁰ gave credit to Orr for equation 7.4. Orr did not publish his findings until he retired in 1972,² but discussed his empirical equation at a Glass Division meeting of the American Ceramic Society in Bedford, PA in September 1955.²¹ Orr told this author in 2001¹⁴ that equation 2 had been extensively used for glass fracture analysis at PPG in the 1940s. In the 1950s and 1960s, many people used a general form of equation 7.4 with the mirror size raised to an arbitrary power. Shand's 1954 and 1959 papers^{17,22} presented an early argument for the $1/2$ power based on stress concentrations at the tip of a sharp crack. These two papers incorporated elements of what become known later as fracture mechanics. Kerper and Scuderi^{18,19} at the National Bureau of Standards in Washington performed meticulous experiments on hundreds of glass laths and rods and showed conclusive evidence that Orr's equation was applicable over a broad range of specimen and mirror sizes. Some have credited Terao²³ with equation 7.4, but a careful reading of his paper fails to back the claim since it shows an exponential form relating mirror size to stress instead. So, although many associate equation 7.4 with Johnson and Holloway¹⁶ in 1966, the relationship had already been in use by Orr for 20 years.

The practical significance of equation 7.4 is that the mirror radius may be measured from a fracture surface, the mirror constant found from a data table, and then the origin stress calculated. The calculated stress is the net tensile stress acting on the flaw and the region around the flaw. It may include several stress sources including mechanical, thermal, and residual stresses. It is possible to discern separate mirror-mist and mist-hackle boundaries in glasses and each has a corresponding mirror constant A . The most common notation is to refer to the mirror-mist boundary as the *inner* mirror boundary and the corresponding mirror constant is designated A_i . The mist-hackle boundary is referred to as the *outer* mirror and the corresponding mirror constant is designated A_o . The mirror-mist boundary is usually not perceivable in polycrystalline ceramics and only the mirror-hackle boundary is usually measured.

At this point it is appropriate to reiterate that equation 7.4 is empirical. In chapter 5, it was noted that there were competing models to account for the mirror formation. Kirchner and colleagues^{24,25} presented compelling evidence that a fracture mechanics criterion based on a critical stress intensity (described later in section 7.5) gives the best fit to data and the exact shape of mirrors in various stress fields. A crucial observation is that the stress intensity model fully accounts for the small inward facing cusp at specimen surfaces

(Figures 5.2 and 7.7), whereas the other models do not. Kirchner et al. argued^{24,25} that a more fundamental material parameter might be K_{IB} , the stress intensity factor at branching, rather than the A 's in equation 7.4 since the latter do not take into account the free surface, geometry factors, and non-uniform stress gradients over the crack surface. There is validity to their argument, but in practice the ease of use of 7.4 has led to its widespread adoption. (The size and shape predictions based on A or K_{IB} match very closely for the limiting cases of small mirrors in tension specimens. This is also true for most of the periphery of small semicircular mirrors centered on surface flaws in strong tension or flexure specimens.)

The accuracy of the stress estimate varies depending upon the material, the experience of the fractographer, the microscopy and illumination used, and component geometry and stress gradient effects. Stress estimates may be accurate to within $\approx 10\%$ with glasses if they form ideal fracture mirrors.

Kirchner and Gruver²⁶ also showed that the relationship holds for elevated temperature fractures in ceramics. The mirror constant was invariant from room temperature to 1400 °C for a hot-pressed alumina with a 1 μm grain size. This is a remarkable finding since the alumina was fired at 1475 °C. Kerper and Scuderi also showed that mirror constants were unaffected by elevated temperature for eight glasses.²⁷

As noted in section 7.3.1, crack branching distances also seem to follow the same trend and crack branching constants A_b have sometimes been reported. The three boundaries correspond to an expanding crack front, and hence, $A_i < A_o < A_b$. Appendix C has a comprehensive compilation of fracture mirror and branching constants. The table shows there is some variability in the published mirror constants, even for model materials such as fused silica or soda lime silica. Some of this is due to the aforementioned metrology and judgment issues, but much of it is due to genuine material-to-material variability. Thus, one should not expect all silicon nitrides or aluminas to have the same mirror constants. Microstructural differences can change the mirror constants considerably.

The word "boundary" must be used with some caution. It is now clear from a number of studies that there probably is not a discrete or sudden transition point on the fracture surface corresponding to a mirror boundary. The mode of viewing and magnification affects the judgment of the boundaries location. The higher the magnification the smaller the mirror seems to be, since fine detail that was washed out or not resolvable at lower power can be discerned at higher power. The mirror-mist boundary probably corresponds to surface

roughness features that are of the order of $0.1\ \mu\text{m}$ to $0.2\ \mu\text{m}$, which is a fraction of the wavelength of light and at the threshold of observable features with an optical microscope. Section D.3 in Appendix D has a discussion of several studies that have used various surface roughness measurement methods to measure mirrors, but these methods have yielded different results.

So, although there is some variability in how different observers judge and measure fracture mirror sizes, most fractographers agree that there is a mirror. Size estimates can vary depending upon the type of microscope used, the mode of illumination, the objective power of the lens, and the judgment criteria of the fractographer. The next section gives a brief outline of how to measure fracture mirror sizes. Very detailed guidelines are presented in Appendix D. The guidelines are intended to bring some consistency to procedures and to improve the precision of the measurements.

7.4.2 How to measure mirror sizes

In principal, a mirror size measurement is a straightforward exercise, but in practice it is not as easy as one would think even with glasses. In addition to the boundary interpretation issue discussed above, component geometry effects, gradients in the stress fields, residual stresses, and origin flaw effects can all contribute to mirror distortions. Most investigators use simple, common sense approaches such as measuring a few mirror radii from the origin. Some have suggested more elaborate schemes. Appendix D has a specific set of instructions on how to measure fracture mirrors. The boundary criteria are:

The mirror-mist boundary in *glasses* is the periphery where one can discern the onset of mist. This boundary corresponds to A_i , the inner mirror constant.

The mist-hackle boundary in *glasses* is the periphery where one can discern the onset of systematic hackle. This boundary corresponds to A_o , the outer mirror constant.

The mirror-hackle boundary in *polycrystalline ceramics* is the periphery where one can discern the onset of systematic new hackle, and there is an obvious roughness change relative to that inside the mirror region. This boundary corresponds to A_o , the outer mirror constant. Ignore premature hackle and/or isolated steps from microstructural irregularities in the mirror or from irregularities at the origin.

Figure 7.8 shows an example in a moderately difficult-to-judge ceramic. The yttria-stabilized zirconia is a difficult to interpret since, although it has a very

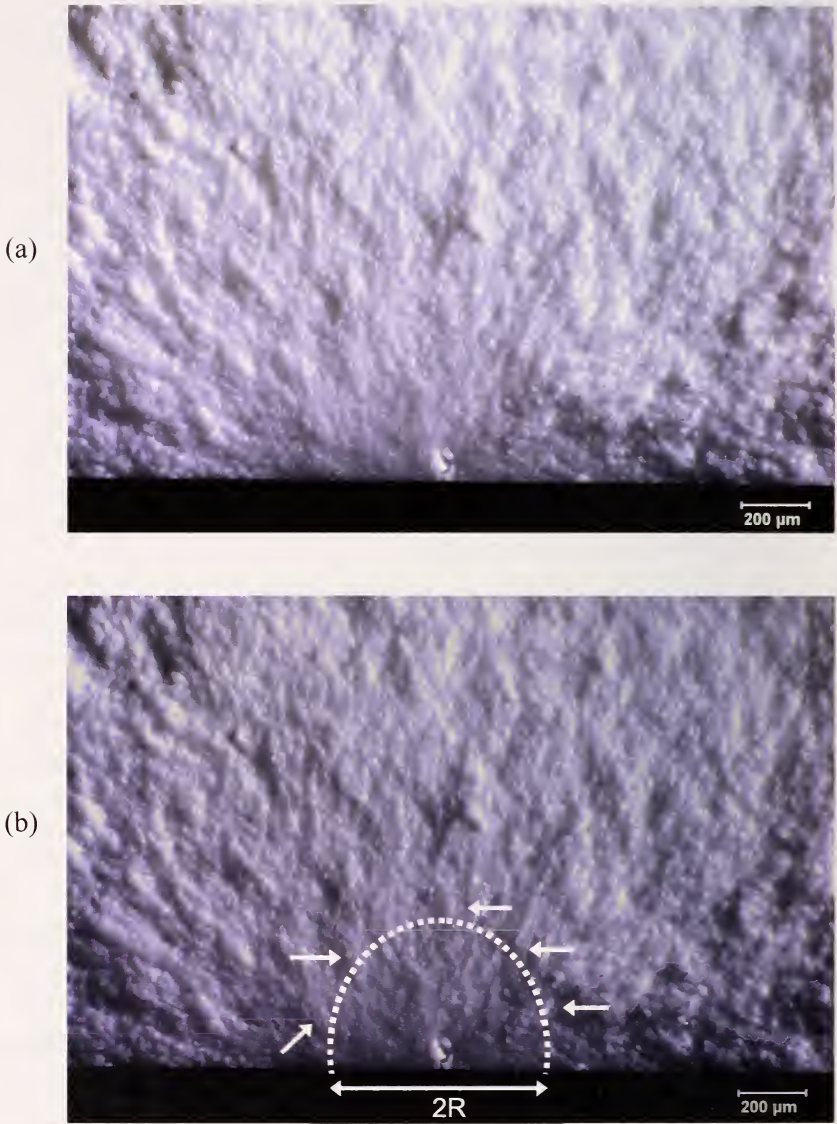


Figure 7.8 Example of a mirror in a ceramic material that is difficult to precisely measure. This is one of the specimens of the 3Y-TZP for the data in Figure 7.11 below. (a) shows the uncoated fracture surface of a 2.8 mm thick bend bar with vicinal illumination (486 MPa). (b) shows an interpretation for a mirror-hackle boundary whereby new hackle is detected (small white arrows) as compared to the roughness inside the mirror: The mirror is slightly elongated into the interior due to the stress gradient. Judgments are best made while viewing the surface through a microscope.

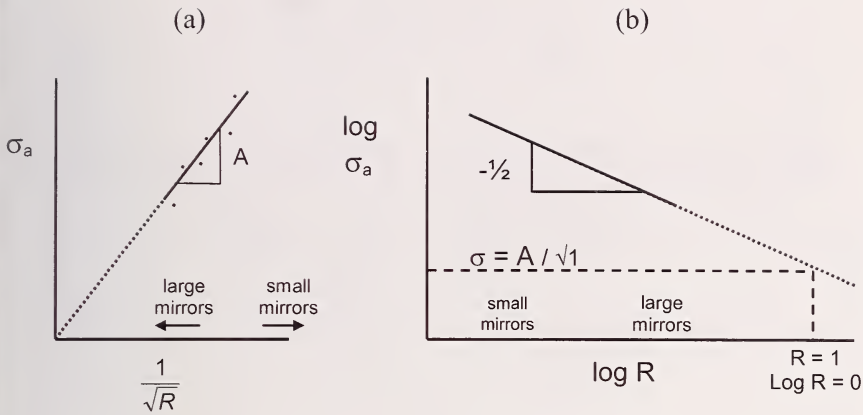


Figure 7.9 Stress and mirror size graphs. (a) shows the preferred graph of applied stress, σ_a , versus inverse square root of mirror radius. The mirror constant is the slope of the line. (b) shows $\log \sigma_a$ versus \log radius as commonly used in the older literature. The mirror constant corresponds to the applied stress necessary to create a mirror of unit radius since $\sigma\sqrt{1} = A$

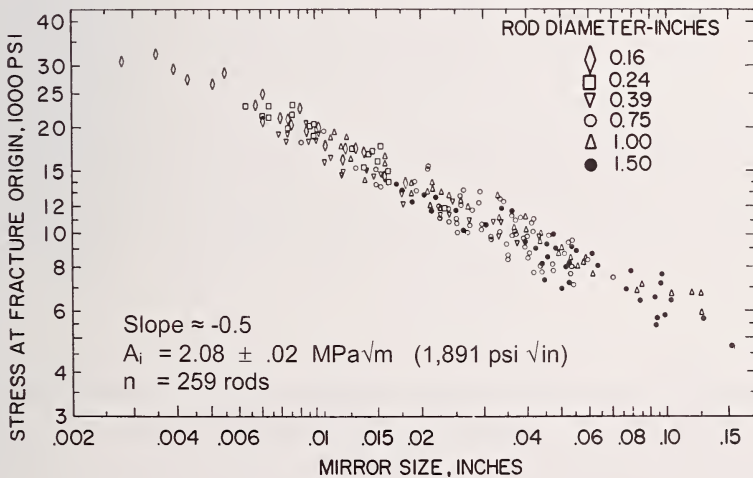


Figure 7.10 A splendid example of fracture mirror-stress correlation for glass rods of a wide variety of sizes and strengths. Two hundred and fifty nine Pyrex 7740 rods that varied in size by almost a factor of ten (4.1 mm to 38.1 mm) were broken in three-point flexure by Kerper and Scuderi.¹⁹ All data fit the same trend. This figure is from the original reference.

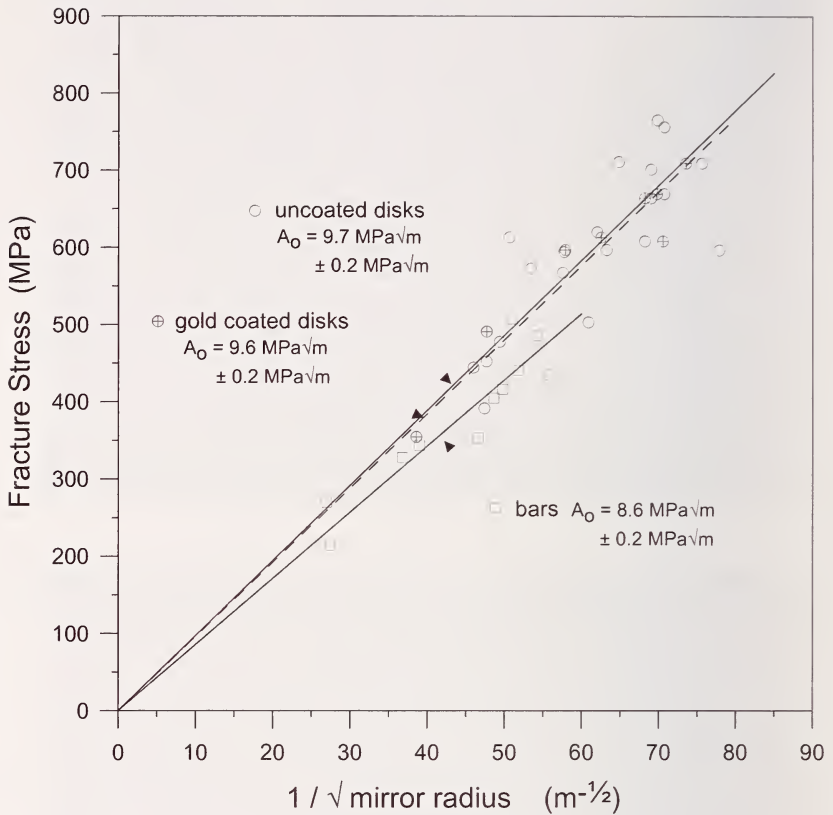


Figure 7.11 Fracture mirror size data for a 3 mol % yttria-stabilized tetragonal zirconia (3Y-TZP) from Ref. 28. Figure 7.9 shows one of the mirrors. Figure 3.20 shows a mirror both coated and uncoated. The bend bars produced had a smaller mirror constant, either due to a geometric effect or simply the scatter in the data.

fine grain size ($< 0.5 \mu\text{m}$), it has a gradual progression of roughness from well within the mirror to the obvious hackle region far from the origin. Keeping in mind the criteria for polycrystalline ceramics above, the first step is to look at a region well *within* the mirror and note the typical, *inherent* roughness due to the microstructure. The next step is to observe the obvious new hackle that is greater in magnitude than anything in the relatively smooth mirror region.

Figure 7.9 shows the two most common graph types that are used to show stress - mirror size relationships. The merits of each approach are discussed in Appendix D. This Guide recommends the use of stress versus $1/\sqrt{R}$.

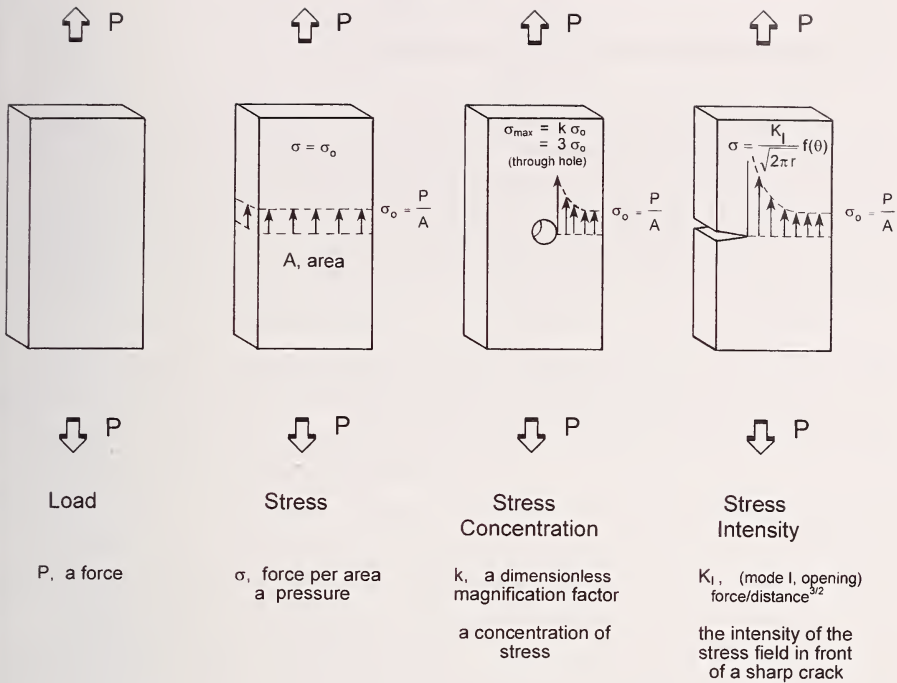


Figure 7.12 The effect of load upon a material. Only a single force P is shown for simplicity. (a) force P acting upon the object. Fracture occurs at a critical force that depends upon the material properties and the object's size. (b) stress is the force normalized by the cross sectional area. (c) discontinuities such as a thorough hole **concentrate** stress and magnify it in the vicinity of the discontinuity. (d) **sharp** discontinuities such as cracks **intensify** the stress field in front of the discontinuity.

Two examples of mirror analysis are shown in Figures 7.10 and 7.11. The glass data in Figure 7.10 is extraordinary since the mirror size range is almost a factor of 100. Figure 7.11 shows that measurements on uncoated and gold coated 3Y-TZP specimens concurred. This was gratifying since the uncoated specimens were difficult to interpret due to material translucency and difficulty in judging a boundary. Not surprisingly, the data scatter was greater for the uncoated specimens. More examples of marked fracture mirrors are shown in Appendix D. Appendix D explains in detail how residual stresses, stress gradients, the origin flaws, and microstructure can affect mirror sizes and shapes.

7.5 Fracture Mechanics Analysis of the Flaw Size

7.5.1 Introduction to fracture mechanics

Fracture mechanics is a powerful analytical tool to aid the fractographer. It can be used to estimate critical flaw sizes and can help determine whether a flaw the fractographer has detected is of appropriate size to cause fracture. It can also be used to estimate the stress in a fractured part. A short introduction of fracture mechanics fundamentals is presented below followed by some practical examples.

Figure 7.10 shows a hypothetical “brick” loaded in tension. A force P may or may not cause breakage depending upon the size and shape of the brick and the material properties. Load divided by the area carrying the load is known as stress. The stress is constant across the cross section throughout the brick in this simple example. Real engineering structures usually have stress variations or gradients and the stresses are magnified or concentrated in the vicinity of geometric discontinuities. So, for example, the through hole shown in the Figure 7.10c concentrates stresses at the side of the hole since “flow lines of stress” are diverted around the hole. Stress concentrations are dimensionless magnification factors usually designated by lower case letter k . For the case of a through hole, $k = 3$, meaning that in the immediate vicinity of the hole, the stress is three times the nominal stress elsewhere in the body. The above conventional analysis is well known to all mechanical engineers. Simple structures may be analyzed by the so-called “strength of materials” analysis, wherein assumptions about the structure (e.g., cross section plane sections remain plane, deflections are small, the structure remains elastic to fracture) lend themselves to simplified analysis. The maximum stress in three- or four-point beams in bending may be readily derived from “simple beam theory” a subset of the strength of materials analysis. More elaborate analyses that are not limited by the simplifying assumptions may be solved by the “theory of elasticity” or by computer analysis using the “finite element analysis” (FEA).

The local stress conditions in the vicinity of sharp discontinuities such as cracks cannot be adequately modeled using the strength of materials analyses. Stress concentration analyses lead to estimates of infinite stress at crack tips. Fracture mechanics is a discipline that deals with the stresses and strains around sharp flaws and has as its roots the 1920s work of Griffith.^{29,30} He showed that the strength of a brittle material with an slender elliptical flaw through crack of size $2c$ in a uniformly stressed plate as shown in Figure 7.13 is:

$$\sigma_f = \sqrt{\frac{2E\gamma_f}{\pi C}} \quad 7.5$$

where γ_f is the fracture stress (the nominal stress in the plate), E is the elastic modulus, and γ_f is the fracture energy that is the energy to create unit surface area. In this Guide, flaw size is denoted as either “a” or “c” following conventional practice in the fracture mechanics literature. Usually the dimensions are the radius or half width as shown in Figure 7.13a. The critical feature of this relationship is that strength is inversely proportional to the square root of flaw size. The larger the flaw, the weaker is the structure. Griffith’s formula was derived on the premise that crack propagation occurs if the elastic strain energy release in a body is greater than the creation of surface energy due to the new surfaces if the crack were to extend. His formula sets a necessary condition for a decrease in overall energy of the system.

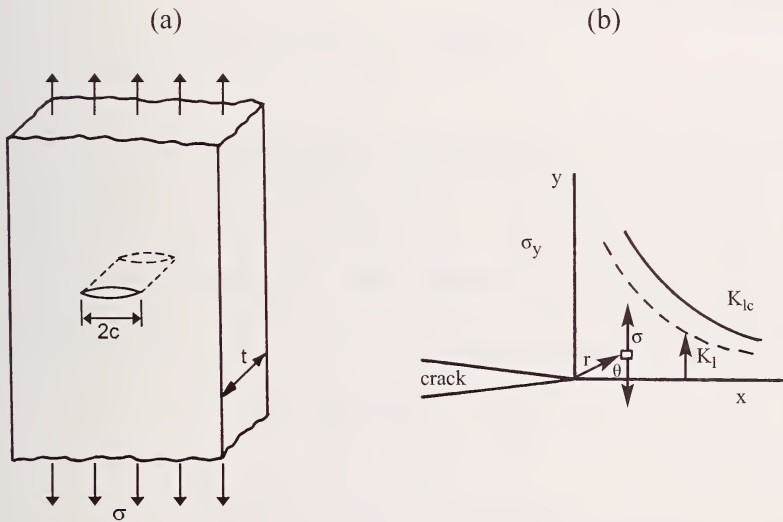


Figure 7.13 Through crack in a plate loaded in tension (a). Long slender elliptical cracks of this type were envisioned by Griffith as flaws. If the crack tips are atomically sharp, fracture mechanics developed by Irwin³¹ in the 1950s must be used to model the stress state in the immediate vicinity for the crack tip as shown in (b). The dashed line shows σ_y directly in front of the crack tip for $y = 0$. The stress intensity K_I quantifies the magnitude of the stress field acting to open up the crack tip. K_I depends upon the far field stress and the geometry of the crack and the structure. Fracture occurs when the intensity of the stress field reaches a limiting value, K_{Ic} , known as the critical fracture toughness, mode I.

Many flaws are atomically sharp and fracture mechanics analyses developed by Irwin in the 1950s are applicable.³¹ This approach analyses the stress field in front of a crack tip. The intensity of the field is quantified by the term K_I , which is called the “stress intensity factor, mode I.” Mode I means the opening mode, whereby the crack faces are pulled directly apart. This mode is of primary concern for most ceramic and glass failures. As figures 7.12 and 7.13 show, the intensity of the stress field in front of the crack tip is proportional to K_I . The flaw will propagate when the stress intensity reaches a critical condition, K_{Ic} . Loading conditions often are such that the extension is sudden and unstable causing fracture. K_{Ic} is called the critical stress intensity factor, Mode I, or more briefly, *fracture toughness*. For a small flaw in a body loaded in tension, σ , the stress intensity acting on the flaw is:

$$K_I = Y \sigma \sqrt{c} \quad 7.6$$

and fracture occurs when:

$$K_{Ic} = Y \sigma_f \sqrt{c} \quad 7.7$$

Y is the stress intensity shape factor, which is a dimensionless parameter that takes into account the shape of the crack and the loading conditions and σ_f is the stress at fracture. In this Guide, Y combines all geometric terms. Examples of Y will be shown below. Fracture occurs when any combination of Y , σ , or c leads to the critical condition. Note that the stress and flaw size dependencies are the same as the Griffith equation. Indeed, it can be shown that the energy and stress intensity approaches are consistent, and for plane strain loading conditions:

$$K_{Ic} = \sqrt{\frac{2E\gamma_f}{(1-\nu^2)}} \quad 7.8$$

Sometimes the fracture mechanics literature uses a related term, G_{Ic} , the critical strain energy release rate. For plane strain conditions, it is simply related to K_{Ic} by:

$$K_{Ic} = \sqrt{\frac{EG_{Ic}}{(1-\nu^2)}} \quad 7.9$$

and $G_{Ic} = 2\gamma_f$. The ceramics and glass technical literature of the 1960s and early 1970s used analyses based on γ_f and the Griffith equation, but few flaws have a simple through-plate elliptical shape. Fracture mechanics analysis based upon stress intensity K_I is more versatile and can model many more complex-shaped cracks. It became more common in the 1970s and is dominant today.

Fracture toughness, K_{Ic} , is an important material property that characterizes a material's intrinsic resistance to fracture. It has units of stress $\sqrt{\text{length}}$ and in SI units is expressed either as $\text{MPa}\sqrt{\text{m}}$ or $\text{MN}/\text{m}^{1.5}$. (The English system of units for fracture toughness is $\text{ksi}\sqrt{\text{in}}$ and the conversion factor to the SI units is only 1.1 as listed in table 7.1) Fracture energies are usually expressed as erg/cm^2 or as J/m^2 . Table 7.2 shows some approximate K_{Ic} values. It is much better, however, to use a value for a specific material, since fracture toughness depends strongly upon composition and microstructure. Figure 7.14 shows some crack-microstructure interactions that can affect crack propagation and hence the fracture toughness.

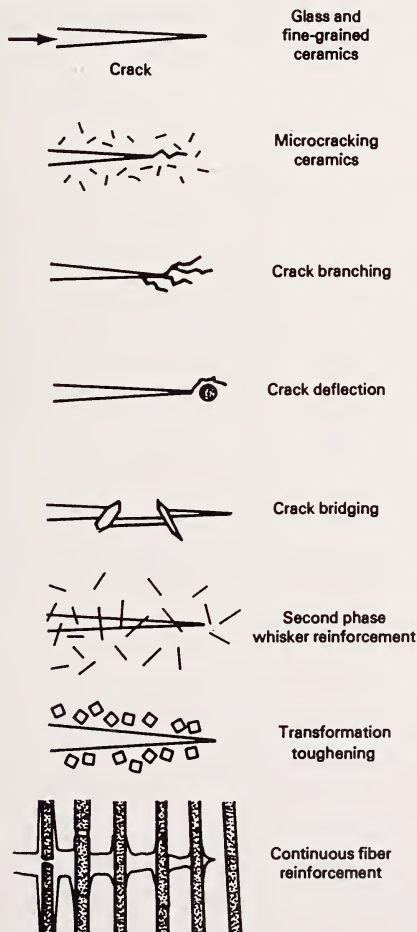


Figure 7.14 Crack interactions with microstructure.

Material	K_{Ic} MPa√m	R-curve?	SCG at room temperature?
Glasses	0.75 - 0.90	No, flat	Yes
Sintered fused silica	0.92	No	Yes
Glass ceramics	2.0 - 2.5	No	Yes
Mullite	2.2	?	?
Alumina, single crystal	2.4 to 4.5 different planes	No	Yes
Alumina (hot pressed or sintered, 99.9% pure, fine grained)	3.0 - 4.0	No	Yes
Alumina (sintered, glass bonded)	2.5 - 5.	No	Yes
Alumina (coarse grained)	3.0 - 5.0	Yes	Yes, especially if there is a glassy boundary phase
Boron carbide (hot pressed)	2.5	No, flat	No
Silicon carbide (solid state sintered)	2.5 - 3.0	No, flat	No
Silicon carbide (liquid phase sintered, elongated grains)	3. - 5.	Yes	Yes
Silicon nitride (equiaxed fine grained)	4.5	No	No
Silicon nitride (elon- gated grains, glassy boundary phase)	5. - 8.0	Yes	Yes
Zirconia, cubic stabilized	3.	No, flat	?
Zirconia, Mg partially stabilized	3. - 18	Yes	Yes
Zirconia, Y tetragonal zirconia polycrystal	4.5. - 5.0	No	Yes
Cast iron	37. - 45.	No	No

Table 7.2 Approximate fracture toughness, K_{Ic} values. Fractographers should obtain a more specific value for the material being examined whenever possible. See sections 5.9.1 and 7.10 for slow crack growth (SCG). See sections 5.9.2 and 7.11 for R-curves. The larger values are usually associated with materials that have rising R-curve behavior, described later in this chapter. If R-curve behavior is suspected for a material, it is best to use small crack fracture toughness in a flaw size calculation

Table 7.2 includes two columns that require explanation. The third column is for R-curve behavior whereby fracture resistance increases as a crack extends. This behavior is caused by several of the crack microstructure interactions shown in Figure 7.14 such as transformation toughening around a crack tip or bridging behind the crack tip. The fourth column is for “slow crack growth” which is a phenomenon whereby cracks grow stably at stress intensities less than K_{Ic} . Both of these phenomena are dependent upon the chemistry and microstructure. It is convenient to categorize materials according to Table 7.3. For now, the discussion will focus on the simplest combination in the top left box: a material that does not have slow crack growth and which has a flat R-curve. Such a material has a single value for fracture resistance, K_{Ic} . Many ceramics (e.g., solid state sintered silicon carbide and many fine grained materials) and all glasses if tested under inert atmosphere conditions fit this category.

Brittle (no R-curve) No SCG K_{Ic}	Brittle (No R-curve) SCG K-V (velocity) curves
Rising R-curve No SCG K_R - a curves	Rising R-curves and SCG K_R - a curves and K-V (velocity) curves

Table 7.3 The fracture resistance of ceramics and glasses may be categorized by whether the material does or does not exhibit slow crack growth (SCG) or rising R-curve behavior. (After Fuller, private communication.)

◆ Fractography of Ceramics and Glasses

Users should be cautioned that much fracture toughness data is unreliable, especially the data obtained from simple saw cut notched bend bars or Vickers indentation crack length methods. The former method almost always overestimates fracture toughness. Vickers indentation fracture toughness data are notoriously faulty. Reliable methods such as single-edged precracked beam, chevron notched beam, or surface crack in flexure, have been refined and standardized. International round robins and reference materials such as NIST Standard Reference Material, SRM 2100, have confirmed their reliability.³² Slow crack growth and R-curve behavior are important phenomena that add complications to fracture analysis, but for now we focus on a straightforward, simple application of equation 7.3 to aid fractographic analysis.

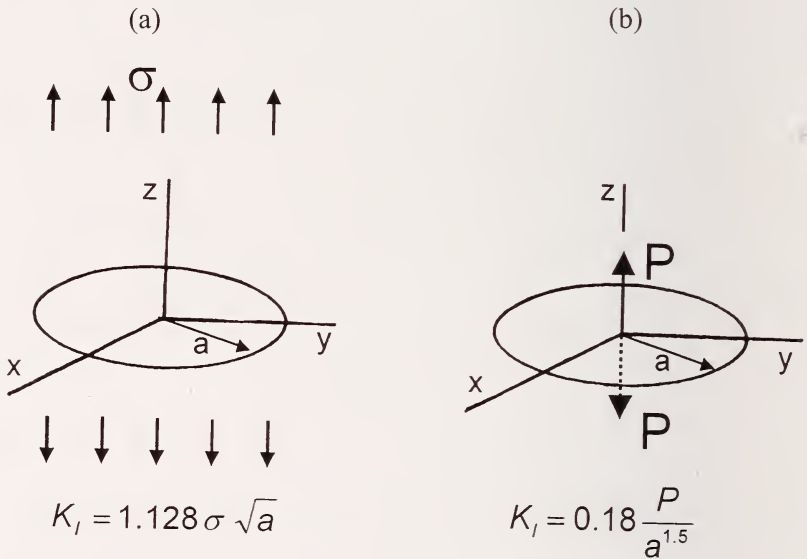


Figure 7.15 The stress intensity for penny-shaped circular cracks for two loading configurations. (The three-dimensional axes make the flaws appear elliptical in this view.) (a) shows a far-field tensile stress σ , and (b) shows opposed forces P pulling directly on the middle of the crack. K_I increases with crack size in (a), but decreases with crack size in case (b).

The stress intensity K_I on a flaw depends upon the flaw size and shape, the stress magnitude and distribution, and on the component size and shape. A remarkable variety of fracture crack shapes and loading configurations have been analyzed and the reference handbooks listed in Appendix A may be consulted for a specific problem. Figure 7.15 illustrates two examples. Figure 7.15a shows a penny-shaped circular flaw, which is a case that is commonly used to simulate internal flaws in ceramics. Equations 7.6 and 7.7 are applicable and the shape factor Y for this configuration is 1.128. Figure 7.15b shows a different loading configuration on the same flaw. This latter case (or more precisely the case for a semicircular surface flaw) is commonly used to represent the effect of concentrated residual indentation stresses from a Vickers indentation on a median crack flaw. Although both cases are for penny-shaped flaws, the nature of the loading leads to radically different K_I formulations.

Surface cracks can often be modeled by semi elliptical flaws as shown in Figure 7.16.

The flaw shape affects the Y factor. Y usually varies around the flaw periphery. A flaw goes critical when one portion of the flaw reaches K_{Ic} , so the maximum Y is of primary concern. The author has seen a number of instances where localized fractographic markings confirmed that fracture indeed had started at the portion of the flaw periphery that had the maximum Y . Figure 7.17 shows maximum shape factors for a variety of elliptical and semi elliptical flaws subjected to a far field tensile stress. In each instance, the flaw size for equation 7.2 is the *depth* for surface flaws, or the *half minor axis length* for internal cracks. Note that for comparably sized internal or surface flaws, the surface flaw has a greater Y factor because it has less supporting material in the vicinity to sustain force and its crack opening displacements are greater.

The model cracks shown in Figures 7.16 and 7.17 may be used with equation 7.6 for small flaws that cause fracture in ceramics and glasses. The equation has four variables: the far field tensile stress, σ ; the flaw size, a or c ; the shape factor, Y ; and the fracture toughness, K_{Ic} . This simple equation may be used in three different ways. Flaw size may be estimated if Y , σ , and K_{Ic} are known. This approach is very useful in laboratory testing, whereby specimens are broken under controlled conditions and break loads are used to compute failure stresses. Alternatively, if the flaw size and shape can be measured fractographically and the fracture toughness is known, the failure stress can be estimated. This approach is useful in estimating stresses in fractured components. Finally, if the flaw size and shape, and the stress are known, then the material's fracture toughness may be computed. Examples will be shown below, but first

◆ Fractography of Ceramics and Glasses

additional information about the flaw shape and stress gradients must be considered so that appropriate Y values may be estimated.

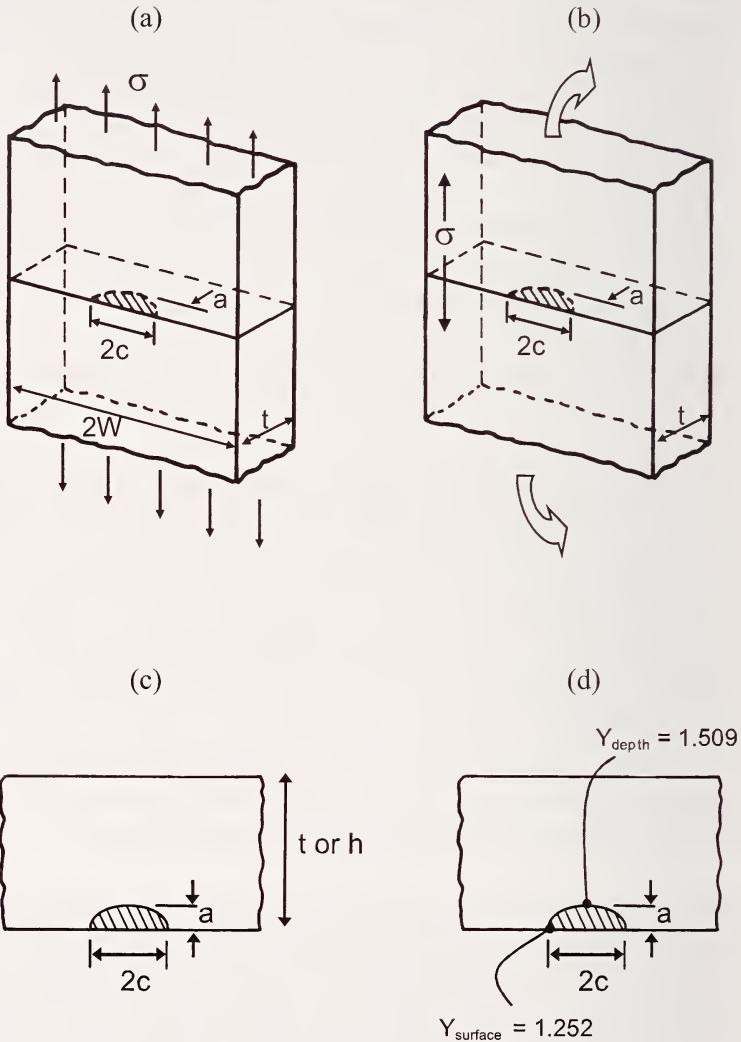


Figure 7.16 Surface cracks in plates or bars in far-field tension (a) or bending (b). The stress intensity factor equations by Newman and Raju³³ are applicable to these configurations. The Y factors for case (a) and (b) are the same for very shallow cracks, $a/t \approx 0$. (c) is a view of the cross section. (d) shows the same but labeled with the Y factors at two locations for the flaw dimensions given in table 7.1

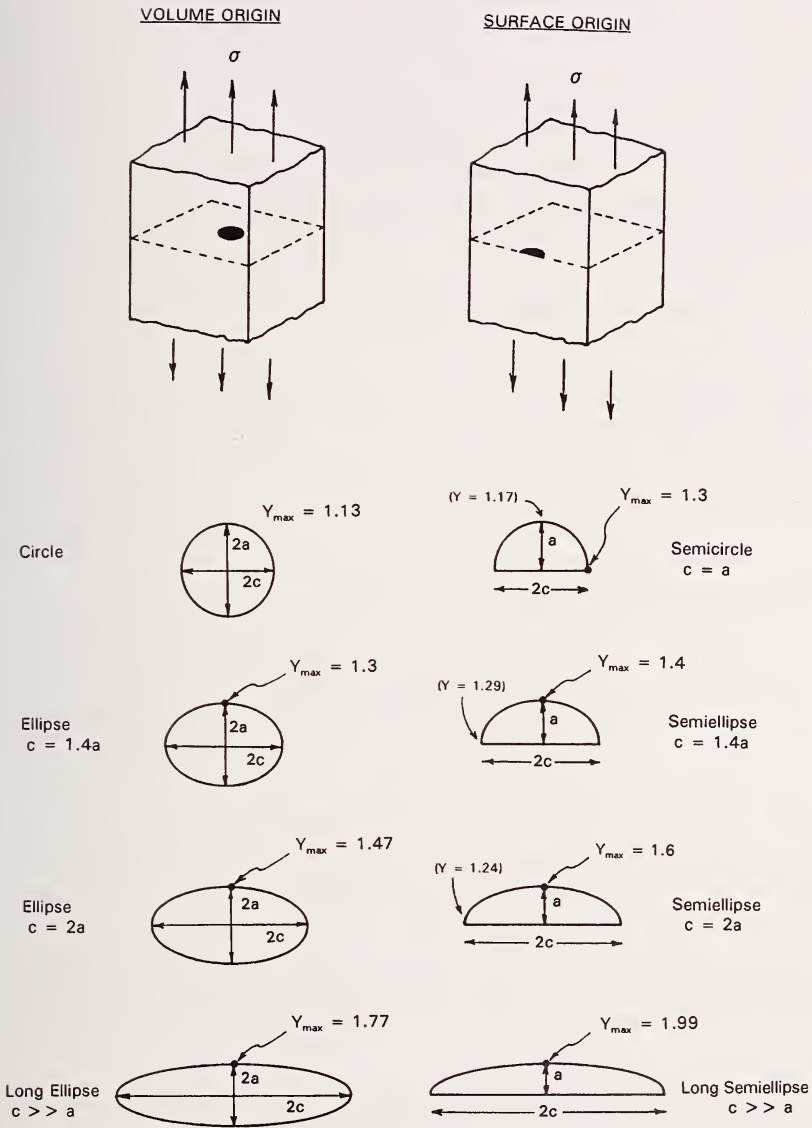


Figure 7.17 The stress intensity shape factors Y for surface and internal round and elliptical for internal (volume) cracks and surface cracks for far-field tension stresses. Minimum Y factors for the surface cracks are shown in parenthesis. The Y factors for the surface flaws may also be used for parts loaded in bending if the flaw depth a is small relative to the specimen thickness.

The reader should be forewarned that there is no consistency in the fracture mechanics and materials science literatures. Crack sizes are usually described by a, b, c, 2c, or other symbol, but sometimes these same symbols are used differently and sometimes they are even used for the component dimensions. Sometimes the Y factor includes π or a $\sqrt{\pi}$ term, but sometimes it does not. (One reference even uses Y as the inverse of how it is used everywhere else.) In this Guide, and in ASTM standards C 1322³⁴ for fractography and C 1421³⁵ for fracture toughness, all geometric terms for the stress intensity shape factor are combined into Y.

7.5.2 The Newman-Raju Y factors

Ceramics and glasses often have surface origins and the stress intensity factor solutions of Newman and Raju³³ for both tension and bending stress fields are very helpful. Their versatile solutions may be applied to tension, bend bar, and biaxial disk specimens, and indeed any component shape wherein a remote stress field causes fracture. With reference to Figure 7.16 for dimensions for surface flaws in a plate or beam in bending, the Y_{depth} and $Y_{surface}$ for locations at deepest part of the crack and at the surface are:

$$Y_{depth} = \frac{M}{\sqrt{Q}} * H_2 * \sqrt{\pi} \quad 7.10$$

$$Y_{surface} = S * \frac{M}{\sqrt{Q}} * H_1 * \sqrt{\pi} \quad 7.11$$

where M, Q, H2, H1, and S are geometric terms:

$$M = \left[1.13 - 0.09 \left(\frac{a}{c} \right) \right] + \left[\frac{0.89}{0.2 + \left(\frac{a}{c} \right)} \right] * \left(\frac{a}{h} \right)^2 + \left[0.5 - \frac{1}{0.65 + \left(\frac{a}{c} \right)} + 14 * \left(1 - \left(\frac{a}{c} \right) \right)^{24} \right] * \left(\frac{a}{h} \right)^4 \quad 7.12$$

$$H_1 = 1 - \left(0.34 + 0.11 \left(\frac{a}{c} \right) \right) * \left(\frac{a}{h} \right) \quad 7.13$$

$$H_2 = 1 - \left(1.22 + 0.12 \left(\frac{a}{c} \right) \right) * \left(\frac{a}{h} \right) + \left[0.55 - 1.05 \left(\frac{a}{c} \right)^{0.75} + 0.47 * \left(\frac{a}{c} \right)^{1.5} \right] * \left(\frac{a}{h} \right)^2 \quad 7.14$$

$$\Phi = \sqrt{Q} = \sqrt{1. + 1.464 * \left(\frac{a}{c}\right)^{1.65}} \quad \text{for } a/c \leq 1 \quad 7.15$$

$$S = [1.1]^* \sqrt{\left(\frac{a}{c}\right)} \quad 7.16$$

(Equations 7.10 and 7.11 do not include an additional term f_w in the original Newman-Raju analysis since, for nearly all cases for ceramics and glasses, the flaw width $2c$ is small relative to the component width and f_w is 1.0.) These polynomials appear intimidating at first glance, but are easily programmed into hand calculators or spreadsheets. The $(1-(a/c))^{24}$ term for M is genuine and not a typographical mistake. The Newman-Raju Y factors have been widely used and are included in several ASTM standards including C 1421 for fracture toughness of ceramics,³⁵ E 740 for metals,³⁶ and ISO standard 18756.³⁷ Experience and subsequent analyses have shown that these factors are very reliable and accurate.

The above equations are for surface cracks in bending stress fields and Newman and Raju listed alternative formulas for direct uniform tension loadings.³³ It is not necessary to list them here. Equations 7.10 – 7.16 may be easily used for cracks in uniform tension loaded parts by the simple expedient of inputting an arbitrary large value (e.g., 1000) for the part thickness, h .

So for example, if a bend bar is broken and it has a surface crack with a depth of $a = 40. \times 10^{-6}$ m; width $2c$ of $144. \times 10^{-6}$ m; and the specimen height is 2.998×10^{-3} m; then $M = 1.080$, $H_1 = 0.995$, $H_2 = 0.983$, $\sqrt{Q} = 1.247$, and $S = 0.820$. Then, $Y_{\text{depth}} = 1.509$, $Y_{\text{surface}} = 1.252$. These are shown in Figure 7.16d. In practice, the more elliptical the flaw, the more likely the maximum Y is at the flaw depth unless the crack penetrates deeply into the specimen interior and into the stress gradient.

Using the larger value for Y and the flexural strength which was 453 MPa; equation 7.7 gives $K_{Ic} = 1.509 * 453 \text{ MPa} * \sqrt{40 \times 10^{-6}} = 4.32 \text{ MPa}\sqrt{\text{m}}$. In this case, the parameters are used to estimate the material's fracture toughness. If instead, the fracture toughness and flexure strength were known, the flaw size could have been estimated. Similarly, if the crack size had been measured and the fracture toughness was known, then the stress of 453 MPa could have been estimated.

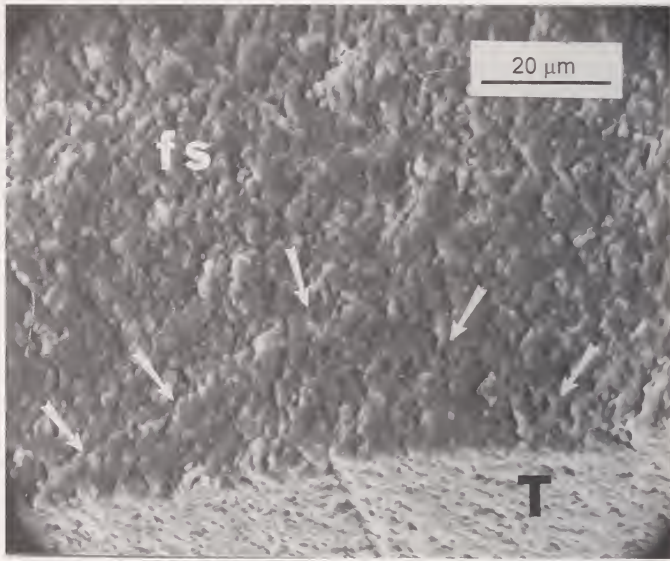


Figure 7.18 Grinding induced crack in a longitudinally-ground silicon carbide bend bar at 649 MPa. This flaw was located directly in the center of a well-defined fracture mirror. The depth a is 23 μm , the width $2c$ is 95 μm and the bar height was 2.2 mm. Y_{max} was at the deepest point and was 1.58. The computed fracture toughness is: $1.58 * 649 \text{ MPa} * \sqrt{23 \times 10^{-6}} = 4.9 \text{ MPa}\sqrt{\text{m}}$, which is reasonably consistent with published average values of 4.0 to 4.5 $\text{MPa}\sqrt{\text{m}}$ for the material. This orthogonal grinding crack is subtle and does not stand out clearly against the background microstructure. There may have been some doubt about its identification, but the fracture mechanics calculation shows it is about the right size.

Figures 7.18, 7.19, and 7.20 show examples of how the calculation can be used to confirm that the right flaw has been identified. Sometimes the calculated and measured flaw sizes agree very closely, but there are a number of reasons why they may differ as will be discussed below. ASTM standard C 1322³⁴ states that if the calculated and measured flaw sizes do not agree within a factor of two or three, then the origin should be reexamined to verify that the correct feature has been identified.

The surface crack in the BK-7 glass disk shown in Figures 6.17 and 7.20 was 7.3 μm deep and the stress at fracture was 146 MPa. For a long surface crack, Y is 1.99. The calculated fracture toughness from these values is 0.78 $\text{MPa}\sqrt{\text{m}}$, which is very close to published values for this particular glass.

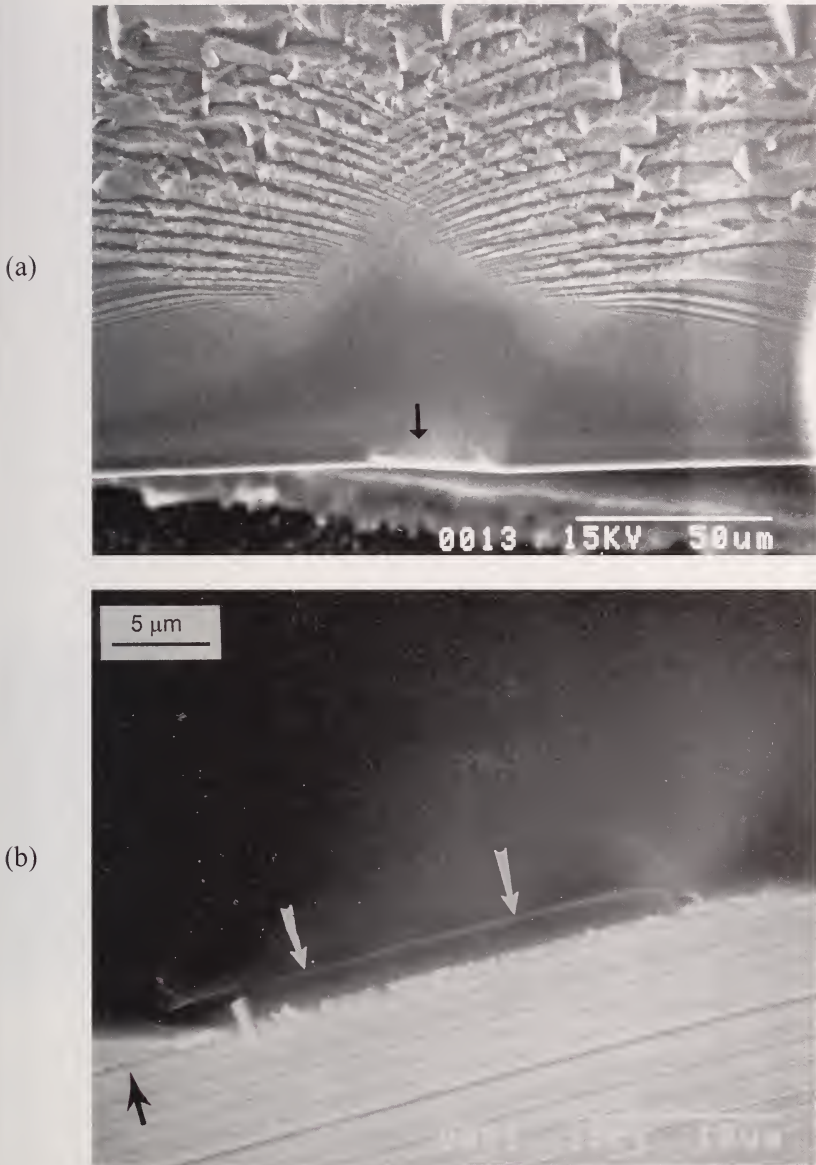


Figure 7.19 Fracture origin in a single crystal silicon wafer. (a) shows the fracture mirror which has a very faceted shape typical of some single crystals. The origin is a grinding crack shown by the white arrows in (b). The specimen was tilted back to show both the fracture and outer ground surfaces. A 3000 X scanning electron microscope photo showed that the crack was 2 micrometers deep, and when combined with a 282 MPa fracture stress and a Y factor of 1.99 gives $K_{Ic} = 0.79 \text{ MPa}\sqrt{\text{m}}$, in reasonable good agreement with published values for fracture on the $\{110\}$ plane.

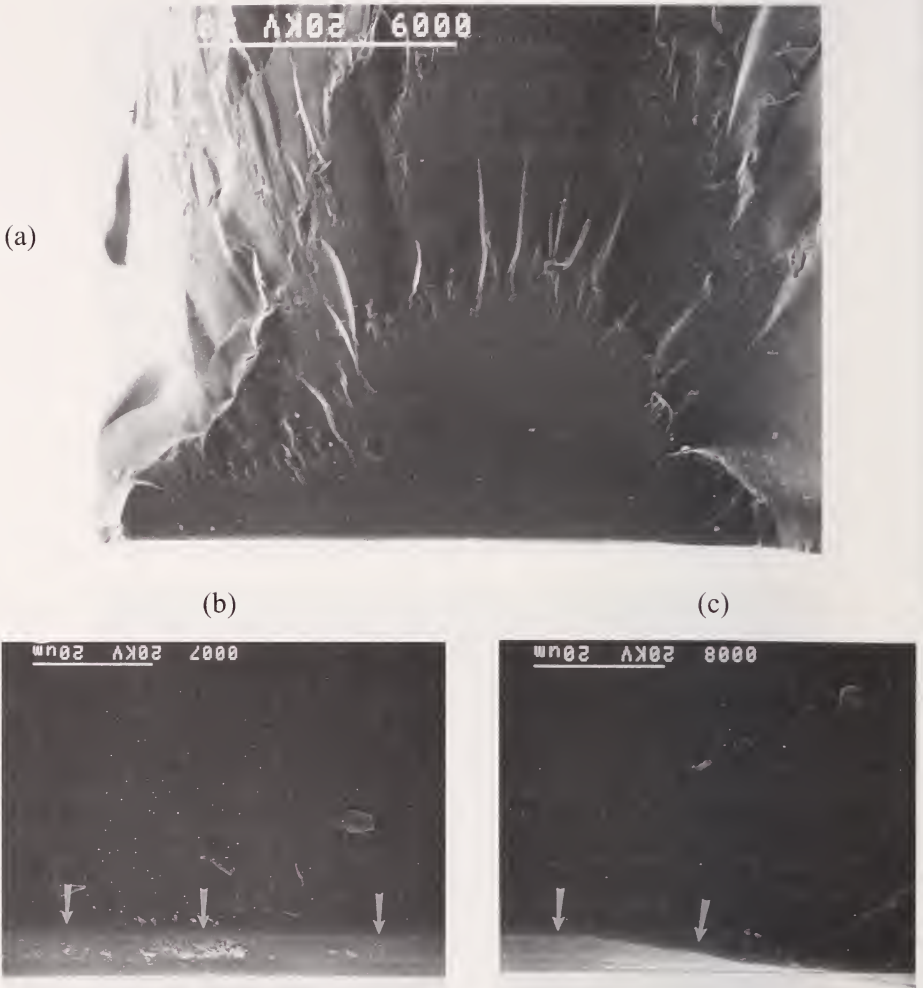


Figure 7.20 Fracture origin crack for the borosilicate crown glass biaxial disk specimen that was broken in inert conditions as shown in Figure 5.15. (a) is an SEM photo of the distorted mirror. (b) and (c) show two portions of the polishing scratch which was 7.3 mm deep (arrows). Using $Y = 1.99$ and the breaking stress of 146 MPa, gives $K_{Ic} = 0.78 \text{ MPa}\sqrt{\text{m}}$. The optical image (see Figure 5.15) showed a slight bulge in the flaw at the center of the mirror suggesting the flaw may have grown slightly before going critical. This growth is not evident in the SEM images.

Figure 7.21 may be useful for those who do not wish to program a calculator or spreadsheet. Y values may be picked off the graph for cracks in bending problems for given a/t and a/c ratios. Notice it demonstrates how Y decreases as a flaw penetrates into the stress gradient (larger a/t). (Y values for small surface flaws in uniform tension fields may be obtained by reading the graph value for an a/t ratio of zero.)

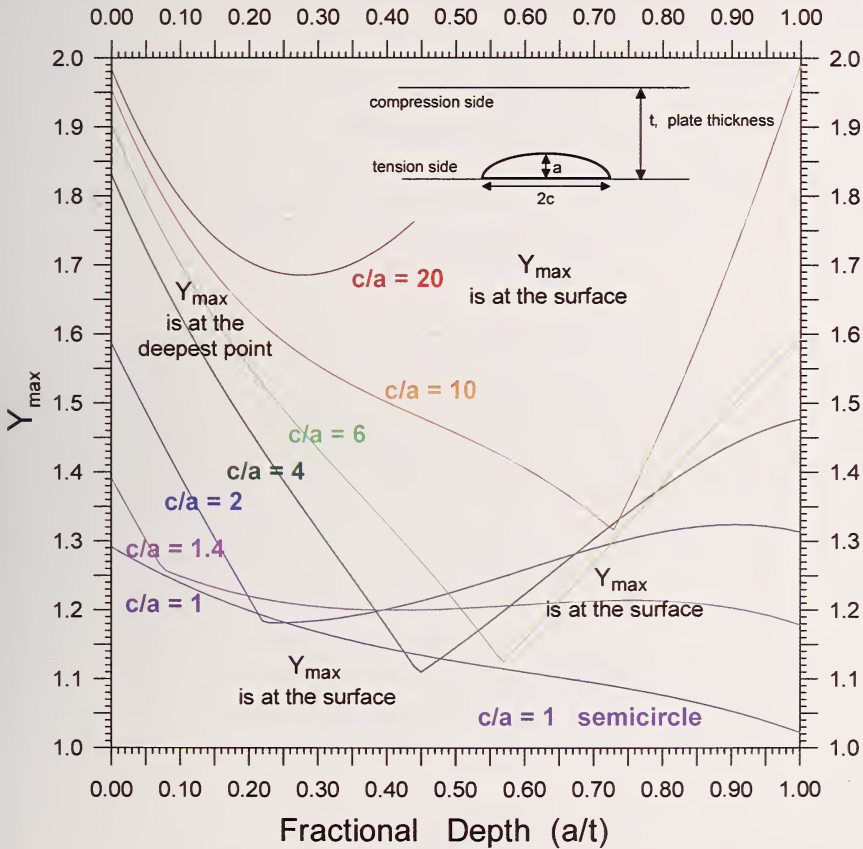


Figure 7.21 The maximum stress intensity shape factor Y for semi elliptical surface cracks in a bending stress field in a plate or bar of thickness t . The kink in the loci corresponds to where the maximum Y changes from the surface to the deepest point in the interior or vice versa.

7.5.3 Irregularly-shaped surface cracks

Fracture mechanics reference books have amazing tabulations of stress intensity formulas and shape factors for a myriad of crack shapes and loading configurations. There are even listings for multiple cracks in proximity to each other that show how the stress intensity fields interact. Real flaws in real materials often do not have convenient shapes, however. Several approximations are very helpful. Figure 7.22 shows a case of an irregular planar surface crack loaded by far-field tension. The stress intensity may be approximated, with a maximum of a 10% error (Poisson's ratio of 0.3), by:³⁸

$$K_i = 1.15 \sigma \sqrt[4]{\text{area}} \quad 7.17$$

For example, if the flaw is semicircular with a radius a , this simplifies to

$$K_i = 1.29 \sigma \sqrt{a} \quad 7.18$$

Numerical analysis showed that the fourth root of area equation 7.17 is an adequate approximation for stress intensity factor solution for such diverse shapes as partial circles, triangles, rectangles and semi ellipses. An analysis for semi-ellipses by Bansal reached a similar conclusion.³⁹ This approximation may also be used for small cracks in bending specimens, provided that the crack does not

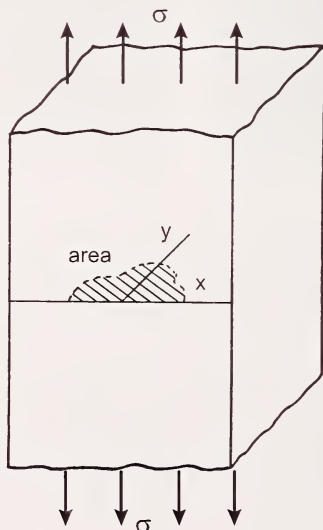


Figure 7.22 An irregular planar shaped surface crack in a tension stress field. (After Murakami, ref. 38.)

penetrate very deeply into the specimen. Insight as to the safe depth for such an approximation may be gained by consulting Figure 7.21. The area function is accurate to within 5% for semi-elliptical surface flaws with $1.0 < c/a < 5.0$. It should not be used for more elongated ($c/a > 5$) flaws.

7.5.4 Three-dimensional, blunt, and inclined flaws

Real flaws are not always flat and planar. Figure 7.23 shows a sphere that is not unlike many pores in ceramics and glasses. Sometimes these are modeled by a penny-shaped crack. This is a gross over-simplification. Indeed, if the pore is round and crack free, it does not act to intensify the stress, but simply concentrates stress around the flaw sides. Smooth round pores require much greater force to cause fracture than the penny-shaped flaw of similar diameter. Round pores may be quite docile and not act as strength-limiting flaws. Figure 7.23c shows another variation that is more apt to be the case for ceramics and glasses if the pore is located on a surface. This is a combined stress concentration-fracture mechanics problem. For small rim cracks, the pore acts as a concentrator of stresses and the rim crack size may be regarded as the crack size in a fracture mechanics calculation. For a very large rim crack, the pore's effect is diminished and the penny shaped crack is a very good approximation. In practice, it is very difficult to detect a rim crack around a pore, much less measure it. It is not unreasonable to expect that rim cracks of one or two grain diameters extend from the pore and in fact many pores in ceramics do have local microstructural irregularities or microporosity in the vicinity. Only very rarely

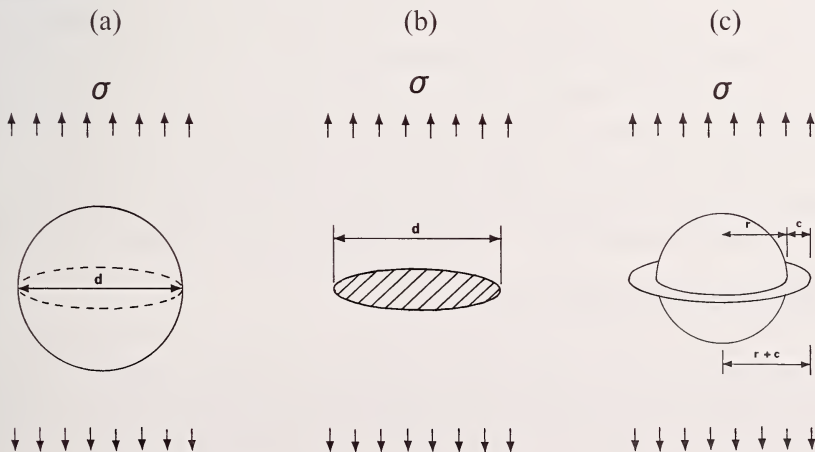


Figure 7.23 Flaws may be three-dimensional and a penny shaped crack is only an approximation.

have fractographers attempted to precisely model such flaws and it is customary to use the penny-shaped cracks as an approximation, but with full cognizance that the actual flaw is much blunter.

The reader may consult fracture mechanics handbooks for more information about flaws that are *inclined* to the stress direction. A slight inclination of 5 degrees does not affect the mode I loading very much, but beyond 10 degrees flaws experience not only mode I loading but varying degrees of modes II and III depending upon the flaw shape and inclination angle. Modes II and III are tearing or shearing actions on a crack and are beyond the scope of this Guide.

7.6 Relationship of K_{Ic} and A

K_{Ic} and the fracture mirror and branching constants are related to $\sigma\sqrt{a}$ or $\sigma\sqrt{R}$ and hence have the same set of units: $\text{MPa}\sqrt{\text{m}}$ (or $\text{ksi}\cdot\sqrt{\text{in}}$). As Figure 7.7 illustrates, K_{Ic} pertains to conditions at the flaw and the A values correspond to events away from the origin as the crack propagates and reaches terminal velocity. Kirchner and Conway²⁵ have shown that mirror shapes can be predicted on the basis of stress intensity at the crack front as it expands outwards from the origin, so it is not unreasonable to expect that K_{Ic} and the A's are related. If they are related, then in principle one can estimate K_{Ic} from A or vice versa. Mecholsky et al.⁴⁰ tabulated A's and K_{Ic} 's for over two dozen ceramics and glasses and showed there was an approximate correlation. On average the A_0 to K_{Ic} ratio was $20/7 = 2.86$, although there was considerable scatter. Bansal and Duckworth^{41,42} carefully measured A_0 to K_{Ic} ratios of 2.2 to 2.4 for a glass ceramic and a sintered alumina, and 2.3 for float glass and a hot-pressed alumina. Subsequent tabulations⁴³ on more contemporary materials, many of which have R-curve behavior, have given ratios as low as 1.5 to 2.0. In a dissenting view, Bradt and colleagues^{44,45} have suggested that A is not really a material constant and they also noted the discrepancies in A/K_{Ic} ratios. In summary, variability in the quality and accuracy of the K_{Ic} and A data, plus genuine microstructural effects probably mean there is no unique A/K_{Ic} ratio.

7.7 Mirror to Flaw Size Ratios

A simple but very useful observation is that mirror and flaw sizes are related. Krohn and Hasselman⁴⁶ showed that the mirror size to flaw size ratio is about 10 for glasses. Mecholsky et al.^{40,47} obtained ratios of 10 to 11.6 using the mirror-mist (inner mirror) boundary in glasses. They estimated the ratio to be about 13 for the mist-hackle (outer) boundary to flaw size ratio for glasses.

Ratios for ceramics are more problematic and depend upon the macrostructure and the ability to judge a specific boundary. Mecholsky et al.⁴⁰ estimated the mirror-mist (inner) boundary to flaw size ratio to be about 6 on average for polycrystalline ceramics, but their values ranged from as low as 3 for a glass ceramic to as large as 10 for spinel. The ratio of the hackle boundary (outer mirror) to flaw size was 13 for polycrystalline ceramics and single crystals, but varied from as low as 8 to as large as 40!

Rice⁴⁸ has pointed out that the bluntness of the flaw may alter the mirror to flaw size ratio. For example, pores often act as blunt flaws and it requires extra energy or stress to overcome the bluntness. The excess energy causes a mirror to form at shorter distances from the origin than if the flaw were sharp.

Slow crack growth can also alter the apparent ratios.⁴⁷ If the mirror to flaw size ratio is much greater than the values listed above, then the flaw should be checked for evidence that it grew stably prior to fracture.

$C_{calc} < C_{meas}$	$C_{calc} > C_{meas}$	$C_{calc} > C_{meas}$ or $C_{calc} < C_{meas}$
Crack blunting	Stable crack extension -SCG	High temperature SCG
Use of 2-D model	Stable crack extension - R curve	Multiple flaws nest or interact
Stress gradients	Flaw causes a local fracture toughness degradation	Residual stresses
	Flaw is within a single grain	Flaw is truncated on the fracture surface
	Flaw links with other flaws or the surface	Flaw shape irregularity
		Flaw elastic properties are different than the matrix
		Faulty fracture toughness data

Table 7.4 Factors that can cause a measured flaw size c_{meas} to differ from the calculated c_{calc} size. (Quinn and Swab, Ref. 49 and 50.)

Residual stresses in the vicinity of the flaw or the mirror also can change the ratios. Unexpected mirror to flaw size ratios may be evidence of residual stresses acting on the flaw or the whole mirror.

The effect of R-curve behavior on these ratios is as yet unexplored. One might expect that the microstructural features that accentuate R-curve behavior may trigger earlier formation of hackle and, hence mirror boundaries at smaller radii than in fine-grained materials or glasses.

7.7 Comparing Measured to Calculated Flaw Sizes

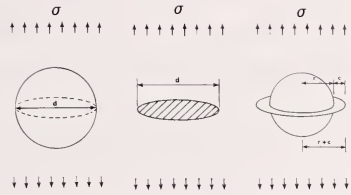
Differences in calculated and measured flaw sizes of 20 % to 50 % should not be considered too serious, but variations greater than a factor of 2 or 3 should prompt the fractographer to study the origin more carefully. Either the wrong feature has been identified as an origin or the origin may be more complicated than expected. Either something about the calculation is wrong or the fractographically-measured size is wrong. Table 7.4 and Figure 7.24 show some of the factors that can cause the discrepancy.^{49,50} These can be appreciated if Equation 7.7 is rewritten:

$$c_{calc} = \left(\frac{K_{Ic}}{Y\sigma_f} \right)^2 \quad 7.19$$

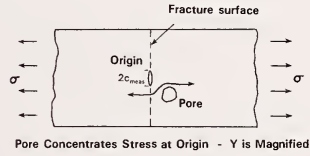
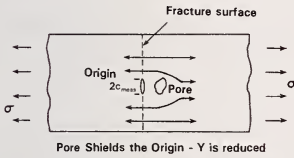
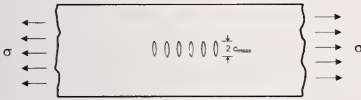
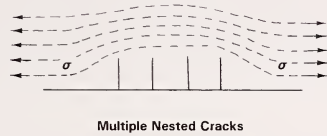
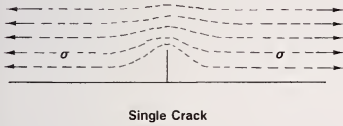
A blunt flaw of actual size c requires a greater stress to cause fracture than a comparably sized sharp flaw. Some flaws are blunt to begin with. Other initially sharp flaws may have been blunted or even partially healed by oxidation or other environmental effects. Inserting the greater stress in equation 7.19 leads to a smaller c_{calc} than the actual flaw size c . Assuming that flaws are penny shaped or are flat ellipses usually leads to Y estimates that are too large, and this also leads to smaller c_{calc} than the actual flaw size c . Unexpected stress gradients can cause σ_f to be overestimated. That in turn will again cause c_{calc} to be too small. The stress at the origin site should be used in equation 7.19.

Slow crack growth and rising R-curve behavior can cause stable crack extension. Using the actual breaking stress in equation 7.7 or equation 7.19 gives a correctly calculated flaw size, but if the fractographer detects and measures only the initial flaw size, then $c_{calc} > c_{meas}$. In this case it is the fractographic size measurement that is off. Alternatively, if stable crack extension due to R-curve behavior does occur, but the fractographer uses a long crack (plateau) value of fracture toughness, then the fracture toughness is overestimated and

(a) Flaw bluntness or 2-D approximations

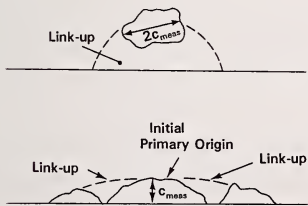
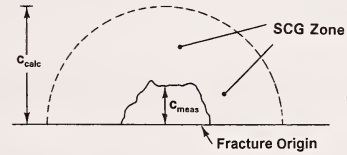
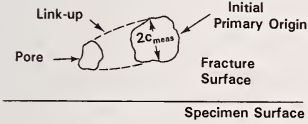


(b) Flaw interactions



(c) Flaw linkage

(d) Flaw slow crack growth



(e) Flaw truncation on the fracture surface

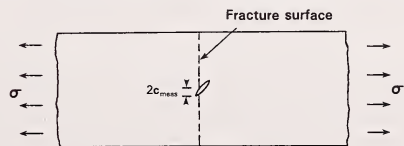


Figure 7.24 Some of the factors that cause calculated and measured crack sizes to differ.

◆ Fractography of Ceramics and Glasses

again $c_{\text{calc}} > c_{\text{meas}}$. R-curve behavior is discussed in more detail in section 7.11. Inclusions or chemical inhomogeneities can be particularly deleterious if they degrade the fracture toughness of the surrounding matrix. If the fractographer uses the baseline K_{Ic} value in equation 7.19, this also leads to $c_{\text{calc}} > c_{\text{meas}}$. In this case, the calculated size is wrong and the observed crack size is correct. The fracture toughness of a single crystal, or a single grain, is almost always less than that of a polycrystal. If a flaw resides within a single grain, but a polycrystalline K_{Ic} value is used in equation 7.19, then c_{calc} will be too large. Flaws may link up with other flaws or a surface weakening the specimen. If the linkage is undetected by the fractographer, then his c_{meas} will be too small compared to the calculated and actual critical flaw size.

Some factors can cause the size discrepancy to go either way. Flaws are often assumed to exist in isolation, but as Figure 7.24b shows they can interact causing either an increase or a decrease in the Y factors that act on them. It all depends upon the geometries and arrangements. If flaws are lined up in a row parallel to the stress, the flaws will shield each other. If they are staggered or lined up sideways, they can intensify the K_I fields and the Y factors. Flaws may be truncated and only a portion detected on the fracture surface. Undetected residual stresses can throw off the calculated flaw size as well. Last, but not least, faulty fracture toughness data can also throw off the correlations.

The point here is that fracture mechanics is a valuable tool to aid fractographic analysis. It can help confirm that the fractographer has found the correct flaw as an origin. A finding that the calculated and measured sizes are appreciably different should prompt further consideration and analysis. What factors caused the discrepancy? Is the discrepancy an isolated outcome or part of a pattern?

7.9 Crack Velocities from Wallner Line Analysis

Wallner lines can be used to estimate crack velocities, whether they are created incidentally during the fracture event or deliberately by ultrasonic fractography. Wallner lines may not be evident in very slow fractures in glass or in ceramics due to their rough fracture surfaces.

Ultrasonic fractography uses a transducer to generate sonic waves that interact with the propagating crack as discussed in sections 5.4.4 and 3.21. Usually the transducer is placed position perpendicular to the crack propagation plane. The sonic waves create tertiary Wallner lines and show the crack front shape. Velocities are easily estimated from the spacing between the Wallner lines.

Richter and Kerkhof^{51,52} and Michalske et al.^{53,54} used this technique over a broad range of crack velocities from terminal velocity down to 10^{-7} m/sec. Indeed Richter and Kerkhof⁵¹ used this technique to show that surface cracks that grow by slow crack growth do evolve in shape in accordance with the Newman-Raju stress intensity shape factors. They also showed Figures 5.36 b and c which proved a semi-elliptical crack could go unstable from one side as shown in Figure 5.44.

Crack terminal velocities are about 50 % to 60 % of the transverse elastic wave speed and range from 1500 m/s for soda lime silica to 2500 m/s for fused silica as listed in Table 5.1. The transverse wave velocity is:

$$v_t = \sqrt{\frac{E}{2\rho(1+\nu)}} \quad 7.20$$

where E is the elastic modulus, ρ is the density, and ν is Poisson's ratio. Richter^{51,52} measured cracks running at terminal velocity at stress intensities above K_{Ic} .

Even in the absence of externally applied sonic pulses, it is possible to interpret *naturally* created Wallner lines to estimate crack velocities as shown in Figures 7.25 – 7.27. The simplest case is for a straight crack front that intersects a discontinuity such as a bubble or inclusion that creates an elastic pulse. The radiating transverse elastic wave always travels faster than the crack front. Figure 7.25 shows how the radiating wave catches up and intersects with other portions of the crack front. The locus of intersections generates Wallner lines that have a telltale “V” pattern centered on the elastic discontinuity. There often is a slight curl at the pulse origin and the net effect is to produce a shape that led to its name: gull wings. The included angle (2β) between the wing segments may be used to calculate crack velocities. Crack velocity is quite simply:

$$v_c = v_t \cos \beta \quad 7.21$$

where v_c and v_t are the velocities of the crack front and the transverse wave. Slowly moving cracks do not advance very far in a time interval Δt , and the elastic pulse quickly overcomes the entire front. The “V” shape is very flat and, if it is assumed that the included angle 2β is $180^\circ - 2^\circ = 178^\circ$, then the slowest velocity that can be measured in a glass with $v_t = 3460$ m/s is $v_{c,\min} = 60$ m/s. Conversely, if the crack is advancing at the terminal velocity of 60%

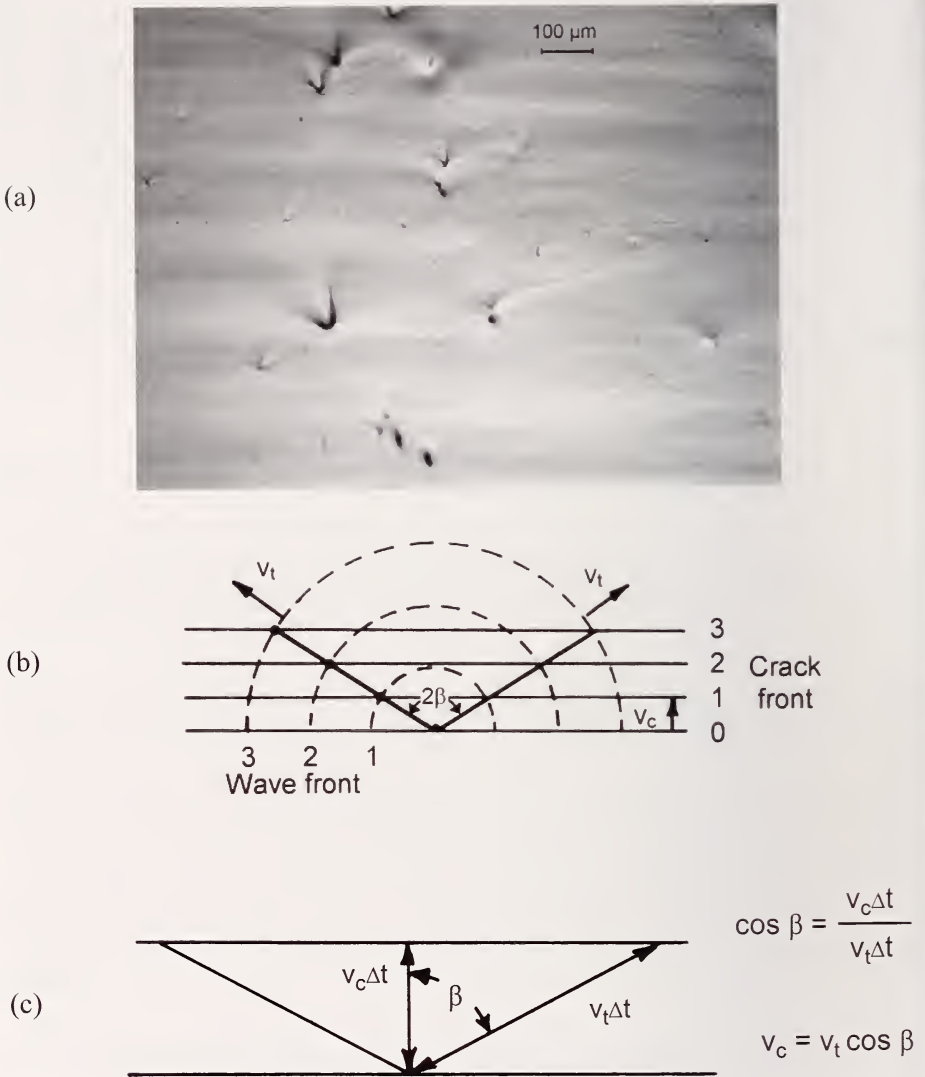


Figure 7.25 Crack velocities may be estimated from Wallner line analysis. Gull wing Wallner lines occur when a straight crack front passes a point discontinuity such as a bubble or inclusion. (a) shows gull wings in knapped obsidian (specimen courtesy A. Tsirk). The direction of crack propagation is from bottom to top. The included angle (2β) of the trailing gull wing lines may be analyzed to estimate crack velocity. Slowly moving cracks have flat (horizontal) wings. Fast moving cracks create wings with a “V” shape. (b) and (c) show the geometries and simple trigonometry used to estimate crack velocity.

of the transverse wave velocity, then the maximum included angle 2β is 106° . Tsirk⁵⁵ has identified hyperbolic “V” shaped Wallner lines in obsidians, created by an elastic pulse generated by secondary fracturing behind the primary fracture front.

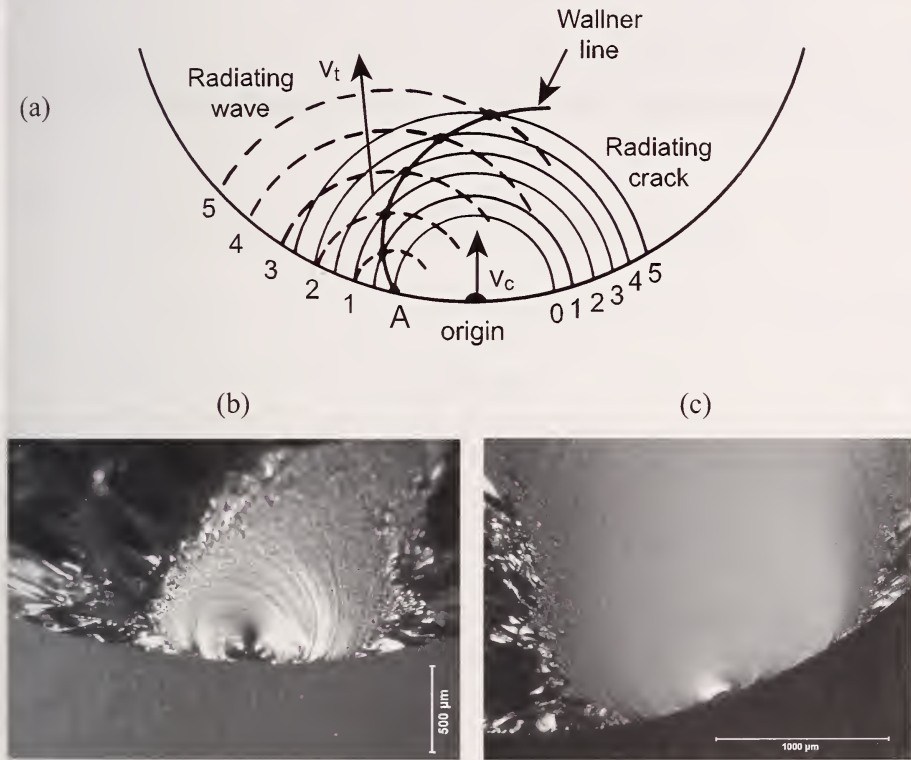


Figure 7.26 Crack velocities can be estimated from Wallner line analysis. (a) shows a crack front that radiates outward at velocity v_c (thin circular lines) and reaches irregularity A. An elastic pulse is generated at A and it radiates a transverse (shear) wave outward from A (dashed lines) with a faster speed v_t than the crack front. The numbers label the crack and elastic pulse fronts at the successive times starting at 0, the instant the crack reaches A. The intersections for the specific times are marked by dots, but of course this is a continuous process and the solid line shows the ensuing Wallner line. The crack front is assumed to be moving at constant velocity $v_c = 0.5 v_t$ in this case. If the crack were accelerating, the Wallner line would be less hooked in the beginning and would extend more towards the upper right. (b) and (c) show Wallner lines inside mirrors in glass rods.

Wallner lines such as those inside a mirror shown in Figure 7.26 may be analyzed as shown in Figure 7.27.^{10,22,56,57} In the case where the exact direction of crack propagation (radiating at speed v_c from origin "O") and the initiation site of the Wallner line (A) are known, then from Figure 7.27a:

$$\frac{v_c}{v_t} = \frac{\sin \gamma}{\cos \beta} \quad 7.22$$

Crack velocity can be determined even if the crack propagation direction is not known. Two intersecting Wallner lines may be analyzed as shown in Figure 7.27b:

$$\frac{v_c}{v_t} = \frac{\sin \varphi}{\sqrt{\cos^2 \beta_1 + \cos^2 \beta_2 + 2 \cos \beta_1 \cos \beta_2 \cos \varphi}} \quad 7.23$$

and if the Wallner line intersection is symmetric ($\beta_1 = \beta_2 = \beta$), then:

$$\frac{v_c}{v_t} = \frac{\sin \left(\frac{\varphi}{2} \right)}{\cos (\beta)} \quad 7.24$$

Elastic waves interactions from slowly moving cracks run across the crack front fairly quickly and thus the Wallner line corresponds closely with the crack front shape. The minimum velocity that can be estimated by Wallner line analysis was estimated by Mencík¹⁰ as $v_c/v_t = 0.175$, using equation 7.24 with $\varphi = 2$, corresponding to nearly flat crossing Wallner lines. For glass with $v_t = 3460$ m/s, then $v_{c,\min} = 60$ m/s. So in general, quantitative Wallner line analysis for crack velocities is most suitable for fast moving cracks.

The spacing between the legs of Wallner lambda lines, discussed in section 5.4.5 and shown in Figure 7.28, can easily be used to estimate a crack velocity. In the time that the crack advances approximately a distance $a/2$, the elastic wave has traveled across the thickness once. For a straight crack front:

$$V_c = V_s \frac{a}{2 \sqrt{\left(\frac{a}{2} \right)^2 + t^2}} \quad 7.25$$

The formula can also be used to approximate crack velocities for slightly curved crack fronts as well.

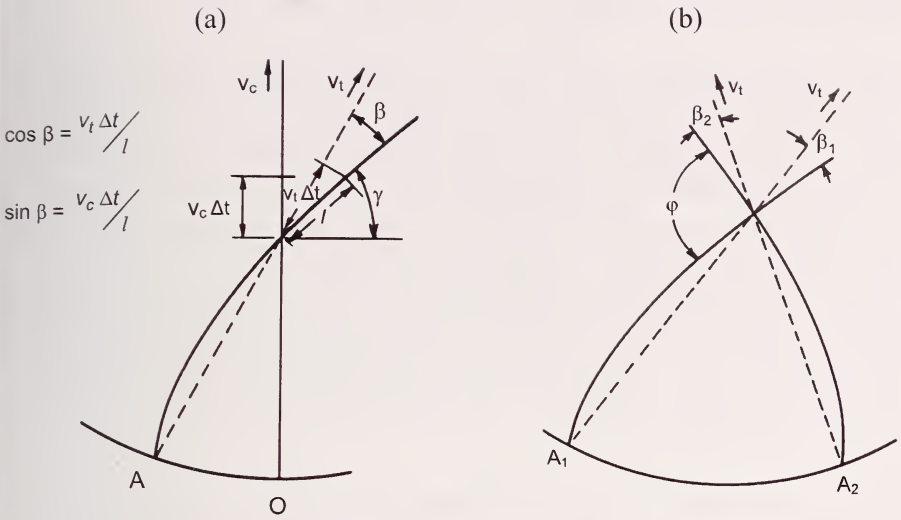


Figure 7.27 Analysis of Wallner lines to determine the crack velocity if a crack radiates outwards from a point origin "O". (a) shows a case where the location of the Wallner line pulse (A) and the direction of the crack extension are known. (b) shows the case where the precise crack growth direction is not known, but the origins of the two Wallner lines (A_1 and A_2) are known.

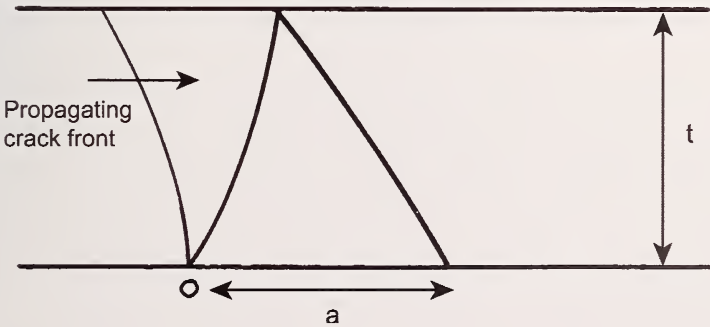


Figure 7.28 The spacing between the lambda line legs can be used to estimate crack velocity.

7.10 Slow Crack Growth

Cracks may grow stably when loaded at stresses and stress intensities less than that necessary for the flaw to become unstable. As discussed in sections 5.9.1 and 5.9.3, glasses, oxide ceramics, and ceramics with glassy boundary phase are susceptible. The mechanism of slow crack growth at ambient temperature is a stress corrosion phenomenon whereby stressed cracks that are open to the environment are attacked by water or another polar molecule. The water may be in the form of liquid or gaseous molecules. The water molecules attack the strained silicate or oxide bonds at the crack tip causing them to rupture which in turn leads to stable crack extension. At elevated temperature, oxidation attack, grain boundary softening, or other mechanisms can lead to slow crack growth.

Crack velocity depends strongly upon the stress intensity and slight changes in the latter can have dramatic effects upon the velocity. As a crack grows larger, the stress intensity also increases in accordance with equation 7.14. If stress and the flaw shape are invariant, the crack will gradually accelerate. Data are often graphed on log - log axes as shown in Figure 7.29a, and straight lines imply a power law dependence of velocity upon stress intensity:

$$V = A K_I^N \quad 7.26$$

Region I crack velocity behavior often controls lifetime or rate effects on strength. The slope of the line, N , is known as the slow crack growth exponent and is a critical parameter for reliability and rate effect analyses. Very high values of N (e.g., > 100) indicate considerable resistance to slow crack growth and hence, little rate sensitivity. Low values (e.g., 5 to 30) indicate high susceptibility. Crack velocity data as shown in Figure 7.29a are usually collected with laboratory specimens under controlled testing conditions. Figure 7.29b shows the effect of slow crack growth on the lifetime of specimens loaded at constant stress levels below the fast fracture strength. The decrease in strength varies with log time to the $-1/N$ power. Slow crack growth can even affect outcomes in ordinary strength tests as shown in Figure 7.29c. The slower the test is run, the weaker are the specimens. The crack can grow a surprising amount during the time of loading. Figure 5.44 showed an example of a flaw in glass that grew as much as 20 times its original size due to slow crack growth in water. Figure 5.43 showed a flaw in alumina that grew a more modest amount. Slow crack growth changes the mirror to initial flaw size ratio, as discussed previously in section 7.7.

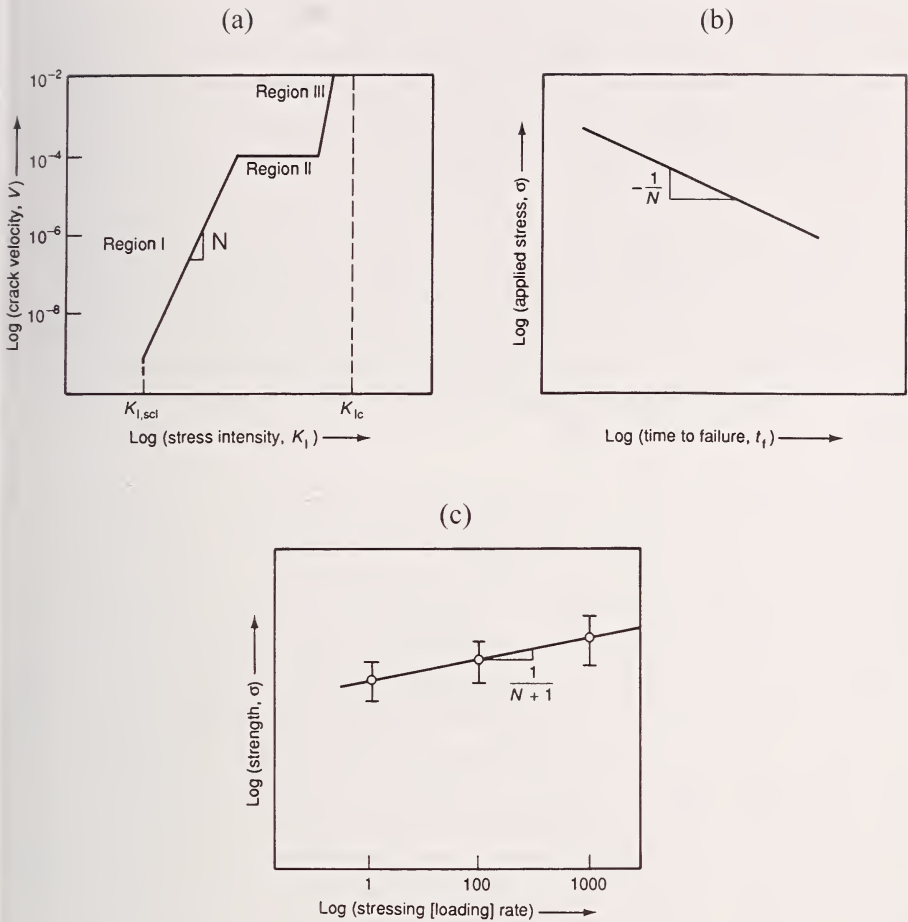


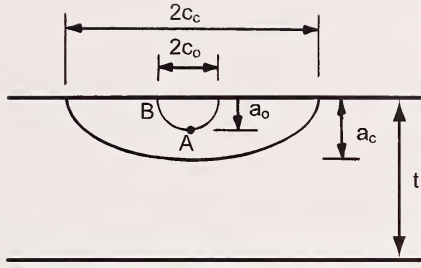
Figure 7.29 Slow crack growth manifests itself in different ways. (a) shows a crack velocity versus stress intensity (K - V) graph showing three regions. Usually such data is plotted on log-log axes. Fracture mechanics type tests are used to collect such data. (b) shows a graph of log stress – log time to failure, also known as a “static fatigue” or “stress rupture” plot. (c) shows a graph of strength as a function of stressing rate also with log - log axes, also known as a “dynamic fatigue” plot. The slow crack growth exponent N features prominently in each instance.

A comprehensive theoretical justification for the power law relationship between K and V is lacking at the present time. There are alternatives, but the power law relationship lends itself to simple integrations and transformations and is usually adequate. It should be used with caution for any extrapolations beyond the times and velocities for which the data was collected, however.

Crack-fluid interactions can cause abrupt changes in crack growth that can create markings such as scarps on fracture surfaces. For example, an accelerating crack may outrun the ability of a fluid to keep up with the crack tip and this may cause cavitation. Conversely, a decelerating crack may slow down enough that water can catch up to the crack causing a scarp. Sometimes a jump in the crack from region I behavior (Figure 7.29a) to region II behavior will create scarps.

The Newman-Raju stress intensity shape factors also explain one commonly observed trend: surface cracks that grow stably evolve shape and become semielliptical. Figure 7.30 illustrates the trend and Figure 5.36b an example. The stress intensity shape factor Y is not constant, but varies around the crack front. For a semicircular flaw, Y is greatest at the point where the crack intersects the outer surface, point B. At the internal point A, there is more material on either side that can share the load, and hence the stress intensity shape factor is about 13 % less. The crack initially grows faster along the outer surface, but then, as the crack shape evolves into a semiellipse, the stress intensity evens itself out around the periphery. Newman and Raju showed examples of this for fatigue crack growth in metals, both for bending and direct tension stress fields. The semi elliptical shapes differ in the two cases, depending upon the size of the crack relative to the specimen thickness. The identical trends have also been observed in ceramics and glasses.^{51, 58-62} Small cracks in large, uniform direct tension loaded specimens or plates will assume a constant semi elliptical shape with an aspect ratio of about 0.83. Cracks in bending stress fields will also gravitate to this shape if they are small relative to the thickness, but if they penetrate into the stress gradient, they will become shallower semi ellipses the deeper they go.

(a)



(b)

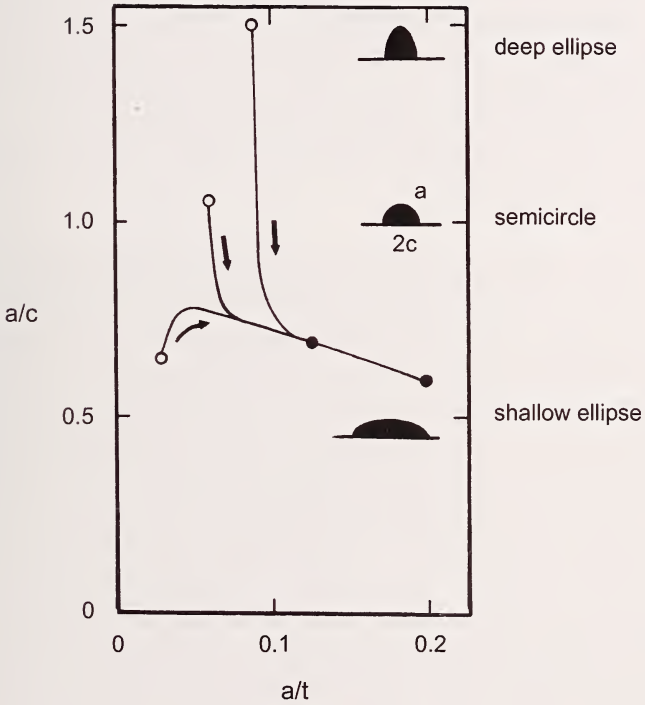


Figure 7.30 Crack shape often changes with growth. (a) shows an initially semicircular crack of size a_o that changes to a semi elliptical shape as it grows in a bending stress field. (b) shows the evolution of crack shapes in glass bend specimens converges to a shallow semiellipse, irrespective of the starting shape (hollow circles). (after Fett, Munz, Keller, Ref. 58)

7.11 R- Curve Behavior

R-curve behavior, which arises from crack-microstructure interactions, is a phenomenon that may improve fracture resistance in ceramics. It can give rise to stable crack extension prior to fracture. It is not operative in glasses. Unfortunately, R-curve behavior does not leave any intrinsic telltale markings on the fracture that the fractographer can interpret.

Figure 7.31 illustrates the general concepts. Flat R-curve materials such as glasses and many fine-grained ceramics behave as shown in Figure 7.31a. Fracture toughness is independent of the crack size and has a specific value, K_{Ic} . When the combination of stress, flaw shape and size reach the critical condition, unstable crack extension usually occurs. If there are substantial tensile stresses throughout the body, it will break. If, on the other hand, if the stresses decrease either temporally as in thermal shock cases or spatially as in localized contact loading cases, the crack initially may be unstable, but then slow down and even stop.

Rising R-curve behavior occurs when the microstructure impedes crack extension. Several crack-microstructure interactions shown in Figure 7.14 can cause this. For example, yttria-stabilized tetragonal zirconia polycrystal (Y-TZP) is carefully processed so that after firing the microstructure is composed of metastable tetragonal grains. These can transform to the monoclinic phase when a crack tip and its stress field approaches. This martensitic phase transformation consumes some energy that might otherwise drive the crack forward. In addition, the transformed grains expand by $\approx 4\%$ thereby putting a compressive constraint on the crack tip. The process zone may only be a few grains wide in Y-TZP. R-curves can arise from other crack-microstructure interactions. For example, sometimes during crack propagation through coarse-grained ceramics, large grains behind the crack tip may not necessarily be immediately cleaved. They may act as bridges across the crack faces that reduce the stress intensity field on the crack tip. They can persist for long crack propagation distances.

Phenomena such as these can lead to behavior shown in Figure 7.30b. Starting with an initial crack size, c_0 , if the stress intensity K_a from an applied stress reaches the level of K_{Ic} , the crack begins to propagate. As it grows, K_a increases in proportion to \sqrt{c} if the stress is invariant. The material's fracture resistance K_R may increase at a greater rate thereby retarding or arresting further crack propagation. Further propagation requires additional stress to

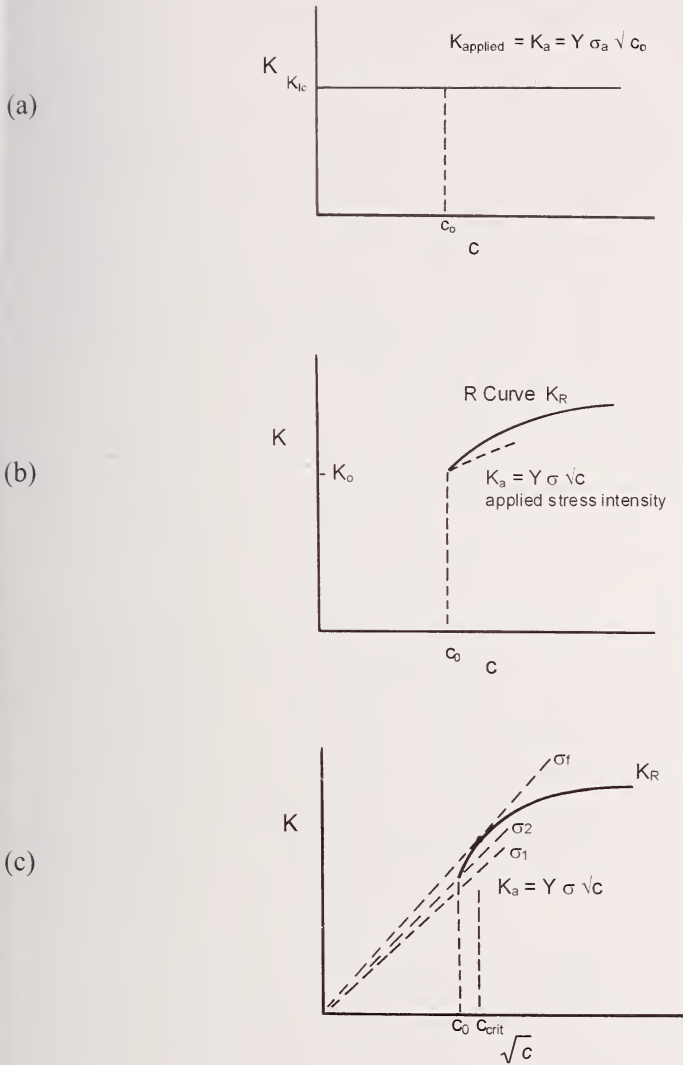


Figure 7.31 R-curve effects in ceramics. (a) shows the case of a material with a constant, or flat R-curve. (b) shows a general schematic of a rising R-curve. Crack extension leads to a greater applied stress intensity K_a , but the material's fracture resistance curve K_R may also increase. (c) shows K_a versus \sqrt{c} , in which case the K_a plots as a straight line with slope proportional to applied stress. Fracture occurs at c_{crit} where the rate of increase of applied K_a is greater than the slope of the K_R curve. Initial flaws larger than c_{crit} may not exhibit any stable crack extension and may immediately go critical.

increase K_a . The R-curve typically reaches a plateau such that further toughening is not possible. Fracture may occur before the plateau is reached if:

$$K_a = K_R \quad 7.27$$

and

$$\frac{dK_a}{dc} > \frac{dK_R}{dc} \quad 7.28$$

In other words fracture occurs when the applied K_a reaches the level of the R-curve *and* the rate of increase in K_a with further extension is greater than the rate of toughening. To better show the relative increases, it is common to plot fracture resistance with K^2 versus c , or K versus \sqrt{c} as shown in Figure 7.31c. In this fashion, the increase in K_a with crack size appears as a straight line with slopes that increase with σ . This K_a line can be more easily compared to the K_R trend. Instability occurs at $c = c_{crit}$, a value well before the plateau is reached, after only a small amount of crack growth has occurred.

There is no universal R-curve for a material.⁶³ The R-curve depends upon the starting size of the crack relative to the microstructure and its prior propagation history. It also depends upon the size, shape, and mode of loading of the specimen. R-curves for large cracks are not the same as those for small cracks. In other words, data from large crack fracture mechanics specimens are usually not applicable to natural small flaws. Large fracture mechanics specimens usually are effective in measuring plateau toughness values. A double-cantilever beam specimen has a dramatically different crack opening displacement than a notched beam or a surface flaw in a bend bar. The number of bridges behind the crack tip bridges depends upon the crack opening displacement and the greater the opening, the fewer the intact bridges. For example, a 20 μm grinding-induced crack may have already interacted with the microstructure and formed bridges or transformed some material during the crack formation. Figure 7.32 shows two possible examples. In contrast, a 20 μm round pore may not have activated any prior toughening.

It is extremely difficult to measure R-curves for small natural-sized flaws, and especially the initial K_0 fracture resistance. The limited data that has been collected suggests the initial K_0 may be very small, approaching single crystal or even grain boundary fracture toughness values. Some materials may have such small toughening zones that, for all practical purposes, they can be treated as having a set fracture toughness value. Many yttria-stabilized tetragonal zirconia (Y-TZP) may be like this since the transformation zone is only a few grains large. On the other hand, magnesia partially-stabilized zirconia (Mg-PSZ) may

have considerable crack extensions prior to fracture.⁶⁴ Many studies have used Vickers indentation artificial flaws, but they often do not behave like genuine flaws as discussed in the next section. The R-curves that are generated are not relevant to natural flaws or are simply wrong. For example, one study showed that without proper care, the usual analysis with Vickers indentation flaws produced the implausible result that a soda lime silica glass has a rising R curve.⁶⁵ The most credible R-curve data to date (that is applicable to strength limiting flaws) has been that collected by careful microscopic examination of crack growth from natural flaws in controlled loading experiments.^{61,62,66,67}

The instability point depends upon the starting crack size and the slope of the R-curve at small crack sizes as shown in Figure 7.31c. Indeed, the overall plateau value may be inconsequential in many cases. A particular crack may grow only a small amount before going unstable^{63,64,68} or it may immediately be unstable. Fett and Munz's mathematical analysis is quite revealing.⁶⁸ They showed that R-curve behavior led to negligible strength enhancements in an alumina that had bridging grains, quite simply because the natural flaws did not have a chance to grow very far before going unstable. Their analytical and experimental results may easily be understood by the simple realization that in strong aluminas the flaws are only 5 to 20 times larger than the average grain size. The stable crack extension may involve only a few grains before the flaw goes critical and it is impossible to generate many behind-the-crack tip bridges. Perceptible strengthening would only occur in very weak specimens ($\sigma < 100$ MPa) with large initial flaws. Fett and Munz also showed that the R-curve behavior in their aluminas had negligible effect on the Weibull distribution⁶⁸ contradicting predictions of dramatic improvements in Weibull modulus based on indentation mechanics analysis.⁶⁹

Mecholsky et al.⁷⁰ and Marshall⁶⁴ suggest that a simple way to measure an effective R-curve is to measure strength and critical flaw size in strength test specimens and compute apparent K_{Ic} at fracture. Rising R-curves will be evident on a plot of K_{Ic} versus crack size. They showed evidence that the mirror to flaw size ratio changed significantly as a function of crack size.

(a)



(b)



Figure 7.32 Grinding cracks in transversely ground rods that show evidence of stable crack extension (arrows) in a silicon nitride with rising R-curve behavior. (a) 657 MPa and (b) 641 MPa. (Ref. 71)

The fractographer should keep the above factors in mind. As noted above, R-curve behavior does not leave any intrinsic telltale markings on the fracture surface. R curve behavior can throw off flaw size calculations if they are based on a single point value for fracture toughness in equations 7.7 or 7.19. In principle, the fractographer may be able to find a region of stable extension around a flaw, but in practice this may be difficult especially if the toughening phenomena and the microstructure produce a rough fracture surface. One indication of potential R-curve behavior may be a systematic $c_{\text{calc}} \neq c_{\text{meas}}$ trend. As noted previously, if the fractographer detects and measures only the initial flaw size, then $c_{\text{calc}} > c_{\text{meas}}$. In this case it is the fractographic size measurement that is off. Alternatively, if stable crack extension due to R-curve behavior does occur, but the fractographer uses a long crack (plateau) value of fracture toughness, then the fracture toughness is overestimated and the calculated crack size is wrong, and again $c_{\text{calc}} > c_{\text{meas}}$.

A rising R-curve does not necessarily translate to superior mechanical properties. Careful microstructural control is usually required. If reinforcing agents are not well dispersed and are clumped together, they can act as strength-limiting flaws. Alternatively, local regions depleted of the reinforcing elements may also have ordinary flaws. Many toughened ceramics have not shown commensurate increases in strength or Weibull moduli (a measure on consistency of strengths as discussed in section 7.15,) contrary to expectations. The reason is simple. The very microstructural changes that enhance crack-microstructure interactions also create non-uniform microstructural regions, flaws, and microflaw concentration regions. That is why Y-TZP with a modest fracture toughness of $5 \text{ MPa}\sqrt{\text{m}}$ to $6 \text{ MPa}\sqrt{\text{m}}$ is stronger than Mg-PSZ. The Y-TZP has a very uniform sub-micron grain size and small $\approx 20 \mu\text{m}$ diameter pore flaws (Figure 6.6f). The Mg-PSZ has a fracture toughness of up to 10 to $20 \text{ MPa}\sqrt{\text{m}}$, but a coarse-grain microstructure loaded with grain boundary faults and concentrations of micropores (Figures 6.13, 6.44, 6.45, 6.46c). The flaw size may be hundreds of μm in size.

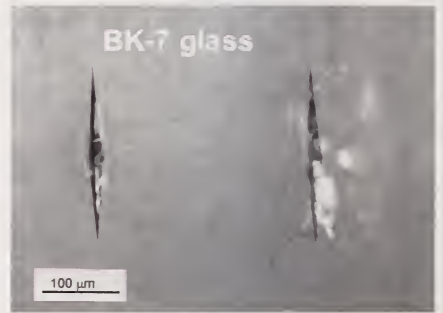
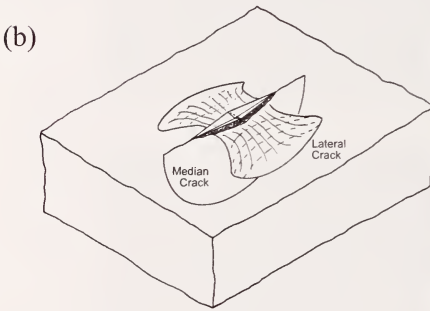
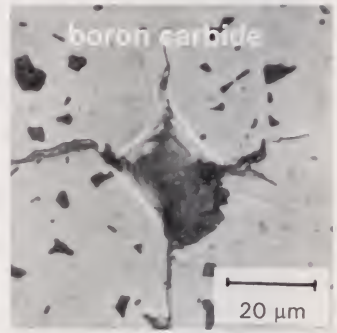
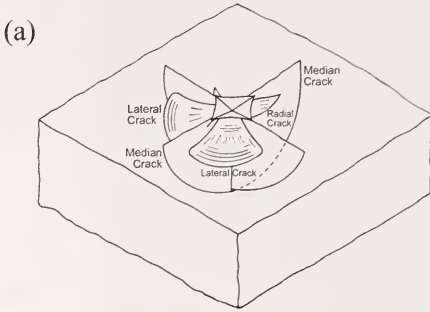
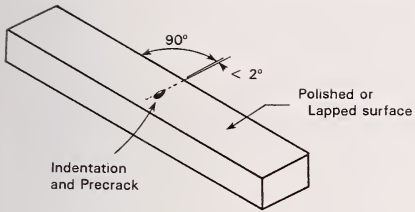
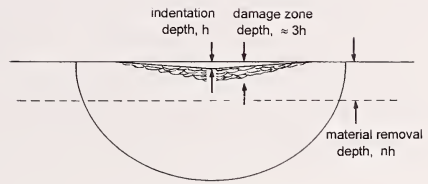


Figure 7.33 Indentation generated damage sites. (a) and (b) show common crack patterns and examples around Vickers and Knoop indentations.

(a)



(b)



(c)

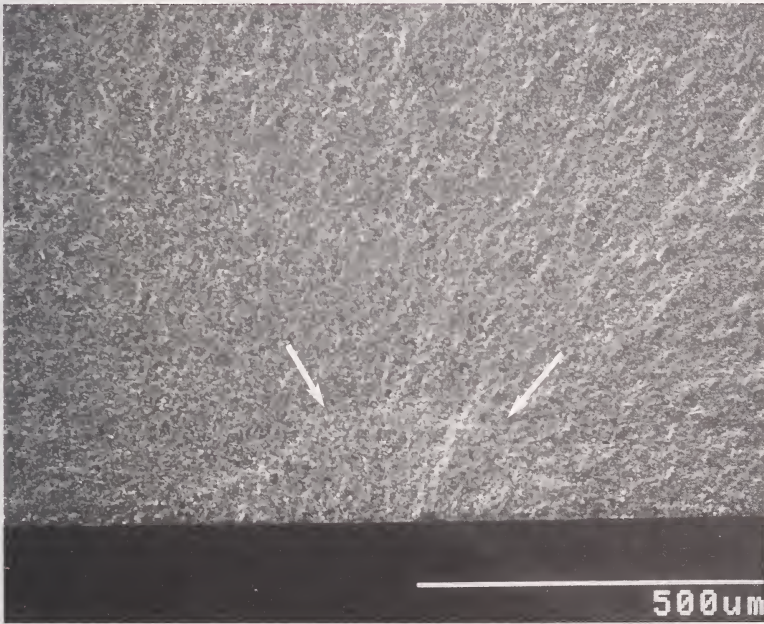


Figure 7.34 The surface crack in flexure method uses a Knoop indenter to create a semi elliptical surface crack in a bend bar (a). (b) shows a section view of the indentation and the median crack below it. The residual stress damage zone is removed by polishing or hand grinding leaving a controlled surface flaw in the test piece. (c) shows a Knoop crack in a silicon nitride (arrows).

7.12 Indentation Mechanics

A substantial literature exists on the mechanics of flaws made with Vickers or Knoop indentations. Figures 7.33 illustrate some of these “controlled flaws.” The indentations create not only a residual impression that is measured in a hardness test, but cracks and a concentrated damage zone directly underneath the indentation.

Controlled flaws for fracture mechanics experiments should be made with the Knoop indenter.^{72,73} The flaw geometry is simpler and more easily controlled. Loads of 9.8 N to 294 N are used to create a semi-elliptical surface cracks in a bend bar (Figure 7.34). The indentation residual stress damage zone and any lateral cracks are removed by polishing and then the test piece broken in flexure. Fractographic techniques are used to find and measure the flaw size. Other precrack examples are shown in Figures 5.43 and 6.30. Calculations are simple. The Newman-Raju stress intensity shape factors described in section 7.5.2 are used with equation 7.6 to compute stress intensities. The name of the method was changed from “controlled surface flaw” to the “surface crack in flexure (SCF)” method by the author in 1994 in order to avoid confusion with some Vickers indentation methods and to also use nomenclature then in use in the fracture mechanics community.^{36,74} The SCF procedure was the primary method used to prepare the world’s first standard reference material for the property fracture toughness, K_{Ic} .⁷⁵ It was formally standardized by the American Society for Testing and Materials^{35,76} the European Committee for Standards⁷⁷, and the International Organization for Standards.³⁷ The method does not work on soft, porous, or very tough materials, since median cracks will not form. Details on the method are in these standards or in Reference 73.

Vickers indentation procedures are widely used since they usually do not require fractographic examination. The method has severe drawbacks, however. Vickers generated flaws are much more complex. Rather than a single median crack, Vickers indentations have multiple median, radial, and lateral cracks. The cracks also have a complex stress residual stress damage associated with them.^{78,79} Rather than envision these Vickers indentation sites as model flaws with discrete median cracks with a modest residual stress pulling on the faces, it is actually more appropriate to regard them as Vickers *damage zones*. A semicircular median crack is typically assumed to pop in underneath the indentation, although the crack type and formation sequence is quite complicated and varies dramatically with material.⁸⁰ The residual stress damage zone is approximated by a point force acting to open the crack. The stress intensity fac-

tor K_{Ir} acting on the flaw in this case has the relationship shown in Figure 7.13b, namely:

$$K_{Ir} = \chi \frac{P}{c^{1.5}} \quad 7.29$$

where c is the crack size, P is the indentation load, and χ is a constant that incorporates geometry and residual stress field factors. This combines with the stress intensity created by a far field tensile stress to produce a net K_I :

$$K_I = Y\sigma_a \sqrt{c} + \chi \frac{P}{c^{1.5}} \quad 7.30$$

The first term on the right dominates for large cracks. The second term is significant for small crack sizes, but rapidly diminishes as the crack extends away from the residual stress damage zone. The net effect of the two terms is to cause a crack to extend stably somewhat prior to catastrophic propagation. The extent of stable propagation has been estimated to be 2.5 times the original flaw size when the testing is done in inert environment and all the assumptions in the analysis are upheld.⁷⁹

It is clear from above that the local residual stresses dramatically alter the local stress intensity field, and that a simple application of equations 7.6 based on only the far field tensile stresses will be faulty. Typically c_{calc} will be larger than c_{meas} , if the latter is the original flaw size and stable crack extension is not detected.

By the time the crack propagates to the extent that it is forming the mirror boundary markings, the effect of the localized residual stress term is insignificant.⁸¹ Hence, the mirror size is unaffected by the indentation residual stresses and the stress-mirror size relationship equation 7.4 is unaffected. The mirror to *initial* flaw size ratio is affected, however, and can be larger than values for annealed flaws.⁸¹ Indentation residual stresses do not affect branching distances or the fragmentation patterns.

Evidence of stable crack extension from indentation localized residual stresses may be difficult to detect on fracture surfaces. Figure 5.45 shows an example in a fine-grained silicon nitride. Stable extension is most often detected in laboratory conditions with careful microscopy on a polished outer surface or through the material if the material is transparent.

The observant reader will note that Vickers indentation flaws do not resemble the majority of origins shown in Chapter 6. Notwithstanding claims to the contrary, it is not at all clear whether indentation damage sites simulate genuine

flaws in ceramics and glasses. It has been claimed that they model contact damage sites and/or machining cracks, but Figure 6.18 in the previous chapter shows that actual contact or impact damage sites are often more irregular than the model flaws, with significant amounts of material removed by lateral cracks and spalls. The contact-generated residual stresses are often partially or completely relieved. Service impact conditions are rarely as controlled as those in an indentation process, where an ideal diamond slowly applies load perpendicular to the surface. The localized indentation residual stress field of a laboratory indentation has a very stabilizing influence on a flaw, allowing it to have extensive stable extension that may not be experienced by genuine flaws. The previous section on R-curve effects mentioned some examples where predictions of enhanced Weibull modulus based on indentation flaw analysis were misleading or wrong. One study⁶⁵ showed that, without proper care, the usual analysis with indentation flaws produced the implausible result that a soda lime silica glass had a rising R curve. There has been an over reliance on Vickers indentation flaws. From some of the literature one might think that are they are more important than genuine flaws. Fractographers know otherwise.

7.13 Fractal Analysis

Fractal analysis is a tool that may be used to characterize irregular surfaces, such as fracture surfaces. It is not used to find and characterize fracture origins, but to characterize the roughness or unevenness of a surface. Fractal geometry is a non-Euclidean geometry that exhibits self similarity and scale invariance. Self similarity means that a geometric shape in one location is similar to a geometric shape elsewhere. Scale invariance means that the geometric shape is similar irrespective of its size. Fractal analysis is unlike classical surface roughness measurements that characterize the heights between peaks and valleys. Fractal analysis measures the extent of the “wiggleness,” “tortuosity,” or irregularity of the surface.^{82,83}

Classical Euclidean geometry has a simple relationship between area and length. So for example, a circle of diameter D has the well-known relationships in accordance with Euclidean geometry:

$$Area = \frac{\pi D^2}{4} \quad 7.31$$

and

$$Perimeter = \pi D \quad 7.32$$

so that

$$Perimeter \propto \sqrt{Area} \quad 7.33$$

This is the case for a perimeter line that is unwavering and follows the circle rim exactly. If on the other hand, the perimeter line had perturbations and wiggles, the perimeter length is greater. If the perimeter line is magnified and studied in greater detail, it is possible that each wiggle or perturbation itself may be seen to have yet smaller wiggles creating additional length and so on. That is the nature of fractal dimensions. The greater the magnification used, and the finer the measuring stick used to measure the lengths, the longer is the overall perimeter length. This leads to the somewhat unsatisfying outcome that the perimeter length actually varies with magnification and the size of the measuring scale. The extra wiggleness or irregularity alters the classical Euclidean geometric relationships and add length by an amount depending upon the fractal dimension and the size of the measuring stick. The perimeter of a fractal shape around an area can be characterized by the following relationship:

$$L = L_0 s^{1-D} \quad 7.34$$

where L is the length of the line, L_0 is a constant, s is the measuring scale or ruler size, and D is the *fractal dimension* which in this instance is between 1 and 2. If the line has no wiggles (and is a Euclidean line) then $D = 1$, and $L = L_0$ irrespective of the size of ruler used to measure it. On the other hand if the line is fractal, and D is between 1 and 2, then L varies with the size of the ruler unit used. The exponent of s is negative and the smaller s is, the larger is L . The same type relationship applies if areas were to be used in equation 7.34, in which case D would have a value between 2 and 3. The value of $D-1$ for lengths (or $D-2$ for areas) is often written as D^* , the fractional part of the fractal dimension.

Two ways to measure the fractal dimension of a fracture surface are the fracture profile technique and the slit island analysis.⁸³ The fracture profile technique simply makes a vertical cross section through a fracture surface. The profile with all its ups and downs is analyzed. In the slit island technique, a horizontal cross section is made through a fracture surface to reveal islands corresponding to the peaks of hills and ridges and their wiggly outlines. This process is repeated and measurements remade much like in a classical metallographic serial section analysis. Both procedures can be tedious, but computer analysis and image analysis software can simplify this task. Confocal optical microscopy would seem to be an ideal tool, since it may be able to examine the fracture surface directly and section it automatically without the need for repetitive polishing.^{84,85} A typical fractal analysis measures a perimeter length or roughness number with finer and finer measuring intervals. A graph of log length versus log measuring interval size is constructed and the slope used to estimate the fractal dimension.

Fractal analysis has usually been used to correlate fracture toughness with the fractal dimensions. The processes that enhance fracture toughness often increase the roughness of a fracture surface. Passoja, Mecholsky and colleagues have pioneered correlations of this type for ceramics.^{82,83,86,87} For example, they have shown that:

$$K_{Ic} = K_o + A(D^*)^{1/2} \quad 7.35$$

where K_o is a baseline toughness of the material for a smooth (Euclidean) fracture surface, D^* is the fractional part of the fractal dimension and A is a constant that can be related to the elastic modulus and the atomic dimensions of the structure of the material. The implication of this relationship is that only a small portion of a fracture surface is needed to determine the fracture toughness. In principal, this could be used in forensic analyses to determine if the material was poorly processed and had a lower than expected fracture toughness. The fractal analysis gives no information about the origin, however.

Mecholsky and Freiman⁸⁷ showed that variations in the mirror to flaw size ratio correlated with the fractal dimension of the fracture surface well outside the mirror:

$$\frac{R}{c} \propto \frac{1}{D^*} \quad 7.36$$

where R is either the mirror-mist, mist-hackle, or branching distance, and c is the flaw size. In other words, the very processes that contribute to formation of roughness at the mirror boundary are related to those that create roughness elsewhere in areas remote from the origin.

At the beginning of this section it was noted that fractal analysis is a tool to characterize fracture surfaces. Most fractal analyses have focused on using the fractal dimension as a materials science tool to study the microstructure or material properties. Additional work showing practical applications is needed.

7.14 Estimation of Residual Stresses

Residual stresses may exist on many levels. They may be local to a flaw, as in a Vickers indentation or an inclusion with a mismatch in properties with the matrix. They may be distributed through the thickness, as in surface compression and internal tension in chemically or thermally tempered glasses. They may be global from differential shrinkage during firing. Their effects on

flaws may be very difficult to analyze unless some assumptions are made about their character and distribution.

For example, residual stresses from grinding vary with direction, whether parallel to or perpendicular to the grinding direction. They typically are strongly compressive right at the surface, but rapidly decrease and become tensile a short distance (5 μm to 20 μm) beneath the surface. A grinding crack tip may be in tension or still in a compression zone depending upon how deep it is. The net effect of the stress gradient on the flaw as a whole is a complex fracture mechanics problem, but analytical attempts have been made to determine the effect on flaws with mixed success. The reader is referred to the work of Holstein et al.⁸⁸ for a good example. It is often difficult to determine whether the net effect is tensile or compressive. The weak point in these analyses is the lack of adequate quantitative information about the residual stress spatial profile.

Empirical estimation of residual stresses by fragmentation patterns has been covered in sections 7.2.2 and 7.3.2.

The usual approach in dealing with residual stress problems is to rely on the principle of superposition. That is, the effect of stresses on a location or flaw in a body is additive, whether the stresses are mechanical, transient thermal, or residual. To a first approximation, residual stresses, σ_r , simply add to or subtract from the applied stresses acting on the flaw from known external sources, σ_a so that the net stress acting on a site or a flaw is:

$$\sigma_{net} = \sigma_a + \sigma_r \quad 7.37$$

Tensile residual stresses add to externally applied tensile stresses and reduce the stresses or forces necessary to cause fracture from a particular flaw. Compressive residual stresses acting on a flaw must be overcome and require greater applied stresses. (The usual convention is that compressive stresses are negative.) For the case of a flaw loaded with a far field stress σ_a with a residual stress σ_r that is constant in the vicinity of the flaw:

$$K_{Ic} = Y \sigma_{net} \sqrt{a} \quad 7.38$$

Rearranging:

$$\sigma_r = \frac{K_{Ic}}{Y \sqrt{a}} - \sigma_a \quad 7.39$$

If a convenient flaw is found that has a shape that is conducive to a fracture mechanics analyses and K_{Ic} , σ_a , and the flaw size are known, then equation 7.39 can be used to estimate σ_r . If the flaws are less ideal, several may be ana-

lyzed as best as possible and any systematic deviation from the calculated and measured flaw sizes may be interpreted as evidence of residual stresses as discussed in section 7.8.

Residual stresses can cause systematic deviations in the stress- mirror size trends presented previously. Trend deviations are shown in Figure 7.35. The easiest interpretation is in Figure 7.35a, whereby a nonzero intercept indicates the magnitude and sign of the residual stress. A compressive residual stress shifts the line upward since a greater applied stress is necessary to cause fracture. If a single mirror is measured and the externally applied stress σ_a is known, then:

$$(\sigma_a + \sigma_r)\sqrt{R} = A \tag{7.40}$$

and

$$\sigma_r = \frac{A}{\sqrt{R}} - \sigma_a \tag{7.41}$$

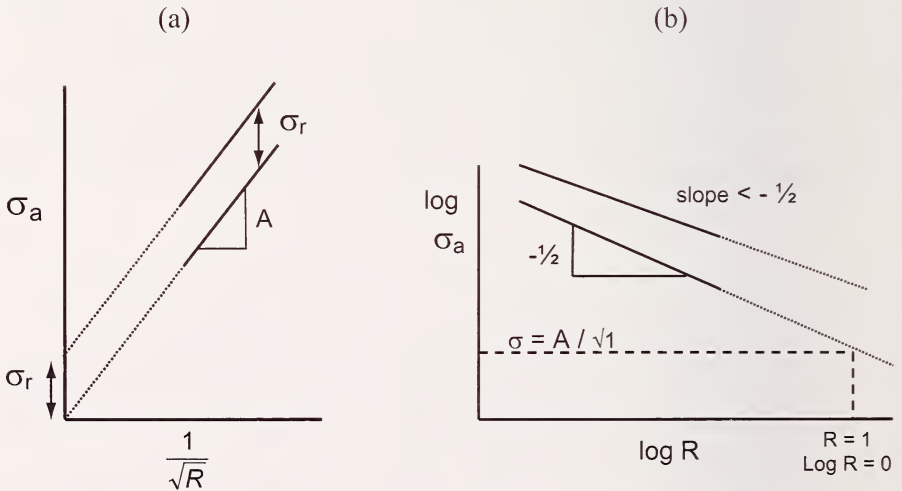


Figure 7.35 Systematic deviations in the fracture mirror size trends for applied stress, σ_a , as a function of mirror radius are indicative of residual stresses. (a) shows that residual stresses create non zero intercepts. (b) shows that residual stresses alter the slope.

Additional details on estimating residual stresses by this method are in Appendix D.

On the other hand, more complex loadings, such as in the case of indentation mechanics problem discussed previously whereby the residual stresses vary dramatically in the vicinity of the flaw, it is necessary to add stress intensities and:

$$K_{Ic} = K_{Ia} + K_{Ir} = Y \sigma_a \sqrt{a} + K_{Ir} \quad 7.41$$

where K_{Ir} is the stress intensity from the residual stress and K_{Ia} is that from the applied tensile stresses.

A qualitative assessments that residual stresses are present can be made from mirror shapes as discussed in section 5.2.3 and also by changes in the mirror to flaw size ratio as discussed in section 7.7.

7.15 Weibull Analysis

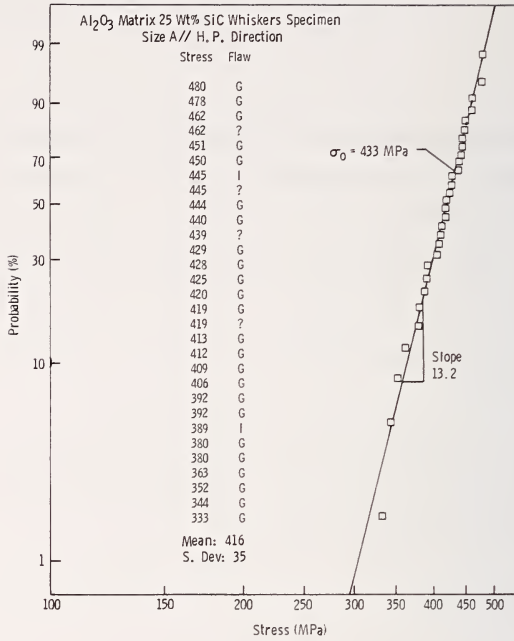
Ceramic and glass strengths depend upon the size and shape of the specimens and the mode of loading. Specimen strengths vary due to variations in the size, severity, location, and density of flaws. Strength variability is usually analyzed in accordance with the Weibull distribution,⁸⁹ which is based on the premise that the weakest link in a body controls strength. A strength test produces two key bits of information: a strength datum and a fracture origin flaw. The flaws are just as important as the strength.

The Weibull two-parameter distribution is:

$$P_f = 1. - \exp\left(-\left(\frac{\sigma_a}{\sigma_\theta}\right)^m\right) \quad 7.43$$

where P_f is the probability of fracture, σ_a is the applied stress, and m and σ_θ are constants called the Weibull modulus and the characteristic strength of the specimen, respectively. Strength data is typically ranked from weakest to strongest and then plotted on a special set of axes intended to linearize the data as shown in Figures 7.36. With Weibull analyses, the maximum nominal stress in the body that is used. Stress is not adjusted for location. If the data fits the Weibull distribution, then it should fit on a line with the slope equal to the Weibull modulus, m , and the characteristic strength σ_θ corresponding to the strength of the specific test specimen configuration at the 63.2 % level.

(a)



(b)

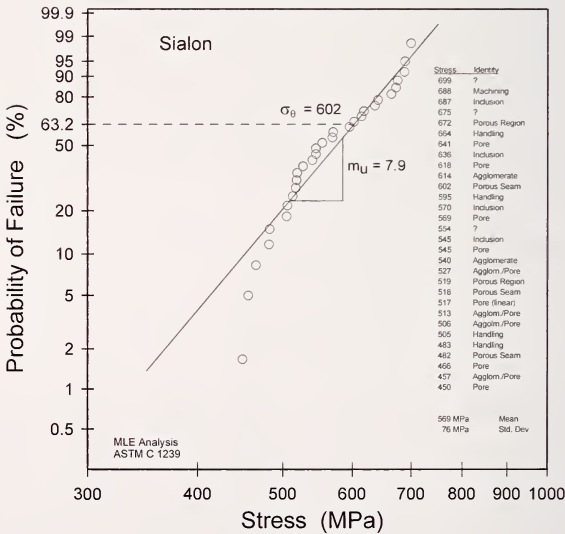


Figure 7.36 Fractographically-labeled Weibull flexural strength distribution plots. (a) is for a SiC whisker-reinforced alumina. “G” is an abbreviation for a large grain origin type, “I” is for inclusion, and “?” is unknown. (b) is for a SiAlON ceramic. The slope of the fitted lines is the important Weibull modulus (m) parameter, a measure of strength variability.

Figure 7.36 shows two sets of strength data as commonly plotted. Such graphs demonstrate the scatter and the goodness of fit to the Weibull function. Both data sets are fractographically labeled Weibull graphs which have not only the strengths, but also flaw information. Figure 7.36a for the alumina with silicon carbide whisker reinforcements shows that the strength-controlling flaws were almost always large alumina grains. The whiskers that were added to enhance K_{Ic} had chemistries or impurities that caused grain growth in the matrix. The good news was that only one flaw type controlled strength and the Weibull distribution fit quite well. In contrast, Figure 7.36b shows a SiAlON material that had many concurrent flaw types and a very low Weibull modulus. Brittle materials design with such a material would be problematic, since each flaw type has its own distribution. Strength scaling with size would be complicated. The tester might have wondered why the curve had so many wiggles. The fractographic analysis makes it clear why the single Weibull line does not fit very well.

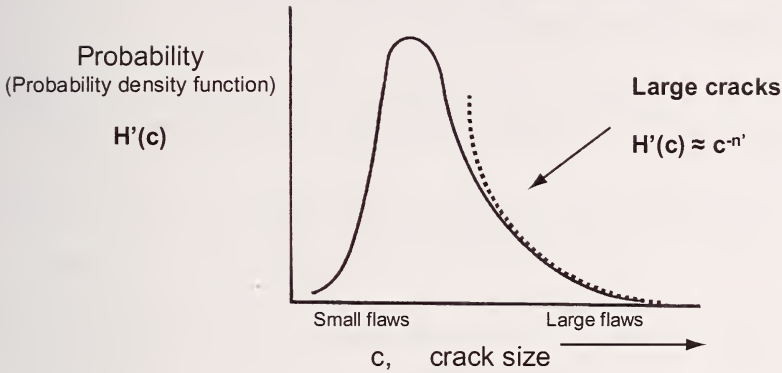
Weibull originally derived his distribution on semi-empirical grounds. No assumptions about flaws or their nature were made. He simply assumed that small elements in a body had a local strength and he assumed a plausible distribution for these local variations. He then integrated to compute the failure probability for the whole specimen assuming that fracture would occur at the weakest link or element. His perceptive analysis has been theoretically verified by subsequent analyses by a number of authors, but most especially by Jayatilaka and Trustrum.^{90,91} They showed that flaw size distributions could have their distribution tails (at large flaw size) matched by an inverse power law distribution as shown in Figure 7.37. Using this inverse power law distribution and applying classical fracture mechanics (equation 7.7) they were able to mathematically derive the Weibull distribution. The Weibull function is now based on a solid theoretical footing. Reference 92 has a useful review of a number of successful applications using Weibull analysis.

Average bulk properties such as density, surface finish, or grain size often do not correlate with strength. Strength often depends upon infrequent or aberrant microstructural features, namely flaws, and not on the average microstructure. In some cases, the aberrant features do scale with the average microstructure, so there may be a correlation between strength and average bulk microstructure or surface finish. One important aspect of the Weibull model is that the larger the structure or test piece is, the more apt it is to contain a severe flaw. Hence, strength usually varies inversely with component size: the larger the component, the weaker it is likely to be. Strengths can be correlated or scaled by comparing effective volumes or effective surfaces. It is beyond the scope of this Guide to delve into this topic, but suffice to say that such strength scaling

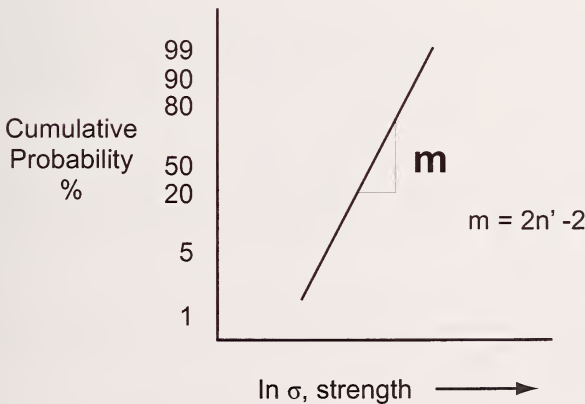
analyses depend upon crucial assumptions. For example, a Weibull effective volume scaling approach is justified if fractography confirms that strength limiting flaws are volume-distributed. One often overlooked assumption in the Weibull analysis is that specimens must contain a minimum number of flaws. There must be a number of "chain links" present in the specimen for it to have strength controlled by a "weakest link." A specimen with a single flaw has only one strength controlling link. For this reason, it is ludicrous to apply Weibull statistics to specimens with single indentation flaws. It is also very dangerous for engineers to ignore or discard a few usually low strength specimens from the low strength tail of a Weibull distribution. These "atypical" or "non representative outcomes" may reflect a genuine flaw type that will ruin many pieces if the product is scaled up for mass production or if the components are designed to have very low probabilities of fracture (e.g., $P_f \ll 1\%$). Finally, strength scaling analyses quickly become very complex if more than one flaw type (e.g., pores and inclusions, or pores, inclusions, and machining damage) controls strength. Various flaw types may suddenly appear or disappear as strength controlling flaws as components sizes are scaled up or down. The reader is referred to the review by Quinn and Morrell⁹² for more information on these fascinating topics.

(a)

$$H'(c) = \text{constant} * \exp\left(-\frac{\alpha}{c}\right) c^{-n'}$$



(b)



The Weibull distribution can be derived from the flaw size distribution shown in (a). $H'(c)$ is the probability for occurrence of a flaw of size c . n' and α are constants. The largest flaws control strength and that portion of the distribution can be modeled by an inverse power law with exponent n' . (b) shows the Weibull distribution for strength. The Weibull modulus m is equal to $2n' - 2$.

Chapter 7 References

- 1 V. D. Fréchet, *Failure Analysis of Brittle Materials*, Advances in Ceramics, Vol.28, American Ceramic Society, Westerville, OH, 1990.
- 2 L. Orr, "Practical Analysis of Fractures in Glass Windows," *Materials Research and Standards*, 12 [1] (1972) 21 - 23.
- 3 V. D. Fréchet and T. A. Michalske, "Fragmentation in Bursting Glass Containers," *Bull. Amer. Ceram. Soc.*, 57 [4] (1978) 427 - 429.
- 4 V. D. Fréchet and S. L. Yates, "Fragmentation of Glass Bottles by Impact," *J. Am. Ceram. Soc.*, 72 [6] (1989) 1060.
- 5 R. Morrell, "Fractography of Brittle Materials," Measurement Good Practice Guide, #15, National Physical Laboratory, Teddington, Middlesex, United Kingdom, 1999.
- 6 R. A. McMaster, D. M. Shetterly, and A. G. Bueno, "Annealed and Tempered Glass," pp. 453 - 459 in *Engineered Materials Handbook, Vol. 4, Ceramics and Glasses*, S. Schneider, ed., ASM, Metals Park, OH, 1991.
- 7 N. Shinkai, "The Fracture and Fractography of Flat Glass," pp. 253-297 in *Fractography of Glass*, eds. R. C. Bradt and R. E. Tressler, Plenum, NY, 1994.
- 8 K. Akeyoshi, E. Kanai, K. Yamamoto, and S. Shima, Asahi Garasu Kenkyu Hokoku, (Report of the Research Lab, Asahi Glass Co., 17 [1] (1967) 23 - 26.
- 9 J. M. Barsom, "Fracture of Tempered Glass," *J. Am. Ceram. Soc.*, 51 [2] (1968) 75 - 78.
- 10 J. Menč, "*Strength and Fracture of Glass and Ceramics*," Glass Science and Technology 12, Elsevier, NY, 1992.
- 11 D. Shetty, A. Rosenfield, and W. Duckworth, "Crack Branching in Ceramic Disks Subjected to Biaxial Flexure," *Comm. Am. Ceram. Soc.*, Jan. 1983, C10 - C12.

- 12 D. Hull, "Influence of Stress Intensity and Crack Speed on the Fracture Surface Topography: Mirror to Mist to Macroscopic Bifurcation," *J. Mat. Sci.*, 31 (1996) 4483 – 4492.
- 13 U. Soltesz, H. Richter, and E. Sommer, "Influence of Internal Stresses on the Development of Cracks in Glasses," pp. 2303 – 2310 in *Advances in Fracture Research*, eds. D. Francois et al., Pergamon Press, NY, 1980.
14. Private Communication. Letter from L. Orr to G. Quinn on December 15, 2001.
- 15 W. C. Levenood, "Effect of Origin Flaw Characterization on Glass Strength," *J. Appl. Phys.*, 29 [5] (1958) 820 – 826.
- 16 J. W. Johnson and D. G. Holloway, "On the Shape and Size of the Fracture Zones on Glass Fracture Surfaces," *Phil. Mag.* 14 731 - 743 (1966).
- 17 E. B. Shand, "Breaking Stress of Glass Determined from Dimensions of Fracture Mirrors," *J. Am. Ceram. Soc.*, 42 [10] (1959) 474 – 477.
- 18 M. J. Kerper and T. G. Scuderi, "Relation of Strength of Thermally Tempered Glass to Fracture Mirror Size," *Bull. Am. Ceram. Soc.*, 44 [12] (1965) 953 – 955.
- 19 M. J. Kerper and T. G. Scuderi, "Relation of Fracture Stress to the Fracture Pattern for Glass Rods of Various Diameters," *Bull. Am. Cer. Soc.*, 45 [12] (1966) 1065 - 1066.
- 20 H. P. Kirchner, R. M. Gruver, and W. A. Sotter, "Fracture Stress-Mirror Size Relations for Polycrystalline Ceramics," *Phil. Mag.*, 33 [5], 775 – 780 (1976).
- 21 *Glass Industry*, 36 [10] (1955) 523.
- 22 E. B. Shand, "Experimental Study of Fracture of Glass: II, Experimental Data," *J. Am. Ceram. Soc.*, 37 [12] (1954) 559 – 572.
- 23 N. Terao, "Sur une Relation entre la Resistance a la Rupture et le Foyer d'Eclatement du Verre," *J. Phys. Soc. Japan.*, 8 [4] (1953) 545 – 549.

- 24 H. P. Kirchner and J. W. Kirchner, "Fracture Mechanics of Fracture Mirrors," *ibid*, 62 [3-4] (1979) 198 – 202.
- 25 H. P. Kirchner and J. C. Conway, Jr., "Criteria for Crack Branching in Cylindrical Rods: I, Tension; and II, Flexure," *ibid*, 70 [6] (1987) 413 – 418 and 419 - 425.
- 26 H. P. Kirchner and R. M. Gruver, "Fracture Mirrors in Alumina Ceramics," *Phil Mag.*, 27 (1973) 1433 – 1446.
- 27 M. J. Kerper and T. G. Scuderi, "Modulus of Rupture of Glass in Relation to Fracture Pattern," *Cer. Bull.*, 43 [9] (1964) 622 – 625.
- 28 G. D. Quinn, J. Eichler, U. Eisele, and J. Rödel, "Fracture Mirrors in a Nanoscale 3Y-TZP," *J. Am. Ceram. Soc.*, 87 [3] (2004) 513-516.
- 29 A. A. Griffith, "The Phenomena of Rupture and Flow in Solids," *Philos. Trans. R. Soc. Lond.*, A221 (1920) 163 – 198.
- 30 A. A. Griffith, "The Theory of Rupture," in *Proc. 1st Int. Congress on Applied Mechanics*, eds. C. B. Biezeno and J. M. Burgers, (1924), 55.
- 31 G. R. Irwin, "Analysis of Stresses and Strains Near the End of a Crack Traversing a Plate," *J. Appl. Phys.*, 24 (1957) 361 – 364.
- 32 SRM 2100, "Fracture Toughness of Ceramics," National Institute for Standards and Technology, Gaithersburg, MD, 1999.
- 33 J. C. Newman and I. S. Raju, "An Empirical Stress Intensity Factor Equation for the Surface Crack," *Eng. Fract. Mech.*, 15, [1-2] (1981) 185-192.
- 34 ASTM C 1322-96, "Standard Practice for Fractography and Characterization of Fracture Origins in Advanced Ceramics," *Annual Book of Standards*, Vol. 15.01, ASTM, West Conshohocken, PA, 1996.
- 35 ASTM C1421-99, "Standard Test Method for the Determination of Fracture Toughness of Advanced Ceramics," *ibid*, 2000.
- 36 ASTM E-740-88, "Standard Practice for Fracture Testing with Surface-Crack Tension Specimens," *Annual Book of Standards*, Vol. 3.01, ASTM, West Conshohocken, PA, 1988.

- 37 ISO 18756, Fine Ceramics (Advanced Ceramics, Advanced Technical Ceramics) – Determination of Fracture Toughness of Monolithic Ceramics at Room Temperature by the Surface Crack in Flexure (SCF) Method, International Organization for Standards, Geneva, SW, 2003.
- 38 Y. Murakami, *Stress Intensity Factors Handbook*, Vols. 1 and 2, ed., Pergamon Press, NY, 1986. (Case 9.49)
- 39 G. K. Bansal, “Effect of Flaw Shape on Strength of Ceramics,” *J. Am. Ceram. Soc.*, 59 [1-2] (1976) 87-88.
- 40 J. J. Mecholsky, Jr., S. W. Freiman, and R. W. Rice, “Fracture Surface Analysis of Ceramics,” *J. Mat. Sci.*, 11 (1976) 1310–1319.
- 41 G. K. Bansal and W. H. Duckworth, “Fracture Stress as Related to Origin and Fracture Mirror Sizes,” *J. Am. Ceram. Soc.*, 60 [7–8] (1977) 304 – 310.
- 42 G. K. Bansal, “On Fracture Mirror Formation in Glass and Polycrystalline Ceramics,” *Phil Mag.*, 35 [4] (1977) 935- 944.
- 43 S. R. Choi and J. P. Gyekenyesi, “Crack Branching and Fracture Mirror Data of Glasses and Advanced Ceramics,” NASA Technical Report TM 1998-206536, 1998.
- 44 A. I. A. Abdel-Latif, R. C. Bradt, and R. E. Tressler, “Dynamics of Fracture Mirror Boundary Formation in Glass,” *Int. J. Fract.*, 13, [3] (1977) 349-359.
- 45 M. Ramulu, R. C. Bradt, A. S. Kobayashi, and K. H. yang, “A Dynamic Fracture Mechanics Interpretation of Multiple Mist Regions on Soda-Lime-Silicate Glass Fracture Features,” pp. 215 – 227 in *Fractography of Glasses and Ceramics, Advances in Ceramics*, Vol. 22, J. Varner, and V. Fréchette, eds., American Ceramic Society, Westerville, OH, 1988.
- 46 D. A. Krohn and D. P. H. Hasselman, “Relation of Flaw Size to Mirror in the Fracture of Glass,” *J. Am. Ceram. Soc.*, 54 [8] (1971) 411.
- 47 J. J. Mecholsky, Jr., A. Gonzalez, and S. W. Freiman, “Fractographic Analysis of Delayed Failure in Soda-Lime Glass,” *J. Am. Ceram. Soc.*, 62 [11-12] (1979) 577 – 580.

- 48 R. W. Rice, "Ceramic Fracture Features, Observations, Mechanism and Uses," pp. 5 – 103 in *Fractography of Ceramic and Metal Failures*, ASTM STP 827, ASTM, 1984.
- 49 G. D. Quinn and J. J. Swab, "Fractography and Estimates of Fracture Origin Size from Fracture Mechanics," *Ceram. Eng. and Sci. Proc.*, 17 [3] (1996) 51 - 58.
- 50 G. D. Quinn and J. J. Swab, "Comparisons of Calculated and Measured Flaw Sizes," pp. 175 – 192 in *Fractography of Glasses and Ceramics IV*, Ceramic Transactions, Vol. 122 eds. J. Varner and G. Quinn, American Ceramic Society, Westerville, OH, 2001.
- 51 H. G. Richter and F. Kerkhof, "Stress Wave Fractography," pp. 75 – 109 in *Fractography of Glass*, eds. R. C. Bradt and R. E. Tressler, Plenum, NY, 1994.
- 52 H. Richter, "Crack Propagation in Glass Under Liquids in an Intermediate Range of Crack Velocities," pp. 219 – 229 in *Strength of Inorganic Glass*, ed. C. R. Kurkjian, Plenum Press, NY, 1985.
- 53 T. A. Michalske, M. Singh, and V. D. Fréchette, "Experimental Observation of Crack Velocity and Crack front Shape Effects in Double-Torsion Fracture Mechanics Tests," pp. 3 - 12 in *Fracture Mechanics for Ceramics, Rocks, and Concrete*, STP 745, American Society for Testing and Materials, West Conshohocken, PA, 1982.
- 54 T. A. Michalske and J. M. Collins, "Fractographic Determination of Crack-Tip Stress Intensity," pp. 229 – 239 in *Fractography of Glasses and Ceramics*, Advances in Ceramics, Vol. 22, eds. J. R. Varner and V. D. Fréchette, American Ceramic Society, Westerville, OH 1988.
- 55 A. Tsirk, "Formation and Utility of a Class of Anomalous Wallner Lines on Obsidian," pp. 57 – 69, *ibid.*
- 56 E. F. Poncelet, "The Markings on Fracture Surfaces," *J. Soc. Glass Technol.*, 42 (1958) 279T – 288T.
- 57 A. Smekal, "Procedure for Measurement of Fracture Surface Propagation Velocities on Fracture Surfaces," *Glastech. Ber.*, 23 [3] (1950) 57 – 67.

- 58 T. Fett, D. Munz, and K. Keller, "Determination of Subcritical Crack Growth on Glass in Water from Lifetime Measurements on Knoop-Cracked Specimens," *J. Mat. Sci.*, 23 (1988) 798 - 803.
- 59 P. J. Dwivedi and D. J. Green, "Determination of Subcritical Crack Growth Parameters from In situ Observation of Indentation Cracks," *J. Am. Ceram. Soc.*, 78 [8] (1995) 2122 - 2128.
- 60 V. M. Sglavo and R. Dal Maschio, "Controlled Indentation-Induced Cracks for the Determination of Fracture Toughness in Alumina," pp. 233 - 244, in *Fracture Mechanics of Ceramics, Vol. 11*, eds. R. C. Bradt et al., Plenum, NY, 1996.
- 61 M. Stech and J. Rödel, "Method for Measuring Short -Crack R-Curves Without Calibration Parameters: Case Studies on Alumina and Alumina/Aluminum Composites," *J. Am. Ceram. Soc.*, 79 [2] (1996) 291 - 297.
- 62 W. Chen, D. Lupascu, J. Rödel, and C. S. Lynch, "Short Crack R-Curves in Ferroelectric and Electrorestrictive PLZT," *ibid*, 84 [3] (2001) 393 - 397.
- 63 A. H. Heuer, "Transformation Toughening in ZrO₂-Containing Ceramics," *ibid*, 70 [10] (1987) 689 - 698.
- 64 D. B. Marshall, "Strength Characteristics of Transformation Toughened Zirconia," *ibid*, 69 [3] (1986) 173 - 180.
- 65 S. M. Smith and R. O. Scattergood, "Controlled Crack Shapes for Indentation Fracture of Soda Lime Glass," *ibid*, 75 [9] (1992) 2593 - 2596.
- 66 R. W. Steinbrech and O. Schmenkel, "Crack-Resistance Curves of Surface Cracks in Alumina," *ibid*, 71 [5] (1988) C271- C273.
- 67 T. Fett, D. Munz, J. Siedel, M. Stech, and J. Rödel, "Correlation Between Long and Short Crack R-Curves in Alumina Using the Crack Opening Displacement and Fracture Mechanical Weight Function Approach," *ibid*, 79 [5] (1996) 1189 -1196.
- 68 T. Fett and D. Munz, "Evaluation of R-curve Effects in Ceramics," *J. Mat. Sci.*, 28 (1993) 742 - 752.

- 69 R. F. Cook and D. R. Clarke, "Fracture Stability, R-Curves and Strength Variability," *Acta Metall.*, 36 [3] (1988) 555 – 562.
- 70 J. J. Mecholsky, Jr., T. J. Hill and Z. Chen, "Application of Quantitative Fractography to the Characterization of R-Curve Behavior," pp. 152 – 167 in *Fracture Resistance Testing of Monolithic and Composite Brittle Materials*, ASTM STP 1409, eds., J. Salem, G. D. Quinn, and M. G. Jenkins, ASTM, West Conshohocken, PA 2002.
- 71 G. D. Quinn, L. K. Ives, and S. Jahanmir, "On the Fractographic Analysis of Machining Cracks in Ground Ceramics: A Case Study on Silicon Nitride," Special Publication SP 996, NIST, Gaithersburg, MD, May, 2003.
- 72 J. J. Petrovic, L. A. Jacobson, P. K. Talty, and A. K. Vasudevan, "Controlled Surface Flaws in Hot-Pressed Si_3N_4 ," *J. Am. Ceram. Soc.*, 58 [3-4] (1975) 113 - 116.
- 73 G. D. Quinn, R. J. Gettings, and J. J. Kübler, "Fractography and the Surface Crack in Flexure (SCF) Method for Evaluating Fracture Toughness of Ceramics," pp. 107 - 144 in *Fractography of Glasses and Ceramics III*, Ceramic Transactions, Vol. 64, eds., J. R. Varner, V. D. Fréchette, and G. D. Quinn, ACS, Westerville, OH, 1996.
- 74 G. Quinn, R. Gettings, and J. Kübler, "Fracture Toughness by the Surface Crack in Flexure (SCF) Method: Results of the VAMAS Round Robin," *Ceram. Eng. and Sci. Proc.*, 15, [5] (1994) 846-855.
- 75 G. D. Quinn, K. Xu, J. A. Salem, and J. J. Swab, "SRM 2100: the World's First Fracture Toughness Reference Material," pp. 499 – 530 in *Fracture Mechanics of Glasses and Ceramics, Vol. 14*, eds. R. C. Bradt, D. Munz, M. Sakai, and K. W. White, Kluwer/Plenum, NY, 2005.
- 76 I. Bar-On, G. D. Quinn, J. Salem, and M. J. Jenkins, "Fracture Toughness Standard Test Method C 1421-99 for Advanced Ceramics," pp. 315-335 in *Fatigue and Fracture Mechanics*, Vol. 32, ASTM STP 1406, ed. R. Chona, American Society for Testing and Materials, West Conshohocken, PA, 2001.

- 77 EN ISO 18756:2005, "Advanced Ceramics, Advanced Technical Ceramics) - ; Determination of Fracture Toughness of Monolithic Ceramics at Room Temperature by the Surface Crack in Flexure (SCF) Method," European Committee for Standards, Brussels.
- 78 B. R. Lawn and D. B. Marshall, "Indentation Fractography," pp. 1–36 in *Fractography of Glass*, eds. R. C. Bradt and R. E. Tressler, Plenum, NY, 1994.
- 79 P. Chantikul, G. R. Anstis, B. R. Lawn and D. B. Marshall, "A Critical Evaluation of Indentation Techniques for Measuring Fracture Toughness: II Strength Method," *J. Am. Ceram. Soc.*, 64 [9] (1981) 539–543.
- 80 R. F. Cook and G. M. Pharr, "Direct Observation and Analysis of Indentation Cracking in Glasses and Ceramics," *J. Am. Ceram. Soc.*, 73 [4] (1990) 787–817.
- 81 D. B. Marshall, B. R. Lawn, and J. J. Mecholsky, "Effect of Residual Stresses on Mirror/Flaw Size Relations," *ibid*, 63 [5-6] 358–360.
- 82 D. E. Passoja, "Fundamental Relationships Between Energy and Geometry in Fracture," pp. 101–126 in *Fractography of Glasses and Ceramics*, eds. J. R. Varner and V. D. Fréchet, Advances in Ceramics Volume 22, American Ceramic Society, Westerville, OH 1988.
- 83 J. J. Mecholsky, T. J. Mackin, and D. E. Passoja, "Self-Similar Crack Propagation in Brittle Materials," *ibid*, pp. 127–134.
- 84 D. A. Lange, H. M. Jennings, and S. P. Shah, "Relationship Between Fracture Surface Roughness and Fracture Behavior of Cement Paste and Mortar," *J. Am. Ceram. Soc.*, 76 [3] (1993) 589–597.
- 85 Y. Xin, K. J. Hsia, and D. A. Lange, "Quantitative Characterization of the Fracture Surface of Si Single Crystals by Confocal Microscopy," *ibid*, 78 [12] (1995) 3201–3208.
- 86 J. J. Mecholsky, D. E. Passoja, and K. S. Feinberg-Ringel, "Quantitative Analysis of Brittle Fracture Surfaces Using Fractal Geometry," *ibid*, 72 [1] (1989) 60–65.

- 87 J. J. Mecholsky, Jr. and S. W. Freiman, "Relationship Between Fractal Geometry and Fractography," *ibid*, 74 [12] (1991) 3136 – 3138.
- 88 T. Hollstein, W. Pfeiffer, M. Rombach, and B. Thielicke: pp. 145-169 in *Fractography of Glasses and Ceramics, III*, Ceramic Transactions, Vol. 64, eds. J. Varner, V. Fréchette and G. Quinn, (ACS, Westerville, OH, 1996).
- 89 W. Weibull, "A Statistical Distribution Function of Wide Applicability," *J. Appl. Mech.*, September, (1951) 293 – 297.
- 90 K. Trustrum and A. De S. Jayatilaka, "Application of Weibull Analysis for Brittle Materials," *J. Mat. Sci.*, 18 (1983) 2765-70.
- 91 A. De S. Jayatilaka and K. Trustrum, "Statistical Approach to Brittle Fracture," *ibid*, 12 (1977) 1426-30.
- 92 G. D. Quinn and R. Morrell, "Design Data for Engineering Ceramics: A Review of the Flexure Test," *J. Am. Ceram. Soc.*, 74 [9] (1991) 2037 2066.

8. SINGLE CRYSTALS

8.1 General

Fractographic procedures for single crystals are similar to those for glasses and polycrystalline ceramics, but there are some nuances and differences. Fracture surfaces may have regions with conchoidal fracture and Wallner lines and twist hackle. Other regions may have dramatic faceting. Fracture resistance often varies significantly between the crystallographic planes, causing jagged fracture patterns as cracks radically change directions onto preferred cleavage planes. Fracture surfaces may be very difficult to interpret. Some examples of the unusual markings are shown in Figure 8.1.

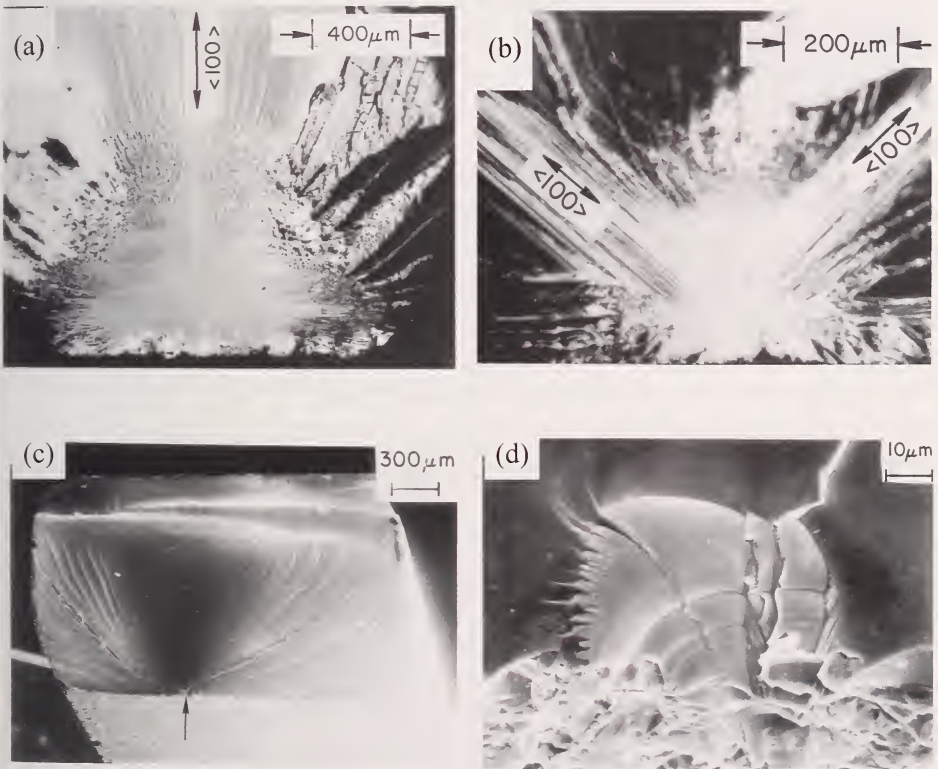


Figure 8.1. Examples of single crystal fractures. (a) and (b) show fracture mirrors on the $\{100\}$ type planes in MgO, but with two different tensile surface orientations. (c) and (d) show a cubic zirconia bend bar with curved linear lance like marking emanating from the origin area and the grinding crack origin. (Courtesy R. Rice)

The overall fracture plane may not necessarily be perpendicular to the direction of principal normal stress, since a preferred cleavage plane may be at an irregular angle to that stress. Sometimes the overall fracture extension may be approximately perpendicular to the maximum principal stresses, but local fracture proceeds in a zigzag fashion on other planes. This crack redirection is different than conventional crack branching in glasses or polycrystalline ceramics. Branching is much less common in single crystals. If the maximum principal stress is perpendicular to a preferred cleavage plane, the fracture surface may be very flat and featureless with little or no hackle, and no branching at all.

Fracture mirrors may be present, but may have odd shapes and markings. There may be no mist or hackle on preferred cleavage planes. Mirror sizes may be extremely difficult or impractical to measure. Cleavage hackle steps may be confused with Wallner lines. Twinning may cause fracture.

8.2 Preferred Cleavage Planes

Bradt et al.^{1,2} have reviewed the various criteria for cleavage and concluded that fracture toughness is the best indicator of the preferred cleavage plane. The energy to propagate cracks along preferred cleavage planes is less than that for less favored planes. Nevertheless, there is contradictory information in the literature on preferred cleavage planes in some crystals, even for such well studied materials as silicon, alumina (sapphire), and magnesium aluminate spinel. Some of contradictory information surely is due to experimental error or specific aspects of the test method. The direction of crack advance on a plane is as important as the plane itself. The speed of crack advance can even determine which plane of fracture is preferred.³ Although the double cantilever beam method and the constant applied moment variation as shown in Figure 8.2 are often used, results are not strictly valid if the crack zigzags down the guiding groove or is tilted to the intended fracture plane.

Knoop indentations in bend bars may be used to generate controlled surface flaws in the surface crack in flexure (SCF) method as shown in Figure 8.2. The specimen axis and cross section and the indentation and precrack plane may be aligned with a particular cleavage plane. The local direction of crack extension may vary along the crack periphery, however. Such micro flaws, which mimic naturally occurring flaws, are valuable in demonstrating just how complex fracture resistance can be in single crystals. A good example is from the work of Chen and Leopold⁴ and Xin et al.⁵ on silicon as summarized in Table 8.1. Xin et al.⁵ showed that the residual stresses from the indentation

could change the propagation plane. Bradt et al.^{6,7,8} have used this method on alumina and spinel. Figure 8.3 shows a Knoop precrack in sapphire. One unresolved issue with the SCF method for single crystals is whether or not indentation residual stresses vary with plane and orientation. Akimune and Bradt⁹ showed that there is considerable hardness anisotropy even on one plane (100) in spinel, but negligible variability on the (111).

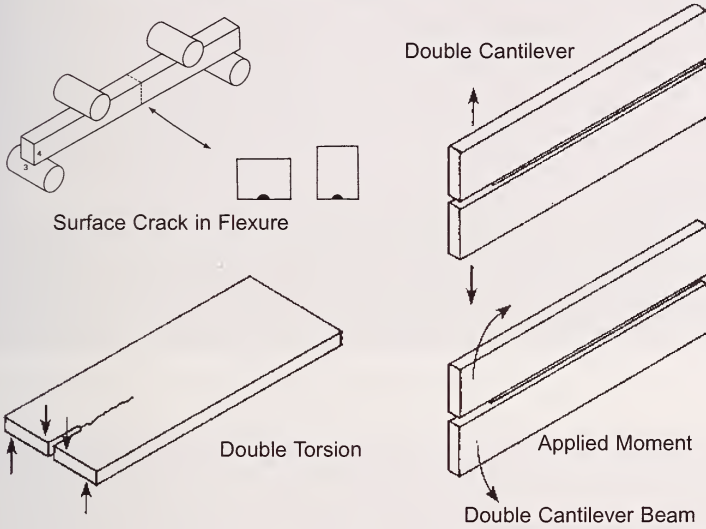
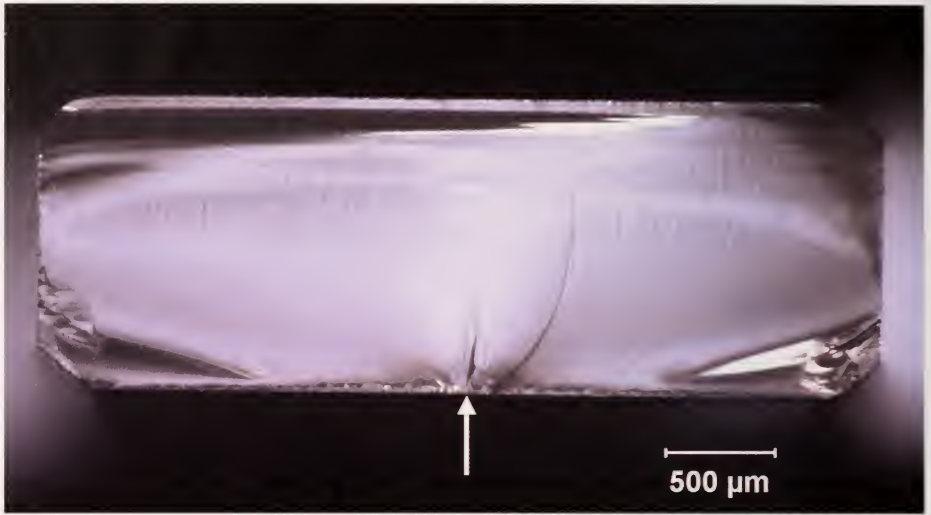


Figure 8.2. Tests methods for single crystal fracture toughness determination.

Table 8.1. Fracture toughness of single crystal silicon from Knoop SCF tests.

Reference	Plane Type	K_{Ic} (MPa \sqrt{m})	Fracture characteristics
Chen and Leipold (4)	{111}	0.82	Flat and smooth fractures. This is the preferred cleavage plane.
Chen and Leipold (4)	{110}	0.90	Large but asymmetric cathedral mirrors centered on the flaws. Propagation switched to {111} planes and zigzagged at the mirror boundaries.
Chen and Leipold (4)	{110}	0.95	A very rough fracture surface. Cracks switched to {111} very quickly.
Xin, Hsia, and Lange (5)	{110}	0.95	Residual indentation stresses intact: Cracks propagated on {110}.
Xin, Hsia, and Lange (5)	{110}	—	Residual indentation stresses removed by annealing. Crack switched to {111}.

(a)



(b)

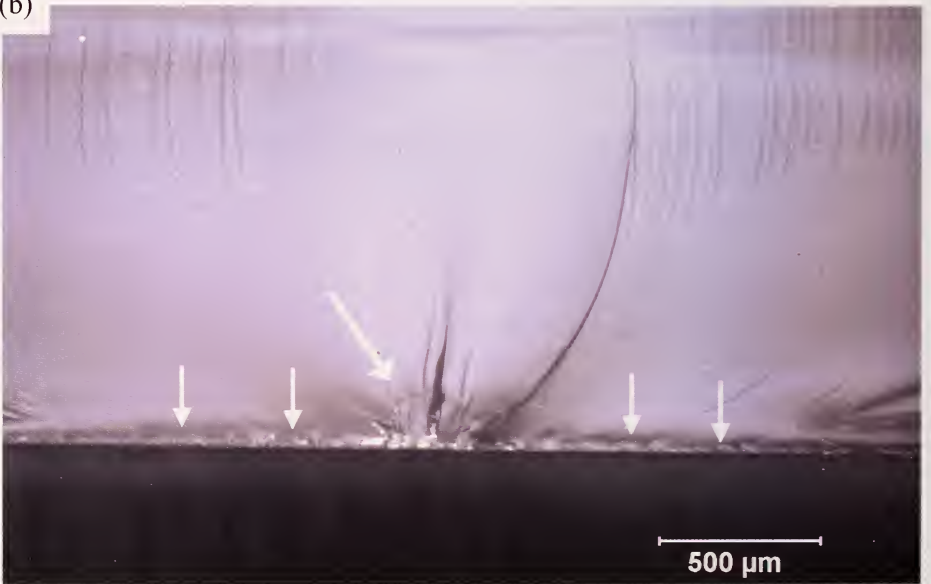


Figure 8.3. Relatively smooth fracture surface (a) of a surface crack in flexure (SCF) sapphire test specimen with a 49 N Knoop indentation as a starter flaw (arrow). The bar tensile surface was the *a*-plane. Fracture occurred on the *m*-plane. (b) is a close-up which shows grinding cracks along the surface (small white arrows), but the indentation crack (large white arrow) was dominant. (Courtesy R. Krause.)

8.3 Fractographic Techniques

Vicinal illumination on cleaved surfaces may be more problematic since fracture surfaces are mirror like and reflect light away from the microscope objective lens. Silicon is a good example of this and the fractographer is confronted with either getting too little or too much light reflected into the eyepieces. When using a stereomicroscope with directional illumination, it is often effective to tilt the specimen at an angle to reflect more light up into the eyepieces. The good depth of field of the stereomicroscope can accommodate the specimen tilt at low to moderate magnifications. Stopping down an aperture can increase the depth of field.

A reflected light compound microscope may be very effective with single crystals if the fracture surface is not too rough. Dark field illumination may aid finding fracture mirrors, since the symmetry of cleavage steps may be accentuated as shown in Figure 8.4.

Confocal microscopes may not be very effective due to the specular reflections.

Transmitted illumination is often useful for transparent single crystals. Polarizers are essential aids to help discern twinning, which may cause fracture in some crystals. Gold coating of a transparent single crystal may aid in interpretation and may make the fracture surface easier to view, but if the surface is very flat, the gold coating may make it behave like a mirror, which will pose problems for inspection and photography.

X-ray topography is a unique tool for single crystals. Imperfections in the crystal and its surface produce image contrast. Figure 8.5 shows an example that reveals handling damage on the polished surface of a sapphire hemispherical dome.¹⁰ The full extent of the handling damage was not readily visible with the optical or scanning electron microscopy.

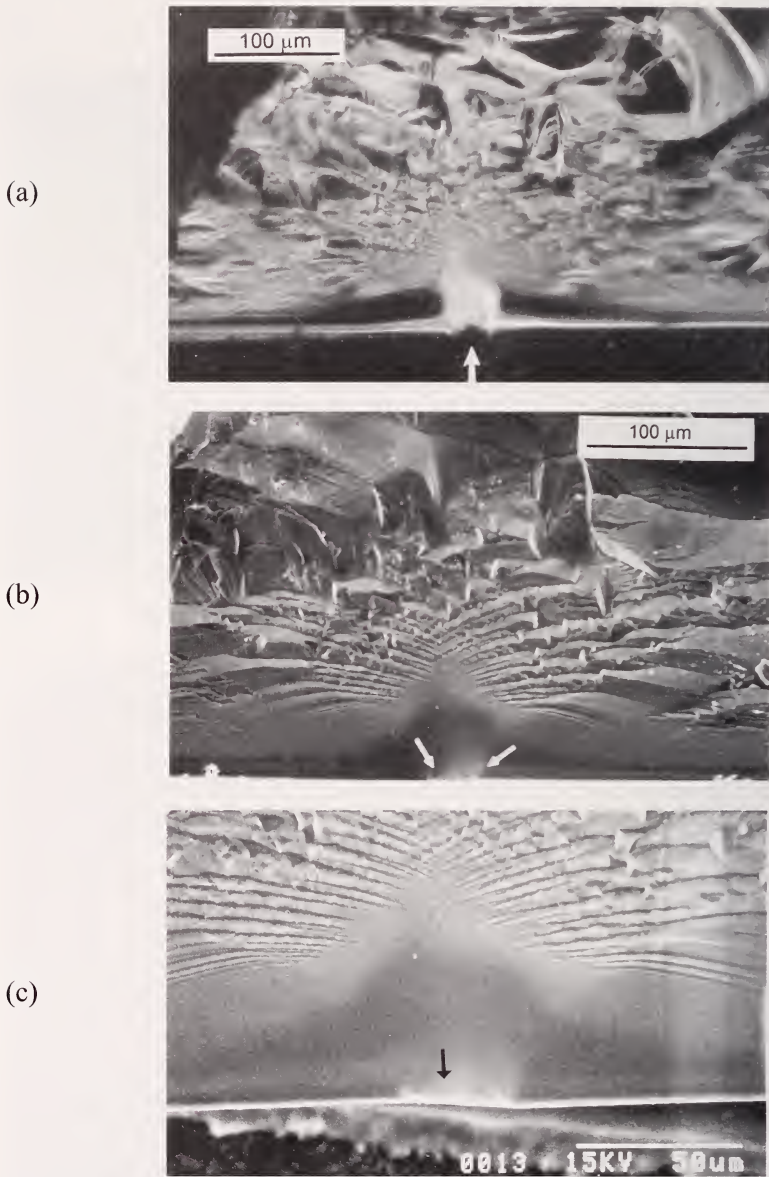


Figure 8.4. Dark field illumination may aid optical examination. Different views of the fracture origin in a silicon wafer tested in a biaxial ring-on-ring mode (282 MPa). Fracture initiated from the surface grinding crack (also shown in Figure 8.17), propagated on a $\{110\}$ type plane, but started to zigzag. (a) is a dark field optical image with a strange appearance that nonetheless has a symmetry that is a tip off to the existence of an origin and mirror. (b) and (c) are SEM images of the origin with arrows calling attention to the flaw.

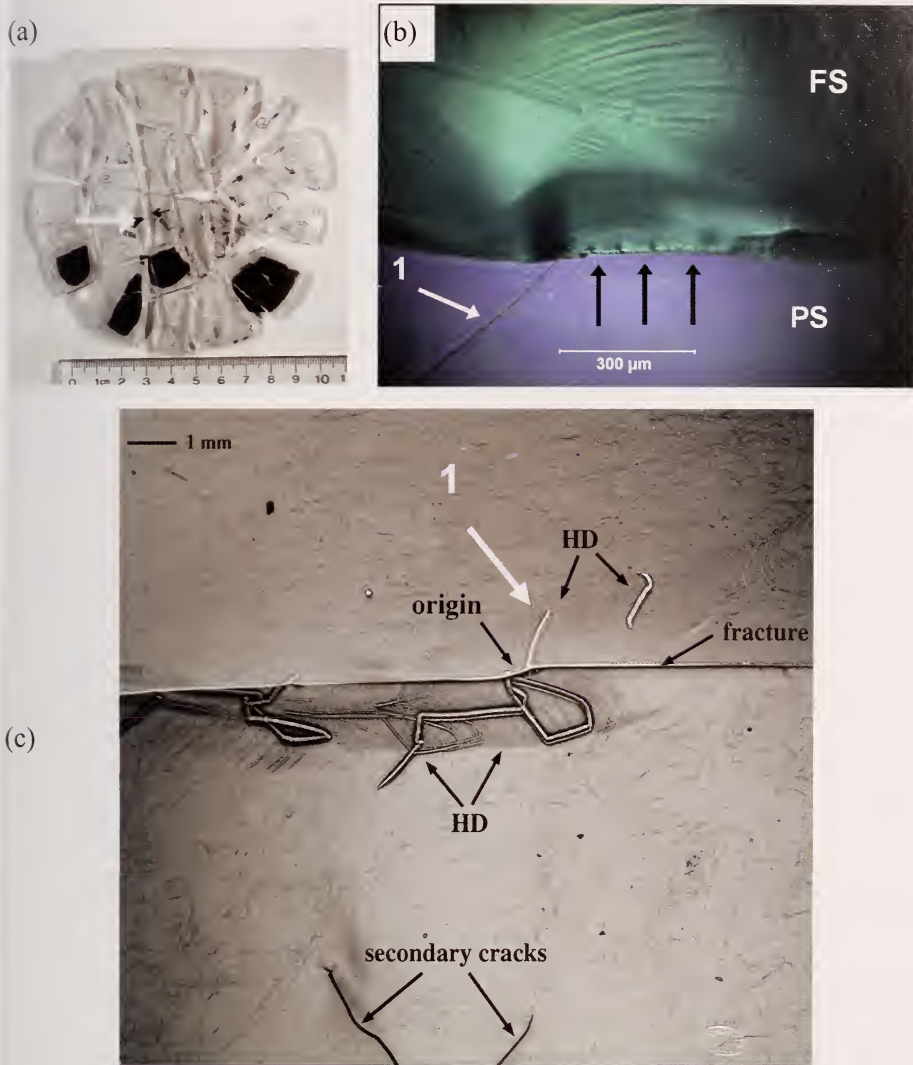


Figure 8.5. Sapphire hemispherical dome that fractured during a thermal stress proof test. (a) shows the fractured dome and the origin (large white arrow). (b) shows an optical fractograph with the origin piece tilted back to show both the fracture surface (FS) and the polished outer surface (PS). The cracking is marked by the black arrows. Another apparently isolated intersecting scratch is marked with the white arrow and the numeral "1." (c) is a composite of two x-ray topographs of the polished outer surface, showing the matching fracture halves where they meet at the origin. Surface and subsurface damage are exposed and the scratch labeled "1" in (b) is revealed to be part of a complex handling damage (HD) network. (c is courtesy of D. Black)

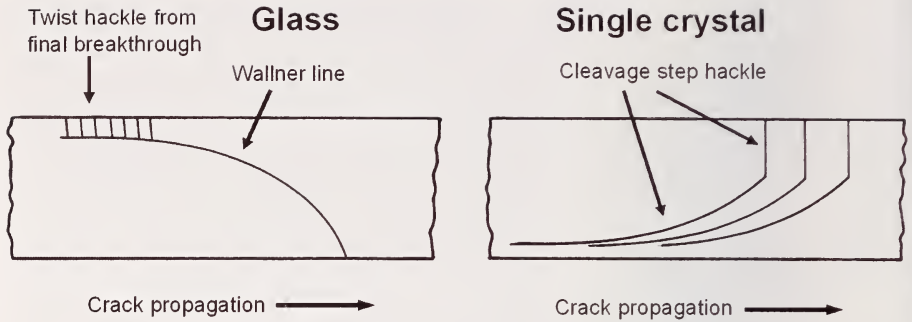


Figure 8.6. Schematics showing (a) a Wallner line and twist hackle in a glass plate loaded in bending and (b) “cleavage step hackle” in a single crystal plate loaded in bending. In both cases the crack was leading on the bottom surface.

8.4 Fracture Surface Markings

Single crystal fracture planes often have small “cleavage step hackle” that may be confused with Wallner lines. Figure 8.6 shows the differences. Cleavage step hackle is often generated by the origin or other surface irregularities and runs parallel to the direction of crack propagation. The hackle may suddenly change from curved lines to parallel segments on the initially compressive loaded side of a specimen. The cleavage step hackle may be very persistent and extend over great distances without merging, unlike twist hackle lines.

Fracture surfaces and fracture mirrors may have extraordinary shapes and facets, but usually have some degree of recognizable symmetry that will help the fractographer identify an origin site. Mirror shapes may vary dramatically within a crystal depending upon the fracture plane. To illustrate these remarkable variations, fracture markings for single crystal cubic spinel are shown in Figures 8.7 through 8.14. These figures follow the recommendations of this Guide and ASTM C 1322.¹¹ They show a picture of the whole fracture surface, the fracture mirror, and a close up of the origin. The fractographic findings are summarized in Table 8.2. These images are from Rice and colleagues^{3,12,13,14} who studied fracture in this material using double cantilever beam and flexural strength specimens. They found a remarkable variety of fracture surfaces with features such as “cathedral mirrors,” “gull wing mirrors,” “skewed cathedral mirrors,” and “whisker lances.” Cathedral and gull wing mirrors have also been observed in other cubic crystals such as

silicon (Figure 8.4) and fully-stabilized zirconia. Gull wing mirrors look like cathedral mirrors that are tilted 90° on the fracture surface. Bear in mind that there may be threshold stresses or stress intensities for the formation of markings on certain planes. Thus the flat fractures shown in figures 8.8 and 8.9 may indicate fracture on a preferred cleavage plane, or that the stresses were too low in each case to generate mirror markings.

The preferred cleavage plane in spinel is the $\{100\}$ which has a fracture toughness of 0.9 to 1.2 $\text{MPa}\sqrt{\text{m}}$ depending upon the method of measurement.^{3,6,7,10,11,12} The fracture toughness of the $\{110\}$ is not much greater at 1.0 to 1.5 $\text{MPa}\sqrt{\text{m}}$. Consequently fracture usually runs on $\{100\}$ or $\{110\}$ type planes. Fracture is not preferred on the $\{111\}$ and the fracture toughness is much greater (1.9 $\text{MPa}\sqrt{\text{m}}$ or more).^{3,6,7,11,12,13}

Table 8.2. Fracture markings in MgAl_2O_4 spinel bend bars. The brackets $\{100\}$ denote the family of (100) planes and the angles $\langle 100 \rangle$ denote the family of [100] directions. (After Wu, McKinney, and Rice, Ref. 3)

Intended fracture plane type (*)	Bend bar tensile surface	Bend bar tensile axis	Fracture type	Figure
$\{100\}$ (A)	$\{100\}$	$\langle 100 \rangle$	Cathedral mirror Major crack redirection beyond the mirror sides	8.7
$\{100\}$ (D)	$\{110\}$	$\langle 100 \rangle$	No mirror Flat and featureless fracture surface	8.8
$\{110\}$ (B)	$\{100\}$	$\langle 110 \rangle$	No mirror Flat and featureless fracture surface	8.9
$\{110\}$ (F) (C)	$\{110\}$	$\langle 110 \rangle$	Skewed fracture mirror and Major crack redirection beyond the mirror sides, or Gull wing mirror and Jagged fracture surface beyond top of mirror	8.10 8.11 8.12
$\{110\}$ (G)	$\{111\}$	$\langle 110 \rangle$	Skewed cathedral mirror Major crack redirection beyond the mirror sides, or flat	8.13 8.14
$\{111\}$ (E)	$\{110\}$	$\langle 111 \rangle$	Gull wing mirror Jagged crack propagation beyond top of mirror	8.15

* Cases A through G are so identified in Figures 8.7 to 8.15

◆ Fractography of Ceramics and Glasses

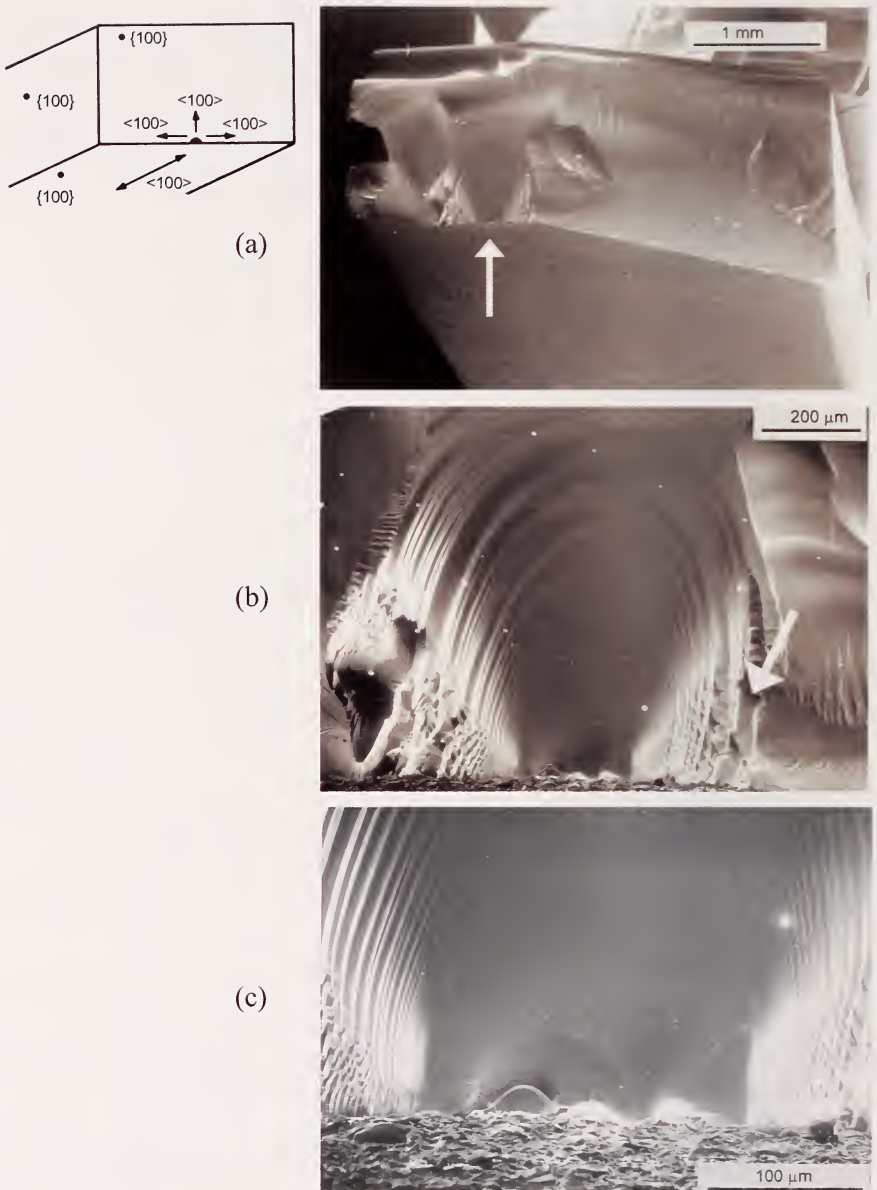
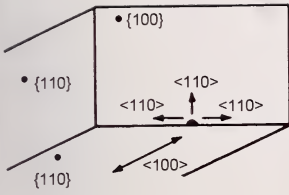
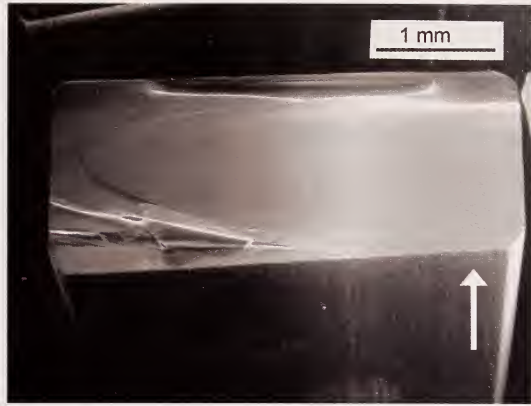


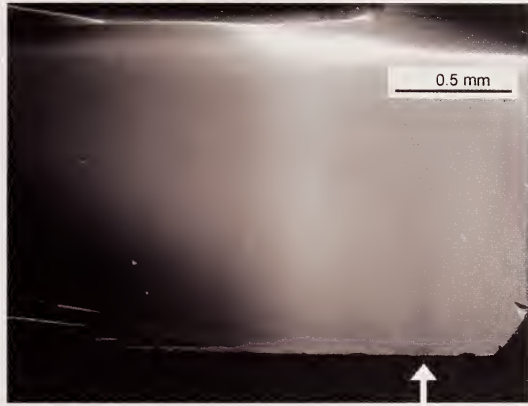
Figure 8.7. Spinel bend bar with a $\{100\}$ tensile surface and $\langle 100 \rangle$ tensile axis designed to cause fracture on a $\{100\}$ plane. (185 MPa) (a) shows the whole fracture surface and origin (arrow). (b) shows the “cathedral mirror” and the arc-ribs that gradually get progressively severer until a branch or major crack redirection occurs (white arrow). (c) shows the grinding crack fracture origin. Fracture starts on the $\{100\}$ but shifts or branches to the $\{110\}$ just beyond the sides of the mirror. (Case A, Table 8.2) (Courtesy R. Rice)



(a)



(b)



(c)

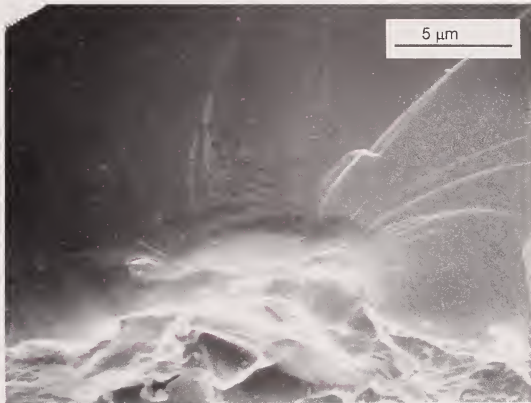


Figure 8.8. Spinel bend bar with a $\{110\}$ tensile surface and $\langle 100 \rangle$ tensile axis designed to cause fracture on a $\{100\}$ plane. (170 MPa) (a) shows the whole fracture surface which is flat except for the cleavage steps on the side and the cantilever curl. Other similar specimens had no cleavage steps. (b) shows the origin site and (c) shows the grinding crack fracture origin. (Case D, Table 8.2) (Courtesy R. Rice)

◆ Fractography of Ceramics and Glasses

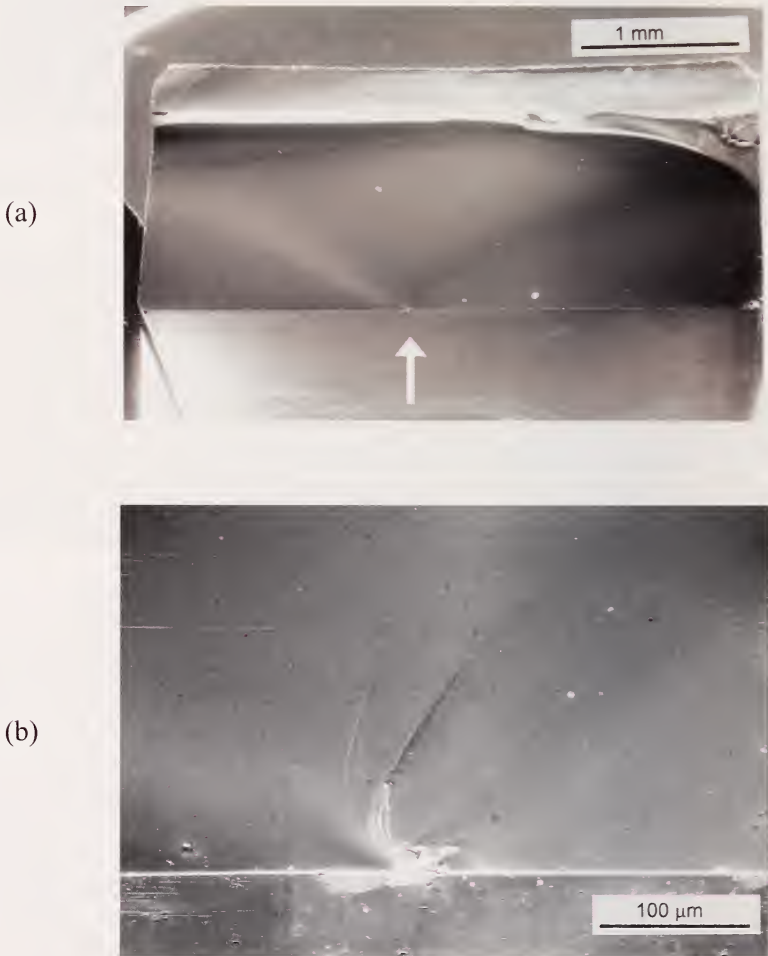
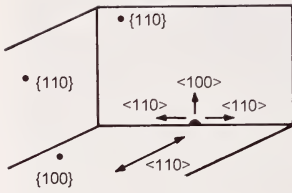
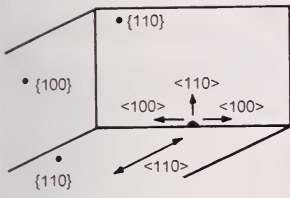
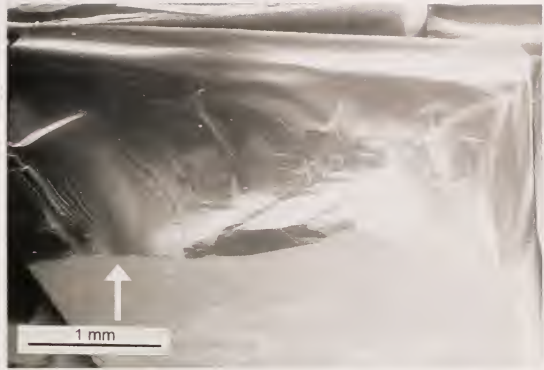


Figure 8.9. Spinel bend bar with a $\{100\}$ tensile surface and $\langle 110 \rangle$ tensile axis designed to cause fracture on a $\{110\}$ type plane. (169 MPa) (a) shows the whole fracture surface which is flat and featureless except for the cantilever curl. The arrow shows the origin. (b) shows the grinding crack fracture origin. Fracture stays on a $\{110\}$ type plane. (Case B, table 8.2) (Courtesy R. Rice)



(a)



(b)

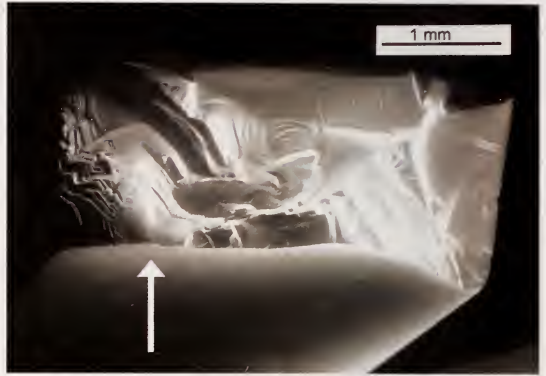
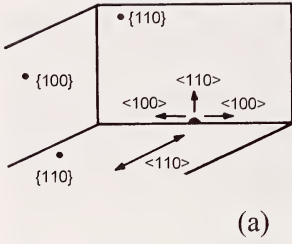


(c)

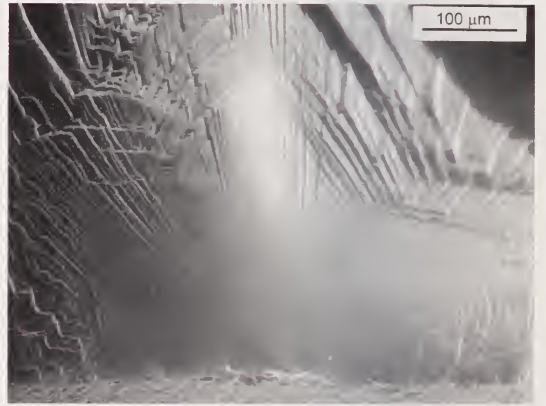


Figure 8.10. Spinel bend bar with a $\{110\}$ tensile surface and $\langle 110 \rangle$ tensile axis designed to cause fracture on a $\{110\}$ plane. (283 MPa) (a) shows the whole fracture surface, (b) shows the mirror with whisker lances radiating outward, and (c) shows the grinding crack fracture origin. (Case F1, table 8.2) (Courtesy R. Rice)

◆ Fractography of Ceramics and Glasses



(a)



(b)

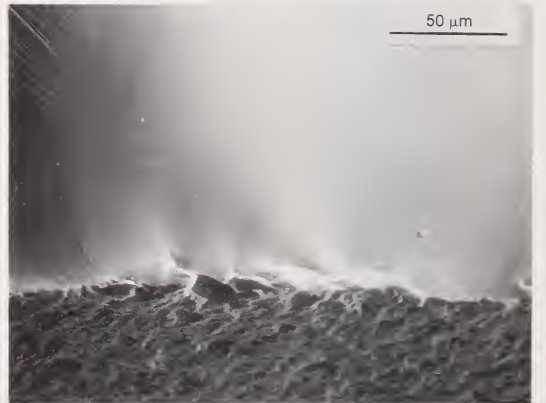
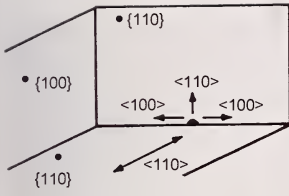
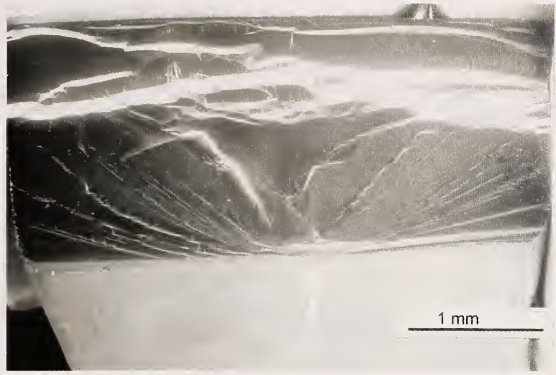


Figure 8.11. A second example of a spinel bend bar with a $\{110\}$ tensile surface and $\langle 110 \rangle$ tensile axis. (172 MPa) The fracture surface (a) is very rough as in the previous figure. The mirror (b) is somewhat more symmetric than in the previous figure. This mirror was shown in an earlier publication (Figure 29 of Ref. 13), but with a typographical mistake identifying it as $\{110\}$ $\langle 100 \rangle$. (Case F2, table 8.2). (Courtesy R. Rice)



(a)



(b)

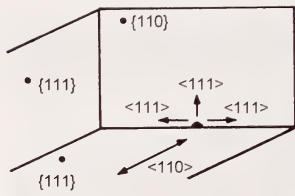


(c)

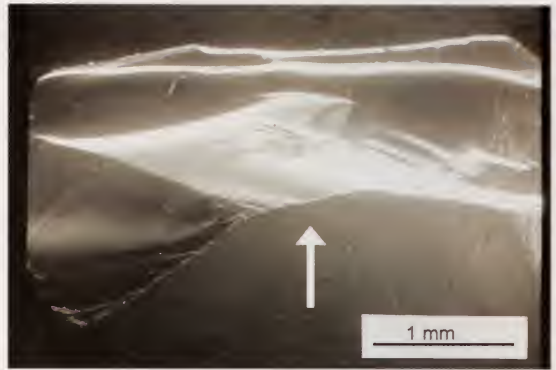


Figure 8.12. Spinel bend bar with a $\{110\}$ tensile surface and $\langle 110 \rangle$ tensile axis designed to cause fracture on a $\{110\}$ plane. (361 MPa) (a) shows the whole fracture surface, (b) shows the “gull wing mirror,” and (c) shows the grinding crack fracture origin. (Case C, table 8.2) (Courtesy R. Rice)

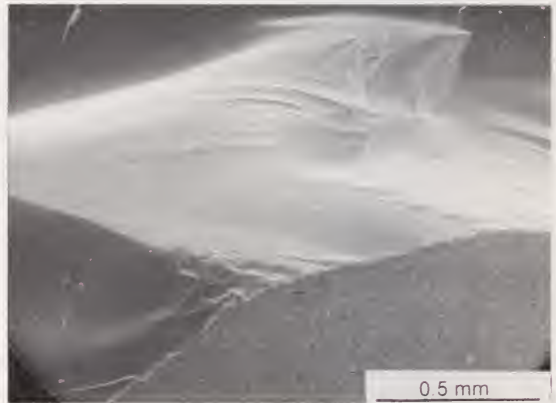
◆ Fractography of Ceramics and Glasses



(a)



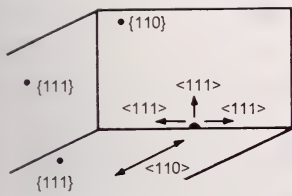
(b)



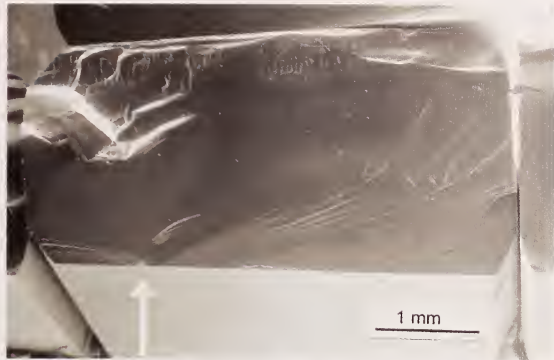
(c)



Figure 8.13. Spinel bend bar with a $\{111\}$ tensile surface and $\langle 110 \rangle$ tensile axis designed to cause fracture on a $\{110\}$ plane. (unknown stress) (a) shows the whole fracture surface and the major crack redirection on the mirror sides. (b) shows the “skewed cathedral mirror;” and (c) shows the grinding crack fracture origin from the matching fracture piece. (Case G1, table 8.2) (Courtesy R. Rice)



(a)



(b)



(c)

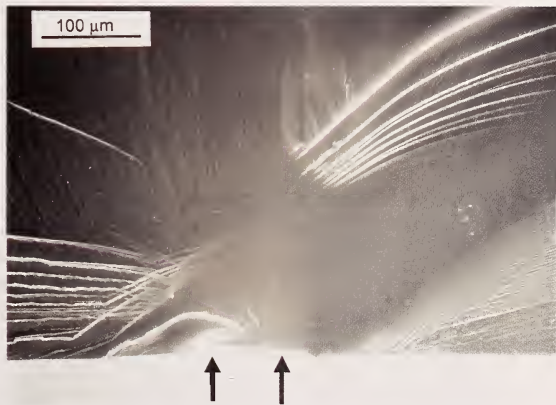
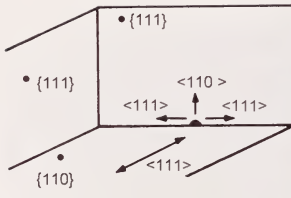


Figure 8.14. Another example of a spinel bend bar with a $\{111\}$ tensile surface and $\langle 110 \rangle$ tensile axis designed to cause fracture on a $\{110\}$ plane. (261 MPa) (a) shows the whole fracture surface, (b) shows a “skewed mirror” with “whisker lances” and (c) shows the grinding crack fracture origin (black arrows) which is at a slight angle to the tensile stress axis and the fracture surface). (Case G2, table 8.2) (Courtesy R. Rice)

◆ Fractography of Ceramics and Glasses



(a)



(b)



(c)

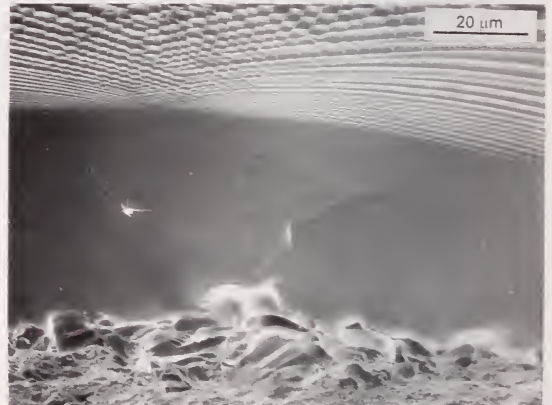


Figure 8.15. Spinel bend bar with a $\{110\}$ tensile surface and $\langle 111 \rangle$ tensile axis designed to cause fracture on a $\{111\}$ plane. (325 MPa) (a) shows the whole fracture surface and the major crack redirection on the top half, (b) shows the “gull wing mirror,” and (c) shows the grinding crack fracture origin. (Case E, table 8.2) (Courtesy R. Rice)

Another distinctive shape seen in some crystals are long hackle lines that extend vertically from the sides of an origin suggesting a “batman mirror” shape as shown in Figure 8.16.

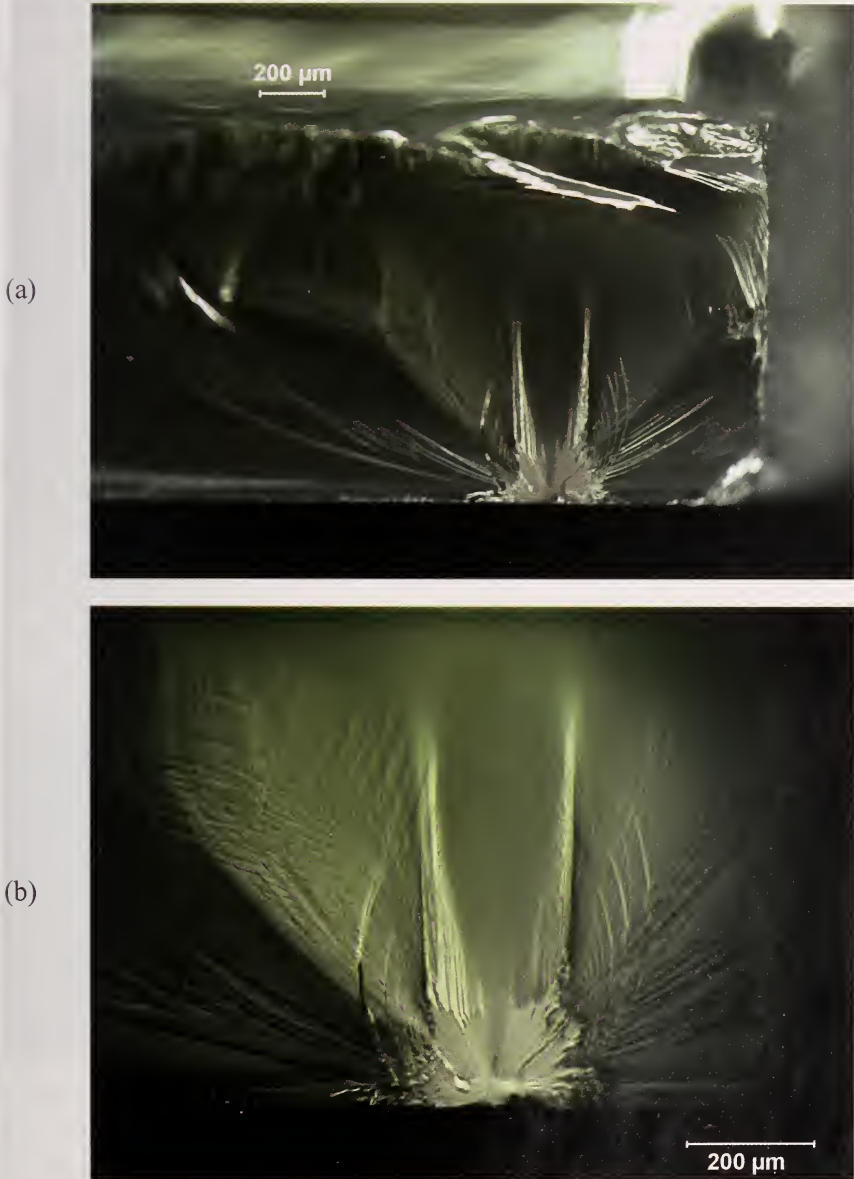


Figure 8.16. “Batman” mirror in a sapphire. (a) shows matching halves of the bend bar with a tensile surface parallel to the a -plane and bend bar sides oriented so as to cause fracture on the r -plane. The tensile direction was the r axis. The origin was grinding damage. (Specimen courtesy R. Krause.)

Mirror shapes seem to correlate with elastic moduli variations in different directions in a fracture plane.¹⁵ The very limited data on fracture mirror constants that have been published are listed in Appendix C. The asymmetry and diversity of fracture mirror shapes and difficulties in judging mirror sizes hamper any attempts to accurately correlate fracture stresses to mirror sizes by the methods described in chapters 7 and appendix D.

Scarps can occur in single crystals and are indicative of the presence of liquid during fracture. Figure 5.39b shows an example of scarps in sapphire.

8.5 Origins

Single crystals are very sensitive to surface contact damage of any type. The low fracture toughness and high stiffness means that tiny strength limiting cracks can easily pop into the crystal. There are no grain boundaries or other microstructural features to impede or redirect surface initiated cracks. Grinding or polishing flaws are common fracture origins. Flexure and tensile specimens are very sensitive to edge flaws and special care must be taken with the edge beveling or rounding procedures. Figure 8.17 shows the grinding crack origin of the silicon wafer shown in Figure 8.4. Single crystals are also

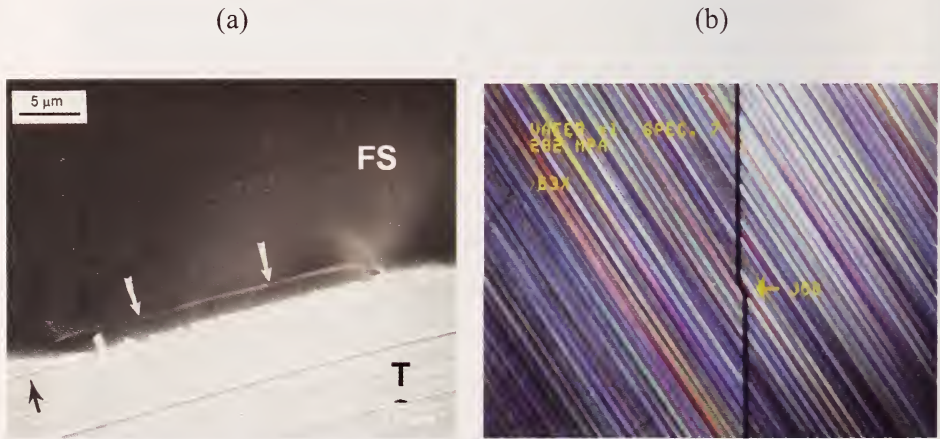


Figure 8.17. Fracture origin of the silicon wafer shown in Figure 8.4. (282 MPa) (a) shows the origin is a grinding crack that extends only 2 μm below the tensile surface (T) and is associated with a striation that seems to be deeper and has caused greater cracking than other nearby striations. The grinding direction is slightly different than the final plane of fracture, which caused the fracture surface to have a jog at the origin as shown in the optical view of the tensile surface (b).

very susceptible to polishing flaws. Subsequent polishing or finishing may eliminate any surface trace or scratch associated with the flaw, rendering optical post finishing inspection ineffective. Figure 8.18 shows an example in a sapphire dome.

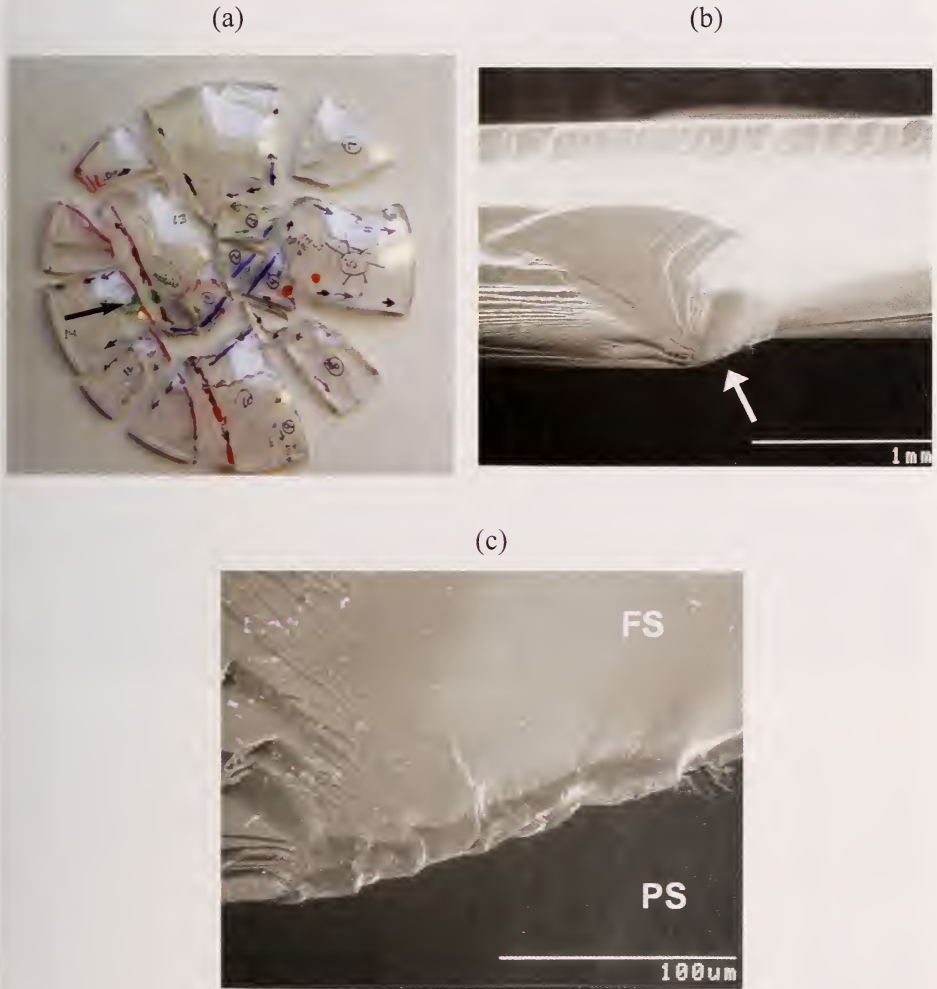


Figure 8.18. Polishing or grinding crack origin in a sapphire dome. (a) shows the entire fractured structure. The origin is marked by the black arrow. (b) shows an SEM photo of the piece with the origin marked by the arrow. Fracture followed the axis of a polishing crack for a short distance, but then quickly shifted to a different plane. (c) is a SEM close-up of the origin. The piece has been tilted back to show not only the fracture surface (FS) but the polished surface (PS) as well. There is no trace of damage on the polished surface.

◆ Fractography of Ceramics and Glasses

Surface impact or contact loading creates strength-limiting flaws. The contact can create cracks that may be extended by subsequent loading. Alternately, there may be stresses already present in the part that can propagate the crack. Figure 8.19 shows an example.

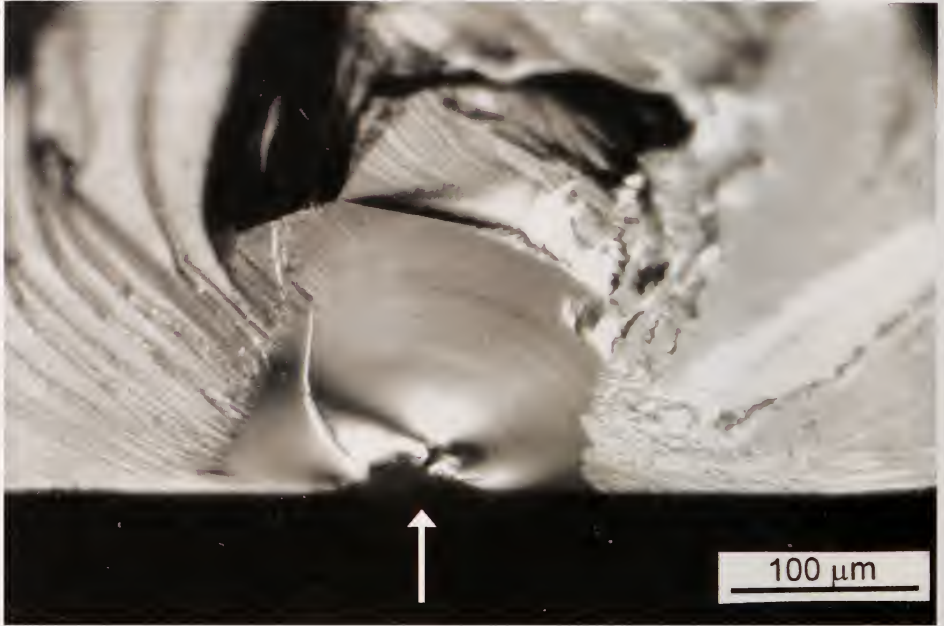


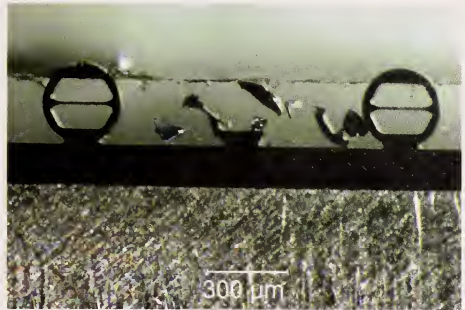
Figure 8.19. Impact crack fracture origin in a hemispherical sapphire dome that was impacted by a small particle while the dome was under thermal stress. The impact site on the surface is missing a small divot (arrow) and the approximately 150 μm deep crack shows concentric semicircular tertiary Wallner lines that are telltale signs of impact.

Other surface flaws may originate as a result of processing conditions. Figure 8.20d shows a crack associated with a groove in a microelectromechanical (MEMS) sized single crystal silicon theta specimen. Deep reactive ion etching (DRIE), which is a lithographic process used to prepare integrated circuits and small structures, was used to fabricate the shape from a standard $\{100\}$ type silicon wafer. The DRIE process created the surface damage that was strength limiting in this case.

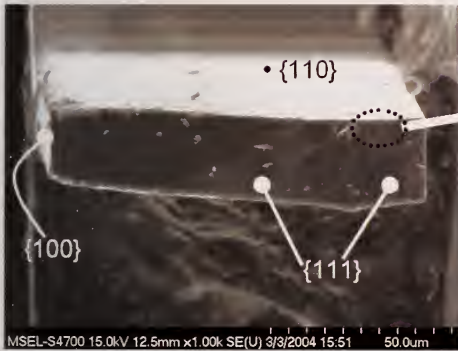
(a)



(b)



(c)



(d)



Figure 8.20. Tiny silicon theta test specimens. The ring shown in (a) is compressed on the top and bottom of its rim in a nanoindenter causing the web-gage section in the middle to stretch in uniaxial tension. (b) shows one fractured specimen on a strip. (c) shows a fragment from a hexagonal variant of the theta specimen. The web tensile strength was approximately 600 MPa. (d) shows the cathedral mirror and origin (arrow), which is a crack from a groove in the surface that was prepared by deep reactive ion etching (DRIE). The face of the silicon specimen is a $\{100\}$ type plane and the web axis pulled in tension is a $\langle 110 \rangle$ type direction. Fracture in the web occurred on $\{111\}$ type planes. (ref. 16)

Volume- distributed flaws such as pores, inclusions or compositional inhomogeneities can also cause fracture. They usually will stand out quite clearly on the fracture surface. Newcomb and Tressler¹⁷ and Rice¹⁸ showed or analyzed pore examples in sapphire fibers. An example of an internal origin in a nonstoichiometric spinel is shown in Figure 8.21.

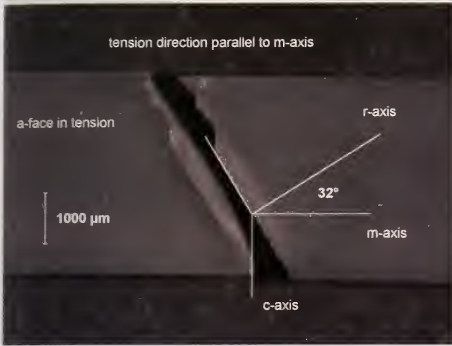
Twinning can initiate fractures, especially if twins from different planes intersect and can nucleate cracks. Figure 8.22 shows twins that controlled the strength in a sapphire bend bar tested at high temperature. This failure mechanism is especially a problem in sapphire since twins are easily nucleated by relatively low compression stresses at fairly low temperatures. They cause drastic reductions of compression and flexure strengths in some orientations.^{19,20} They sometimes form with an audible pop.²¹ Chapter 10 includes a case study of a sapphire tube that fractured from intersecting twins.

Figure 8.23 is a good example of a fracture occurring on a sapphire preferred cleavage plane that was not perpendicular to the maximum principal stresses. Alternately, the loading conditions or part geometry may be such that fracture is forced on an unfavorable plane such as the basal plane in sapphire. Fracture surfaces will be very rough as shown in Figure 8.24. Other examples of basal plane fracture in sapphire are shown in references 8, 18, and 22.

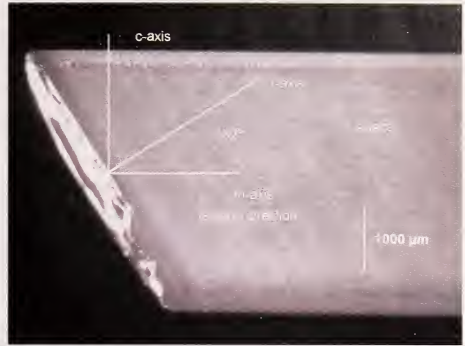


Figure 8.21. Internal origin in a flame polished non-stoichiometric (alumina rich) spinel single crystal. The bend bar strength was 238 MPa (courtesy R. Rice)

(a)



(b)



(c)

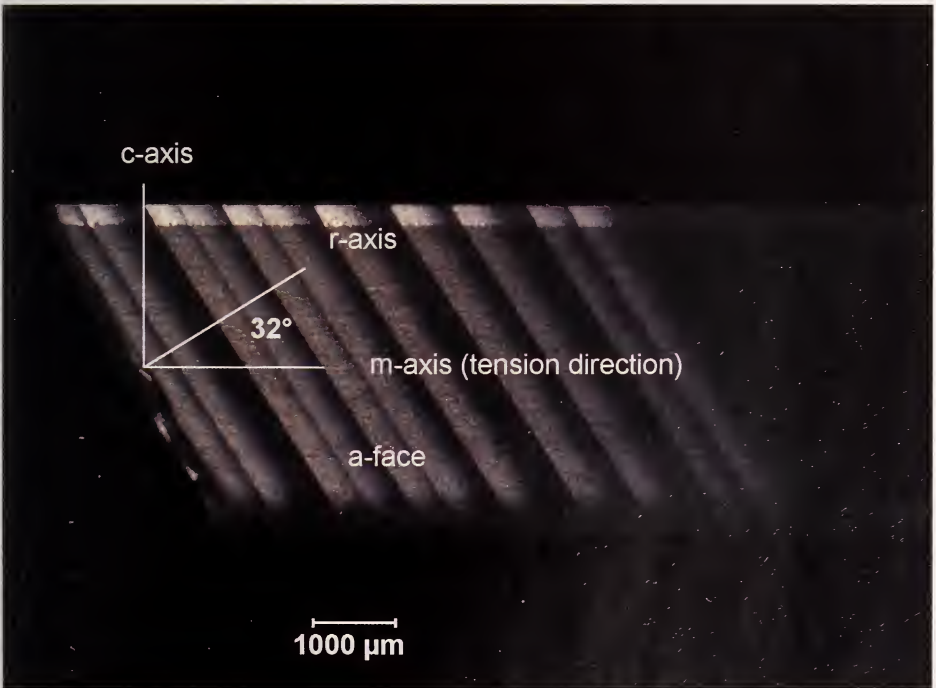


Figure 8.22. Twinning in sapphire bend bars in an elevated temperature bend bar specimen. The bar was cut with an *a*-plane tensile surface and an intended *m*-plane fracture surface. The specimen instead broke on the *r*-plane from cracks initiated by twins probably from the compression side of the specimen. (a) shows the tensile face under ordinary lighting. (b) shows the same specimens but with lighting adjusted to reflect off the twins. (c) shows the bar between crossed polarizers. (Courtesy R. Krause)

◆ Fractography of Ceramics and Glasses

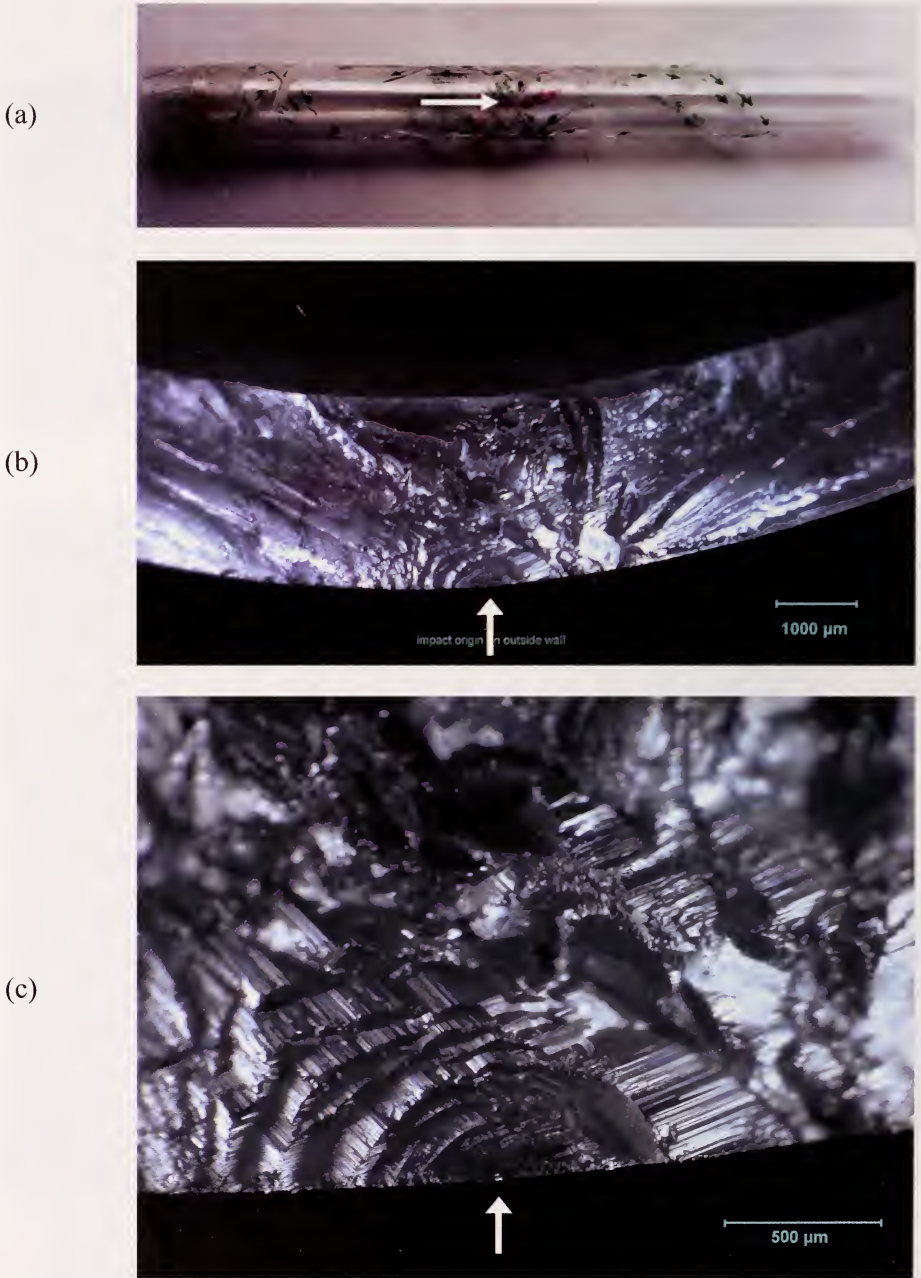


Figure 8.23. Example of basal plane fracture in a *c*-axis sapphire tube that fractured from severe thermal shock (a). The origin is at the tube mid length (large arrow) and is perpendicular to the tube axis. The thermal stresses acted in the axial direction. (b) and (c) show the mirror and origin on the outer tube surface.

Good estimates of the fracture toughness K_{Ic} may be obtained from fracture mechanics analyses of flaws. For example, the long uniform $2\ \mu\text{m}$ deep surface crack in the silicon wafer shown in Figure 8.17a combined with a breaking stress of 282 MPa and a shape factor $Y = 1.99$ produced an estimate of $K_{Ic} = 1.99 (282) \sqrt{2} \times 10^{-6} = 0.79\ \text{MPa}\sqrt{\text{m}}$ in good agreement with values in table 8.1. Rice showed several good examples^{12,18} and Newcomb and Tressler¹⁷ were able to measure fracture toughness on the basal plane of sapphire by this approach, when other methods usually fail due to the difficulty of controlling fracture on this plane. Many groups have effectively used Knoop indentation surface crack in flexure tests to study fracture behavior and measure fracture toughness of single crystals since the small semi elliptical flaws mimic the behavior of other flaws.

8.6 Other Sources

Rice has written several outstanding, richly illustrated papers on single crystal fracture and fractography. Reference 13 is a book length article with over thirty figures showing single crystal fracture surfaces in MgO , MgAl_2O_4 , Si , SiC , Al_2O_3 , ZrO_2 , CaF_2 , and W . Reference 14 has six pages of illustrations and a discussion of fracture markings in various single crystal ceramics.

Chapter 8 References

1. R. A. Schultz, M. C. Jensen, and R. C. Bradt, "Single Crystal Cleavage of Brittle Materials," *Int. J. Fract.*, **65** (1994) 291 – 312.
2. R. C. Bradt, "Cleavage of Ceramic and Mineral Single Crystals," pp. 355 – 365 in *Cleavage Fracture*, Proceedings of a Symposium at the 1997 TMS Fall meeting, Indianapolis, IN, Sept. 15-17, 1997, ed. K. S. Chan, The Minerals, Metals, and Materials Society, Warrendale, PA, 1997.
3. C. C. M. Wu, K. R. McKinney, and R. W. Rice, "Zig-zag Crack Propagation in MgAl_2O_4 Crystals," *J. Mat. Sci. Ltrrs.*, **14** (1995) 474 – 477.
4. C. P. Chen and M. H. Leipold, "Fracture Toughness of Silicon," *Bull. Am. Ceram. Soc.*, **59** [4] (1980) 469 – 472.
5. Y-B. Xin, K. J. Hsia, and D. A. Lange, "Quantitative Characterization of the Fracture Surfaces of Silicon Single Crystals by Confocal Microscopy," *J. Am. Ceram. Soc.*, **78** [12] (1995) 3210 – 3208.

6. R. L. Stewart, M. Iwasa, and R. C. Bradt, "Room Temperature K_{Ic} Values for Single-Crystal and Polycrystalline $MgAl_2O_4$," *Comm. Am. Ceram. Soc.*, Feb. 1981, C22 – 23.
7. R. L. Stewart and R. C. Bradt, "Fracture of Single Crystal $MgAl_2O_4$," *J. Mat. Sci.*, **15** (1980) 67 – 72.
8. M. Iwasa and R. C. Bradt, "Fracture Toughness of Single-Crystal Alumina," pp. 767 – 779 in *Advances in Ceramics*, Vol. 10, ed. W. Kingery, American Ceramic Society, Westerville, OH, 1984.
9. Y. Akimune and R. C. Bradt, "Knoop Microhardness Anisotropy of Single-Crystal Stoichiometric $MgAl_2O_4$ Spinel," *J. Amer. Ceram. Soc.*, **70** [4] (1987) C84 – C86.
10. D. Black and G. D. Quinn, "X-ray Topography for Fractography of Single-Crystal Components," accepted by *J. Failure Anal. and Prevention*, **6** [3] (2006) 79 – 86.
11. ASTM C 1322-96, "Standard Practice for Fractography and Characterization of Fracture Origins in Advanced Ceramics," *Annual Book of Standards*, Vol. 15.01, ASTM Int., West Conshohocken, PA (1996).
12. R. W. Rice, "Fractographic Determination of K_{Ic} and Effects of Microstructural Stresses in Ceramics," pp. 509 – 545 in *Fractography of Glasses and Ceramics II*, eds. V. Fréchet and J. Varner, 1991
13. R. W. Rice, "Ceramic Fracture Features, Observations, Mechanisms and Uses," pp. 5 – 102 in *Fractography of Ceramic and Metal Failures*, ASTM STP 827, eds. J. Mecholsky and Powell, 1984, American Society for Testing and Materials, West Conshohocken, PA, 1984.
14. R. W. Rice, "Perspectives in Fractography," pp. 3 – 56 in *Fractography of Glasses and Ceramics*, Advances in Ceramics, Vol. 22, eds. J. Varner and V. Fréchet, American Ceramic Society, Westerville, OH, (1988).
15. S. W. Freiman, J. J. Mecholsky, and P. Becher, "Fractography: A Quantitative Measure of the Fracture Process," pp. 55 – 78 in *Fractography of Glasses and Ceramics, II*, eds. V. Fréchet and J. Varner, American Ceramic Society, Westerville, OH, 1991.

16. G. D. Quinn, E. Fuller, D. Xiang, A. Jilavenkatessa, L. Ma, D. Smith, and J. Beall, "A Novel Test Method for Measuring Mechanical Properties at the Small -Scale: The Theta Specimen," *Ceram Eng. and Sci Proc.*, **26** [2] (2005) 117 – 126.
17. S. A. Newcomb and R. E. Tressler, "High-Temperature Fracture Toughness of Sapphire," *J. Amer. Ceram. Soc.*, **77** [11] (1994) 3030 – 3032.
18. R. W. Rice, "Corroboration and Extension of Analysis of c-Axis Sapphire Filament Fractures from Pores," *J. Mat. Sci. Lttrs.*, **16** (1997) 202 – 205.
19. F. Schmid and D. C. Harris, "Effects of Crystal Orientation and Temperature on the Strength of Sapphire," *J. Am. Ceram. Soc.*, **81** [4] (1998) 885 – 93.
20. P. F. Becher, "Fracture Strength Anisotropy of Sapphire," *J. Am. Ceram. Soc.*, **59** [1-2] (1976) 59 – 61.
21. J. A. Salem, Private Communication 2005
22. R. W. Rice and P. F. Becher, "Comment on Creep Deformation of 0° Sapphire," *J. Am. Ceram. Soc.*, **60** [3-4] (1977) 186 – 188.



9 CERAMIC AND GLASS COMPOSITES

9.1 Particulate, Whisker, or Self-Reinforced Ceramic Composites

Ceramics or glasses that are reinforced by second phases, whiskers, or particulates may be examined using the same equipment and techniques as used for monolithic materials. The reinforcing agents act to deflect or bridge cracks and create very rough fracture surfaces that may mask classical fracture surface features such as Wallner or hackle lines.

The composite ideally should have a controlled microstructure such that the reinforcing phase is uniformly distributed. This is routinely achieved with glass ceramics, but is more problematic with fiber or particulate-reinforced ceramics since the reinforcing agent forms clumps or aggregates. These can act as strength-limiting flaws as shown in Figure 9.1. Flaws of this type may be broadly described as compositional inhomogeneities using the logic in chapter 6, but more specific descriptors are probably better (fiber clump, fiber tangle, platelet cluster, etc.).

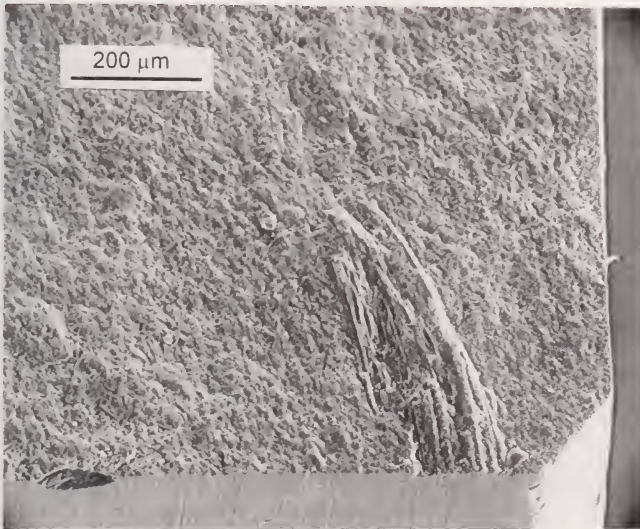


Figure 9.1. Nonuniform dispersal of toughening agents often causes strength limiting flaws in ceramic composites. This figure shows a whisker clump that was the strength-limiting flaw in a siliconized SiC bend bar. The material was made by mixing chopped carbon fibers with SiC starting powders and then infiltrating with silicon. The carbon fibers were intended to react with the silicon to form dispersed silicon carbide fibers that would toughen the matrix.

Second phase aggregates can also inhibit local sintering causing pockets of porosity that also act as strength limiting flaws. Self-reinforced materials that rely on interconnected elongated-grain microstructures may develop excessively large grains that control strength as shown in Figures 6.12c and d. Very often reinforcing agents such as SiC whiskers can create local chemistry imbalances in the matrix leading to exaggerated grain growth. These large grains then can act as flaws. Although few would argue against reinforcing ceramics to enhance fracture toughness, this approach sometimes comes with a price. The very agents used to reinforce the material can create flaws that limit the material's strength.

9.2 Fiber-Reinforced Composites

Fiber-reinforced ceramics and glasses may have much greater resistance to fracture if stressed in the same direction as the fiber reinforcements. Usually the fibers have greater strength and elastic modulus than the matrix. Optimum bonding does not necessarily mean perfect bonding, however, since the latter would lead to cleavage through the reinforcing fibers. Optimum bonding is such that the fiber-matrix interface is able to transmit some load, but then fractures or debonds along the interface. The fibers pull out of the matrix with additional loading. While pulling out they exert frictional or mechanical interlocking resistance so that more energy is consumed. The microstructure is designed to shed load from the matrix to the strong fibers and to divert cracks in the matrix to run along the matrix fiber interface. The processing must be done carefully so that the interface strength is controlled and that the fiber does not deteriorate too much from microstructural changes, surface pitting, or interactions with the matrix.

Fractography of fiber-reinforced ceramics and glasses is different than that for monolithic materials. Fracture surfaces are often very rough and there often is no point looking for a specific fracture origin. There are exceptions. Figures 9.2 and 9.3 shows a silicon carbide filament-reinforced silicon nitride that did have discrete fracture origins.

Fracture typically entails damage accumulation and coalescence leading to rupture. Often the objective is to observe the general fracture mode and to ascertain whether it was due to tensile fiber pull out and fiber rupture, shear delamination in the matrix parallel to the fibers, compression buckling of fibers, or buckling of a protective coating in compression. The failure mode depends upon whether the structure is one-, two- or three-dimensionally reinforced and the size and shape of the component and the loading conditions. Although bend testing is reliable for creating tensile fractures in

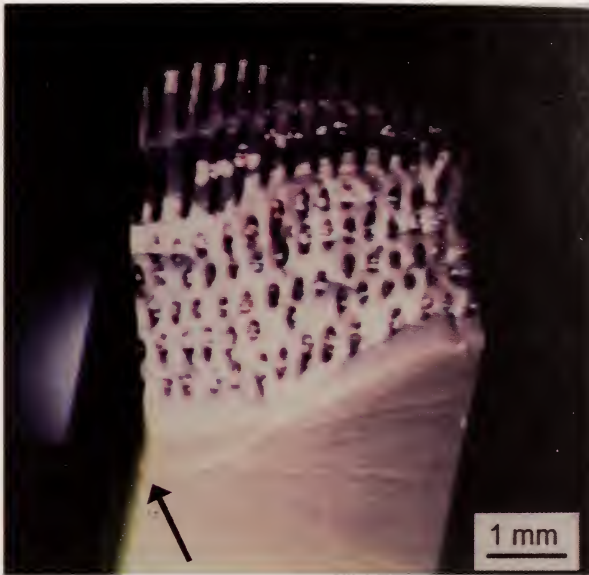


Figure 9.2. A SiC filament reinforced Si_3N_4 bend bar tilted back at an angle so as to view the fracture and tensile surfaces. A series of branching cracks radiate outwards from one origin site (arrow).

(a)

(b)

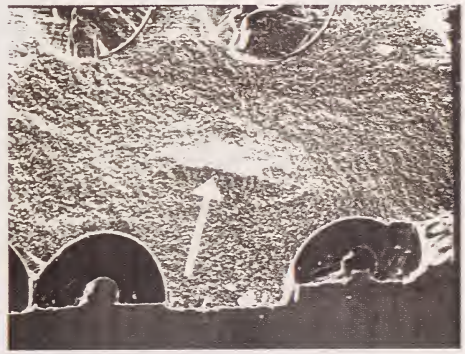


Figure 9.3. Fracture surface of CVD SiC filament reinforced Si_3N_4 bend bar. (Ref. 1) (a) shows that there was not very much fiber pullout in this case. Wake hackle in the matrix behind the filaments are telltale indicators of the local direction of crack propagation through the matrix and lead back to the origin, which is a porous seam in the matrix shown by the white arrows in (a) and (b).

monolithic ceramics and glasses, composites are more susceptible to alternative failure modes when loaded in bending. Figures 9.4 and 9.5 shows tensile stress fractures with good pull-out in a fiber-reinforced epoxy and a ceramic, respectively.

Images such as these can be used to qualitatively assess the fiber-matrix interface bonding and also if any damage has been done to the fibers during processing. Very often the fibers have fracture mirrors and it is instructive to ascertain whether the fibers have fractured from surface or internal flaws. Furthermore, the fracture mirror sizes in the fibers may be analyzed and used to obtain good estimates of the stress at fracture in the fibers. This strength can be compared to analytical predictions for the composite behavior to determine whether the load redistribution to the fibers was as expected. The strength of the fibers in the matrix may be compared to the strength of virgin fibers tested alone. Often processing and interactions with the matrix or with a fiber coating weakens the fibers.^{2,3,4,5,6,7}

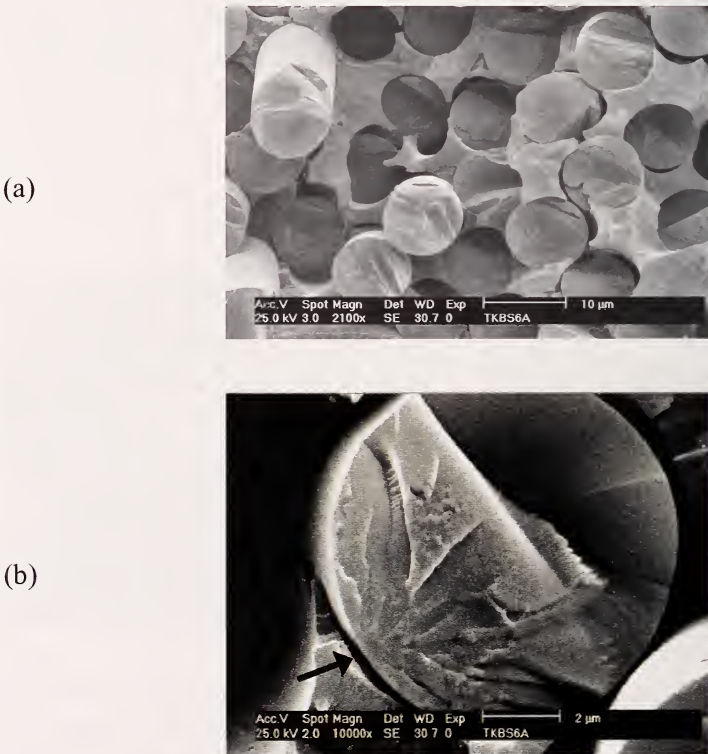


Figure 9.4. Fracture surface of an E-glass fiber reinforced epoxy matrix one-dimensional composite. The arrow marks the origin in (b). (courtesy of S. Scherrer)

Some material science or material development investigations focus on crack interactions with the structure. The scanning electron microscope is the preferred tool. Emphasis is placed on cracking in the fibers, the fiber pullout lengths, cracking in and around the fiber-matrix interface, or the microcrack density in the matrix. Micro-analytical chemical analyses are often used to study the chemistry of the fibers and the interfaces.

As stated above, the usual desired mode of fracture is one with a very rough fracture surface with ample fiber pullout. Observation that portions of a composite structure have fractured in a planar fashion with minimal pull out is often a sign that some deterioration in the composite has occurred or that the fiber-matrix bond is too strong. For example, Glass et al.⁸ analyzed a spectacular rupture of a large fiberglass-epoxy tank that stored pressurized sulphuric acid. Large portions of the tank had the classic rough fracture fractures with extensive fiber pullout, but the origin region had flat planar fracture zones. Incidental spilled acid on the exterior surface penetrated matrix microcracks and reached and degraded the reinforcing E-glass fibers. Fracture mirror analysis showed the fibers broke at only 20% to 40% of the baseline fiber strengths. Progressive fracture from the exterior occurred over a period of time as outer fibers broke, matrix microcracks opened up, and more acid penetrated and damaged more fibers until the vessel ruptured.



Figure 9.5. SEM image of the fracture surface of a SiC (Nicalon) ceramic fiber – zirconia matrix composite. The arrows mark fracture origins and mirrors in several fibers. (Ref.13, Courtesy of R. Rice)

Composites that are exposed to elevated temperature sometimes fracture with planar fracture regions near the surface surrounding a core of rough fibrous fracture in the core.^{9,10,11} Oxidation, corrosion, or surface reactions can alter the fiber–matrix bonding or fiber strength causing composite degradation.

Composites that are tested transversely, that is with tensile stresses perpendicular to the fiber directions, are usually very weak. Fractography in such cases often is focused on the crack propagation paths around or through the fiber and the fiber-matrix interface. Hull shows several examples in section 7.2 in his book on fractography.¹²

Chapter 9 References

1. J. J. Swab, G. D. Quinn, and D. J. Snoha, “Mechanical Behavior of a SiC Fiber/Si₃N₄ Composite,” U. S. Army MTL Technical Note TN 90 2, Watertown, MA, Sept. 1990.
2. M. D. Thouless, O Sbaizero, L. S. Sigl, and A. G. Evans, “Effect of Interface Mechanical Properties on Pullout in a SiC-Fiber-Reinforced Lithium Alumino Silicate Glass-Ceramic,” *J. Am. Ceram. Soc.*, **72** [4] (1989) 525 – 532.
3. W. A. Curtin, “In situ Fiber Strengths in Ceramic-Matrix Composites from Fracture Mirrors,” *J. Am. Ceram. Soc.*, **77** [1] (1994) 1075 – 1078.
4. I. J. Davies and T. Ishikawa, “Mirror Constant for Tyranno Silicon-Titanium-Carbon-Oxygen Fibers Measured *In Situ* in a Three Dimensional Woven Silicon Carbide/Silicon Carbide Composite,” *J. Am. Ceram. Soc.*, **85** [3] (2002) 691 – 693.
5. A. J. Eckel and R. C. Bradt, “Strength Distribution of Reinforcing Fibers in a Nicalon Fiber/Chemically Vapor Infiltrated Silicon Carbide Matrix Composite,” *J. Am. Ceram. Soc.*, **72** [3] (1989) 455 – 458.
6. J. F. Jamet, D. Lewis, and E. Y. Luh, “Characterization of Mechanical Behavior and Fractographic Observations on Compoglas SiC/LAS Composites,” *Ceram. Eng. Sci. Proc.*, **5** [7] (1984) 625 – 642.
7. A. C. Jaras, B. J. Norman, and S. C. Simmens, “The Measurement of Glass Fibre Strength in Composites from Studies of their Fracture Surfaces,” *J. Mat. Sci.*, **18** (1983) 2459 – 2465.

8. S. J. Glass, E. K. Beauchamp, M. J. Carr, T. R. Guess, S. L. Munroe, R. J. Moore, A. Slavin, and N. R. Sorenson, "Failure Analysis of A Fiberglass-Reinforced Plastic Pressure Vessel," pp. 527 – 541 in *Fractography of Glasses and Ceramics, III, Ceramic Transactions*, Vol. 64, J. Varner, Fréchette, V., and G. Quinn, eds., American Ceramic Society, Westerville, OH, 1996.
9. K. M. Prewo, "Tension and Flexural Strength of Silicon Carbide Fibre-Reinforced Glass Ceramics," *J. Mat. Sci.*, (1986) 3590 – 3600.
10. T. Mah, M. G. Mendiratta, A. P. Katz, R. Ruh, and K. S. Mazdiyasi, "High-Temperature Mechanical Behavior of Fiber-reinforced Glass-Ceramic Matrix Composites," *Comm. Am. Ceram. Soc.*, **68** [9] (1985) C 248 – 251.
11. T. Mah, M. Mendiratta, A. Katz, and K. Mazdiyasi, "Recent Developments in Fiber-Reinforced High Temperature Ceramic Composites," *Bull Am. Ceram. Soc.*, **66** [2] (1987) 304 – 308, 317.
12. D. Hull, Fractography, Observing, Measuring and Interpreting Fracture Surface Topography, Cambridge University Press, Cambridge, 1999.
13. R. W. Rice and D. Lewis, III, "Ceramic Fiber Composite Based Upon Refractory Polycrystalline Ceramic Matrices," pp. 117 – 142 in *Reference Book for Composite Technologies, Vol. 1*, ed S. N. Lee, Technomic Publ. Co., Lancaster, PSA 1989.

10. Case Studies

The following case studies illustrate the application of fractographic techniques for failure analysis. Most have not been published. Many additional case studies may be found in Appendix B. The proceedings of the Alfred University Fractography of Glasses and Ceramics conference series have dozens of additional cases and are listed in Appendix A.

- Case 1 Ruptured Rotor (Ceramic gas turbine rotor)
- Case 2 Busted Barrel (Silicon carbide gun liner)
- Case 3 Conflicting Carbide Data (Silicon carbide flaws and slow crack growth)
- Case 4 Vulnerable Vials (Broken medicinal vials)
- Case 5 Troublesome Tubes (Sapphire tubes in a plasma asher)
- Case 6 Suffering Setter Plate (Silicon carbide furnace plate)
- Case 7 Ruptured Radomes (Fused silica missile nosecones)
- Case 8 Maligned machinists (Bend bars made by different machine shops)
- Case 9 Modeler's Match (Fracture origins in MEMS scale micro tensile specimens)
- Case 10 Fractious Fractographers (A VAMAS fractography round robin)
- Case 11 Perilous Prostheses (Four All-ceramic dental crowns)

Case 1: Ruptured Rotor (Ceramic Gas Turbine Rotor)

Figure 10.1 shows a model gas turbine rotor made of hot-pressed silicon nitride that was designed to fail. It was one of twelve such model structures made by the Ford Motor Company's scientific research laboratory in the late 1970s to mid 1980s.^{1,2} It was part of a much larger ambitious endeavor to incorporate advanced ceramics into automotive gas turbine engines. Considerable effort was expended on improving ceramic materials, developing reliability codes, generating data bases, fabricating parts, and running them in test rigs. Full scale engine testing was expensive and risky, so a small project was set up to verify the ceramic design and reliability codes by using a realistic model rotor. This simulated gas turbine rotor was mounted in a hot spin rig shown in Figure 10.2 and rotated at 50,000 rpm while heated by hot gasses to a peak rim temperature of 1260 °C (2300 °F). These conditions were representative of the turbine operating conditions and the speed, mass and shape of the part were designed so that some of the rotors would fracture in a time dependent manner, from slow crack growth of preexisting flaws. The goal was to correlate failure times to predictions based on life prediction computer models.



Figure 10.1. A Ford silicon nitride model gas turbine rotor which survived 25 h intact. The model rotor has a 95 mm diameter.

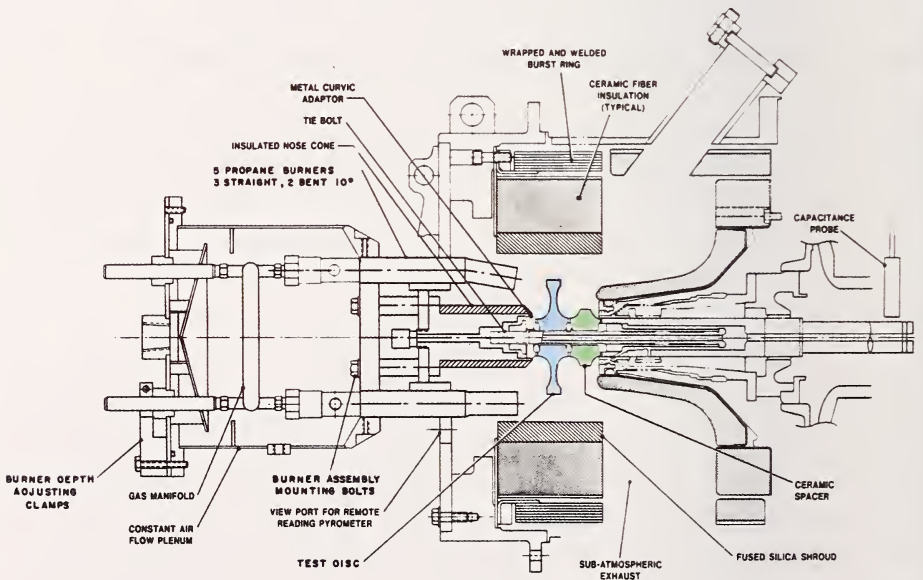


Figure 10.2. The Ford hot spin test rig (Ref. 2).

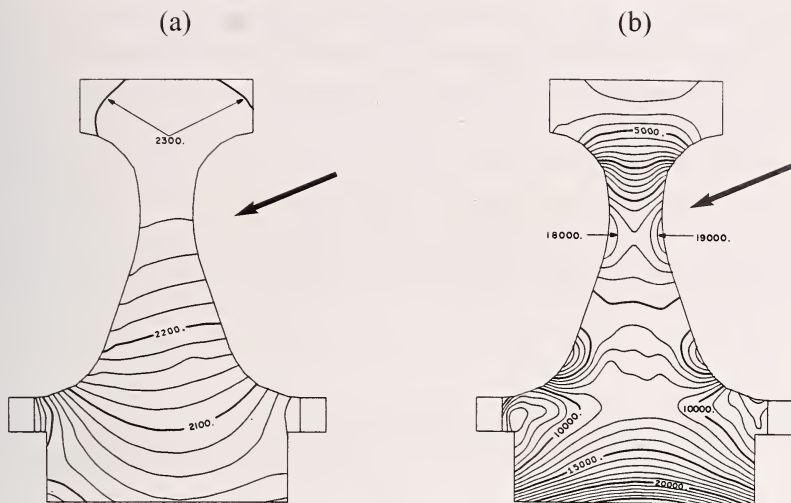


Figure 10.3. Isotherms ($^{\circ}\text{F}$) (a), and maximum principal stresses (psi), (b) in the rotor. (These figures are from the original references which used the older units.) Failure was expected to occur in the thin web (large arrows) (Ref. 1,2). The maximum stress in the web was oriented primarily in a radial direction.

Twelve model rotors were fabricated and tested. Figure 10.3 shows the temperature and principal stresses from the heat transfer and finite element models, respectively. The maximum principal steady state stress was 131 MPa (19 ksi). Six broke in a time dependent manner as intended. Three were run out and did not fail in the allotted times. They were treated as censored outcomes. One other did not break when a test run was terminated early and it too was treated as a censored outcome. Two rotors broke on initial start up. The rotors were designed to have a high probability of survival on loading (>95 %), but to probably fail within 25 h. The design analysis assumed that failure would occur due to slow crack growth of preexisting volume-distributed flaws. It was expected that fracture would occur from the thin web portion of the rotor where the stress and temperature were both high.

The model rotor was made of a state of the art hot-pressed silicon nitride^a that was carefully machined to final dimensions. The particular grade was one of the most thoroughly analyzed structural ceramics of all time and was eventually used as the world's first reference material for the property fracture toughness.³ Eventually enough data was available that a comprehensive

^a Grade NC 132, Norton Co., now St. Gobain Advanced Ceramics, Worcester, MA.

fracture mechanism map was constructed,⁴ but that was after the conclusion of the Ford study. A substantial amount of laboratory test coupon data were available including flexural and tensile strengths, elastic properties, and slow crack growth parameters. All were available as a function of temperature. Slow crack growth data were available from three types of tests: variable stressing rate strength tests (dynamic fatigue), crack velocity - fracture mechanics tests (double torsion), and stress rupture (flexural and tensile). The model rotor did not have turbine vanes, but an increased rim mass to simulate their effect.

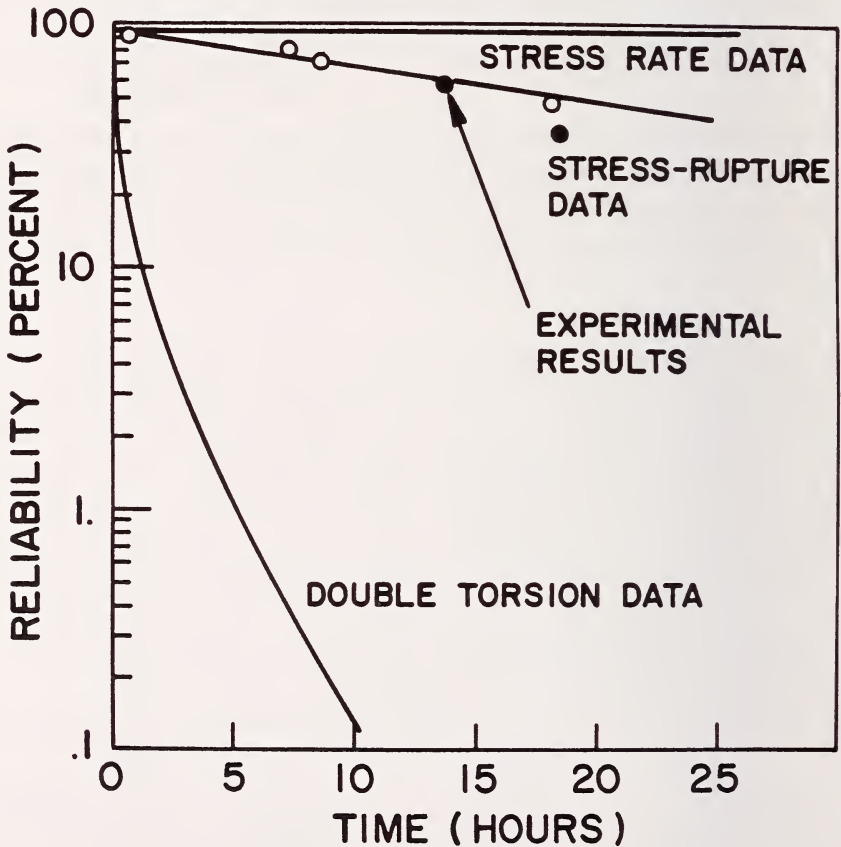


Figure 10.4. Reliability versus time showing reliability predictions based on three different types of laboratory test data (solid lines) versus the actual outcomes for six rotors that failed.(Refs. 1,2) The two solid points are the rotors that were fractographically analyzed by the author.

Figure 10.4 shows the reliability as a function of time. An estimate of the error in the calculated reliabilities was made using estimated temperature errors of $\pm 11\text{ }^{\circ}\text{C}$ ($\pm 20\text{ }^{\circ}\text{F}$). The reliability, R , for the i^{th} rotor was:

$$R = \prod_{i=1}^N \frac{N-i}{N+1-i}$$

where $N = 10$ is for the ten rotors that survived the initial startup. The three types of slow crack growth data gave very divergent predictions. The six data points show the outcomes for the six rotors that failed at times from 0.2 h to 18.6 h. The predictions made with the stress rupture data set gave the best correlation to the actual lifetimes and the authors concluded that stress rupture data was the best for predicting reliability versus time.^{1,2}

The fractographic analysis revealed that fracture did not occur quite as anticipated. The test rig was constructed in such a manner that most of the fragments were retrievable. The longest (18.6 h) and third longest (13.8 h) rotors were sent to the author for fractographic evaluation. It was felt that these would have large slow crack growth zones that would be easy to find. One virtue of NC 132 is that it was a very fine-grained fully-dense material with minimal second phase.

Fracture markings were quite clear and the local direction of crack propagation could be assessed in every piece. One rotor (18.6 h) was reconstructed piece by piece over the course of one week culminating in the assembly shown in Figure 10.5. Many fragments from the rim were missing, but it did not matter. The figure also shows that the spacer had also fractured and its pieces were commingled with the rotor thereby hampering the assembly. Nevertheless, the central and web portions of the rotor were almost completely reassembled. After completion, the rotor was taken apart again and a map of crack propagation directions was made.

The interpretation was clear. Primary fracture commenced at the bore or the curvic coupling teeth and cracks branched and ran out to the rim as shown in the Figure 10.5 schematic. Every single fragment was examined in a futile search for a web origin with a slow crack growth zone, but none were found. All primary fractures started from the bore or coupling area. There were three origins from the inner part of the rotor. Origin "A" at the exact edge of the bore which although chamfered nonetheless had surface grinding cracks (Figure 10.6 and 10.7). It could not be determined whether slow crack growth had enlarged the grinding cracks. The other two origins were located on the

◆ Fractography of Ceramics and Glasses

other side of the bore and were from the curvic coupling teeth machined into the rotor (figure 10.8). These were part of the attachment scheme. One origin was a parallel machining crack (aligned parallel to the axis of grinding) in the tooth and the other was an impact – contact crack also on a tooth (Figure 10.8).

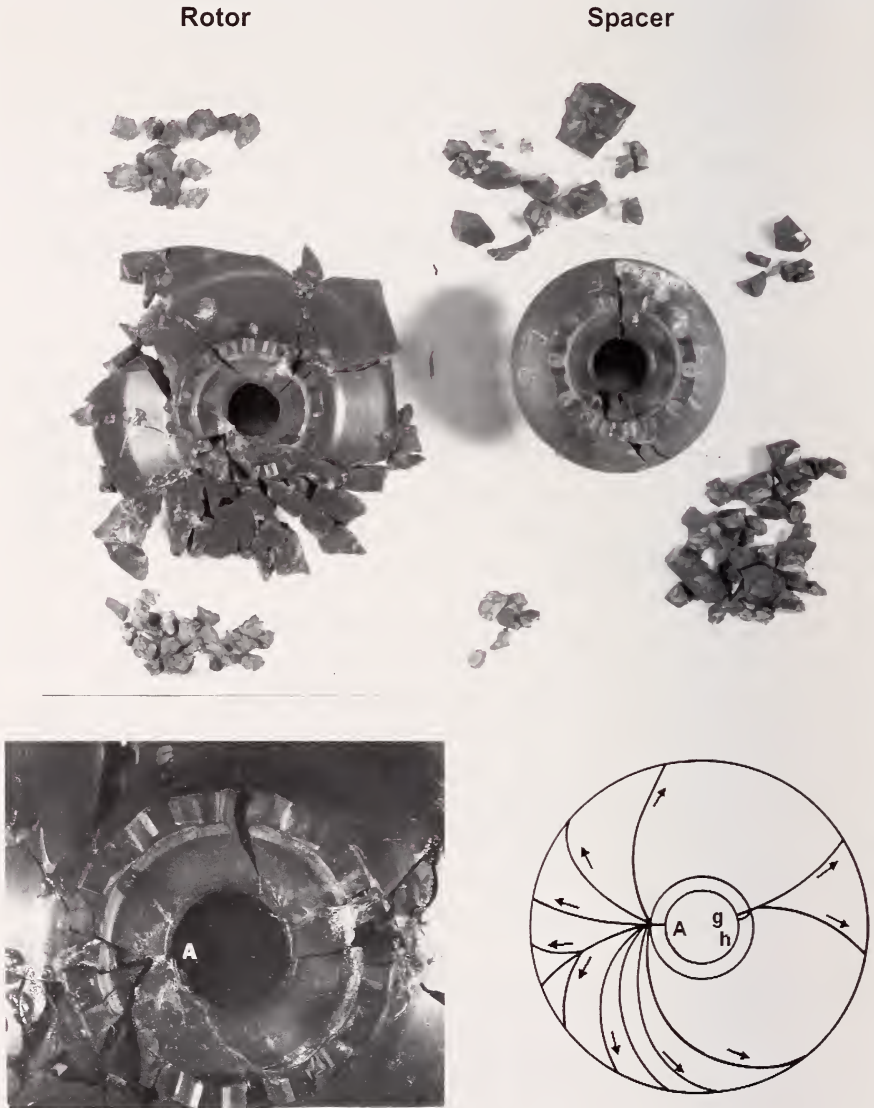


Figure 10.5. Reconstructed model rotor and spacer. Fracture initiated either at location “A” on the left side of the bore of the rotor or at two locations “g” or “h” on the opposite side. “g” occurred after “h.” The lower schematic shows the overall fracture pattern in the rotor.

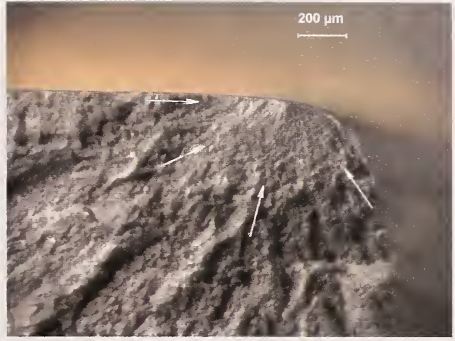
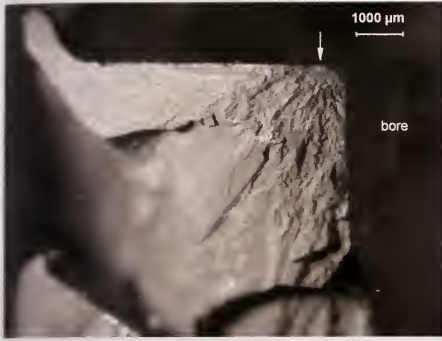


Figure 10.6. Fracture surfaces showing a fracture mirror and the origin site A, which is a surface crack from grinding. The right figure highlights the mirror and fracture origin which was a grinding crack. The next figure has a close-up.

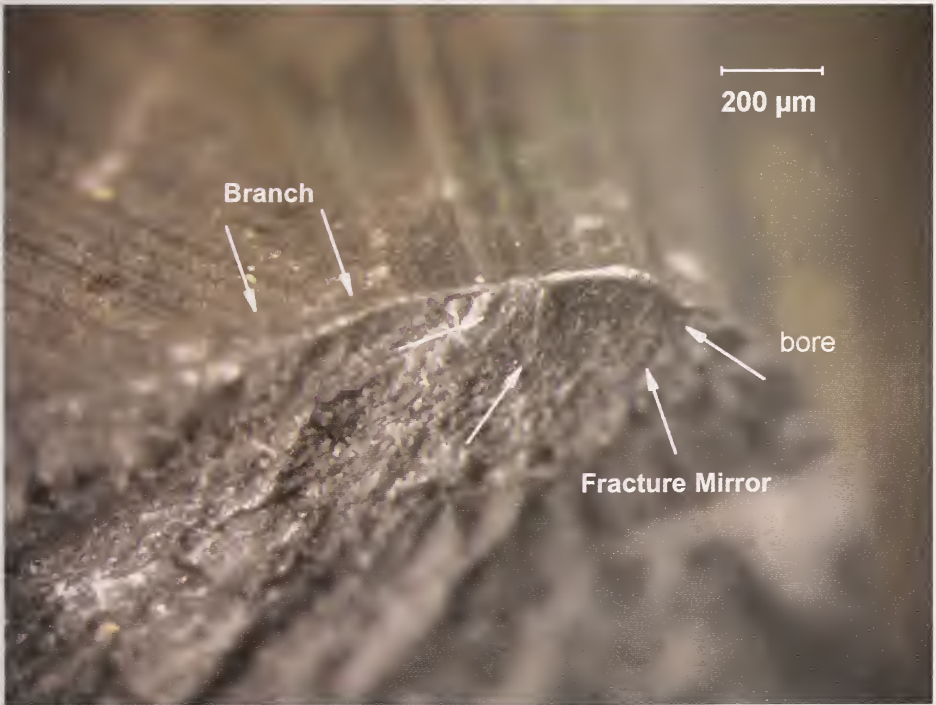


Figure 10.7. Origin A was at the inside bore. The part has been tilted to show both the fracture surface and the ground surfaces.

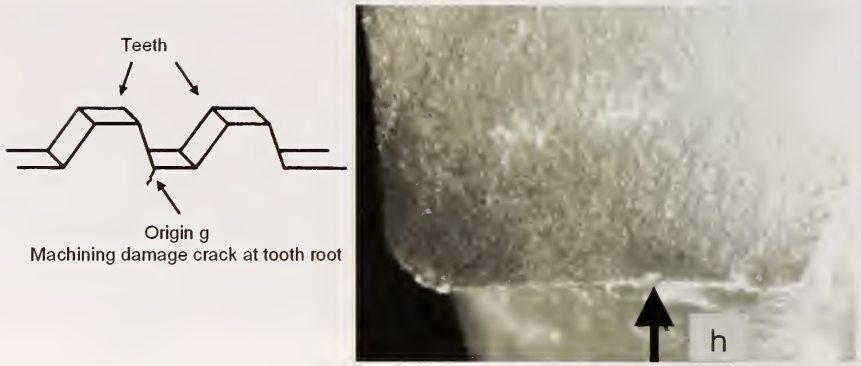


Figure 10.8. Origins *g* and *h* on the opposite side of the rotor were a grinding crack at the root of a tooth (*g*) and a contact crack (arrow) at a root of a tooth slot (*h*).

Thus, fracture started on one side of the rotor, thereby opening up the disk structure whereupon unbalanced forces triggered a rupture on the opposite side. Origin A had a well-defined small fracture mirror allowing an stress estimate of a 630 MPa (92 ksi) which is much greater than the model estimated bore stress of ≈ 172 MPa (25 ksi) from Figure 10.3. This, plus the violent branching from site A, suggests it was a secondary fracture. Primary fracture occurred on the other side of the bore, causing the rotor to go completely out of balance leading to the overstress fracture at point A. Origin *h* was a large contact crack flaw with a very large mirror. The local stress was estimated to be 500 MPa (72 ksi) from the flaw size and approximately 580 MPa (84 ksi) from the fracture mirror. Origin *g* was determined to have fractured after site *h* since the crack from *g* stopped when it encountered the prior crack from *h*. Figure 10.3 shows there were modest bore stresses (≈ 138 MPa, 20 ksi) and temperatures (1150 °C, 2200 °F), but the stress does not match fractographic estimates.

One other possibility is suggested by an observation from the fractographic examination. When the rotor and spacer were assembled in the hot test rig, it was customary to separate them with a thin platinum foil to prevent direct ceramic-to-ceramic contact. The fractographic examination showed uneven platinum wear traces and even some bare spots. Could it be that the foil deformed or crept with time such that ceramic-to-ceramic contact eventually occurred? If so, then the rotor stress distribution may have become unbalanced or local stress concentrations or contact stresses may have contributed to cause an initial contact crack and fracture at site *h*.

This exercise was a good example of one of the author's laws of fractography: "The first one is the hardest." While at first glance reassembly of a burst rotor may appear to be a formidable task, it was merely time consuming. The second rotor took less time to analyze. It also had fracture initiation sites at the bore or at the teeth. Years later, the author became aware of comparable work done on model silicon nitride rotors at Daimler-Benz.⁵ They also reconstructed burst silicon nitride rotors and used fractography to find that grinding cracks in the bores sometimes were fracture origins.

Some lessons learned from this case study were:

- a. Fracture occurred from a different cause than expected and modeled.
- b. Stress rupture data may have been the best for reliability estimation, but the correlation of failure times was fortuitous for the two rotors examined.
- c. Volume flaws were not found in the two fractured rotors. Surface machining cracks were found and Weibull area scaling should also have been included in the reliability model.

Case 2: Busted Barrel (Silicon Carbide Gun Liner)

The U. S. Army has off and on over the past twenty-five years investigated ceramic liners to improve gun barrel life and reduce mass. The low density, high compression strength, refractoriness, and erosion and wear resistance of ceramics could be advantageous. Figures 10.9 and 10.10 show drawings for a 50-caliber machine gun breech with a ceramic liner from a project conducted for the U. S. Army in the 1980s.⁶ One design placed the ceramic into compression by shrink fitting a steel sleeve around the ceramic. The steel sleeve was heated and placed over the cool ceramic tube. As the assembly cooled, the steel contracted and put the ceramic liner into axial, radial, and hoop compression. The dimensions and temperature differentials were chosen so that the ceramic liner was always in compression, even when firing a projectile. Several ceramics were tried, but most testing was on a sintered α -SiC. Figure 10.10 shows the maximum *axial* stresses in the three components of the assembly from combining the residual shrink fit and projectile firing stresses. The maximum axial stress was 670 MPa in compression in the ceramic liner mid portion. This stress tapered to zero at each end. The axial stress maximums were 112 MPa tensile in the steel sleeve and 154 MPa tensile in the steel jacket. The maximum *radial* stress in the ceramic sleeve was 345 MPa compression, and the maximum *hoop* stress was 590 MPa compression during projectile firing. The environment is severe, but if the ceramic was always under compression, perhaps it would not fracture.

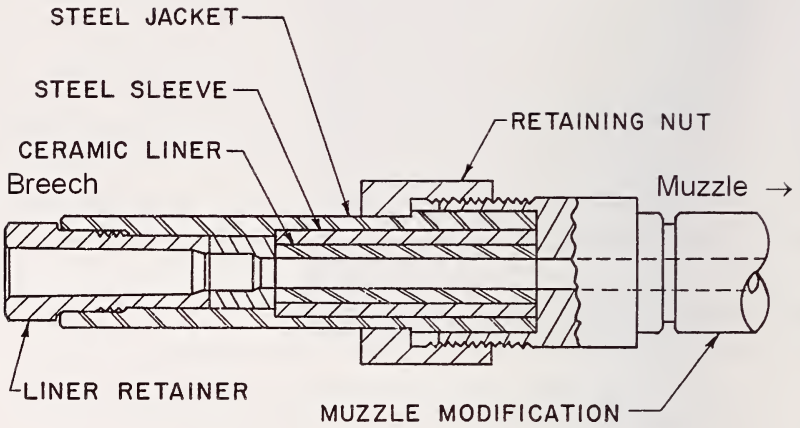


Figure 10.9. Schematic of the breech end of the 50 caliber (12.7 mm) gun barrel (Ref. 6).

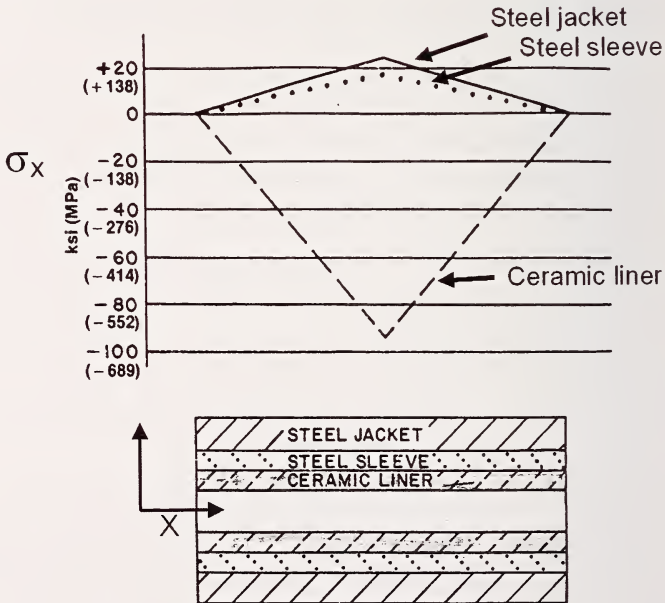


Figure 10.10. Axial stress distribution, σ_x , as a function of position x in the assembly along the bore (a). The stresses correspond to the three parts shown in a sectional view in (b) which is a simplified version of the assembly shown in the previous figure. The stresses included those from shrink fitting and projectile firing. (Figure from Ref. 6)

Some assemblies survived as many as a thousand single-shot firings, confounding some skeptics who felt that the assembly would not survive one shot. One assembly that did develop ceramic cracking after a few hundred shots had circumferential fractures as shown in Figure 10.11a. The steel sleeve and jacket were machined away to allow extraction of the ceramic as shown in Figure 10.11b. The fracture planes were perpendicular to the axial direction, suggesting that hoop stresses from internal pressure during projectile firing were not the cause of failure. The latter would have created radial cracking. Fractographic analyses showed that every fragment fractured from one or more contact cracks that were periodically spaced on the *outer rim* of the ceramic where it contacted the steel sleeve.

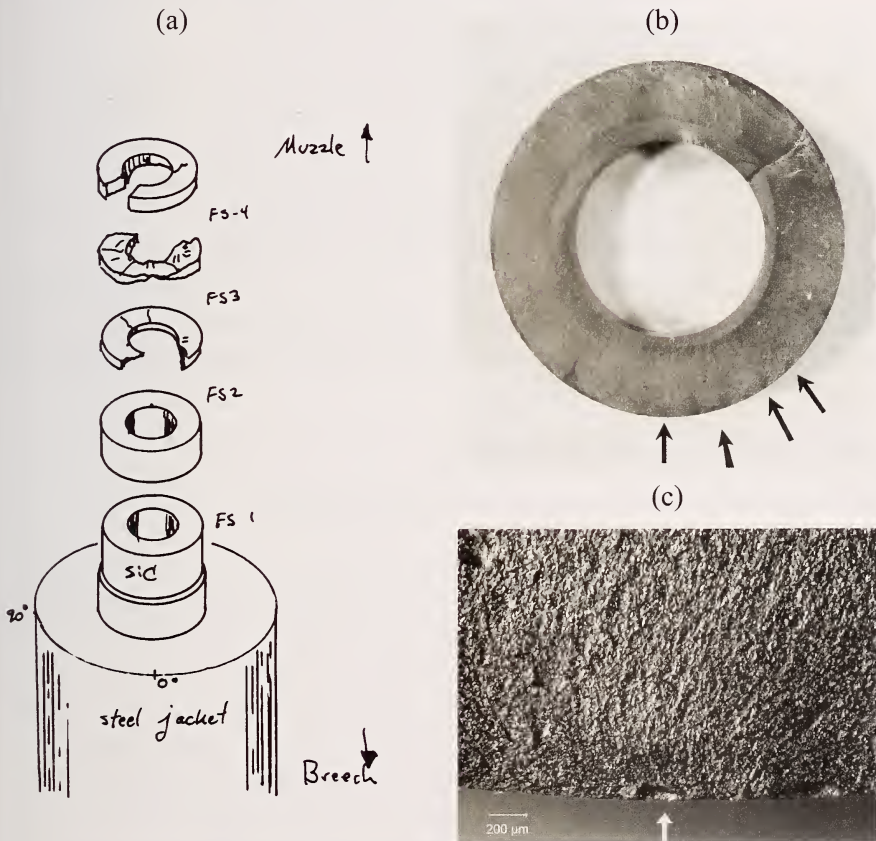


Figure 10.11. Fractured α -SiC gun barrel. (a) is a schematic sketch. (b) shows the fracture surface of one of the ring shaped fragments. Contact cracks are spaced periodically around the outer rim and appear as shadows in this view (arrows). The bore diameter is 12.7 mm. (c) shows a close-up of one of the contact cracks.

So if the shrink fitting created compressive stresses, where did the tensile stresses come from? The plane of the fractured surfaces and also of the initial semi elliptical contact cracks indicated that the tensile stresses were axial. Figure 10.10 shows that the axial residual compressive stresses did taper off towards the tube ends. The most likely sources of tensile stresses are dynamic stress waves generated during the firing of a bullet. Even if these are initially compressive, they can change phase and become tensile when the stress wave reflects off of the end faces. Furthermore, the elastic wave velocity and impedance of the silicon carbide and the steel sleeve are not matched and stress waves propagated axially at different rates. Hence, a dynamic tensile stress could develop at the interface due to mismatch of the transient elastic strains.

The contact stress cracks often were periodic around the rim. Although the parts were machined to tight tolerances, it is likely that slight variations in the mating surfaces led to an uneven fit and stress concentration sites that triggered the contact cracks. So, in this case, the ceramic was designed to always be in compression, but fractography showed otherwise. Some design and modeling improvements were suggested. The tolerances and surface specifications for the mating parts could be changed. The elastic properties of the ceramic and the confining sleeve could be matched better. More sophisticated stress models could examine the transient stress states in the assembly.

Case 3: Conflicting Carbide Data (Silicon carbide flaws and slow crack growth)

This case is not about a specific component, but about the risk of treating all flaws as if they behave the same. As part of a program on characterization of structural ceramics for heat engine ceramics in the 1980s, the author conducted extensive stress rupture testing of pressureless sintered α -SiC.^{b 7,8,9} Stress rupture testing entails applying a constant stress to a specimen at a level below that needed to cause fast fracture and measuring the time to failure. Slow crack growth can cause flaw enlargement and time dependent fracture. Sometimes such tests are termed creep rupture if the loading conditions are such that bulk creep deformation leads to accumulated damage and fracture.

^b Hexoloy SA, Carborundum, Co., Niagara Falls, NY. Now St. Gobain Advanced Ceramics

The author's data^{7,8,9} at 1300 °C in air was consistent with data published by another team.¹⁰ Both teams detected time-dependent fractures due to intergranular slow crack growth of preexisting flaws as shown in Figure 10.12. A much different story emerged at 1200 °C. This author recorded time dependent fractures such as shown in Figure 10.13, but the other team did not observe any time-dependent fractures in their experiments. Why did the two groups have such contrasting outcomes at 1200 °C?

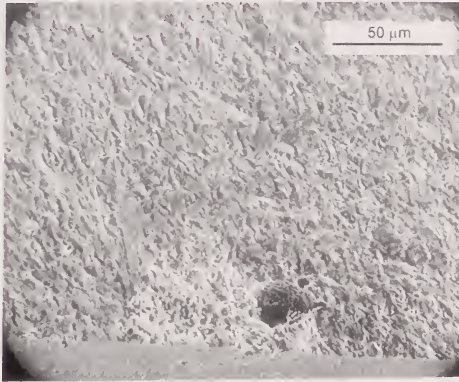


Figure 10.12. Fracture origin in a 1300 °C stress rupture specimen. The origin is a large intergranular slow crack growth region that may have started from the side of or beneath the large pore.

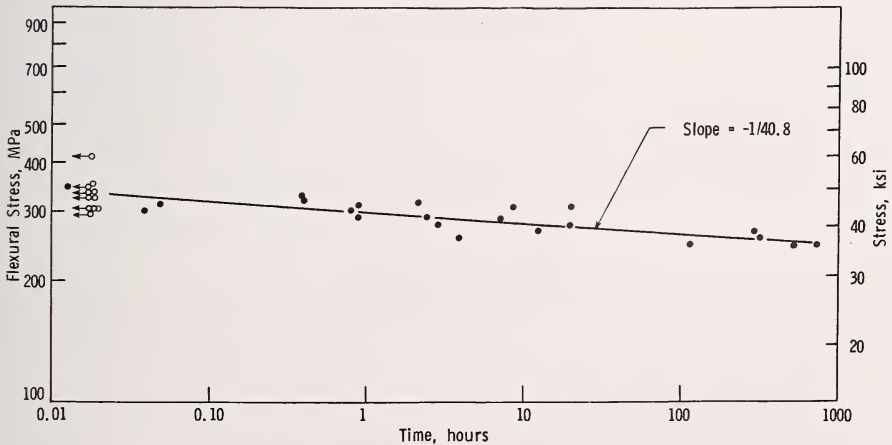


Figure 10.13. Stress rupture curve at 1200 °C in air for sintered α -SiC.⁷⁻⁹ Every time-dependent fracture was from a pore or porous zone and only if it was surface connected. The hollow points with arrows to the left are breaks on loading and are consistent with the fast fracture strength which was about 350 MPa. The slow crack growth exponent N was 40.8.

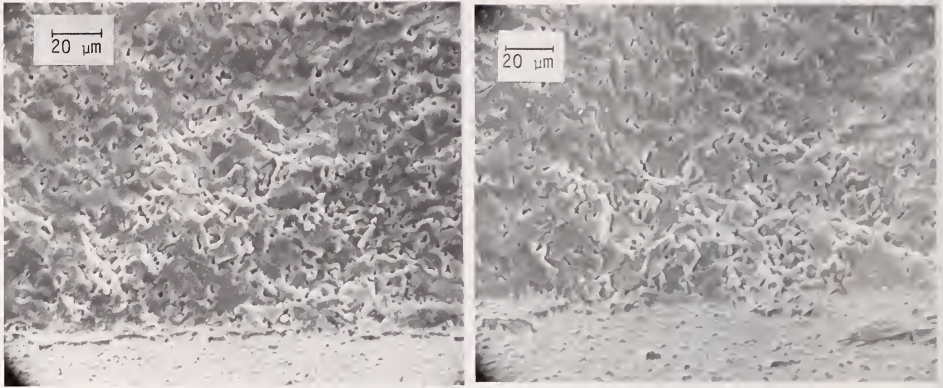


Figure 10.14. Fracture origins in 1200 °C α -SiC specimens that fractured at 863 h (left) and 1460 h (right) from surface-connected porous regions.

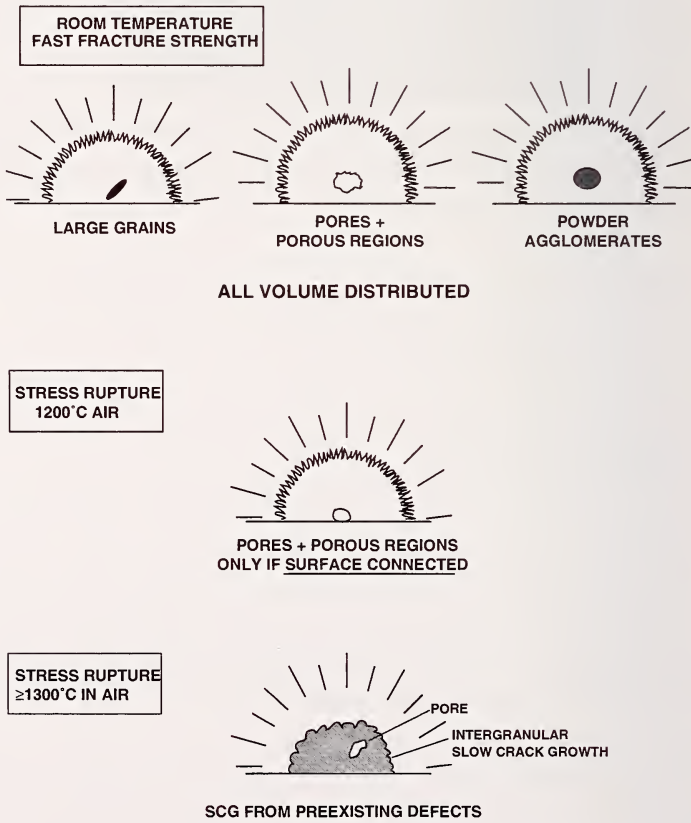


Figure 10.15. Fracture origins in α -SiC.

Fractographic analysis provided the answer. At 1300 °C and above, easily detected intergranular slow crack growth from volume-distributed flaws such as large grains, pores, or agglomerates caused fracture such as shown in Figure 10.12. Some of these volume origins were located in the bulk. Both teams detected this behavior.

On the other hand, every one of the 1200 °C time-dependent fracture origins was a pore or porous region connected to the outer surface as shown in Figure 10.14. These flaws did not have slow crack growth markings. Evidently these flaws were susceptible to very localized stress-corrosion crack extension (from oxidation) that sharpened or locally extended tiny microcracks on the pore periphery. These flaws did not need much change in flaw size or severity for them to go critical, since the failures occurred at stresses very close to the fast fracture strength as shown in Figure 10.13. Figure 10.15 summarizes the fractographic findings.

The other testing team did not detect the 1200 °C stress corrosion mechanism since they used Knoop artificial flaws in all of their bend specimens.¹⁰ Artificial flaws often are effective tools for studying fracture, but in this instance they produced misleading results. The Knoop flaws did grow by slow crack growth at 1300 °C and above. They did not grow by slow crack growth or by stress corrosion at 1200 °C. The Knoop flaws were not susceptible to the same failure mechanism as the pores and porous zones in the as-machined specimens.

One might ask why the Knoop flawed specimens did not fracture from the pores and porous regions that were undoubtedly present. The answer is that the large Knoop flaws reduced the strength of the specimens to less than 200 MPa, a stress well below that necessary to activate the pore flaw stress corrosion mechanism.

In summary, large grains, agglomerates, pores and porous zones controlled the room temperature strength and were sources of time dependent fracture at 1300 °C, but only the latter two flaw types were vulnerable to time dependent stress corrosion cracking at 1200 °C, and only if they were connected to the surface. A reliability model that assumed no time dependent failure at 1200 °C in air would have been faulty. This case demonstrates that it is often best to let a material reveal what type of flaws it is apt to fail from, rather than force it to fail from artificial indentation flaws.

Case 4: Vulnerable Vials (Broken Medicinal Bottles)

A pharmaceutical company had a problem with neck rim cracking in 17 mm diameter medicinal vials. The cracking rarely caused the vials to break, but the trace leakage and loss of the airtight seal due to through-cracks in the rim caused great concern. Loss of seal carries a risk of contamination with potential fatal consequences in medical containers (e.g., see case 10.8 in Fréchette, Ref. 11).

Optical stereomicroscope examination of vials with either intact or severed caps revealed a circumferential damage zone in the glass just under the aluminum cap seal (Figure 10.16 a,b). Focusing through the glass revealed that some cracks had penetrated deep beneath the surface although the full extent of the penetration was difficult to assess with tight intact cracks. Examination of a vial with a severed cap confirmed the contact cracks could

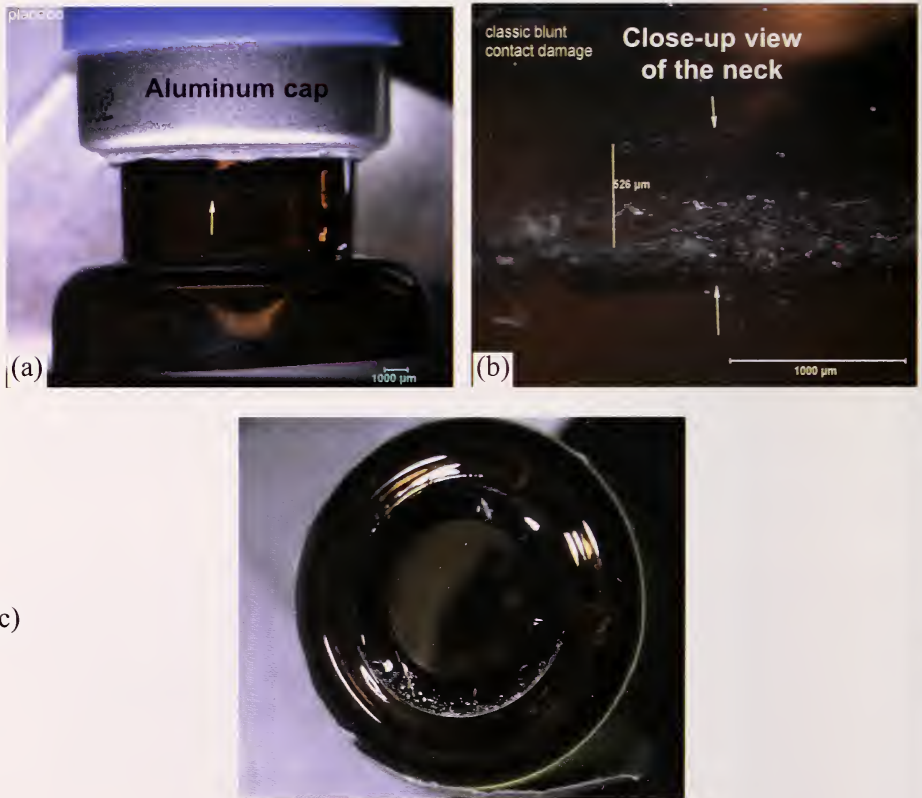


Figure 10.16. Rim cracking in glass medicinal vials. (a) and (b) show blunt contact cracking damage (arrows). (c) shows a top view of the fracture surface of a vial with a severed cap.

reach all the way to the interior. No defects in the glass were detected and the concentricity of the neck with the vial body was within specifications. The source of the fractures was traced to a misalignment of the cap crimping machine star wheel assembly.

An incidental finding was the beautiful example of scarps, shown previously as Figure 5.39a, on one of the fracture surfaces of a severed cap. The presence of the scarps was consistent with the outer surface cracks having reached the vial interior and the fluid therein aiding the final fracture of the remainder of the glass neck.

Case 5: Troublesome Tubes (Sapphire in a Plasma Asher)

Single crystal c-axis sapphire tubes, 38 mm diameter and 400 mm long, fractured during two runs of a prototype plasma asher. This is a device used to dry-remove photoresist from 300 mm diameter silicon wafers during manufacture of integrated circuits. The tubes contained oxygen and nitrogen gasses which were energized into a plasma state by a 2.5 kW microwave chamber. The plasma was used to ash (dry-removal) photoresist from 300 mm diameter silicon wafers. The microwave power was cycled on and off in 60 s intervals and the sapphire tubes reached temperatures of 600 °C to 700 °C. One tube broke during a gas purge step three seconds after the shutdown of the microwave energy. The second tube broke two minutes after a shutdown. The tubes that broke had shorter lengths than those in the earlier models. The longer tubes had lifetimes in excess of 400,000 cycles.

Figure 10.17 shows the fractured tubes. Many of the large cracks were approximately axial, suggesting that hoop stresses caused breakage. The breakage during cool down suggested thermal stresses had caused fracture. The cracks curved and wiggled at the tube ends, indicating the cracks slowed down and arrested. Some of the cracks crossed over each other, indicating that primary cracks did not run all the way through the wall thickness.

During optical microscopic examination of the fracture surfaces, a chance reflection off one surface revealed thin parallel reflective lines that ran counter to the fracture surface faceting as shown in Figure 10.17c. This was a sure sign of twinning and the next step was to view the tubes between crossed polarizers with the results shown in Figure 10.18. Multiple twins in the hot region triggered crack formation at twin intersections. The twins were oriented at 32 ° to the sapphire tube axis corresponding to classic r-plane twinning in sapphire, which can be caused by rather low compression stresses at temperatures as low as 300 ° to 500 °C.¹²

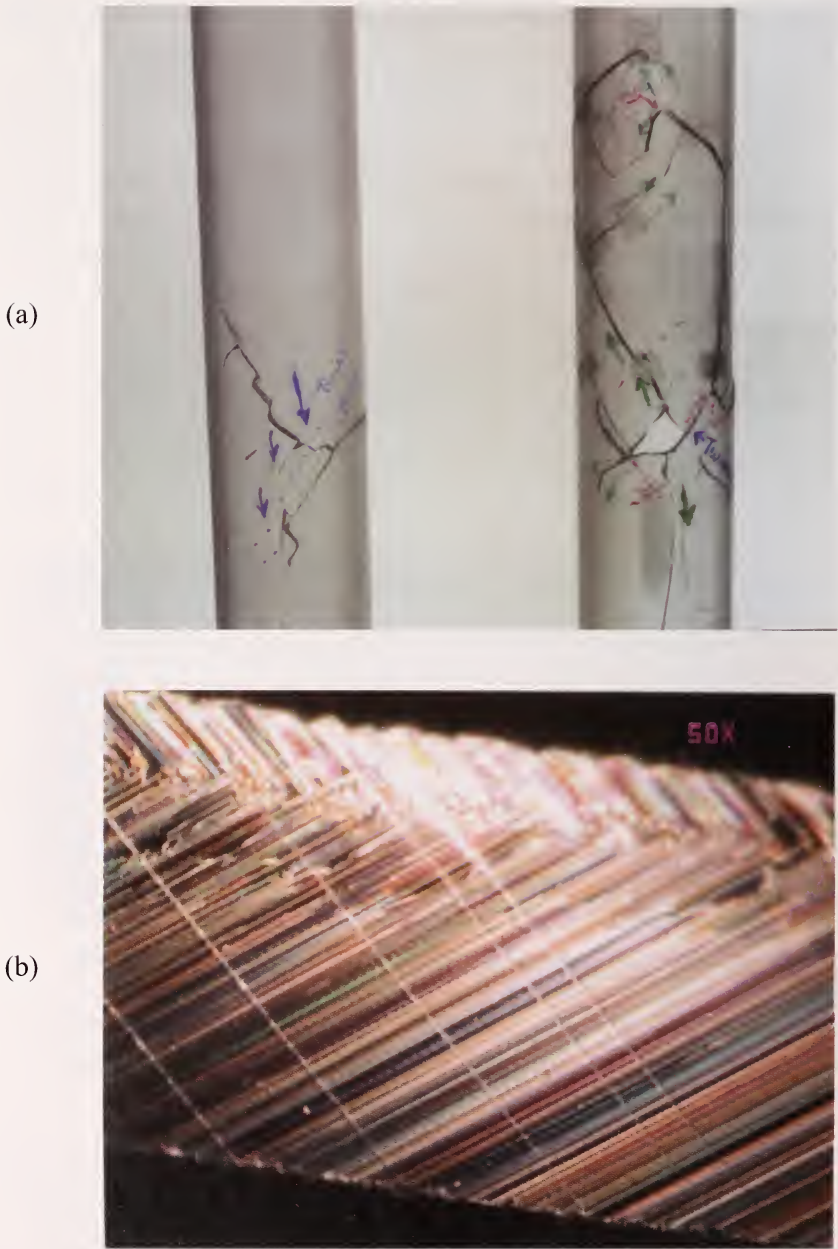


Figure 10.17. Two broken 38 mm diameter sapphire tubes from an integrated circuit plasma asher are shown. (b) shows a stereoptical microscope photo close-up of the fracture surface of a fragment from the middle of one tube in normal white light illumination at just the right angle. Five thin twin bands are visible against the very faceted fracture surface.



Figure 10.18. Twin bands became very apparent when the tubes were illuminated by light from crossed polarizers. Cracks initiated at twin band intersections (white arrows) and then were propagated by cool down thermal stresses. (Photos courtesy R. Pingree)

◆ Fractography of Ceramics and Glasses

Fracture occurred in two stages. First, axial constraint from a new type of seal at the tube ends prevented the free expansion of the tubes during the heating portion of the operating cycle. The earlier model ashers that did not have breakages used a different seal design that allowed expansion. The constraint in the new design created compression stresses which created the intersecting twins that generated cracks. The cracks propagated by cool down thermal stresses until the tube ruptured. The tube seal design was changed to eliminate the end constraints, thereby solving the problem.

Case 6: Suffering Setter Plate (Silicon Carbide Furnace Plate)

A large silicon carbide furnace setter plate fractured during a furnace run. Was the material faulty or was there some other cause? Figure 10.19 shows one half of the broken plate. It has the wavy fracture that is a telltale sign of a



Figure 10.19. Fractured SiC furnace setter plate (a). The curvy pattern is typical of a center heated plate fracture as shown in Chapter 4. The arrow marks the origin which is a hole through the plate. The machined grooves were chipped and had ragged edges as shown in (b). The plate was 36 cm round and 1.9 cm thick. (c) shows the origin hole from the bottom surface. There is spall and evidence of a chemical reaction with a mounting bolt or washer. (plate courtesy of B. Mikijelj)



(a)



(b)



(c)

Figure 10.20. Fracture surface of the SiC setter plate. A fracture mirror at the origin (arrows) attests to a moderate stress level. Hoop tensile stresses on the rim were generated by thermal strains. Thermal expansion of the hot plate center was resisted by the cooler rim. As the crack propagated towards the plate middle it slowed since it reached hot regions that were originally in compression. The fracture surface became relatively featureless and the crack meandered. The hole through the plate at the origin had chipping and grinding damage that weakened the plate. The mirror is centered on grinding damage on the inside of the hole shown by the arrow in (c).

center-heated plate fracture. Figure 10.20 shows the fracture surface revealing that fracture initiated from grinding damage at a hole near the rim. No material flaws of consequence were detected. The material was completely satisfactory, but the machining, grinding, and attachments were not. This failure analysis required only a visual inspection.

Case 7: Ruptured Radomes (Fused Silica Missile Nosecones)

First generation U. S. Army Patriot air defense missiles in the early 1980's utilized sintered fused silica radomes (Figure 10.21). Radomes are nosecones that are radar transmissive. Although fused silica is weak, it was selected since it had a low coefficient of thermal expansion. It would be less susceptible to thermal stresses from aerodynamic heating. The radome was prepared by sintering silica particles to greater than 85% density. This porous structure had a low but acceptable strength and, like an insulating firebrick, was more effective in arresting cracks than if the radome were a fully-dense glassy body. Selected radomes were deliberately loaded to fracture or proof tested as part of the engineering development program. This was done by attaching a sling to the side of the radome and pulling it laterally several times in different directions. Unexpected fractures occasionally occurred. Most fractures occurred in the ceramic where it was joined to a threaded fiber-epoxy thread ring attachment part (Figure 10.22). Fractography was difficult in the porous weak ceramic since it had a rough fracture surface, but a number of fractures were successfully diagnosed. Figure 10.22 shows an instance where atypical grinding damage created strength limiting cracks. Better control of



Figure 10.21. U. S. Army first generation Patriot air defense missile. The radome was 1.1 m tall with a 40 cm diameter. (a) courtesy U. S. Army. (b) courtesy Raytheon.

the surface grinding eliminated the problem. Figure 10.23 shows a different example wherein excessive shrinkage of the epoxy bond caused debonding. This created a stress concentration site in the ceramic that initiated fracture. The remedy in this case was to adjust the bond cure thermal cycle.

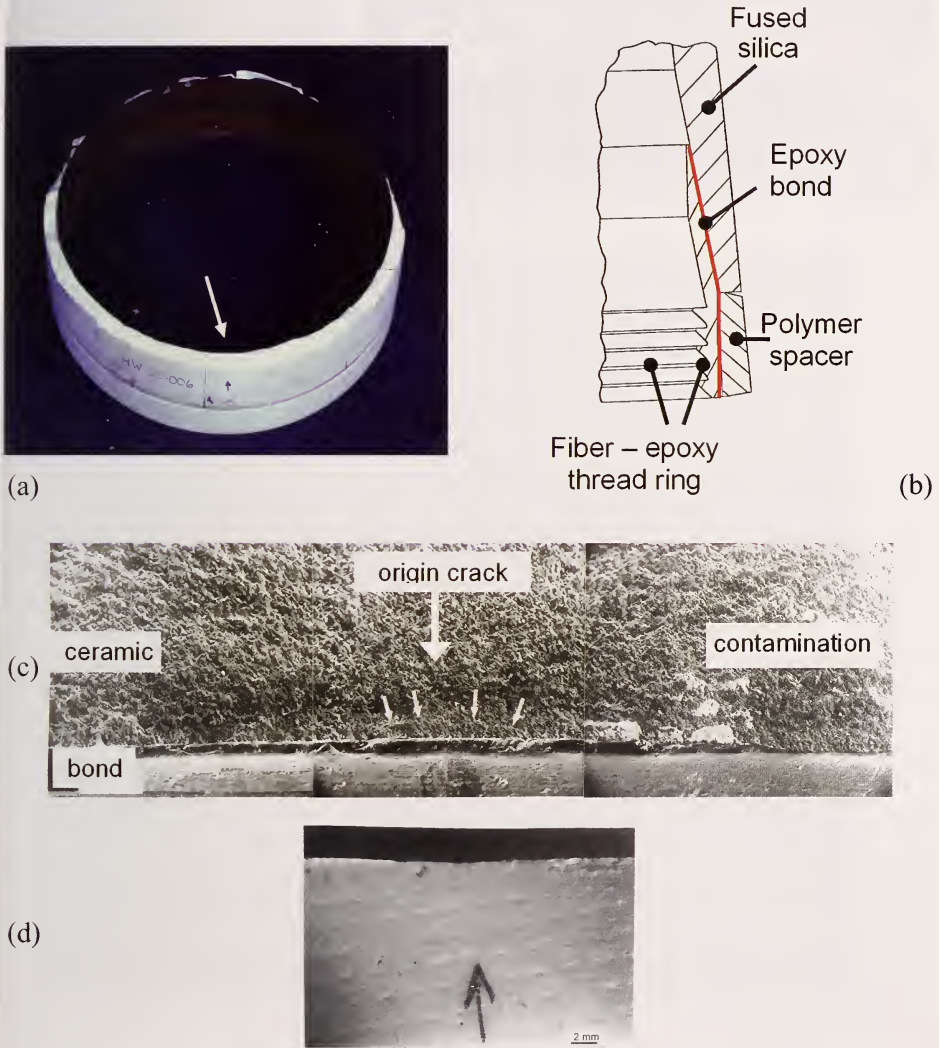


Figure 10.22. Sintered fused silica radome that fractured during a proof test. (a) is a top view with the origin region marked by the arrow. The ceramic is bonded on the inside to a fiber epoxy attachment ring. (b) is a schematic showing the attachment scheme. Fractures in the ceramic typically occurred near the top of the thread ring. (c) shows a grinding crack at the origin area (arrows). (d) shows a grinding pattern on the inside ceramic surface.

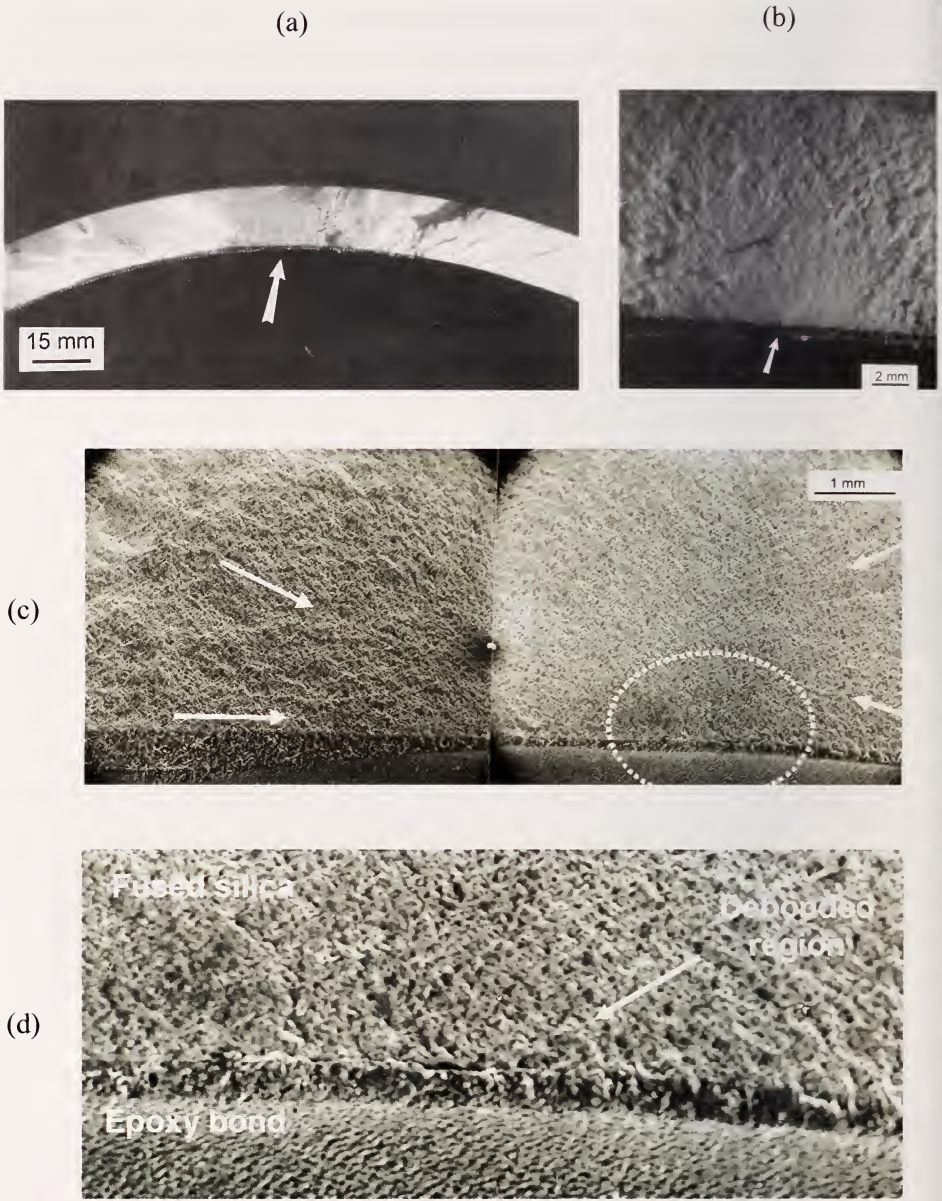


Figure 10.23. Sintered fused silica radome fracture. (a) shows the origin site on the inside wall. (b) is a close-up showing a fracture mirror centered on a feature on the inside wall of the ceramic at the top of the bond line. (c) is a composite of two SEM photos of the origin area. The origin is less obvious, but hackle lines point back (white arrows) to the circled area. (d) shows there is no significant material flaw at the origin, but the ceramic and the epoxy are debonded at the origin.

Case 8 Maligned Machinists (Bend Bars Made by Different Machine Shops)

This case was part of an investigation whether different machine shops could prepare common bend bars to a set of specifications, with minimal damage and at a reasonable cost. The work described here was done in the 1980s in support of the first standard test method for flexural strength of high performance ceramics in the United States, MIL STD 1942(MR).¹³ The standard, which was adopted by the U.S. Army in 1983, served as a basis for American Society for Testing and Materials standard C 1161 in 1990¹⁴ and (along with elements from analogous European and Japanese standards) was used as the basis for International Organization for Standards ISO 14704 in 2000.¹⁵ Prior to standardization in 1983, a myriad of procedures were in use and data comparability was poor. Much of the data were erroneous. Standardization has led to dramatic improvements in the quality of data and significant cost savings. Bend bar costs decreased as machine shops prepared specimens to a common reliable procedure.

As part of the standardization work, a major international round robin with 11 labs around the world was conducted in 1984 and 1985.^{16,17} Several thousand specimens of 99.9 % pressureless sintered alumina and reaction bonded silicon nitride were tested. Among the principal findings of the round robin was the conclusion that consistent results could be obtained if the standard procedure with defined test fixtures and alignments were used. It has long been known that grinding during specimen preparation could introduce strength limiting damage. A side topic investigated in the round robin was whether different machine shops could meet the grinding specifications and prepare damage free B type bend bars (3 mm x 4 mm x 50 mm). Spare sintered 99.9 % purity pressureless sintered alumina plates of size 100 mm x 100 mm x 25 mm from the same batch used in the round robin were available. Requests for price quotations were sent to eight machine shops for them to prepare 20 specimens according to the MIL STD 1942. The specifications were for a multi step grinding process ranging from coarse initial grinding to final finishing. Finer grinding wheels with reduced depths of cut were used at each step with the objective of removing prior damage and minimizing final residual damage.

Although the standard recommend thirty specimens for statistical analysis, only twenty specimens were required since it was felt that this twenty would be adequate to reveal machining problems. One shop did not bid. Two others bid \$101 and \$112 per bar and were not contracted since these prices were exorbitant. In 1984 – 1985 the typical price for bend bars from experienced

shops were in the \$12 to \$25 range. A single plate from the common batch was sent to each of the remaining five shops which bid from \$15 to \$50 per bar. The bars that they machined were then broken in four-point flexure on 20 mm x 40 mm spans in accordance with MIL STD 1942. The surfaces and edges of all bars were inspected beforehand to ascertain whether the bars met specifications or if there were any signs of machining damage. The results are shown in Table 10.2.

The initial visual examination showed that the five vendors did meet all of the specifications for the most part. Deviations were usually on isolated specimens. Machining damage can be hidden, however, and the strength testing was intended to reveal the damage. A comparison of the average strength values suggested that vendors B, C, and D damaged their specimens since their specimen strengths were much lower than those from shops A and

Table 10.2. Flexural strengths of sintered 99.9% alumina from test sets prepared by different machine shops. The flaws that were strength limiting are listed in their order of frequency in each set.

Shop	Bar Price \$	Specifications met?	Plate	Avg. MPa	Std. Dev. MPa	Char. Str. MPa	Weibull Modulus	Origins
A	15	Yes	P	372	42	391	10.3	Round pores Porous zones Porous seams 2 machining
B	19	Yes, a, b	2	315	22	325	17.1	Porous zones Porous seams Agglomerates 4 machining
C	20	Yes, c	1	301	30	314	11.5	Porous seams Pores Agglomerates
D	41	Yes, b	3	335	32	350	12.0	Porous seams Porous zones Agglomerates
E	50	Yes, b	4	373	36	389	11.9	Pores Agglomerates 2 machining

- a Minor edge chips on some
- b Some skip marks or deep striations
- c Chamfers a bit uneven

E. It would have been tempting to reject vendors B, C, and D for further jobs on the basis of the strength outcomes, but the fractographic analysis revealed a surprising explanation for the outcomes.

Optical examination of the fracture surfaces revealed that machining damage was not the prime factor in any of the five samples sets. Machining cracks did cause fracture in a few specimens, but strength-limiting flaws were volume distributed sintering flaws such as pores, porous zones, porous seams, agglomerates, and occasional inclusions. Figures 6.6a, 6.8, and 6.40a and e show some of these. The crucial difference was that the *flaws varied between the plates*. Porosity was the most common flaw type, but it manifested itself differently in the plates. In some plates the flaws were primarily round discrete pores. In other plates, the flaws were equiaxed regions of microporosity, porous seams, or porosity associated with inclusions. The plates were prepared from the same powder lot by the identical procedure and to all external appearances were identical. Only when the specimens were fractured was the true flaw character revealed.

This case illustrates the hazards of interpreting strength results without supportive fractographic analysis. The variability in flaw character between billets and its effect on strength also underscores a serious problem for structural ceramic designers. If the flaws in a material vary between nominally identical ceramics pieces, this does not bode well for the success of reliability analyses.

Case 9 Modeler's Match (Fracture Origins in MEMS Scale SiC Micro Tension Specimens)

Testing methodologies must keep pace with emerging technologies for miniature devices and structures for microelectromechanical systems (MEMS) and even smaller devices. Sharpe et al.¹⁸ recently investigated the strength of miniature silicon carbide specimens shown in Figure 10.24. These had cross section sizes of $\approx 200 \mu\text{m}$ or less and were prepared by Beheim at NASA-Glenn by chemical vapor deposition (CVD) followed by deep reactive ion etching (DRIE) to final shape.¹⁹ Specimens with straight, curved, and notched gage sections were tested in direct tension and fractured in a special miniature tensile tester. Weibull statistics were applied to scale the strengths and to determine whether surface or volume flaw scaling gave better correlation. The Weibull analysis using area scaling worked reasonably well for the curved and straight specimens, but gave a poor correlation for the notched specimens, which were much weaker than expected.

◆ Fractography of Ceramics and Glasses

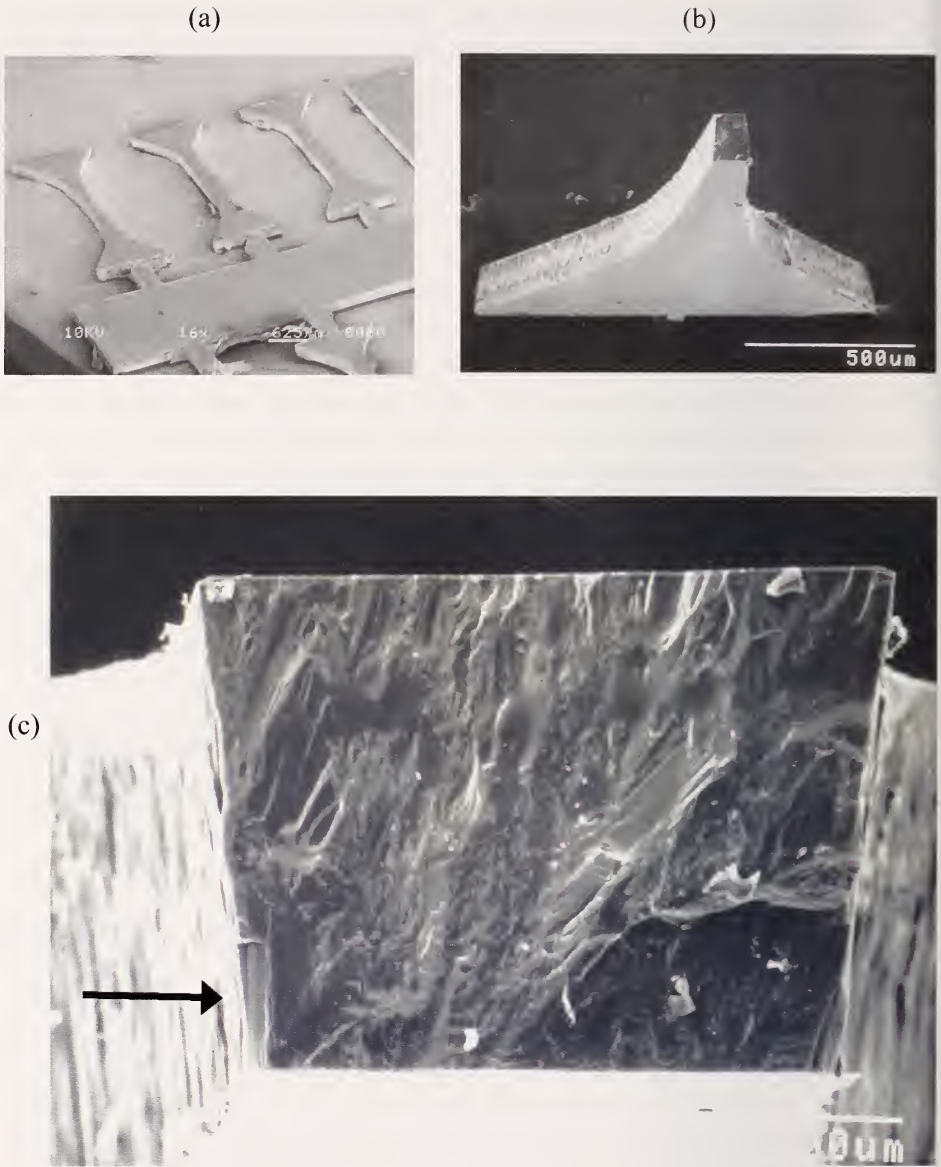


Figure 10.24. Miniature 3.1 mm long SiC tensile test specimens. (a) shows from the left: curved, straight and small notched gage sections. The notch is too small to see in this view. (b) shows a fractured curved gage length specimen (c) shows the fracture surface of a straight section specimen. The arrow shows the origin is a 25 μm x 50 μm large grain at the root of an etch groove. (photos a and b, courtesy of W. Sharpe)

Fractographic analysis was difficult, but productive.^{19,20} The CVD SiC had a coarse microstructure that created a very rough fracture surface that masked common fracture markings. Large SiC grains affected the crack propagation across the fracture surface, causing significant crack redirection and severe roughness as the propagating crack sought out preferred cleavage planes. The most helpful features for pinpointing the origin were twist hackle lines on cleaved grains and occasional large hackle lines that showed the local direction of crack propagation. These markings led back to the origin.

The fracture origins in all three specimen types usually were a combination of a deep etch groove that combined with a large, favorably-oriented columnar grain. Cracks popped in on a preferred cleavage plane in such grains. Thus, most critical flaws were a hybrid surface-volume type flaw: a sidewall groove and a large grain as shown in Figure 10.24c. The fractographic results supported the Weibull area scaling for comparing the straight and curved specimens, and the best correlation was obtained if only the etched *sidewall* areas were used in the calculation.

The reason the Weibull strength scaling did not work for the notched specimens became obvious as shown in Figure 10.25. The notches were quite small (15 μm to 25 μm radius). They concentrated stress to a very small region directly under and around the notches. Hence, the Weibull effective volumes or areas were tiny, and comparable to the size of some of the single columnar grains. Hence, one cannot assume there is a well-distributed set of flaws scattered throughout the stressed volume, as is assumed in conventional Weibull analysis. There probably was only one flaw in the Weibull volume! Furthermore, an analysis based on continuum mechanics assuming the material was isotropic and homogeneous is questionable.

Case 10 Fractious Fractographers (A Fractography Round Robin)

Can different fractographers agree on fracture origin analysis? Can they reach similar conclusions? How do they exercise their craft?

These were questions addressed in an international round robin conducted in the mid 1990's.²¹ Round robins are interlaboratory exercises using a common procedure. There are many reasons for conducting a round robin, but usually the goals are to evaluate whether different laboratories can apply a prescribed procedure and obtain consistent results, or to generate test method uncertainty data such as repeatability or reproducibility precision estimates. Fractography round robins are extremely rare. D. Lewis of the Naval

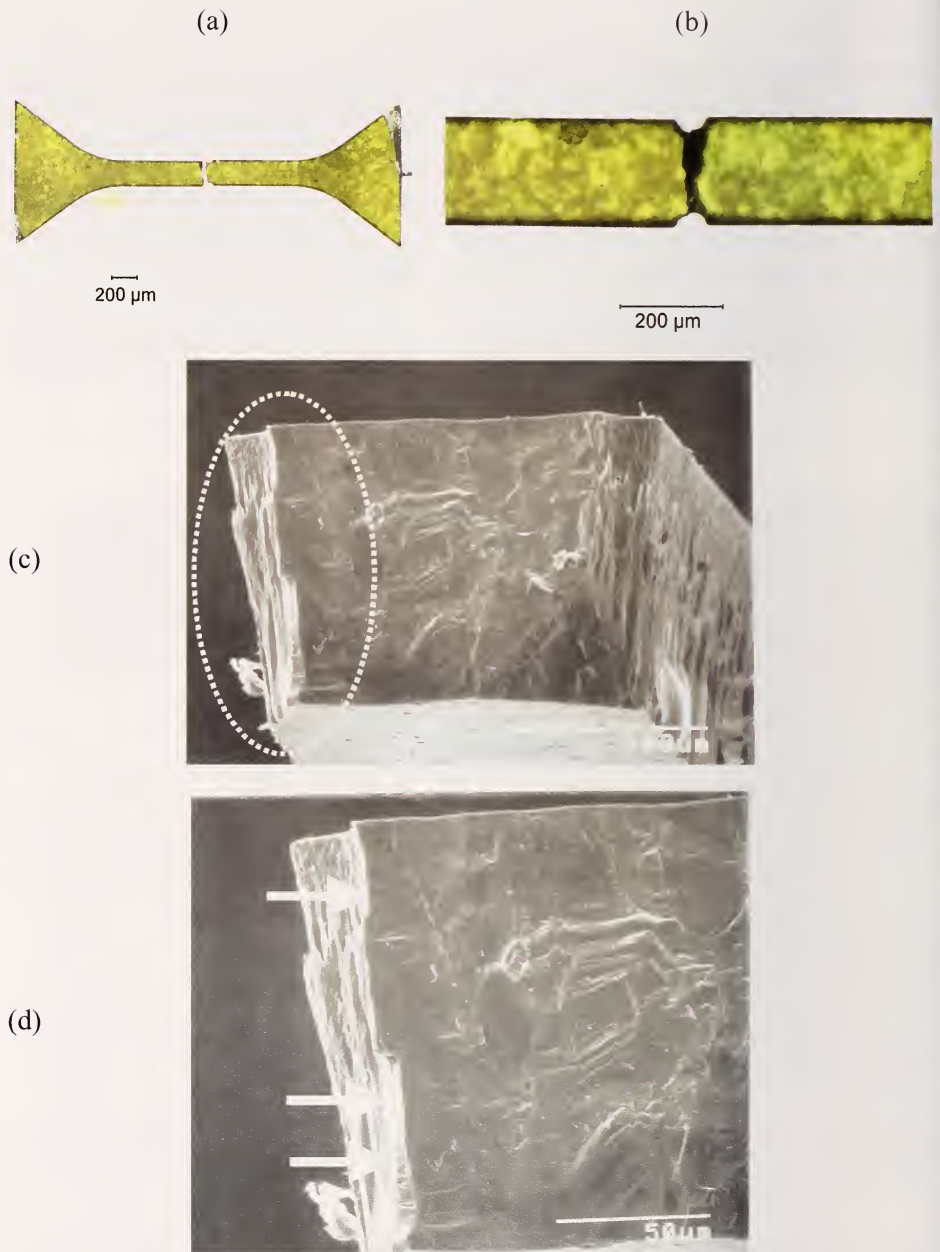


Figure 10.25. A broken notched miniature SiC tensile specimen. (a) shows the whole specimen. (b) shows a close-up of the gage section notches. Transillumination through the green single crystal SiC grains created the light patches. (c) and (d) show the fracture surface. Fracture started at the bottom of the round notch (arrows), from an etch groove linked with a single long and large columnar SiC grain that ran from the top to the bottom.

Research Laboratory coordinated one on photo analysis of ceramics in the mid 1980s for the then ASTM subcommittee E24.07, Fracture of Brittle Materials. Results were mixed and the results were never published.

This author and Dr. J. Swab of the U.S. Army Materials Technology Laboratory (now with U. S. Army Research Lab, Aberdeen, MD) conducted a major international round robin on characterization of fracture origins of advanced ceramics in 1994-1995. Seventeen laboratories participated. The participants had experience that ranged from zero to thirty-five years. The project was coordinated under the auspices of the Versailles Advanced Materials and Standards (VAMAS) program. This work evaluated a new (1992) set of guidelines for finding and characterizing fracture origins in ceramics: "Fractography and Characterization of Fracture Origins in Advanced Structural Ceramics," Military Handbook MIL HDBK 790.²²

The round robin was conducted to determine if the guidelines in the MIL HDBK were reasonable and whether they could be improved. In this respect, the round robin was successful. Weak points in the MIL HDBK were identified. Sometimes participants interpreted the origins the same way the organizers did, but in other cases there was disagreement or confusion. The causes of the latter were identified. Improvements were made to the guidelines and they were eventually adopted by ASTM as Standard Practice C 1322,²³ the world's first fractography standard for characterizing fracture origins.

Topic 1 of the VAMAS round robin was a photo interpretation exercise with focus on detection and characterization of grinding damage in bend bars. Photos of one specimen each of silicon nitride, a zirconia-alumina composite, and an alumina were furnished. Six photos of each specimen were provided showing for each half, a low magnification overall shot, a picture of the fracture mirror area, and a close-up of the origin area. Results were mixed. There was consensus that the origins were machining cracks, but there was considerable variability in how they were marked and measured. Some participants disagreed and felt the origins were not grinding damage. Although a short paragraph on each specimen with strength and fracture toughness information was furnished along with the photos, very few of the participants used this information to estimate a critical crack size. Participants were also asked to mark and measure the fracture mirror sizes on the photos. The organizers were surprised at the scatter in mirror size estimates. Evidently many participants were not familiar with measuring fracture mirrors.

Topic 2 was an actual examination of six bend bar strength specimens by each laboratory. Each participant received one example of the specimens listed in Table 10.3. Most were carefully prepared (no small feat) by Dr. Swab. Again, results varied. Most participants had no trouble identifying the pore as the fracture origin in specimen 3. Many had difficulty with the others. For example, the scratch that caused cracking damage in specimen 2 was sometimes identified as machining damage or even a pore or large grain. Figure 6.16c shows one of these scratched specimens. The scratch should have been obvious. Dr. Swab had made it with a diamond indenter and it stood out very clearly on the tension surface of the bend bar. Evidently some participants did not bother looking at the external surface and only looked at the fracture surface. In other specimens, participants looked at only one half. Sometimes this was satisfactory, but in just as many cases observers looked at the less clear half.

Table 10.3. Bend bar specimen types distributed in Topic 2 of the VAMAS round robin.

Specime	Material	Flaw Origin
1	Hot-pressed alumina with silicon carbide whiskers	Large grain
2	Sintered 99.9% alumina	Handling damage (scratch)
3	Sintered 3 mol% yttria stabilized zirconia (Y-TZP)	Pore
4	Reaction bonded silicon carbide	Surface Pit
5	Hot isopressed silicon nitride	Machining damage
6	Sintered titanium diboride	Porous seam or porous region

Many participants evidently did not read the brief four to six sentences of information furnished with each specimen, including treatments if any and the breaking stress and fracture toughness. For example, the pit origin specimens had been exposed to an oxidizing environment at high temperatures. Some labeled the origin a pore and ignored the surface condition and reaction zones around the pits. Few estimated flaw sizes from fracture mechanics and compared them to their fractographically-measured sizes for verification.

The entire exercise was a learning experience for the organizers. Some participants did very well, but many had difficulty. Much was learned by

studying the causes of the misinterpretations. Even for such mundane objects as bend bars, there was considerable variability in how the participants analyzed the photos, the specimens, and the ancillary information provided. Some simply looked at the fracture surfaces and ignored everything else. Some of these participants reached the correct conclusion, but just as many did not. The organizers came to realize that fractographic analysis (and failure analysis in general) is a process whereby an expert integrates all information including, but not limited to, fracture surface examination. This realization led the author and Dr. Swab to prepare Figures 1.1 (the fractographer as detective) and 1.2 (the fractographic analysis puzzle) of this Guide. The organizers also came to the realization that they had a huge advantage compared to the participants. The organizers could look at many specimens of a type, and were not limited to a solitary example. Furthermore, there is no substitute for actually looking at a specimen in ones own hands under a microscope, as opposed to looking at two-dimensional photographs as in topic 1. Several of the authors fractographic Rules of Thumb listed in the next chapter stem from this exercise.

Case 11 Perilous Prostheses (Four Ceramic Dental Crowns)

All-ceramic dental crowns are increasingly being used as alternatives to gold or porcelain fused-to-metal restorations (Figure 10.26). A variety of ceramic materials have been used including feldspathic or leucite porcelains, glass ceramics, alumina and zirconia. These ceramics function as the main load bearing and structural elements of the crown, but the crowns also have a glassy exterior veneer layer added for cosmetic purposes. The fracture resistance and durability of the new ceramic crowns are a primary concern. Despite the sanguine claims of the manufacturers, premature fractures do occur, much to the consternation of the patient and his or her dentist.



Figure 10.26. A fractured Dicor^c glass ceramic molar crown.
(Courtesy S. Scherrer)

^c Dentsply Int., York, PA.

◆ Fractography of Ceramics and Glasses

Progress in the field has been typified by a trial and error approach. The usual approach has been to statistically analyze the rates of failures and infer or guess causes of failures. There are conflicting explanations as to why the crowns do or do not fail. It is not even clear what properties are desired and what are the best laboratory-scale tests to evaluate these properties. Until recently, postmortem failure analyses have been quite rare. One key reason for this is that dental ceramic crown fractures are in fact among the most challenging problems to solve.

Many dental ceramics have coarse-grained and/or porous microstructures. They often fracture at low stress. Stress states in the crowns are transient and uneven. Classic fractographic markings are often masked by the roughness of the fracture surface. Fracture mirrors are almost never observed in a clinical fracture. Another difficulty is that key fragments are often missing, either due to loss in the mouth or damage during crown extraction. Crowns usually accumulate damage from multiple events at multiple sites, creating complex, conflicting fracture networks. For example, the author has often detected Hertzian cone crack damage sites on crown occlusal and facial surfaces, but has only seen a few instances where the cone acted as an actual crown fracture origin. The Hertzian cones crack damage sites usually are dormant. Contact damage does occur and cause clinical failures, but it almost always in due to *edge chipping*.

Fractographic analysis of all-ceramic dental prostheses is a field where recent fractographic analyses have been very productive.^{24,25,26,27,28, 29} The author has had the pleasure of collaborating with a small team of experienced clinicians and scientists who have step-by-step, crown-by-crown, and bridge-by-bridge, expanded this knowledge. The following four crown fracture case studies illustrate the progress that has recently been made.

Figure 10.27 shows a Cerestore^d alumina-magnesia spinel fractured molar crown that was documented by J. Quinn et al., in Ref. 24. (In this and the following three examples, gold coating has made the veneer look dark in the optical images and the core material lighter.) The origin was located at the margin (or bottom) of the crown and the vertical split nature of the fracture suggests that hoop stresses around the bottom of the crown, where the crown was the thinnest, caused the breakage. A specific material flaw could not be identified. By the time the crack propagated over to the opposite side, the two halves hinged apart in bending creating the cantilever curl.

^d Originally developed by Coors Biomedical, Lakewood, Co., Available later from Ceramco Inc., East Windsor, NJ.

Figure 10.28 shows a similar case, also from Ref. 24, but for a Procera 99.9% purity alumina.^e It also split vertically, evidently in response to a hoop stress. The fractographic markings again lead to a margin origin site. A specific single material flaw is not evident. The origin site coincides with the end of the cement bond to the core material, on the inside of the crown. This undoubtedly is a stress concentration site.

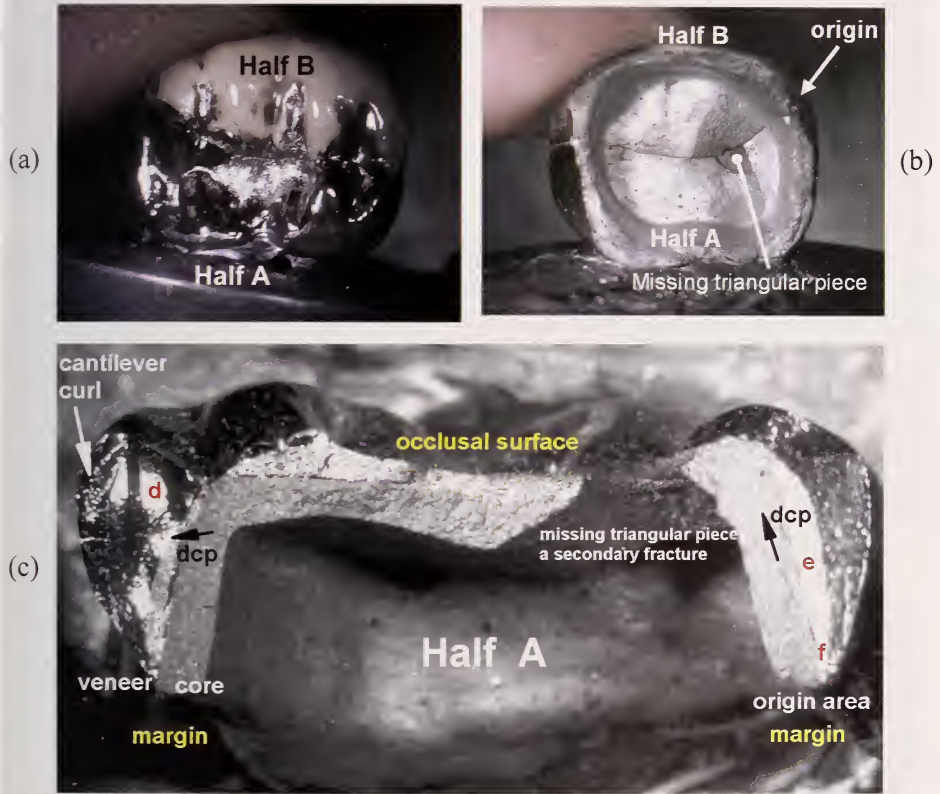


Figure 10.27 a-c. Fractured Cerestore alumina-spinel molar crown with an origin on the margin. (a) is a top occlusal surface view showing the two cleaved halves held together. Half A is fully- and half B is partially-gold coated. (b) shows a view of the interior looking up into the crown. The missing triangular piece was caused by secondary breakage. The origin was on the margin, at the bottom of the crown. (c) shows an optical photo of the fracture surface. Arrows show the local direction of crack propagation (dcp). The dark outer regions are the gold-coated glassy veneer. The lighter gray portions are the gold-coated core ceramic material. The letters d, e, f identify regions shown in Figures (d) – (f) on the next page. (Courtesy J. Quinn)

^e Nobel Bicare, Stockholm, Sweden.

◆ Fractography of Ceramics and Glasses

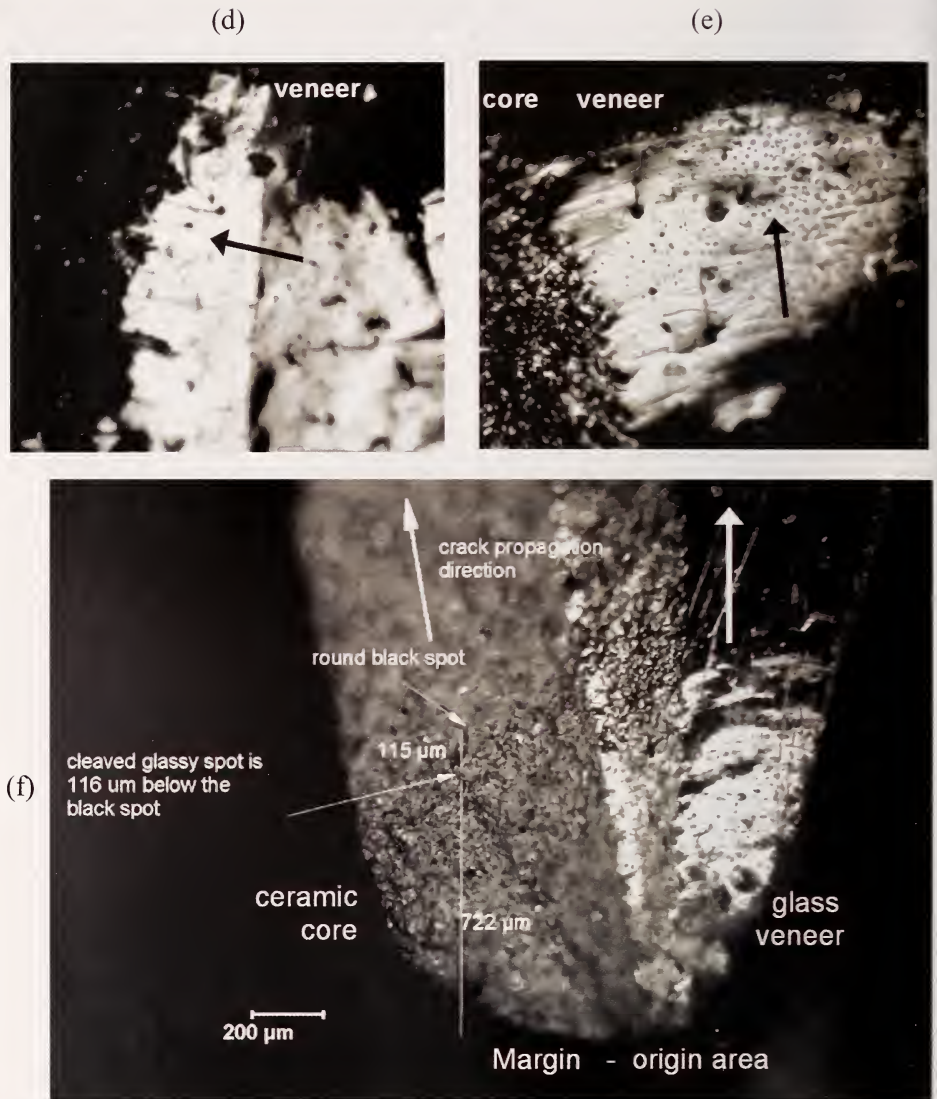
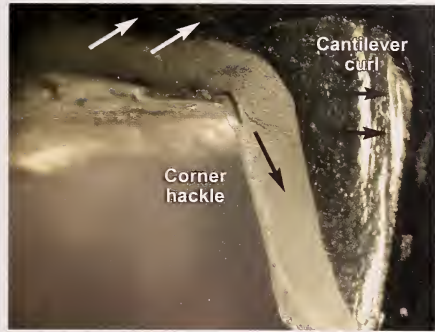


Figure 10.27 d-f. Fractured Cerestore alumina-spinel molar crown (continued). (d) shows wake hackle from tiny bubbles in the veneer glass. This location is on the left of view (c) and indicates the crack moved right to left (arrow). (e) shows wake hackle and gull wings from bubbles in the veneer on the right side of the crown. At this location the crack was running in the direction of the arrow from the margin (bottom) of the crown to the top. Careful scrutiny of the adjacent core ceramic material showed that it also had wake hackle generated by pores in the ceramic, and pointed in the same direction. (f) is an optical image with working notes of the origin area at the margin. A distinct flaw is not recognizable in either the veneer or the core.

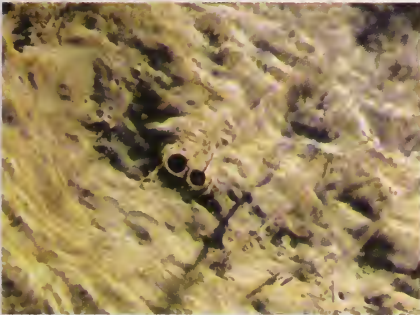
(a)



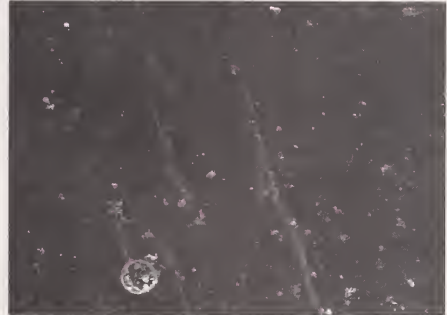
(b)



(c)



(d)



(e)



(f)



Figure 10.28. Procera alumina molar crown. The crown split vertically into two halves. (a) and (b) show the fracture surface after gold coating. The veneer glass is dark and the core ceramic is a lighter shade. The arrows show the local direction of crack propagation from corner hackle around the inside corner, the cantilever curl, and from wake hackle markings in the veneer. (c) and (d) are examples of wake hackle from pores in the veneer. (e) and (f) show optical and SEM images of the margin, respectively. The origin is the stress concentration site at the end of the cement bond to the core (arrow). (Courtesy J. Quinn and S. Scherrer)

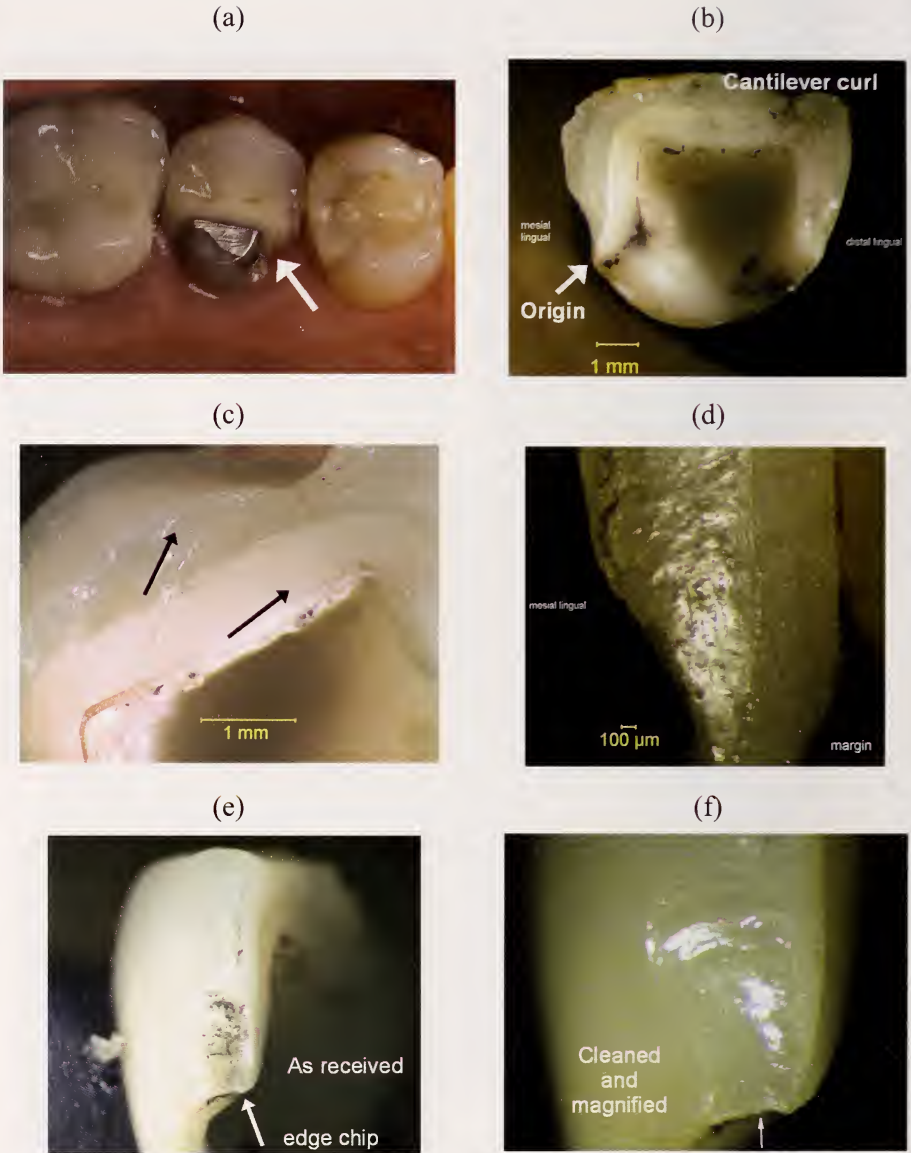


Figure 10.29. Procera alumina molar crown that broke from a margin chip. (a-f) are optical images without any coatings. (a) is a clinical view with the origin marked. (b) is one half of the fractured crown. (c) shows a fanlike array of corner hackle (between the two arrows which show the propagation direction) in both the veneer and core emanating from the top inside corner. (d) is from near the margin on the left side and shows tiny wake hackle from veneer pores. The crack ran from bottom to top. (e) and (f) show the origin was an edge chip from a force applied on the bottom of the margin aimed upwards.

(g)



(h)

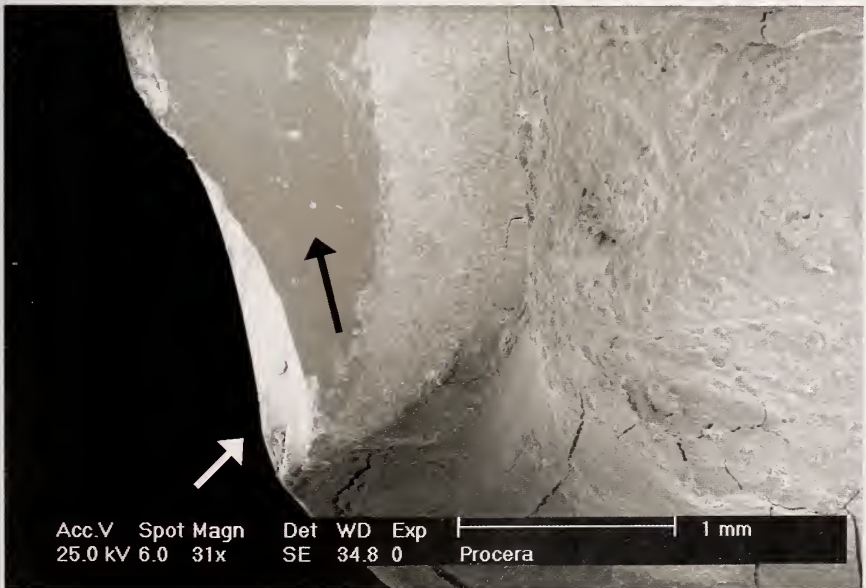


Figure 10.29 (cont'd). (f) and (g) SEM views of the margin chip (arrows). The fracture that cleaved the crown started at the bottom at the margin, from part of the margin chip, and ran as shown by the black arrow. (photos a, g, h courtesy of S. Scherrer)

The third crown, also a Procera alumina, is shown in Figure 10.29. It also has a margin origin site that led to crack propagation by hoop stresses. Images 10.29 a-f are all optical images of the crown without coatings. As such, some of the details were “washed out” and did not photograph well. Nevertheless, this crown failure was diagnosed solely on the basis of an optical examination with a stereo optical microscope. Subsequent SEM examination produced the sharper images shown in Figures 10.29 f and g. Corner hackle around the inside corners of the core, a cantilever curl, and wake hackle again led back to a margin initiated fracture origin. A well-defined edge chip on the veneer was the origin. The edge chip was discolored suggesting that it had been present for quite some time. The direction of the edge chip was puzzling as well. It appeared to have been from a force directed upwards on the crown. Such a loading is not likely in the mouth since the margin is protected by the gum line and jaw. The chip was probably created during fabrication or installation.

The fourth crown shown in Figure 10.30 is an Empress II lithium silicate glass ceramic incisor.^f The crown had been in service only 4 months when it split into two pieces. No information was furnished on how the fracture event occurred or on the installation or fabrication of the crown. The fracture plane was vertical and perpendicular to the dental arch. The two halves fitted closely together. A few small chips were missing, probably from secondary fracture, and were inconsequential to the analysis.

The lingual surface (the side that faces the tongue) had some surface damage and also an unusually thick veneer. There were several shallow depressions ($\approx 1 \text{ mm}^2$ square area) as well as numerous conchoidal chip fractures, small pits and gouges at mid crown height. The shallow depressions had tool marks indicating they were from adjustments to the lingual surface by the dentist once the crown had been cemented in place and opposing tooth contact checked. This adjustment was only partially successful in relieving contact from the opposing tooth as evidenced by the numerous pits, chips and gouges. This location was eventually determined to be near the fracture origin region.

The facial surface (the surface that faces outwards) was in good condition and had little damage or evidence of abuse. The unusually thin veneer had a few secondary spall chips and one harmless Hertzian cone crack that did not penetrate into the core material. The chips were noted on one fragment but not on the other, indicating that they were secondary fractures that occurred after the crown had broken.

^f Ivoclar, Schaan, Liechtenstein.

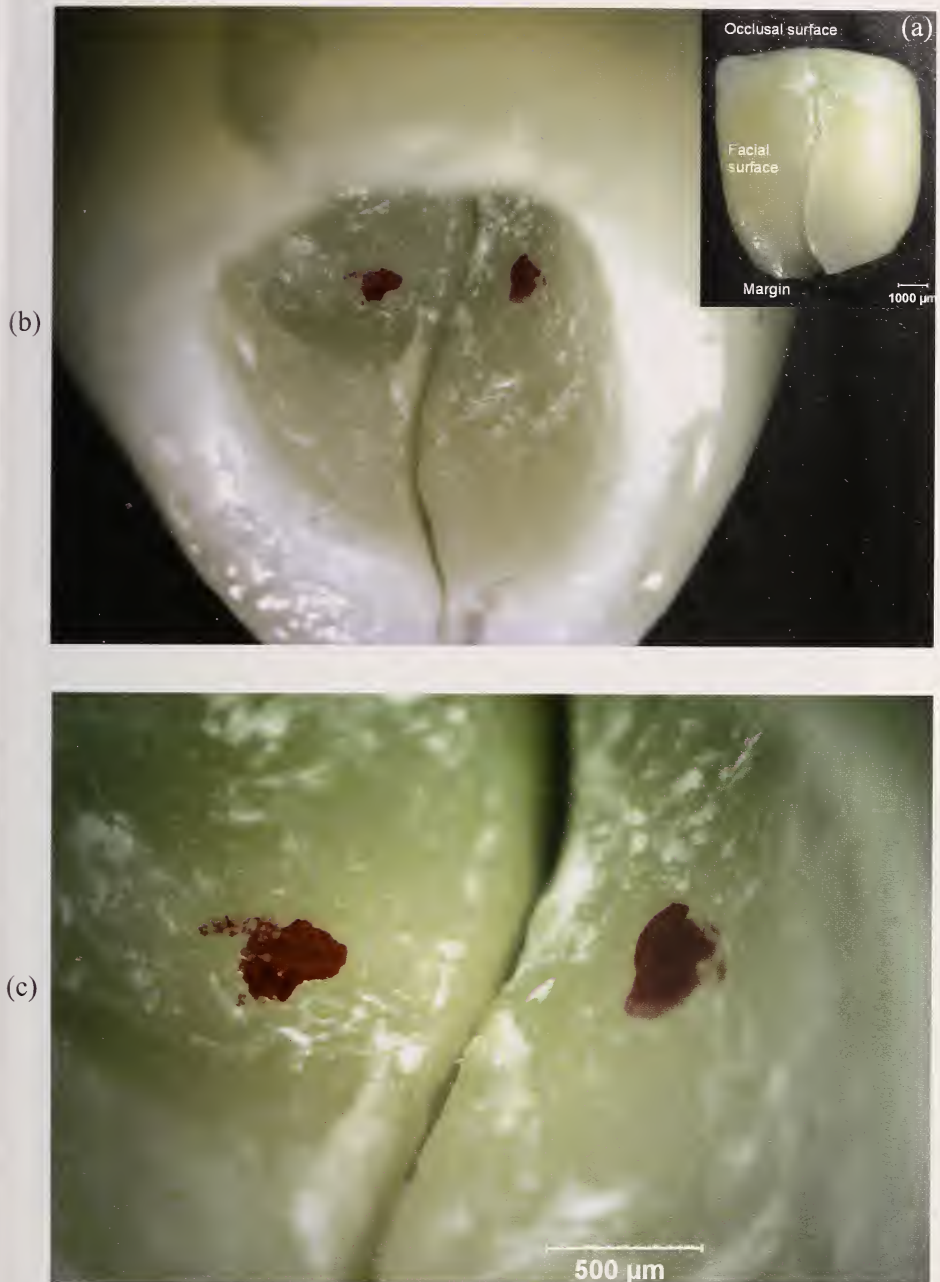


Figure 10.30 a-c. Fractured Empress II glass ceramic anterior (#7) incisor cemented crown. The insert (a) shows a facial view of the cleaved crown. (b) and (c) show views looking up into the interior with the two halves together. The origin is located between the two red dots on the inside surface.

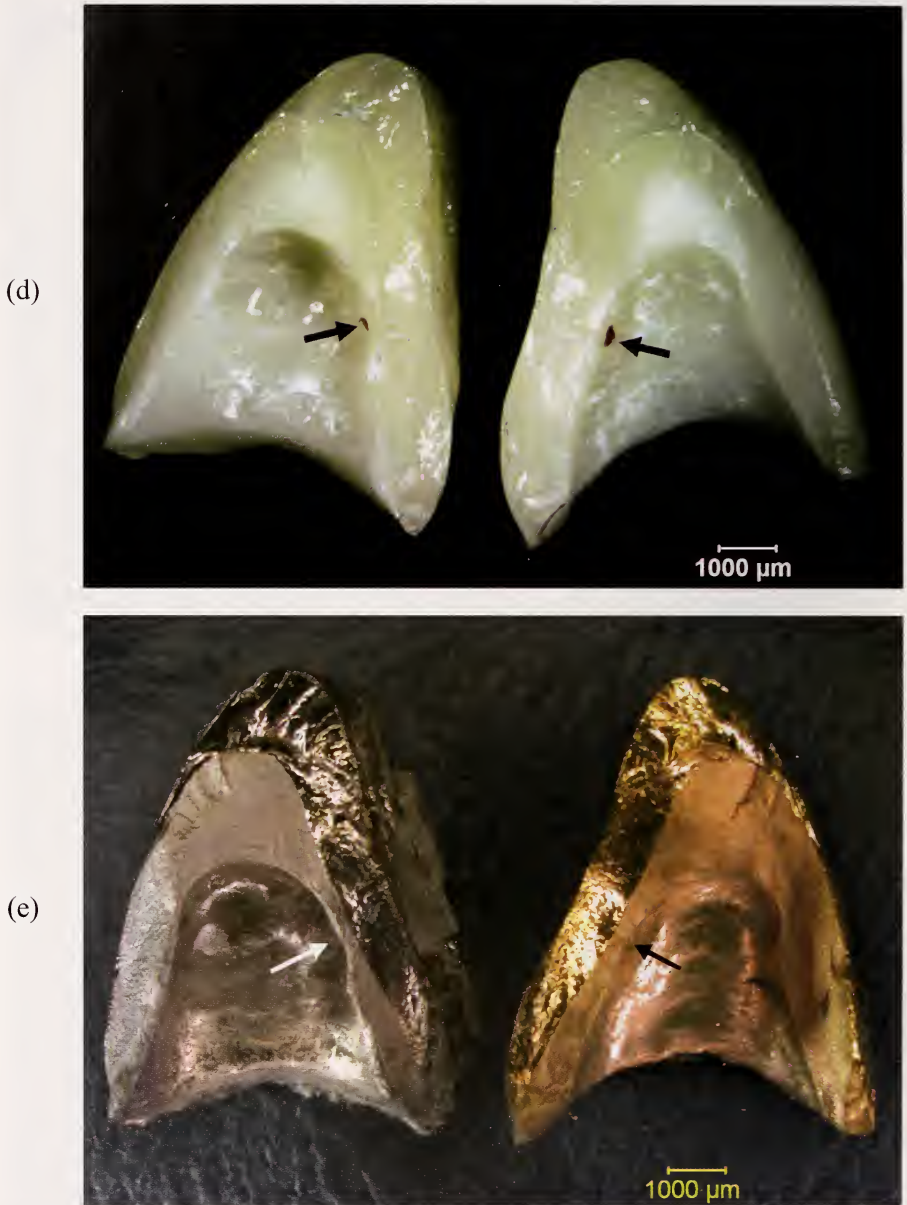


Figure 10.30 d-e. (d) and (e) show the fracture surfaces of the two halves. (d) shows an optical photo of the uncoated halves, and (e) shows gold coated surfaces. Two different coaters were used causing the different coloration. The gold coating of the glassy veneer reflects more and it is evident the veneer thickness is very uneven and out of normal guidelines. It is very thick on the labial side and very thin on the facial side. The arrows mark the origin site located at the thinnest part of the core ceramic material.

(f)



(g)

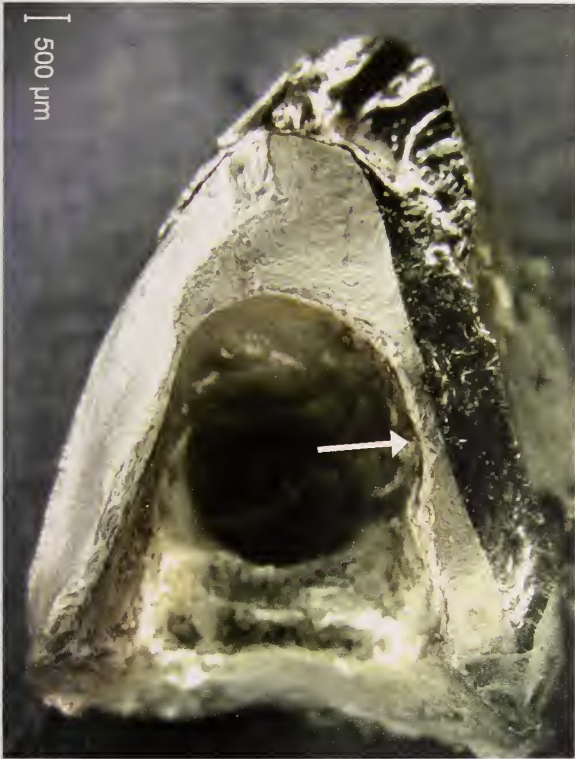
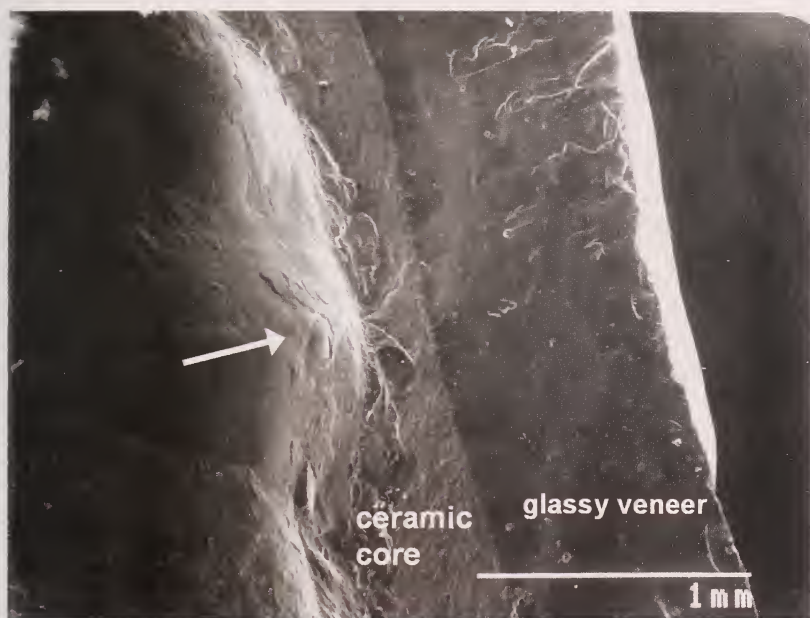


Figure 10.30 f-g. (f) shows an SEM image wake hackle in the glassy veneer from a region near the top (occlusal) surface of the A half. The wake hackle shows that the crack was running in the direction of the arrow in this region. All the wake hackle in the entire crown showed fracture was from the inside to the outside. (g) shows the origin site is a cone crack on the inside surface (arrow). The following photos show this site in more detail.



Figure 10.30 h-i. (h) and (i) are optical images of the origin which originated from a contact on the inside of the crown at the thinnest point of the core.

(j)



(k)

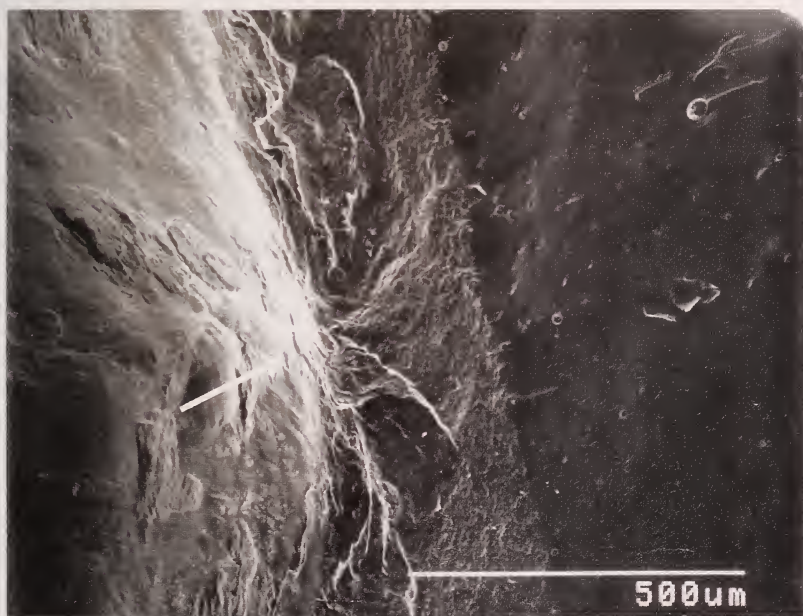


Figure 10.30 j-k. (j) and (k) are SEM images of the origin. Notice all the wake hackle in the veneer aiming away from the interior. The crack ran from the inside to the outside. The inside surface is uneven and there are mold or tool marks in the vicinity. This region is directly opposite a region of extensive localized contact damage on the exterior lingual veneer surface.

◆ Fractography of Ceramics and Glasses

There was negligible damage on the occlusal (top) surface. Some residual porous powdery material was detected on the inside surface of the crown and was the remnants of the cement. Tool grinding marks and/or casting impression marks were detected on the inside of the crown.

The application of green tinting dye for an optical examination and a subsequent SEM examination brought out a number of telltale brittle material fracture features. Fractographic markings in the glass ceramic core material were difficult to detect, but subtle hackle markings were similar to features observed on bend strength test specimens of the same material. Extensive wake hackle was detected from bubbles in portions of the glassy veneer as shown in Figure 10.28g. Seven or eight crack arrest lines were also detected.

This was a difficult analysis. Initial examinations had only limited success, but with repeated careful scrutiny of the fragments using different examination techniques (optical, optical green dye coated, optical gold coated, and SEM) enabled the author and J. Quinn to find the origin region. Once again, maps of crack propagation direction were constructed, primarily through observations of the wake hackle markings in the veneer. Fracture initiated in the core material (where it was very thin) from an *internal* surface Hertzian cone crack. This location was in the same vicinity where *external* lingual surface damage has also been detected. Fracture then radiated upwards and downwards in response to hoop stresses causing the crown to split into two halves.

This internal contact damage origin had initially been dismissed as secondary chipping damage, created during extraction or handling. Only after repeated examination was it realized that both halves showed matching damage features characteristic of blunt contact damage at the exact same location on the inside (cementation) surface of the crown. It was further observed that the inside crown surface was uneven and had raised hills, ridges and depressions.

In summary, the Empress II crown had uneven veneer and core wall thickness. Fracture initiated from contact damage on the inside of the crown, probably due to an uneven fit or improper placement. Opposing tooth contact in the same vicinity on the crown exterior surface (as evidenced by shallow pit and chip damage) created the stresses in the origin area. Surface grinding adjustments made to the same area suggested a fitting problem.

These four crowns cases have been published and are part of a growing body of fractographic analyses of crown failures. All four broke from hoop stresses

and split vertically, perpendicular to the dental arch. Specific gross material flaw origins were not detected in any of the four. Fractographic analysis of dental crowns is very challenging, but promises to be very rewarding. Patience and persistence will pay off as we continue to learn to recognize the failure modes and their telltale fractographic signs.

Chapter 10 References

1. R. R. Baker, L. R. Swank, and J. C. Caverly, "Ceramic Life Prediction Methodology - Hot Spin Disk Life Program," AMMRC TR 83-44, Army Materials and Mechanics Research Center, Watertown, MA, August, 1983.
2. L. R. Swank, R. R. Baker, and E. M. Lenoe, "Ceramic Life Prediction Methodology," pp. 323 - 330 in *Proceedings of the 21st Automotive Technology Development Contractors Coordination Meeting*, Society of Automotive Engineers, Warrendale, PA, 1984.
3. G. D. Quinn, K. Xu, R. J. Gettings, J. A. Salem, and J. J. Swab, "Does Anyone Know the Real Fracture Toughness? SRM 2100: The World's First Ceramic Fracture Toughness Reference Material," pp. 76 - 93 in *Fracture Resistance Testing of Monolithic and Composite Brittle Materials*, ASTM STP 1409, J. A. Salem, G. D. Quinn, and M. G. Jenkins, eds. ASTM Int., West Conshohocken, PA, 2002.
4. G. D. Quinn, "Fracture Mechanism Maps for Advanced Structural Ceramics, Part I, Methodology and Hot Pressed Silicon Nitride," *J. Mat. Sci.*, **25** (1990) 4361 - 4376.
5. K. D. Mörghenthaler and E. Tiefenbacher, "Bauteile Aus Keramik Für Gasturbinen," (Ceramic Components for Gas Turbines), Final Report of Phase III, Daimler-Benz AG, Technical Report, Stuttgart, 1983.
6. E. J. Bunning, D. R. Claxton, and R. A. Giles, "Liners for Gun Tubes - A Feasibility Study," *Ceram. Eng. and Sci. Proc.*, **2** [7-8] (1981) 509 - 519.
7. G. D. Quinn, "Characterization of Turbine Ceramics After Long Term Environmental Exposure," AMMRC TR 80 15, Army Materials and Mechanics Research Center, Watertown, MA, May 1980.
8. G. D. Quinn, "Review of Static Fatigue in Silicon Nitride and Silicon Carbide," *Ceram. Eng. and Sci. Proc.*, **3** [1 2] (1982) 77 - 98.

9. G. D. Quinn and R. N. Katz, "Time Dependent High Temperature Strength of Sintered Alpha SiC," *J. Amer. Ceram. Soc.*, **63** [1 2] (1980) 117 – 119.
10. J. Coppola, M. Srinivasan, K. Faber, and R. Smoak, "High Temperature Properties of Sintered Alpha Silicon Carbide," presented at the *International Symposium on Factors in Densification and Sintering of Oxide and Non-Oxide Ceramics*, Hakone, Japan, October, 1978.
11. V. D. Fréchette, *Failure Analysis of Brittle Materials*, Advances in Ceramics, Vol. 28, American Ceramic Society, Westerville, OH 1990.
12. F. Schmid and D. C. Harris, "Effects of Crystal Orientation and Temperature on the Strength of Sapphire," *J. Am. Ceram. Soc.*, **81** [4] (1998) 885 – 93.
13. MIL STD 1942 (MR), "Flexural Strength of High Performance Ceramics at Ambient Temperature," U. S. Army Materials Technology Laboratory, Watertown, MA, 21 Nov. 1983.
14. ASTM C 1161 90, "Standard Test Method for Flexural Strength of Advanced Ceramics at Ambient Temperature," ASTM Int., West Conshohocken, PA, 1990.
15. ISO 14704, "Fine Ceramics (Advanced Ceramics, Advanced Technical Ceramics) – Test Method for Flexural Strength of Monolithic Ceramics at Room Temperature," Int. Org. for Standards, Geneva, SW, 2000.
16. G. D. Quinn, "Fractography and the Army Flexure Standard," pp. 319 – 334 in *Fractography of Glasses and Ceramics*, eds. J. Varner and V. Fréchette, American Ceramic Society, Westerville Ohio, (1988).
17. G. D. Quinn, "Flexure Strength of Advanced Structural Ceramics: A Round Robin," *J. Am. Ceram. Soc.*, **73** [8] (1990) 2374 – 2384.
18. W. N. Sharpe, Jr., O. Jadaan, N. N. Nemeth, G. M. Beheim, and G. D. Quinn, "Fracture Strength of Silicon Carbide Microspecimens," *J. Microelectromechanical Systems*, **14** [5] (2005) 903 – 913.
19. G. D. Quinn, W. Sharpe, Jr., G. Beheim, N. Nemeth, and O. Jadaan, "Fracture Origins in Miniature Silicon Carbide Structures," pp. 62 – 69 in *Fractography of Advanced Ceramics, II*, ed. J. Dusza, R. Danzer, and R. Morrell TransTech Publ., Zurich, 2005.

20. G. D. Quinn, "Design and Reliability of Ceramics, Do Modelers, Designers and Fractographers See the Same World?" *Ceram. Eng. and Sci. Proc.*, **26** [2] (2005) 239 – 252.
21. J. J. Swab and G. D. Quinn, "The VAMAS Fractography Round Robin: A Piece of the Fractography Puzzle," pp. 55 – 70 in *Fractography of Glasses and Ceramics III*, Ceramic Transactions, Vol. 64, eds., J. R. Varner, V. D. Fréchette, and G. D. Quinn, ACS, Westerville, OH, 1996.
22. MIL HBK 790, "Fractography and Characterization of Fracture Origins in Advanced Structural Ceramics," U. S. Army Materials Technology Laboratory, Watertown, MA, June, 1992.
23. ASTM C 1322-96, "Standard Practice for Fractography and Characterization of Fracture Origins in Advanced Ceramics," *Annual Book of Standards*, Vol. 15.01, ASTM Int., West Conshohocken, PA.
24. J. B. Quinn, G. D. Quinn, J. R. Kelly, and S. S. Scherrer, "Fractographic Analyses of Three Ceramic Whole Crown Restoration Failures," *Dental Materials*, **21** (2005) 920 – 929.
25. S. S. Scherrer, J. B. Quinn, G. D. Quinn, and J. R. Kelly, "Failure Analysis of Ceramic Clinical Cases Using Qualitative Fractography," *Int. J. Prosthodont.*, **19** [2] (2006) 151 – 158.
26. J. B. Quinn, G. D. Quinn, J. R. Kelly, and S. S. Scherrer, "Useful Tools for Dental Failure Investigation," pp. 36 – 53 in *Proceedings of the Conference on Scientific Insights and Dental Ceramics and Photopolymer Networks*, ed. D. C. Starrett, Trans. Academy of Dental Materials, Vol. 16, 2004.
27. J. R. Kelly, "Fractography of Dental Ceramics," pp. 241 – 251 in *Fractography of Glasses and Ceramics, IV*, eds. J. R. Varner and G. D. Quinn, American Ceramic Society, Westerville, OH, 2001.
28. J. B. Quinn, "Failure Analysis of a Broken Tooth," *J. Fail. Anal. Prev.*, **4** [1] (2004) 41 – 46.
29. J. Y. Thompson, K. J. Anusavice, A. Naman, and H. F. Morris, "Fracture Surface Characterization of Clinically Failed All-ceramic Crowns," *J. Dent. Res.*, **73** [12] (1994) 1824 – 1832.



11. CONCLUSIONS

This Guide is intended to introduce engineers and scientists to the science of fractographic analysis of brittle materials as a tool to solve fracture problems. This tool may be applied to a broad range of practical problems including component failure analyses, materials processing refinements, routine materials characterization, laboratory scale mechanical testing, and reliability and design. Fractography is the examination of fracture surfaces, the examination of the general crack patterns, other part surfaces, other specimens, and a review of processing, exposure, and testing conditions. Much like the master detective, the fractographer starts with an open mind, integrates and analyzes the available information and relates it to similar episodes from his own experience and to what is published in the literature. The fractographer applies deductive logic to arrive at a conclusion.



The author's fractographic experiences over a number of years have been distilled into the following rules of thumb for fractography:

1. The first one is the hardest.

The more examples of a particular fracture problem that are examined the better. This is true for both experienced and novice fractographers. Patterns may be recognized that are not apparent in a single example. An unfamiliar or subtle feature may be overlooked in one example. When the fractographer sees a curious or unfamiliar marking in multiple examples, he is less likely to dismiss it as a random artifact. One of the most gratifying experiences a fractographer has is when he or she first recognizes and understands a new marking and adds it to his or her personal experience base.

2. The more experience the fractographer has the better.

The job gets easier with experience. Fractography is a cumulative learning experience. The more one learns, the easier and faster becomes the learning process. The fractographer should look at as many different test specimens, components, and materials as possible.

3. Photos almost never show all there is to see.

Photos are two-dimensional representations of a three-dimensional world and perspective is inevitably lost.

4. Good equipment makes the job easier or even possible, but is no substitute for skill and experience.

One must know where to look and great pictures of the wrong things are worthless. Many published close-up SEM images fit this category.

5. Good fractography under laboratory testing situations begins even before the specimen is broken.

The specimen should be tested in clean conditions to minimize contamination of the fracture surfaces. It should be cushioned or restrained so that secondary fractures are prevented if at all possible. Specimen orientation and loading points should be marked on the specimens. The key fragments should be recovered and stored to minimize additional breakage, contamination, or identity mix-ups.

6. Fractography is more than looking at fracture surfaces.

7. A good fractographer is patient.

Don't be afraid to reexamine the pieces. Look at all the pieces, even the ones that may not seem to be relevant. Sometimes, in a group of laboratory tested specimens, a key feature is discerned or recognized on the last specimen. Fractographers in a rush often overlook important details.

8. It's better to let the material tell you why it failed than the other way around. Theoretical modelers cause the most trouble. They already know why something should fail since it is in their computer model.

9. A good fractographer does not overreach, guess, or force an interpretation. Don't let other people put words in your mouth.

The good fractographer is not afraid to say: "I don't know." It is often a good idea to say up front: "I'll take a look, but I make no promises." The credibility of the fractographer is a precious commodity.

10. Fractography may seem subjective to the uninitiated, but it is very objective.

One last metaphor to summarize the fractographic craft is offered. When a fractographer first sees broken fragments, he or she sees pieces that are trying to tell a tale. With the tools of the trade and with the fractographic skills summarized in this Guide, a fractographer can listen to the pieces, interpret their story, and unlock the secrets of the fracture.

APPENDIX A. BIBLIOGRAPHY

Books on Glass and Ceramic Fractography

V. D. Fréchette, *Failure Analysis of Brittle Materials, Advances in Ceramics*, Vol.28, American Ceramic Society, Westerville, OH, 1990.

A must for the serious fractographer. This book covers all aspects of the fractography of glasses including fundamental markings on crack surfaces (Wallner lines, hackle, and so forth), crack forking, failure origins, and estimates of stress at fracture and fractographic techniques. Superbly illustrated with a number of service failures and amazing case histories.

Fractography of Glass, Ed. R. C. Bradt and R. E. Tressler, Plenum Press, NY, 1994.

Eight technical articles on glass fractography.

Fractography, D. Hull, Cambridge University Press, 1999.

A superbly illustrated and laid out textbook on the fractography of metals, ceramics, and polymers. Strong on the physics underlying the fracture markings, but weak on practical applications.

Fractography, Vol. 12 ASM Handbook, ASM International, Materials Park, OH, 1987.

The seminal work for metals fractography. Expensive. Includes a large atlas of metal failures but only a few examples for ceramics or glasses. Includes excellent chapters on the history of fractography, metal models of fracture, photographic equipment and techniques, optical and electron microscopy that are directly relevant to ceramics and glasses. Caution: Some cleaning and preparation techniques such as surface coatings, replicating tapes, replicating tape stripping, and aggressive detergent cleaning prescribed for metals are not recommended for ceramic fracture surfaces.

Failure Analysis and Prevention, Vol. 11, ASM Handbook ASM International, Materials Park, OH, 2002.

Includes sections on fractography, and fractographic equipment and techniques, but deals more with the broader issues of failure analysis: why a component fails to perform its intended function. Fracture is but one of many failure modes. Includes sections on failure analysis philosophies and approaches. Has one brief chapter on ceramics. The fracture mechanics chapter is tailored towards metals fracture and not ceramic or glass fracture.

Conference Series Books on Fractography of Glasses and Ceramics

Fractography of Glasses and Ceramics, Advances in Ceramics, Vol. 22, J. Varner, and V. Fréchet, eds., American Ceramic Society, Westerville, OH, 1988.

Proceedings of the first of a quadrennial-quinquennial conference series by the same name held at Alfred University in 1986. Sections on: fundamental phenomena, high-temperature fracture, fractography and fracture mechanics, fractography in materials development and testing, and component failures.

Fractography of Glasses and Ceramics, II, Ceramic Transactions, Vol. 17, V. Fréchet, and J. Varner, eds., American Ceramic Society, Westerville, OH, 1991.

Twenty-six papers from the second Alfred university conference, held in 1990.

Fractography of Glasses and Ceramics, III, Ceramic Transactions, Vol. 64, J. Varner, V. Fréchet, and G. D. Quinn, eds., American Ceramic Society, Westerville, OH, 1996.

Twenty-five papers from the third Alfred university conference, held in 1995.

Fractography of Glasses and Ceramics, IV, Ceramic Transactions, Vol. 122, J. Varner, and G. D. Quinn, eds., American Ceramic Society, Westerville, OH, 2001.

Thirty-two papers from the fourth Alfred university conference, held in 2000. Special session on edge chipping.

Fractography of Advanced Ceramics, ed., J. Dusza, Trans Tech Publ., Zurich, 2002.

First (2001) of a new conference series in Stará Lesná, Slovakia.

Thirty six papers, many of which are on mechanical testing and have no fractography. Excellent papers including a bioceramics fracture paper by H. Richter and a paper by R. Morrell and J. Kübler on the background of the then new CEN prEN 843-6 fractography standard.

Fractography of Advanced Ceramics II, eds. J. Dusza, R. Danzer, and R. Morrell, Trans Tech Publ. Zurich, 2005.

Second (2004) of the Stará Lesná, Slovakia conference series. Sixty one short papers. Notable papers by Quinn et al. on machining damage

detection and characterization, Wang et al. on ZnO varistor failures, Supanic *et al.*, on fractures in stacked PZT piezoceramic actuators, and Tatami *et al.* on nanofractography of alumina by scanning probe microscopy. Many of the papers have negligible fractography, however, and deal more with mechanical properties, processing, and indentation.

Fractography of Ceramic and Metal Failures, J. Mecholsky, Jr., and S. Powell, Jr., eds., ASTM STP 827, ASTM, Philadelphia, PA, 1984.

Eight papers on ceramics from a 1982 symposium at ASTM headquarters in Philadelphia. Includes an outstanding, comprehensive, and well-illustrated review paper by Rice, and papers by Pantano and Kelso, and Healy and Mecholsky (cited below).

Fracture Mechanics of Ceramics, Vol. 1, R. Bradt, D. Hasselman, and F. Lange, eds., Plenum Press, NY, 1974.

Proceedings of a conference at Pennsylvania State University in 1973 with twenty-three papers on fracture mechanics applied to origin detection and fractography in ceramics. The later volumes of this quadrennial series also have some fractography papers.

Microscopy Techniques

C. G. Pantano, and J. F. Kelso, "Chemical Analysis of Fracture Surfaces," *Fractography of Ceramic and Metal Failures*, ASTM STP 827, ASTM, 1984, pp. 139 – 156.

The applicability of various instrumental techniques for chemical analysis of fracture surfaces is reviewed. The relative merits and spatial and depth resolutions of Auger microscopy and energy or wavelength dispersive electron microscopy are given.

J. T. Healy, and J. J. Mecholsky, Jr., "Scanning Electron Microscopy Techniques and Their Application to Failure Analysis of Brittle Materials," *Fractography of Ceramic and Metal Failures*, ASTM STP 827, ASTM, 1984, pp. 157 – 181.

Discusses cleaning, coating, and other procedures for SEM specimens. The merits and differential emphases of secondary and backscattered electron imaging are presented.

C. R. Brooks and B. L. McGill, "The Application of Scanning Electron Microscopy to Fractography," *Materials Characterization*, Vol. 33, 1994, pp. 195 – 243.

An excellent, well illustrated review of the application of scanning electron

microscopy for topographical and chemical analysis of fracture surfaces of ceramics, metals, and polymers. Includes a good discussion of stereo SEM fractography.

Fractography of Ceramics and Glasses - Overview Papers

J. J. Mecholsky, Jr., and S. W. Freiman, "Determination of Fracture Mechanics Parameters Through Fractographic Analysis of Ceramics," pp. 136 – 150 in *Fracture Mechanics of Ceramics Applied to Brittle Materials*, S. Freiman, ed., ASTM STP 678, ASTM, 1979.

A short but useful overview of the utility of fractography as a quantitative tool to determine strength-limiting origins, the stress at failure, and critical fracture toughness.

R. W. Rice, "Fractographic Identification of Strength Controlling Flaws and Microstructure," pp. 323 – 345 in *Fracture Mechanics of Ceramics*, Vol. 1, R. Bradt, D. Hasselman, and F. Lange, eds., Plenum Press, NY, 1974.

A short but valuable discussion of several key origins (pores, pore groups, and large grains) and their relationship to fracture energy. The fracture energy can either be a single-crystal or polycrystalline value depending upon the relative sizes of origin and microstructure.

G. D. Quinn, J. J. Swab, and M. J. Slavin, "A Proposed Standard Practice for Fractographic Analysis of Monolithic Advanced Ceramics," MTL TR 90-57, November 1990, NTIS Access No. ADA-231989.

Discusses Military Standard MIL HDBK 790, the predecessor of ASTM standard C1322. Discusses essential background information and the rationale for consistency in characterization. A standard nomenclature and origin characterization scheme are proposed.

R. W. Rice, "Topography of Ceramics," pp. 439 – 472 in *Surfaces and Interfaces of Glass and Ceramics*, V. Fréchette, W. LaCourse, and V. Burdick, eds., Plenum Press, NY, 1974.

A very helpful introduction describes the role of unaided eye, hand lens, optical, scanning, and transmission electron microscopy. Fig. 1 shows optical and SEM photos of the same origin. Fracture surface features such as transgranular and intergranular fracture, crack microstructure interactions, crack branching, mirrors, and single crystal fractography are discussed.

R. W. Rice, "Ceramic Fracture Features, Observations, Mechanism and Uses," *Fractography of Ceramic and Metal Failures, ASTM STP 827*, ASTM, 1984, pp. 5 – 103.

T. A. Michalske, "Quantitative Fracture Surface Analysis," pp. 653 – 662 in *Ceramics and Glasses, Engineered Materials Handbook*, Vol. 4, ed. S. Schneider, ASM, Metals Park, OH, 1991.

J. R. Varner, "Descriptive Fractography," pp. 635 – 644 in *Ceramics and Glasses, Engineered Materials Handbook*, Vol. 4, ed. S. Schneider, ASM, Metals Park, OH, 1991.

J. S. Wasyluk, "Special Terminology Used in Fractography," pp. 632 – 634 in *Ceramics and Glasses, Engineered Materials Handbook*, Vol. 4, ed. S. Schneider, ASM, Metals Park, OH, 1991.

Fractography Round Robins

J. J. Swab and G. D. Quinn, "Fractography of Advanced Structural Ceramics, Results from the VAMAS Round Robin Exercise," U.S. Army Technical Report, ARL-TR-656, Dec. 1994.

An international -Versailles Advanced Materials and Standards Round Robin on the identification of fracture origins in test coupons and photographs. Many lessons were learned.

J. J. Swab and G. D. Quinn, "Fractography of Advanced Structural Ceramics: Results From Topic #2 of the VAMAS Round Robin Exercise" *Ceramic Engineering and Science Proceedings.*, Vol. 16 [5] (1995), 929-938.

A short summary of findings from the 1994 VAMAS round robin.

J. J. Swab and G. D. Quinn, "Results of a Round Robin Exercise on the Fractography of Advanced Structural Ceramics," *Ceramic Engineering and Science Proceedings*, Vol. 15, [5] (1994), 867-876.

A short summary of findings from the 1994 VAMAS round robin.

J. J. Swab and G. D. Quinn, "The VAMAS Fractography Round Robin: A Piece of the Fractography Puzzle," pp. 55 – 70 in *Fractography of Glasses and Ceramics III*, eds. J. Varner and G. D. Quinn, American Ceramic Society, Westerville, OH, Ceramic Transactions, Vol. 64 (1996).

Origins in Ceramics

H. Kirchner, R. Gruver, and W. Sotter, "Characteristics of Flaws at Fracture Origins and Fracture Stress—Flaw Size Relations in Various Ceramics," *Material Science and Engineering*, Vol. 22, 1976, pp. 147 – 156.

A concise but useful report on strength-limiting origins in alumina, silicon nitride, and silicon carbide with a detailed tabulation of different types of origins. Emphasis is on porosity, large grains, and machining origins. An important observation (Fig. 1b) is that origins in the center of fracture mirrors may intersect the fracture surface at an angle and a true view of the origin may not be seen.

H. Baumgartner, and D. Richerson, "Inclusion Effects on the Strength of Hot Pressed Si₃N₄," *Fracture Mechanics of Ceramics*, Vol. 1, 1974, pp. 367 – 386.

Good characterization of machining damage and inclusions in silicon nitride. The inclusions are much smaller than expected the result of locally-degraded fracture toughness.

M. G. Gee, and R. Morrell, "Fracture Mechanics and Microstructures," pp. 1 – 22 in *Fracture Mechanics of Ceramics*, Vol. 8, R. Bradt, A. Evans, D. Hasselman, and F. Lange, eds., Plenum Press, NY, 1986.

Principally a discussion of the application of fracture mechanics theories to strength. Microstructural influences significantly complicate matters and may limit utility to qualitative issues. The nature of strength-limiting origins and their severity is discussed. In some instances, sharp cracks will not form until the stress is applied.

A. G. Evans, "Structural Reliability, A Processing Dependent Phenomenon," *Journal of the American Ceramic Society*, Vol. 65, No. 3, (1982), 127 – 139.

Emphasis on the micromechanics of fracture with a good discussion of the effect of thermal and mechanical property mismatches between an origin and the matrix. Graph of stress versus origin size for silicon nitride showing the relative severity of different origins (WC, Fe, Si, C inclusions, porosity, and machining damage).

G. D. Quinn, L. K. Ives, and S. Jahanmir, "On the Fractographic Analysis of Machining Cracks in Ground Ceramics: A Case Study on Silicon Nitride," Special Publication SP 996, NIST, Gaithersburg, MD, May, 2003.

An exhaustive, well-illustrated treatment of the nature of machining flaws in ground ceramics and how to find them. Photos and many schematics.

G. D. Quinn, L. K. Ives, and S. Jahanmir, "On the Nature of Machining Cracks in Ground Ceramics: Part I: SRBSN Strengths and Fractographic Analysis," *Machining Science and Technology*, 9 (2005) 169 – 210.

G. D. Quinn, L. K. Ives, and S. Jahanmir, "On the Nature of Machining Cracks in Ground Ceramics: Part II: Comparison to Other Silicon Nitrides and Damage Maps," *Machining Science and Technology*, 9 (2005) 211 – 237.

G. D. Quinn, L. K. Ives, and S. Jahanmir, "Machining Damage Cracks: How to Find and Characterize Them by Fractography," *Ceram. Eng. Sci Proc.*, 24 [4] (2003) 383 – 394.

A short summary of the work in the previous references.

G. D. Quinn, L. K. Ives, and S. Jahanmir, "Machining Cracks in Finished Ceramics," pp. 1 – 14 in *Fractography of Advanced Ceramics, II*, eds. J. Dusza, R. Danzer, and R. Morrell, TransTech Publ., Zurich, 2005.

A short summary of the work in the previous references.

R. W. Rice, "Failure Initiation in Ceramics: Challenges of NDE and Processing," and "Ceramic Developments," C. Sorrell, and B. Ben-Nissan, eds., *Materials Science Forum*, Vol. 34 – 36, Trans. Tech. Publ. Ltd. Switzerland, 1988, pp. 1057 – 1064.

A comprehensive, well-illustrated review of failure-initiating origins. Nearly an encyclopedia of flaws. Origins include: agglomerates, pores, large grains, inclusions, machining damage, handling damage, thermocouple beads, ball mills, dandruff, insects, feces, inadequate mixing of constituents, etc.

R. W. Rice, "Processing Induced Sources of Mechanical Failure in Ceramics," pp. 303 – 319 in *Processing of Crystalline Ceramics*, eds. H. Palmour, R. Davis, and T. Hare, Plenum Press, NY, 1978.

A short, well-illustrated review of origins. A good starting point.

R. W. Rice, J. J. Mecholsky, Jr., and P. F. Becher, "The Effect of Grinding Direction on Flaw Character and Strength of Single Crystal and Polycrystalline Ceramics," *Journal of Material Science*, Vol. 16, (1981), 853 – 862.

Machining damage in a variety of ceramics is well illustrated by nine figures.

J. J. Mecholsky, Jr., S. W. Freiman, and R. W. Rice, "Effects of Grinding on Flaw Geometry and Fracture of Glass," *Journal of the American Ceramic*

Society, Vol. 60, Nos. 3 – 4, (1977), 114 – 117.

Two primary sets of cracks result from surface grinding. These are schematically shown and complemented by SEM photos and related to fracture mechanics parameters.

R. W. Rice, “Pores as Fracture Origins in Ceramics,” *Journal of Material Science*, Vol. 19, (1984), 895 – 914.

A well-illustrated examination of pores in glassy and polycrystalline materials. Pores tend to be “sharper” in the latter than in the former.

D. Munz, O. Rosenfelder, K. Goebells, and H. Reiter, “Assessment of Flaws in Ceramic Materials on the Basis of Non-Destructive Evaluation,” pp. 265 – 283 in *Fracture Mechanics of Ceramics*, Vol. 1, eds. R. Bradt, D. Hasselman, and F. Lange, F., Plenum Press, NY, 1986.

Six different flaw types were characterized in reaction bonded and sintered silicon nitrides. Some flaws were artificially created to support a fracture mechanics analysis. Pores have a different effect upon strength than inclusions.

Origins in Glass

J. R. Varner, “The Practical Strength of Glass,” pp. 389 – 406 in *Strength of Inorganic Glass*, ed. C. Kurkjian, Plenum, NY, 1986.

V. D. Fréchet, *Failure Analysis of Brittle Materials, Advances in Ceramics*, Vol.28, American Ceramic Society, Westerville, OH, 1990.

Fracture Mirrors

J. J. Mecholsky, Jr., S. W. Freiman, and R. W. Rice, “Fracture Surface Analysis of Ceramics,” *Journal of Material Science*, Vol. 11, (1976), 1310 – 1319.

A detailed correlation of origin size, fracture mirror sizes and characterization, and fracture mechanics parameters for single and polycrystalline ceramics. A table of mirror constants is given for a range of ceramics, and it is demonstrated that the outer mirror (hackle) to origin size ratio is about 13 to 1. The inner mirror (mist) ratio is between 6 to 1 and 10 to 1.

J. J. Mecholsky, Jr., R. W. Rice, and S. W. Freiman, “Prediction of Fracture Energy and Flaw Sizes in Glasses from Measurements of Mirror Size,” *Journal of the American Ceramic Society*, Vol. 57, No. 10, (1974), 440 – 443.

Details of fracture mirror features are discussed and related to fracture mechanics parameters for glasses. A table of mirror constants for glasses is included.

H. P. Kirchner, R. M. Gruver, and W. A. Sotter, "Fracture Stress—Mirror Size Relations for Polycrystalline Ceramics," *Philosophical Magazine*, Vol. 33, No. 5, (1976), 775 – 780.

Many mirror constants for a range of ceramics.

H. P. Kirchner, and J. C. Conway, Jr., "Fracture Mechanics of Crack Branching in Ceramics," pp. 187 – 213 in *Fractography of Glass and Ceramics, Advances in Ceramics*, Vol. 22, American Ceramic Society, Westerville, OH, 1988.

Analysis that fracture mirror features are controlled by stress intensity.

J. J. Mecholsky, Jr., and S. W. Freiman, "Determination of Fracture Mechanics Parameters Through Fractographic Analysis of Ceramics," pp. 136 – 150 in *Fracture Mechanics Applied to Brittle Materials, ASTM STP 678*, S. Freiman, ed., ASTM, 1979.

A short discussion of fracture mirrors and mirror constants with a comparative table of mirror constants. Comments on useful techniques to measure mirror parameters.

Fracture Mechanics—Estimates of Flaw Size

D. W. Richerson, *Modern Ceramic Engineering*, Marcel Dekker Inc., NY, 1982.

Chapter 3 is a good primer on strength and fracture toughness measurements and their applicability to fractographic analysis. Several numerical examples are given for estimating the strength of a specimen on the basis of a fracture mechanics calculation using the measured flaw size.

H. K. Baumgartner and D. W. Richerson, "Inclusion Effects on the Strength of Hot Pressed Si₃N₄," *Fracture Mechanics of Ceramics*, Vol. 1, eds. R. Bradt, D. Hasselman, and F. Lange, Plenum Press, NY, 1974, pp. 367 – 386.

Applies fracture mechanics to one class of flaws with several numerical examples. The strength-limiting inclusions are smaller than expected from fracture mechanics, suggesting that the fracture toughness is altered in the vicinity of the inclusions.

◆ Fractography of Ceramics and Glasses

J. J. Mecholsky, Jr., S. W. Freiman, and R. W. Rice, "Fracture Surface Analysis of Ceramics," *Journal of Material Science*, Vol. 11, (1976), 1310 – 1319.

Compares measured flaw sizes to fracture mechanics estimates for a range of ceramics and glasses.

H. P. Kirchner, R. M. Gruver, and W. A. Sotter, "Characteristics of Flaws at Fracture Origins and Fracture Stress-Flaw Size Relations in Various Ceramics," *Material Science and Engineering*, Vol. 22, (1976), 147 – 156.

Measured flaw sizes are compared to fracture mechanics estimates for several different types of flaws in alumina, silicon nitride, and silicon carbide.

A. G. Evans, and G. Tappin, "Effects of Microstructure on the Stress to Propagate Inherent Flaws," *Proceedings of British Ceramic Society*, Vol. 20, (1972), 275 – 297.

Discusses flaws in alumina ceramics and compares the stress needed to cause fracture-to-fracture mechanics estimates. Microstructural factors such as flaw linking prior to catastrophic fracture are discussed.

D. Munz, O. Rosenfelder, K. Goebells, and H. Reiter, "Assessment of Flaws in Ceramic Materials on the Basis of Non-Destructive Evaluation," pp. 265 – 283 in *Fracture Mechanics of Ceramics*, Vol. 1, eds. R. Bradt, D. Hasselman, and F. Lange, Plenum Press, NY, 1986.

A superb, comprehensive fracture mechanics analysis of six different flaw types in two silicon nitrides. Fractographic size measurements agreed with fracture mechanics estimates for some flaw types, but not others. Over 100 specimens. Discusses the different crack models that can be used to simulate real flaws as well as the shortcomings of such models. Includes Raju-Newman and elliptical integral flaw stress intensity factor solutions.

G. D. Quinn and J. J. Swab, "Fractography and Estimates of Fracture Origin Size from Fracture Mechanics," *Ceram. Eng. and Sci. Proc.*, Vol. 17, 3, (1996), 51 – 58.

Fracture mechanics should be used routinely in fractographic analyses to verify that the correct feature has been identified as the fracture origin. This paper reviews the factors that may cause calculated and measured flaw sizes to differ.

Fracture Mechanics—Stress Intensity Factors

Y. Murakami, *Stress Intensity Factors Handbook*, Vols. 1 and 2, Pergamon Press, NY, 1986.

A collection of stress intensity factors for various cracks under different loading conditions.

H. Tada, P. C. Paris, and G. R. Irwin, *The Stress Analysis of Cracks Handbook, 3rd edition*, ASM International, Metals Park, OH, 2000.

An update of their 1973 collection of stress intensity factors for various cracks under different loading conditions.

T. Fett, and D. Munz, *Stress Intensity Factors and Weight Functions*, Wessex Institute of Technology, Southampton, UK, 1997.

A collection of stress intensity factors for various cracks under different loading conditions.

D. P. Rooke, and D. J. Cartwright, *Compendium of Stress Intensity Factors*, Her Majesty's Stationary Office, London, 1976.

A collection of stress intensity factors for various cracks under different loading conditions.

G. C. Sih, *Handbook of Stress Intensity Factors*, Lehigh University, Bethlehem, PA, 1973.

An older but still useful collection of stress intensity factors for various cracks under different loading conditions.

I. Bar-on, "Applied Fracture Mechanics," *Engineered Materials Handbook*, Vol. 4, Ceramics and Glasses, S. Schneider, ed., ASM, Metals Park, OH, 1991, pp. 645 – 651.

A good introduction to the application of fracture mechanics analysis to idealized crack configurations. Stress intensity shape factors are given for through slits, surface cracks, and pores with rim cracks.

J. C. Newman, Jr., and I. S. Raju, "An Experimental Stress-Intensity Factor Equation for the Surface Crack," *Engineering Fracture Mechanics*, Vol. 15 [1 – 2], (1981), 185 – 192.

Presents an equation for the calculation of the shape factor (Y) for surface semicircular or semielliptical cracks. Y is given for the location where the origin meets the surface and at the deepest point of the origin.



APPENDIX B. FRACTOGRAPHIC CASE STUDIES

Case studies for components and structures are organized by topic. The compilation is undoubtedly incomplete and the author invites readers to recommend open technical literature additions to this list for inclusion in future revisions of this guide.

Glass Windows

Automotive and building windows

N. Shinkai, "The Fracture and Fractography of Flat Glass," pp. 253 – 297 in *Fractography of Glass*, eds. R. C. Bradt and R. E. Tressler, Plenum Press, NY, 1994.

A superb practical article on annealed, tempered, and laminated glass for automobiles or building windows.

V. D. Fréchette and M. Donovan, "Some Effects of the Glue Chipping Process on Strength," pp. 407 – 411 in *Fractography of Glasses and Ceramics II*, Ceramic Transactions Vol. 17, eds. V. D. Fréchette and J. R. Varner, American Ceramic Society, Westerville, OH, 1991.

Fractures of hundreds of very large float glass windows in a famous Boston skyscraper.

V. D. Fréchette, *Failure Analysis of Brittle Materials*, Advances in Ceramics, Vol. 28, American Ceramic Society, Westerville, OH, 1990, pp. 119 – 120.

Fractures in large float glass windows in a skyscraper. Glue chips.

T. Sakai, M. Ramulu, A. Ghosh, and R. C. Bradt, "A Fractal Approach to Crack Branching (bifurcation) in Glass," pp. 131 – 146 in *Fractography of Glasses and Ceramics II*, Ceramic Transactions Vol. 17, eds., V. D. Fréchette and J. R. Varner, American Ceramic Society, Westerville, OH, 1991.

Fracture patterns in laminated safety glass for bus passenger shelters.

S. T. Gulati, R. Akcakaya, and J. Varner, "Fracture Behavior of Tin vs. Air Side of Glass," pp. 317 – 325 in *Fractography of Glasses and Ceramics, IV*, eds., J. R. Varner and G. D. Quinn, American Ceramic Society, Westerville, OH, 2001.

S. T. Gulati, J. D. Helfinstine, T. A. Roe, "Strength Degradation of Automotive Windshield from Manufacturing to On-Road Service," *Glass Technol.*, 43C (2002) 303 – 308.

Testing of singlets and windshield coupons. Edging, scoring, solder tabs.

◆ Fractography of Ceramics and Glasses

T. Cleary and S. Gulati, "Influence of Glass Score and Seam Orientation on Edge Strength of Multi-Layered Glass Articles," pp. 327 – 341 in *Fractography of Glasses and Ceramics, IV*, eds. J. R. Varner and G. D. Quinn, American Ceramic Society, Westerville, OH, 2001.

Fracture patterns in laminated safety glass (sandwich of two glass plates and a central plastic sheet).

R. A. Allaire and T. Ono, "Fracture Analysis of the Glass Scoring Process," pp. 467 – 471 in *Fractography of Glasses and Ceramics, IV*, eds. J. R. Varner and G. D. Quinn, American Ceramic Society, Westerville, OH, 2001.

Fracture patterns on scored glass plates.

M. E. Stevenson, S. E. Jones, and R. C. Bradt, "Fracture Patterns of a Composite Safety Glass Panel During High Velocity Projectile Impacts," pp. 473 – 488 in *Fractography of Glasses and Ceramics, IV*, eds. J. R. Varner and G. D. Quinn, American Ceramic Society, Westerville, OH, 2001.

Sight glass windows, water hammer

V. D. Fréchette, *Failure Analysis of Brittle Materials*, Advances in Ceramics, Vol. 28, American Ceramic Society, Westerville, OH, 1990, pp. 112.

Tempered glass spontaneous failure

R. C. Bradt, "Macro- and Microfracture Patterns of Thermally Tempered Plate Glass Falling from Nickel Sulfide Inclusions," pp. 417 – 426 in *Fractography of Glasses and Ceramics, Advances in Ceramics*, Vol. 22, ed. J. D. Varner and V. D. Fréchette, American Ceramic Society, Westerville, OH, 1988.

C. C. Hsiao, "Spontaneous Fracture of Tempered Glass," pp. 985 – 992 in *Fracture 1977*, Volume 3, International Congress on Fracture 4, Waterloo, Canada, 1977.

Plate glass mirrors for solar cells

V. D. Fréchette, *Failure Analysis of Brittle Materials*, Advances in Ceramics, Vol. 28, American Ceramic Society, Westerville, OH, 1990, p. 117.

Hail stones, thermal stresses, and edge cracks.

Laser glass slabs

J. E. Marion, "Fracture Mechanisms of Solid State Slab Lasers," pp. 307 – 318 in *Fractography of Glasses and Ceramics, Advances in Ceramics*, Vol. 22, ed. J. D. Varner and V. D. Fréchette, American Ceramic Society, Westerville, OH, 1988.

J. E. Marion, "Fracture of Solid State Laser Slabs," *J. Appl. Phys.*, 60 [1] (1986) 69 – 77.

Ceramic Windows, IR Domes, Radomes

Magnesium Fluoride IR window test coupons

R. W. Rice, "Failure Analysis of Ceramics," pp. 369 – 388 in *Fractography of Glasses and Ceramics, IV*, eds. J. R. Varner and G. D. Quinn, American Ceramic Society, Westerville, OH, 2001.

Glass ceramic missile radome, thermal shock

R. W. Rice, "Failure Analysis of Ceramics," pp. 369 – 388 in *Fractography of Glasses and Ceramics, IV*, eds. J. R. Varner and G. D. Quinn, American Ceramic Society, Westerville, OH, 2001.

Fused silica Missile radome

This Guide. Chapter 10, case 7.

Grinding flaws and joint debonding.

Glass Containers, Lamps, and Pressure Vessels

Bottles and flasks

V. D. Fréchette, *Failure Analysis of Brittle Materials*, Advances in Ceramics, Vol. 28, American Ceramic Society, Westerville, OH, 1990, pp. 94 – 101, 112, 118, 123.

Internal pressure, water hammer, thermal shock, and impact fractures.

Various bottles including intravenous medical bottles, wine bottles, frozen citrus fruit concentrate bottles, malformed bottles.

F. W. Preston, "Bottle Breakage – Causes and Types of Fractures," *Am. Ceram. Soc. Bull.*, 18 [2] (1939) 35 – 60.

An early paper but with an exceptional treatment of a variety of failure causes.

V. D. Fréchette and T. A. Michalske, "Fragmentation in Bursting Glass Containers," *Bull. Amer. Ceram. Soc.*, 57 [4] (1978) 427 – 429.

Four different sizes of internally pressurized, water filled bottles.

V. D. Fréchette and S. L. Yates, "Fragmentation of Glass Bottles by Impact," *J. Am. Ceram. Soc.*, 72 [6] (1989) 1060.

Three different sizes of water filled bottles were swung at different velocities against a stationary steel rod.

J. B. Kepple, and J. S. Wasylyk, "Fracture of Glass Containers," pp. 207 – 252 in *Fractography of Glass*, eds. R. C. Bradt and R. E. Tressler, Plenum Press, NY, 1994.

An excellent, multifaceted treatment. Many fracture causes and patterns are shown.

R. E. Mould, "The Behavior of Glass bottles Under Impact," *J. Amer. Ceram. Soc.*, 35 [9] (1952) 230 – 235.

A well illustrated paper on controlled breakages of bottles. This article (and Dimmick's that followed it) proved that hinge origins away from the impact site were sources of breakage in some cases.

G. D. Quinn, This Guide, Chapter 10. Medicinal Glass Vials
Neck cracking from the cap sealing operation.

Fluorescent lamps

D. Johnson, "Arc Induced Fractures from Lampmaking Test Equipment," pp. 517 – 525 in *Fractography of Glasses and Ceramics, III*, Ceramic Transactions, Vol. 64, J.R. Varner, V.D. Fréchet, and G. D. Quinn, eds., American Ceramic Society, Westerville, OH, 1996.

Cathode Ray Tube

A. Ghosh, C. Y. Cha, Vaidyanathan, and R. C. Bradt, "Finite Element Stress Analysis and Crack Path Prediction of Imploding CRT," pp. 1 – 24 in *Fractography of Glasses and Ceramics II*, Ceramic Transactions Vol. 17, eds. V. D. Fréchet and J. R. Varner, American Ceramic Society, Westerville, OH, 1991.

Glass cooking thermometer

V. D. Fréchet, *Failure Analysis of Brittle Materials*, Advances in Ceramics, Vol. 28, American Ceramic Society, Westerville, OH, 1990, p. 120.

Tempered glass cylinders

V. D. Fréchet, *Failure Analysis of Brittle Materials*, Advances in Ceramics, Vol. 28, American Ceramic Society, Westerville, OH, 1990, pp. 120 – 121, 123 – 124.

Uneven thermal temper in a structural cylinder and also a high power gymnasium lamp that lost its temper due to heating.

Ceramic Seals

Tetragonal zirconia polycrystalline (TZP) hydraulic seal disks

R. W. Rice, "Failure Analysis of Ceramics," pp. 369 – 388 in *Fractography of Glasses and Ceramics, IV*, eds. J. R. Varner and G. D. Quinn, American Ceramic Society, Westerville, OH, 2001.

Mechanical seal rings – silicon carbide

R. Morrell, "Fractography of Brittle Materials," R. Morrell, Measurement Good Practice Guide 15, National Physical Laboratory, Teddington, Middlesex, United Kingdom, 1999, pp. 76 – 85.

Large open rotating rings with shoulders and notches. Impact damage - chipping, preexisting cracks, grinding cracks, handling damage.

Microwave tube (alumina)

R. W. Rice, "Failure Analysis of Ceramics," pp. 369 – 388 in *Fractography of Glasses and Ceramics, IV*, eds. J. R. Varner and G. D. Quinn, American Ceramic Society, Westerville, OH, 2001.

Ceramic Containers, Lamps, and Pressure Vessels

Large porcelain tubes

V. D. Fréchette, *Failure Analysis of Brittle Materials*, Advances in Ceramics, Vol. 28, American Ceramic Society, Westerville, OH, 1990, pp. 125 – 126.

"Spontaneous" fracture during end-face machining. Internal residual stresses.

Beta alumina hollow cylinders, burst pressure loading

B. J. McEntire, R. H. Snow, J. L. Huang, L. Viswanathan, and A. V. Virkar, "Characterization of Processing Flaws in Beta Alumina," pp 335 – 349 in *Fractography of Glasses and Ceramics*, Advances in Ceramics, Vol. 22, ed. J. D. Varner and V. D. Fréchette, American Ceramic Society, Westerville, OH, 1988.

Beta alumina electrolyte tubes, service failures

E. K. Beauchamp, "Beta Alumina failures in Sodium/Sulfur Batteries," pp. 377 – 387 in *Fractography of Glasses and Ceramics*, Advances in Ceramics, Vol. 22, ed. J. D. Varner and V. D. Fréchette, American Ceramic Society, Westerville, OH, 1988.

Ceramic Armor Plates

S. Winkler, H. Senf, and H. Rothenhäusler, "High Velocity Fracture Investigation in Alumina," pp. 165 – 183 in *Fractography of Glasses and Ceramics II*, Ceramic Transactions Vol. 17, eds. V. D. Fréchet and J. R. Varner, American Ceramic Society, Westerville, OH, 1991.

High-speed photography of alumina and glass plates hit on end.

M. E. Stevenson, S. E. Jones, and R. C. Bradt, "Fracture Patterns of a Composite Safety Glass Panel During High Velocity Projectile Impacts," pp. 473 – 488 in *Fractography of Glasses and Ceramics, IV*, eds. J. R. Varner and G. D. Quinn, American Ceramic Society, Westerville, OH, 2001.

J. J. Swab, G. A., Glide, P. J. Patel, A. A. Wereszczak, J. W. McCauley, and J. D. Risner, "Fracture Analysis of Transparent Armor Ceramics," pp. 489 – 508 in *Fractography of Glasses and Ceramics, IV*, eds. J. R. Varner and G. D. Quinn, American Ceramic Society, Westerville, OH, 2001.

Biaxial strength tests on sapphire, aluminum oxynitride, and magnesium alumina spinel.

R. L. Woodward, R. G. O'Donnell, B. J. Baxter, B. Nicol, and S. D. Pattie, "Energy Absorption in the failure of Ceramic Composite Armors," *Mater. Forum*, 13 (1989) 174 – 181.

M. J. Slavin, "Fractographic Analysis of Long Rod Penetrator – Armor Ceramics Interactions," U. S. Army Technical Report, TR 89 – 93, U.S. Army Materials Technology Laboratory, Watertown, MA, Oct. 1989.

C. Tracy, M. Slavin, and D. Viechnicki, "Ceramic Fracture During Ballistic Impact," pp. 295 – 306 in *Fractography of Glasses and Ceramics*, Advances in Ceramics, Vol. 22, ed. J. D. Varner and V. D. Fréchet, American Ceramic Society, Westerville, OH, 1988.

S. Rodriguez, V. B. Munoz, E. V. Esquivel, L. E. Muir, and N. L. Rupert, "Microstructural Characterization of TiB₂ Armor Targets," *J. Mat. Sci. Ltrts.*, 21 (2002) 1161 – 1666.

V. D. Fréchet and C. F. Cline, "Fractography of Ballistically Tested Ceramics," *J. Am. Ceram. Soc.*, 49 [11] (1970) 994 – 997.

V. D. Fréchet, "Fractography and Quality Assurance of Glass and Ceramics," pp. 227 – 236 in *Quality Assurance in Ceramic Industries*,

eds. V. D. Fréchette, L. D. Pye, and D. E. Rase, Plenum, NY, 1978.

Hot-pressed boron carbide blanks fractured during machining. Internal residual stresses were created by too rapid a cool down from the firing temperature.

R. N. Katz and W. A. Brantley, "Fractography of High Boron Ceramics Subjected to Ballistic Loading," pp. 271 – 282 in *Materials Science Research*, Vol. 5, ed. W. W. Kriegel, Plenum, NY, 1971.

D. G. Christie and H. Kolsky, "The Fractures Produced in Glass and Plastics by the Passage of Stress Waves," *J. Soc. Glass Technol.*, Vol. 36, (1952) 65 – 73.

Ceramic Ball Bearings

J. J. Swab and M. P. Sweeney, "Fracture Analysis of An All-Ceramic Bearing System," U. S. Army Research Laboratory Technical Report, ARL TR 512, September 1994.

Y. Wang and M. Hadfield, "Rolling Contact Fatigue Failure Modes of Lubricated Silicon Nitride in Relation to Ring Crack Defects," *Wear*, 225 – 229 (1999) 1284 – 1292.

Y. Wang and M. Hadfield, "The Influence of Ring Crack Location on the Rolling Contact Fatigue Failure of Lubricated Silicon Nitride: Experimental Studies," *Wear*, 243 (2000) 157 – 166.

Cellular Ceramics, Catalytic Converters, Filters

D. J. Green and R. Brezny, "Fractographic Determination of Strut Strength in Cellular Ceramics," pp. 199 – 129 in *Fractography of Glasses and Ceramics II*, Ceramic Transactions Vol. 17, eds. V. D. Fréchette and J. R. Varner, American Ceramic Society, Westerville, OH, 1991.

J. Kübler, R. Baechtold, G. Blugan, L. Lemster, and S. Fuso, "Failure Analysis on a De-Nox Catalyst of a Large Waste Burner," pp. 78 – 85 in *Fractography of Advanced Ceramics II*, eds. J. Dusza, R. Danzer and R. Morrell, Transtech, Zurich, 2005.

Fibers - Glass Optical

H. C. Chandan, R. D. Parker, and D. Kalish, "Fractography of Optical Fibers," pp. 143 – 184 in *Fractography of Glass*, Ed. R. C. Bradt and R. E. Tressler, Plenum Press, NY, 1994.

W. R. Wagner, "Failure Analysis of Fiber Optic Connectors," pp. 389 – 402 in *Fractography of Glasses and Ceramics*, Advances in Ceramics, Vol. 22, ed. J. D. Varner and V. D. Fréchet, American Ceramic Society, Westerville, OH, 1988.

J. J. Mecholsky, "Fracture Surface Analysis of Optical Fibers," pp. 663 – 668 in *Ceramics and Glasses, Engineered Materials Handbook*, Vol. 4, ed. S. Schneider, ASM, Metals Park, OH, 1991.

Fibers – Nonoptical

P. K. Gupta, "Fractography of Fiberglass," pp. 185 – 206 in *Fractography of Glass*, ed. R. C. Bradt and R. E. Tressler, Plenum Press, NY, 1994.

G. V. Srinivasan and V. Venkateswaren, "Fractographic Investigation of Flaws in Sintered SiC Fiber," pp 317 –337 in *Fractography of Glasses and Ceramics, III, Ceramic Transactions*, Vol. 64, J. R. Varner, V. D. Fréchet, and G. D. Quinn, eds., American Ceramic Society, Westerville, OH, 1996.

C-T. Li and N. R. Langley, "Development of a Fractographic Method for the Study of High-Temperature Failure of Ceramic Fibers," pp. 177 – 184 in *Fractography of Glasses and Ceramics*, Advances in Ceramics, Vol. 22, ed. J. D. Varner and V. D. Fréchet, American Ceramic Society, Westerville, OH, 1988.

T. Clark, "Fracture Properties of Thermally Aged Ceramic Fiber Produced by Polymer Pyrolysis," pp. 279 – 305 in *Fractography of Glasses and Ceramics*, Advances in Ceramics, Vol. 22, ed. J. D. Varner and V. D. Fréchet, American Ceramic Society, Westerville, OH, 1988.

Fiber Composites

A. S. Fareed, M. J. Koczak, F. Ko, and G. Layden, "Fracture of SiC/LAS Ceramic Composites," pp. 261 – 293 in *Fractography of Glasses and Ceramics*, Advances in Ceramics, Vol. 22, ed. J. D. Varner and V. D. Fréchet, American Ceramic Society, Westerville, OH, 1988.

Special Components

MEMS structures

S. J. Glass, D. A. LaVan, T. E. Buchheit, and K. Jackson, "Strength Testing and Fractography of MEMS Materials," pp. 227 – 240 in *Fractography of Glasses and Ceramics, IV*, eds. J. R. Varner and G. D. Quinn, American Ceramic Society, Westerville, OH, 2001.

G. Quinn, W. Sharpe, G. M. Beheim, N. Nemeth and O. Jadaan, "Fracture Origins in Miniature Silicon Carbide Structures," pp. 62 – 69 in *Fractography of Advanced Ceramics II*, eds. J. Dusza, R. Danzer and R. Morrell, Transtech, Zurich, 2005.

Ceramic automotive valves

R. Danzer, M. Hangl, and R. Paar, "Edge Chipping of Brittle Materials," pp. 43 – 55 in *Fractography of Glasses and Ceramics, IV*, eds. J. R. Varner and G. D. Quinn, American Ceramic Society, Westerville, OH, 2001.

M. J. Andrews, A. A. Wereszczak, K. Breder, and T. P. Kirkland, "Fractographic Analysis Applied to Ceramic Component Life Prediction," pp. 301 – 315 in *Fractography of Glasses and Ceramics, IV*, eds. J. R. Varner and G. D. Quinn, American Ceramic Society, Westerville, OH, 2001.

Ceramic gas turbine model rotor

G. D. Quinn, This Guide, Chapter 10, and
G. D. Quinn, "Design and Reliability of Ceramics, Do Modelers, Designers and Fractographers See the Same World?" *Ceram. Eng. and Sci. Proc.*, 26 [8] (2005) 239 – 252.

α – silicon carbide heat exchanger tube

K. Breder and J. R. Kaiser, "Failure Analysis of an α -SiC Tube Subjected to Thermal Cycling in and Oxygen-Steam Atmosphere," pp. 301 – 15 in *Fractography of Glasses and Ceramics, III, Ceramic Transactions*, Vol. 64, J. R. Varner, V. D. Fréchette, G. D. Quinn, eds., American Ceramic Society, Westerville, OH, 1996.

Silicon carbide machine gun barrel

G. D. Quinn, This Guide, Chapter 10, and
G. D. Quinn, "Design and Reliability of Ceramics, Do Modelers, Designers and Fractographers See the Same World?" *Ceram. Eng. and Sci. Proc.*, 26 [8] (2005) 239 – 252.

Contact cracks from shrink fitting and stress reverberations.

Silicon nitride rolling mill rollers

M. Lengauer, R. Danzer, D. Rubesa, W. Harrer, and W. Zleppnig, "Failure Analysis of Si₃N₄ Rolls for Wire Hot Rolling by Numerical Simulation of Thermal and Mechanical Stresses," pp. 94 – 101 in *Fractography of Advanced Ceramics II*, eds. J. Dusza, R. Danzer and R. Morrell, Transtech, Zurich, 2005.

Lead zirconate titanate (PZT) sonar rings

R. W. Rice, "Failure Analysis of Ceramics," pp. 369 – 388 in *Fractography of Glasses and Ceramics, IV*, eds. J. R. Varner and G. D. Quinn, American Ceramic Society, Westerville, OH, 2001.

Epoxy bonding stresses.

Coatings and Glazes

Diamond coatings

H. A. Hoff, K. A. Snail, A. A. Morrish, and J. E. Butler, "Fractography and Fracture Mechanics of Combustion Grown Diamond Thin Films," pp. 25 – 54 in *Fractography of Glasses and Ceramics II, Ceramic Transactions*, Vol. 17, eds. V. D. Fréchette and J. R. Varner, American Ceramic Society, Westerville, OH, 1991.

Whiteware glazes

V. D. Fréchette, *Failure Analysis of Brittle Materials*, Advances in Ceramics, Vol. 28, American Ceramic Society, Westerville, OH, 1990, pp. 94 – 101.

Internal pressure, water hammer, thermal shock, and impact fractures.

Electronic Ceramics

Porcelain railroad electrical insulator

J. Woodtli, K. Beroth, and T. Luthi, "Combination of Fractography and Computed Tomography for the Determination of the Cause of Fracture," pp. 257 – 271 in *Fractography of Glasses and Ceramics, III, Ceramic Transactions*, Vol. 64, J. R. Varner, V. D. Fréchette, and G. D. Quinn, eds., American Ceramic Society, Westerville, OH, 1996.

Porcelain insulator, high tension power line

J. R. Varner and V. D. Fréchette, "Fractography of Whitewares," pp. 305 – 315 in *Science of Whitewares*, eds. V. Henkes, G. Onoda, and W. Carty, American Ceramic Society, Westerville, OH, 1996.

Material fault, a clump of feldspar grains.

Silicon wafers

R. E. Moore, P. G. Hansen, W. Carty, and J. W. Ha, "Fracture of Thermally Shocked Silicon Disks," pp. 351 – 361 in *Fractography of Glasses and Ceramics*, Advances in Ceramics, Vol. 22, ed. J. D. Varner and V. D. Fréchet, American Ceramic Society, Westerville, OH, 1988.

Stacked PZT piezoelectric actuator material

P. Supancic, Z. Wang, W. Harrer, K. Reichmann, and R. Danzer, "Strength and Fractography of Piezoceramic Multilayer Stacks," pp. 46 – 53 in *Fractography of Advanced Ceramics II*, eds. J. Dusza, R. Danzer and R. Morrell, Transtech, Zurich, 2005.

PTC (Positive Temperature Coefficient) thermistors – barium titanate

A. Platzer, P. Supancic, C. Lembacher, U. Theiszi, and R. Danzer, "Thermography and Simulation as a Combined Method for Failure Analysis of PTCs," pp. 54 – 61 in *Fractography of Advanced Ceramics II*, eds. J. Dusza, R. Danzer and R. Morrell, Transtech, Zurich, 2005.

ZnO varistors

Z. Wang, P. Supancic, F. Aldrian, A. Schriener and R. Danzer, "Strength and Fractography of High Power Varistors," pp. 358 – 365 in *Fractography of Advanced Ceramics II*, eds. J. Dusza, R. Danzer and R. Morrell, Transtech, Zurich, 2005.

R. W. Rice, "Failure Analyses of Ceramics," pp. 369 – 388 in *Fractography of Glasses and Ceramics, IV*, eds. J. R. Varner and G. D. Quinn, American Ceramic Society, Westerville, OH, 2001.

Components suffer dielectric breakdown.

Bioceramics**Ceramic hip joint ball heads**

H. G. Richter, "Fractography of Bioceramics," pp. 157 – 180 in *Fractography of Advanced Ceramics*, ed. J. Dusza, Trans Tech Publ., Zurich, 2002.

R. Morrell, L. Byrne, and M. Murray, "Fractography of Ceramic Femoral Heads," pp. 253 – 266 in *Fractography of Glasses and Ceramics, IV*, eds. J. R. Varner and G. D. Quinn, American Ceramic Society, Westerville, OH, 2001.

A. Walter, "Fracture Phenomena in Orthopedic Alumina," pp. 403 – 414 in *Fractography of Glasses and Ceramics*, Advances in Ceramics, Vol. 22,

ed. J. R. Varner and V. D. Fréchet, American Ceramic Society, Westerville, OH, 1988.

Dental Ceramics

J. R. Kelly, "Fractography of Dental Ceramics," pp. 241 – 251 in *Fractography of Glasses and Ceramics*, IV, eds. J. R. Varner and G. D. Quinn, American Ceramic Society, Westerville, OH, 2001.

J. B. Quinn, "Failure Analysis of a Broken Tooth," *J. Failure Analysis and Prevention*, 4 [1] (2004) 41 – 46.

A patient's tooth fractured days after open-heart surgery. Was the laryngoscopy by the anesthesiologist done correctly?

S. S. Scherrer, J. B. Quinn, G. D. Quinn, and J. R. Kelly, "Failure Analysis of Ceramic Clinical Cases Using Qualitative Fractography," *Int. J. Prosthodont.*, 19 [2] (2006) 151 – 158.

Five dental crown restorations that failed in service were analyzed. The materials were: Procera alumina, Cerestore alumina-spinel, In-ceram glass in-fused alumina, and porcelain fused to metal. Fractography identified the failure causes that were correlated to clinical observations and crown design.

J. B. Quinn, G. D. Quinn, J. R. Kelly, and S. S. Scherrer, "Fractographic Analyses of Three Ceramic Whole Crown Restorations," *Dental Materials*, 21 (2005) 920 – 929.

Three dental crown restorations that failed in service were analyzed. The materials were Procera alumina, Cerestore alumina-spinel, and Empress II lithium disilicate. Origin sites were found in each case.

J. B. Quinn, G. D. Quinn, J. R. Kelly, and S. S. Scherrer, "Useful Tools for Dental Failure Investigation," pp. 36 – 53 in *Proceedings of the Conference on Scientific Insights and Dental Ceramics and Photopolymer Networks*, ed. D. C. Starrett, Transactions of the Academy of Dental Materials, Vol. 16, 2004.

B. Taskonak, J. J. Mecholsky, Jr., and K. J. Anusavice, "Fracture Surface Analysis of Clinically Failed Fixed Partial Dentures," *J. Dental. Res.*, 3 (2006) 277 – 281.

J. Y. Thompson, K. J. Anusavice, A. Naman, and H. F. Morris, "Fracture Surface Characterization of Clinically Failed All-Ceramics Crowns,

J. Dent. Res., 73 [12] (1994) 1824 - 1832.

Ten Dicor crown were fractographically analyzed in accordance with MIL HDBK 790 and the principles outline by Frechette. Fracture initiated on the inside surfaces from abrasive damage or failure of the cement at restoration/cement interface. Twelve Cerestore crowns were more difficult to analyze, but appeared to break from porcelain/core interface or inside the core material. Laboratory scale strength tests with biaxial disk specimens furnished valuable property and fractographic information.

Whitewares and Kitchenware

J. S. Banda and P. F. Messer, "Fracture-Initiating Flaws in Whitewares," pp. 363 – 375 in *Fractography of Glasses and Ceramics*, Advances in Ceramics, Vol. 22, ed. J. D. Varner and V. D. Fréchet, American Ceramic Society, Westerville, OH, 1988.

P. B. Adams and S. E. DeMartino, "Glass-Ceramic Cookware Failure Analysis," pp. 669 – 673 in *Ceramics and Glasses, Engineered Materials Handbook*, Vol. 4, ed. S. Schneider, ASM, Metals Park, OH, 1991.

V. D. Fréchet, *Failure Analysis of Brittle Materials*, Advances in Ceramics, Vol. 28, American Ceramic Society, Westerville, OH, 1990, pp. 113 – 114.
Teapots on stoves – thermal stresses.

V. D. Fréchet, *Failure Analysis of Brittle Materials*, Advances in Ceramics, Vol. 28, American Ceramic Society, Westerville, OH, 1990, pp. 114 – 115.
Lasagna dish, cone crack – impact.

J. R. Varner and V. D. Frechette, "Fractography of Whitewares," pp. 305 – 315 in *Science of Whitewares*, eds. V. Henkes, G. Onoda, and W. Carty, American Ceramic Society, Westerville, OH, 1996.

Porcelain Coffee Storage Jars – contact damage from a metal band cover seal.

Porcelain Bushing, 2.7 m long by 0.9 m diameter – residual stresses from firing.

Porcelain Bushing, small-screw holes acted as origins.

Toilet Bowl – water hammer.

Toilet Tank – mounting-bolt hole failure from mechanical overloading.

◆ Fractography of Ceramics and Glasses

V. D. Fréchet, *Failure Analysis of Brittle Materials*, Advances in Ceramics, Vol. 28, American Ceramic Society, Westerville, OH, 1990, p. 113.

Porcelain faucet handles.

See also electronic ceramic insulators and dental ceramics

Rocks, Lithic Materials

J. B. Quinn, J. W. Hatch, and R. C. Bradt, "The Edge Flaking Test as an Assessment of the Thermal Alteration of Lithic Materials, Bald Eagle Jasper," pp. 73 – 85 in *Fractography of Glasses and Ceramics, IV*, eds. J. R. Varner and G. D. Quinn, American Ceramic Society, Westerville, OH, 2001.

A. Tsirk, "An Exploration of Liquid-Induced Fracture Markings," pp. 87 – 101 in *Fractography of Glasses and Ceramics, IV*, eds. J. R. Varner and G. D. Quinn, American Ceramic Society, Westerville, OH, 2001.

Obsidian tools.

A. Tsirk, "Fractographic Evidence for Liquid on Obsidian Tools," *J. Archeol. Sci.*, 27 (2000) 987 – 991.

A. Tsirk, "Formation and Utility of a Class of Anomalous Wallner Lines on Obsidian," pp. 57 – 69 in *Fractography of Glasses and Ceramics*, Advances in Ceramics, Vol. 22, ed. J. D. Varner and V. D. Fréchet, American Ceramic Society, Westerville, OH, 1988.

Geological, Tectonic Structures

(Bahat's book is a good starting point but readers should be warned that some of the interpretations are controversial and are not settled. A sampling of other representative publications is listed.)

D. Bahat, *Tectono-fractography*, Springer-Verlag, Berlin, 1991.

B. R. Kulander, "Hackle Plume Geometry and Joint Propagation Dynamics," pp. 85 – 94 in *Proceedings of the International symposium on Fundamentals of Rock Joints*, Björkilden, 15 – 20 September 1985.

O. H. Muller, "Fractography Applied to Large Scale (m to km) Cracks in the Earth," pp. 427 – 438 in *Fractography of Glasses and Ceramics*, Advances in Ceramics, Vol. 22, ed. J. D. Varner and V. D. Fréchet, American Ceramic Society, Westerville, OH, 1988.

Similar features observed over nine orders of magnitude of size.

A. I. Younes and T. Engelder, "Fringe Cracks: Key Structures for the Interpretation of the Progressive Alleghanian Deformation of the Appalachian Plateau," *Geological Society of America Bulletin*, 111 [2] (1999) 219 – 239.

D. Bahat, T. Bankwitz, and E. Bankwitz, "Preuplift Joints in Granites: Evidence for Subcritical and Postcritical Fracture Growth," *Geological Society of America Bulletin*, 115 [2] (2003) 148 – 165.

D. T. McConaughy and T. Engelder, "Joint Initiation in Bedded Clastic Rocks," *J. Struct. Geology*, 23 (2001) 203 – 221.

T. Engelder, "Tectonic Implication Drawn from Differences in the Surface Morphology on Two Joint Sets in the Appalachian Valley and Ridge, Virginia," *Geology*, 32 (2004) 413 - 416.

T. Engelder, "The Propagation Velocity of Joints vis-a-vis Fractography of Rock," to be pub., *Fractography of Glasses and Ceramics V*, eds., G. D. Quinn, J. R. Varner, M. Wightman, American Ceramic Society, Westesville, OH. 2007.

Other

Glass fibers in a fiberglass-reinforced plastic pressure vessel

S. J. Glass, E. K. Beauchamp, M. J. Carr, T. R. Guess, S. L. Munroe, R. J. Moore, A. Slavin, and N. R. Sorenson, "Failure Analysis of A Fiberglass-Reinforced Plastic Pressure Vessel," pp. 527 – 541 in *Fractography of Glasses and Ceramics, III*, Ceramic Transactions, Vol. 64, Varner, J, Fréchette, V., and Quinn, G. eds., American Ceramic Society, Westerville, OH, 1996.

Violent rupture of a pressurized tank holding sulphuric acid. Occasional and incidental spillage penetrated microcracks in the matrix and caused progressive degradation in glass fiber strengths.

Stoneware reactor catalyst media balls

R. W. Rice, "Failure Analysis of Ceramics," pp. 369 – 388 in *Fractography of Glasses and Ceramics, IV*, eds. J. R. Varner and G. D. Quinn, American Ceramic Society, Westerville, OH, 2001.

Emerald gemstone (3.66 carat)

R. W. Rice, "Failure Analysis of Ceramics," pp. 369 – 388 in *Fractography of Glasses and Ceramics, IV*, eds. J. R. Varner and G. D. Quinn, American Ceramic Society, Westerville, OH, 2001.

Impact on ceramic kitchen tile countertop caused cracking.

Jade

D. J. Rowcliffe and V. Frühauf, "The Fracture of Jade," *J. Mat. Sci.*, 12 (1977) 35 – 42.

Gemstones

J. E. Field, "Brittle Fracture: Its Study and Application," *Contemp. Phys.*, 12 [1] (1971) 1 – 31.

Porcelain faucet handles

V. D. Fréchette, *Failure Analysis of Brittle Materials*, Advances in Ceramics, Vol. 28, American Ceramic Society, Westerville, OH, 1990, p. 113.

Earthenware sewer pipe

V. D. Fréchette, *Failure Analysis of Brittle Materials*, Advances in Ceramics, Vol. 28, American Ceramic Society, Westerville, OH, 1990, p. 116.

Uranium dioxide fuel element – bushing

V. D. Fréchette, *Failure Analysis of Brittle Materials*, Advances in Ceramics, Vol. 28, American Ceramic Society, Westerville, OH, 1990, pp. 120 – 121.
Thermal fracture.

Beryllium oxide hollow cylinder

J. R. Varner and V. D. Fréchette, "Fractography of Whitewares," pp. 305 – 315 in *Science of Whitewares*, eds. V. Henkes, G. Onoda, and W. Carty, American Ceramic Society, Westerville, OH, 1996.

Hollow cylinder loaded at high temperature under laboratory conditions.

Ceramic machine base (Electrically insulating base)

R. Morrell, "Fractography of Brittle Materials," R. Morrell, *Measurement Good Practice Guide 15*, National Physical Laboratory, Teddington, Middlesex, United Kingdom, 1999, pp. 67 – 69.

Bending failure from bolt holes.

Ceramic ball valve – alumina

R. Morrell, "Fractography of Brittle Materials," R. Morrell, *Measurement Good Practice Guide 15*, National Physical Laboratory, Teddington, Middlesex, United Kingdom, 1999, pp. 70 – 71.

150 mm alumina ball with slots and large hole, internal pressure.

Gas valve plate - alumina

R. Morrell, "Fractography of Brittle Materials," R. Morrell, *Measurement Good Practice Guide 15*, National Physical Laboratory, Teddington,

Middlesex, United Kingdom, 1999, pp. 72 – 74.

Possible grinding or lapping damage near a complex hole.

Steel continuous casting nozzles – Carbon-bonded alumina, zirconia, magnesia, graphite

A. Mašelejová and A. Leško, “Fracture Characteristics of Isostatic Pressed Submerged Entry Nozzle,” pp. 370 – 373 in *Fractography of Advanced Ceramics II*, eds. J. Dusza, R. Danzer and R. Morrell, Transtech, Zurich, 2005.



APPENDIX C. FRACTURE MIRROR AND BRANCH CONSTANTS

The following table includes all the published values of mirror and branching constants that the author could find up to mid 2006 when this Guide went to press. The original reference is listed for each entry.

The mirror and branching constants were analyzed assuming:

$$\sigma \sqrt{R} = A \quad (\text{C.1})$$

Mirror-mist (or inner mirror) A_i and mist-hackle (or outer mirror) A_o constants are listed for glass and glass ceramics. Mist is difficult or impossible to discern in most ceramics and the mirror constant A_o that is listed corresponds to the mirror-hackle boundary.

Entries where a modified version of equation C.1 was used are noted by a footnote.

No judgment is made of the veracity of the listed values. Some of the values may be inaccurate. Even for ideal materials such as fused silica and soda lime silica there are unsettling variations in reported values. The variations probably are caused by:

1. Differences in viewing mode, including type of microscope, magnifications, illumination techniques, and magnification accuracy and precision.
2. Differences in observer judgment.
3. Differences in the radii measured (e.g., along the surface, into the depth, or other) and the accuracy and precision of the length measurements.
4. Differences in test method (e.g., flexure, tension, biaxial plate) and accuracy and precision of the strength data.
5. Differences in whether or not corrections were made for stress gradients and the stress at the origin location.
6. Unaccounted for residual stresses.
7. Differences in the analysis used including whether data were plotted and regressed as log stress versus log mirror radius, or linear stress versus inverse square root of radius.
8. Variations in density, microstructure, or fracture toughness between nominally identical materials.
9. Variations in the number of specimens tested.

One is tempted to conclude that most of the discrepancies are due to viewer judgment, but this cannot account for all of the variability. The mirror

constant is only sensitive to the square root of the measured radii. In other words, a 10% systematic error in radii measurements causes only a 5% error in the mirror constant.

All values in the table are listed with the same number of significant figures as in the original reference. Uncertainties (\pm one standard deviation) are listed when available from the original reference. Multiple entries in a cell denote estimates by different microscopy techniques or analysis. For polycrystalline ceramics, the mirror constants taken from the reference sources are assumed to be for the mist-hackle boundary unless otherwise stated.

If the user cannot find the mirror constant for a particular material, he or she may consider values for comparable materials within the same class. For example, if a particular glass is not listed, then use the value for a glass of similar composition. For polycrystalline ceramics, microstructure plays an important role in determining a mirror constant. Conscientious readers should check the references listed for more details on a particular material.

Readers are encouraged to send unlisted mirror constant data to the author for inclusion in future versions of this Guide.

Mr. George D. Quinn
MSEL, STOP 852
NIST
Gaithersburg, MD 20899

Material	Technique	Mirror-Mist A_i (MPa $\cdot\sqrt{m}$)	Mist-Hackle or Mirror-Hackle A_o (MPa $\cdot\sqrt{m}$)	Branching A_b (MPa $\cdot\sqrt{m}$)	Reference
Glasses					
Flint (Kimble R6 soda lime)	Flexure (Rods)		2.0		Kirchner, 8
Flint (Kimble R6 soda lime)	Flexure (Rods)		1.9		Kirchner, 9
Flint (Kimble R6 soda lime)	Flexure (Rods)		2.3		Kirchner, 10
Soda-Lime Silicate – window glass	Flexure (biaxial ring-on ring, large)	2.09			Orr, 5
Soda-Lime Silica (window, sheet, and plate)	Flexure (Bars or laths)	2.05			Shand, 4
Soda-Lime Silicate – float, plate, sheet	Flexure (biaxial ring-on ring and bend bars)		2.09		Barsom, 62
Soda-Lime Silicate – window glass	Pressurized windows, large	1.96			Reed, 39
Soda-Lime Silicate	Flexure (Bars)	1.74			Bansal, 14
Soda-Lime Silicate A – plate glass Soda-Lime Silicate B – plate glass	Flexure (Bars – large) Room Temperature to Strain Point	1.86 \pm 0.66 1.82 \pm 0.91			Kerper, Scuderi 6
Soda-Lime Silica Float	Flexure (Bars)	1.80 \pm 0.15 * 1.81 \pm 0.25	2.42 \pm 0.16 * 2.29 \pm 0.24		Ball, 40
Soda-Lime Silica Float (G.E.C. – X8)	Tension (Rods) Flexure (Bars)	1.89 \pm 0.06	2.04 \pm 0.06 2.09		Johnson, Holloway, 1
Soda-Lime Silica Float	Flexure (Bars) Flexure–Delayed failure (Bars)	1.92 2.0 \pm 0.1	2.21 2.2 \pm 0.1		Mecholsky, 18,21 Mecholsky, 21
Soda-Lime Silica	Flexure	1.8	2.0	2.3	Mecholsky, 22
Soda Lime Silica Float	Flexure (Many bars, large and small, 3-point and 4-point)	2.06 \pm 0.07	2.29 \pm 0.19		Duckworth, 16
Soda-Lime Silica	Tension (Plates)			1.2 – 1.6	Congleton, Petch, 2
Soda-Lime Silica	Flexure (Bars) Flexure (Biaxial ring-on ring plates)	1.81 \pm 0.28		3.54 \pm 0.64	Choi, 33
Soda-Lime Silica	Tension			1.9	Clark, 34
Soda-Lime Silica	Pressurized Tube			2.0	Aoki, 35
Soda-Lime Silica	Flexure (Biaxial ring-on ring disks) 3 environments, Vickers indented	1.82 – 1.94	2.03 – 2.13	2.28 – 2.42	Marshall, 19
Soda-Lime Silica	Flexure (Biaxial ring-on ring disks)			2.1 *	Shetty, 15
Soda-Lime Silica	Flexure (rods)	1.8			Terao, 63
Soda-Lime Silica	Flexure (rods)	1.85 \pm 0.21			Varner, 68
Soda-Lime Silica	Flexure (3-point rods) Flexure (4-point rods) Tension (Fibers)	3.15 \pm 0.11 2.74 \pm 0.15 1.72 \pm 0.28			Abdel-Latif, 49
Soda-Lime Silica	Flexure (3-point, laths)	(2.9 ***)			Levengood, 64
Borosilicate A (P 3235) Borosilicate B (C 7740)	Flexure (Bars – large; Room Temperature to Strain Point)	1.98 \pm 0.46 2.04 \pm 0.75			Kerper, Scuderi, 6
Borosilicate (C 7740)	Flexure (Rods, many diameters)	2.08 \pm 0.02			Kerper, Scuderi, 7

◆ Fractography of Ceramics and Glasses

Material	Technique	Mirror-Mist A_i (MPa $\cdot\sqrt{m}$)	Mist-Hackle or Mirror-Hackle A_o (MPa $\cdot\sqrt{m}$)	Branching A_b (MPa $\cdot\sqrt{m}$)	Reference
Borosilicate (C 7740)	Flexure (Bars)	1.87 \pm 0.3	2.10		Mecholsky, 17, 18
Borosilicate (C 7740)	Flexure (Bars) and Biaxial disks	1.9 \pm 0.3	1.9		Mecholsky, 20
Borosilicate (C 7740)	Flexure (Rods)	2.2, 2.35			Shand, 3
Borosilicate	Flexure and Tension (Rods)	1.9*			Alarc3n et al. 56
Borosilicate crown (Schott BK-7)	Flexure (Biaxial ring-on ring disks)*	1.98 \pm 0.02 *	2.11 \pm 0.03 * 2.3	2.28 \pm 0.03 *	Quinn, 25
Aluminosilicate (C 1723)	Flexure (Bars)	2.14	2.40		Mecholsky, 18
Aluminosilicate A (P 6695) Aluminosilicate B (C 1723)	Flexure (Bars – large) Room Temperature to Strain Point	2.31 \pm 0.76 2.34 \pm 0.97			Kerper, Scuderi, 6
Alkali-borosilicate	Tension (Fibers)	1.33 *			Jaras et al., 12
Alkaline-earth boro aluminosilicate (C1737)	Flexure (Biaxial ring-on- ring)	2.07 \pm 0.01			Gulati et al., 57
Barium silicate 3BaO-5SiO ₂	NR (Flexure Bars?)	1.3	1.5		Mecholsky, 22
E glass CaO-Al ₂ O ₃ -B ₂ O ₃ alumina borosilicate	Tension (Fibers)	1.47 *			Jaras et al., 12
Lead silicate (G.E.C. L1)	Tension (Rods)	1.71 \pm 0.06			Johnson, Holloway, 1
Lead silicate	Flexure (Bars)	1.61	1.78		Mecholsky, 18
Lithium silicate Li ₂ O-2SiO ₂	Flexure Bars (3-point)	2.2	2.6		Mecholsky, 22
Zinc silicate	Flexure Bars	2.1	2.6	3.2	Mecholsky, 22
Zirconia silicate (Cem-FIL AR)	Tension (Fibers)	2.37 *			Jaras et al., 12
Yttrium-Alumino- Silica Oxyntride (2Y-Al-Si-O-N)	Flexure (Bars)	1.5 \pm 0.2			Coon, 48
Fused Silica (C 7940)	Flexure (Bars)	2.23	2.42	2.7	Mecholsky, 18, 22
Fused Silica (C 7940)	Flexure (Bars – large; Room Temperature to Strain Point)	1.89 \pm 0.51			Kerper, Scuderi, 6
Fused silica (Vitreosil)	Tension (Rods)	2.33 \pm 0.06			Johnson, Holloway, 1
Fused silica	Flexure (Rods)	2.20 \pm 0.33			Choi, 33
Fused silica	Flexure and Tension (Rods)	1.2 *			Alarc3n et al. 56
Fused silica fibers	Tension	2.10			Choi, 33
Fused silica clad fibers	Tension	1.96 \pm 0.13			Baker, 29
Fused silica fibers	Tension	1.83			Castilone, 30
Fused silica fibers, bars, disks	Tension (Fibers) Flexure (Bars) Flexure (Biaxial, piston on 3 balls)	2.2 \pm 0.5 2.3 \pm 0.5 2.4 \pm 0.3			Mecholsky, 20

Material	Technique	Mirror-Mist A_i (MPa $\cdot\sqrt{m}$)	Mist-Hackle or Mirror-Hackle A_o (MPa $\cdot\sqrt{m}$)	Branching A_b (MPa $\cdot\sqrt{m}$)	Reference
Fused silica fibers	Tension	2.224			Chandan, 37
Leached High Silica (C 7930)	Flexure (Bars)	0.91	1.19		Mecholsky, 18
96% Silica (C 7900)	Flexure (Bars – large; Room Temperature to Strain Point)	1.84 \pm 0.65			Kerper, Scuderi, 6
Glassy Carbon	Flexure (Bars)	1.17	1.67		Mecholsky, 17,18
Glassy Carbon	Flexure (Bars)			2.1	Bullock, Kaae, 61
As ₂ Se ₃ chalcogenide glass, untreated	Tension	0.69 0.35	0.69 0.35	0.77 0.38	Hulderman, 45
As ₂ Se ₃ chalcogenide glass, UV treated					
As ₂ Se ₃	Flexure (Bars)	0.56	0.65		Mecholsky, 18
Ge ₃₃ As ₁₂ Se ₅₅	Flexure (Bars)	0.55	0.65		Mecholsky, 18
0.3PbSe - 0.7Ge _{1.5} As _{0.5} Se ₃	Flexure (Bars)	0.48	0.55		Mecholsky, 18
ZBLA (halide glass)	Flexure (Bars)	0.8			Mecholsky, 22
Lead Borate glass 30PbO-70B ₂ O ₃ (mol) 40PbO-60B ₂ O ₃ 50PbO-50B ₂ O ₃ 60PbO-40B ₂ O ₃ 70PbO-30B ₂ O ₃	Flexure (Bars)	1.7 \pm 0.05 1.45 \pm 0.05 1.15 \pm 0.05 0.85 \pm 0.01 0.65 \pm 0.01			Shinkai, Ishikawa, 60 **
Glass Ceramics					
Pyroceram 9608 (Li, Mg, Al silicate)	NR		2.8		Adams + DeMartino, 27
Pyroceram 9607 (Li, Mg, Zn, Al silicate)	NR		2.1 *		Adams + DeMartino, 27
Pyroceram 9606 (Cordierite, Mg, Al silicate)	Flexure	3.6	6.5		Mecholsky, 17
Pyroceram 9606 (Cordierite, Mg, Al silicate)	Flexure (Bars)		6.5		Lewis, 44
Pyroceram 9606 (Cordierite, Mg, Al silicate)	Flexure (Bars)		5.7		Bansal, 13,14
Pyroceram 9606 (Cordierite, Mg, Al silicate)	Flexure (Bars) and Flexure (Biaxial, piston on 3 balls)		6.3		Mecholsky, 20
Pyroceram 9606 (Cordierite, Mg, Al silicate)	Flexure (Biaxial, ring on ring)			3.1 \pm 0.2 *	Shetty, 15
Pyroceram 9606 (Cordierite, Mg, Al silicate)	Flexure (Rods)		4.8		Shand, 3
Li ₂ O-SiO ₂ (NPL glass ceramic, 2 grades)	Flexure (Bars)	3.3, 3.8	4.5, 5.4		Mecholsky, 17
Dental Ceramics					
Dicor (dental, tetra silica fluoromica) glass ceramic	Flexure (Bars)		0.97		Kelly, 47

◆ Fractography of Ceramics and Glasses

Material	Technique	Mirror-Mist A_i (MPa $\cdot\sqrt{m}$)	Mist-Hackle or Mirror-Hackle A_o (MPa $\cdot\sqrt{m}$)	Branching A_b (MPa $\cdot\sqrt{m}$)	Reference
Dental Ceramics					
Feldspathic Porcelain (alumina filled, Vitadur N 338)	Flexure (Bars)		2.82		Kelly, 47
Feldspathic Leucite Porcelain, Optec OPC	Flexure (Bars)		2.1		Fischer, 52
Empress I Leucite glass ceramic	Flexure (Bars)		1.7		Fischer, 52
Empress II Lithium disilicate glass ceramic	Flexure (Bars)		3.9		Fischer, 52
Omega - Opaker	Flexure (Bars)		1.3		Fischer, 52
Cerec Mark II Porcelain	Flexure (Bars)		1.6		Fischer, 52
Glass infused Alumina, In-Ceram	Flexure (Bars)		6.6		Fischer, 52
Dental resin, 85 wt% zirconia-silica filler in bisGMA-TEGDMA	Flexure (Bars)		2.6		Quinn, Scherrer, 59
Silicon Carbide					
Sintered SiC (Hexoloy SA)	Flexure (Bars)		5.39		Quinn, 23
Sintered SiC (Hexoloy SA)	Flexure (Biaxial ring-on- ring plates)			6.30 \pm 0.54	Salem, 31
Sintered SiC (Hexoloy SA)	Flexure (Biaxial ring-on- ring plates)			5.45 \pm 0.30	Choi, 33
Sintered SiC (Hexoloy SA)	C-ring	5.50 \pm 0.94	8.20 \pm 0.54	10.48 \pm 0.97	Conway et al. 67
Sintered Si toughened (Hexoloy SX)	Tension (Rods) and Flexure (Bars)		7.0?	7.0?	Srinivasan, 42
Sintered with Al (Rioceram SiC)	C-ring	5.67 \pm 0.60	8.16 \pm 0.54	11.60 \pm 0.75	Conway et al. 67
Sintered (Carolt S)	Flexure (Bars, optical, SEM)		6.1, 6.8		Woodtli, 36
Hot-pressed SiC (NC-203)	Flexure (Rods) Flexure-Delayed Fracture (Rods)		11.4 11.9		Kirchner, 8
Hot-pressed SiC (NC-203)	Flexure (Rods)		11.5		Kirchner, 9
Hot-pressed SiC (ACE)	Flexure (Rods)		10.8		Kirchner, 10
Siliconized SiC (KT)	Flexure		10.7		Mecholsky, 17
Reaction bonded SiC (Coors SCRB205)	C-ring	4.11 \pm 0.31	5.22 \pm 0.23	6.41 \pm 0.36	Conway et al. 67
Zirconia					
Yttria stabilized (3Y-TZP)	Flexure (Bars)		9.95		Morrell, 43
Yttria stabilized (3Y-TZP)	Flexure (Bars) Flexure (Biaxial piston on 3 ball)		8.6 \pm 0.23 9.6 \pm 0.23		Quinn, 50
Yttria stabilized (3Y-TZP, Lava)	Flexure (Bars)		10.7		Quinn, 58

Material	Technique	Mirror-Mist A_i (MPa $\cdot\sqrt{m}$)	Mist-Hackle or Mirror-Hackle A_o (MPa $\cdot\sqrt{m}$)	Branching A_b (MPa $\cdot\sqrt{m}$)	Reference
Yttria stabilized (3.5Y-TZP)	Flexure (Biaxial ring-on-ring disks)			11.48 \pm 1.46	Choi, 33
Zircar (Alfred-Union Carbide, 0.4 μ m, 5-6 mol% Y TZP)	Flexure (Bars)		15.2		Mecholsky, 17
Zyttrite (AFML, 10 μ m, cubic)	Flexure (Bars)		7.4		Mecholsky, 17
Silicon Nitride					
Sintered Reaction Bonded (Ceralloy 147-31N)	Flexure (Rods) Flexure (Bars)		8.47 \pm 0.07 7.79 \pm 0.02		Quinn, 26
Sintered (SSN-500 yttria/alumina)	Flexure (Bars)		5.8		Quinn, 23
Sintered (SN 220)	Flexure (Biaxial ring-on-ring disks)			8.13 \pm 2.36	Choi, 33
Sintered (AS 44)	Flexure (Biaxial ring-on-ring disks)			10.85 \pm 2.71	Choi, 33
Hot-pressed (Ceralloy 147A)	Flexure (Bars)		7.83		Quinn, 23
Hot-pressed (NC-132)	Flexure (Rods)		9.2		Kirchner, 9
Hot pressed (NC-132)	Flexure (Rods) Flexure-Delayed Fracture (Rods)		8.9 9.2		Kirchner, 8
Hot-pressed (NC-132)	Flexure (Rods)		14.3		Kirchner, 10
Hot-pressed (NC-132)	Flexure (Bars, 1100°C) Flexure (Biaxial ring-on-ring, 1100°C)		9.40 \pm 1.19	7.92 \pm 2.08	Choi, 33 ****
Hot-pressed (HS-130)	Flexure		18.1		Mecholsky, 17
Hot-pressed (HS-130)	Flexure (Rods)		9.1		Kirchner, 8
Hot-isopressed (NT 154)	Flexure (Bars)		5.88 \pm 0.14		Choi, 32,33
Hot-isopressed + 30vol% SiC whiskers	Flexure (Bars)		6.63 \pm 0.11		Choi, 32,33
Hot-isopressed (GN-10)	Flexure (Biaxial ring-on-ring) Tension (Rods)		11.78 \pm 1.41	10.32	Choi, 33 ****
Reaction Bonded (NC 350)	Flexure (Bars)		3.89		Messier, 24
Reaction Bonded (NC 350)	Flexure (Bars)		3.19		Larsen, 28
Reaction Bonded (AME A25B)	Flexure (Rods)		4.2		Kirchner, 8
Alumina					
Sapphire (average of several planes)	Flexure		6.1		Mecholsky 17
Sapphire (Tyco filaments, c-axis parallel to fiber axis)	Tension Flexure		5.5 10.0		Abdel-Latif, 38
Sapphire (Ruby rods, c axis ~60° off rod axis)	Flexure (Rods)		3.3		Abdel-Latif, 38

◆ Fractography of Ceramics and Glasses

Material	Technique	Mirror-Mist A_i (MPa $\cdot\sqrt{m}$)	Mist-Hackle or Mirror-Hackle A_o (MPa $\cdot\sqrt{m}$)	Branching A_B (MPa $\cdot\sqrt{m}$)	Reference
Sapphire Filament, c-axis parallel to fiber axis	Tension, 800 to 1000°C	2.4	3.2		Rice, 51
β -Al ₂ O ₃	Flexure		~ 6.5		Mecholsky, 17
Hot-pressed (1 μ m, Cer. Fin.)	Flexure (Rods, 4-point) 25 to 1400°C		10.4		Kirchner, 11
Hot-pressed (99+% pure, Cer. Fin.)	Flexure (Rods, 4-point) Flexure-Delayed Fracture (Rods)		10.3 9.9		Kirchner, 8.9 Kirchner, 8
Hot-pressed (99+% pure, Cer. Fin.)	Flexure (Rods-3 point)		9.1		Kirchner, 10
Hot-pressed (99+% pure)	Flexure	5.2	12		Mecholsky, 17
Hot pressed	Flexure (Rods)		10.4		Mecholsky, 11
Hot-pressed (Avco, 1-2 μ m)	Flexure		9.8		Bansal, 14
Sintered (Lucalox)	Tension (Plates)			7.3	Congleton, Petch, 2
Sintered (96%) (Alsimag 614)	Flexure (Rods)		8.5		Kirchner, 9
Sintered (96%) (Alsimag 614)	Flexure (Rods) Flexure-Delayed Fracture (Rods)		8.3 8.9		Kirchner, 8
Sintered (96%) (Alsimag 614)	Flexure (Bars)		9.0		Bansal, 13,14
Sintered (96%) (Alsimag 614)	Flexure (Rods)		9.1		Kirchner, 10
Sintered (96%) (Alsimag 614)	Flexure (Bars)		13.1		Mecholsky, 17
Sintered (96%) (Alsimag 614)	Flexure (Bars), Flexure (Biaxial ball-on- ring), Flexure (Biaxial ring-on- ring)		7.64 \pm 0.53	7.39 \pm 0.55 7.24 \pm 0.66	Choi, 33 ****
Sintered 96% (Alsimag 614)	Flexure (Biaxial ring-on- ring disks)			4.0 \pm 0.28 *	Shetty, 15
Other					
Ammonium diphosphate, single crystal	Flexure (Bars)		0.5		Mecholsky, 17
WC-Co (various Co contents)	Flexure		24 – 87		Luyckx, 41
WC (No Co)	Flexure		10		Swab, 46
Mullite	Flexure		6.1		Mecholsky, 17
MgO	Flexure		9.6		Mecholsky, 17
MgO	Tension (Plates)			4.3	Congleton, Petch, 2
MgO, single crystal	Flexure (Bars)		5		Mecholsky, 17
MgF ₂ (Kodak)	Flexure (Bars)	1.8	3.1		Mecholsky, 17
MgF ₂ (Kodak, IRTRAN 1)	Flexure (Bars) and Biaxial Disks			4.4	Mecholsky, 20
MgAl ₂ O ₄ Spinel	Flexure (Bars)	4.0	7.8		Mecholsky, 17
MgAl ₂ O ₄ Spinel, single crystal	Flexure (Bars)		2.6		Mecholsky, 17

Material	Technique	Mirror-Mist A_i (MPa $\cdot\sqrt{m}$)	Mist-Hackle or Mirror-Hackle A_o (MPa $\cdot\sqrt{m}$)	Branching A_b (MPa $\cdot\sqrt{m}$)	Reference
B ₄ C hot-pressed	Flexure (bars)	4.8	9.27		Mecholsky, 17
3BaO-SiO ₂	Flexure (Bars)	3.9	6.0		Mecholsky, 17
PZT	Flexure	1.7	3.7		Mecholsky, 17
Graphite (POCO)	Flexure		3.32		Mecholsky, 17
BaTiO ₂ (2 grades)	Flexure (Bars)		5.0, 5.4		Mecholsky, 17
SrZrO ₃	Flexure (Bars)	4.4	6.0		Mecholsky, 17
Sleatite (Mg silicate insulator, DC - 144)	Flexure (Rods)		4.8 4.5		Kirchner, 8,9 Kirchner, 10
Yttrium Aluminum Garnet, polycrystal. (2.2 μ m)	Flexure (Bars)		2.15 \pm 0.08		Mezeix and Green, 66
Yttrium Aluminum Garnet, single crystal (111)	Flexure (Bars)		2.20 \pm 0.06		Mezeix and Green, 66
Zircon Porcelain (Alsimag 475)	Flexure (Rods)		4.0		Kirchner, 8,9
ZnSe	Flexure (Bars)			1.7	Mecholsky, 17
ZnSe (44 μ m)	Flexure (Biaxial ring-on-ring disks)			0.8, 1.0 #	Salem, 65
Fibers					
E glass CaO-Al ₂ O ₃ -B ₂ O ₃ alumina borosilicate	Tension (Fibers)	1.47 *			Jaras et al., 12
Alkali-borosilicate	Tension (Fibers)	1.33 *			Jaras et al., 12
Zirconia silicate (Cem-FIL AR)	Tension (Fibers)	2.37 *			Jaras et al., 12
Fused silica fibers	Tension	2.10			Choi, 33
Fused silica clad fibers	Tension	1.96 \pm 0.13			Baker, 29
Fused silica fibers	Tension	1.83			Castlone, 30
Fused silica fibers	Tension (Fibers)	2.2 \pm 0.5			Mecholsky, 20
Fused silica fibers	Tension	2.224			Chandan, 37
Si-Ti-C-O (Tyranno LoxM) fiber	Fibers in 3-D SiC matrix composite		2.50 \pm 0.09		Davies, 53
Si-C-O fibers (Nicalon), Si-C-N-O fibers, Si-N-C-O fibers	Tension		~2		Sawyer, 54
Si-C-O, (Nicalon)	Fibers in 2-D CVI SiC matrix composite		2.51		Eckel + Bradt, 55
Sapphire filament, c-axis parallel to fiber axis	Tension, 800 to 1000°C	2.4	3.2		Rice, 51

* A non-zero intercept was detected on the graph of stress versus inverse square root radius. Mirror or branching constants calculated with non-zero intercepts are usually different than those calculated with intercepts through the ordinate. Consult the original reference for more information.

** Additional mirror constants for the lead borate glasses are available at liquid nitrogen temperature (-196°C) in the original reference.

*** Mostly likely an overestimate since stresses were not adjusted for failure location in the 3-point rod specimens.

**** A_1 was indeed reported to be $> A_b$.

Alternative analyses are in the original reference.

NR Not reported

REFERENCES

1. J. W. Johnson, and D. G. Holloway, "On the Shape and Size of the Fracture Zones on Glass Fracture Surfaces," *Phil. Mag.*, **14** [130] (1966) 731 – 743.
2. J. Congleton, and N. J. Petch, "Crack Branching," *Phil. Mag.*, **16** [142] (1967) 749 – 760.
3. E. B. Shand, "Breaking Stress of Glass Determined from Dimensions of Fracture Mirrors," *J. Amer. Ceram. Soc.*, **42** [10] (1959) 474 – 477.
4. E. B. Shand, "Breaking Stresses of Glass Determined from Fracture Surfaces," *The Glass Industry*, April 1967, 90 – 194.
5. L. Orr, "Practical Analysis of Fractures in Glass Windows," *Materials Research and Standards*, **12** [1] (1972) 21 – 23.
6. M. J. Kerper, and T. G. Scuderi, "Modulus of Rupture of Glass in Relation to Fracture Pattern," *Bull. Amer. Ceram. Soc.*, **43** [9] (1964) 622 – 625.
7. M. J. Kerper, and T. G. Scuderi, "Relation of Fracture Stress to the Fracture Pattern for Glass Rods of Various Diameters," *Bull. Amer. Ceram. Soc.*, **45** [12] (1966) 1065 – 1066.
8. H. P. Kirchner, R. M. Gruver, and W. A. Sotter, "Fracture Stress-Mirror Size Relations for Polycrystalline Ceramics," *Phil. Mag.*, **33** [5] (1976) 775 – 780.
9. H. P. Kirchner, R. M. Gruver, and W. A. Sotter, "Use of Fracture Mirrors to Interpret Impact Fracture in Brittle Materials," *J. Amer. Ceram. Soc.*, **58** [5-6] (1975) 188 – 191.
10. H. P. Kirchner, and R. M. Gruver, "Fracture Mirrors in Polycrystalline Ceramics and Glass," pp. 309 – 321 in *Fracture Mechanics of Ceramics 1*, eds. R. C. Bradt, D. P. H. Hasselman, and F. F. Lange, Plenum, NY, 1973.

11. H. P. Kirchner, and R. M. Gruver, "Fracture Mirrors in Alumina Ceramics," *Phil. Mag.*, **27** [6] (1973)1433 – 1446.
12. A. C. Jaras, B. J. Norman, and S. C. Simmons, "The Measurement of Glass Fibre Strength in Composites from Studies of Their Fracture Surfaces," *J. Mat. Sci.*, **18** (1983) 2459 – 2465.
13. G. K. Bansal, and W. H. Duckworth, "Fracture Stress as Related to Origin and Fracture Mirror Sizes," *J. Amer. Ceram. Soc.*, **60** [7–8] (1977) 304 – 310.
14. G. K. Bansal, "On Fracture Mirror Formation in Glass and Polycrystalline Ceramics," *Phil. Mag.*, **35** [4] (1977) 935 – 944.
15. D. K. Shetty, A. R. Rosenfeld, and W. H. Duckworth, "Crack Branching in Ceramic Disks Subjected to Biaxial Flexure," *Comm. of the Amer. Ceram. Soc.*, Jan. 1983, C10 – C13.
16. W. H. Duckworth, D. K. Shetty, and A. R. Rosenfeld, "Influence of Stress Gradients on the Relationship Between Fracture Stress and Mirror Size for Float Glass," *Glass Technology*, **24** [5] (1983) 263 – 273.
17. J. J. Mecholsky, Jr., S. W. Freiman, and R. W. Rice, "Fracture Surface Analysis of Ceramics," *J. Mat. Sci.*, **11** (1976) 1310 – 1319.
18. J. J. Mecholsky, R. W. Rice, and S. W. Freiman, "Prediction of Fracture Energy and Flaw Size in Glasses from Measurements of Mirror Size," *J. Amer. Ceram. Soc.*, **57** [10] (1974) 440 – 443.
19. D. B. Marshall, B. R. Lawn, and J. J. Mecholsky, "Effect of Residual Contact Stresses on Mirror/Flaw Size Relations," *J. Amer. Ceram. Soc.*, **63** [5–6] (1980) 358 – 360.
20. J. J. Mecholsky, Jr., and R. W. Rice, "Fractographic Analysis of Biaxial Failure in Ceramics," in *Fractography of Ceramics and Glass Failures*, ASTM STP 827, eds. J. Mecholsky and S. Powell, ASTM, Westerville, OH, 1984 185 – 193.
21. J. J. Mecholsky, A. C. Gonzalez, and S. W. Freiman, "Fractographic Analysis of Delayed Failure in Soda Lime Glass," *J. Amer. Ceram. Soc.*, **62** [11–12] (1979) 577 – 580.

◆ Fractography of Ceramics and Glasses

22. J. J. Mecholsky, "Quantitative Fractographic Analysis of Fracture Origins in Glass," pp. 37 – 173 in *Fractography of Glass*, eds. R. C. Bradt and R. E. Tressler, Plenum, NY, 1994.
23. G. D. Quinn, D. R. Messier, and L. J. Schioler, "Characterization of Ceramic Vane Materials for 10 kW Turboalternator," U.S. Army Materials and Mechanics Research Center Technical Report TR 83-18, April 1983.
24. D. R. Messier, L. J. Schioler, and G. D. Quinn, "Fracture Behavior and Strength of Reaction-Bonded Si₃N₄ Turbine Shrouds," *Bull. Amer. Ceram. Soc. Bulletin*, **60** [8] (1981) 812 – 817.
25. J. B. Quinn, "Extrapolation of Fracture Mirror and Crack-Branch Sizes to Large Dimensions in Biaxial Strength Tests of Glass," *J. Amer. Ceram. Soc.*, **82** [8] (1999) 2126 – 2132.
26. G. D. Quinn, L. K. Ives, S. Jahanmir, and P. Koshy, "Fractographic Analysis of Machining Cracks in Silicon Nitride Rods and Bars," in *Fractography of Glasses and Ceramics, IV, Ceramic Transactions*, Vol. 122, eds., J. R. Varner and G. D. Quinn, American Ceramic Society, Westerville, OH, 2001 343 – 365.
27. P. B. Adams, and S. E. DeMartino, "Glass-Ceramic Cookware Failure Analysis," in *Engineered Materials Handbook, Vol. 4, Ceramics and Glasses*, ASM, Metals Park, OH, 1991 669 – 673.
28. D. C. Larsen, and G. C. Walther, "Property Screening and evaluation of Ceramic Turbine Engine Materials," IIT Research Institute, Chicago IL, Interim Technical Report No. 5, IITRI D 6114-ITR-30, 1978.
29. L. K. Baker, and G. S. Glaesemann, "Break Source Analysis, Alternate Mirror Measurement Method," *Proceedings of the International Wire and Cable Symposium*, Philadelphia, PA 1998 933 – 937.
30. R. J. Castilone, G. S. Glaesemann, and T. A. Hanson, "Relationship Between Mirror Dimensions and Failure Stress for Optical Fibers," pp. 11 – 20 in *Optical Fiber and Fiber Component Mechanical Reliability and Testing II*, eds. J. Matthewson and C. R. Kurkjian, Proc. of SPIE, Vol. 4639, (2002).
31. J. A. Salem, S. R. Choi, and L. M. Powers, "Toughened Ceramics Life Prediction," in Ceramic Technology Project Semiannual Progress Report for

October 1992 Through March 1993, Oak Ridge National Laboratory Technical Report TM 12428, September 1993, 307 – 316.

32. S. R. Choi, and J. A. Salem, "Indentation Flaw Formation and Strength Response of Silicon Nitride Ceramics at Low Indentation Loads," *Journal of Material Science Letters*, **11** (1992) 1398–1400.
33. S. R. Choi, and J. P. Gyekenyesi, "Crack Branching and Fracture Mirror Data of Glasses and Advanced Ceramics," NASA Technical Report TM 1998-206536, 1998.
34. A. B. J. Clark, and G. R. Irwin, "Crack Propagation Behaviors," *Experimental Mechanics*, **6** [6] (1966) 321 – 330.
35. S. Aoki, and M. Sakata, "Crack Bifurcation Under Hydrostatic Pressure," *Engineering Fracture Mechanics*, **13** [3] (1980) 491 – 499.
36. J. Woodtli, "Quantitative Fractographie in Keramik: Auswertung von Spiegelzonen in SiC," Swiss Federal Laboratories for Materials Testing and Research, Report 157361, Dec. 1997.
37. H. C. Chandan, and R. D. Parker, "Fractography of Optical Fibers," pp. 143 – 184 in *Fractography of Glass*, eds. R. C. Bradt and R. E. Tressler, Plenum Press, NY, 1994.
38. A. I. A. Abdel-Latif, R. E. Tressler, and R. C. Bradt, "Fracture Mirror Formation in Single Crystal Alumina," in *Fracture 1977*, ed. D. Taplin, University of Waterloo Press, 1977, 933 – 939.
39. D. A. Reed, and R. C. Bradt, "Fracture Mirror-Failure Stress Relations in Weathered and Unweathered Window Glass Panels," *Comm. Amer. Ceram. Soc.*, Nov. 1984, C 227 – C 229.
40. M. J. Ball, D. J. Landini, and R. C. Bradt, "Fracture Mist Region in a Soda-Lime Silica Float Glass," pp. 110 – 120 in *Fractography of Ceramic and Metal Failures*, ASTM STP 827, J. Mecholsky, Jr., and S. Powell, eds., ASTM, 1984.
41. S. Bartolucci Luyckx, and A. Sannino, "Crack Branching and Fracture Mirrors in Cemented Tungsten Carbide," *J. Mat. Sci.*, **23** (1988) 1243 – 1247.

42. G. V. Srinivasan, J. Gibson, and S. K. Lau, "The Origin of Strength Limiting Defects in a Toughened SiC (Hexoloy SX-SiC), in *Fractography of Glasses and Ceramics III, Ceramic Transactions* Vol. 64, eds, J. R. Varner, V. D. Fréchette, and G. D. Quinn, American Ceramic Society, Westerville, OH, 1996, 181 – 192.
43. R. Morrell, L. Byrne, and M. Murray, "Fractography of Ceramic Femoral Heads," in *Fractography of Glasses and Ceramics, IV, Ceramic Transactions* Vol. 122, eds., J. R. Varner and G. D. Quinn, American Ceramic Society, Westerville, OH, 2001, 253 – 266.
44. D. Lewis, III, "Fracture Strength and Mirror Size in a Commercial Glass-Ceramic," *J. Amer. Ceram. Soc.*, **64** [2] (1961) 82 – 86.
45. F. Hulderman, J. S. Sanghera, and J. D. Mackenzie, "The Effect of UV Radiation on the Mechanical Strength of As₂Se₃ Glass Fibers," *J. Non-Crystalline Solids*, **127**, (1991) 312 – 322.
46. J. J. Swab, J. C. LaSalvia, and W. A. Gooch, "Characterization of WC-Based Armor Ceramics," to be published as a Technical Report by the Army Research Laboratory, Aberdeen Proving Ground, MD 21005.
47. J. R. Kelly, "Fractography of Dental Ceramics," pp. 241 – 251 in *Fractography of Glasses and Ceramics, IV*, eds. J. R. Varner and G. D. Quinn, Ceramic Transactions Vol. 122, American Ceramic Society, Westerville, OH 43081, 2001.
48. D. N. Coon, "Mirror/Mist Radius Constant for Y-Al-Si-O-N Glass," *J. Mat. Sci. Letters.*, **21**, (2002) 1121 – 1122.
49. A. I. A. Abdel-Latif, R. C. Bradt, and R. E. Tressler, "Dynamics of Fracture Mirror Boundary Formation in Glass," *Int. J. Fract.*, **13**, [3] (1977) 349 – 359.
50. G. D. Quinn, J. Eichler, U. Eisele, and J. Rödel, "Fracture Mirrors in a Nanoscale 3Y-TZP," *J. Amer. Ceram. Soc.*, **87** [3] (2004) 513 – 516.
51. R. W. Rice, "Corroboration and Extension of Analysis of c-Axis Sapphire Filament Fractures from Pores," *J. Mat. Sci. Lttrs.*, **16** (1997) 202 – 205.

52. H. Fischer, J. Gröbel, and R. Marx, "Fraktograpische Schadensanalyse an Dentalkeramik," *Deutsche Zahnarztl. Zeitschrift*, **55** [10] (2000) 667 – 670.
53. I. J. Davies, and T. Ishikawa, "Mirror Constant for Tyranno Silicon-Titanium-Carbon-Oxygen Fibers Measured in Situ in a Three-Dimensional Woven Silicon Carbide/Silicon Carbide Composite," *J. Amer. Ceram. Soc.*, **85** [3] (2002) 691 – 693.
54. L. C. Sawyer, M. Jamieson, D. Brikowski, M. I. Haider, and R. T. Chen, "Strength, Structure, and Fracture Properties of Ceramic Fibers Produced from Polymeric Precursors: I: Base-Line Studies," *J. Amer. Ceram. Soc.*, **70** [11] (1987) 798 – 810.
55. A. J. Eckel, and R. C. Bradt, "Strength Distribution of Reinforcing Fibers in a Nicalon Fiber/Chemically Vapor Infiltrated Silicon Carbide Matrix Composite," *J. Amer. Ceram. Soc.*, **72** [3] (1989) 455 – 458.
56. O. E. Alarcón, R. E. Medrano, and P. P. Gillis, "Fracture of Glass in Tensile and Bending Tests," *Metall. Mat. Trans. A*, **25A**, May (1994) 961 – 967.
57. S. T. Gulati, J. F. Bayne, W. R. Powell, and J. D. Helfinstine, "Mirror Constant for AMLCD Glass," *Bull. Amer. Ceram. Soc.*, **83** [5] (2004) 14 – 15.
58. J. B. Quinn, D. Cheng, R. Rusin, and D. Suttor, "Fractographic Analysis and Material Properties of a Dental Zirconia," International Association for Dental Research (IADR) paper, 0560, Baltimore, MD, March, 2005.
59. J. B. Quinn and S. Scherrer, "Fractography of Dental Resin Composites," Unpubl. 2005.
60. N. Shinkai, and H. Ishikawa, "Crack Branching of Binary PbO-B2O3 Glasses," *J. Noncryst. Solids*, **52** (1–3) (1982) 385 – 394.
61. R. E. Bullock, and J. L. Kaae, "Size Effect on the Strength of Glassy Carbon," *J. Mat. Sci.*, (1979) 920 – 930.
62. J. M. Barsom, "Fracture of Tempered Glass," *J. Amer. Ceram. Soc.*, **51** [2] (1968) 75 – 78.
63. N. Terao, "Sur une Relation entre la Résistance à la Rupture et le Foyer d'Eclatement du Verre," *J. Phys. Soc. Jap.*, **8** [4] (1953) 545 – 549.

64. W. C. Levengood, "Effect of Origin Flaw Characteristics on Glass Strength," *J. Appl. Phys.*, **29** [1] (1958) 820 – 826.
65. J. A. Salem, "Mechanical Characterization of ZnSe Windows for Use With the Flow Enclosure Accommodating Novel Investigations in Combustion of Solids (FEANICS) Module," NASA Technical Report TM-2006-214100, NASA-Glenn Center, Cleveland, OH, 2006.
66. L. Mezeix and D. J. Green, "Comparison of the Mechanical Properties of Single Crystal and Polycrystalline Yttrium Aluminum Garnet," *Int. J. Appl. Ceram. Technol.*, **3** [2] (2006) 166 – 176.
67. J. C. Conway, Jr., J. J. Mecholsky, O. M. Jadaan, and D. L. Shelleman, "Test Methodology for Ceramic Tubular Components," Center for Advanced Materials Research Report, Pennsylvania State University, 1989.
68. J. R. Varner and H. J. Oel, "Einfluss von Oberflächenbeschädigungen auf die Festigkeit von Glasstäben," *Grastechn. Ber.*, **48** [5] (1975) 73 – 78.

APPENDIX D GUIDELINES FOR MEASURING FRACTURE MIRRORS

D.1 Introduction

Mirrors are circular in ideal loading conditions such as uniform tension specimens. On the other hand, they often are elongated or distorted due to stress gradients or geometrical effects. There is a strong subjective element to estimating the location of the mirror boundary. Johnson and Holloway¹ noted that: "The position assigned to the boundary between mirror and mist zones depends upon the illumination and the magnification at which the fracture is examined, even within the range of the optical microscope. However, under given conditions a reproducible position for the boundary can be assigned." Since many of the early mirror measurements were made while viewing through the optical microscope, it is safe to say that the first perception of a mirror boundary was where the surface roughness was a fraction of the wavelength of light (0.39 μm - 0.80 μm). Threshold levels of detectability have been estimated to be as small as a few tens of nanometers to as much as 0.25 μm . Attempts to make objective determinations of the mirror boundary by quantitative surface roughness characterization are discussed in section D.3 below, but a single threshold roughness value cannot be specified.

Despite these problems, it cannot be denied that fracture mirror measurements are a powerful diagnostic tool for quantitative analysis. Therefore some guidelines are needed to bring some long overdue consistency to this procedure. Some of the following recommendations are based on common sense. Others are based upon the experiences of the author and other experts. The empirical mirror relationship for a residual stress free part is:

$$\sigma \sqrt{R} = A \quad (\text{D.1})$$

where σ is the stress at the origin, R is the mirror radius, and A is the appropriate mirror constant. The boundary criteria are:

The mirror-mist boundary in glasses is the periphery where one can discern the onset of mist. This boundary corresponds to A_i , the inner mirror constant.

The mist-hackle boundary in glasses is the periphery where one can discern the onset of systematic hackle. This boundary corresponds to A_o , the outer mirror constant.

The mirror-hackle boundary in polycrystalline ceramics is the periphery where one can discern the onset of systematic new hackle and there is an obvious roughness change relative to that inside the mirror region. This boundary corresponds to A_0 , the outer mirror constant. Ignore premature hackle and/or isolated steps from microstructural irregularities in the mirror or irregularities at the origin.

In coarse-grained or porous materials, it may be impossible to identify a mirror boundary. In polycrystalline ceramics, it is highly unlikely that a mirror-mist boundary can be detected due to the inherent roughness created by the crack-microstructure interactions even within the mirror. In very weak materials, the mirror may be larger than the specimen or component and the boundaries will not be present.

If the mirror is being measured for a component failure analysis, and if the mirror constant A is known, follow steps 1 through 9 in the next section and compute the stress *at the origin* in accordance with equation D.1. Note that this origin stress may or may not necessarily be the *maximum* stress in the part.

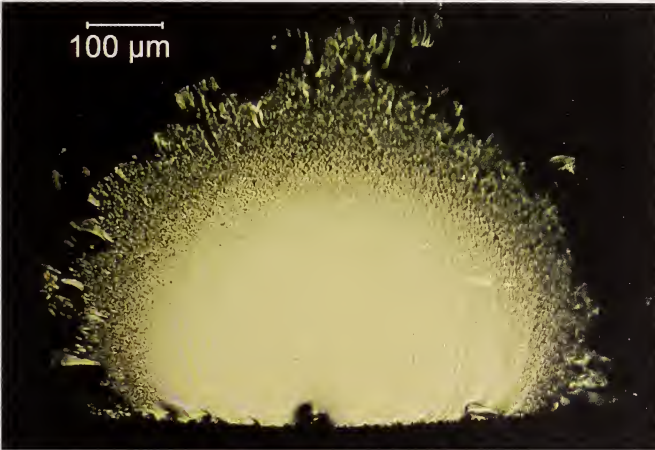
On the other hand, if the fracture mirror constant A is being evaluated by means of testing laboratory specimens and the origin stresses are known, follow steps 1 through 12 in the following section.

Examples of how to judge the boundaries are shown in Figures D.1 through D.6 on the following pages. Low power images are also shown to provide an overview. In each example, matching unmarked and marked images are shown so that the reader can make a judgment for comparison. The boundaries were assessed while looking through a microscope and the digital images in Figures D.1 to D.6 were marked. Mirrors should be evaluated while looking in a microscope. Alternatively, they may be measured on a high-resolution computer monitor, but preferably while the fracture surface can be also viewed through the microscope. Interpretation from two-dimensional photos only should only be done as a last resort.

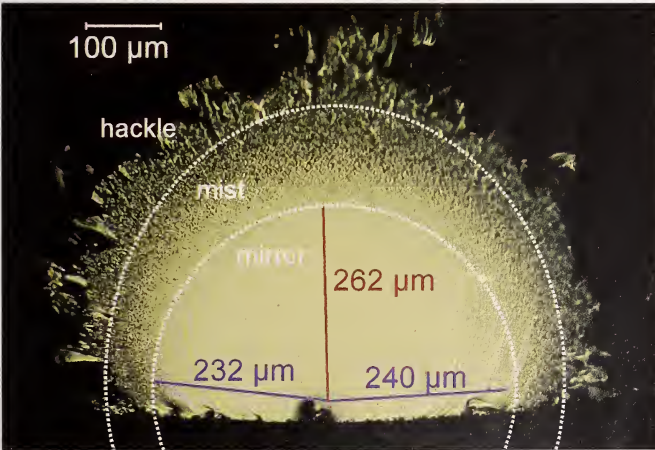
Although some of the mirrors are approximately circular or semicircular, examples of common alternative shapes are presented. Kirchner et al.^{2,3}, have presented compelling evidence that fracture mechanics analyses account for stress gradient and geometric effects upon mirror shapes.



(a)



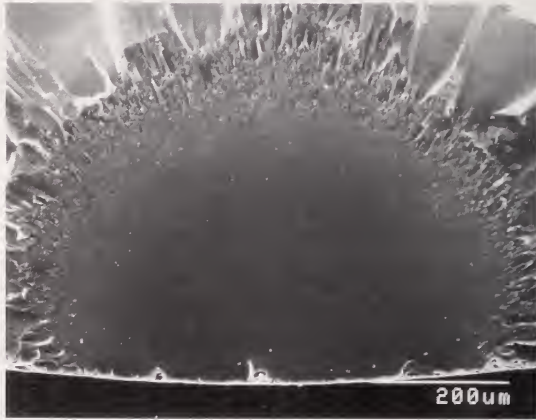
(b)



(c)

Figure D.1. Fused silica rod broken in flexure (122 MPa). The origin is a surface flaw located at the bottom of the specimen (a) where the stress was a maximum. A stress correction is unnecessary. The mirror-mist boundary is small relative to the cross section size and is approximated by a circle in (c). The inward cusps at the surface are ignored as discussed in section D.3. The mist – hackle boundary is slightly elongated towards the top. Close examination of the fracture surface in the vicinity of the flaw (not shown) showed that fracture started from the deepest part of the flaw.

(d)



(e)

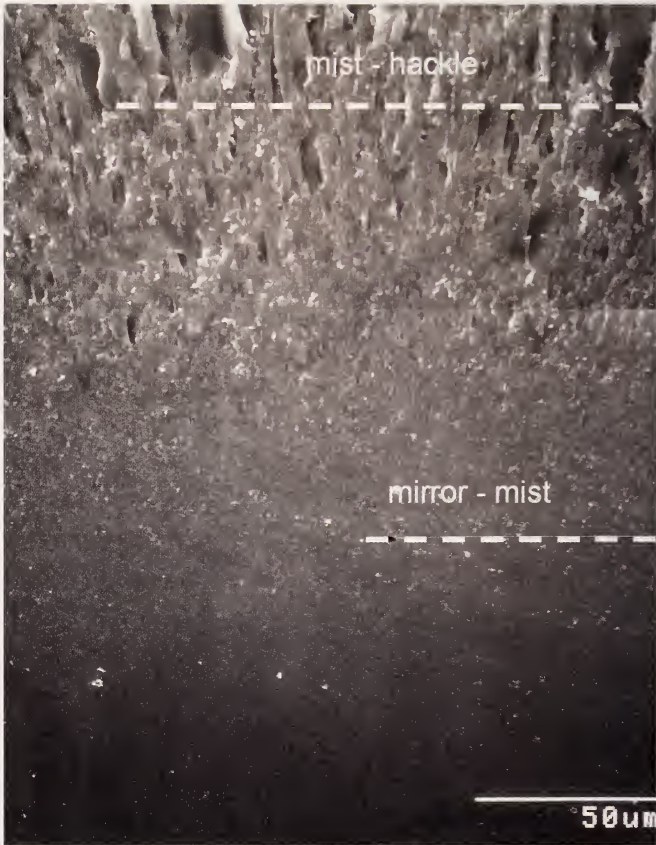


Figure D.1 (continued). (d) is an SEM image of the same mirror and at the same magnification as (b) and (c). The mist is indistinct in the SEM image. (e) is a composite of two SEM images showing the transition from mirror to mist to hackle. The locations of the boundaries as assessed by optical microscopy are marked by dashed lines on the SEM images.

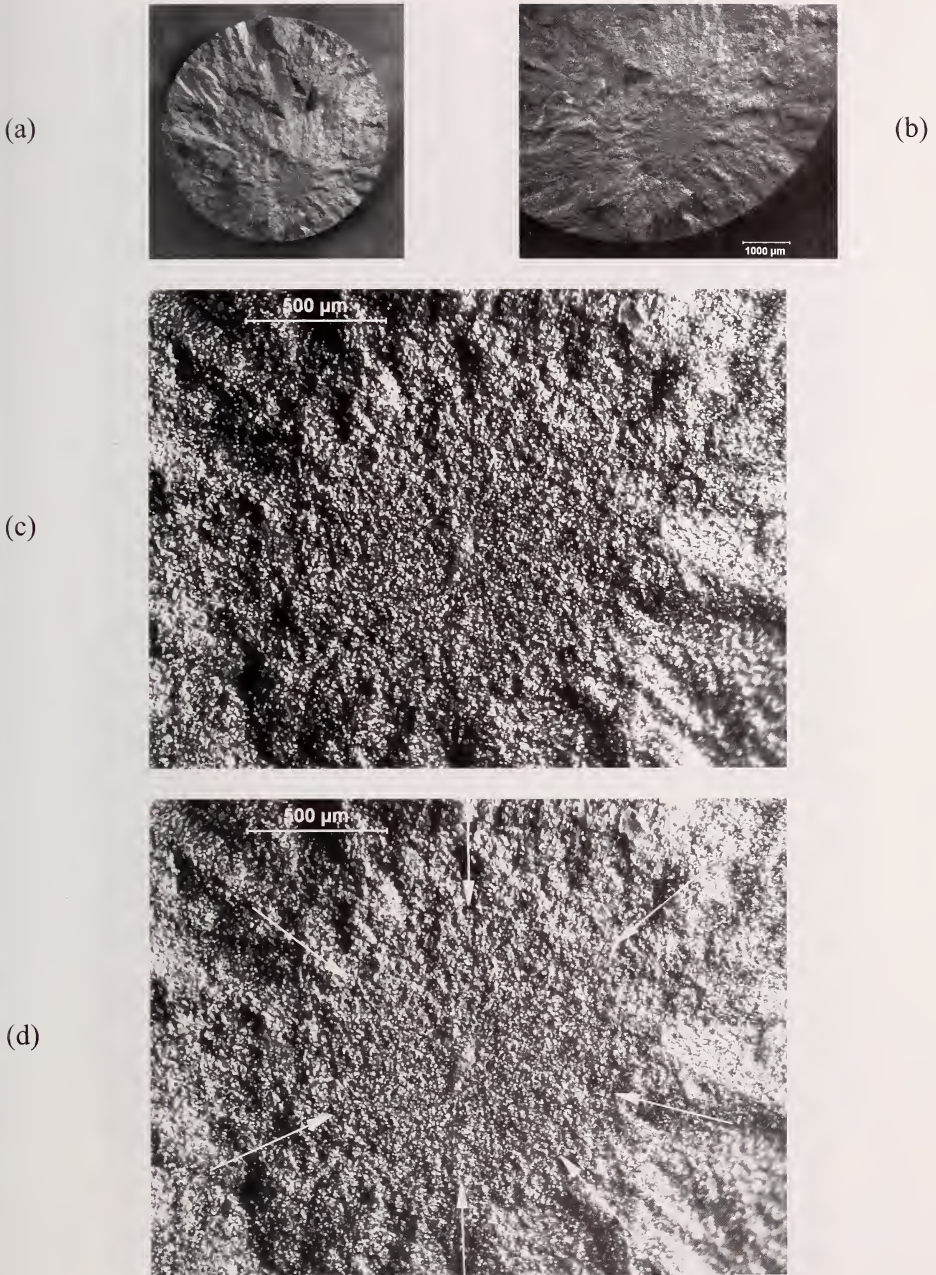


Figure D.2. Silicon carbide tension strength specimen (371 MPa) with a mirror centered on a compositional inhomogeneity flaw shown in Figure 6.11b. Note how clear the mirror is in the low power images. The mirror boundary (arrows in d) is where systematic new hackle forms and there is an obvious difference compared to the roughness inside the mirror region.

◆ Fractography of Ceramics and Glasses

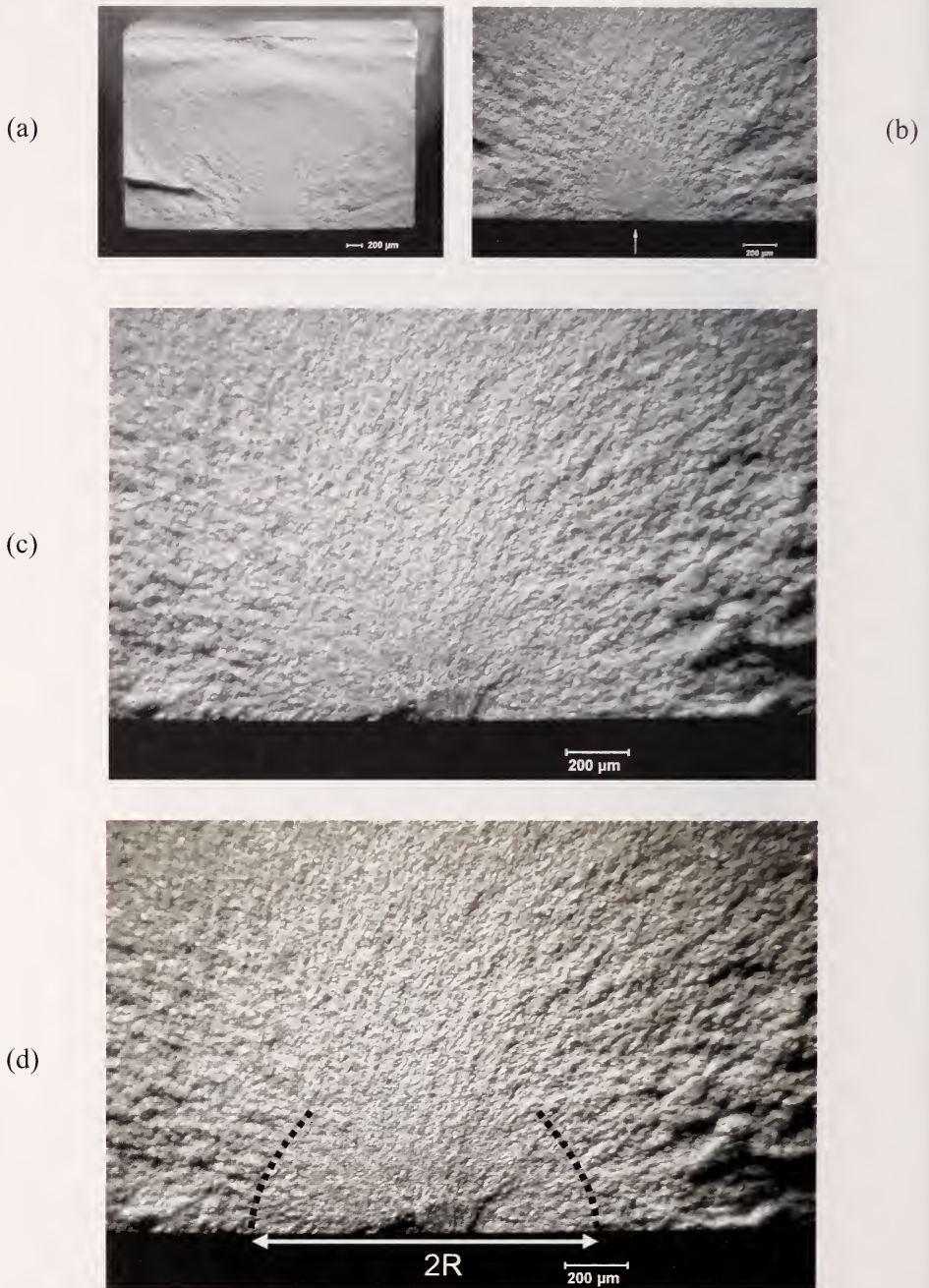


Figure D.3. Silicon nitride bend bar with a Knoop surface crack (449 MPa, Ceralloy 147-31N, Refs. 4,5). The mirror is incomplete into the stress gradient, but the mirror sides can be used to construct boundary arcs in (d). Radii are measured in the direction of constant stress along the bottom.

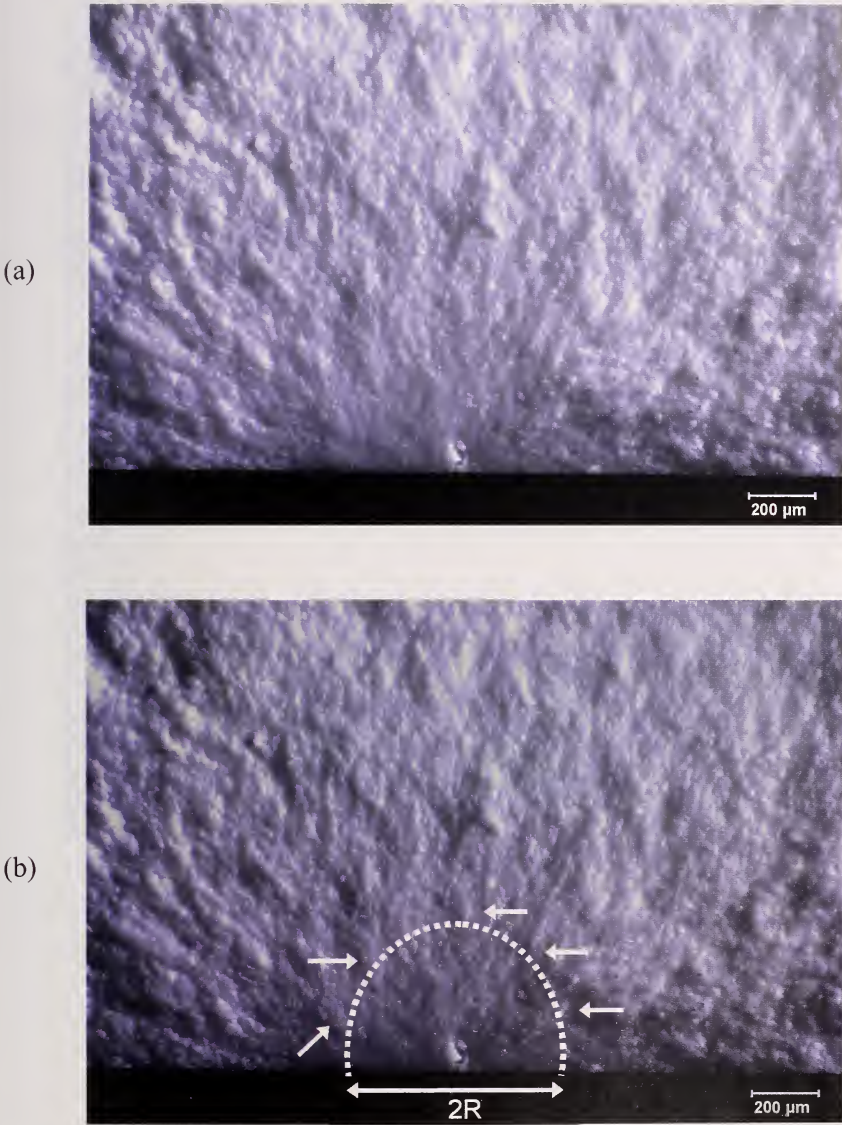


Figure D.4. Example of a mirror in a fine-grained 3 mol % yttria-stabilized tetragonal zirconia (3Y-TZP) polycrystal (Bosch, Ref. 6). The mirror is difficult to mark in this material. (a) shows the uncoated fracture surface of a 2.8 mm thick flexural strength specimen (486 MPa) with vicinal illumination. (b) shows an interpretation for a mirror-hackle boundary where systematic new hackle is detected (small white arrows) as compared to the roughness inside the mirror. The marked circle is elongated somewhat into the depth due to the stress gradient. The radius was 345 μm .

◆ Fractography of Ceramics and Glasses

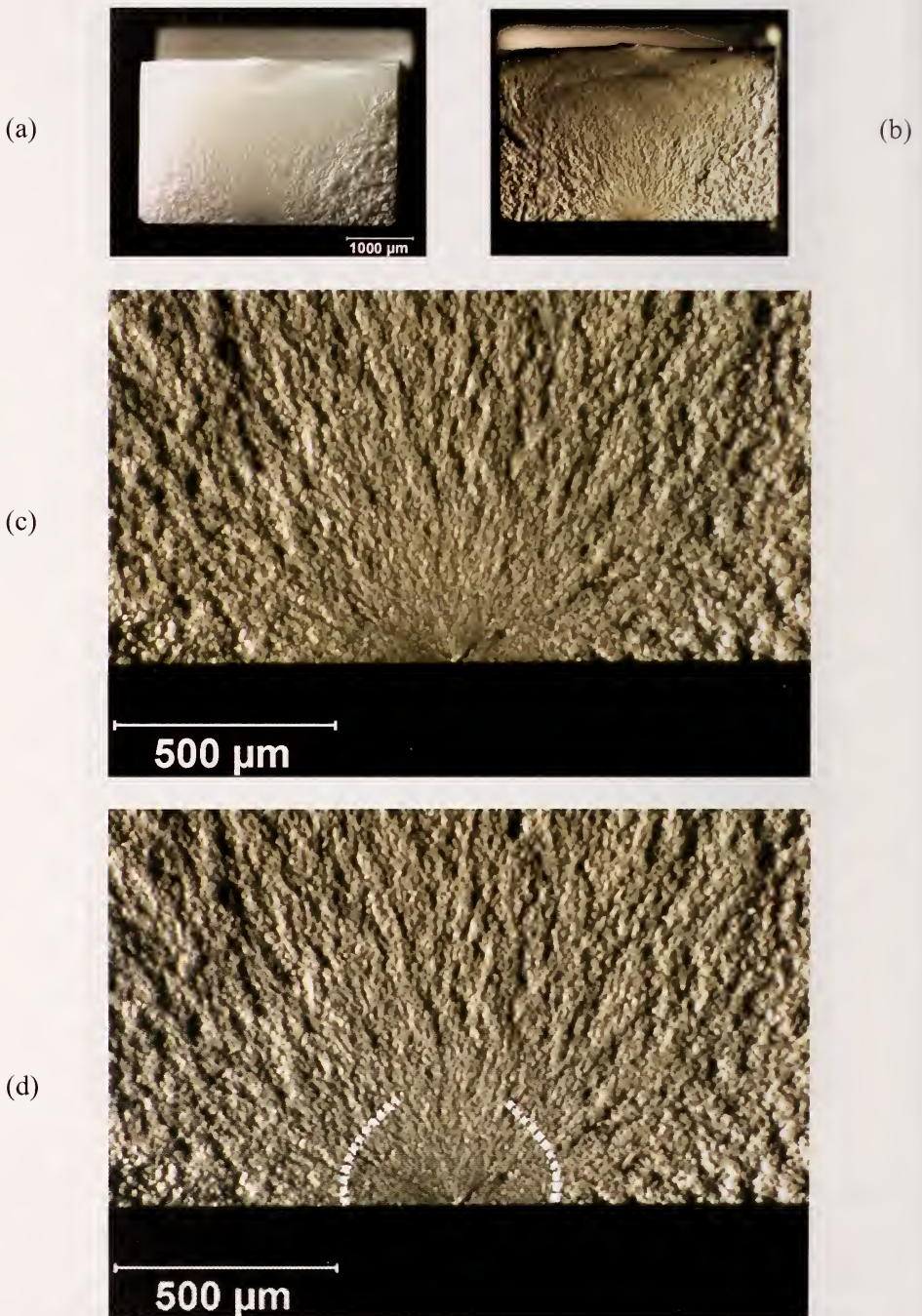


Figure D.5. Fracture mirror in a 3Y-TZP zirconia flexural strength specimen (Lava, 798 MPa). (a) and (b) are uncoated and gold coated images of the whole fracture surface, respectively. (Images courtesy J. Quinn)

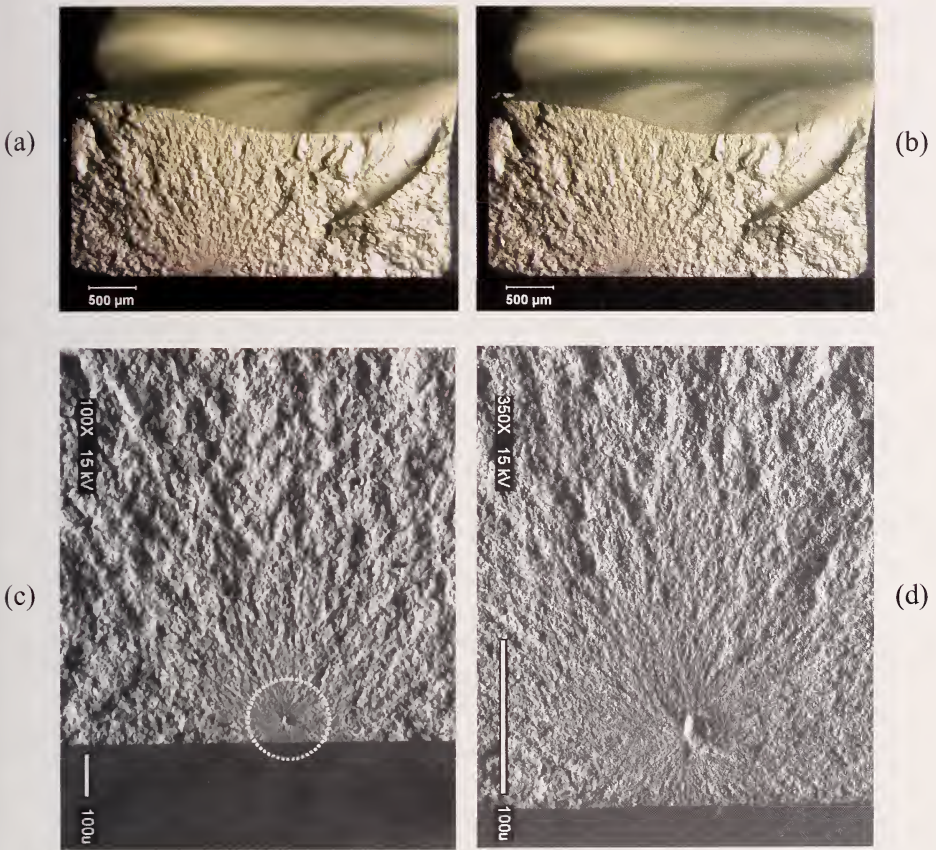


Figure D.6. Fracture mirror in another 3Y-TZP bend bar. (Lava, 1059 MPa maximum stress, 1024 MPa at the origin). (a) and (b) are stereo optical microscope images. (c) and (d) are SEM images. The flaw is a pore. Fine hackle lines in the mirror run right to the origin. They are created by the flaw itself and the microstructure. The mirror boundary is where systematic new hackle forms and there is an obvious difference compared to the roughness inside the mirror region. This is a very difficult example. One interpretation is shown in the lower magnification SEM image. (SEM images (c) and (d) courtesy J. Quinn)

D.2 Measure the Mirror Size

Use the following steps to measure mirror sizes. These steps are repeated, but with detailed notes, clarifications, and illustrations in section D.3 immediately following this section.

1. **Use an optical microscope whenever possible.** A compound optical microscope is best for glasses. A stereoptical microscope is best for ceramics. A thin coating may be applied to translucent or transparent ceramics. A scanning electron microscope may be used if optical microscopy is not feasible.
2. **The fracture surface should be approximately perpendicular to the microscope optical path or camera.**
3. **Optimize the illumination to accentuate topographical detail.** Ceramics may be coated with gold or carbon.
4. **Use a magnification such that the fracture mirror area occupies about 75% to 90% of the width of the field of view for glasses, and approximately 33% to 67% of the width of the field of view for ceramics.** An additional, lower-power image may be helpful for ceramics.
5. **Measure the mirror size while viewing the fracture surface with an optical microscope whenever possible.**

Use either calibrated reticules in the eyepieces or traversing stages with micrometer-positioning heads. Alternatively, measurements may be made on digital images on a high-resolution computer monitor, preferably while the fracture surface can be simultaneously viewed through the microscope eyepieces in order to aid judgment.

Measurements from photos may be used as a last resort if the steps above cannot be followed. This may be necessary for very small specimens or very strong specimens with tiny mirrors and a scanning electron microscope must be used to photograph the mirror.

Measurements from other devices may be used provided that the criterion used for identifying the mirror boundary is carefully documented.

6. **Measure radii in directions of approximately constant stress whenever possible.** A mirror diameter may be measured and halved to estimate the radius if the origin site is indistinct or complex.

7. Exercise caution when mirrors are large relative to the specimen cross-section size.
8. Show at least one photo with arrows or lines marking the mirror size.
9. Report how the mirrors were measured.

Additional steps for the determination of fracture mirror constants:

10. Use the stress at the origin site.

Correct the stress for location in specimens with stress gradients.

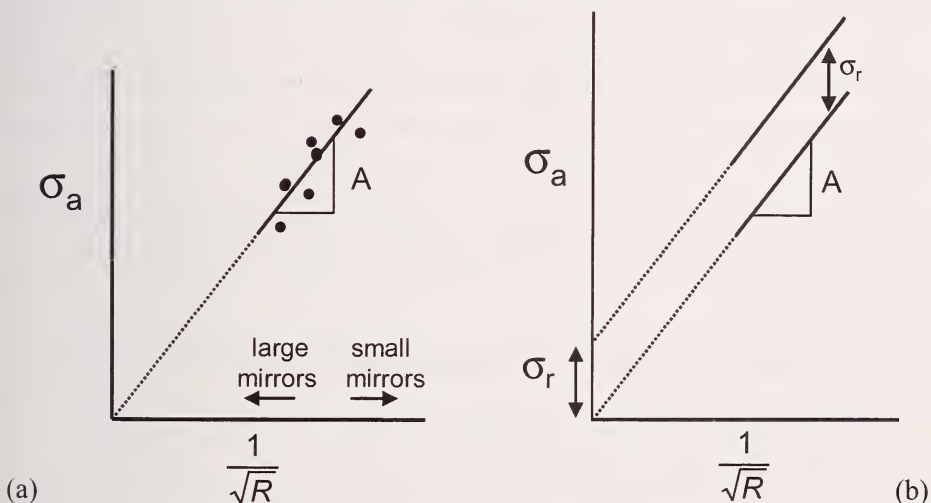


Figure D.7. Plot of applied stress σ_a (at the origin) versus $1/\sqrt{R}$. (a) shows the trend for residual stress-free parts. (b) shows it for parts with residual stresses. Compressive residual stresses move the locus up with a positive intercept σ_r , but with the same slope. Tensile residual stresses shift the data downwards with a negative intercept (not shown).

11. Evaluate the fracture mirror constants by regressing stress on inverse square root of mirror radius. (Preferred method)

Use linear regression methods to obtain A in accordance with equation D.2 with a forced zero intercept as shown in Figure D.7. A is the slope of the regression line.

$$\sigma_a = \frac{A}{\sqrt{R}} \quad (\text{D.2})$$

where σ_a is the stress at the origin site, computed from the known applied

stresses. A is the mirror constant and R is the mirror radius in the direction of constant stress.

Use some judgment in the regression analysis since fracture mirror data frequently has moderate scatter. If the data does not appear to fit a trend that has a zero intercept, regress the data with a non-zero intercept and equation D.3. Report the intercept if it deviates significantly (> 10 MPa) from zero. Investigate possible residual stresses or specimen size or shape issues if the intercept deviates significantly from zero.

$$\sigma_a = \frac{A}{\sqrt{R}} - \sigma_r \quad (\text{D.3})$$

where σ_a is the stress at the origin estimated from known applied stresses, σ_r is the residual stress at the origin location, and R and A are the same as before. A negative σ_r is a compressive residual stress and a positive σ_r is tensile.

12. Mirrors sizes should be collected over a broad range of sizes and fracture stresses if possible. Data from different specimen types and sizes may be combined.

D.3 Clarifications, Additional Notes, and Illustrations

1. Use an optical microscope whenever possible. A compound optical microscope with bright field illumination is best for glasses. A stereoptical microscope is best for ceramics. A thin coating may be applied to translucent or transparent ceramics. A scanning electron microscope may be used if optical microscopy is not feasible.

Differential interference contrast (DIC, also known as Nomarski) mode viewing with a research compound microscope *is not recommended* by this Guide. It is not suitable for rough ceramic fracture surfaces. It also creates complications with glass fracture surfaces. There is no question that DIC mode viewing can discern very subtle mist features in glasses, but the threshold of mist detectability is highly dependent upon how the polarizing sliders are positioned. Hence, DIC measured radii are quite variable. DIC measured radii can be substantially smaller than those obtained with conventional viewing modes. It also must be borne in mind that not all users have access to interference contrast microscopes.

Dark-field illumination may be used with glasses, but dark-field images may lose a little resolution with glasses and radii may be slightly larger as a result. It is very effective with highly-reflective mirror surfaces in single crystals.

Confocal optical microscopes and optical interferometers have been occasionally used to examine fracture mirrors, but the author is unaware of any systematic study to correlate apparent mirror sizes from these tools to those measured with conventional optical microscopes. The quantitative surface roughness capabilities of these instruments in principle could be used to correlate an average or root mean square roughness to the mist or hackle boundaries.

Scanning electron microscope images of mirrors are not recommended for measuring the mirror-mist boundary in glasses since the boundary is usually indiscernible at the magnifications needed to see the overall mirror. SEM images often appear flat and do not have adequate contrast to see the fine mist detail. SEM images may be used to measure mirror hackle boundaries with very small mirrors that would be difficult to see with optical microscopy, e.g., as in high strength optical fibers.

Scanning electron microscope images may be used for ceramics if necessary, but steps should be taken to enhance contrast and shadowing to produce images such as shown in Figures D-6c and d.

Attempts to correlate the mirror boundaries with a simple surface roughness parameter have produced mixed results. The work has been limited to glasses. Duckworth et al.⁷ carefully studied mirror sizes in float glass using optical photographs and a conventional surface profilometer. They obtained a good correlation with optical boundary estimates when the surface roughness reached a level of $0.25\ \mu\text{m}$ for the mirror- mist A_i boundary, and $5\ \mu\text{m}$ for the mist-hackle A_o boundary. Kuluwansa et al.⁸ used scanning tunneling microscopy (STM) to study mirror features and suggested the transition from a nano-mist region to the mist-hackle region with its rougher features (that were observable in the SEM) may be sharp. The characteristic scale of crack branching in the mirror to mist-hackle transition region ranged from $50\ \text{nm}$ (the size of typical nano-mist features) to about $50\ \mu\text{m}$ (the size of typical hackle features. Hull^{9,10} and Wünsche et al.¹¹ used atomic force microscopy to show that the mist region in glass or brittle epoxy has a roughness of as small as a few tens of nanometers, which is much less than the wavelength of visible light ($390\ \text{nm}$ to $800\ \text{nm}$). The scanned regions were quite small, however, and both groups noted that if the AFM scans a small region between hackle or river line steps, then the measured roughness is much less than if the latter are included. Hull pointed out that the greater undulations from Wallner lines need to be factored out when evaluating the intrinsic mist roughness. His study showed that roughness increased continuously and there were no

dramatic jumps in roughness at the boundaries, but the *rate of change* of roughness did change significantly at the mirror-mist boundary. Surface roughness measurements should be taken perpendicular to the direction of crack propagation since high-resolution transmission microscope images^{12,13,14} of the mist and hackle show the surface features are elongated in the direction of crack propagation.

Hull¹⁰ pointed out that different surface roughness characterization devices such as atomic force microscopes (AFMs), mechanical profilometers, and laser optical profilometers all have different advantages, disadvantages, sensitivities and scanning zone sizes. AFM's can measure tiny regions with very high sensitivities, but may miss large hackle steps in a mist or hackle zone. These latter features can dramatically alter the average or root mean square roughness. A mechanical stylus profilometer or laser profilometer with a 1 μm spot size may miss the small undulations and be more sensitive to larger hackle steps on the fracture surface. Mist and hackle regions may have different roughness at different scales. Hull discusses these various scales of roughness in some detail in his book.¹⁰

The author is not aware of any systematic studies comparing fracture mirror sizes as a function of the viewing mode or microscope type. Readers are encouraged to contact the author if they have more information on this topic.

2. The fracture surface should be approximately perpendicular to the microscope optical path or camera.

This simple and fairly obvious requirement is intended to avoid the foreshortening that can occur if the specimen is tilted. A small amount of tilting is acceptable in order to get a favorable reflection in a glass piece.

A compound optical microscope is best for glasses. A stereo optical microscope is best for ceramics.

The requirement poses a small problem if the mirrors are examined with stereo binocular microscopes. These have two different tilted optical paths. If viewing with both eyes in a stereomicroscope, the specimen should be flat and facing directly upwards. The observer's brain will interpret the image as though he is facing it directly.

Alternatively, if a camera is mounted on one light path of the stereomicroscope and it is used to capture or display the mirror, then the specimen should be tilted so that the camera axis is normal to the fracture surface.

For example, tilt the specimen to the right if the camera is attached to the right optical path.

3. Optimize the illumination to accentuate topographical detail.

The mist and hackle features should be accentuated. Glasses may either be illuminated from directly down onto a fracture surface or by grazing angle, vicinal illumination. Ceramics should not be directly illuminated since the light will reduce contrast, especially in translucent or transparent materials. Ceramics should be illuminated with vicinal illumination. Stereoptical microscopes are strongly preferred for ceramics. Vicinal illumination is less convenient with compound light microscopes. The observer should experiment with whatever illumination options are available to accentuate subtle surface roughness and topography features. Contrast and topographic detail should be emphasized with the SEM if it is necessary to use this mode of examination because the mirror is too small to be measured optically.

4. Use a magnification such that the fracture mirror area occupies about 75 % to 90 % of the width of the field of view for glasses, and approximately 33 % to 67 % of the width of the field of view for ceramics. An additional, lower-power image may be helpful for ceramics.

Observers usually mark the mirror boundaries closer to the origin at greater magnifications than they would at lower magnifications. This is because mist or micro hackle markings are easier to see at distances closer to the origin at high magnification. This is particularly the case with glasses. Conversely, at very low magnifications, much detail is lost and observers typically overestimate the mirror size.

Fracture mirrors are reasonably easy to see in glasses and magnifications should be used such that they nearly fill the field of view.

Mirror interpretation is more problematic with polycrystalline ceramics. Excessive magnification often leads to confusion as to where the boundary is located. Even though a mirror may be obvious at low or moderate magnifications, at higher magnifications it may be impossible to judge a boundary. It is more practical to view the mirror region (and the natural microstructural roughness therein) relative to the hackle roughness in the regions outside the mirror. "Stepping back" and using the 33 % to 67 % rule should help an observer better detect the topography differences. Images recorded at these magnifications are also more convincing when shown to other fractographers or engineers. Even lower magnification images may also be made to aid interpretation such as shown in Figures D-2b, D-3b, and D-6b. The images

should not be more than 5 times different in magnification; otherwise it is difficult to correlate features in one image to another.

Sometimes the microstructure of polycrystalline ceramics creates even worse judgment problems in ceramic matrix composites (particulate, whisker or platelet) or self-reinforced ceramics whereby elongated and interlocking grains impart greater fracture resistance. These difficulties were experienced in studies of the fracture surfaces of a self-reinforced silicon nitride^{2,3} and also a yttria-stabilized tetragonal zirconia polycrystal.⁴ Mirrors were plainly evident at low magnifications, but accurate assessment of their size was difficult. The mirror region itself was somewhat bumpy in the self-reinforced silicon nitride, so some judgment as to what was the mirror boundary was necessary. The zirconia had intrinsic micro hackle lines well within the mirror. The criterion for the mirror boundaries was as follows: *The mirror boundary was judged to be the point where systematic new radiating hackle commenced and there was an obvious roughness change relative to the inside-mirror region.*

The word systematic requires some elaboration. Mirror boundary hackle lines are velocity hackle lines created after the radiating crack reaches terminal velocity. Premature, isolated hackle can in some instances be generated well within a mirror, however. It should be disregarded when judging the mirror boundary. Wake hackle from an isolated obstacle inside the mirror (such as a large grain or agglomerate) can trigger early “premature” hackle lines such as shown in Figure 5.5. Steps in scratches or grinding flaws can trigger hackle lines that emanate from the origin itself.

5. Measure the mirror size while viewing the fracture surface with an optical microscope whenever possible.

A compound optical microscope is best for glasses. A stereoptical microscope is best for ceramics. Use either calibrated reticules in the eyepieces or traversing stages with micrometer-positioning heads. For routine measurements for ceramics, the author uses a stereo binocular microscope with a traversing X-Y stage with digital micrometer heads that read out to 0.001 mm (1 μm). Alternatively, measurements may be made on digital images projected onto a high resolution computer monitor preferably while the fracture surface can be simultaneously viewed through the microscope eyepieces in order to aid judgment.

Measurements from photos may be necessary for very small specimens or very strong specimens with tiny mirrors, such as in fibers or microelectro-mechanical system (MEMS) devices. Scanning electron microscope images may be

used. Again, the fractographer should take an overall framing photograph or image shot in accordance with the 75 % to 90 % rule for glasses and 33 % to 67 % rule for ceramics. Higher and lower magnification images may be used to help aid in interpretation.

Mirror size measurements from photographs are usually less accurate. They frequently overestimate mirror sizes unless conditions are carefully optimized to accentuate contrast and topographic detail. Two-dimensional photographic renditions of a three-dimensional fracture surface usually lose much of the topographic detail discernable by the eye with a compound optical or stereomicroscope.

Mirror size measurements made on computer monitor screens are also subject to inaccuracies, also because they are two-dimensional renditions of a three-dimensional fracture surface. Video cameras should not be used to capture mirror images since they lack adequate resolution. High-resolution cameras and monitors are beginning to match the capabilities and accuracy of an observer peering through the optical microscope.

6. Measure radii in directions of approximately constant stress whenever possible. A mirror diameter may be measured and halved to estimate the radius if the origin site is indistinct or complex.

There is no consensus on how many mirror radii measurements should be taken and in how many directions. Ideally, measurements should be taken from the center of the mirror region, but some judgment may be necessary. A common practice is to make a judgment whether a mirror is indeed approximately semicircular or circular. If it is, then multiple radii measurements may be made in different directions and averaged to obtain the mirror size estimate.

The center of the mirror may not necessarily be the center of the flaw at the origin. Careful inspection of tiny localized fracture surface markings (Wallner lines and micro hackle lines) right around the origin may reveal that fracture started at one spot on a flaw periphery. For example, fracture from grinding or impact surface cracks in glass often starts from the deepest point of the flaw and not at the specimen outer surface. Figure D.1 shows an example. Large pores often trigger unstable fracture from one side. An example is the pore in Figure D.6d, where fracture seems to have started on the left side of this internal flaw. If an exact mirror center cannot be determined, it is adequate to measure a mirror diameter and halve the measurement. This is commonly done for semicircular mirrors centered on irregular surface-located flaws whereby the mirror center may be difficult to judge.

Circular embedded mirrors are easiest to interpret (such as in Figure 5.7). Small semicircular mirrors on the surface of a part, such as in a bend bar or a flexurally loaded plate, are also not too difficult to interpret. The mirror relationship holds up remarkably well in glass optical fibers tested in tension for mirror radii almost as large as the fiber diameter.¹⁵ The mirror radius should simply be measured from the origin to the mirror-mist or mist-hackle boundary on the opposite side of the fiber, R_d as shown in Figure D.8.

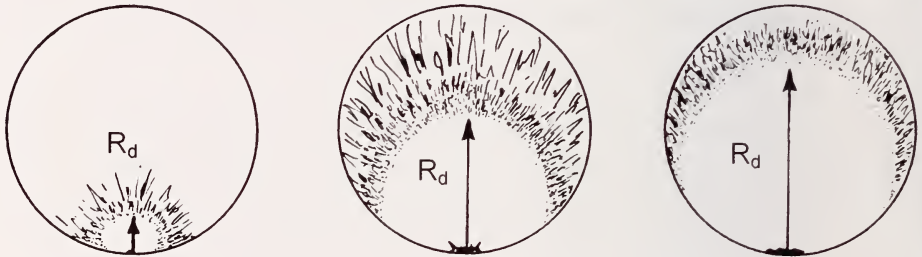


Figure D.8. Mirrors surrounding surface origins in rods or fibers loaded in direct tension. (After Ref. 12) Measure both the mirror-mist radius (shown) and mist hackle radii into the depth as shown.

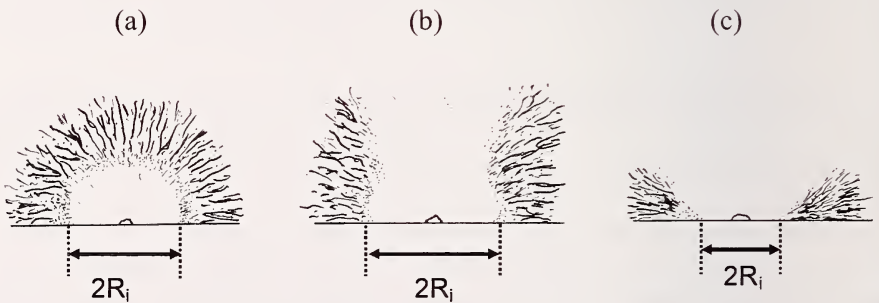


Figure D.9. Elongated mirrors in bending stress fields. If the mirror is small relative to the part size (i.e., a strong part), then the mirror may be semicircular as shown in (a). Weaker parts have larger mirrors that flare into the interior and are incomplete as shown in (b) and (c). Measure the mirror size (R_i or $2R_i$ for the mirror-mist in the illustrations here) in the direction of constant stress. (Note: special guidance on how to deal with small inward bending cusps at the surface is shown in Figure D.12 below.)

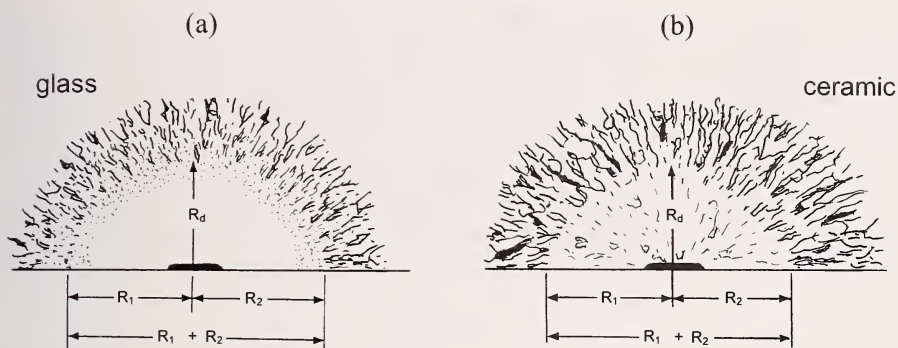


Figure D.10. Grinding cracks and scratches can cause mirror elongations along the surface, even in bend bars with stress gradients. (a) shows a schematic of such a mirror with the mist-hackle boundary marked in glass, and (b) shows a comparable image in a polycrystalline ceramic. It has some intrinsic microstructural roughness inside the mirror and the mirror-hackle boundary is marked. Use an average radius: $R_{avg} = \{(R_1 + R_2 + R_d)/3\}$.

Quarter circular mirrors centered on an edge or chamfer should be measured from the origin.

On the other hand, mirror shapes are commonly affected by stress gradients in a plate or a beam. Mirror radii are elongated in the direction of decreasing stress. Examples are shown in Figure D.9b and c. In such cases, measure the mirror radius along the tensile surface where the stress is constant. Do not measure the mirror radii into the gradient. Even with this precaution, there is considerable evidence that the data begins to depart from the stress-mirror size curves and the relationship in equation D.1 when the sizes approach the plate, beam, or rod thickness. For mirrors radii larger than the plate thickness, data points fall above the trend on a log stress – log mirror size plot which means that mirrors are larger than they would otherwise be if the part were loaded in uniform tension.

A trend for mirrors to elongate the opposite way, along the external surface of a specimen, was detected by the author in recent work on the fractographic analysis of grinding flaws in structural ceramics.^{2,3} Long surface cracks often caused mirrors to have perceptible deviations from a semicircular shape as shown in Figure D.10. In such cases, measure an average radius:

$$R_{avg} = (R_1 + R_2 + R_d) / 3.$$

In some cases, it may be difficult to measure mirrors in directions of constant stress. The two sides of a mirror may have unequal lengths since the stresses are different on either side of the mirror. Figure D.11 shows examples from the author's research of round rods broken in flexure. Many origins were not at the rod bottom where the stresses were a maximum, but part way up the side of the specimen. The specimen orientation was easily determined from observation of the cantilever curl. The maximum tensile stress on the bottom of the specimen was on the rod directly opposite the cantilever curl. It was a simple task (see section 9 below) to compute the actual stress at the origin location. The mirror radii had obviously different lengths due to the stress gradient. *Use a radius in the direction of constant stress, R_h , as shown in Figure D.11, if the mirror is centered on a well-defined origin site.*

If there is any doubt, then an average radius may be computed.

Use $R_{\text{avg}} = (R_1 + R_2 + R_d) / 3$ if the mirror is nearly semicircular.

Use $R_{\text{avg}} = (R_1 + R_2) / 2$ if the mirror is elongated into the interior and R_d is large or is incomplete.

For origins located in the interior of a rod broken in flexure, *only use the radii in the direction of constant stress.* As a check, and only if the mirror is a complete ellipse, one may measure two orthogonal mirror diameters and compute an average diameter and halve this to obtain an average radius.

There is one important detail about mirror sizes that warrants discussion. Mirrors located on a specimen external surface have *small cusps* at the intersection with the outer surface as shown in Figure D.12a. Cusps are often detected in glass mirrors, but they are rarely if ever discerned in polycrystalline ceramic mirrors. The small cusp is a consequence of fracture mechanics. A small element of material near the tip of a crack at the specimen exterior surface experiences greater stress intensity than a similar element buried in the interior whereby neighboring elements can "share the load." Kirchner et al.^{2,3} discussed the shapes of fracture mirrors that intersect outer surfaces and they showed that the local enhancement of the stress intensity K_I accounts for the cusps. The slightly-greater stress intensity at the surface triggers the mirror markings a bit sooner than for interior elements. *The usual convention, and the one adopted in this Guide, is to truncate the cusp. Extend the semicircular (or other mirror shape) arcs as shown in Figure D.12c.* Another reason to be wary of measurements right along the surface is that surface roughness, machining damage, or other surface irregularities may trigger mist or hackle formation a bit earlier than in the interior. Others have noted that measurements taken right on an exterior surface are slightly

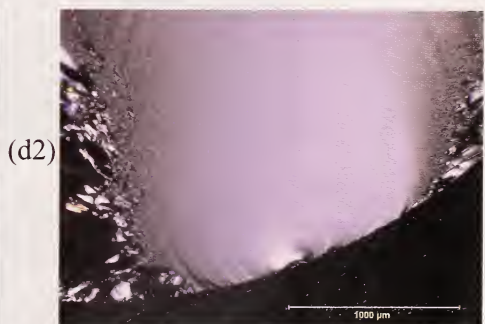
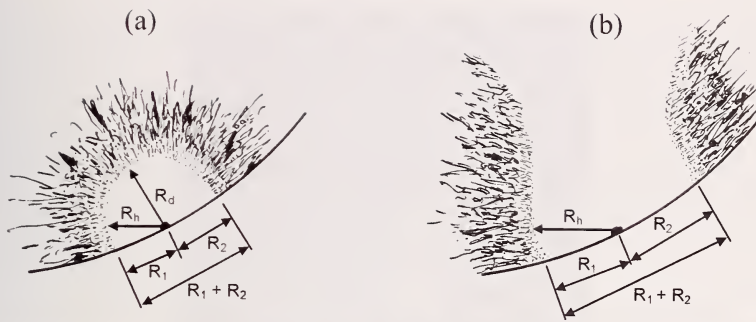
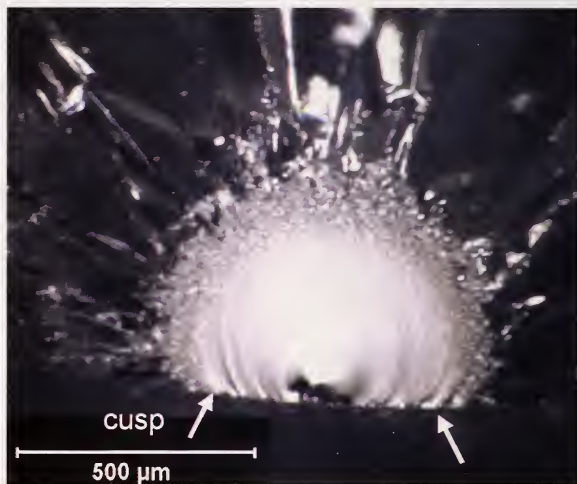


Figure D.11. Fracture mirrors in rods tested in flexure. The load was applied in a vertical direction and the maximum tensile stresses are at the bottom center. Fractures started at flaws part way up the sides of the rods causing the mirrors to have unequal radii. Schematics (a and b) are similar to two glass rods (c and d). The rod shown in (c) was sufficiently strong that a nearly semicircular mirror formed, but with unequal radii due to the stress gradient. Use $R = R_h$ if the origin and mirror center is distinct. Otherwise use $R_{avg} = (R_1 + R_2 + R_d) / 3$ if the mirror is nearly semicircular. Use $R_{avg} = (R_1 + R_2) / 2$ if the mirror is elongated into the interior and R_d is large. (d) shows a weaker glass rod. Use $R = R_h$ if the origin and mirror center are distinct, otherwise use $R_{avg} = (R_1 + R_2) / 2$.

(a)



(b)



(c)

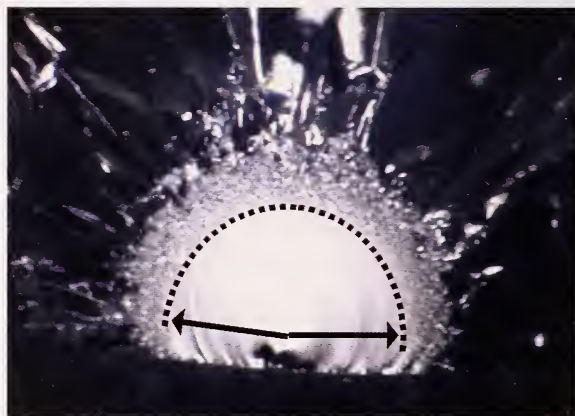


Figure D.12. Fracture mirror in a fused silica rod (a), illustrating the cusps in the mirror near the outer surface (b). Mirror measurements should not include the inward bend of the mirror and may be made as shown in (c).

different than those taken into the interior. Even Shand¹⁶ recommended in 1959 that size measurements be taken 0.1 mm (.004 in) beneath the exterior surface. Mecholsky and Freiman¹⁷ in 1979 recommended ignoring the cusp at the surface on the basis of fracture mechanics considerations: “In measuring the mirror-mist and mist-hackle boundaries, these should be projected to the tensile surface to compete a circular arc, since there is curvature at the surface due to free surface effects.”

A dilemma occurs when mirrors are large in plates or beams broken in flexure as shown in Figure D.9c. Cusps cannot be detected. In this case the only plausible way to measure a mirror radius is directly along the surface. In such cases, the general warning of step 7 applies.

It is worth reiterating that equations D.1 and D.2 are empirical. Kirchner and colleagues^{2,3} showed a more rigorous fracture mechanics analysis (based on a critical stress intensity for branching) completely explained the mirror shapes and distortions including the cusp mirrors in various stress fields. Despite the merits of their rigorous fracture mechanics analysis, there is significant practical advantage to using the simpler mirror size - stress relationships D.1 and D.2 even if some rigorousness is sacrificed. In addition, for small mirror sizes relative to the specimen dimensions, the simpler approach is almost as rigorous.

Residual stresses alter mirror shapes. If the mirror is very small relative to the stress gradient, the mirror shape may remain circular or semicircular if along the surface. On the other hand, if the mirror is larger or the stress gradient is steep, then the gradient alters the mirror shape as shown in Figure D.13. Figure D.13a shows an annealed plate that requires an applied stress of $\sigma_a = \sigma_f$ to cause fracture. Figure D.13b shows the case where the same plate has residual surface compression stress $\sigma_r = \sigma_c$ from ion exchange or thermal tempering, so that an applied stress to cause fracture is $\sigma_a = \sigma_f + \sigma_c$. In other words, the applied stress must be increased to overcome the residual surface stress. Nevertheless, the net stress at the surface at the moment of fracture is $\sigma = \sigma_a - \sigma_c = (\sigma_f + \sigma_c) - \sigma_c = \sigma_f$, the same stress as in the annealed plate. Hence the mirror radii along the surface are unchanged compared to the annealed plate. In contrast, in the direction into the interior, tensile stresses combine with the applied tensile stress to cause the mirror markings to form sooner, at a shorter radius into the interior than in the annealed plate. In this example, the mirror shape is flattened to a semiellipse. Mirror radii should be measured *only along the surface* (or just beneath the surface if there is a cusp) in these cases.

7. Exercise caution when mirrors are large relative to the specimen cross-section size.

At some point, one can expect departures from the stress - mirror size relationship. The point where the departure occurs depends upon the loading geometry and the stress state.

Pronounced deviations occur once the mirror size approaches or is greater than the component thickness in plate or beam *bending* fractures. Experimentally measured radii are much greater than predicted by equation D.1. Shand recommended that the maximum mirror size should be no more than 15% of the rod diameter (or 30% of the distance to the centroid) for *flexure* tests.^{16,18} Kirchner and Conway³ warned about limitations in the fracture mechanics models for mirror radii exceeding 20% of a rod diameter tested in flexure. On the other hand, Castilone et al.¹⁵ had success with mirrors that were almost as large as the fiber diameters for fibers tested in direct *tension*.

There is merit to measuring and recording mirrors even if they are large relative to a cross section size. The data may have value for use with analyzing genuine component fractures.

Mecholsky and Freiman¹⁷ warned that systematic deviations from the mirror size relationship occur at large mirror sizes but also at very small sizes, the latter due to internal stress effects, e.g., from thermal expansion anisotropy of grains in ceramics.

8. Show at least one photo with arrows or lines marking the mirror size.

This simple step will help clear up a lot of the doubt and confusion about what an investigator has actually measured.

9. Report how the mirrors were measured.

This simple last step is often overlooked or ignored, and the reader is left wondering exactly what had been done. The fractographer should report the microscope used, whether interpretation was made while looking through the microscope or from photos, and approximately what magnifications were used. The direction the mirror radii were measured should be documented. The approximate shape of the mirrors (semicircular, circular, or elliptical) should be noted. It should also be noted whether the mirrors were an appreciable fraction of the size of the cross section or not. Lastly, and most importantly, the judgment criterion used should be reported.

10. Use the stress at the origin site. (additional steps to determine A)

If the specimen was broken in controlled conditions where the stress distribution was known (e.g., beams, rods, or plates in flexural loadings) correct the stress for location in specimens with stress gradients.

No correction is needed if a part was stressed in uniform tension. On the other hand, many parts or laboratory specimens do have stress gradients. The general principle that should be followed is that the mirror formation is guided by the stresses that acted on and in the immediate vicinity of the flaw origin. While this may seem obvious, it is probable that some analysts in the past have erroneously used *nominal stresses* in a specimen or component rather than the *actual stress* that was acting upon the mirror region in a body. In contrast, some researchers have correlated the stress at every site along the mirror periphery with the mirror radius at that periphery site, but this complex process is not practical on a routine basis.

Example 1: Flexural strength test specimens

The nominal flexural strength is the maximum stress at the outer fiber or tensile surface of the bar. The stress correction for locations beneath the surface is simple if the material is linearly elastic. The stress decreases from a maximum at the outer tensile surface to zero at the middle “neutral axis” which corresponds to the centroid in a square, rectangular, or circular cross-section beam specimen as shown in Figure D.14. At the origin, $\sigma = (2y/h) * \sigma_{\max}$ where y is the distance from the centroid and h is the beam thickness or rod diameter. Alternatively, in terms of the distance from the tensile surface, y' : $\sigma = (1 - 2y'/h) * \sigma_{\max}$.

In similar fashion, if a fracture origin is not directly under the middle loading point in three-point bending, or if the origin is outside the inner gage length in four-point bending, then the stress should be correspondingly adjusted to the stress that actually acted on the origin site. Corrections for breaks outside the gage section or away from the middle loading point are also linear. The stress is reduced in proportion to the distance from the fracture plane to the outer loading points. This correction requires knowledge of the loading point locations. This is an important reason why loading points should be marked on any test piece prior to its fracture. For three-point loading:

$\sigma = (2x/L) * \sigma_{\max}$, where x is the distance from the outer loading point to the fracture plane and L is the total three-point span. For four-point flexure, $\sigma = (x/a) * \sigma_{\max}$, where x is the distance from an outer loading point to the fracture plane, and a is the distance from the outer loading point to an inner

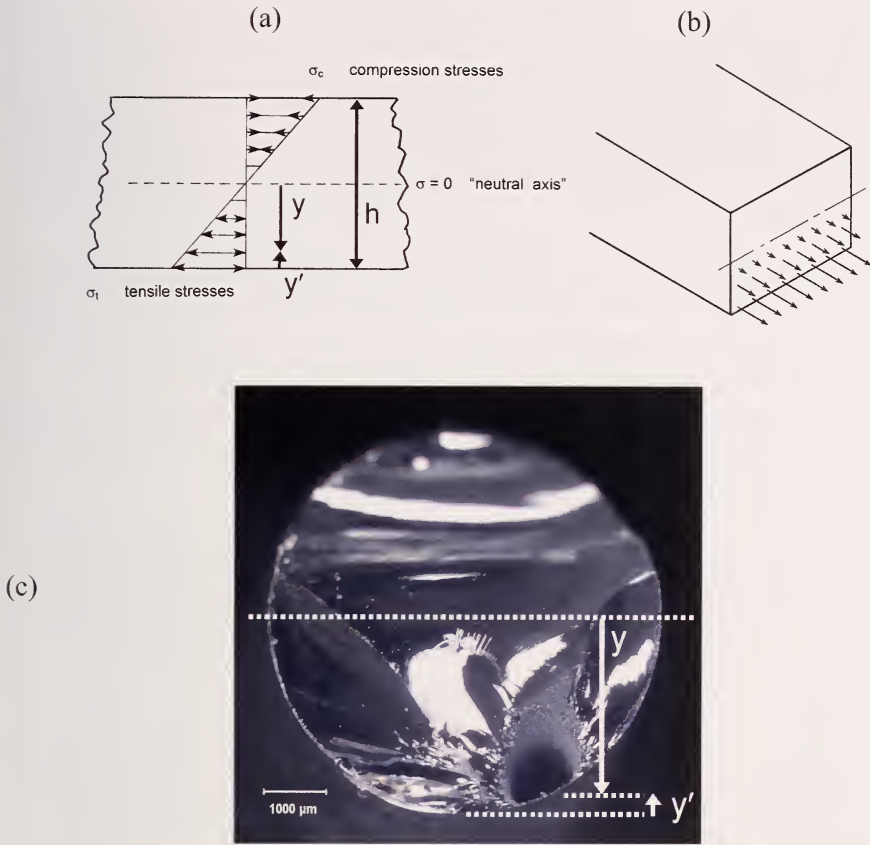


Figure D.14. The flexural stress gradient is shown in (a) and (b) for a rectangular beam. (c) shows how the origin location may be measured from a rod neutral axis.

loading point. If an origin in a flexural beam is subsurface and outside the inner span, then both corrections should be applied. If the origin is on the tensile surface, within the inner span length, and the mirror size is small and semicircular, then no stress correction is needed.

Example 2: Ring-on-ring biaxial strength test specimens

If the origin is on the tensile surface in the inner loading circle, and the mirror size is small and semicircular, then no stress correction is needed. Fracture mirrors from volume flaws located beneath the tensile surface should be corrected in the same manner as above for the uniaxial bend test methods. Corrections for mirrors located outside the inner loading ring also should be

corrected for location. The corrections are not as simple in this case, however. In the annulus outside the inner loading ring, the radial and circumferential (hoop) stresses decrease out to the specimen rim but at different rates.¹⁹ Radial stresses decrease faster, and are zero at the outer rim, and are therefore less likely to induce fracture. Fracture planes and mirrors will usually be perpendicular to the hoop stresses outside the inner ring, so use the hoop stress in the analysis.

On the other hand, hoop stresses decrease more slowly and *are non-zero at the outer circumference* of the specimen. So although the outer hoop stresses are only 10% to 50% of the maximum stress in the inner circle (depending upon the disk and fixture geometries, and especially the disk thickness), large grinding or handling flaws on the specimen rim can cause fracture. The notion that ring-on-ring biaxial strength specimens do not require edge treatments is a common misconception.

The same comments apply to piston on three-balls, ball on three balls, or even pressure loaded plates in bending. Consult appropriate references as needed for the stress distributions in these configurations.

Example 3: Component failure analyses

If the mirror constant for the material is known and a mirror size is measured, the stress at the origin site can be calculated. The peak stress or the nominal stress in the part may be different, however. So as a rudimentary example, imagine a bend bar that broke from an internal origin site, but at an unknown stress. The fractographer uses the mirror size and the mirror constant to estimate the stress at the origin site. The nominal strength of the beam (the maximum outer fiber stress) or the “flexural strength” is greater, however. In this case, the stress adjustment should use σ , A , h , x , y or y' to compute the greater nominal stress, σ_{\max} .

11. Evaluate the Fracture Mirror Constants.

Once a set of matching mirror radii and fracture stresses is compiled, it is customary to plot the data on either a graph of log stress versus log mirror size or linear stress versus inverse square root of mirror size as shown in Figure D.7. A linear regression analysis is then performed and a mirror constant calculated from the regressed line. The mirror constants should be reported as either $\text{MPa}\sqrt{\text{m}}$ (or $\text{ksi}\sqrt{\text{in}}$ if the older units are in use). There is no consensus as to which graphical representation is better. Both are widely found in the literature. Each is discussed in turn and it is this author's conclusion that *the stress versus inverse square root of size procedure is better*.

11a. Plot σ versus $1/\sqrt{R}$. (Preferred)

Use linear regression methods to obtain A in accordance with equation D.2 with a zero intercept. In a typical strength test experiment in a laboratory, applied stress, σ_a , and mirror radius, R , are independently measured. It is customary to regress σ_a on R and this procedure shall be followed in this Guide. A is the slope of the regression line.

$$\sigma_a = \frac{A}{\sqrt{R}} - \sigma_r \quad (\text{D.2})$$

Use some judgment in the regression analysis since fracture mirror data usually has moderate scatter. If the data does not appear to fit a trend that has a zero intercept, regress the data with a non-zero intercept as shown in Figure D.7b. Again use some judgment in the interpretation, since a strict linear regression fit may produce implausible outcomes, particularly if the data is collected over a limited range of mirror sizes and stresses. Report the intercept if it deviates significantly (>10 MPa) from zero. Investigate possible residual stresses or specimen size or shape issues if the intercept deviates significantly from zero.

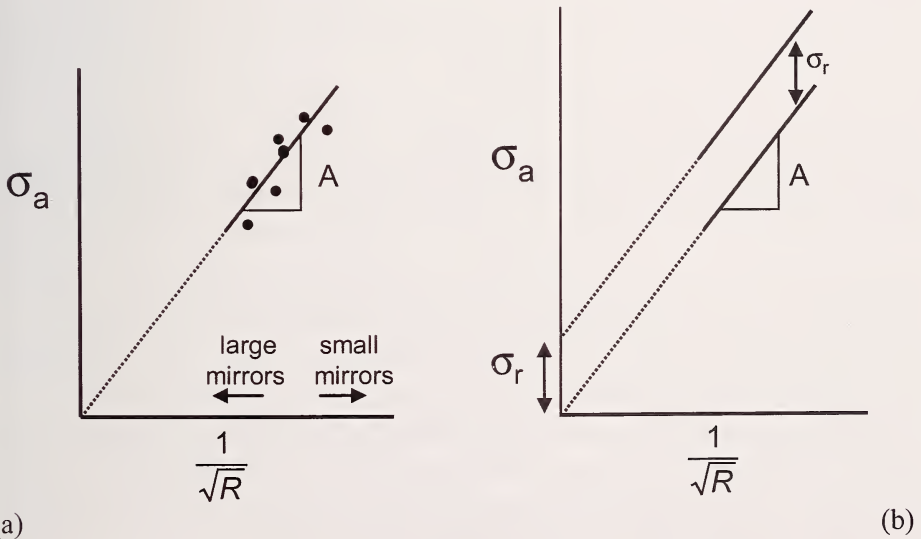


Figure D.7 (duplicate) Plot of applied stress, σ_a , versus $1/\sqrt{R}$, the preferred regression method. (a) shows the trend for residual stress-free parts. (b) shows it for parts with residual stresses. Compressive residual stresses move the locus up with a positive intercept σ_r , but with the same slope. Tensile residual stresses shift the data downwards with a negative intercept (not shown).

Consistent units should be used with this approach. That is to say, if the stress axis is MN/m^2 or MPa , then the abscissa (horizontal axis) should be $1/\sqrt{R}$ where radius is in units of *meters*. If the mirror is measured in mm or μm , then appropriate conversion factors should be added, but this is not trivial and can cause confusion, since the square root of a conversion factor of 1000 (e.g., meters to mm) is an odd value. (If the stress units are psi or ksi , the mirror radii should be measured in inches.)

The mirror constant as a slope is easily visualized. In addition, deviations from the trend usually cause a nonzero intercept, which may be conveniently interpreted as an effective residual stress. If residual stresses σ_r are present in addition to the externally applied stress, σ_a , then the net stress acting on the origin site is: $\sigma_a + \sigma_r$. The fracture and the mirror markings respond to the actual net stress, σ_{net} :

$$\sigma_{\text{net}} = (\sigma_a + \sigma_r) = \frac{A}{\sqrt{R}} \quad (\text{D.3})$$

and:

$$\sigma_a = \frac{A}{\sqrt{R}} - \sigma_r \quad (\text{D.4})$$

An intercept below the origin corresponds to a net tensile residual stress. A positive intercept corresponds to residual compressive stress since the usual sign convention is for compressive stresses to have a negative sign.

Some caution is advised since residual stresses are often nonuniform. The residual stress estimated from the intercept is an effective residual stress, which in reality may vary in magnitude through the mirror region. If the mirror is in a heat strengthened or tempered piece (where stress may be constant along the surface, but change dramatically through the thickness) the mirrors should only be measured along the surface or just underneath to avoid the cusp. Residual stresses from an indentation or impact site are very local to the origin and may have very little effect on a mirror size.

Although most researchers have felt that the regressed lines should go through the origin in annealed test pieces, there is evidence by J. Quinn²⁰ that a small but measurable intercept may exist in even annealed materials. The intrinsic intercept was evaluated as 10 MPa (1,500 psi) for glass, a value that

interestingly concurs with Orr's²¹ estimate of the minimum stress necessary for branching in glass.

11b. Plot $\log \sigma$ versus $\log R$. (Alternative method)

Use linear regression methods to fit the data in accordance with equation D.5 (slope set at $-\frac{1}{2}$) as shown in Figure D.14a. The mirror constant A corresponds to the stress that would create a mirror of size = 1.

$$\log \sigma_a = -\frac{1}{2} \log R + \log A \quad (\text{D.5})$$

where σ_a is the stress at the origin site, A is the mirror constant and R is the mirror radius in the direction of constant stress.

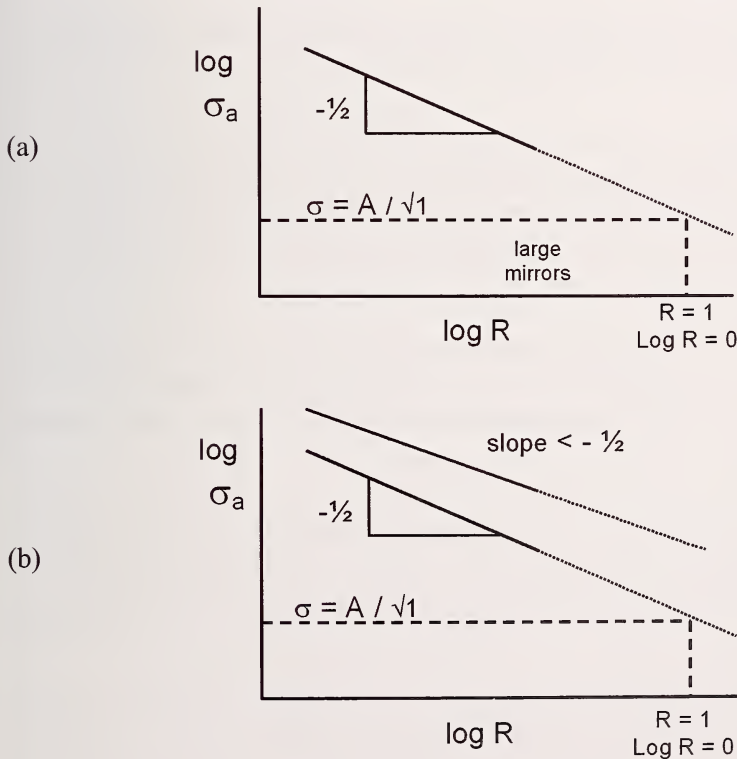


Figure D.15. Plot of $\log \sigma_a$ versus $\log R$ for residual stress-free parts (a) and parts with residual stress (b). Compressive residual stresses move the locus upwards, but with a different slope and intercept. Tensile residual stresses move the loci below the baseline curve (not shown).

Use some judgment in the regression analysis since fracture mirror data frequently has moderate scatter. If the data does not appear to fit a trend with slope $-1/2$, then regress the data with equation D.6:

$$\log \sigma_a = m \log R + \log A' \quad (D.6)$$

where σ_a is the stress at the origin estimated from known applied stresses, R is the mirror radius in the direction of constant stress. A' is a modified mirror constant.

Report the slope m and the alternative constant A' . Again use some judgment in the interpretation, since a strict linear regression fit may produce implausible outcomes, particularly if the data is collected over a limited range of mirror sizes and stresses.

Investigate possible residual stresses or specimen size or shape issues if m deviates significantly from the value $-1/2$.

If stresses are in units of MN/m^2 (MPa) and the mirror size is measured in meters, then the mirror constant A has units of $\text{MN/m}^{1.5}$ or $\text{MPa}\sqrt{\text{m}}$. If the mirror size is 1 m, then $\log R = 0$. Then $\log \sigma = \log A$ and hence, $\sigma = A$. Hence, the mirror constant A corresponds to the value of stress that would create a mirror of size 1 m.

Consistent units also should be used with this approach for the same reasons mentioned in section 11a. If the stresses are in MPa, then the abscissa (horizontal axis) should be with radii in units of *meters*. (If the stress units are psi or ksi, the mirror radii should be in inches.)

Since most actual mirrors that are measured are usually much smaller than unit size, it is apparent from Figure D.15 that the mirror constant (or the stress at $R = 1$) lies somewhat beyond the range of data usually collected. This method of showing the results and calculating a mirror constant was common in the older technical literature and is occasionally still found today. Deviations from the linear relationship on a log - log plot occur when residual stresses are present but unaccounted for (since the plotted stress may not be the true stress at the origin), or when the mirror size becomes large relative to the component size, or when there are stress gradients. The residual stress deviations cause the line to have a slope other than $-1/2$ as shown in Figure D.15b. Attempts to compute the residual stresses may then be made by guessing values of the residual stresses σ_r , replotting the data, with a vertical

axis of: $\sigma_a - \sigma_r$ and checking the goodness of fit of a line of slope $-1/2$. This is a fairly cumbersome process and the alternative procedure in section 11a and Figure D.7b may be simpler and more effective.

If a single mirror is measured, and the externally applied stress, σ_a , and the mirror constant A are both known, then:

$$(\sigma_a + \sigma_r)\sqrt{R} = A \quad (\text{D.7})$$

and

$$\sigma_a = \frac{A}{\sqrt{R}} - \sigma_r \quad (\text{D.8})$$

Mecholsky and colleagues^{22, 23} have shown excellent examples how residual surface stresses in tempered or clad glasses may be estimated from equation D.8 and fracture mechanics analysis.

11c. Comparison of the two curve fitting and regression approaches.

The merits of the two plotting - regression schemes have not been directly compared to the best of the author's knowledge. The regression analyses put different weights on large and small mirror measurements. In one case the mirror constant is a slope of a line, in the other it is an intercept at $R = 1$, a rather large mirror size not likely to be realized in practice. Some of the variability in published mirror constants that are tabulated in Appendix C probably is due to the use of the two different curve-fitting schemes.

It is also certain that some researchers have evaluated unannealed test pieces and then force fitted regression lines through the data with zero intercepts in the former scheme or lines of slope $-1/2$ through the data in the latter scheme. This undoubtedly also has contributed to variability in published mirror constants.

Data from flexurally-loaded specimens frequently deviate from the trends when mirror sizes are large and are a significant fraction (50 % or greater) of the cross section size. Upward deviations from the log stress - log radius graphs have been noted in a number of studies (e.g., Shand^{18,24}, Orr²¹). The experimentally measured mirrors are larger than they otherwise would be in a uniform tension stress field. Regression lines chase the upward deviations from the trend and dramatically alter the estimate of the mirror constant. On the other hand, with the σ versus $1/\sqrt{R}$ graph, large or oversized mirror

data points are closer to the origin and have less influence on the regression line, and hence have less effect upon the slope.

Regression analysis with the σ versus $1/\sqrt{R}$ approach minimizes the deviations of σ from the fitted line. Regression analysis for the $\log \sigma$ versus $\log R$ approach minimizes deviations of $\log \sigma$ from the fitted line. The former is preferred from a mathematical perspective.

In the 1950s and 1960s many researchers plotted log stress versus log radius probably because they were not confident of the theoretical justification for the $-1/2$ slope. They let the exponent vary on the log-log plots and discussed the differences, if any, relative to $-1/2$ power. Any differences were usually due to residual stresses or overly-large mirrors relative to the specimen size. Gradually the case for the $\sigma\sqrt{R}$ relationship solidified and more researchers began to plot stress versus $1/\sqrt{R}$. The case for the relationship is now very strong and there is no reason not to use it.

In summary, *the linear stress versus inverse square root radius approach is superior and is adopted in this Guide*. Analyses are simple and intuitive. The mirror constant is the slope of the regressed line. Residual stresses may be interpreted from non-zero intercepts. The uncertainty of the slope can be estimated from routine analyses available in many statistical software packages. Data deviations due to large mirrors in flexure specimens have less effect upon the regression process and the mirror constant estimates. The alternative method (log stress – log radius) may be useful in some cases for displaying data with an unusually large range of mirror sizes and stresses.²⁵

12. Mirrors sizes should be collected over a broad range of sizes and fracture stresses if possible. Data from different specimen types and sizes may be combined.

This is a fairly obvious conclusion in light of the discussion in the previous paragraph. Superb examples are shown by Kerper and Scuderi²³, for borosilicate glass rods with diameters that varied by a factor of ten, and by Mecholsky and Rice²⁶ for various sized fused silica rods, disks, and fibers.

Ideally, data from many small specimens could be complemented by judicious testing of a few large specimens. Another common procedure is to anneal or fine grind/polish some specimens to obtain high strengths, but also abrade or damage others to obtain low strengths. Sometimes the mode of loading can be changed to alter the fracture stress. For example, some studies have generated

mirrors with large four-point and small three-point flexure specimens. Some specimens may be tested in inert conditions and others tested in conditions conducive to slow crack growth.

D.4 Some Final thoughts

The goal of these guidelines is to bring some consistency to procedures used to measure fracture mirrors. This should facilitate improved data bases and better estimates of failure stresses. Appendix C of this guide is simply a compilation that lists all mirror constants known to the author. It is not an evaluated data base, however. Some of the entries are probably faulty or wrong.

These Guidelines have been prepared on the basis of the author's own experiences as well as a careful review of sixty years of literature. One is struck by the conclusion, which nearly all writers have reached, that measurement of the mirror sizes requires subjective interpretation. The perception of the observer and the type of equipment are important factors. Although advanced microscopy and software tools hold considerable promise in the future, it is unlikely that a simple definitive criterion (such as a set level of surface roughness) will emerge. Despite this, most students of the technique have concluded that consistent readings are possible between observers. The quotation from Johnson and Holloway¹ at the start of this Appendix is one example. Another is from Mecholsky and Freiman¹⁷ who said:

“While one might think initially that the measurements of a mirror boundary using a microscope is quite a qualitative operation and would vary from observer to observer; in fact, experiments performed over a number of years by a large number of investigators have shown that the values of mirror constants obtained in different laboratories are quite nearly the same.”

They then listed some values for a few glasses and ceramics that did in fact vary as much as 20% to 30%. For example, the soda-lime glass values varied by 23%. Hopefully, adoption of the guidelines in this Guide will improve the consistency of future data to within 10%.

One positive conclusion is that fracture mechanics principles do seem to account for the observed shape variations in mirrors.^{2,3} (A caveat is that the fracture mechanics analyses have been based on static loading, whereas the mirror boundaries are formed by a very dynamic crack traveling at or near terminal velocity.) A logical conclusion of this finding is that equation 1 is

over simplistic, since it does not account for stress gradients or geometric effects. Nevertheless, it *does have the proper functional form* for the stress intensity of a crack in a far-field tension stress. For a small mirror in a uniform tensile stress field, equation 1 is completely justifiable.

Another interesting finding from the literature review is how few authors have shown good fracture mirror photos and how even fewer have marked them. One is left with the conclusion that the authors themselves were not sure or were hesitant to show an interpretation for fear of criticism. Hopefully, step 8 of this Guide (which requires marked photos be presented) and the examples shown in this Guide will help future authors improve their reporting. One is also struck by the fact that nearly all the mirrors shown in the literature, even in the classical papers, are not exactly semicircular or circular, despite all the schematics that imply that they are. So future fractographers should not be alarmed if their mirrors are not perfect.

Many of the steps in this Guide have already been proposed. Shand recommended that stresses be corrected for the origin location,¹⁸ that radii be measured beneath the surface to avoid surface effects,¹⁶ that low angle vicinal illumination be used.¹⁸ He also warned about deviations from the trends if the mirror sizes were too large relative to the component thickness.¹⁸ Shand also said that mist could not be discerned in glass ceramics.¹⁸ Morrell et al.²⁷ agonized over the interpretation of mirrors in Y-TZP zirconia (such as shown in Figures D.4 – D.6), but settled on a set of specific criteria. Optical microscopy with a stereo optical microscope at a fixed magnification was used, with grazing incidence illumination. No reflective coating was applied to the surface, but the specimen sides were masked to block transmitted light scatter. Matching fracture halves were mounted together to aid the interpretation. The best set of recommendations predating this Guide were crafted by Mecholsky and Freiman.¹⁷ Six of their recommendations match steps in this Guide: optical microscopy is preferred over scanning electron microscopy whenever possible, suitable magnifications should be used, mirror boundary arcs should be projected to the outer surface to complete a circular arc to eliminate the surface cusps, lighting should be varied to obtain optimum contrast, radii should be measured in directions of constant stress and not into gradients, and that deviations of the trends can be expected for large mirrors relative to part thickness.

Appendix D References

1. J. W. Johnson and D. G. Holloway, "On the Shape and Size of the Fracture Zones on Glass Fracture Surfaces," *Phil. Mag.* **14** (1966) 731 – 743.
2. H. P. Kirchner and J. W. Kirchner, "Fracture Mechanics of Fracture Mirrors," *J. Am. Ceram. Soc.*, **62** [3-4] (1979) 198 – 202.
3. H. P. Kirchner and J. C. Conway, Jr., "Criteria for Crack Branching in Cylindrical Rods: I, Tension and II, Flexure," *J. Amer. Ceram. Soc.*, **70** [6] (1987) 413 – 418 and 419 – 425.
4. G. D. Quinn, L. K. Ives, and S. Jahanmir, "On the Fractographic Analysis of Machining Cracks in Ground Ceramics: A Case Study on Silicon Nitride," SP 996, NIST, Gaithersburg, MD, May, 2003.
5. G. D. Quinn, L. K. Ives, S. Jahanmir, and P. Koshy, "Fractographic Analysis of Machining Cracks in Silicon Nitride Rods and Bars," pp. 343 – 365 in *Fractography of Glasses and Ceramics IV*, Ceramic Transactions, Vol. 122, eds, J. Varner and G. Quinn, American Ceramic Society, Westerville, OH, 2001.
6. G. D. Quinn, J. Eichler, U. Eisele, and J. Rödel, "Fracture Mirrors in a Nanoscale 3Y-TZP," *J. Amer. Ceram. Soc.*, **87** [3] (2004) 513 – 516.
7. W. H. Duckworth, D. K. Shetty, and A. R. Rosenfeld, "Influence of Stress Gradients on the Relationship Between Fracture Stress and Mirror Size for Float Glass," *Glass Technology*, **24** [5] (1983) 263 – 273.
8. D. M. Kuluwansa, L. C. Jensen, S. C. Langford, and J. T. Dickinson, "Scanning Tunneling Microscope Observations of the Mirror Region of Silicate Glass Fracture Surfaces," *J. Mater. Res.*, **9** [2] (1994) 476 – 485.
9. D. Hull, "Influence of Stress Intensity and Crack Speed on Fracture Surface Topography: Mirror to Mist Transition," *J. Mat. Sci.*, **31** (1996) 1829 – 1841.
10. D. Hull, Chapter 5, in *Fractography, Observing, Measuring and Interpreting Fracture Surface Topography*, Cambridge Univ. Press., Cambridge, 1999.

11. C. Wünsche, E. Rädlein, and G.H. Frischat, "Morphology of Silica and Borosilicate Glass Fracture Surfaces by Atomic Force Microscopy," *Glastech. Ber. Glass Sci. Technol.*, **72** (1999) [2] 9 – 54.
12. E. Gölz, "Übermikroskopische Feinstructuren an Glasbruchflächen," *Zeitschrift für Physik*, **120** (1943) 773 – 777.
13. E. K. Beauchamp, "Mechanisms of Hackle Formation and Crack Branching," pp. 409 – 446 in *Fractography of Glasses and Ceramics III*, eds. Varner, Fréchette, Quinn, Ceramic Transactions, vol. 64, 1996, American Ceramic Society, Westerville, OH.
14. E. K. Beauchamp, "Fracture Branching and Dicing in Stressed Glass," Sandia Research Report SC-RR-70-766, January 1971, Sandia National Laboratory, Albuquerque, NM.
15. R. J. Castilone, G. S. Glaesemann, and T. A. Hanson, "Relationship Between Mirror Dimensions and Failure Stress for Optical Fibers," pp. 11 – 20 in *Optical Fiber and Fiber Component Mechanical Reliability and Testing II*, eds., M. J. Matthewson and C. R. Kurkjian, Proc. SPIE, 4639 (2002).
16. E. B. Shand, "Strength of Glass – The Griffith Method Revised," *J. Amer. Ceram. Soc.*, **48** [1] (1965) 43 – 48.
17. J. J. Mecholsky and S. W. Freiman, "Determination of Fracture Mechanics Parameters Through Fractographic Analysis of Ceramics," pp. 136 – 150 in *Fracture Mechanics Applied to Brittle Materials*, ASTM STP 678, S. W. Freiman, ed, ASTM, Int., West Conshohocken, PA, 1979.
18. E. B. Shand, "Breaking Stress of Glass Determined from Dimensions of Fracture Mirrors," *J. Am. Ceram. Soc.*, **42** [10] (1959) 474 – 477.
19. H. Fessler and D. C. Fricker, "A Theoretical Analysis of the Ring-On-Ring Loading Disk Test," *J. Am. Ceram. Soc.*, **67** [9] (1984) 582 – 588.
20. J. B. Quinn, "Extrapolation of Fracture Mirror and Crack-Branch Sizes to Large Dimensions in Biaxial Strength Tests of Glass," *J. Am. Ceram. Soc.*, **82** [8] (1999) 2126 – 2132.
21. L. Orr, "Practical Analysis of Fractures in Glass Windows," *Materials Research and Standards*, **12** [1] (1972) 21 – 23, 47.

22. J. C. Conway, Jr. and J. J. Mecholsky, Jr., "Use of Crack Branching Data for Measuring Near-Surface Residual Stresses in Tempered Glass," *J. Am. Ceram. Soc.*, **72** [9] (1989) 1584 – 87.
23. J. J. Mecholsky and M. G. Drexhage, "Comparisons of Optical and Fractographic Measurements of Residual Stress in Compressively Clad Glass Rods," *J. Am. Ceram. Soc.*, **63** [5-6] (1980) 347 – 349.
24. E. B. Shand, "Breaking Stresses of Glass Determined from Fracture Surfaces," *The Glass Industry*, April (1967) 190 – 194.
25. M. J. Kerper and T. G. Scuderi, "Relation of Fracture Stress to the Fracture Pattern for Glass Rods of Various Diameters," *Bull. Am. Ceram. Soc.*, **45** [12] (1966) 1065 – 1066.
26. J. J. Mecholsky, Jr. and R. W. Rice, "Fractographic Analysis of Biaxial Failure in Ceramics," pp. 185 – 193 in *Fractography of Ceramic and Metal Failures*, eds. J. J. Mecholsky, Jr. and S. R. Powell, ASTM STP 827 American Society for Testing and Materials, West Conshohocken, PA, 1984.
27. R. Morrell, L. Byrne, and M. Murray, "Fractography of Ceramic Femoral Heads," pp. 253 – 266 in *Fractography of Glasses and Ceramics, IV*, Ceramic Transactions Vol. 122, eds., J. R. Varner and G. D. Quinn, American Ceramic Society, Westerville, OH, 2001.



INDEX:**A**

- Abrasion 6-43 – 6-47
 Acid storage tank 9-4
 Agglomerate, see origins, agglomerate
 Alumina 4-18, 4-32, 5-17,
 5-62, 5-64, 6-8, 6-10,
 6-15, 6-33, 6-50,
 10-25 – 10-27,
 10-35 – 10-38
 Alumina furnace plate 4-32
 Alumina single crystal, see sapphire
 Alumina, whisker reinforced 7-66
 Aluminum oxynitride 5-32, 5-61, 5-67, 6-8,
 6-9, 6-53
 Armor, ceramic B-6
 Artificial flaws, see origins,
 Knoop indentation and Vickers indentation
 Arrest lines 5-55, 5-56
 Atomic Force Microscope 3-52
 Automobile window 4-31, 7-9

B

- Ball bearings B-7
 Ball mill 6-48
 Ball valve B-15
 Barium titanate B-11
 Baseline microstructural flaws 6-53
 Bend bar 4-14 – 4-18,
 10-26 – 10-28
 Bevels, see chamfers
 Biaxial disk 3-21, 4-5, 4-7, 4-9,
 4-18 – 4-21, 5-65, 7-4
 Biaxial stress 1-3, 1-4, 4-18 – 4-21
 Bifurcation
 Bioceramics, see also dental B-11
 Black light 3-58
 Blanchard grinding 6-28
 Blisters, see origins
 Blood 5-58

◆ Fractography of Ceramics and Glasses

Boron carbide	4-43, 7-56
Bottles	4-7, 4-33, 7-3, 10-16, 10-17, B-3, B-4
Boundary phases, ceramics	5-71, 5-72
Branching	4-4 – 4-10, 7-7 – 7-9
Branching angles	4-6 – 4-9
Branching constant	7-7, C-1
Branching distance	4-10, 7-7, 7-9
Branching constants	4-10, Appendix C
Brick, Roman	4-38
Brittleness	
C	
Camera	3-7 – 3-11
Camera, single lens reflex	3-7
Camera stand	3-9
Cantilever curl	4-15 – 4-17, 5-2
Catalytic converter	B-7
Cathode ray tube	B-4
Cavitation, scarp	5-57, 5-58, 7-48
Cellular ceramics	B-7
Center heated plate	4-31, 4-32
Chamfers	6-13, 6-15, 6-19, 6-28, 6-37, 6-52
Characteristic strength	7-65
Chatter marks, see origins chatter marks	
Chill checks, see origins chill check	
Chips, chipping, see edge chips	
Clay	3-5, 6-49 – 6-51
Cleaning agents	3-59
Cleaner, ultrasonic	3-59
Cleavage	5-2, 8-1, 8-2, 8-5
Cleavage step hackle	8-8
Coatings	3-20 – 3-22, 3-39, 3-40
Combination flaw	6-49, 6-52
Component fracture patterns	4-22, 4-40
Composites	7-21, 7-66, 9-1 – 9-6
Compositional inhomogeneity, see origins, compositional inhomogeneity	
Compound optical microscope	3-26 – 3-29

- Compression curl 4-15 – 4-17
 Conchoidal fracture 5-2
 Cone cracks, see Hertzian cone crack
 Confocal microscope 3-53, 3-55
 Contact cracks 4-28, 4-42,
 6-21– 6-27, 10-8,
 10-11, 10-16, 10-17,
 10-40, 10-46, 10-47
 Contaminants, see also clay 6-49 – 6-51
 Continuous casting nozzle B-17
 Controlled flaws,
 see origins, Knoop and Vickers indentations
 Conversion factors 7-1
 Cords, see origins
 Corrosion flaws 4-43, 6-17
 Crack branching 4-3 – 4-10, 7-21
 Crack bridging 7-21, 7-50
 Crack front shape 5-42
 Crack, processing 4-11, 6-38
 Cracks, intersecting 4-26, 4-27
 Crack velocity 7-40 – 7-49
 Crack velocity, terminal 5-3, 5-6, 7-41
 Creep fracture 5-70, 5-71
 Critical strain energy release rate, G_{IC} 7-20
 Crossing cracks 4-27
 Crowns, see dental
- D**
- Damage wave 5-6
 Dandruff 6-48
 Dark field illumination 3-18, 3-26, 8-5, 8-6
 Debonding 10-23 – 10-24
 Deep Reactive Ion Etching (DRIE) 8-23, 10-27 – 10-29
 Deer 4-23
 Defect, see also flaws and origins 6-1
 Dental ceramics, crowns, bridges 3-34, 10-33 – 10-47,
 B-12
 Alumina, porcelain 6-61, 10-35,
 10-37 – 10-40
 Bovine dentin 4-15
 Bridge, alumina 4-11

◆ Fractography of Ceramics and Glasses

Cerestore alumina-magnesia spinel	10-34 – 10.36
Dicor	10-33
Empress II glass ceramic	5-32, 10-40 – 10-46
Human enamel	4-4
Lithium silicate glass ceramic	4-38
Porcelain	4-38
Replicas	3-32, 3-34
Veneers	5-31, 6-61
Zirconia, see zirconia	
Devitrification stones, see origins	
Discussion stereo microscope	3-15, 3-16
Digital camera, photos	3-9 – 3-11, 3-29
Digital image formats	3-10, 3-11
Digital image processing	3-29
Disk specimen, see biaxial disk	
Dome, IR	B-3
Dome, see sapphire domes	
Double torsion specimen	5-45, 8-3
Dunt crack	6-38
Dye staining	3-21 – 3-23
Dye penetration	3-56 – 3-59
Dynamic fatigue (variable rate strength test)	7-46, 7-47

E

E-glass composite	9-4, 9-5
Earthenware, sewer pipe	B-16
Edges	6-1, 6-2, 6-28, 6-37
Edge chips	4-37 – 4-39, 10-38 – 10-40
Elastic waves	5-3, 5-6, 5-40, 7-40 – 7-45
Electrical insulators	6-8, 6-26
Emerald gemstone	B-15
Environmental scanning electron microscope	3-50
Extrinsic flaws	6-3, 6-4

F

Failure analysis	1-5 – 1-7
Fatigue crack	3-18, 5-56, 5-57
Faucet handle	B-16

Fiber composite	9-1 – 9-6, B-8
Fiberglass- epoxy composite	9-4, 9-5
Fiber reinforcement	7-21, 9-1, 9-2
Field emission scanning electron microscope	3-50
File formats, digital images	3-10, 3-11
Filter, ceramic	B-7
Finite element analysis	4-40, 4-41, 7-18
Firing stresses	6-38
Flaw	6-1
Flaw bluntness	7-35 – 7-37
Flaw linkage	6-49, 6-52, 6-55 – 6-57, 7-39
Flaw shielding	7-39, 7-40
Flaw size	6-58
Flaw size distribution	7-67, 7-69
Flaw truncation	6-54, 7-39, 7-40
Flexural strength	4-14 – 4-18, 5-14
Flexural stress gradient	D-18, D-19
Fluorescent dye penetration	3-57, 3-58
Fractal analysis	7-60 – 7-62
Fractography, definition	1-4
Fractography, Laws of	11-1 – 11-3
Fractography standards, see Standards	
Fracture, conchoidal	5-2
Fracture energy	7-19, 7-20
Fracture map	5-73
Fracture mirror, definition	5-1
Fracture mirror	5-2 – 5-28,
Appendices C and D, see also mirror	
Fracture origin, definition	4-1
Fracture origins, see origins	
Fracture toughness	7-20 – 7-25, 7-36
Fracture toughness, single crystal	8-2, 8-3
Fracture toughness, standard reference material	7-24
Fragmentation	4-10 – 4-12, 4-19, 7-2 – 7-7
Furnace plate	4-32, 10-20 – 10-22
G	
Gas turbine rotor	10-1 – 10-9
Gemstone	B-14 – B-16

◆ Fractography of Ceramics and Glasses

Glass

Borosilicate, Pyrex	7-15
Borosilicate crown	4-5, 4-21, 6-40, 7-4, 7-32, 7-56
Fused silica	5-2, 5-4, 5-5, 6-7
Fused silica, sintered	10-22 – 10-24
Soda lime	4-23, 6-13, 6-25, 6-44, 6-47, 7-3, 7-5, 7-6, 7-9
Glass bottles, see bottles	
Glass ceramic, dental	3-23
Glass disk, see biaxial disk	
Glass rod, flexure	4-15
Glass tube	4-35
Glass windows, see windows	
Glazes	5-30
Gloves, cotton	3-2, 3-7
Glue, specimen reconstruction	4-2, 4-3
Glue chips	5-59, 5-60
Green pen, dyes	3-21 – 3-23, 10-46
Griffith flaw	6-1, 7-18, 7-19
Griffith criterion, equation	7-18 - 7-20
Grinding cracks, see origins, grinding cracks	
Grinding damage, glass disks	4-20, 4-21
Gull wings	5-41, 5-46, 7-41, 7-43
Gun Barrel	10-9 – 10-12

H

Hackle	5-7 – 5-13, 5-29, 5-40
cleavage step	8-8
definition	5-11
coarse hackle	5-29, 5-30
grinding crack	6-30, 6-32, 6-34, 6-35
microstructural	5-29, 5-33
mist hackle	5-11
shear hackle	5-40
twist hackle	5-34 – 5-39
velocity hackle, definition	5-12
wake hackle	5-31 – 5-33, 5-46
Hailstone	7-4
Hair	6-48
Halo, slow crack growth	5-63, 5-64

- Hand magnifier 3-2
 Handling damage 6-17, 6-25,
 6-43 – 6-47, 8-7
 Heat exchanger tube B-9
 Hertzian cone cracks 6-23 – 6-27, 10-11,
 10-12, 10-40 – 10-46
 High speed photography 3-56
 Hinge fracture 4-34, 4-35
 Hip joints B-11
 Holders 3-5, 3-6
 Human enamel 4-3
 Human skin contamination 6-50
 Hybrid flaws 6-49, 6-52
- I**
- Illumination 3-15 – 3-19
 Impact 4-29, 4-34, 4-42
 Impact origins, see origins impact
 Impact, tertiary Wallner lines 5-50, 5-51
 Inclusion, see origins-inclusion
 Indentation flaws,
 see origins Knoop and Vickers indentation
 Indentation fracture mechanics 7-24, 7-58 – 7-60
 Insect 6-48
 Intrinsic flaws 6-3, 6-4
 Intergranular fracture 5-60 - 5-64
 Intersecting cracks 4-25
 Invisible cracks 4-27
- J**
- Jade B-14
 Jeweler's Loupe 3-3, 3-4
 Joint 5-2, 10-22 – 10-24
 JPEG format 3-10
- K**
- Kitchenware 6-42, 6-45, B-13
 Knoop indentation crack, see origins
 K-V diagram (slow crack growth) 7-46 – 7-47

L	
Laboratory fractures	4-12, 4-40
Lambda lines	5-55
Lamp fracture	4-11, 7-7, B-3, B-4
Lances, see also hackle	5-35, 8-8, 8-13, 8-17
Laser glass	B-2
Laws of fractography, see Fractography Laws	
Lead zirconium titanate (PZT)	5-33, B-10, B-11
Leader crack	4-34, 4-35
Lithic fractures	5-2, 5-58, B-14
Obsidian	5-46, 5-58
Longitudinal grinding	6-28 – 6-31
Loupes	3-3
M	
Machine gun barrel	10-9 – 10-12
Machine shops	10-25 – 10-27
Machining cracks, see origins	
Machinist loupe	3-3
Macrofractography camera stand	3-9
Magnesium oxide	8-1
Magnesium aluminum oxide spinel, see spinel	
Magnifying glass	3-2
Mandelbrot relationship	7-61
Mechanical overload	4-41
Medicinal vial	10-16, 10-17
Microcracking	7-21, 9-5
Microelectromechanical structures (MEMS)	8-23 – 8-24, 10-28, B-9
Microflaw pocket	6-55 – 6-57
Micrometer, damage from	6-25
Micrometer, stage	3-24
Microscope	
Atomic force	3-51
Compound optical	3-26 – 3-29
Confocal	3-55
Discussion stereo optical	3-15
Environmental scanning electron	3-50
Field emission scanning electron	3-50
Scanning electron	3-35 – 3-48
Stereo optical	3-11 – 3-15

- Transmission electron 3-50, 3-51
 Microwave tube B-5
 Mirror, fracture
 Alumina bend bar 5-17
 Borosilicate crown glass 5-20, 5-24
 Bent 5-20
 Glass rod 3-54, 3-55, 5-22
 Multiple 5-18, 5-19
 Silicon carbide 5-16
 Silicon nitride 5-19, 5-25, 5-34
 Tempered glass 5-28
 Zirconia 3-21, 5-15, 5-17
 Mirrors, single crystals 8-2, 8-6, 8-8, 8-9
 Batman 8-19
 Cathedral 8-8 – 8-10, 8-16, 8-17
 Gull wings 8-8, 8-15, 8-18
 Skewed cathedral 8-8, 8-16, 8-17
 Mirror constants 5-12, 7-10 – 7-16,
 7-36, 7-37,
 Appendices C and D
 D-20 – D-23
 Mirror cusp D-20 – D-23
 Mirror, fibers 9-5, 9-6
 Mirror size, radius 7-10 – 7-16,
 Appendix D
 Mirror size, residual stresses 7-59, D-22 – D-24
 Missile domes, see sapphire domes and IR domes
 Missile radomes 10-22 – 10-24
 Mist 5-8 – 5-14
 Mist hackle, definition 5-11
 Montages 6-60
- N**
- Near surface 6-3
 Neutral axis, bending 4-14 – 4-16
 Newman-Raju factors,
 see stress intensity shape factors
 Nickel sulfide 6-13
- O**
- Obsidian 5-46, 5-58

◆ Fractography of Ceramics and Glasses

Optical comparator	3-3
Optical microscope, see microscope	
Optical profilometer	3-52 – 3-54
Origin	6-1
Abrasion tracks	6-45 – 6-47
Agglomerate	3-44, 6-5, 6-11, 9-1
Ball mills	6-4, 6-48
Baseline microstructure	6-53
Blisters, glass	6-41
Chatter marks, cracks	5-27, 6-43 – 6-47
Chill checks	4-27, 4-42, 6-43, 6-44
Cords, glass	6-41
Compositional inhomogeneity	3-44, 6-12, 6-14
Dandruff	6-48
Delaminations	6-38, 6-39
Devitrification stones, inclusions, glass	6-41
Dunt cracks	6-38
Etch groove	8-22, 8-23, 10-28 – 10-30
Fatigue crack	3-18
Feces	6-48
Fiber	6-8
Grinding cracks, see origins, machining cracks	
Grain boundary	6-16, 6-53
Hair	6-8
Handling damage	6-17, 6-25, 6-43 – 6-47, 8-7
Hybrid	6-49, 6-52
Insect	6-48
Impact, blunt	4-28, 4-29, 6-23 – 6-27
Impact, sharp	4-28, 4-29, 6-21, 6-22, 8-23
Inclusion	3-45 – 3-47, 6-12, 6-13, 6-59
Knoop indentation crack	3-23, 3-43, 3-59, 5-33, 5-64, 5-66, 6-39, 6-40, 7-57, 7-58, 8-2 – 8-4, 10-15
Large grain	6-12, 6-15
Machining cracks	6-28 – 6-36, 10-6, 10-7, 10-20 – 10-27

Orthogonal cracks	6-28 – 6-31
Parallel cracks	6-28 – 6-36
V-grinding cracks	6-30, 6-34, 6-35
Zipper cracks	6-32 – 6-34
Machining crack skin zone	6-33
Microflaw pockets	6-55 – 6-57
Nickel sulfide, glass	6-13
Pits	6-17, 6-18
Polishing surface flaws	3-57, 5-65, 6-17, 6-20, 6-21, 8-21
Pore	6-3, 6-6, 6-8
Porous region	6-6, 6-9, 10-14, 10-15
Porous seam	6-6, 6-10, 9-3
Processing cracks	4-11, 6-38, 6-39
Scratch	6-7 6-17, 6-19 – 6-21, 8-7
Seeds, glass	6-41
Silicon vein	6-48
Skin	6-50
Stones, glass	6-41
Straie, glass	6-41
Surface void	6-17, 6-18
Thermocouple beads	6-48
Vickers indentation cracks	5-20, 6-21, 7-24, 7-25, 7-56, 7-58 – 7-60
Whisker clump	9-1
Origin, fracture definition	4-1
Orthogonal machining crack, see origins	
Oxidation	4-43, 6-17, 6-18
P	
Parallel machining crack, see origins	
Parting	5-2
Patriot missile	10-22
Pattern recognition	1-3
Penny shape cracks	7-24, 7-35
Phase instability	6-48
Photos, Photography	3-7
Pits, see origins	
Plasma asher	10-17 – 10-19
Plate fracture patterns	4-28, 4-29

Plate fracture patterns, thermal	4-31, 4-32
Polarizer	3-19, 3-20, 8-5, 10-17
Polished microstructural section	6-5, 6-53, 6-57, 6-58
Polishing surface flaws, see origins	
Porcelain	3-33, 3-58, 4-38, 6-8, 6-26, B-13
Porcelain electrical insulator	3-33, 6-8, B-10, 6-26
Pore, see origins	
Porous region, see origins	
Porous seam, see origins	
Pressure flaking	5-58
Pressure vessel	4-7, 4-33
Proof test, radome	10-22
PZT, see Lead zirconium titanate	

Q

Quartz lamp fracture, see Lamp fracture

R

R-curve	5-66, 7-22, 7-23, 7-50 – 7-53
Radome, fused silica	10-22 – 10-24
Rayleigh wave velocity	5-3
RAW format	3-10
Reliability	10-1 – 10-5, 10-15
Replicas	3-30 – 3-34
Residual stress	4-43
Compression induced cracking	5-59
Estimates of magnitude	7-62 – 7-65
Firing	6-39
Grinding	7-63
Heat strengthened glass	5-26, 5-27
Indentation	6-38, 7-58 – 7-60, 7-65
Mirror shapes, effect on	5-26, 5-27, D-22 – D-24
Stable crack extension from	5-66
Tempered glass	4-29 – 4-31, 5-28
Rib marks	5-41, 5-55
Ripples	5-41
River deltas	5-1, 5-34

- Rock fracture, see lithic fracture
- Roller, silicon nitride B-10
- Roman brick 4-38
- Rotor, gas turbine 10-1 – 10-9
- Round robin, flexural strength 10-25 – 10-27
- Round robin, fractography 10-29 – 10-33
- Round robin, machining 10-25 – 10-27
- S**
- Saliva 5-58
- Sapphire, single crystal alumina 3-57, 6-21, 8-4, 8-7, 8-19, 8-21, 8-22, 8-25, 8-26, 10-17 – 10-20
- Sapphire dome 3-57, 4-25, 5-58, 6-20, 8-7, 8-21, 8-22
- Sapphire scarp 5-58
- Scanner 3-59
- Scanning electron microscope 3-35 – 3-50
- Scarps 5-56, 5-57, 7-46, 8-20, 10-16
- Scratch, see origin
- Secondary fracture, edge chips 4-37
- Secondary origins 4-4, 4-16, 4-17, 4-37
- Secondary Wallner line 5-47 – 5-50
- Seeds, see origins
- Self-toughened ceramics 9-2
- Shark's teeth 6-30, 6-34
- Shear hackle 5-39, 5-40
- Shrink fit 10-9 – 10-12
- Sialon 6-13, 7-66
- Sierra scarp 5-57, 5-58
- Silica, fused 10-22 – 10-24
- Silicon 7-31, 8-2, 8-3, 8-6, 8-20, 8-23, 8-27, B-11
- Silicon carbide 4-4, 5-16, 5-38, 5-61, 5-68, 6-5, 6-8, 6-9, 6-11, 6-14, 6-15, 6-31, 6-37, 6-40, 6-48, 6-50, 6-52, 6-58, 7-30, 9-1, 10-9 – 10-15
- Silicon carbide, CVD 5-38, 9-3,

	10-27 – 10-29
Silicon carbide, fibers	9-1 – 9-3, 9-6
Silicon carbide machine gun barrel	10-9 – 10-12
Silicon carbide furnace plate	10-20 – 10-22
Silicon nitride	3-40, 3-44, 3-46, 4-9, 4-15, 5-15, 5-19, 5-25, 5-30, 5-62, 5-66, 5-69, 5-70, 5-72, 5-73, 6-4, 6-7, 6-8, 6-12 – 6-15, 6-18, 6-19, 6-25, 6-31 – 6-33, 6-35, 6-37, 6-39, 6-40, 6-48, 6-58, 6-59, 7-54, 9-3, 10-1 – 10-9, B-10
Single crystals	8-1 – 8-27
Alumina, see sapphire	
Spinel	8-9 – 8-18, 8-24
Silicon	7-31, 8-2, 8-3, 8-6, 8-20, 8-23, 8-27, B-11
Zirconia	8-1
Sketches	4-25
Slow crack growth	4-44, 5-63 – 5-69, 7-22, 7-23, 7-46 – 7-48, 10-1 – 10-4, 10-12 – 10-15
Slow crack growth exponent, N	7-46, 7-47
Soda Lime silica, see glass	
Solar cells	B-2
Sonar rings, PZT	B-10
Spinel, magnesium aluminum oxide	8-9 – 8-18, 8-24, 10-34 – 10-36
Stable crack extension	5-56, 5-57, 7-37, 7-38, 7-50 – 7-55
Staining	3-21– 3-23, 3-57, 3-60
Standards	
ASTM C 1322, fractography	7-28, 8-8, 10-31
ASTM C 1421, fracture toughness	7-28, 7-29
ISO 14704, flexural strength	10-25
ISO 18756, fracture toughness	7-29
MIL STD 1942 (MR), flexural strength	10-25, 10-26
MIL HDBK 790, fractography	10-31

- Standard Reference Material, fracture toughness 7-24
- Stage micrometer 3-23 – 3-24
- Stage, traversing 3-25, 3-28
- Static fatigue 7-46, 7-47,
10-12 – 10-15
- Steel, fatigue crack 3-18
- Stereoptical microscope 3-1, 3-11 – 3-15
- Stereo scanning electron microscope images 3-5, 3-49
- Stereoscope 3-49
- Stones, glass, see origins
- Stress 1-4, 7-17 – 7-19
- Stress concentration 7-17, 7-18
- Stress, biaxial 1-4
- Stress corrosion 10-15
- Stress, flexural 5-14
- Stress intensity 7-20, 7-24 – 7-26
- Stress intensity shape factor 7-20, 7-25,
7-26 – 7-29, 7-33,
7-34
- Stress intensity shape factor, Newman-Raju 7-26 – 7-29, 7-48
- Stress rupture 10-4, 10-12 – 10-15
- Stress state 1-4
- Stress uniaxial 1-4
- Stress wave fractography 3-52
- Straie, see origins
- Striations, fatigue cracks 5-56
- Striations, grinding 6-7, 6-28, 6-29, 6-31
- Subcavitation hackle 5-58
- Surface crack – fracture mechanics 7-26 – 7-33
- Surface crack in flexure, see origins, Knoop
- Surface external 6-6
- Surface finish 6-28
- Surface grinding 6-28 – 6-36
- Surface void, see origins
- T**
- Teeth 4-4, 5-28, 10-8
- Tempered glass 4-29 – 4-31, 6-12,
6-13, 6-42, 7-5, 7-6,
7-9, B-2, B-4
- Tension strength 4-13, 10-27 – 10-29

◆ Fractography of Ceramics and Glasses

Terminal velocity	5-3 – 5-6
Tertiary Wallner lines	5-50 – 5-54
Thermal fracture	4-31, 4-32, 4-34, 4-41, 4-42, 10-20, 10-21
Thermal shock	4-42, 8-26
Thermal stresses	6-43, 8-7, 8-26, 10-17 – 10-20
Thermocouple bead, see origins	
Thermometer	B-4
Theta specimen strength specimen	8-23
Time dependent fracture	4-44
TIFF format	3-10
Torsion	4-7, 4-18, 4-36, 4-37
Transformation toughening	7-21, 7-50
Transgranular fracture	5-60, 5-61, 5-64, 5-68
Transillumination	3-19, 3-20, 4-3, 4-4, 8-5, 10-30
Transmission electron microscope	3-51, 5-72
Transmitted illumination	3-19, 4-4, 8-5, 10-30
Transverse grinding	6-28 – 6-36
Tube fracture	4-35, 8-26, 10-9 – 10-12, 10-17 – 10-19, B-5
Twinning	8-5, 8-24, 8-25, 10-17 – 10-19
Twist hackle	5-34 – 5-39
U	
Ultrasonic cleaner	3-61
Ultrasonic fractography	3-53, 5-53, 5-54
Uniaxial stress	1-4
Uranium dioxide	B-16
V	
Valves, automotive	B-9
Varistors, Zinc oxide	B-11
Velocity hackle	5-8, 5-12, 5-28
Velocity, terminal	5-3, 5-6
VAMAS	10-31
Vials, medicinal	10-16 – 10-17

- Vicinal illumination 3-12, 3-17, 3-18, 6-33, 8-5
- Vickers indentation flaws, see origins
- V machining crack, see origins, machining
- W**
- Wake hackle 5-31 – 5-33, 9-3, 10-36, 10-37, 10-43
- Wallner lines 5-41– 5-55, 7-40 – 7-45, 8-8
- Gull wings 5-46
- Lambda 5-55
- Primary, definition 5-43 – 5-45
- Secondary, definition 5-47 – 5-50
- Tertiary, definition 5-50 – 5-54, 8-22
- Water hammer 4-33, 4-34, B-2
- Wave velocity, see elastic waves
- Weakest link theory, see Weibull distribution
- Weibull distribution 7-65 – 7-67
- Weibull modulus 7-53, 7-55, 7-65 – 7-67
- Whisker lances, single crystal 8-8, 8-13, 8-17
- Whisker reinforcement 7-21, 9-1, 9-2
- Whitewares B-10, B-13
- Window failure 4-23, 4-28 – 4-31, B-1, B-2
- Window failure, glue chips 5-60
- Window patterns 4-27, 4-28
- Window, thermal fracture 4-31, 7-2
- Witness marks 4-20, 4-23, 4-42, 6-21
- X**
- X-ray topography 3-57, 8-5, 8-7
- X-Y stage, traversing 3-24, 3-35, 3-28
- Z**
- Zinc oxide Varistors B-10
- Zipper crack, see origins, machining
- Zirconia, cubic single crystal 8-1

◆ Fractography of Ceramics and Glasses

Zirconia disk seals	B-5
Zirconia, magnesia stabilized	5-29, 6-16, 6-17, 6-56, 6-57, 7-55
Zirconia, fiber reinforced	9-6
Zirconia, yttria stabilized	5-15, 5-17, 6-8, 6-9, 6-51, 7-13, 7-14, 7-16, 7-55



April 2007